

Fracture Patterns in Cooling Intrusions

Thermomechanical Modelling and Fracture Orientations



A thesis submitted to Cardiff University in
candidature for the degree of Doctor of
Philosophy

November 2019

Jennifer Frances Ellis-Evans

School of Earth and Ocean Sciences, Cardiff
University, Main Building, Park Place,
Cardiff, CF10 3AT

This document includes minor post-viva edits made February 2020.

Abstract

Understanding fracture patterns in intrusions has multiple industrial applications where knowledge of geotechnical stability or sub-surface fluid flow is required. This study advances the understanding of the influence of thermal stress on the evolution of early fractures, important as they are likely to influence early fluid flow and later fracturing events, in cooling plutonic bodies. This study involves numerical modelling, field work and analogue modelling studies.

Finite element modelling in COMSOL® is used to predict thermal stresses that result from the cooling of hot intrusive bodies within a cooler crust. The models extend existing two-dimensional approaches into the third dimension. Models predict that stress magnitudes can cause fracturing and the minimum principal stress direction may change during cooling. The change in principal stress orientation is influenced by the geometry and depth of the modelled intrusive body and may result in multiple fracture orientations forming. Analogue modelling, using drying corn-starch patties, produces both radial and tangential fractures, which supports the idea that multiple fracture orientations may result from the cooling of intrusive bodies.

Numerical models are applied to the Alta stock and Bingham Canyon copper porphyry deposit in Utah. Fracture orientations inferred from principal stresses and failure criterion are comparable to the field data. Application of the Griffith failure criterion to models of the Alta stock predicts that shear and hybrid failure conditions always precede tensile failure. High fluid pressure is the only parameter that may alter the sequence of failure, allowing tensile failure to occur independently of shear or hybrid failure. Hybrid and tensile failure-modes are inferred from the field observations. Application of the models at Bingham Canyon, a system in which high fluid pressures are likely, highlights that thermal stress may have controlled early vein orientations, providing an explanation for the spatial and temporal variation of early formed fractures.

Table of Contents

Chapter 1. Thesis Overview	1
1.1. Fractures in Intrusions	1
1.2. Approaches to the Study of Cooling Fractures	3
1.2.1. Field Studies	3
1.2.2. Analogue Modelling	3
1.2.3. Experimental	4
1.2.4. Numerical Modelling	4
1.3. Motivation.....	6
1.4. Field Location	7
1.5. Aims and Objectives.....	11
1.6. Thesis Structure	12
Chapter 2. Fracturing in Pluton Rocks – A Review	13
2.1. Conceptual Models	14
2.1.1. The Cloos Model	14
2.1.2. The Heidrick and Titley Model	19
2.2. Characteristics of Fractures in Plutonic Rocks	21
2.2.1. Geometry	21
2.2.2. Aperture	22
2.2.3. Spacing and Density	22
2.3. Classification of Fractures in Plutonic Rocks.....	23
2.3.1. Cooling Fractures	25
2.3.2. Tectonic Fractures	25
2.3.3. Exhumation Fractures	25
2.4. Plutonic Rock Emplacement, Geometry and Cooling Histories	27
2.4.1. Emplacement and Geometry	27
2.4.2. Cooling History	27
2.5. Origin of Cooling Fractures	29
2.5.1. In-situ stress.....	30
2.5.2. Cooling	30
2.5.3. Fluid Pressure.....	31
2.6. Experimental Cooling Fractures and Temperature Dependent Properties	32

2.6.1. Experimental Cooling Fractures.....	32
2.6.2. Temperature Dependent Material and Mechanical Properties	32
2.7. Summary	34
 Chapter 3. Thermomechanical Modelling	35
3.1. Published Models of Fracturing Related to Cooling of Plutonic Bodies	38
 Part 1	
3.2. COMSOL® Model Setup	47
3.2.1. Software	47
3.2.2. Model Overview	50
3.2.3. Model Calculations	50
3.3. Example Models 1 – 3	56
3.3.1. Model Geometry.....	56
3.3.2. Initial Conditions	56
3.4. Example Models 1 – 3 Results.....	58
3.4.1. Thermal History	60
3.4.2. Principal Stress Orientations.....	64
3.4.3. Stress Magnitudes.....	66
3.4.4. Elastic Strain Energy.....	67
3.4.5. Failure Criterion	69
3.4.6. Grid Resolution and Timesteps.....	62
3.4.7. Model Run Time.....	62
3.4.8. Summary	72
 Part 2	
3.5. COMSOL® Models Based on Published Models	73
3.5.1. Infinite Dyke, Knapp (1978)	74
3.5.2. Pressured Cylinder and the Diamond Joe Stock, Gerla (1983)	81
3.5.3. Geometric shapes, Cartridge Pass and Lake Edison granodiorites, Bergbauer (1998).....	89
3.5.4. The Tanvald Pluton, Žák et al. (2006)	97
3.6. Summary	103
 Part 3	
3.7. COMSOL® Model Variations	105
3.8. Modelling Results.....	115

3.8.1. Intrusion Depth	115
3.8.2. Initial Temperature Distribution	117
3.8.3. In-situ Stress	117
3.8.4. Temperature Dependent Mechanical Properties	120
3.8.5. Temperature Dependent Material Properties.....	124
3.8.6. Pluton Geometry.....	124
3.9. Discussion.....	129
3.9.1. Rotation of the Principal Stress Axes	129
3.9.2. Stress Magnitudes.....	131
3.9.3. Failure Criteria	131
3.9.4. Implications of Numerical Models for Understanding Fracturing in Cooling Plutons	134
3.10. Conclusions	135
Chapter 4. The Alta Stock	136
4.1. Introduction	137
4.2. Geological Overview	142
4.3. Field Data	144
4.3.1. Primary Structures (foliations, lineations and enclaves)	147
4.3.2. Aplite Dykes	151
4.3.3. Mineralized and Non-mineralized Fracture and Veins	154
4.3.4. Significance of the Structural Data	163
4.4. Numerical Modelling	165
4.4.1. Overview	165
4.4.2. Modelling Geometry	166
4.4.3. Material and Mechanical Properties	168
4.4.4. Gravitational and Tectonic Loads	170
4.4.5. Initial Temperature Distributions	170
4.4.6. Grid Size and Modelling Time Steps	170
4.4.7. Modelling Outputs.....	171
4.5. Numerical Modelling Results	173
4.5.1. Cooling History.....	173
4.5.2. Principal Stress Orientations.....	176
4.5.3. Stress Magnitudes and Failure Modes.....	184
4.5.4. Elastic Strain Energy.....	187
4.6. Comparison of Numerical Models to Field Data	188

4.6.1. Orientation Comparison	188
4.6.2. Elastic Strain Energy Compare to Fracture Density	195
4.7. Discussion	196
4.7.1. Failure Sequence.....	196
4.7.2. Cooling History.....	199
4.7.3. Stress Field and Tectonic Setting during Cooling.....	201
4.8. Conclusions	203
Chapter 5. Bingham Canyon	205
5.1. Introduction	206
5.2. Geological Overview	207
5.3. Early Fracturing in and around the Bingham Canyon Magmatic Complex	212
5.4. Methodology	216
5.4.1. Numerical Modelling	217
5.4.2. Field Data and Estimation of Paleostress	222
5.4.3. Comparison of Numerical Models	225
5.4.4. Comparison of Numerical Models to Field Data.....	225
5.5. Numerical Modelling Results	226
5.5.1. Cooling History.....	226
5.5.2. Principal Stress Orientations.....	229
5.5.3. Elastic Strain Energy.....	231
5.6. Comparison of Numerical Models to Field Data	234
5.7. Discussion	236
5.7.1. Stress Evolution.....	236
5.7.2. Cooling History.....	238
5.7.3. Comparison of Field Data and Numerical Models.....	238
5.8. Conclusions	240
Chapter 6. Analogue Modelling	241
6.1. Modelling Aims and Approach.....	242
6.2. Theoretical Background of Fracture Formation in Starch Flours.....	244
6.3. Method.....	247
6.4. Scaling	251
6.4.1. Geometric Scaling	251
6.4.2. Dynamic Scaling	251

6.4.3. Kinematic Scaling	251
6.5. Results	253
6.5.1. Geometry A	253
6.4.2. Geometries B - E	267
6.6. Discussion.....	269
6.6.1. Experimental Results	269
6.6.2. Experimental Uncertainties	269
6.6.3. Additional Modelling	270
6.6.4. Comparison to Fracture Orientations in Conceptual Models.....	271
6.6.5. Comparison to Numerical Models	272
6.6.6. Comparison to Columnar Joint Formation in Drying Corn-Starch	272
6.7. Conclusions	275
 Chapter 7. Synthesis.....	 276
7.1. Addressing the Hypotheses	276
7.2. Limitations with Numerical Modelling.....	280
7.3. Summary	282
7.4. Future Research	283
7.4.1. Application of Numerical Models	283
7.4.2. Extension of Numerical Models.....	283
 References	 285
 Appendix	
A. Chapter 3 Appendix	304
B. Chapter 4 Appendix	332
C. Chapter 5 Appendix	336
D. Chapter 6 Appendix.....	346
E. Digital Appendix	359

List of Figures

Figure 1.1. Photos of various forms of fractures in igneous rocks	2
Figure 1.2. Regional map depicting Central Wasatch mountains and surrounding region	8
Figure 1.3. Photos from field locations	9
Figure 2.1. The Cloos Model of fractures in plutonic rocks, redrawn after Žák et al. (2006)	14
Figure 2.2. Schematic block diagrams showing the characteristics of the three fundamental types of mesoscopic joint sets and dykes, veins and fault-veins identified in the Heidrick and Titley model.....	19
Figure 2.3. Possible brittle fracture planes formed in compression tests, related to principal stress directions	23
Figure 2.4. Feedback loop controlling cool rates in pluton-host rock systems	29
Figure 3.1. Numerical model of the Tanvald pluton contoured for the maximum (P1) and minimum (P3) principal stresses (MPa), compression negative	41
Figure 3.2. Development of stresses within plutons (grey) and host rock in map view for given time steps for a circular, rectangular and hourglass intrusions.....	42
Figure 3.3. Vertical slice through an infinitely elongate dyke (two-dimensional plane strain model) showing the computed state of stress in terms of brittle failure regimes	43
Figure 3.4. Comparison of numerical models (short black ticks) and photolineament interpretation (grey lines).....	44
Figure 3.5. Stress and strain energy predicted in a pressured cylinder for varying chamber radius	45
Figure 3.6. Modelling dimensions and boundary set up in COMSOL®	48
Figure 3.7. Failure criterion.....	55
Figure 3.8. Examples of meshes used for models 1 – 3	56
Figure 3.9. Models 1 – 3, showing location of map and sections and line and points used in graphs.....	59
Figure 3.10 Modelled temperature distributions shown as colour map and contours for selected time steps 1000 years, 10,000 years and 100,000 years.....	61
Figure 3.11. Temperature profiles through the pluton and host rock	62
Figure 3.12. Temperature over time for selected points.....	63
Figure 3.13. Principal stress orientations plotted on maps and sections.	65
Figure 3.14. Stress paths for selected points on a maximum (σ_1) – minimum (σ_3) principal stress plot, compression positive.	66
Figure 3.15. Elastic strain energy (J/m^3) contoured for given time steps.....	67
Figure 3.16. Elastic strain energy (J/m^3) over time for selected points	68
Figure 3.17. Stress paths for selected points on a maximum (σ_1) – minimum (σ_3) principal stress plot for model 2.....	70
Figure 3.18. Failure domains for selected time steps for model 2	71

Figure 3.19. Isotherms showing the cooling of the plutonic body for models K-1 and K-2 at selected time steps in years after model	75
Figure 3.20. In the bottom row of images contours the COMSOL® models are compared to contours calculated by Knapp (1978).....	75
Figure 3.21. Temperature vs time graphs for selected points within the host rock and pluton.....	76
Figure 3.22. Principal stress trajectories in the cooling pluton for models K-1 and K-2 at selected time steps in years after model initiation and temperature contours (grey).....	77
Figure 3.23. Stress paths calculated at selected locations within the COMSOL® model (tensile positive)	78
Figure 3.24. Calculated failure domains for the Coulomb-Navier failure criterion in the cooling pluton for models K-1 and K-2 at selected time steps in years after model initiation	79
Figure 3.25. Comparison of COMSOL® model K-1 to Knapp models for selected time steps	80
Figure 3.26. Plan view of temperature, stress and strain energy (J/m ³) values calculated in COMSOL® models G-1 to G-3 at 100,000 years after model initiation.....	82
Figure 3.27 Stress and strain energy predicted in a pressured cylinder for varying chamber radius	83
Figure 3.28. Variations of model G-2 showing effect of not accounting for magma pressure and lowering the regional load.....	84
Figure 3.29. Lineament interpretation of the Diamond Joe stock.....	86
Figure 3.30. Numerical models of the Diamond Joe stock and comparison to lineament maps	87
Figure 3.31. Calculated failure domains for the Coulomb-Navier failure criterion in the cooling pluton for models G-4 and G-5 at selected time steps in years after model initiation.....	88
Figure 3.32 A. Development of stresses within plutons and host rock in map view for given time steps for a circular intrusion, rectangular intrusion hourglass intrusions (after Bergbauer et al., 1998) ..	90
Figure 3.32 B. Development of stresses within plutons (grey) and host rock in map view for given time steps for a circular, rectangular and hourglass intrusions (from Bergbauer et al., 1998)	91
Figure 3.33. Numerical models of the Cartridge Pass granodiorite 50,000 years after model initiation...	92
Figure 3.34. Numerical models of the Lake Edison granodiorite 1,000,000 years after model initiation	93
Figure 3.35. Comparisons of lineament interpretation from (A) Cartridge Pass granodiorite (top row) and (B) Lake Edison granodiorite (bottom row) with modelled thermal and thermal and tectonic stresses from COMSOL® and modelling results from Bergbauer and Martel (1999).....	94
Figure 3.36. Calculated failure domains for the Coulomb-Navier failure criterion in the cooling pluton for models B-6 and B-10 at selected time steps in years after model initiation	96
Figure 3.37. Geometry and grid used in COMSOL® to model the Tanvald pluton	97
Figure 3.38. Comparison of Maximum and minimum principal stress values 10,000 and 50,000 year after model initiation in years of COMSOL® and Žák et al., 2006 models.....	99

Figure 3.39. Influence of mechanical properties on material constants calculated of the Drucker-Prager yield criterion.....	100
Figure 3.40. A. sketch map of the Tanvald plutonic body showing fracture trajectories interpolated from outcrops. B. numerical models of the Tanvald pluton, using mapped boundary.....	102
Figure 3.41. Thermal history predicted from two-dimensional modelling of the Diamond Joe stock (model G-4), Cartridge Pass granodiorite (model B-5), Lake Edison granodiorite (model B-9) and the Tanvald pluton (model Z-2).....	103
Figure 3.42. Schematic diagram showing variation in model geometry (A) thickness and volumes of modelled cylinders (models 2, 21 – 23) (B) other geometries (models 24 – 30).....	107
Figure 3.43. Schematic diagram showing variation in model depth (models 2, 4 – 6).....	108
Figure 3.44. Schematic diagram showing variation in initial temperatures (models 2, 4 – 6)	109
Figure 3.45. Graphs of material property variation with temperature	113
Figure 3.46. Graphs of mechanical property variation with temperature	114
Figure 3.47. Stress paths for selected points (point 4, at varying depths as labelled) on a maximum (σ_1) – minimum (σ_3) principal stress plot (compression positive) with the Griffith failure domain plots	115
Figure 3.48. Influence of depth on failure domains of the Griffith and Griffith-Murrell criterion accounting for temperature dependent mechanical properties.....	116
Figure 3.49. Influence of initial temperature distribution on failure domains of the Griffith and Griffith-Murrell criterion accounting for temperature dependent mechanical properties	118
Figure 3.50. Influence of regional stress on failure domains of the Griffith criterion in three-dimensional models.....	119
Figure 3.51. Griffith and Griffith-Murrell failure domains for selected time steps for models 13 – 18 with selected temperature dependent material properties, as labelled	121
Figure 3.52. Influence of depth for the applied failure criterion. Material properties are temperature dependent and mechanical properties in these models are temperature independent.....	122
Figure 3.53. Graph of the solid thermal mechanical parameter and its influence on Griffith and Griffith-Murrell failure domains	123
Figure 3.54. Influence of temperature dependent mechanical properties for the applied failure criterion for varying depths	125
Figure 3.55. Model 2 (temperature independent material properties) and model 19 (temperature dependent material properties) for the 3D Griffith-Murrell criterion, assuming temperature dependent mechanical properties.....	126
Figure 3.56. Influence of cylindrical geometry on stress orientation and the predicted Griffith domains failure domains	127
Figure 3.57. Influence of non-cylindrical geometries on stress orientation and the predicted Griffith domains failure domains	128
Figure 3.58. Schematic diagram of planes perpendicular to minimum tensile stress in cooling plutonic bodies of model	129

Figure 3.59. Schematic diagram of planes perpendicular to minimum tensile stress in cooling plutonic bodies of varying geometries and depths	130
Figure 3.60. Schematic diagram of planes perpendicular to minimum tensile stress in cooling plutonic bodies with anisotropic horizontal stress	131
Figure 3.61. Effect of initial conditions on failure mode.....	132
Figure 4.1. Summary of workflow, comparison of numerical models and field data.....	137
Figure 4.2. Geological map of the Alta stock and surrounding area	139
Figure 4.3. Published mapping of orientation data of joints and veins recorded by Wilson (1961)	140
Figure 4.4. Published mapping of joints and veins recorded by John (1991) separated by mineral fill ...	141
Figure 4.5. Tectonic evolution of the Wasatch fault and surrounding area	143
Figure 4.6. Annotated panoramic photos of the field area around Alta	145/146
Figure 4.7. Summary field map of lineation's, foliation and enclave data	148
Figure 4.8. Photos of schlieren	149
Figure 4.9. Photos of enclaves	150
Figure 4.10. Summary field map of aplites	152
Figure 4.11. Photos of aplites	153
Figure 4.12. Summary field map of joint data	155
Figure 4.13. Photos of joints	156
Figure 4.14. Photos of selected outcrops	157
Figure 4.15. Interpretation of lineaments on satellite image.....	159
Figure 4.16. Interpretation of lineaments on aerial photos at selected locations A - G	160
Figure 4.17. Topology plot based on data collected from circular scan lines.....	161
Figure 4.18. Circular scan line analysis and topological analysis	162
Figure 4.19. Kinematics that may result shear offset on conjugate dykes comparable with the shorting direction in the obtuse angle.....	164
Figure 4.20 Modelled stock geometry	167
Figure 4.21. 3D models of stock for numerical modelling showing variations in thickness.....	168
Figure 4.22. Field locations	172
Figure 4.23. Thermal models for slices taken from models A1 – A4 at selected time steps	174
Figure 4.24. Thermal history of model A1	175
Figure 4.25. Principal stress directions over time for model A1.....	177
Figure 4.26. Comparison of principal stress directions over time for models A1 – A4 on a horizontal plane	178
Figure 4.27. Principal stress directions over time for model A5.....	180
Figure 4.28. Principal stress directions over time for model A6.....	181

Figure 4.29. Principal stress directions over time for model A7	182
Figure 4.30. Comparison of principal stress directions over time for models A6, A8 – A10 on a horizontal plane	183
Figure 4.31. Principal stress magnitudes for selected time steps of a NE-SW 2D line cut through numerical models A1 – A7	185
Figure 4.32. Calculated failure modes within the stock for oblique view, looking north, of the numerical models for selected times from model initiation	186
Figure 4.33. Strain energy (J/m^3) plotted for models A1 – A10	187
Figure 4.34. Comparison of satellite interpretation (left) and Wilson (1961) schematic representation of joint direction and spacing (see Figure 4.3) (right) with numerical model orientation at a depth of 5 km at 1000 years, 10,000 years and 100,000 years for models A1, A5 and A6.....	189
Figure 4.35. Comparison of satellite interpretation and strike of the maximum-intermediate principal plane for numerical model orientation at a depth of 5 km at 1000 years, 10,000 years and 100,000 years for models A1, A5 and A6.....	190
Figure 4.36. Comparison of kinematic dyke interpretation and numerical model orientations at 1000 years, 10,000 years and 100,000 years for models A1, A5 and A6.....	192
Figure 4.37. Poles predicted for fracture orientations based on failure criterion from numerical models are overlain on stereonets of field data.....	194
Figure 4.38. Comparison of (A) calculated joint density based on schematic representation of joint direction and spacing (Wilson, 1961) and (B) strain energy predicted from numerical modelling.....	195
Figure 4.39. Griffith-Murrell failure criteria plotted on σ_1 - σ_3 graph	198
Figure 4.40. Alternative thermal models with initially non uniform thermal distributions	200
Figure 4.41. Paleostress orientations from (A) Ren et al., 1989 and (B) redrawn from Kowallis et al., 1995	202
Figure 5.1. Regional geological map and section of the Bingham Canyon magmatic complex.....	209
Figure 5.2. Local geological map and section of the Bingham Canyon magmatic complex	210
Figure 5.3. Veins plotted as poles on equal area lower hemisphere Schmidt nets.....	214
Figure 5.4. Map sketches illustrating the sequence of vein formation at the Bingham Canyon deposit after Gruen et al. (2010)	215
Figure 5.5. Workflow.....	216
Figure 5.6. Monzonite (MZ) and Quartz Monzonite Porphyry (QMP) from the 3D Kennecott Utah Copper (KUC) 2017 the three-dimensional mine.....	218
Figure 5.7. Levels sliced from KUC 2017 mine model used as geometries in models BC-1 to BC-4.....	219
Figure 5.8. Geometry used in models BC-5 to BC-7.....	220
Figure 5.9. Summary of surface measurements (poles) and estimated paleostress orientations.....	224
Figure 5.10. Colour map of temperature distribution over time. Model BC-5 includes enclaves and model BC-6 excludes enclaves	227

Figure 5.11. Temperature over time for sections A-A' and B-B'	228
Figure 5.12. Results and comparison between numerical models presented as maps with lines perpendicular to the predicted direction of least compressive stress for models BC-5 to BC-7	230
Figure 5.13. Strain energy (J/m ³) plotted for models BC-5 – BC-7.....	232
Figure 5.14. Density plots from Grün (2007)	233
Figure 5.15. Comparison of field data and numerical model predictions	235/236
Figure 5.16. Map sketches illustrating the evolution of the stress field related to thermal cooling over time and resulting fracture orientations	237
Figure 6.1. Examples of experimental results from drying corn starch and field examples of columnar joints	243
Figure 6.2. Mechanisms of fracture formation in drying corn-starch	245
Figure 6.3. Experimental set-up.....	248
Figure 6.4. Comparison of drying methods for 40 mm by 40 mm cylinders	253
Figure 6.5. Graph of normalised weight against drying time for selected samples given in Figure 6.4...254	
Figure 6.6. Line diagrams of surface fracture patterns.....	256
Figure 6.7. Plots of number of trace length and total number of sample edge fractures against burial depth.....	257
Figure 6.8. Plot of top surface fracture intensity value (Table 6.2) plotted against burial depth	259
Figure 6.9. Comparison of top and side fracture patterning, (i) top surface of dried corn-starch patties (ii) side fracture pattern. (A) air dried out of mould (sample 6) and (B) sand buried (sample 32)	260
Figure 6.10. Topological analysis for top surface fractures plotted on a I-Y-X diagram.....	261
Figure 6.11. Line diagrams of internal fracture patterns.....	262
Figure 6.12. Comparison of varying internal fracture patterns with burial depth for 40 mm by 40 mm cylinders.....	264
Figure 6.13. Sketches for selected fracture patterns presented on a grid of burial depth versus drying rate.....	265
Figure 6.14. Example of samples in which no fractures formed.....	266
Figure 6.15. Examples of fractures extending the entire height of the geometry with plumose pattering on surfaces	266
Figure 6.16. Comparison of fractures formed for geometries B and D for various drying methods.....	267
Figure 6.17. Rice starch flat cylinder 10 cm diameter, thickness 2 cm.....	268
Figure 6.18. Sketch of key internal fracture orientations produced in sand buried corn-starch patties	271
Figure 6.19. Comparison of analogue and numerical models	273
Figure 6.20. Comparison of corn-starch columnar joints to columnar joints found in the field	274

List of Tables

Table 2.1. Characteristic and origin of the four joints sets that form primary fracture system of the Cloos Model (as defined in Balk 1937).....	16
Table 2.2. Fracture systems of the Cloos Model referred to as planes of primary expansion (as defined in Balk 1937)	17
Table 2.3. Fracture systems in other plutonic bodies as defined by Cloos and co-workers (as defined in Balk 1937).....	17
Table 2.4. Alternative classifications to the Cloos Model suggested for foliations and limitations (Hutton, 1988), Fractures (Žák et al., 2006) and Faults (Crider, 2015) found in plutons	18
Table 2.5. Fracture sets of the Heidrick and Titley model	20
Table 2.6. Classification of fracture types after Nelson, 2001	24
Table 3.1. Published models of fracturing related to cooling of plutonic bodies.....	39
Table 3.2. Elastic material properties for models given in Table 3.1	40
Table 3.3. Publications using COMSOL® to solve thermal and mechanical problems in volcanology	49
Table 3.4. Temperature independent material and mechanical properties	57
Table 3.5. COMSOL® models based on published models.....	73
Table 3.6. Initial temperatures, material properties	89
Table 3.7. Temperature dependent material and mechanical properties	98
Table 3.8. COMSOL® models run	106
Table 3.9. Initial temperature and assumed liquidus solidus temperatures from previous publications	110
Table 3.10. Initial in-situ stresses assumed in previous publications	111
Table 3.11. Temperature dependent material and mechanical properties	112
Table 4.1. COMSOL® models run	165
Table 4.2. Reasoning for variations in modelled geometry	166
Table 4.3. Material properties	169
Table 4.4. Mechanical properties	169
Table 5.1. Basin and Range rotation estimates	211
Table 5.2. COMSOL® models run	217
Table 5.3. Material properties of the domains defined in the thermomechanical model	221
Table 5.4. Wilcoxon signed-rank test.....	234
Table 6.1. Acetate mould geometries.....	247
Table 6.2. Quantitative analysis of top surface pattern	255
Table 6.3. Temperature and humidity values for Cardiff for July and December 2017	270

Publications

Peer-reviewed journals

Ellis, J.F. and Blenkinsop, T. 2019. Analogue modelling of fracturing in cooling plutonic bodies. *Tectonophysics*, v.766, p14-19. doi.org/10.1016/j.tecto.2019.05.019

Conference posters and presentations

Ellis, J.F. and Blenkinsop, T., Analogue modelling of fractures in cooling intrusions. Tectonics Study Group 2018.

Ellis, J.F., Blenkinsop, T. and Davies, H. Numerical modelling of stress and fracture evolution in 3-dimensional cooling bodies. Tectonics Study Group 2018.

Ellis, J.F., Blenkinsop, T. and Davies, H. The Origin of Fractures in Plutonic Rocks: field evidence and three-dimensional numerical modelling of the Alta Stock, Utah. AGU 2018.

Ellis, J.F. and Blenkinsop, T., The influence of thermal stresses on vein orientation at the Bingham Canyon porphyry copper deposit, Utah. Materials Network Modelling Workshop 2019

Acknowledgements

Firstly, I would like to thank my research supervisors, Professor Thomas Blenkinsop and Professor J Huw Davies for their continued support and constructive criticism throughout my time at Cardiff University. Their guidance and motivation helped me during research and writing of the thesis. In addition, I would like to thank the Advanced Research Computing at Cardiff (ARCCA) for the technical support offered throughout the research period and specifically thank Ian Thomas (Geoscience High End Computing Research Development Officer, School of Earth and Ocean Sciences, Cardiff University) for converting the STRESSTAT program (Lisle and Orife, 2002; Orife and Lisle, 2003) into Python, making it possible for the software to compare a large number of data points automatically.

I gratefully acknowledge the funding received for the PhD. Including funding from Midland Valley Exploration Ltd (now owned by Petroleum Experts Ltd), Petroleum Experts Ltd and Cardiff University. Funding for field work was also provided by the Society of Economic Geologists, who awarded me the Hugh McKinstry Fund for my field work in 2017. My sincere thanks also goes to Alasdair Pope (Principal Geologist at Rio Tinto) and Verne Pere (Principal Geotechnical Engineer at Rio Tinto, now Principal Rock Mechanics Engineer at Golders) without whose support it would not have been possible to collect the data used to conduct the research presented in chapter 5. I am also grateful for the funding received from the Society of Economic Geologists and the Cardiff Undergraduate Research Opportunities Programme (CUROP).

I thank my fellow researchers at the School of Earth and Ocean Sciences, for interesting and stimulating discussion. My parents, husband, sister and in-laws are those I thank for their unconditional support throughout writing this thesis.

1. Thesis Overview

1.1. Fractures in Intrusions

Plutonic rocks are pervaded by fracture systems (Figure 1.1). Fracture systems commonly have some regularity or patterns which can be described and mathematically modelled (e.g., Bonnet et al., 2001; Berkowitz, 2002). In plutonic rocks fracture systems are often the primary control on the characteristics of the rock mass i.e., rock strength, porosity and permeability. These characteristics often have a critical control on the formation of ore deposits (e.g., McCaffrey et al., 1999), ground water aquifers (e.g., Gustafson and Krásný, 1994), hydrocarbon (e.g., Petford and McCaffrey, 2003) and geothermal systems (e.g., Genter et al., 2010; Villeneuve et al., 2018). Knowledge of these fractures is also important for radioactive waste disposal (e.g., Price, 1979; Shen and Stephansson, 1996; Huotari and Kukkonen, 2004; Mariner et al., 2011; Wang et al., 2018), and understanding processes related to natural hazards such as earthquakes (i.e., Segall and Pollard, 1983b; Christiansen and Pollard, 1997; Crider, 2015).

Plutonic rocks provide a unique challenge when describing and modelling fracture systems. Fractures in plutonic rocks may result from thermal, tectonic, hydraulic or exhumation-induced stresses, or combinations of these types, so that the origin of specific fracture sets, and the evolution of fracture networks, is generally far from obvious. Early formed fractures in plutons are particularly significant as they may control rock behaviour (Segall and Pollard, 1983a; Bergbauer and Martel, 1999; Crider, 2015) and it is likely that they influence later fracturing events (Segall and Pollard, 1983a,b; Pollard and Aydin, 1988; Moir et al., 2010; Jackson et al., 1992). The earliest fractures formed in plutonic bodies are likely to be related to thermal processes (e.g., Balk, 1937; Bergbauer and Martel, 1999; Sanders et al., 2003).

Early formed cooling fractures are unlike tectonic, hydraulic or exhumation-induced fractures and require their own classification and generic models as given in Balk (1937) and Bahat et al. (2005). However, this classification is incomplete as the characteristics and evolution of early plutonic fracture sets are generally far from obvious. This is due to the diversity of styles of plutonic bodies and because of later overprinting from tectonic and exhumation fracture histories (e.g., Price and Cosgrove, 1990).

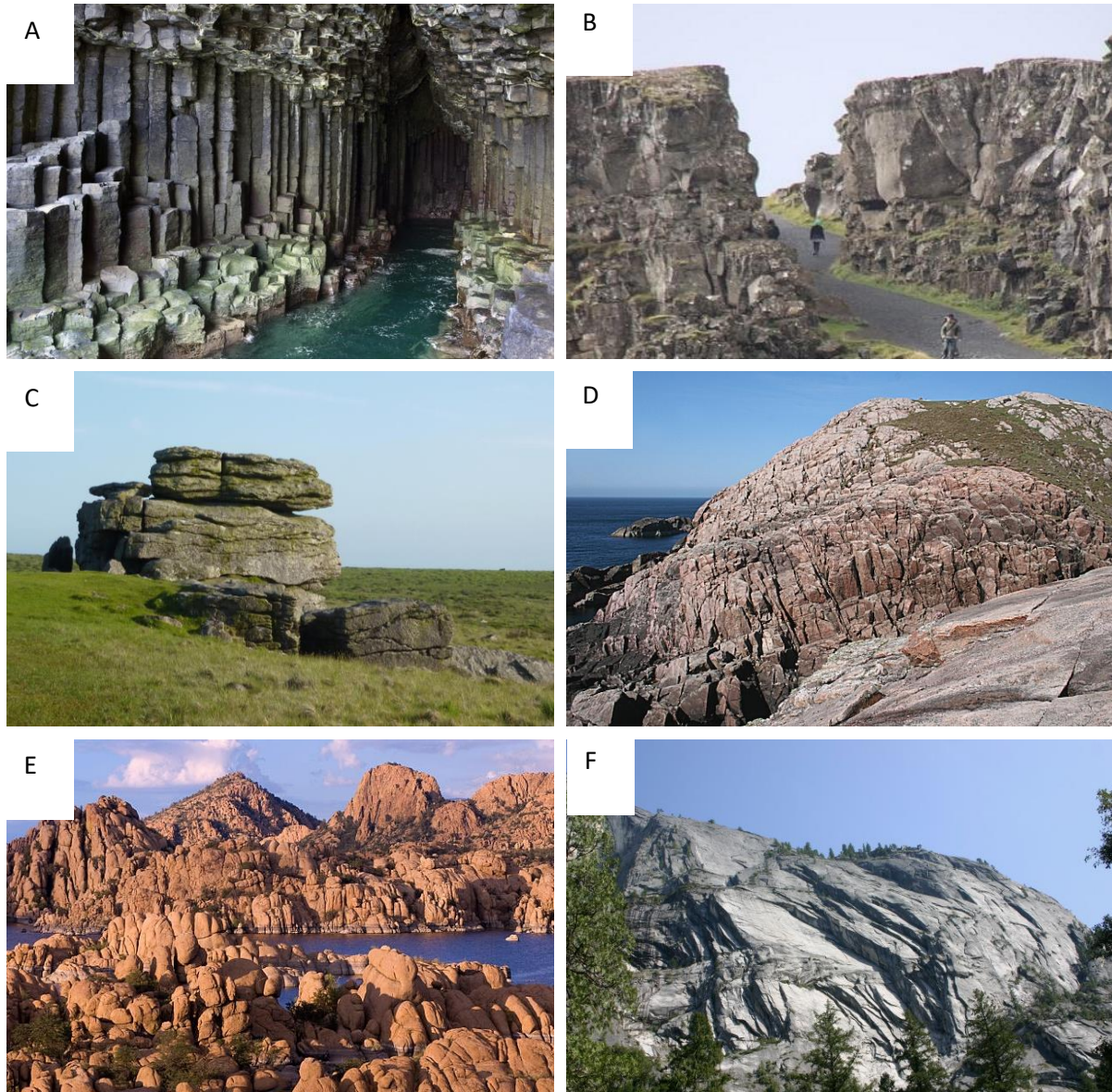


Figure 1.1. Photos of various forms of fractures in igneous rocks: (A) Columnar joints Fingal's cave, Scotland UK; (B) tectonic and cooling joints Thingvellir Iceland; (C) cooling or unloading joints, Dartmoor UK; (D) tectonic joints, Droman Scotland UK; (E) cooling or unloading joints, Watson Lake, Prescott Arizona; (F) Sheet jointing, Yosemite California.

1.2. Approaches to the Study of Cooling Fractures

1.2.1. Field Studies

Multiple fracture sets, which are often orthogonal, are typically identified in plutonic rocks. The orientation of these sets are typically assumed to have been affected by cooling, regional tectonic loads, the pluton emplacement depth (e.g., Balk, 1937; Heidrick and Titley, 1982) and controversially to the formation of magmatic fabrics (e.g., Hutton, 1988; Bahat et al., 2005; Žák et al., 2006).

Identification of early formed fractures in the field may be aided by the presence of aplite intrusions, and at lower temperatures, hydrothermal fluids may preserve a record of fracturing via mineralization (e.g., Balk, 1937; Hutchinson, 1956; Hibbard and Watters, 1985). Without the presence of such infills, these fractures may be annealed if the pluton is in a “semiplastic” state when temperatures are at or near the brittle viscous transition (Price, 1966; Hibbard and Watters, 1985) or difficult to distinguish from fractures formed by later mechanisms. Cooling fractures are typically attributed to opening mode failure and shear failure is inferred to result from the forces of emplacement (Balk, 1937; Price, 1966), or later reactivation of joints (e.g., Segall and Pollard, 1983b).

Studies on the formation of columnar joints (e.g., Spry, 1962; DeGraff and Aydin, 1987; Lore et al., 2000; Goehring and Morris, 2005; Goehring et al., 2006; Hetényi et al., 2012; Woodell, 2012; Phillips et al., 2013; Jiang et al., 2014; Závada et al., 2015; Christensen et al., 2016; Lamur et al., 2018; Weinberger and Burg, 2019) and crack patterns in cooling lava lakes (e.g., Grossenbacher and McDuffie, 1995) provides additional field evidence of early formation of fractures in cooling igneous rocks.

1.2.2. Analogue Modelling

Scaled analogue models are useful for investigating processes that cannot be directly observed and that operate over geological time frames (Hubbert, 1937; Merle, 2015). Of the many analogue models run to investigate fracture processes there are only a few that have been directly used to investigate fracturing within cooling igneous rocks. These include i) the movement of wet clays in order to compare with fracture sets defined in the Cloos model, which are linked to the mode of intrusive emplacement as cooling and crystallisation occurs (Riedel, 1929; Balk, 1937 *p.29 pl 12*), ii) the interactions of contracting two-dimensional films investigating the formation of micro-scale joints in cooling volcanic rocks (Samanta, 2001), iii) the desiccation of air-exposed starch flour investigating the processes of columnar joint formation and tensile-crack morphology (e.g., Müller, 2001), and iv)

the recording crack energy released during the heated and cooling of basaltic rocks by acoustic emission (e.g., Browning et al., 2016).

1.2.3. Experimental

There is a vast amount of literature in experimental rock failure mechanics that addresses brittle failure in granites e.g., Paterson and Wong (2005). Many aspects of the thermal response of crystalline rocks and thermally cracked rocks have been experimentally tested. These experiments generally focus on reheating crystalline rocks. Properties derived from these experiments i.e., Young's modulus, compressive strength, tensile strength, Poisson's ratio, thermal expansion, density, permeability, thermal conductivity and thermal diffusivity are used to define parameters in numerical modelling (Knapp and Norton, 1981; Gerla, 1988; Bergbauer et al., 1998; Bergbauer and Martel, 1999; Žák et al., 2006). The temperature dependence of thermal mechanical properties of granitic rocks have been compiled by Heuze (1983), Dwivedi et al. (2008) and Wang and Konietzky (2019).

1.2.4. Numerical Modelling

Thermomechanical modelling, in which conductive thermal stresses are calculated, is used to predict stress orientation and magnitude in cooling plutonic bodies. The predicted stress is then used to infer fracture orientations (e.g., Knapp, 1978; Gerla, 1983; Bergbauer, 1998; Koenders and Petford, 2003). Studies where numerical models are compared to field examples include the analysis of the Diamond Joe Stock in western Arizona (Gerla, 1983, 1988), the Lake Edison Granodiorite and the Granodiorite of Cartridge Pass in California (Bergbauer et al., 1998; Bergbauer and Martel, 1999), the Tanvald pluton and Liberec granite in the Czech Republic (Žák et al., 2006), and the Chitradurga granite in the Dharwar Craton southern India (Mondal and Acharyya, 2018).

Except for numerical modelling by Žák et al., 2006 it has been shown that predicted thermal stresses would be enough to result in fracture. Results highlight that the initial pluton geometry and orientation of regional loads influence the magnitude and orientation of the developed stress field (Gerla, 1983; Bergbauer, 1998; Bergbauer et al., 1998). Numerical models by Žák et al. (2006) are different from the other models as modelling accounts for temperature dependent properties and uses the Drucker-Prague yield criteria for a deep (8 km) plutonic body.

For a given point within the pluton numerical models only result in the prediction of one fracture orientation (Bergbauer, 1998) i.e., they do not predict the formation of orthogonal sets as observed in the field. Conversely, numerical models where the Navier-Coulomb failure criterion is applied show that the failure mechanism (i.e., shear or tensile failure) may vary over time for any given point with the pluton. As a result, the orientation of predicted fractures may vary over time and with

depth (Knapp, 1978; Gerla, 1983). Questions of the influence of three-dimensional geometry, modelling depth, selected failure criterion and the influence of the temperature dependence of material and mechanical properties have still to be addressed.

1.3. Motivation

The work presented in this thesis was developed from consulting work completed at Midland Valley Exploration (now Petex). The consultancy work looked at developing geological fracture models within intrusive units associated with copper porphyry deposits (Kloppenburg et al., 2010a,b; Grocott and Johnson, 2012; Ellis et al., 2016).

Geological fracture modelling involves identifying sets of characteristically similar fractures. For each fracture set a unique range of properties are assigned (i.e., orientation, aperture, frequency) which are linked to a geological deformation mechanism (e.g., Price and Cosgrove, 1990; Swaby and Rawnsley, 1996). The numerically modelled fracture networks take account of the strain history and geological evolution. Understanding the association between fractures and their origins provides an important tool for inferring the state of stress, the regional tectonic evolution and mechanical behaviour of rocks (Hafner, 1951; Odé, 1957). Physical or mathematical models of deformation can be used to produce proxies which provide predictive constraint in areas without direct observations. These proxies can then be used to predict fracture orientation and distribution optimizing representation of fractures for industrial applications.

Geological fracture modelling has primarily been applied to understand fracture orientations and distributions in faulted and folded sedimentary rocks (e.g., Hennings et al., 2000; Sanders et al., 2004; Ringrose et al., 2011; Mannino et al., 2012; Hennings et al., 2012; Bond et al., 2013; Ou et al., 2018; Watkins et al., 2018). This is a well-established technique in the oil and gas industry and used in several commercially available software packages e.g., Igeoss Structural geology software (Schlumberger¹), Kine3D and SKUA-GOCAD (Emerson, previously Paradigm²), LithoTect[®] Structural modelling (Halliburton³), MOVE™ (Petex⁴) and TrapTester (Badleys⁵).

Thermomechanical modelling of cooling plutons may be a useful attribute for controlling the orientation of fractures modelled in Discrete Fracture Network (DFN) models (Sanders et al., 2003; Grocott and Johnson, 2012). These models may be used to understand fluid flow and later fracturing events (e.g., Titley, 1982; Crider, 2015).

¹ <https://www.software.slb.com/products/igeoss>

² <http://www.pdgm.com/>

³ <https://www.landmark.solutions/LithoTect-Advanced-Structural-Modeling>

⁴ <http://www.petex.com/products/move-suite/>

⁵ <http://www.badleys.co.uk/T7-FRAC.php>

1.4. Field Locations

To confirm the practical application of the numerical models developed in this thesis two field locations have been studied. These are the Alta stock and the Bingham Canyon porphyry in Utah (Figures 1.2 and 1.3). These stocks are found along the same structural axis (Uinta-axis) and provide comparisons of varying size, depth and mineralisation (Steinberger et al., 2013). The selected locations provide interesting case studies for the following reasons:

Alta stock:

- Extensive exposure of relatively non-weathered and unaltered rocks that are accessible.
- Previous study of the stock and its surrounding metamorphic aureole (John, 1991 and references therein; Cook and Bowman, 1994; Vogel et al., 2001; Bartley et al., 2008; Johnson, 2009). This information provides useful constraints for numerical modelling.
- Previously identified vein and joint patterns in outcrops (Wilson, 1961; John, 1991) and microfracture orientations (Ren et al., 1989; Kowallis et al., 1995) which have been linked to the cooling history.

Bingham Canyon:

- Abundance of data available to constrain modelling parameters as it is one of the most studied copper porphyry systems in the world (Steinberger et al., 2013; Krahulec, 1997).
- Mapped spatially and temporally variable fracture and vein system (Gruen et al., 2010; Redmond and Einaudi, 2010).
- The three-dimensional geometry of the intrusions are well constrained from drill-hole data.

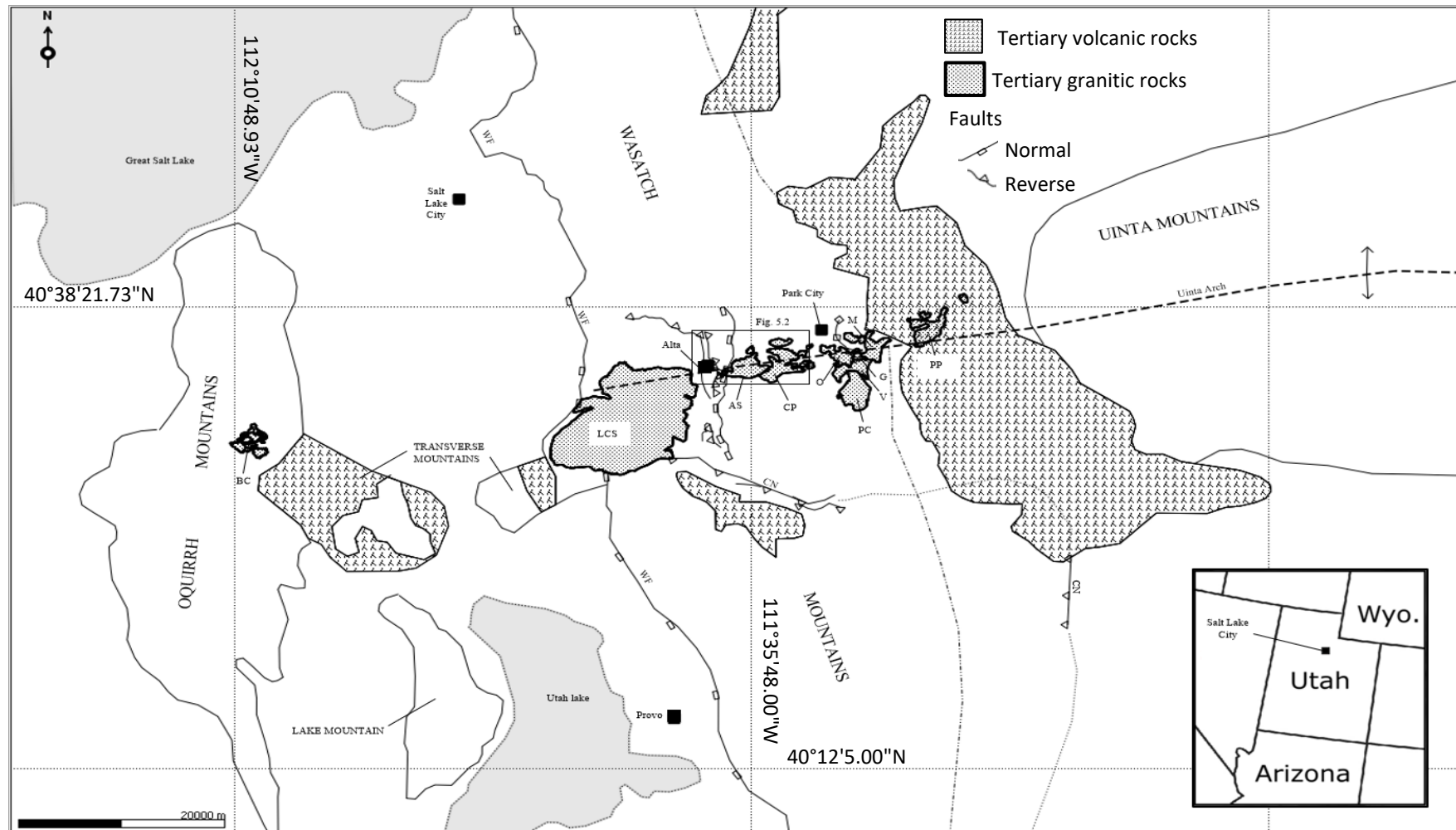


Figure 1.2. Regional map depicting Central Wasatch mountains and surrounding region, highlighting the distribution of the mid-Tertiary igneous rocks and major structures, after John (1989, 1991). Abbreviations: BC – Bingham Canyon stock, LCS – Little Cottonwood stock, AS – Alta stock, CP – Clayton Peak stock, FS – Flagstaff stock, PC – Pine Creek stock, V – Valeo stock, O – Ontario stock; G, Glencoe stock, M – Mayflower stock, PP – Park Premier stock, CN – Charleston-Nebo thrust fault, WF – Wasatch fault zone.



Figure 1.3. Photos from field locations. Top: Lake Mary Alta stock, August 2017. Middle: Looking west down the Little Cottonwood Canyon from the Alta stock towards Bingham Canyon, September 2016. Bottom: Bingham Mine from the mine overlook, October 2011.

1.5. Aims and Objectives

This research aims to advance the understanding of fracturing related to thermal stresses in cooling intrusive rocks. Hypotheses have been developed based on previous numerical modelling and field studies.

Hypothesis 1

Fracture sets of various orientations may be generated as stresses evolve in plutonic bodies during cooling.

Hypothesis 2

The relative importance of thermal and regional stresses that result in failure and fracture formation may vary during plutonic cooling.

Hypothesis 3

Stress paths for a given point within a plutonic body may pass through different failure fields i.e., fail in tension or shear.

Hypothesis 4

Depth and temperature-dependent material properties will influence stress path evolution and control the resulting failure mechanism and timing.

In order to investigate these hypotheses, numerical modelling, field studies and analogue modelling have been applied to the following research objectives:

- Extension of numerical models into the third dimension. To investigate the influence of depth, temperature dependent properties and three-dimensional failure criteria on modelling results (chapter 3).

- Application of the numerical models to case study examples and comparison of predicted fracture orientations and failure mechanisms to fracture sets identified in field work (chapters 4 and 5).
- Determination of the control of thermal stresses in early fracture formation in porphyry deposits (chapter 5).
- Development of analogue models to clarify if multiple fracture sets may develop in cooling bodies (chapter 6).

1.6. Thesis Structure

This thesis is organised into seven chapters.

Chapter 1 is an introduction to the thesis. A summary of approaches to study, motivation, the thesis aim, hypotheses and objectives, and an overview of the thesis structure is given (this chapter).

Chapter 2 reviews available literature outlining conceptual models, characteristics, classification and causes of fractures in plutonic rocks.

Chapter 3 outlines the two- and three-dimensional numerical modelling workflow developed with the finite element code COMSOL Multiphysics®. Workflows applied to previously published two-dimensional models are extended into three-dimensions. The influence of model variables including geometry, depth, in-situ stress and temperature dependent material and mechanical properties are tested. The implications of the assumptions made in the numerical models are assessed.

Chapter 4 describes the application and results of the COMSOL Multiphysics® three-dimensional models as applied to the Alta stock in Utah. Modelling is compared to new field studies, which record the orientations of aplite dykes and early mineralized and later non-mineralized joints. Multiple models are run to address uncertainties in the modelling parameters.

Chapter 5 illustrates the potential influence of thermal stress on porphyry vein orientations. Thermomechanical stress models are compared to estimates of paleostress orientation calculated from vein orientations which are well exposed at the Bingham Canyon copper mine, Utah.

Chapter 6 documents results from scaled analogue experiments developed to address questions of expected fracture propagation directions in contracting bodies. Dehydration of buried starch flour is used as the analogue material. The effects of the geometry and burial depth on resulting fracture patterns created in a contracting body are investigated.

Chapter 7 is a summary of the major findings. Responses to hypotheses are presented, model limitations are summarised and suggestions for further research are made.

Appendix files contain supporting information. The digital appendix includes all data used in the analysis, examples of numerical model files and animations of the numerical models presented in chapter 3.

2. Fracturing in Plutonic Rocks – A Review

Emphasis in this review is placed on the development and evolution of early formed fractures in plutonic rocks. The Cloos and Hedrick and Tiltley conceptual models of fracturing in plutonic rocks are outlined in section 2.1 (p.14). The characteristics of fractures found within igneous rocks are described in section 2.2 (p.21). Fracture classification in intrusive rocks as cooling, tectonic or exhumation is given in section 2.3 (p.23). An overview of plutonic emplacement, geometry and cooling history is given in section 2.4 (p.27) as the plutonic geometry and thermal history have been shown to be important for the formation of early fractures in plutonic rocks. Stresses related to the origins of early formed cooling fracture are outlined in section 2.5 (p.29). Results from experimental cooling fractures and the influence of temperature dependent properties are outlined in section 2.6 (p.32). The review is summarised in section 2.7 (p.34).

Additional reviews are given in relevant chapters: chapter 3 summarises previous thermomechanical models (p.38.- 46), chapters 4 and 5 give an overview of the geology of the Alta and Bingham Canyon magmatic complex (p.137 – 143 and p.206 – 215) and in chapter 6 analogue models of fracturing in cooling material are reviewed (p.242 – 246).

2.1. Conceptual Models

2.1.1. The Cloos Model

The Cloos Model is based on studies of plutonic rocks in Europe and North America. It was the first model to classify fractures in granitic rocks as integrated patterns (Cloos, 1922, 1925). The work is primarily published in German but has been summarised and translated into English by Balk (1937). This model is commonly reproduced in texts as a general explanation of fracture orientations and patterns within plutonic rocks (e.g., Hills, 1972; Pollard and Aydin, 1988; Price and Cosgrove, 1990; Bahat et al., 2005; Figure 2.2). This model forms the basis for classification of fractures in many batholiths (Balk, 1937 and references therein; Hutchinson, 1956; Marre, 1986; Mazzoli et al., 2009).

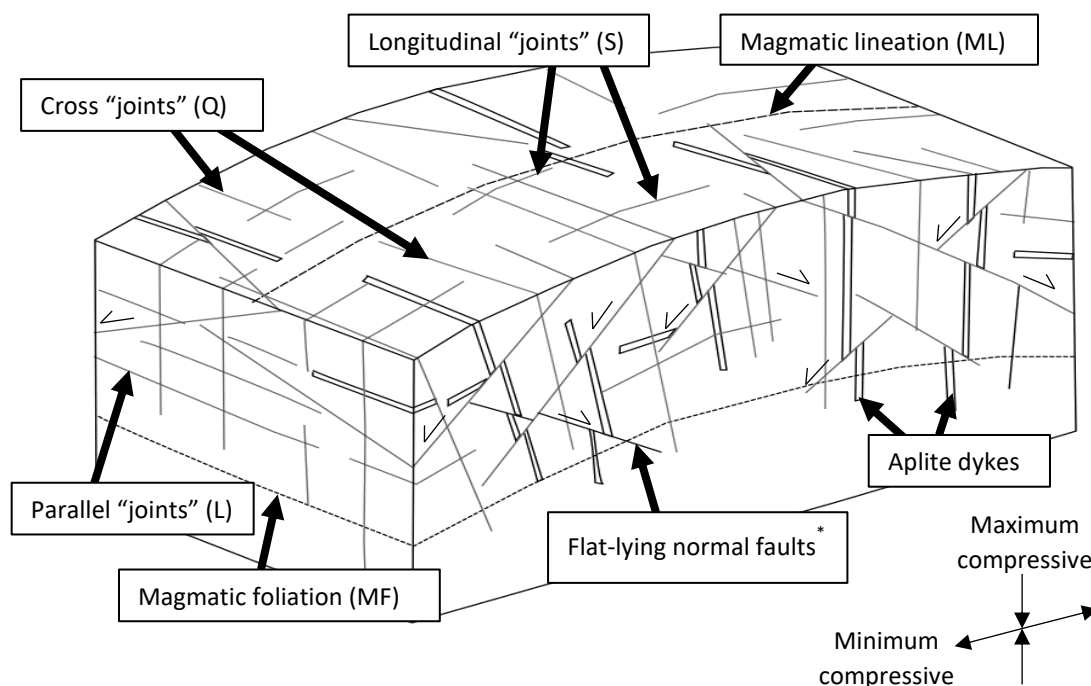


Figure 2.1. The Cloos Model of fractures in plutonic rocks, redrawn after Žák et al. (2006)*. The model highlights the genetic relationship between magmatic fabric (MF and ML) and fractures in a granite pluton. This model is based on field relationships of the Strehlen massif (Balk, 1937 p.75). See the note on next page regarding the use of the term "joint".

* Žák et al., 2006 and Bahat et al., 2005 label this type diagonal faults, here the Cloos label of flat-lying normal faults is used as given in Balk, 1937.

Note: The term “joint” is given in quotations as these fractures do not necessarily comply to the strict definition of a joint as discontinuities across which there is no visible displacement. These fractures often display evidence of shear movement and may form when the rock is in a plastic state (i.e., Price, 1966; Price, 1979; Pollard and Aydin, 1988; Price and Cosgrove, 1990).

Fracture patterns recognised in the Cloos model (Figure 2.1) are formed of three to four “joint” sets: two orthogonal steeply dipping and one horizontal, with or without the additional fourth shallowly dipping fracture set (Balk, 1937). The model distinguishes between primary fracture systems (Table 2.1) and fracture systems (planes of primary expansion) (Table 2.2). Planes of primary expansion are suggested to accommodate vertical (marginal “joints”) and horizontal expansion (flat-lying normal faults) of emplacing batholiths. The observations made by Cloos and his co-workers on intrusive bodies of other geometries are summarised in Table 2.3 (Balk, 1937).

The primary fracture system (cross “joints” (Q), longitudinal “joints” (S), diagonal “joints” (D), flat lying “joints” and faults (L); Figure 2.1, Table 2.1) typically have nearly no displacement. They are inferred to form during solidification, resulting from stresses developed during pluton emplacement (Balk, 1937). Early formation of these “joint” systems is suggested from the presence of hydrothermal mineral assemblages and aplite dykes. Orientations of these “joint” sets are related to those of the primary flow structures and result from stress build up during the inward solidification of a crystallising pluton (Balk, 1937).

The close relationship of the cross- (Q), longitudinal- (S) and diagonal- (D) “joints” to magmatic lineation and foliation related to emplacement strains is disputed (e.g., Hutton, 1988; Bahat et al., 2005; Žák et al., 2006). The main objection to a fracture classification related to primary flow structures is that foliations and lineations may be produced by a number of internal and external forces at various times so that the relationship between fractures and foliation is not simple (Paterson et al., 1998; Correa-Gomes et al., 2001). Alternative observational based classifications of fractures according to time of occurrence have therefore been suggested (Table 2.4).

Table 2.1. Characteristic and origin of the four joints sets that form primary fracture system of the Cloos Model (as defined in Balk, 1937)

Primary fracture system	Characteristics	Origin
Q Cross “joints” or tension “joints” when flow lines absent	Dip often reflects margin geometry (i.e. steeply dipping top surface or horizontal dipping long vertical edges). Perpendicular to flow lines when present. Longer and straighter than the other joints and may extend into host rock. Presence of hydrothermal minerals and aplite’s. Variable spacing.	Tension “joints” resulting from the upward push of liquid or plastic magma in the centre or the cooling body. If dome or arch developed, then cross “joints” may fan and converge towards the centre of the arch.
S Longitudinal “joints”	Steeply dipping. Parallel to flow lines. Displacements are rare. Presence of aplite, pegmatites or other dykes. Best developed when flow lines approach horizontal (near the roof of large intrusions).	Not clearly understood but assumed to be formed during transition of rock from fluid to solid.
D Diagonal “joints”	Steep planes. Trending approximately 45° or more to trends of flow lines. May approach the direction of cross “joints”. One conjugate system may be locally suppressed. Commonly filled with aplite or hydrothermal minerals.	Elongate the rock mass in the direction of flow line trend, likely to be the result of lateral compressive stress normal to the trend of the flow lines. Displacements show the mass of rock, may be regarded as shear planes. May develop instead of cross “joints” in a pluton that is hemmed in preventing lateral expansion. Movement along them may be primary or secondary.
L Flat-lying “joints” or parallel “joints”	Primary May follow gently inclined flow lines, contain dykes or veins. Secondary Sheeting curved “joints” divide rock into flat lying approximately parallel to topographic surface. Less pronounced with depth.	Two types: Primary, formed during emplacement, possibly due to volume change. Secondary, due to (a) weathering and erosion probably due to expansion of feldspars or ferromagnesian minerals or removal of load and seasonal temperature variation of the rock or (b) horizontal compression acting on the massif in which “joints” may potentially fail as shear planes.

Table 2.2. Fracture systems of the Cloos Model referred to as planes of primary expansion (as defined in Balk, 1937)

Fracture system	Characteristics	Origin
Marginal fractures: fissures / joints and up-thrusts	<p>Found along steep contacts.</p> <p>Dip inwards at angles between 20° and 45°.</p> <p>Accompanied by aplite's, pegmatites, quartz veins or barren fissures and can be important hosts to mineralisation.</p> <p>Displacement occurs along upthrusts.</p>	<p>Result from domal expansion or arching. Probably in same process that forms cross "joints", but cross "joints" would be horizontal.</p> <p>Upthrusts envisaged to form in zones where the intrusive mass raises at a faster rate than can be accommodated by stretching.</p>
Flat-lying normal faults (planes of stretching)	<p>Restricted to the upper parts of the intrusion. Favour flat-topped masses but are also found along steep contacts.</p> <p>Dip at 45° or less.</p> <p>Strike and locations apparently random.</p>	<p>Formed by of the border zone of large intrusions parallel to the flow lines.</p> <p>Resulting in horizontal widening of the intrusion. May be caused by the continual intrusion of magma in to the core of a massif.</p> <p>Probably older than cross "joints" but may overlap in age.</p>

Table 2.3. Fracture systems in other plutonic bodies as defined by Cloos and co-workers (as defined in Balk 1937)

Plutonic geometry	Fracture systems present
Dykes	<p>Cross "joints" where flow lines can be recognized, gash veins normal to dike walls and diagonal fractures may form.</p>
Stocks and plugs	<p>Lack regular order to fracture systems.</p> <p>Flat-lying "joints" found near contacts and probably related to tension. In plugs radial tension joints may form and are vertical and radiate around the stock.</p> <p>Inward dipping marginal fractures similar to marginal "joints".</p> <p>Normal faulting may occur in some.</p>
Flat lying sills and intrusion sheets	<p>Flat normal faults found in symmetric zones near contacts.</p> <p>Displacement related to flow of interior portion past the solidified outer zones.</p>

Table 2.4 Alternative classifications to the Cloos Model suggested for foliations and limitations (Hutton, 1988), Fractures (Žák et al., 2006) and Faults (Crider, 2015) found in plutons

Foliation and lineation's Hutton, 1988	Fractures Žák et al., 2006	Faults Crider, 2015
<p>Pre-full deformation Particle suspension alignment resulting in aligned euhedral phenocryst (typically feldspar and mafic phenocrysts) and unaligned late matrix (typically quartz).</p>	<p>Cooling fractures * Form from thermal contraction during pluton cooling. Fractures terminate against margins. Orientation are predictable from thermo-mechanical modelling.</p>	<p>Inherited pre-existing Pre-existing flow structures or cooling joints related to plastic deformation.</p>
<p>Crystal-plastic-strain Deformation affects granite after all phases have crystallised but system may align due to ductile plastic deformation.</p>	<p>Syn-tectonic fractures * Regional tectonic stresses are superimposed on crystallising or solidified pluton. Fractures cut across pluton boundaries. Fracture orientation is arbitrary relative to pluton geometry.</p>	<p>Early-formed Precursory structures formed prior to but in the same stress conditions as later tectonically formed brittle faults.</p>
<p>Syn-kinematic-strain Patterns formed in plutons emplaced synchronously with deformation in the host rock.</p>	<p>Uplift fractures Resulting from the release of stress due to exhumation of the pluton.</p> <p>Post-uplift fractures For example, sheeting or exfoliation joint due to near surface processes.</p>	

* It should be noted that despite the distinction here between cooling fractures and syn-tectonic fractures, thermal-mechanical modelling has shown that the orientation of cooling fractures may be influenced by syn-tectonic forces (Gerla, 1988; Bergbauer, 1998) and that cooling fractures have the potential to extend into the host rock in plutonic geometries that centrally narrow (i.e. hour glass geometries) (Bergbauer, 1998; Bergbauer et al., 1998).

2.1.2. The Heidrick and Titley Model

Heidrick and Titley, 1982 developed a model for fracture systems found in shallow (3 – 5 km) felsic porphyry copper systems based on field studies in the American Southwest (Figure 2.2). Fracture patterns in the model are formed from three mineralized and un-mineralized joint sets and veins, faults, fault-veins, dykes and fault-dykes (Figure 2.2, Table 2.5).

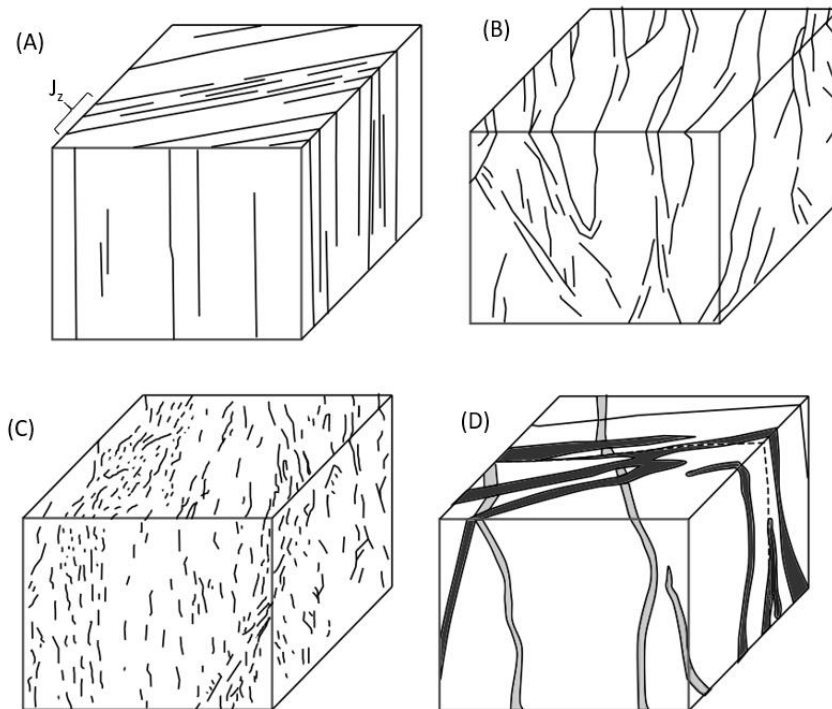


Figure 2.2. Schematic block diagrams showing the characteristics of the three fundamental types of mesoscopic joint sets and dykes, veins and fault-veins identified in the Heidrick and Titley model. (A) Joint set 1 and joint zone (J_z), characterised by smooth planar surfaces which are mineralised, (B) Joint set 2, rough discontinuous curviplanar joints that are rarely altered (C) Joint set 3, irregular discontinuous microfractures and hairline cracks (D) dykes, veins and fault veins. Redrawn after Heidrick and Titley (1982).

Two types of patterns based on fracture orientations are distinguished: intrusion-centred fractures and strike parallel fractures. Intrusion-centred patterns may be either systematic (radial and concentric) or non-systematic (Heidrick and Titley, 1982). Intrusion-centred patterns are generally related to the release of fluid pressure and volatiles during pluton emplacement and cooling. Strike-parallel systems are typically related to regional tectonic activity, commonly interpreted to trend parallel to the direction of the regional horizontal maximum compressive stress (Price and Cosgrove, 1990; Hou, 2012). In shallow level porphyry intrusions, a continuum between intrusion-centred

fractures and repetitive strike parallel fractures has been observed (Heidrick and Titley, 1982; Titley, 1990). The relative occurrence of each type is considered to be dependent on the fluid pressures, depth and regional tectonic activity (Heidrick and Titley, 1982).

Table 2.5. Fracture sets of the Heidrick and Titley model (as defined in Heidrick and Titley, 1982)

Fracture set	Characteristics	Origin
Joint set 1	Smooth-surface. Continuous and planar. Alteration selvages vary from 1 – 10 mm. Spacing and abundance variable, fracture intensity on the order of 0.2 – 0.4 cm ⁻¹ Control and localises mineralization and alteration.	Intrusion stresses are related directly to emplacement and cooling. Intrusions rarely have recognisable foliation, flow lines indicative of rapid emplacement. Joint Set 2 considered to formed between mineralising phases. Episodic nature of fracturing can be identified from overprinting of mineral phases, where assemblages relate to cooling. In the host rock stress distribution results from regional tectonics and local mechanical rock responses to emplacement.
Joint set 2	Rough-surface. Discontinuous and curvilinear. Rarely mineralised or altered. More abundant in non-mineralised areas.	
Joint set 3	Irregular microfractures. Discontinuous and sinuous. Related to joint set one as alteration assemblages are similar, alteration selvages are thin in comparison ~0.1 mm. Most abundant of the joint sets.	
Dykes, veins and Fault veins	Persistent and through going. Continuous planar to curvilinear. Widths of 2 – 15 m Poorly defined <i>en-echelon</i> sets, and swarms may be present and when present lateral offset predominantly strike-slip. Aplite and aplites-pegmatites common in pluton and uncommon in host rocks.	Aplite, aplites-pegmatites and aplites porphyry dykes form in response to brittle fracturing during pluton cooling and follow early breaks in the intrusion, may form before Joint sets.

2.2. Characteristics of Fractures in Plutonic Rocks

Fractures may be characterised by description of their geometric form (e.g., Bahat, 2012), represented statistically in terms of the rock mass properties (e.g., Bonnet et al., 2001; Berkowitz, 2002), or described in terms of fracture set interaction (network topology; e.g., Andresen et al., 2013; Hafver et al., 2014; Sanderson and Nixon, 2015). Variability in these characteristics is dependent on the geological history experienced by the rock mass.

The scale of fracture analysis in plutonic rocks varies from megascopic (i.e., lineament maps) to microscale analysis (Kranz, 1983). Fractal analysis of lineament maps have been used to show that fractures within igneous rocks have similar patterns at different scales (e.g., Velde et al., 1991; Barton and Zoback, 1992; Ledésert et al., 1993; Genter and Castaing, 1997; Ehlen, 1998, 2000; Gerrard and Ehlen, 1999; Viruete et al., 2001; Park et al., 2010; Le Garzic et al., 2011; Bertrand et al., 2015). Analysis of microfractures in plutonic rocks has been used to infer paleostress histories (e.g., Ren et al., 1989; Kowallis et al., 1995; Nadan and Engelder, 2009). The characteristics (i.e., geometry, aperture and spacing and density) of fractures within plutons outlined below are primarily related to meso-scale analysis.

2.2.1. Geometry

Little is known about the three-dimensional geometry of fracture planes in massive rocks (Gonzalez-Garcia et al., 2000; Dowd et al., 2009). The characterisation of geometry is often limited to the fracture trace. Fracture trace geometry is dependent on the relative orientation of the joint surface to that of the exposed surface. Traces may be straight or curved and continuous or segmented (Segall and Pollard, 1983a,b). Three-dimensional fracture geometry is commonly considered to be either elliptical or rectangular. Elliptical hydrofractures have been observed in granite quarries (e.g., Bahat, 2012). Fracture planes forming the sides of columnar joints are often rectangular in shape (e.g., DeGraff and Aydin, 1987).

Fractographic markings (fracture surface markings) can be used to infer the mechanism, rates of deformation in materials, relative timing of development of fractures and, orientation of principle stresses during fracture initiation and growth (Bahat et al., 2005; Ziegler, 2010). Undulations and plumes on the surface are typically assumed to reflect opening (Mode I Failure) (Bahat et al., 2005) as significant shear (Mode II or III failure) would have erased surface markings. Markings in granitic rocks have been studied in detail by Bankwitz and Bankwitz (1995), Bahat et al. (1999), Bankwitz et al. (2004), Bahat et al. (2004), Bankwitz and Bankwitz (2004), Bahat et al. (2005) and Bahat (2012). It has

been suggested that the characteristics of the fracture margins can be used to infer the depth of formation (Bankwitz and Bankwitz, 2004; Bankwitz et al., 2004).

The surface morphology of early formed fractures is typically not visible in plutonic rock masses. However, thin section study of the growth relationships between dyke and wall rocks show that fractures may form both post magmatic (wall rock crystal truncated) or during late magmatic crystallisation (wall rock crystal not truncated) (Hibbard and Watters, 1985).

2.2.2. Aperture

Igneous rocks typically have poor primary porosity so that fluid flow is generally confined to fractures (Petford, 2003; Crider, 2015). As porosity and permeability are dependent on the fracture network a wide range of values can be expected which may be variable over time, as determined by the geological history. Fracture planes and joint surfaces may be coated by thin veneers of surface minerals and alteration products. Others may be filled with minerals (veins) or intrusive material (dykes). Veins are often up to centimetres wide and dykes may be 10s of meters wide. Without the presence of fill many early formed fractures may not be able to be identified in otherwise homogenous rocks (Balk, 1937).

2.2.3. Spacing and Density

The distance between subparallel fracture sets in intrusive igneous rocks are commonly not uniform (Balk, 1937; Segall and Pollard, 1983a; Everitt and Lajtai, 2004). This results in clusters or corridors of fractures in-between areas of widely spaced fractures. In addition it has been shown that columnar joints formed in cooling igneous material often increase in spacing away from the initiation surface (e.g., Spry, 1962). This suggests that the spacing of cooling fractures may also change spatially as the cooling front moves.

2.3. Classification of Fractures in Plutonic Rocks

Fractures are often classified into sets of similar characteristics (i.e., orientation, spacing, mineral fill etc.) and classified by relationship to geological processes such as cooling, faulting, folding, hydraulic pressure, unloading and weathering (Nelson, 2001).

Fractures in plutonic rocks can be defined as experimental or natural (Table 2.6). Experimental fractures form at consistent and predictable angles to imposed principal stress directions (Figure 2.3), while natural fractures are linked to the geological process responsible for their formation (e.g., Nelson, 2001). The naturally occurring fracture classification (Table 2.6) is dependent on the experimental fracture classification.

It is assumed that naturally occurring fracture patterns represent the local state of stress at the time of fracturing and are similar in form to laboratory tests on equivalent rocks under analogue conditions (Nelson, 2001). Fractures within igneous rocks are generally defined as being related to cooling, tectonic or exhumation processes. This subdivision is however often complicated by overprinting of these fractures (Price and Cosgrove, 1990). The characteristics of fracture types related to geological processes are outlined in sections 2.3.1 to 2.3.3 p.25 – 26.

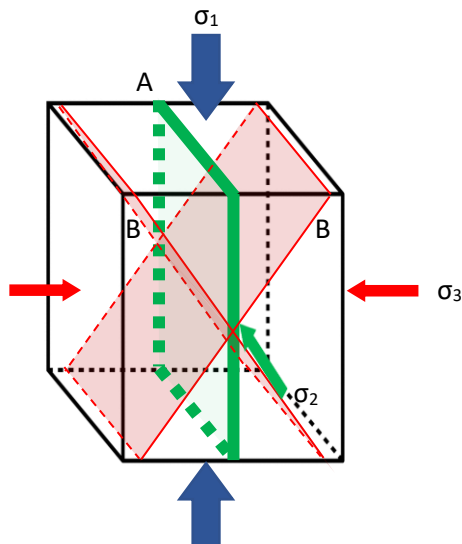


Figure 2.3. Possible brittle fracture planes formed in compression tests, related to principal stress directions for: (A) extensional fractures (green plane), (B) shear fractures (red planes). $\sigma_1 > \sigma_2 > \sigma_3$, compression positive. Redrawn after Anderson, 1951.

Table 2.6 Classification of fracture types after Nelson, 2001

Classification	Characteristics	Origin
Experimental Fracture classification		
Shear fractures	Displacement parallel to fracture plane. Dip at an acute angle to maximum compressive stress and strike parallel to intermediate stress.	All three principal stresses are compressive. Conjugate angle dependent on the: mechanical properties, the absolute magnitude minimum principal stress and the magnitude of the intermediate stress relative to maximum and minimum principal stresses.
Extension fractures	Displacement perpendicular to and away from fracture plane Form parallel to maximum compressive and intermediate and perpendicular to the minimum compressive.	Form when all three principal stresses are compressive. May form synchronously with shear fractures.
Tensile fractures	Orientation and displacement equivalent to extension fractures.	At least one principal stress (the minimum compressive principal stress) must be tensile.
Naturally occurring Fracture classification		
Tectonic fractures (surface forces)	Orders of magnitude size 9 - 10.	Associated with local tectonic events. formed by application of surface forces and related to faults and folds.
Regional fractures (surface or body forces)	Orders of magnitude size 5 Develop in consistent and simple geometry relatively large spacing crosscut local structures over large areas.	Related to tectonic loading at the edge of basins (but would expect intensity to vary from basin margins to centre and many basins do not have structural belts at the edge to form fracturing). Normal basin compaction processes due to loss of vertical dimension. Patterns and azimuth related to the basin shape.
Contractional fractures (body forces)	Orders of magnitude size 2 Tensile or extension fractures.	Due to bulk volume reduction: Desiccation (tensile fractures) Syneresis (tensile or extension fractures). Thermal gradients (tensile or extension fractures depending on depth of burial). Mineral phase changes (tensile or extension fractures)
Surface-related fractures (body forces)	Orders of magnitude size 4-5 Tensile or extension fractures.	Unloading of stored stress and strain.

2.3.1. Cooling Fractures

Cooling fractures may be identified by distinctive geometry (i.e., columnar joints) or identified by dyke or vein infills. Columnar jointing is one of the most characteristic patterns related to cooling (Figure 1.1 A, p.2). Columnar joints are typically formed in lava flows under approximately homogenous stresses (National Research Council, 1996). The columns form polygonal shapes, tending to be pentagons, heptagons, and hexagons or forming as triangular, cubes, and octagons shaped columns (Spry, 1962; Goehring and Morris, 2005; Hetényi et al., 2012; Phillips et al., 2013; Jiang et al., 2014). Columnar joints are vertically elongate relative to their horizontal width (e.g., Pollard and Aydin, 1988). Plumose structures that may form on vertical fracture segments have been interpreted to show the incremental propagation of joints perpendicular to the unit surfaces or cooling isotherms (DeGraft and Aydin, 1987; Grossenbacher and McDuffie, 1995).

Fracture patterns influenced by lithostatic or tectonic forces during cooling, are less well defined but are often orthogonal to the margin geometry of the intrusive body (Balk, 1937; Gerla, 1988; Martel and Bergbauer, 1997; Koenders and Petford, 2003). Without the presence of early fill or characteristic columnar joint geometry, cooling joints may be annealed or difficult to distinguish from tectonic fractures which may overprint them.

2.3.2. Tectonic Fractures

Faults and shear zones formed in granitic rocks may be dependent on the presence of pre-existing joints or dykes (e.g., Segall and Pollard, 1983a; Pennacchioni and Mancktelow, 2007; Crider, 2015). This topic is reviewed in detail by Crider (2015). The requirement of pre-existing joints, likely to be related to cooling, highlights the importance of understanding these early formed fractures but also the complication of field identification due to overprinting.

2.3.3. Exhumation Fractures

Exhumation fractures (Figure 1.1 F, p.2) are fractures with orientations that form close to (within 100 m) and subparallel with the topographic surface (e.g., Gilbert, 1904; Dale, 1923; Holzhausen, 1989). This type of fracture has been studied for assessing rock fall hazards (Cohen, 1993; Bahat et al., 1999; Everitt and Lajtai, 2004; Martel, 2006, and references therein; Collins and Stock, 2016). Exhumation fractures are typically the youngest natural fractures formed.

Their characteristics include increasing joint spacing with depth and lack of hydrothermal mineralisation on open surfaces (e.g., Holzhausen, 1989; Bahat et al., 2005). Lengths may continue for

more than 200 m (Martel, 2006). Fractographic surface markings may display a unique merger of early circular crack and fans (Bahat et al., 1999).

The origin of exhumation fractures has been attributed to various erosion-induced or paleo-stresses (e.g., Dale, 1923; Bruner, 1984), high differential stress (e.g., Holzhausen, 1989), a combination of regional compressive stress and topographic curvature (e.g., Martel, 2006, 2011, or thermal contraction (e.g., Haxby and Turcotte, 1976; Nadan and Engelder, 2009). Although the exact processes are often debated they are related to unloading conditions and are different from other types of fractures which occur due to increasing load (Bahat et al., 1999).

2.4. Plutonic Rock Emplacement, Geometry and Cooling Histories

2.4.1. Emplacement and Geometry

Igneous bodies occur in a wide variety of tectonic settings (e.g., Hutton, 1988) i.e., extensional (e.g., Hogan et al., 1998), compressional (e.g., Musumeci et al., 2005; Tibaldi, 2008; Montanari et al., 2010) and transcurrent (e.g., Brown and Solar, 1999; Corti et al., 2003) which influence the magmatic composition, structural framework (i.e., host rock geometry and structure), thermal gradients and emplacement mechanisms (e.g., Pitcher, 1979; Castro, 1987; Hutton, 1988; Paterson and Fowler, 1993; Petford et al., 2000; Weinberg, 2004; Zellmer and Annen, 2008; Burchardt, 2009; Menand et al., 2011; Menand, 2011; Annen et al., 2015; Cruden and Weinberg, 2018). These factors result in a wide variety of plutonic geometries, defined by size, shape and depth.

External stress conditions defined from the tectonic setting may influence the shape of crustal plutons (Vigneresse, 2006). For example, Montanari et al., 2010 have used analogue modelling to show that intrusion shapes in compressional environments are directly controlled by the shortening and injection rate. However, the fact that magmatic and tectonic rates do not operate on the same time scales has been used to suggest that magmatic emplacement is independent from the tectonic setting (McCaffrey and Petford, 1997; Gudmundsson, 2006; De Saint Blanquat et al., 2011). Although, the complex link between intrusion geometry and tectonic processes is not fully understood it is important to recognise that incremental emplacement of plutonic bodies, shown by compositional variation and presence of internal contacts (Coleman et al., 2004; Glazner et al., 2004; Miller et al., 2007; Miller, 2008; Annen, 2011; Aragón et al., 2019), will likely modify the regional stress field (e.g., Vigneresse et al., 1999) and the thermal history (e.g., Miller, 2008; Menand, 2011).

In numerical models of plutonic bodies geometries are often simplified and the emplacement history ignored (e.g., Gudmundsson, 2012). Cylindrical shapes are commonly used to represent the magma bodies (e.g., Pitcher, 1979; Kohsmann and Mitchell, 1986; Petford et al. 2000; Annen, 2011; Caricchi et al. 2012; Aragón et al., 2019).

2.4.2. Cooling History

Calculations of cooling have been widely applied to estimate the cooling rates of magma bodies and their surrounding rocks (Ingersoll and Zobel, 1913; Lovering, 1935; Jaeger and Carslaw, 1959; Jaeger, 1961). These calculations are commonly simplified to problems of heat conduction away from a homogenous body (e.g., Jaeger and Carslaw, 1959; Knapp and Norton, 1981; Gerla, 1988;

Bergbauer et al., 1998; Bergbauer and Martel, 1999; Koenders and Petford, 2003; Žák et al., 2006). Models of heat conduction include both one- and two-dimensional methods (Norton and Knight, 1977; Harrison and Clarke, 1979; Barton and Hanson, 1989; Hanson and Barton, 1989; Stowell and Pike, 2000; Nabelek et al., 2012). In order to calculate the heat conduction from a hot body these models are simplified so that at model initiation the intrusion, of a uniform temperature, is assumed to be instantaneously emplaced (e.g., Lovering, 1935). The geometry of the body controls the rate of heat transfer and shape of the resulting isotherms which are both suggested to have an important influence on joint geometry and density (e.g., Tomkeieff, 1940; Knapp and Norton, 1981; Gerla, 1988; Bergbauer et al., 1998; Bergbauer and Martel, 1999; Koenders and Petford, 2003).

Convective cooling within a magma body is minimised as heating of the wall rocks reduces the differential temperature gradient (Annen, 2009). Additionally, convective hydrothermal circulation within host rock and plutons remains low until the pluton is significantly fractured and permeable to fluid flow (Cathles, 1981; Clemens and Mawer 1992; Martel and Bergbauer, 1997). Estimates of the time for full-scale convective hydrothermal flow to establish are on the order of $> 10^5$ to 10^6 years, dependent on temperature and host rock permeability (e.g., Furlong et al., 1991). When established, convective hydrothermal circulation, may lead to an increase in pluton cooling rates (Cathles, 1981).

The assumption of instantaneous emplacement is justified where pluton emplacement is considered to be rapid ($< 100,000$ years; Petford et al., 2000) relative to the time required for cooling on the order of millions of years (e.g., Martel and Bergbauer, 1997; Vernikovskaya et al., 2009). Despite this justification at least some plutonic bodies are emplaced incrementally over long periods of time (i.e., > 1 million years; Glazner et al., 2004; Annen 2009, 2011; de Saint Blanquat et al., 2011). The growth sequence of incrementally emplaced bodies may lead to different thermal evolutions (Jaeger 1961; Hanson and Glazner, 1995; Annen and Scaillet, 2006; Annen, 2009; Menand, 2011; Barboni et al., 2015; Ratschbacher et al., 2018). Cooling rate is directly controlled by the magma injection (de Saint Blanquat et al., 2011). Emplacement rates of > 2 cm /year are required so that the temperature remains above the solidus and the thermal history is not significantly different than assuming instantaneous emplacement (Norton and Knight, 1977; Hanson and Glazner, 1995).

Additional model simplifications include using constants for material properties which are not temperature dependent and ignoring the latent heat of crystallization which would increase temperatures (e.g., Lovering, 1935; Knapp, 1978; Nabelek et al., 2012). Errors associated with assuming temperature independent material properties can be minimized by using average values. The magnitude of the error associated with neglecting the latent heat of crystallisation is dependent on the value, which can be up to $\frac{1}{4}$ of the total heat in a magmatic mass (Lovering, 1935).

2.5. Origin of Cooling Fractures

Fracturing events are determined by the local stress conditions experienced over time and the mechanical properties of the rock mass. Fracture patterns can be predicted if the stresses acting on the rock during fracture formation are known (Swaby and Rawnsley, 1996; Price and Cosgrove, 1990). Fractures will form when tectonic, thermal stresses and fluid pressures exceed the lithostatic pressure. The driving stress (ΔS) for fracturing can be defined as:

$$\Delta S = \sigma_{\text{overburden}} + \sigma_{\text{regional}} + \sigma_{\text{thermal}} + P_{\text{fluid}}$$

Where, σ is stress and P is pressure (Martel and Bergbauer, 1997; Bergbauer and Martel, 1999). Evaluating the stress can be complicated due to the wide range of possible values for each of the causing stresses and fluid pressure (e.g., 0–500 MPa; Burnham, 1979) which contributes to the driving stress (Bergbauer and Martel, 1999). Fluid pressure increase results in fractures being brought closer to failure (e.g., Burnham, 1979). The rate of cooling and thermal stress build-up is influenced by a coupled thermal, mechanical, and chemical processes (Figure 2.4; Knapp, 1978).

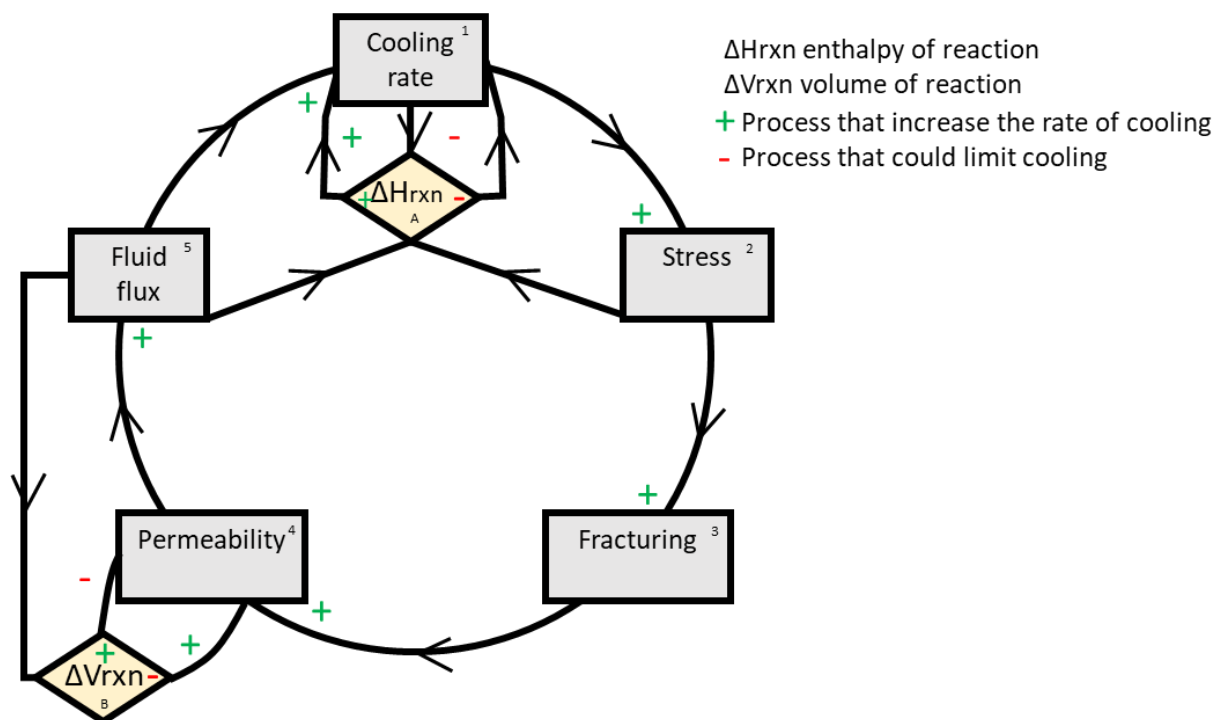


Figure 2.4. Feedback loop controlling cool rates in pluton-host rock systems. Redrawn from Knapp (1978).

2.5.1. In-situ Stress

The overburden in-situ stresses are commonly defined in terms of vertical stress (σ_V), maximum horizontal stress (σ_H) and minimum horizontal stress (σ_h) (e.g., Gudmundsson, 2011, 2012). Vertical stress and horizontal stress can be approximate from the weight of overlying rocks:

$$\text{Vertical stress,} \quad \sigma_V = \int_0^z P(z) g dz \quad (1)$$

$$\text{Horizontal stress,} \quad \sigma_H = \sigma_h = \int \frac{\nu^* p g z}{1-\nu} \quad (2)$$

Where p is density (kg/m^3) of the overburden, g is the gravitational acceleration (9.8066 m/s^2), z is depth (positive downwards) and ν is the Poisson's ratio (Gudmundsson, 2012).

The in-situ stress field may be modified by regional tectonic loading or as a result of local structures such and faults and folds (e.g., Price and Cosgrove, 1990) influencing the orientation and magnitude of the resulting principal stress. Stresses in the host rock may also be modified by or during the emplacement of intrusive bodies (e.g., Anderson, 1951; Ode 1957; Robson and Barr, 1964; Cummings, 1968; Roberts 1970; Gudmundsson, 2006, 2012). As magma has low shear strength under static conditions (Poisson's ratio ~ 0.5), the initial conditions at the point of solidification are typically lithostatic where $\sigma_V = \sigma_h = \sigma_H$.

2.5.2. Cooling

Fracturing is expected where thermal stress change overcomes the sum of material tensile strength (typically in the range of 7 – 25 MPa) and compressive crustal stress. The lateral normal stress change ($\Delta\sigma$) for a given temperature change (ΔT) of a laterally constrained, isotropic cooling material under constant pressure is (Haxby and Turcotte, 1976):

$$\Delta\sigma = \frac{\alpha E}{1-\nu} \Delta T \quad (3)$$

Where α is the coefficient of thermal expansion and E is the Young's modulus.

For intact granite with a Young's modulus (E) of 10 – 70 GPa, Poisson's ratio (ν) 0.25 and coefficient of thermal expansion (α) $8 \times 10^{-6} \text{ } ^\circ\text{C}^{-1}$ (Skinner 1966) then tensile stress occurs at a rate

between 11 MPa and 75 MPa per 100°C temperature decrease. The temperature drop required to counteract crustal load would also be greater at depth and for smaller values of E or larger values of ν and α (Nadan and Engelder, 2009). Changes in stress caused by thermal gradients will therefore decrease with cooling of the pluton until normal crustal temperature is attained (Knapp and Norton, 1981).

2.5.3. Fluid Pressure

Fluid pressure increase results in fractures being brought closer to failure (e.g., Hickman et al. 1995 and references therein). Fluid exsolution from hydrous magmas and later meteoric waters are important for economic mineralisation. A wide range of fluid pressures associated with intrusive bodies can be expected (e.g., 0 – 500 MPa: Burnham, 1979). Uncertainty exists in understanding the time and pressure of initial fluid exsolution and transition from the magmatic to hydrothermal stage of fluids in plutonic systems (e.g., Fournier, 1999, 2007).

Pore fluid pressure is generally considered to be hydrostatic (equal to the weight of a column of water). This may be maintained to depths of ~ 12 km (Zoback and Townsend, 2001). In magmatic systems, pore fluid pressures may also exceed hydrostatic conditions to become suprahydrostatic (Hantschel and Kauerauf, 2009) or trend toward lithostatic conditions (equal to vertical stress equation 1 p.30). In and around magmatic bodies pore fluid pressure is likely to be heterogeneous; pore fluid pressure around magma bodies is likely to be similar to the magma pressure but may quickly decrease within tens of meters to hydrostatic or suprahydrostatic conditions, dependent on the depth (confining pressure) and the presence of a hydrothermal systems (Albino et al., 2018). Increasing pore fluid pressure reduces normal stress and favours Coulomb shear failure. The two commonly applied end-member numerical models of pore fluid pressures round magmatic bodies are (1) some fluid present in host rocks and pore fluid equals lithostatic pressure and (2) at the contact of a magmatic body and host rock, the presence of pre-existing fluid is negligible resulting in zero fluid pressure. Both models are applied to understand failure around magmatic bodies or the propagation and eruption of magmatic chambers (e.g., Gudmundsson, 2012 and references there in).

Models of early fracturing within plutonic rocks, as a result of thermal stresses, focus on conductive cooling and do not account for fluid pressures (See section 2.4.2 p.27 – 28). This is because conductive cooling is likely to dominate the early cooling history of plutonic bodies and early thermal stress history prior to the development of advective cooling processes (e.g., Jaeger and Carslaw, 1959; Knapp and Norton, 1981; Gerla, 1988; Bergbauer et al., 1998). This assumption allows simplification of numerical models.

2.6. Experimental Cooling Fractures and Temperature Dependent Properties

2.6.1. Experimental Cooling Fractures

Rock fracture experiments investigating the response of rocks to high temperature and differential cooling have application to rock excavation (i.e., tunnelling and drilling) generally highlight the weakening of the bulk strength of rocks due to an increase in microcracking (e.g., Bahr et al., 2010; Ge and Sun, 2018; Liu et al., 2020 and references there in). Experiments also highlight changes in the material and mechanical properties as a result of temperature change (see section 2.6.2 p.32 – 33). Acoustic emission data recorded from experimental studies of heated and cooling igneous rock samples can be used to accurately determine the internal damage as a result of microcracking within the rock. Results of these experiments suggest that mechanisms of crack fraction during cooling are different from those formed by heating as the rate, as the energy of acoustic emission is consistently much higher during cooling than during heating (e.g., Browning et al., 2006, Ge and Sun, 2018). Results have also been used to infer that seismogenic faulting may occur within magmas at eruptive temperatures (e.g., Tuffen, 2008) suggesting that high temperature fracturing occurs during cooling and solidification of magmatic bodies.

Thermal fractures are also well studied in material science for metals (e.g., Collin and Rowcliffe, 2002), cements (e.g., Fu et al., 2007; Hubbell and Glisic, 2013), ceramics (e.g., Bazazzadeh et al., 2020, and references there in), glass (e.g., McJunkins and Thornton, 1973; Dembele et al., 2012) and ice (e.g., Petrovic, 2003; Xu and Prakash, 2015), applicable to a wide range of manufacturing, engineering and stability studies. Results from these studies, in relation to rock failure, can only be considered in a general way as unlike rocks materials are typically homogenous and isotropic.

2.6.2. Temperature Dependent Material and Mechanical Properties

Temperature-related physical and mechanical properties influence the mechanical behaviour of rocks and may therefore impact the failure of a rock mass. Changes in temperature dependent material and mechanical properties of rocks are highlighted in experimental studies (e.g., Hezue, 1983; Saiang, 2012; Waig and Konietzky 2019). Temperature influences both the material (i.e., heat capacity at constant pressure, thermal conductivity, coefficient of thermal expansion, Young's modulus and Poisson's ratio) and mechanical properties (i.e., tensile strength, uniaxial compressive strength, cohesion and friction angle).

Temperature dependent material properties (See appendix A Tables A3-2 to A3-4 p.305 - 306 for tabulated values) are variably influenced by temperature and may either increase (i.e., heat capacity at constant pressure), decrease with increasing temperature (i.e., thermal conductivity and Young's modulus), both increase and decrease (i.e., coefficient of thermal expansion) or vary depending on the rock type (i.e., Poisson's ratio) (e.g., Hezue, 1983; Saiang, 2012; Waig and Konietzky 2019). Accounting for the temperature dependence of material properties, the solid elastic thermomechanical parameter (the product of the Young's modulus and coefficient of thermal expansion), which transforms thermal energy changes into initial stresses in cooling plutons (Knapp 1978), will initially increase with decreasing temperature before increasing. Accounting for temperature dependent material properties will therefore initially increase the values of predicted thermal stress. Properties influencing the mechanical response of the rock (i.e., tensile strength, uniaxial compressive strength, cohesion and friction angle) all decrease as temperature increases (see appendix A Table A3-5 p.306 for tabulated values) reducing the strength characteristic of the rock mass and increasing the likelihood of failure.

Large variations in temperature (> 500 °C) as plutons cool can cause a significant variation in the material and mechanical properties of rocks. Equations based on data collected from experimental studies of rocks at high temperature can be incorporated directly into modelling software (e.g., Žák et al., 2006; Nabelek et al., 2012; Gelman et al., 2013). For example, in the case of work by Nabelek et al., (2012) including temperature dependent properties (thermal diffusivity and heat capacity) is shown to increase the longevities of magmatic systems prior to crystallisation and cooling.

2.7. Summary

Fractures in plutonic rocks are important in governing the characteristics of the rock mass including the porosity and permeability which control fluid flow. Being able to define patterns and predict spatial variability of fractures is key for the study of sub-surface fluid flow and geotechnical construction projects.

Early fractures formed in plutonic rocks are likely to be related to cooling processes. Early fractures are important as they are likely to influence later fracturing events. The processes of natural fracture formation in plutonic rocks cannot be observed, so understanding the processes can only be addressed through field observations, experimental and numerical modelling. By understanding stress histories and likely fracture styles related to cooling it should be possible to determine, by comparison with field examples, if thermomechanical modelling provides a useful tool to produce attribute maps for the numerical modelling of fracture networks in plutonic rocks. Comparison between numerical models and field data is likely to be complicated due to the diversity of styles of plutonic bodies, later overprinting from tectonic and exhumation fracture histories, and the ability to identify early formed fractures, which is generally far from obvious.

3. Thermomechanical Modelling

This chapter focuses on development of numerical models for prediction of stress build-up in cooling plutonic bodies. Predicted stress values are compared to failure criteria to determine the potential for fracturing and failure mode. The models are set up in COMSOL Multiphysics® (part 1 p.47 - 72). COMSOL Multiphysics® is a commercial finite element software (www.comsol.com) allowing multi-physics (i.e., heat transfer, solid mechanics, fluid flow etc) problems to be solved. The software can be used to calculate the distribution of stress, strain related to thermal and mechanical forces and to assess the location of rock failure. COMSOL Multiphysics® provides a platform for models to be extended into three-dimensions allowing the influence of geometry and emplacement depth. Comparison of previously published two-dimensional models and equivalent models set up in COMSOL Multiphysics® is given in part 2 (p.73 – 104). A full assessment of the effect of temperature dependent material and mechanical properties is carried out (part 3 p.105 - 130) and the impact of applying different failure criteria is assessed (parts 1 and 3). The modelling workflow developed in this chapter is applied to two examples in chapters 4 and 5.

Results presented in parts 1 and 3, were given as a talk at the 2018 Tectonic Studies Group meeting (Ellis, J.F, Blenkinsop, T. and Davies, H. Numerical modelling of stress and fracture evolution in 3-dimensional cooling bodies).

Appendix A (p.304 - 331) contains additional information on the failure criterion setup in COMSOL®, tables of the applied material and mechanical properties and figures of temperature, stress and strain magnitudes for selected points in each of the models run.

Numerical models in COMSOL Multiphysics® are calculated using the engineering convention where that σ_1 is the most tensile stress and σ_3 in the most compressive stress. Results of models presented in part 3 of this chapter are however converted to the geological convention where σ_3 is the minimum tensile stress and σ_1 in the maximum compressive stress.

List of notations given in chapter 3

Notation	SI unit	Variable Description
ρ	kg/m ³	Density
C_p	J/(kg.K)	Specific heat capacity
T	K	Absolute temperature
t	years (a)	Time
\mathbf{u}	m/s	Velocity vector of translational motion
\mathbf{q}	W/m ²	Heat flux
k	W/(m.K)	Thermal conductivity
Q	W/m ⁻³	Heat at source or sink
F	N/m ³	Body force per volume
σ_c	Pa	Cauchy stress tensor
σ	Pa	Stress tensor
σ_0	Pa	Initial stress
I_1	Pa	first invariant of the stress tensor
J_2	kg ² /(m ² *s ⁴)	second invariant of the deviatoric stress tensor
σ_1	Pa	Maximum principal stress † (red)
σ_2	Pa	Intermediate principal stress † (green)
σ_3	Pa	Minimum principal stress † (blue)
ϵ_e	-	Elastic strain
ϵ_{th}	-	Thermal strain tensors
ϵ	-	Infinitesimal strain tensor
ϵ_0	-	Initial strain
D	Pa	Stiffness or elasticity matrix
E	Pa	Young's modulus
ν	-	Poisson's ratio
α	1/K	Coefficient of thermal expansion
$E\alpha$	Pa	Solid thermo-mechanical parameter
T_{ref}	K	Strain-free reference temperature
sV	Pa	Vertical load
sH	Pa	Maximum horizontal stress
sh	Pa	Minimum horizontal stress

g	m/s ²	Gravitational constant given as -9.8066
z	m	Depth (surface at 0, subsurface negative values)
μ	-	Coefficient of internal friction
C_0	Pa	Uniaxial compressive stress
T_0	Pa	Uniaxial tensile strength
S_0	Pa	Cohesion
ϕ	°	Internal friction angle
$\pm\theta$	°	Shear angle with respect to the maximum compressive stress
A	Pa	Material parameters of the Drucker-Prager criterion as defined in text
B	-	

3.1. Published Models of Fracturing Related to Cooling of Plutonic Bodies

As outlined in chapter 1 (section 1.2.4, p.4 – 5) thermomechanical modelling is used to predict stress orientation and magnitude in cooling plutonic bodies. The predicted stress is then used to infer fracture orientations (Knapp, 1978; Gerla, 1983; Bergbauer, 1998; Koenders and Petford, 2003; Žák et al., 2006; Mondal and Acharyya, 2018). In these models (Table 3.1) thermal histories are calculated based on the conductive cooling of an instantaneously emplaced hot body within a gravitationally loaded elastic crust.

The models are simplified to problems of heat conduction (e.g., Jaeger and Carslaw, 1959; Knapp and Norton, 1981; Gerla, 1988; Bergbauer et al., 1998; Bergbauer and Martel, 1999; Koenders and Petford, 2003; Žák et al., 2006) and discount other processes that may influence the cooling rate of the pluton (see section 2.5 chapter 2 p.29). This simplification is justified as conductive cooling is most likely to be the dominate mechanism of cooling in the early history of plutonic bodies (e.g., Jaeger and Carslaw, 1959; Knapp and Norton, 1981; Gerla, 1988; Bergbauer et al., 1998). As these numerical models only account for instantaneous emplacement and conductive cooling the models are most comparable to plutonic bodies that are (1) emplaced at rates greater than 2 cm / year, (2) have limited time gaps between incremental emplacement and, (3) in systems at early stages of cooling before significant fracturing of the host rock and/or development of hydrothermal systems.

Some of these models (Table 3.1) include regional tectonic loading (Gerla, 1983; Bergbauer, 1998; Bergbauer et al., 1998; Bergbauer and Martel, 1999) and magmatic pressure (Knapp, 1978; Gerla, 1983; Žák et al., 2006). Apart from the model by Knapp (1978) phase change of the plutonic body is not considered and the material properties of the pluton are defined as elastic. Material properties (i.e., Young's modulus, Poisson's ratio, coefficient of thermal expansion) are only defined as temperature-dependent in models by Knapp, 1987 and Žák et al., 2006. Mechanical properties (i.e., tensile strength and compressive strength) are only defined as temperature-dependent by Žák et al., (2006). Temperature dependence of material and mechanical properties are not accounted for in any of the other numerical models (Table 3.2).

Failure criteria are specified by Knapp (1978); modified Navier-Coulomb, Gerla (1983); Navier-Coulomb and Žák et al. (2006); Drucker-Prager. Martel and Bergbauer (1997) assume that all fracturing is tensile, resulting in vertical fractures parallel to the modelled maximum principal stress direction (Table 3.1).

Table 3.1. Published models of fracturing related to cooling of plutonic bodies

Geometry	Software Method	Modelled Behaviour	Failure Criterion	Reference
2D vertical elongate dyke Emplacement depth 4.5 km Dimensions 4.5 km by 3 km	Bespoke Finite difference	viscoelastic to elastic	modified Navier- Coulomb	Knapp (1978) Knapp and Norton (1981)
2D map of a statically pressured hole, representation of the Diamond Joe stock, Arizona Emplacement depth 1 – 2 km Dimensions radius 4 km	Bespoke Unknown	elastic	Navier- Coulomb	Gerla (1983, 1988)
2D map; circle, rectangle, hourglass Emplacement depth 8.6 km Lake Edison Granodiorite, California Emplacement depth 8 km Dimensions ~50 km up to 4 km Cartridge Pass Granodiorite, California Depth 8 km Dimensions ~50 km up to 4 km	MATLAB Fast Fourier transform	elastic	assumed to be tensile	Martel and Bergbauer (1997) Bergbauer (1998) Bergbauer et al. (1998) Bergbauer and Martel (1999)
2D section rectangle Dimension ratio 2:1	Bespoke Analytical	elastic	none	Koenders and Petford (2003)
2.5D horizontal slice of the Tanvald pluton, Bohemian Massif Europe Emplacement depth 8 km Dimensions ~70 km by 2.5 km	ADINA v. 8.3.1 Finite element	elastic	Drucker- Prager	Žák et al. (2006)
2D map of the Chaitradurga granite Dharwar craton, south India Emplacement depth 6 km Dimensions ~60 km by 10 km	Fast Fourier transform after Bergbauer and Martel (1999)	elastic	Assumed to be tensile	Mondal and Acharyya (2018)

Table 3.2. Elastic material properties for models given in Table 3.1

Reference	Rock type	Poisson's ratio	Young's Modulus	Coefficient of thermal expansion	Solid thermo-mechanical parameter *	Thermal diffusivity
			GPa	1/K	MPa °C ⁻¹	m ² /s
Knapp (1978) §	Tonalite	0.22 †			0.25 – 0.5 ‡	
Gerla (1988)	Granitic	0.22 †			0.48	
Martel and Bergbauer (1997)	Granodiorite	0.3 ††	30.4 ††	8 x 10 ⁻⁶ ††	0.24	1.4 x 10 ⁻⁶ §§
Bergbauer et al. (1998)	Granodiorite	0.25	30.4 ††	1.8 x 10 ⁻⁶ **	0.24 ***	1.37 x 10 ⁻⁶ †††
Mondal et al. (2018) ††††						
Bergbauer and Martel (1999)	Granodiorite	0.25	30.4 ††	8 x 10 ⁻⁶ ††	0.24	2.45 x 10 ⁻⁶ †††
Zak et al., (2006) ****	Granite §§§	0.11 0.449 when temperature > intrusion temperature	Linear decreases from 56 at 20 °C ^ to 0 at 1100 °C	Linear increase from 0 at 20 °C ^ to 15e-6 at 700 °C	0.011 at 21 °C to 0.2 at 874 °C below and above these temperature then 0	
	Phyllite §§§	0.2	Linear decreases from 76.5 at 20 °C ^ to 0 at 1100 °C	Not given assumed to be the same as granite	0.015 at 21 °C to 0.27 at 874 °C below and above these temperature then 0	

* Product of the Young's Modulus and coefficient of thermal expansion. Increasing in the solid thermomechanical parameters increases the thermal stress magnitude

** Value reproduced from paper, however this is likely to be a type error, the value should be 8 x 10⁻⁶

*** Value calculated using correct coefficient of thermal expansion value, 8 x 10⁻⁶

**** only model to include different material properties in host rock.

† Birch (1966)

†† Carmichael (1989)

††† Carslaw and Jaeger (1959)

†††† Values after Bergbauer et al. (1998)

‡ range dependent on temperature, lower value at lower temperatures and higher pressures.

‡† Skinner (1966)

‡†† Calculated by trail and error

§ only elastic properties shown, applies different values for magmatic liquid phase.

§§ Incropera and DeWitt (1990)

§§§ Values modelled with a temperature dependence based on measurements published in Heuze (1983)

^ Assumed temperature, just stated as room temperature in the paper.

With the exception of Žák et al. (2006) (Figure 3.1), numerical models convincingly demonstrate that thermal stress plays an important role in the formation of fractures in cooling plutons (Knapp, 1978; Gerla, 1983; Bergbauer, 1998; Koenders and Petford, 2003). Importantly, these models highlight that the initial geometry of the pluton and orientation of regional loads influence the magnitude and orientation of the developed stress field (Gerla, 1983; Bergbauer, 1998; Bergbauer et al., 1998). Models of idealised two-dimensional geometries (e.g., circles, rectangles) reveal that the most compressive stress direction within a cooling body preferentially align to the margin geometry (Figure 3.2).

Variation in the predicted orientations with depth in the vertical section of an infinitely elongate dyke is also observed (Knapp, 1978); being vertical at the top, horizontal in the middle and both vertical and horizontal near the bottom (Figure 3.3 A). In the host rocks which experience initial heating and then cooling the most compressive stress direction preferentially parallels the margin of the plutonic body (Figure 3.3 A). Application of the Navier-Coulomb failure criterion (Knapp, 1978; Gerla, 1983) predicts that within the pluton, shear failure is likely to occur prior to tensile failure (Figure 3.3 B).

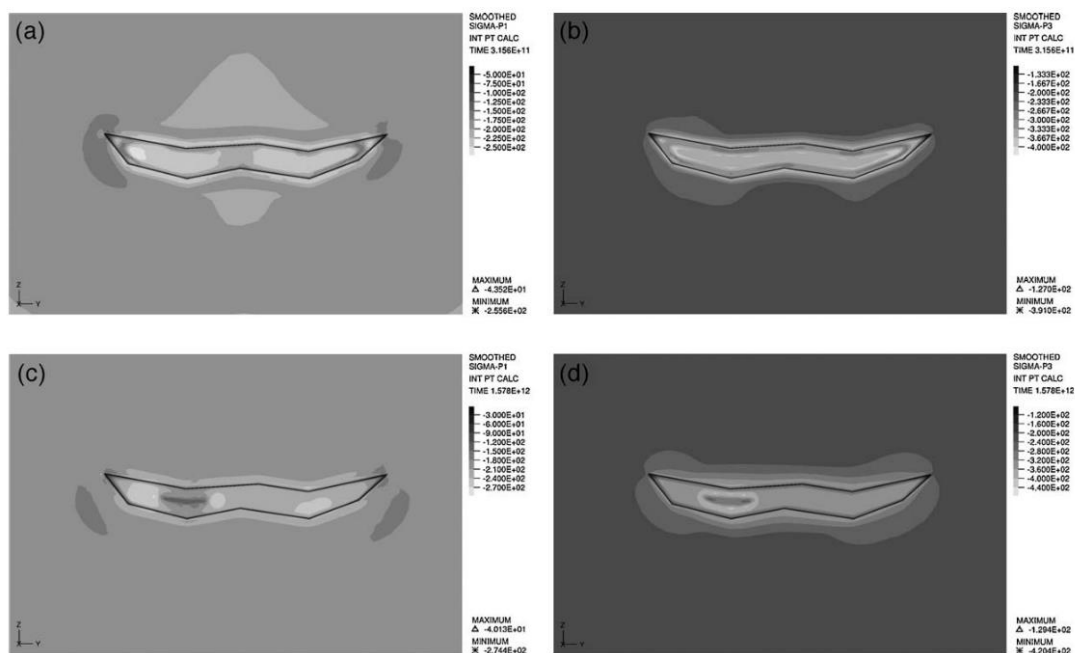


Figure 3.1. Numerical model of the Tanvald pluton contoured for the maximum (P1) and minimum (P3) principal stresses (MPa), compression negative. Top row (a & b), 10,000 years after model initiation and bottom row (c & d) 50,000 years after model initiation. Principal stress remain compressive over time and the Drucker-Prager yield criterion is not exceeded. Image from Žák et al. (2006). Copyright (2006), *Fig.19 p.303* with permission from Elsevier.

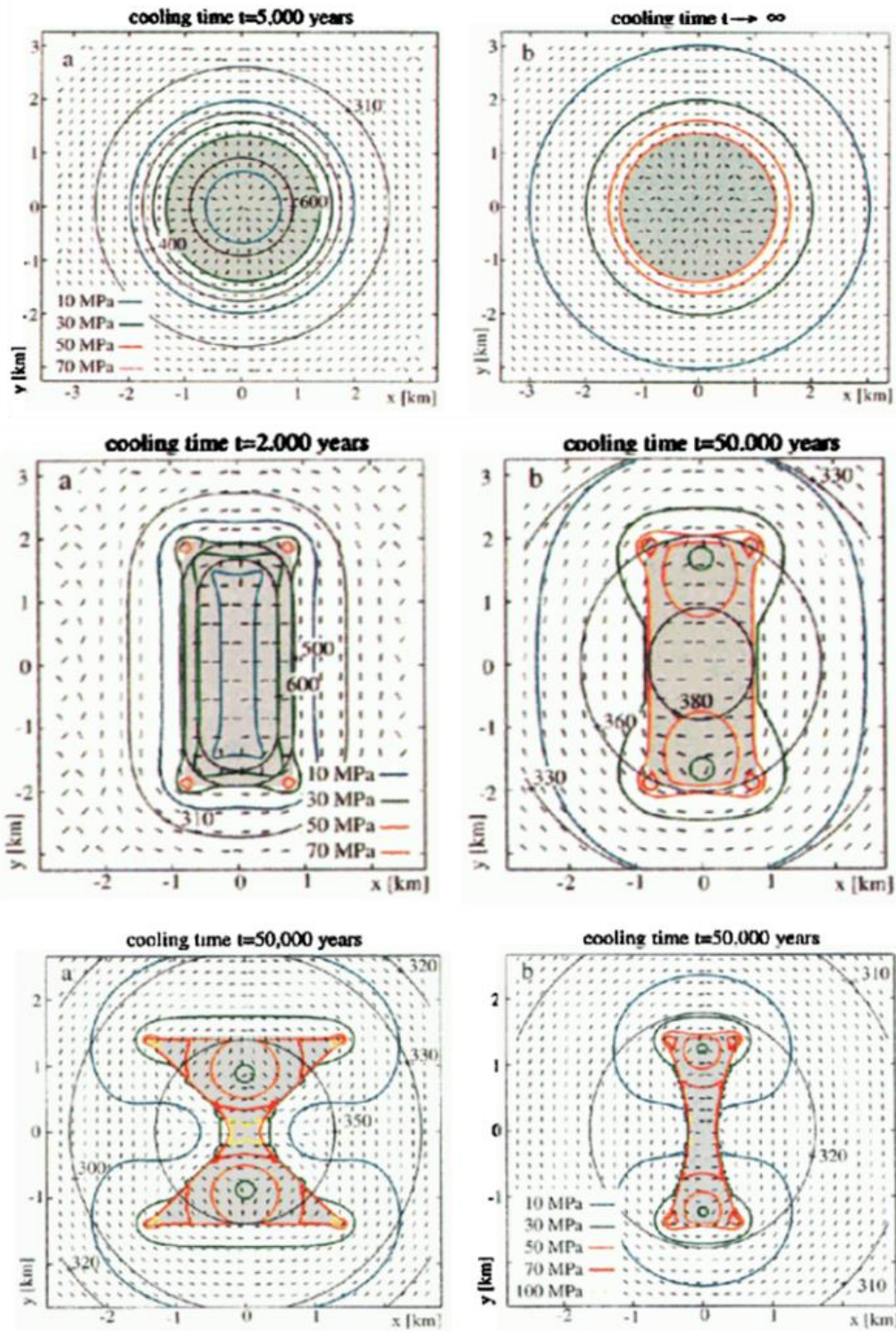


Figure 3.2. Development of stresses within plutons (grey) and host rock in map view for given time steps for a circular, rectangular and hourglass intrusions. Coloured contours show most tensile stress magnitudes and black contours the temperature for the given time after emplacement. Tick marks are perpendicular to the direction of most tensile stress. In circular intrusions, the direction of maximum compressive stress is therefore radial. In rectangular geometries, away from the margins, the maximum principal stress preferentially aligns to the short axis. From Bergbauer et al. (1998). Copyright (1998) *Fig.1 - 3 p.709 AGU.*

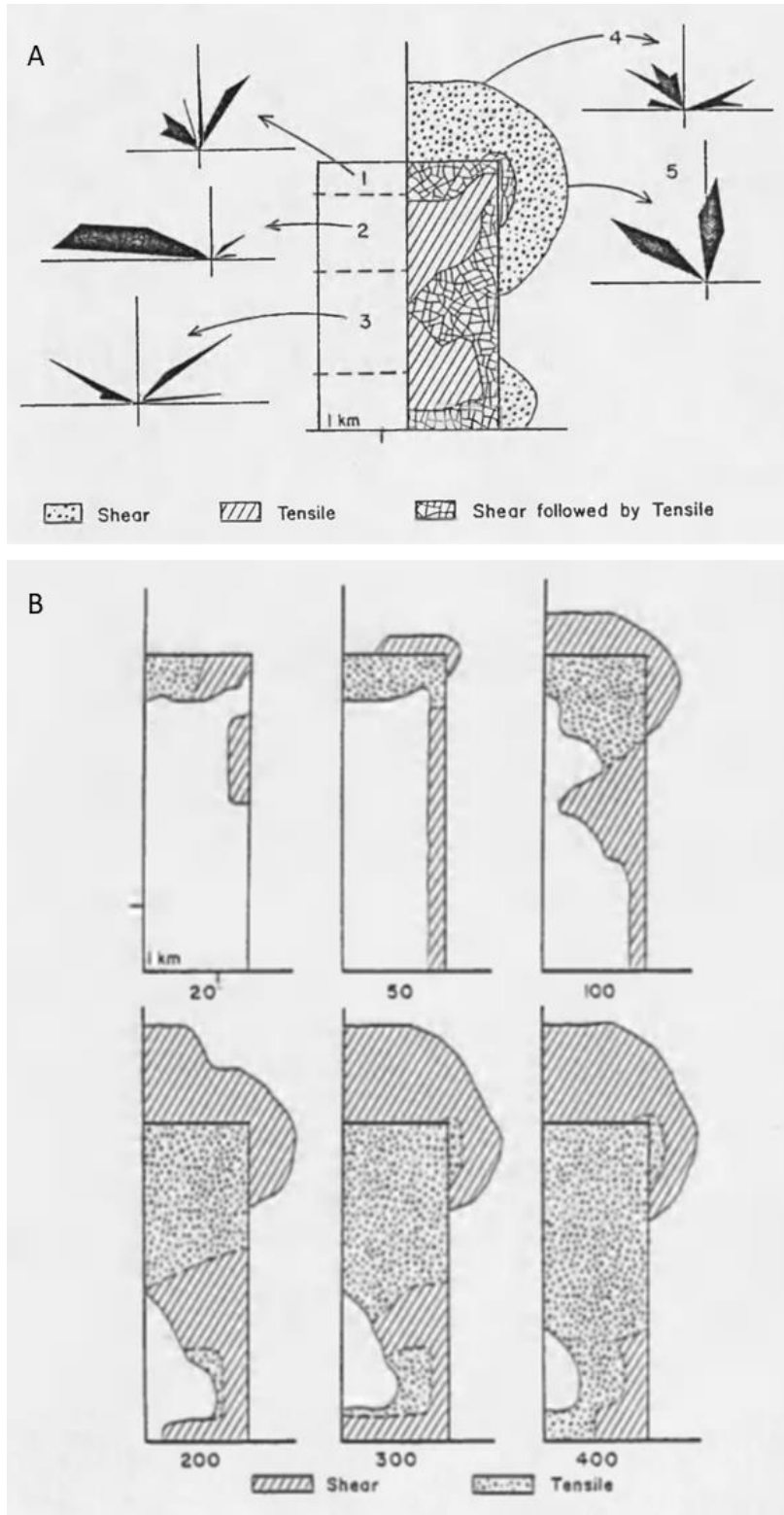


Figure 3.3. Vertical slice through an infinitely elongate dyke (two-dimensional plane strain model) showing the computed state of stress in terms of brittle failure regimes, (A) dips of thermal fracture planes, the rose diagrams represent the relative abundance of thermal fracturing events. (B) variation in brittle failure regimes over time, shown for pluton around the symmetry axis, numbers are for thousands of years since model initiation. Images from Knapp 1978. Copyright (1978) *Fig.25 p.100 Fig.24 p.98* granted by R. Knapp.

Martel and Bergbauer (1997) were the first to apply a numerical model to a mapped pluton boundary (also see Bergbauer, 1998; Bergbauer et al., 1998; Bergbauer and Martel, 1999). Modelling results were interpreted to show a better match between the orientations of photolineament orientations when a tectonic load was applied to the numerical model (Figure 3.4). Mondal and Acharyya (2018) applied the workflow developed by Bergbauer et al. (1998) to the Chaitradurga granite. Modelling results were used as evidence that joints found within enclaves could be used as a reliable paleostress indicator (Mondal and Acharyya, 2018).

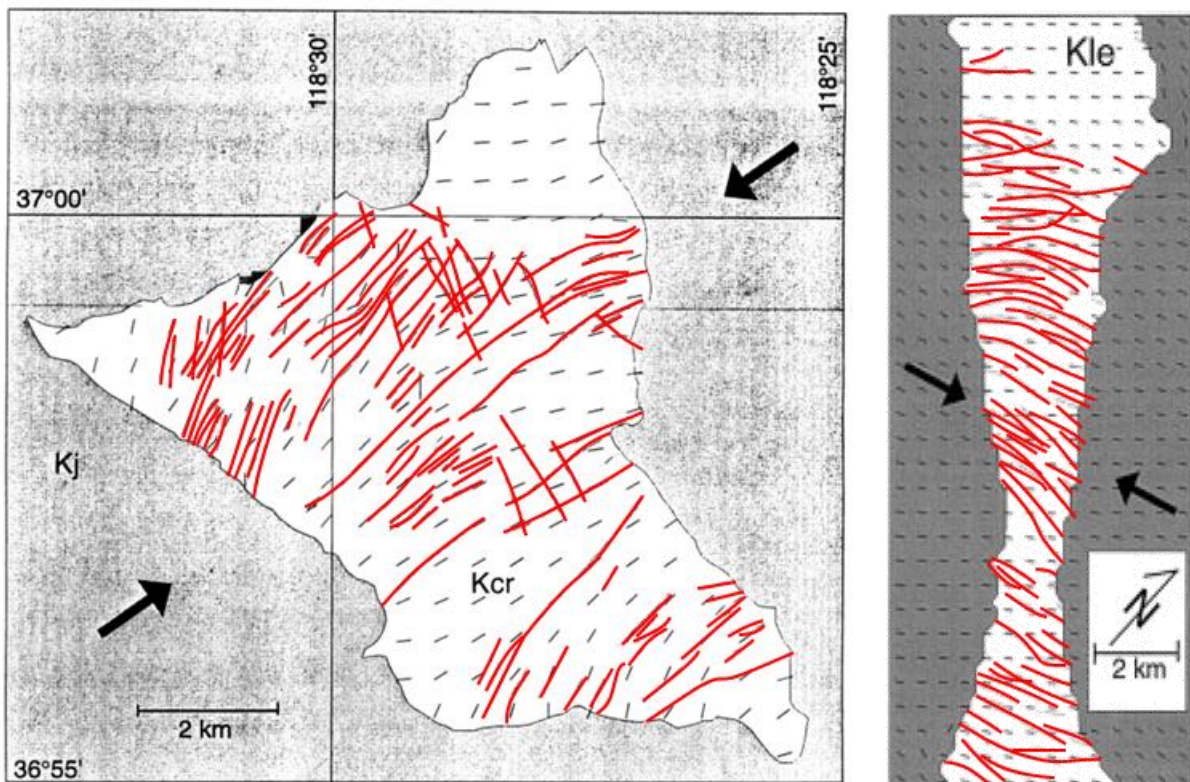


Figure 3.4. Comparison of numerical models (short black ticks) and photolineament interpretation (red lines). Short black ticks are the modelled most compressive stress trajectories due to thermal and regional tectonic stresses. (A) Granodiorite of Cartridge Pass at 0.9 million years after cooling and (B) Lake Edison Granodiorite after 86 million years of cooling. Black arrows show the direction of the applied regional most compressive horizontal stress. Images modified from Bergbauer and Martel (1999). Copyright (1999) *Fig.7 p.831 Fig.8 p.833* with permission from Elsevier.

As well as predicting fracture orientation and failure mode in cooling plutons Gerla (1983) suggested that calculated strain energy (J/m^3) can be used to predict relative fracture densities (Figure 3.5), where the maximum strain energies predicted are assumed to correspond the highest fracture densities. In the numerical models the highest strain energies are located near pluton margins (Gerla, 1983; Bergbauer and Martel, 1999; Koenders and Petford, 2003) and in locations where the direction of thermal and tectonic maximum principal stresses align (Gerla, 1983).

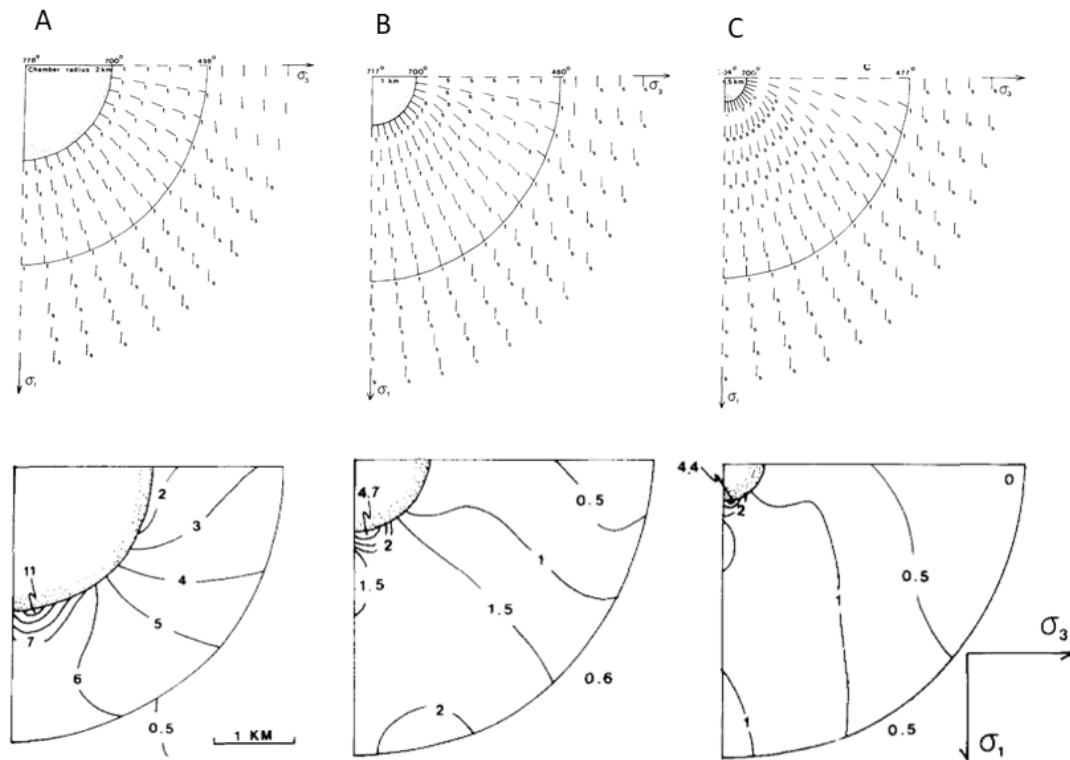


Figure 3.5. Stress and strain energy predicted in a pressured cylinder for varying chamber radius. Top row: Solid lines strike of predicted vertical fractures based on the direction of maximum compressive stress, dashed lines represent areas that are not in failure. Horizontal stresses are set to 135 MPa in the y direction and 45 MPa in the x direction. For 4 km radius pluton with (A) 2 km radius magma chamber, (B) 1 km radius magma chamber and (C) 0.5 km radius magma chamber. Magma pressure is set to 135 MPa in models with a 2 and 1 km radius magma chamber and 162 MPa for the model with a 0.5 km radius magma chamber. Bottom row: Contoured theoretical elastic strain energy at three stages of crystallization (J/cm^3). Dotted contour lines indicate values of strain in areas that are predicted not to fracture. From Gerla (1988). Copyright (1988) *Fig.9 p.278* with permission from Elsevier.

Suggested extensions to thermomechanical modelling as outlined in previous publications include accounting for:

- (1) three-dimensional geometry and the influence of depth on stress magnitudes and orientations (e.g., Bergbauer et al., 1998; Žák et al., 2006)
- (2) material property variation (Knapp and Norton, 1981; Bergbauer et al., 1998), including both the spatial and temporal variation of material properties (Bergbauer et al., 1998)
- (3) the effect of stress redistribution due to fracturing (Bergbauer et al., 1998)
- (4) the effect of convective heat transfer during and after fracturing (Knapp and Norton, 1981; Bergbauer et al., 1998)
- (5) incremental emplacement of magma bodies of different sizes (Knapp & Norton 1981, Bergbauer et al., 1998, Koenders & Petford 2003)

The first two suggestions are investigated in this chapter in parts 1 and parts 3, respectively.

Part 1

3.2. COMSOL® Model Setup

3.2.1. Software

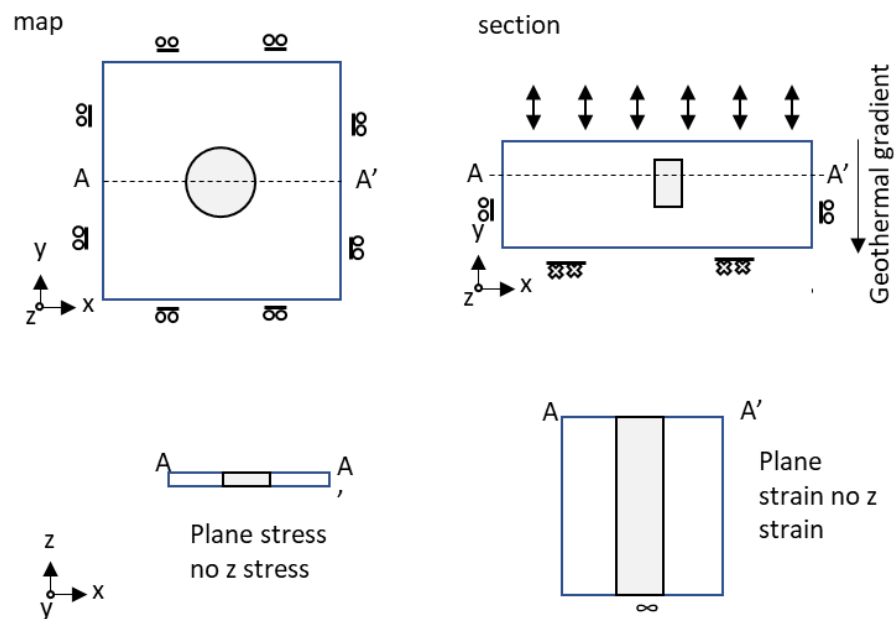
Three-dimensional thermomechanical modelling is used to assess the effect of geometry, emplacement depth and material and mechanical properties on likely fracture patterns resulting from the cooling of plutonic bodies. In this study numerical models are run using COMSOL® Multiphysics (version 5.3).

The commercial software package COMSOL Multiphysics® uses the finite element method (FEM) to solve constituent partial differential equations (PDEs) which describe physical phenomena (Zimmerman, 2006). The Heat Transfer and Structural Mechanics Modules are used to compute temperature and stress (orientation and magnitude) in a cooling volume over time. Problems can be solved in two- and three-dimensions (Figure 3.6).

The theory behind COMSOL Multiphysics® is well document (e.g., Pepper and Heinrich, 2017) and the workflows detailed in published manuals (e.g., Introduction to COMSOL Multiphysics © 1998–2019 COMSOL and COMSOL Multiphysics User’s Guide © 1998–2012 COMSOL). The theory and constitutive equations used for the thermomechanical modelling of cooling plutons are outlined in section 3.2.3 (p.50 – 51). A fully coupled approach can be implemented to solve all set of equations for thermal change and mechanical stress in the same simulation. An implicit backwards differentiated formula (BDF) method is used to integrate the PDEs in time (Zimmerman, 2006).

COMSOL Multiphysics® was selected for modelling as it has been widely used for solving thermal and mechanical problems in volcanology (Table 3.3) and allows focus to be placed on modelling rather than coding. COMSOL Multiphysics® provides a platform for potential model extension through the additional of additional physics modules, such as including fluids or accounting for phase change.

Two-dimensional



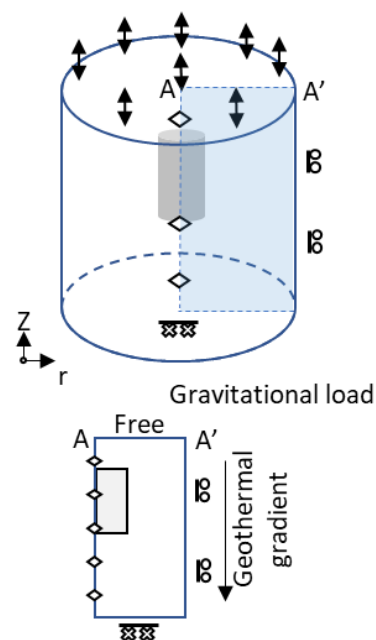
Modelling domain 2D

Modelling plane strain $\sigma_H = \sigma_h > \sigma_V$ OR $\sigma_h < \sigma_H < \sigma_V$
 or stress $\sigma_H = \sigma_h$ or $\sigma_H > \sigma_h, \sigma_V = 0$

Plane stress assumes thin plate

Plane strain model is infinitely long in out of plane direction i.e. dyke

Axisymmetric

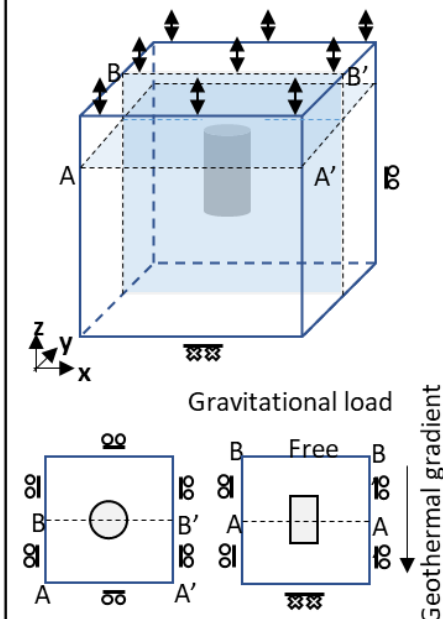


Modelling domain 2D

axisymmetric
 $\sigma_H = \sigma_h > \sigma_V$

Model pluton with central symmetry i.e. cylinder or sphere

Three-dimensional



Modelling domain 3D

$\sigma_H = \sigma_h < \sigma_V$
 $\sigma_h < \sigma_H < \sigma_V$ where σ_h can be extensional or compressional

Allows for 3D non symmetrical models

Figure 3.6. Modelling dimensions and boundary set up in COMSOL Multiphysics®

Table 3.3. Publications using COMSOL® to solve thermal and mechanical problems in volcanology

Reference	Study purpose	Modelling dimensions	Naiver-stocks chemical transport	Thermal conduction	Thermal convection	Stress
Bazargan et al. (2019)	Crystal orientation in viscous flow	2D	x			
Elshaafi and Gudmundsson (2018)	Distribution of stress field between magma reservoirs in Libya	2D and 3D				x
Launay et al. (2018)	Relationship between fluid velocity and growth rates in Panasqueira ore deposit Portugal	1D	x			
de Wall et al. (2018)	Thermal modelling granites Fanconian Basin, Bayreuth Granite	2D		x		
Vachon (2018)	Modelling physical processes in magmatic systems	2D Asymmetrical				x
Mattsson et al. (2018)	Cooling of the Sandfell-laccolith, Iceland	Asymmetrical		x		
Browning and Gudmundsson (2015)	Crustal and ice-sheet response to vertical displacement in chamber roof	Asymmetrical				x
Molina et al. (2015)	Thermal cooling of the Caleu pluton	Asymmetrical		x		
Závada et al. (2015)	Conductive cooling model for intrusive and extrusive bodies for comparison with the pattern of columnar joints formed at the Devils Tower	2D – section		x		
Hickley and Gottsmann (2014)	Benchmarking volcanic deformation in COMSOL®	Asymmetrical		x		x
Gelman et al. (2013)	Conductive cooling of incrementally assembled magma chamber	Asymmetrical		x		
Gutierrez et al. (2013) Similar modelling extended by Payacan et al. (2015) Aravena et al. (2017)	Magmatic fluid dynamic numerical simulation in La Gloria Pluton Chile	2D	x		x	
Alvarado et al. (2013)	Thermal modelling Central System batholith Spain to constrain the thermal effects of newly emplaced magma batches on previously emplacement magma bodies	2D – section		x		
Hickley et al. (2013)	Uplift above the Uturuncu volcano	Asymmetrical				x
Steinberger et al., (2013)	Estimate maximum cooling time of laccolith in Utah based on conductive cooling	2D – section		x		
Bea (2010)	Crystallization dynamics in cooling magma chamber	2D section			x	
Annen (2009)	Conductive cooling of incrementally assembled magma chamber (note modelling software not specifically stated in this paper but assumed to be COMSOL® based on Gelman et al 2013)	Asymmetrical		x		
Burchardt (2009)	Testing mechanical aspects of conceptual model of evolution of the Njardvik Sill.	2D – section				x
Gutiérrez and Parada (2008)	Differentiation and crystallization dynamics in cooling magma chamber	Asymmetrical	x		X	

3.2.2. Model Overview

Numerical models are extended into three-dimensions based on the two-dimensional workflows presented in Martel and Bergbauer (1997), Bergbauer (1998), Bergbauer et al. (1998) and Bergbauer and Martel (1999). A hot body of a given geometry, representing the plutonic body, is modelled inside a gravitationally loaded block representing the host rock with a given geothermal gradient. Elastic stress and strains as a result of cooling of the plutonic body are calculated and provide time-dependent values of magnitude and orientation for the predicted thermomechanical stress at any given point within the model. These values are compared against failure criterion and the likelihood of fracture, as a result of plutonic cooling, is assessed.

The defined plutonic body is assumed to be emplaced instantaneously within the isotropic host rock. The host rock boundaries are extended to ensure that edge effects are negligible. Applied boundary conditions are dependent on the modelling domain (Figure 3.6). The initial conditions of geometry, depth, initial temperature of the pluton, initial geothermal gradient of the host rock, tectonic load, material properties, mechanical properties and failure criteria are defined (section 3.3.2). The initial conditions are varied to test the implications of geometry, depth, regional load, and the material and mechanical properties (part 3).

3.2.3. Model Calculations

Calculation of Thermal Stresses

In COMSOL® thermal stress analysis (using the engineering convention of tension positive) is completed by coupling the Heat Transfer in Solids (i.e., the temperature field) with Solid Mechanics (i.e., structural mechanics analysis) modules (equations 4 to 7). The model is fully coupled and solves the localised heat balance (equation 4) for heat transfer in solids over time:

$$\rho C_p \frac{\partial T}{\partial t} + \rho C_p \mathbf{u} \cdot \nabla T + \nabla \cdot \mathbf{q} = Q$$

$$\mathbf{q} = -k \nabla T \quad (4)$$

Heat equation of heat transfer in solids

Where ρ is the density (kg/m^3), C_p the specific heat capacity at constant pressure ($\text{J}/(\text{kg}\cdot\text{K})$), T absolute temperature (K), t time, \mathbf{u} the velocity vector of translational motion (m/s and is = 0 in the

case of pure conduction), \mathbf{q} is the heat flux by conduction (W/m^2), k is the solid thermal conductivity (W/(m.K)) and Q is the heat source or sink (W/m^3). The first term on of equation 4 accounts for thermoelastic damping. The displacement rate \mathbf{u} is given in terms of the Cauchy stress tensor σ_c :

$$\rho \frac{\partial^2 U}{\partial t^2} - \nabla \cdot \sigma_c = F \quad (5)$$

Equation of motion for linear elasticity

where F is the body force per volume. Hooke's law (proportionality between stress and strain) is used to relate the stress and strain tensors. D is a symmetric 6×6 matrix. In the most general anisotropic case, the matrix contains 21 independent constants. For the isotropic case, it is a function of E and ν

$$\begin{bmatrix} \sigma_{xx} \\ \sigma_{yy} \\ \sigma_{zz} \\ \sigma_{xy} \\ \sigma_{yz} \\ \sigma_{xz} \end{bmatrix} = \mathbf{D} \begin{bmatrix} \varepsilon_{xx} \\ \varepsilon_{yy} \\ \varepsilon_{zz} \\ \varepsilon_{xy} \\ \varepsilon_{yz} \\ \varepsilon_{xz} \end{bmatrix} \quad \mathbf{D} = \frac{E}{(1+\nu)(1-2\nu)} \begin{bmatrix} (1-\nu) & \nu & \nu & 0 & 0 & 0 \\ \nu & (1-\nu) & \nu & 0 & 0 & 0 \\ \nu & \nu & (1-\nu) & 0 & 0 & 0 \\ 0 & 0 & 0 & \frac{(1-2\nu)}{2} & 0 & 0 \\ 0 & 0 & 0 & 0 & \frac{(1-2\nu)}{2} & 0 \\ 0 & 0 & 0 & 0 & 0 & \frac{(1-2\nu)}{2} \end{bmatrix}$$

3D generalization of Hooke's law

The infinitesimal strain theory relates the strain tensor and displacement gradient vectors as:

$$\varepsilon = \frac{1}{2} [\nabla u + \nabla u^T] \quad (6)$$

$$\varepsilon_{th} = \alpha(T - T_{ref}) \quad (7)$$

Thermal expansion

where α is the thermal expansion tensor and T_{ref} is the strain-free reference temperature. Thermal stress accumulates because of conductive cooling over time. It is assumed that thermal stresses are initially zero.

In-situ Stress

The gravitational load is set up as a uniaxial stress state (equations 1 & 2, p.30). In vertical sections, axisymmetric or three-dimensions, gravity is applied as a body load. The tectonic load may be added to the stress tensor.

Failure Criteria

By comparing the computed stresses with failure criteria the timing, location, orientation and failure mode of thermal-mechanical fractures can be predicted (Knapp, 1978; Gerla, 1983). For this study three failure criteria were selected and compared: Coulomb-Navier, Griffith & Griffith-Murrell and Drucker-Prager yield criteria.

The Coulomb-Navier and the Drucker-Prager yield criteria were selected for comparison with previous numerical modelling of fractures in cooling plutonic bodies (Knapp, 1978; Gerla, 1983; Žák et al., 2006). The Griffith failure was applied for domains of shear, extensional shear and tensile failure. The Griffith-Murrell criterion was selected as it accounts for the effect of the intermediate principal stress (Murrell 1963, 1964a,b) and allows for tensile failure at higher differential stress and is often considered to be geologically reasonable (Roberts, 1970; Colmenares and Zoback, 2002; Ma et al., 2012; Rahimi and Nygaard, 2015). In comparison the Coulomb-Navier criterion does not account for the intermediate principal stress and it tends to underestimate rock strength. While the Drucker-Prager criterion accounts for all three principal stresses, it tends to overestimate rock strength and when one or more of the principal stresses are tensile it does not give accurate predictions (Alejano and Bobet, 2012; Wojciechowshi, 2018).

These failure criteria are outlined below and presented on maximum and minimum compressive stress (σ_1 - σ_3) plots (assuming geological convention of compression positive) (Figure 3.7). Plotting in this way allows the stress variation for selected points over time to be graphically presented (Knapp, 1978; Gerla, 1983). These failure criteria are outlined below and application of the failure criterion in COMSOL® is given in the appendix A, Table A3-1 (p.304).

Coulomb-Navier Criterion

Failure is expressed in terms of the maximum (σ_1) and minimum (σ_3) compressive principal stress, for shear failure defined as:

$$\sigma_1 = C_0 + \sigma_3 \cdot \tan^2\left(\frac{\pi}{4} + \frac{\phi}{2}\right) \quad (8)$$

$$\text{When, } \sigma_1 < C_0 + T_0 \cdot \tan^2\left(\frac{\pi}{4} + \frac{\phi}{2}\right)$$

and for tensile failure:

$$\sigma_3 = -T_0 \quad (9)$$

$$\text{When, } \sigma_1 > C_0 + T_0 \cdot \tan^2\left(\frac{\pi}{4} + \frac{\phi}{2}\right)$$

where C_0 is the uniaxial compressive strength, T_0 is the uniaxial tensile strength and ϕ is the angle of internal friction (Paul, 1961; Jaeger and Cook, 1969). Tensile failure occurs perpendicular to the minimum principal stress direction. The angle of shear failure, with respect to the direction of maximum principal stress, is equal to:

$$\theta = \frac{1}{2} \tan^{-1} \left[\frac{1}{\mu} \right] \quad (10)$$

Shear failure angle with respect to the direction of maximum principal stress

Thus, the orientation of shear failure is related to the coefficient of internal friction. For $\mu = 1$ shear failure planes form at an angle (θ) of 22.5° to the direction of maximum principal stress and for $\mu = 0.6$ shear failure planes form at $\theta = 29.5^\circ$ to the direction of maximum principal stress.

The failure criteria for tensile strengths of 5 MPa and 13.5 MPa are represented on a σ_1 - σ_3 plot (Figure 3.7 A).

Griffith and Griffith-Murrell Criterion

The Griffith theory expressed in the form of principal stress is

$$(\sigma_1 - \sigma_3)^2 = 8T_0 (\sigma_1 + \sigma_3) \quad (11)$$

$$\text{When, } \sigma_1 + 3\sigma_3 > 0$$

and for tensile failure

$$\sigma_3 = -T_0 \quad (12)$$

$$\text{When, } \sigma_1 + 3\sigma_3 < 0$$

The shear domain can be further divided into conditions representing extensional-shear and shear (Murrell 1963, 1964)

$$\sigma_1 + 3\sigma_3 > 0 \text{ and } 4.828\sigma_3 < 0 \quad (13)$$

The shear angle $\pm\theta$ with respect to the maximum principal stress is related to the tensile strength and the difference of the maximum and minimal principal stresses and defined as;

$$\pm\theta = \frac{1}{2} \arccos \frac{4T_0}{\sigma_1 - \sigma_3} \quad (14)$$

This failure criterion has been extended into three dimensions by Murrell (1963):

$$(\sigma_1 - \sigma_2)^2 + (\sigma_1 - \sigma_3)^2 + (\sigma_2 - \sigma_3)^2 = 24T_0 (\sigma_1 + \sigma_2 + \sigma_3) \quad (15)$$

See Figure 3.7 B for graphic representation of equation 11 to 14.

Drucker-Prager Criterion

The Drucker-Prager criterion is a smooth approximation of the Mohr-Coulomb law (Figure 3.7. C; Alejano and Bobet, 2012). Plastic yielding begins when the stress state satisfies the Drucker-Prager criterion:

$$BI_1 + \sqrt{J_2} - A \geq 0 \quad (16)$$

where I_1 is the first invariant of the stress tensor, J_2 is the second invariant of the deviatoric stress tensor and A and B are material parameters. Material parameters in terms of compressive and tensile strength are

$$A = \frac{2}{\sqrt{3}} \left(\frac{C_0 T_0}{C_0 + T_0} \right) \quad B = \frac{1}{\sqrt{3}} \left(\frac{T_0 - C_0}{C_0 + T_0} \right) \quad (17)$$

and in terms of cohesion and friction angle

$$A = \frac{2 \sin \phi}{\sqrt{3}(3 - \sin \phi)} \quad B = \frac{6 S_0 \cos \phi}{\sqrt{3}(3 - \sin \phi)} \quad (18)$$

Circumscribes the Mohr-Coulomb surface

$$A = \frac{2 \sin \phi}{\sqrt{3}(3 + \sin \phi)} \quad B = \frac{6 S_0 \cos \phi}{\sqrt{3}(3 + \sin \phi)} \quad (19)$$

Middle circumscribes the Mohr-Coulomb surface

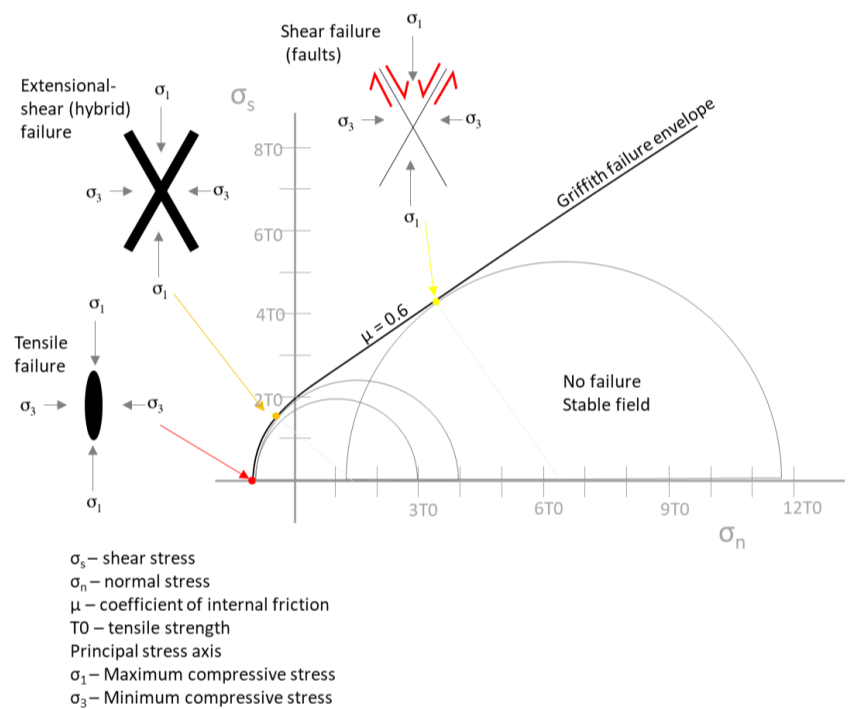
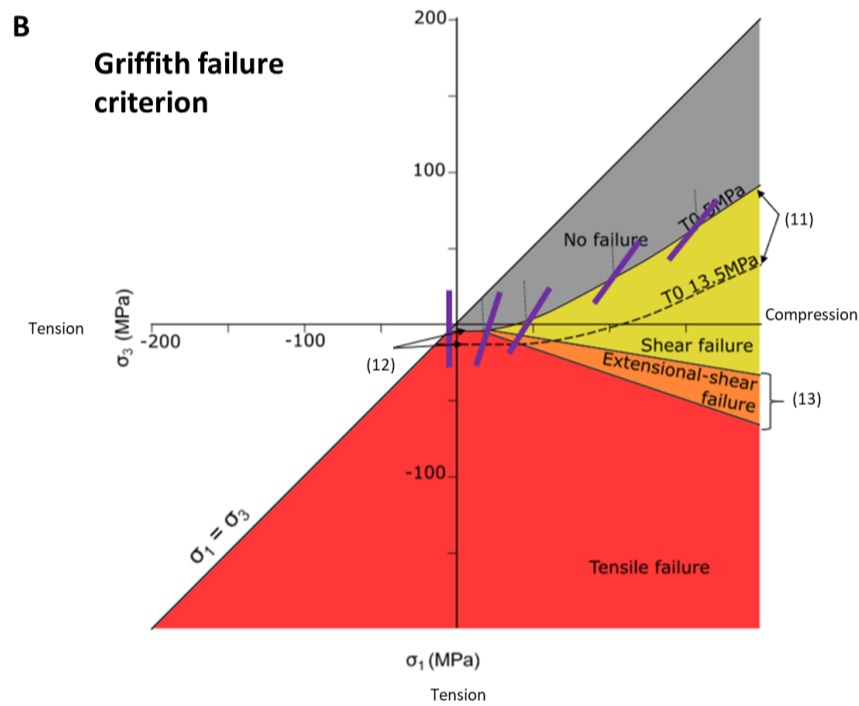
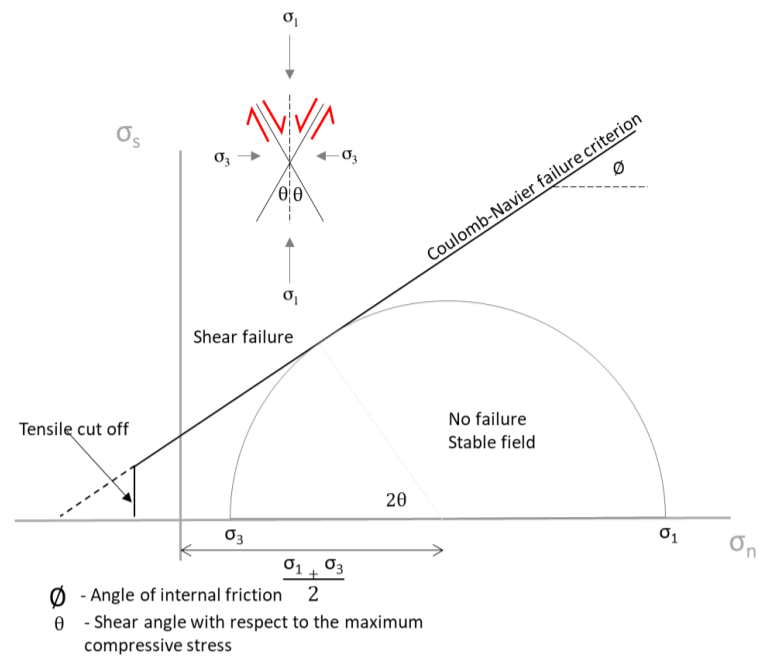
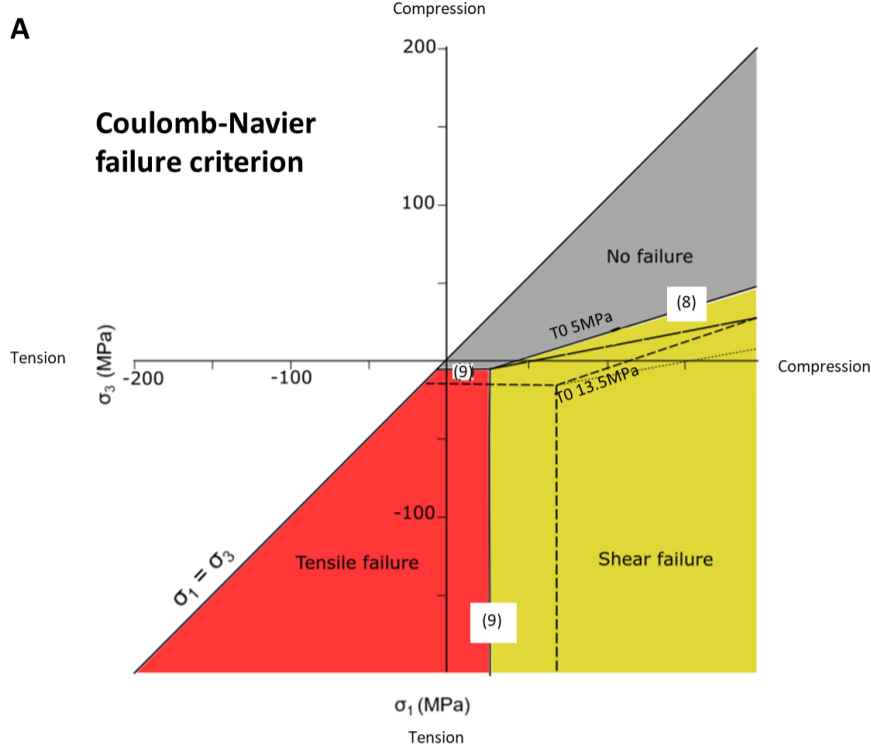
$$A = \frac{\sin \phi}{\sqrt{9 + 3 \sin^2 \phi}} \quad B = \frac{3 S_0 \cos \phi}{\sqrt{9 + 3 \sin^2 \phi}} \quad (20)$$

Inscribes the Mohr-Coulomb yield surface

where S_0 is the material cohesion and ϕ is the internal friction angle (Alejano and Bobet, 2012). See appendix Figure A3-8. (P.329) for sensitivity testing using equation (18) – (20).

Failure criterion of intact rock plotted in terms of major and minor principal stresses

Failure criterion of intact rock plotted on Mohr diagram



Failure criterion of intact rock plotted in three-dimensional stress space

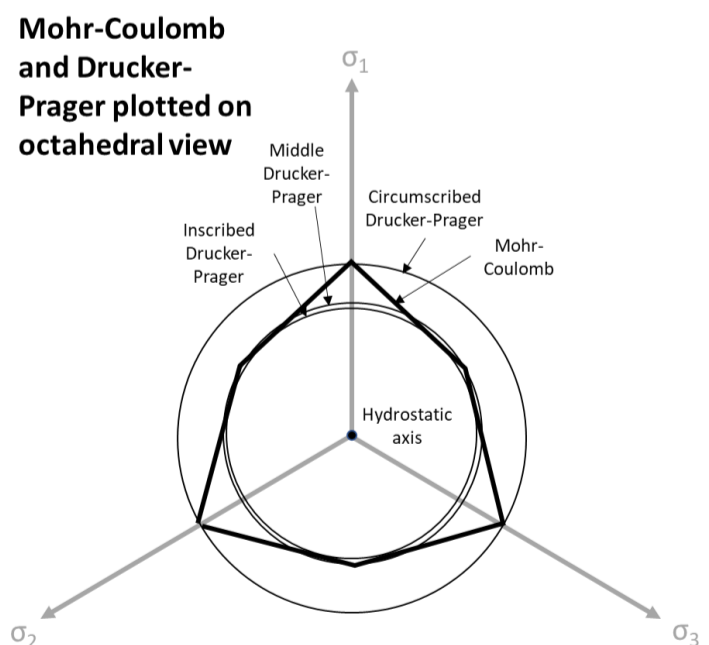
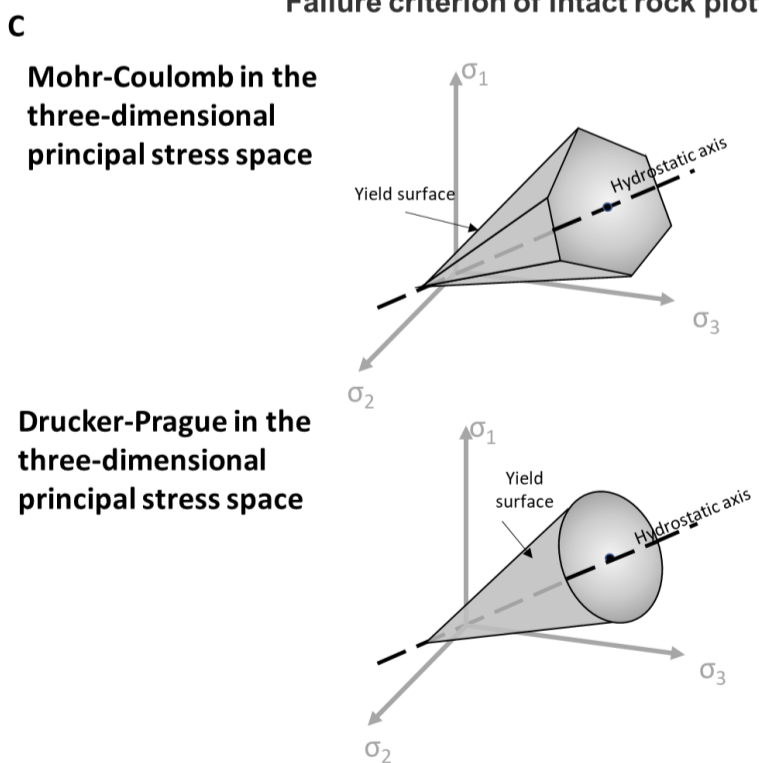


Figure 3.7. Failure criterion. Plotted in terms of major and minor principal stress (σ_1 - σ_3 plot) and Mohr diagrams. σ_1 - σ_3 plots highlight domains of tensile (red) and shear (yellow) failure. Lines are numbered with the equation numbers defining the lines as given in the text. (A) Coulomb-Navier criterion defines the failure domains for a tensile strength (T0) value of 5 MPa. The dashed black line is the domain boundaries for T0 13.5 MPa, dotted black line for T0 13 MPa and coefficient of internal friction (μ) of 0.6. (B) Griffith criterion. Colour fill defines the failure domains for a tensile strength (T0) value of 5 MPa. The dashed black line are the domain boundaries for T0 13.5MPa. Red tensile failure domain, yellow shear failure domain and grey no failure domain. Purple lines represent the angle of failure based on equation (14) relative to a vertical maximum principal stress (σ_1 , blue dotted line). (C) Mohr-Coulomb and Drucker Prager criterion plotted in three-dimensional space.

3.3. Example Models 1 – 3

3.3.1. Model Geometry

Three models comparing the modelling dimensions are presented here, a two-dimensional circle (model 1), and a cylinder as an axisymmetric and three-dimensional model (models 2 and 3, respectively). In model 1 the pluton is defined as a circle with a radius of 1.5 km and in models 2 & 3 a cylinder with a radius of 1.5 km and thickness of 3 km. The top of the cylinder is set to 3 km (Figure 3.8). Model 1 is set a two-dimensional plane strain model and can be considered to represent a slice through an infinitely long cylinder. A horizontal slice at a depth of 4.5 km is assumed to be equivalent to a slice through the centre of the cylinders in models 2 and 3.

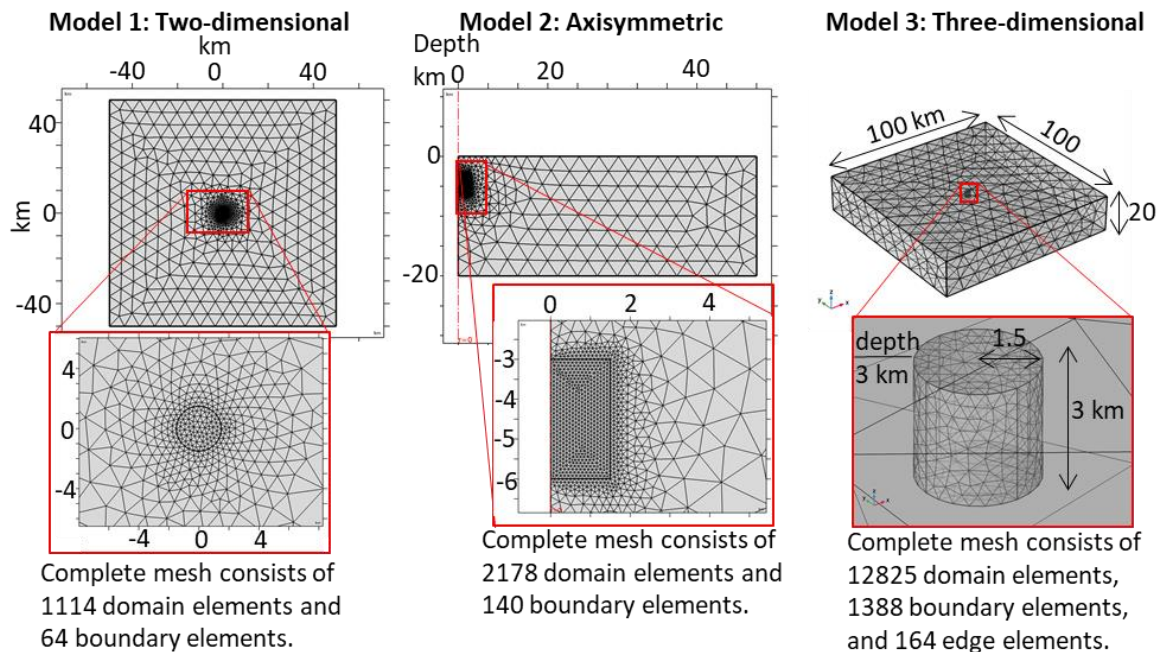


Figure 3.8. Examples of meshes used for models 1 – 3. Element size in the Pluton maximum size 100 m and minimum size 1 m, in the host rock maximum element size 10 km and minimum element size 15 m.

3.3.2. Initial Conditions

The material and mechanical properties of the pluton and host rock are identical and assumed to be temperature independent (Table 3.4). The pluton is set to a homogenous initial temperature of 750 °C. The initial temperature of the host rock is based on an assumed geothermal gradient of 35 °C/km.

In model 1 the host rock is set to 157.5°C. The reasons for the choice of these initial conditions are outlined in part 3.

Table 3.4. Temperature independent material and mechanical properties defined in models 1 - 3

Density *	kg/m ³	2700
Heat capacity at constant pressure *	J/(kg.K)	1150 ‡
Thermal conductivity *	W/(m.K)	1.8
Young's modulus †	MPa	3.04e4
Poisson's ratio †		0.25
Coefficient of thermal expansion †	1/°C	8e-6
Tensile strength **	MPa	5
Compressive strength **	MPa	100
Cohesion	MPa	20
Angle of internal friction	°	30

* Values after Cook and Bowman (1994)
† Values after Bergbauer et al. (1998)
‡ Includes 300 J/(kg.K) to account for latent heat of crystallization
** after Knapp (1978)

Grid size is defined so that the minimum element size in the pluton was 1 m and a maximum of 100m. In the host rock the maximum element size 10 km and minimum element size 15 m (Figure 3.8). A time step of 1000 years over 1 million years was set for each of the models. These sizes are based on sensitivity testing for modelled time steps and grid resolution run for models (appendix, A3-8 & A3-9, p.331).

3.4. Example Models 1 – 3 Results

Modelling outputs include the cooling history, orientations of the principal stress axes, the magnitude of principal stresses, the strain energy and colour maps of failure domains. The time steps presented are chosen to highlight key changes in the direction of the principal stresses over time. The modelling results are presented as map and sections or as graphs along lines or for selected points in the model (Figure 3.9). Map images for models 2 and 3 are sliced horizontally through the model at a depth of 4.5 km, equivalent to the depth assumed in model 1. For axisymmetric models only one half of the model about the central axis is shown.

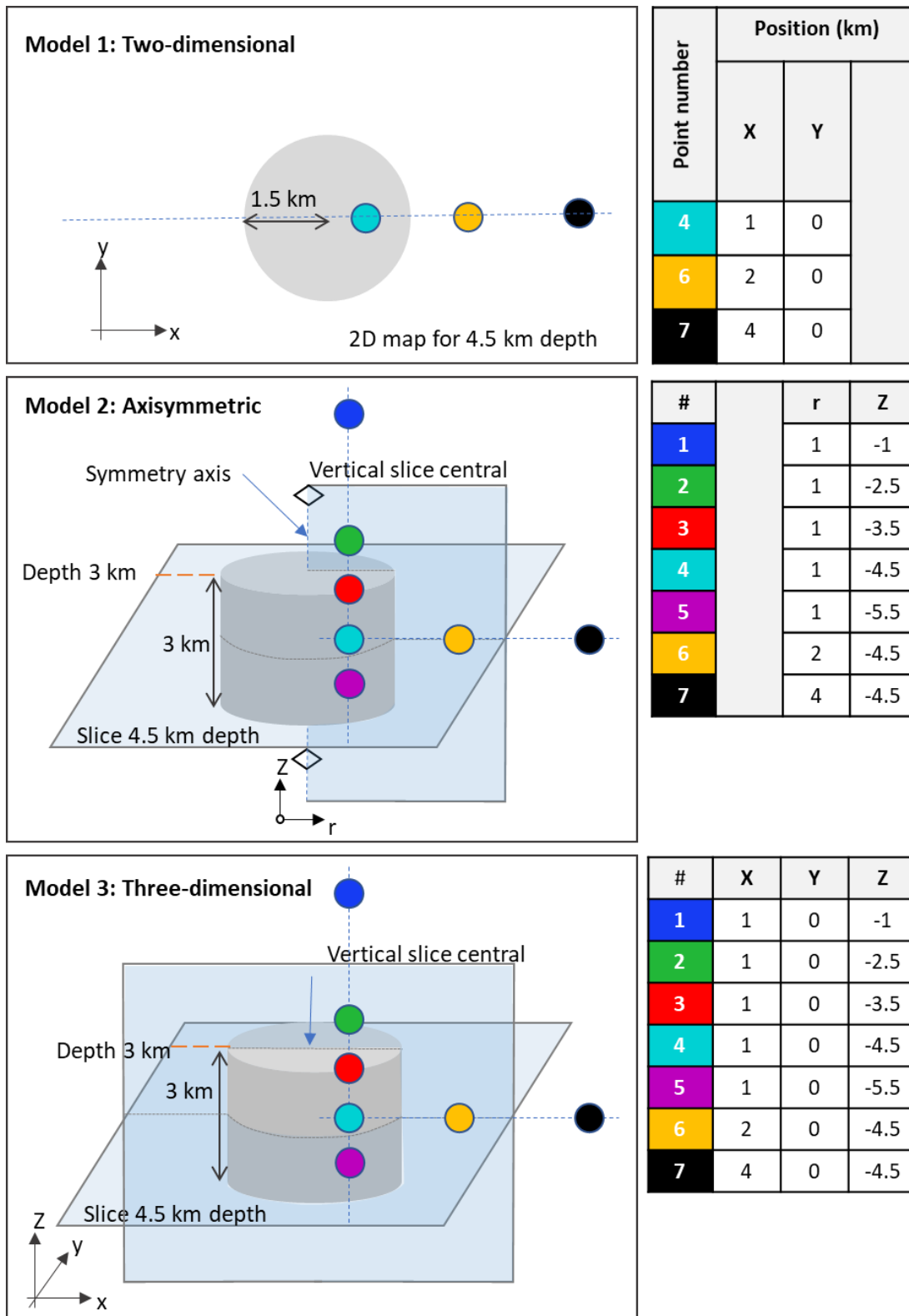


Figure 3.9. Models 1 – 3, showing location of map and sections and line and points used in graphs. Origin at centre of circle (model 1) $x=0, y=0$ and axis of models 2 and 3, marked by blue arrow in model 2 and 3.

3.4.1. Thermal History

The thermal regimes of the pluton and host rock differ. The pluton continuously cools, while the temperature of the host rock, close to the pluton, increases and then decreases (Figures 3.10 to 3.12). The influence of temperature redistribution in the host rock extends for 20 km from the intrusion centre in the two-dimensional model and up to 10 km from the intrusion centre in the axisymmetric and three-dimensional models (Figure 3.11). The magnitude of thermal maximum and thermal decay is inversely proportional to the distance from the pluton margins.

The rate of cooling is also influenced by the modelling dimension. Axisymmetric and three-dimensional models (models 2 and 3) cool faster than the two-dimensional model (model 1). For example point 4, in the two-dimensional model (model 1) cools by 400 °C in the first 50,000 years after model initiation and the same point in the axisymmetric and three-dimensional model (models 2 and 3) cools by approximately 500 °C in the same time interval (also see appendix A, Table A3-6, p.307).

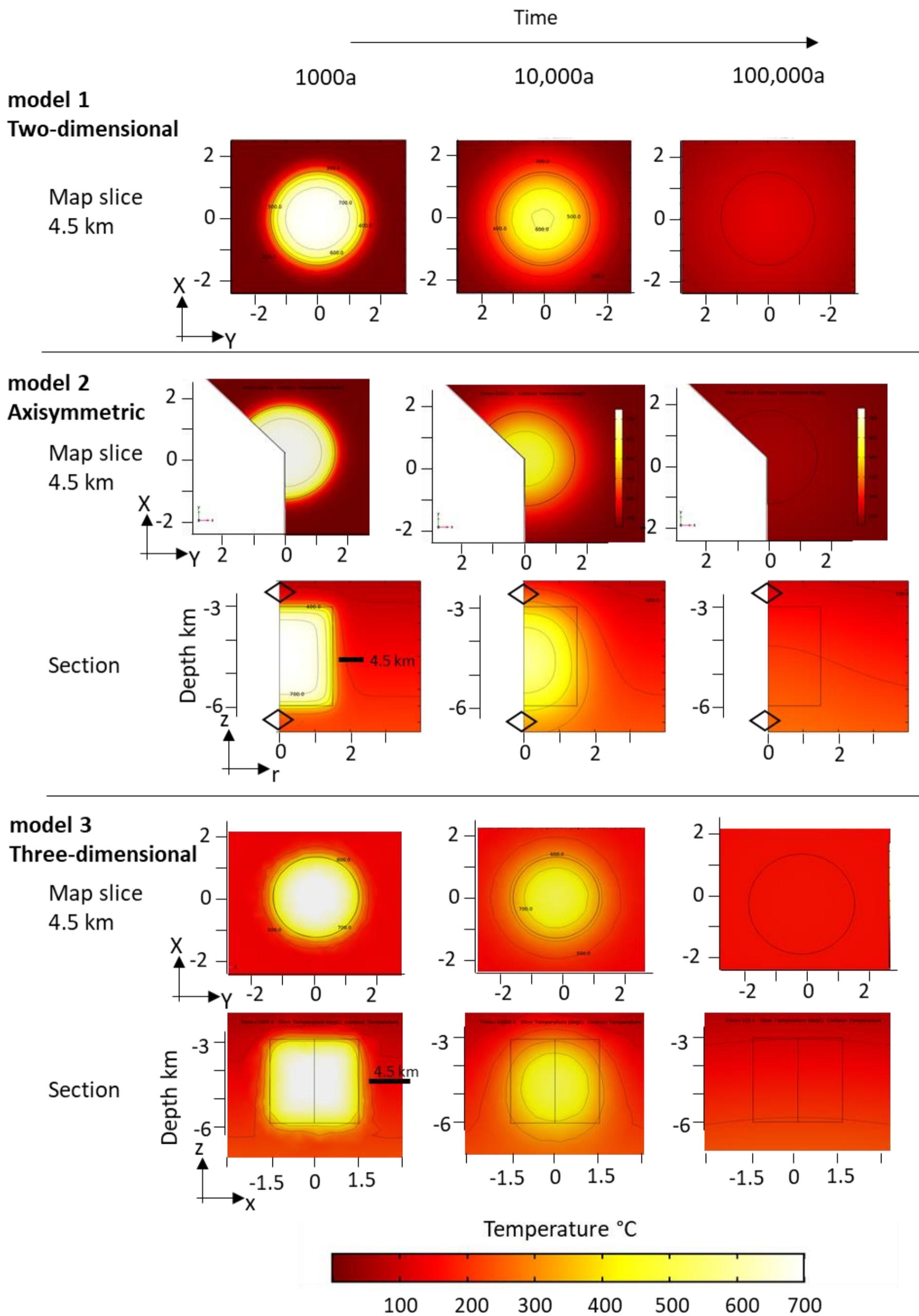


Figure 3.10. Modelled temperature distributions shown as colour map and contours for selected time steps 1000 years, 10,000 years and 100,000 years. (model 1 two-dimensional strain, model 2 axisymmetric and model 3 three-dimensional modelling). For models 2 and 3 top row images are a map slices at 4.5 km depth and the bottom row sections are sliced through the centre of the pluton.

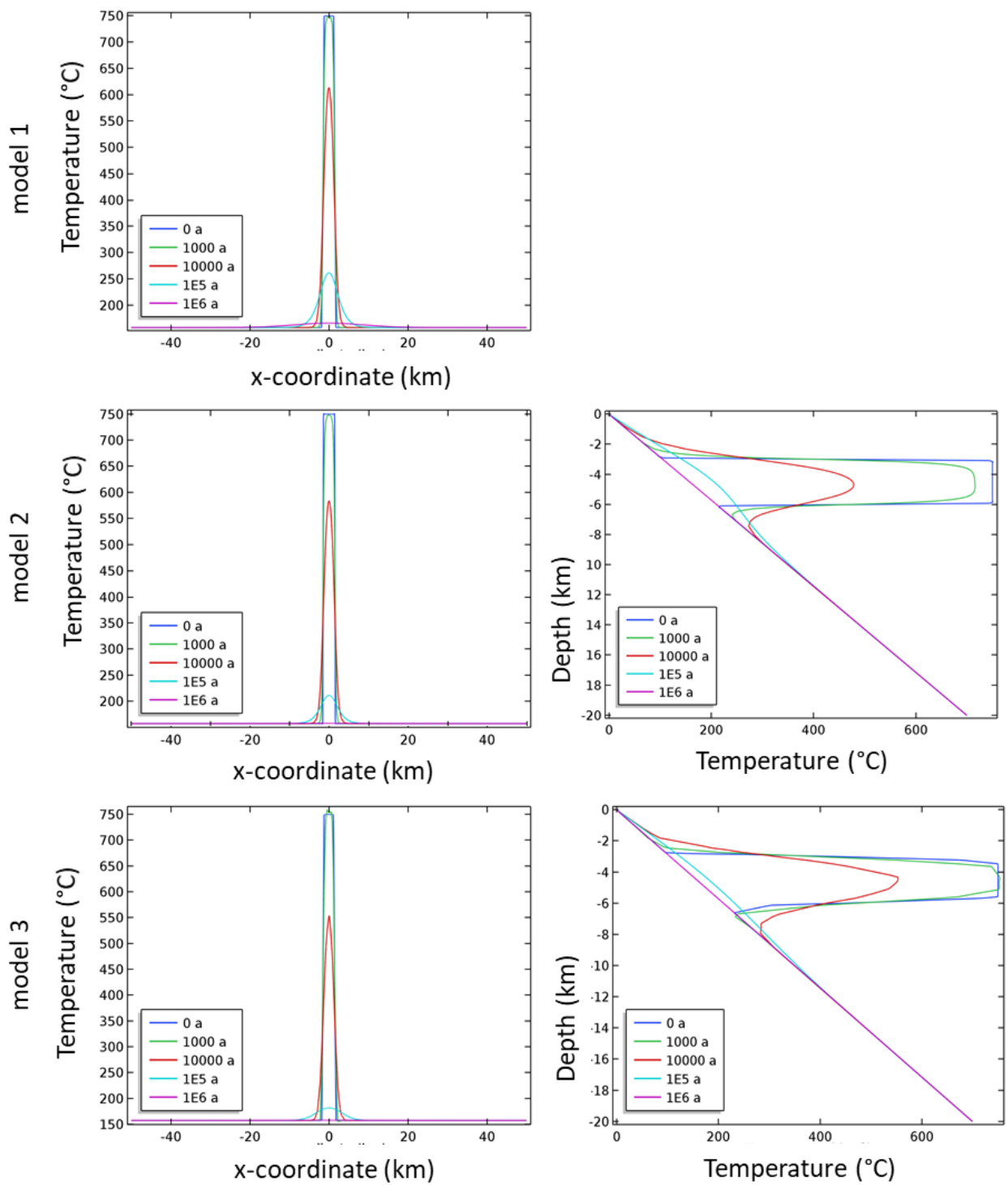


Figure 3.11. Temperature profiles through the pluton and host rock. For a horizontal line (left) and vertical line (right) temperature profiles through the pluton and host rock, (see Figure 3.9). Lines are coloured for selected time steps 0a, 1000a, 10,000a and 100,000a, 1,000,000a.

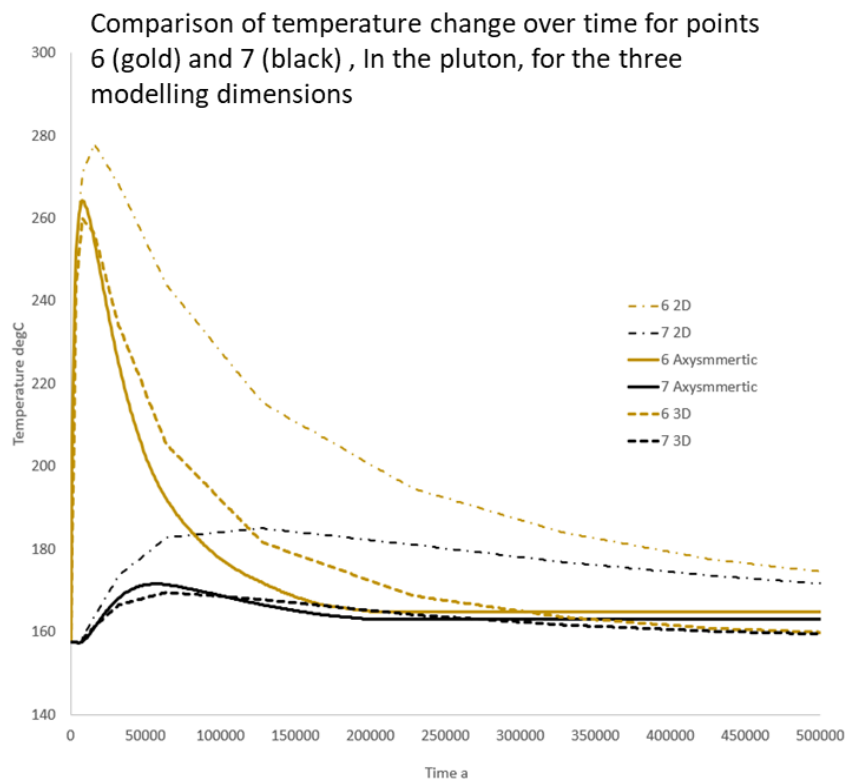
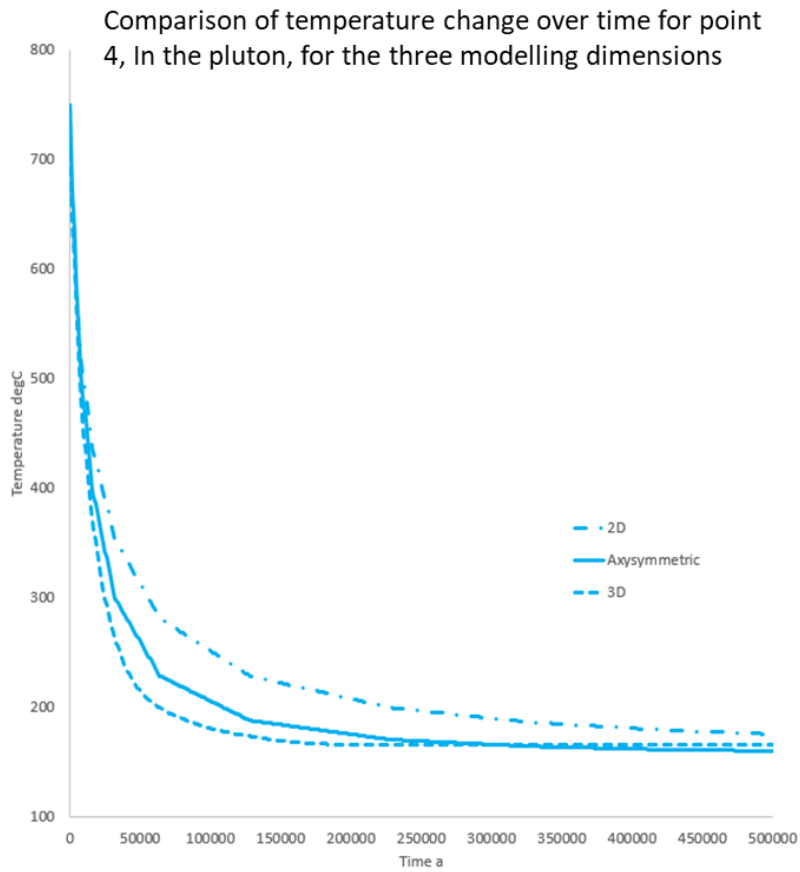


Figure 3.12. Temperature at point 4 (blue) in the pluton and in the host rock points 6 (gold) and 7 (black) through time. This figure highlights the differences in temperature change between modelling dimensions (models 1 – 3). See Appendix A Figure A-3-8 (p.330) for temperature of all points.

3.4.2. Principal Stress Orientations

Principal stress orientations within a cylindrical intrusion rotate over time (Figure 3.13). Initially the maximum compressive stress is vertical. Within the pluton the minimum compressive stress is concentric and in the host rock around the pluton radial.

As the pluton cools, in models 2 & 3, the orientation of the maximum tensile stress switches near the top and base to become radial and the maximum compressive stress / minimum tensile stress inclines away from vertical. In the host rock, around the top and base of the pluton the maximum compressive stress rotates to horizontal and the minimum compressive stress becomes vertical. The maximum compressive stress remains radial around the vertical edge of the pluton.

As the minimum compressive stress is initially concentric around the pluton, assuming tensile failure, joints would be expected to form radially within the pluton (i.e., perpendicular to the direction of maximum tensile stress). The switch in principal stress orientations at the top and base of the pluton mean that jointing may also form concentrically in these locations. In the host rock joints would form parallel to the pluton margins.

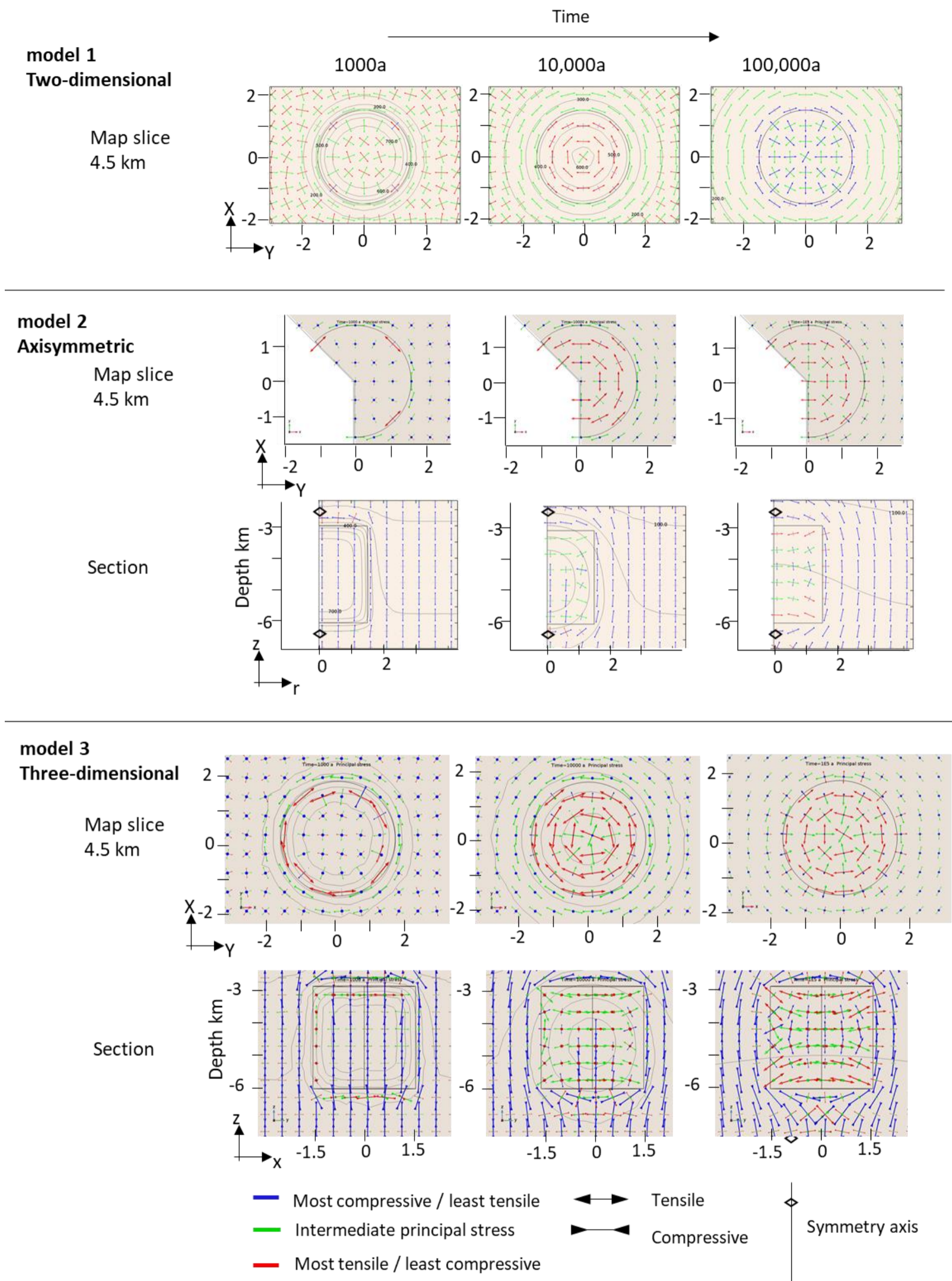


Figure 3.13. Principal stress orientations plotted on maps and sections. Colours represent most compressive stress (blue), intermediate compressive stress (green) and most tensile stress (red). Shown for selected time steps 1000a, 10,000a and 100,000a. For models 2 and 3 top row images are horizontal map slices at 4.5 km depth and the bottom row are vertical sections sliced through the centre of the pluton (see Figure 3.10 for sketches showing location of sliced map and sections).

3.4.3. Stress Magnitudes

Stresses within the intrusion are initially compressional but as cooling progresses all the principal stresses become tensile (Figures 3.13 and 3.14). This change occurs progressively, propagating in towards the centre of the intrusion. In the host rock at distances greater than 1 km from the pluton margins the minimum principal stress remains compressive. The magnitude of stress change is on the order of 200 MPa (Figure 3.14) and is great enough to result in rock failure.

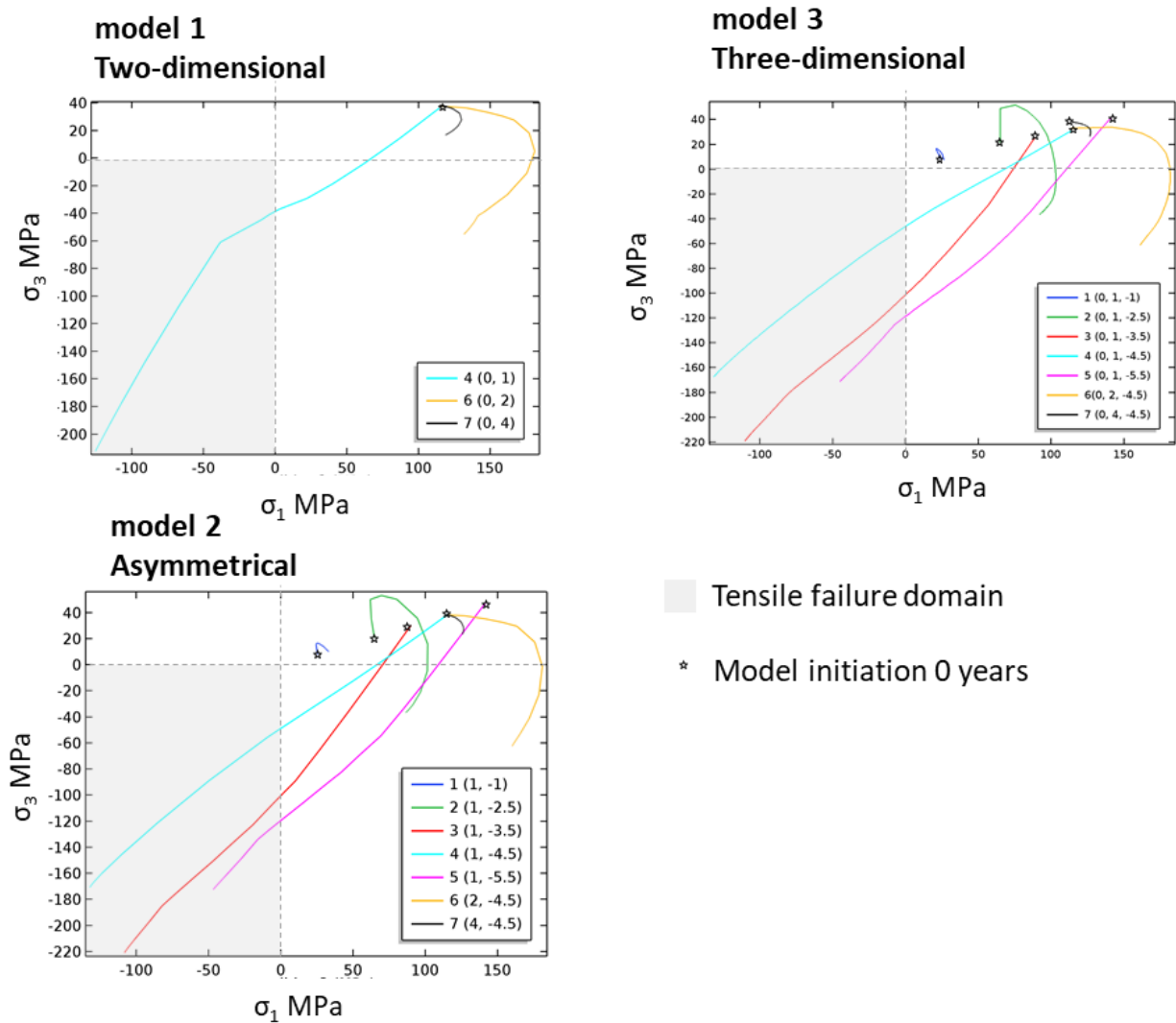


Figure 3.14. Stress paths for selected points on a maximum (σ_1) – minimum (σ_3) principal stress plot, compression positive. See appendix A, Figure A3-8 A p.330 for overlay of points 4, 6 & 7. Modelling dimension has limited influence on predicted stress paths and magnitude.

3.4.4. Elastic Strain Energy

Elastic strain energy increase over time and are highest near to the top as the pluton cools. In the host rock, elastic strain energy initially decreases as the rock is heated and then increases as it cools. Elastic strain energy in the host rock is highest around the pluton corners (Figure 3.15 & 3.16). Elastic strain energy for a given point in the two-dimensional model (model 1) is lower than the strain energy of the equivalent axisymmetric and three-dimensional models (models 2 & 3) (see appendix A, Figure A3-8 B p.330).

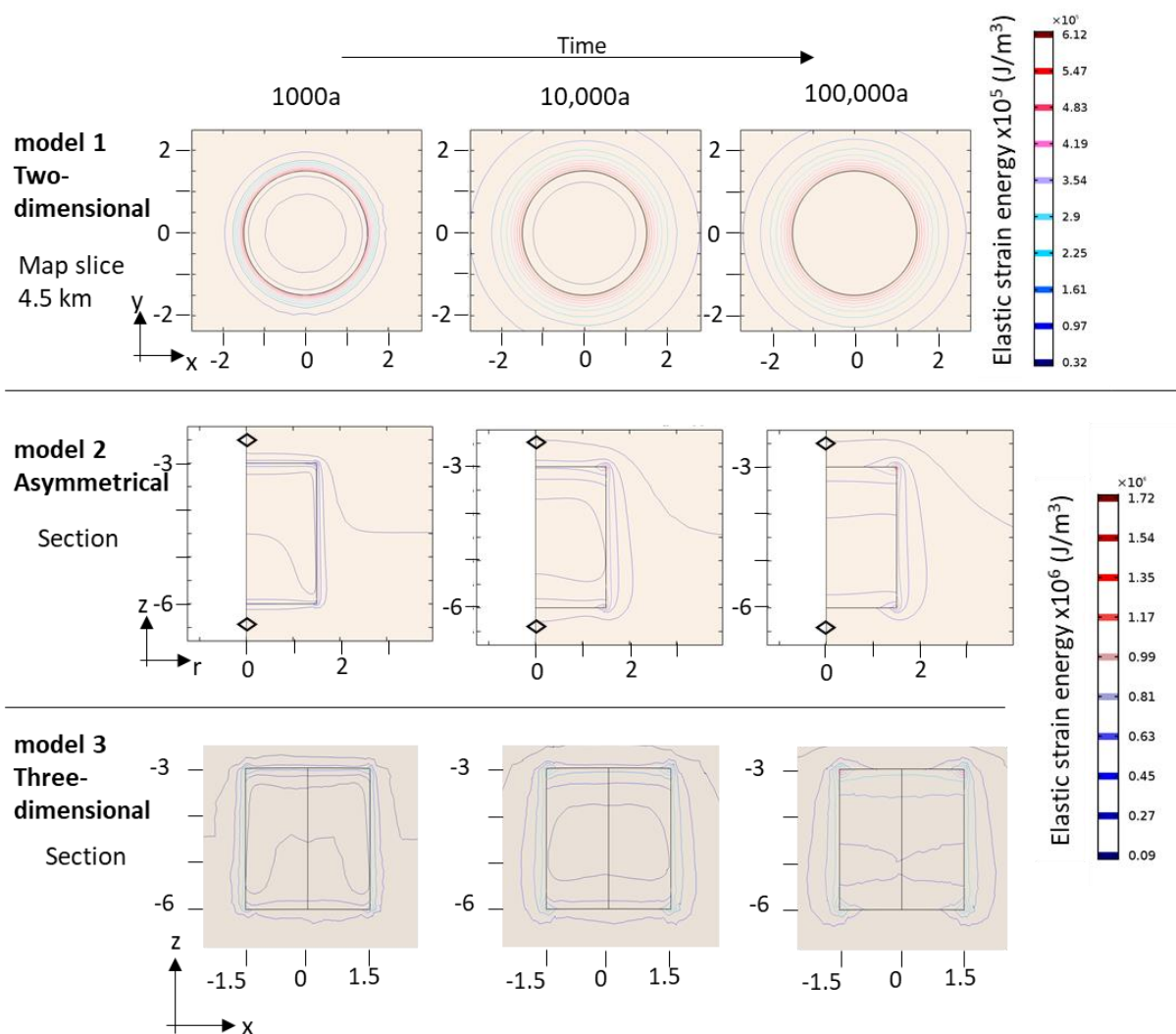
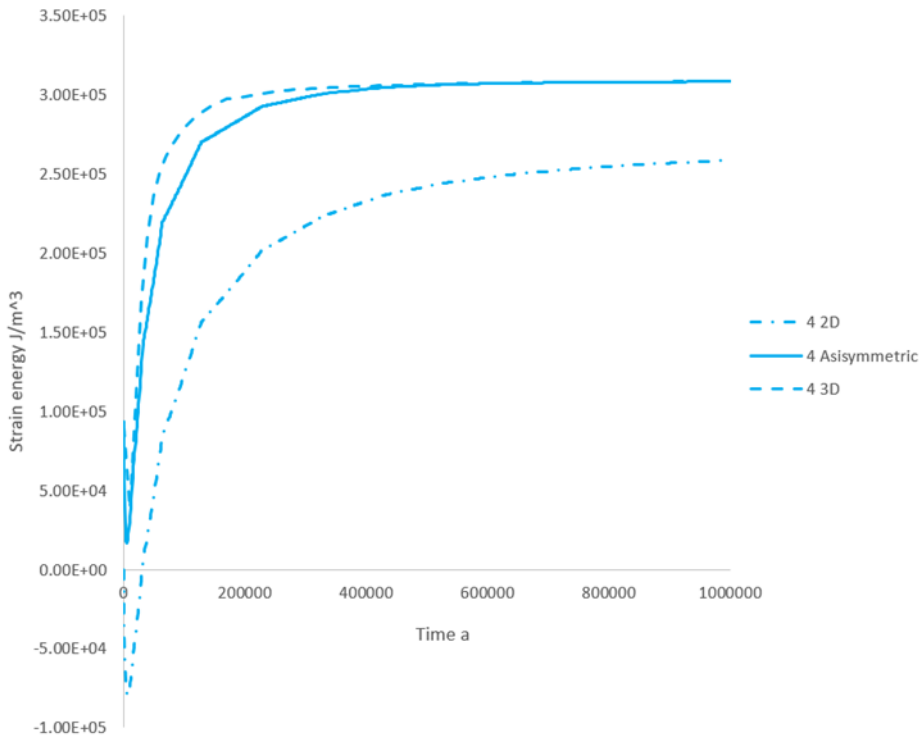


Figure 3.15. Elastic strain energy (J/m³) contoured for given time steps. Models 2 and 3 are shown as vertical slices through the centre of the pluton.

Comparison of elastic strain energy over time for point 4, In the pluton, for the three modelling dimensions



Comparison of elastic strain energy over time for points 6 (gold) and 7 (black), In the pluton, for the three modelling dimensions

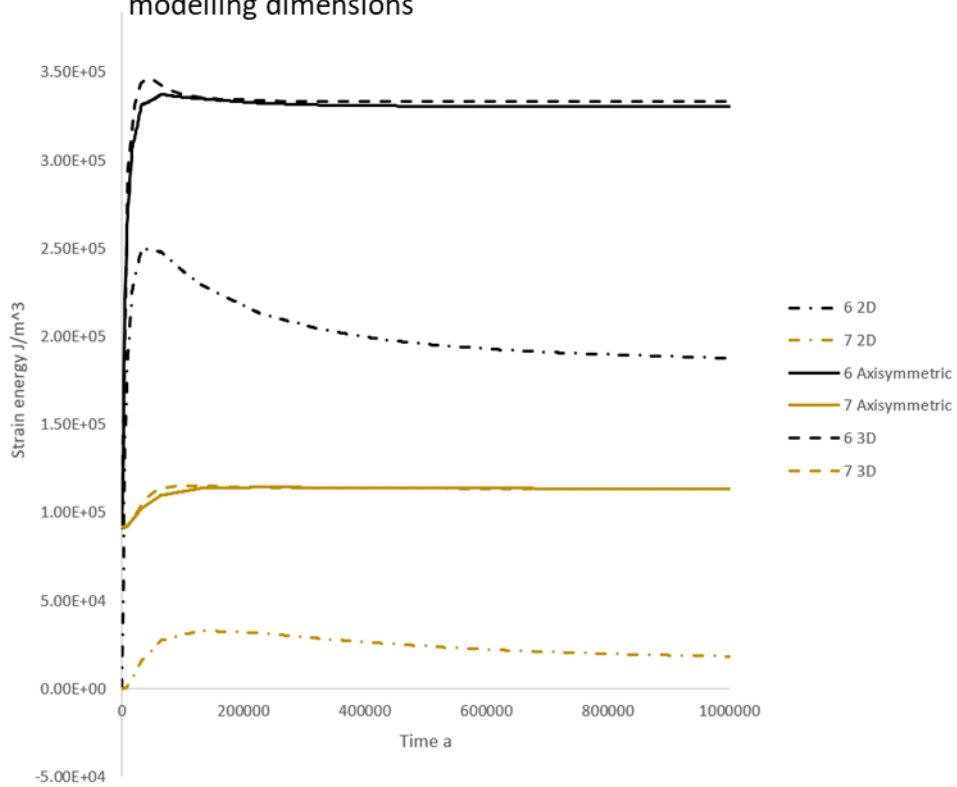


Figure 3.16. Elastic strain energy (J/m^3) over time at point 4 (blue) in the pluton and in the host rock points 6 (gold) and 7 (black). See Appendix A Figure A-3-8 (p.330) for temperature of all points.

3.4.5. Failure Criterion

Cooling drives the pluton towards failure. Stress paths for a given point progressively move through failure domains (Figure 3.17). Brittle failure propagates inwards from the pluton margins and outwards in the host rock (Figure 3.18). The applied failure criterion indicates the timing of failure and the failure mode at a given point in the model as cooling occurs is variable (Figure 3.17 & 3.18).

The predicted domain of failure in the pluton for the applied Coulomb-Navier criterion is like that of the Drucker-Prager yield criterion. In the host rock the Drucker-Prager yield criterion predicts a smaller failure area. The domain of no failure of the Griffith-Murrell criterion is vertically narrower than that of the Coulomb-Navier criterion and Drucker-Prager yield criterion. When the intermediate principal stress is not accounted for using the Griffith criterion the failure domain is larger (Figure 3.18). The time and mode of failure experienced by a given point is also influenced by pluton depth and the applied material and mechanical properties, discussed further in part 3.

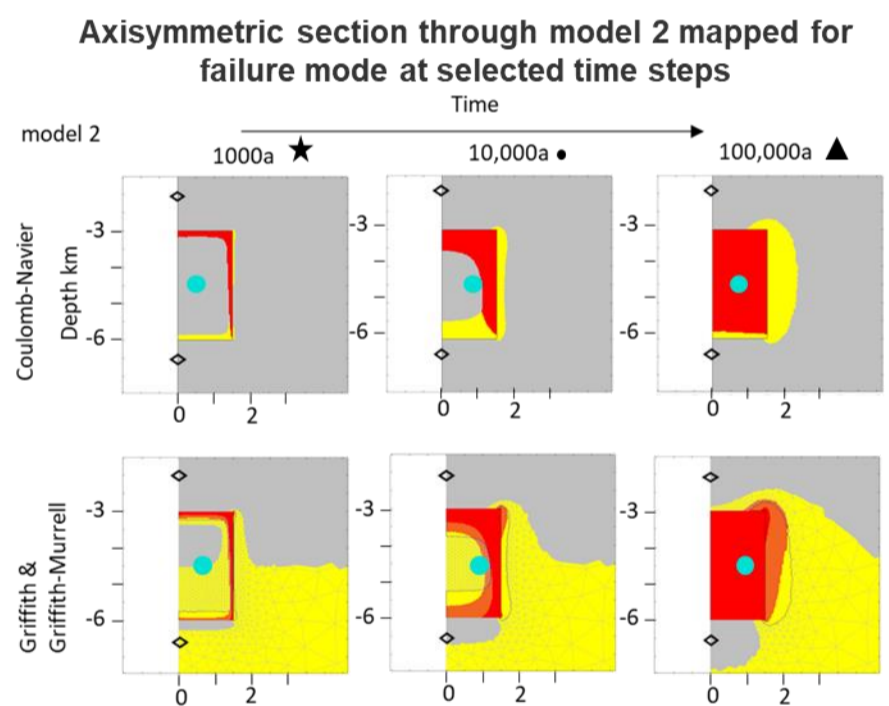
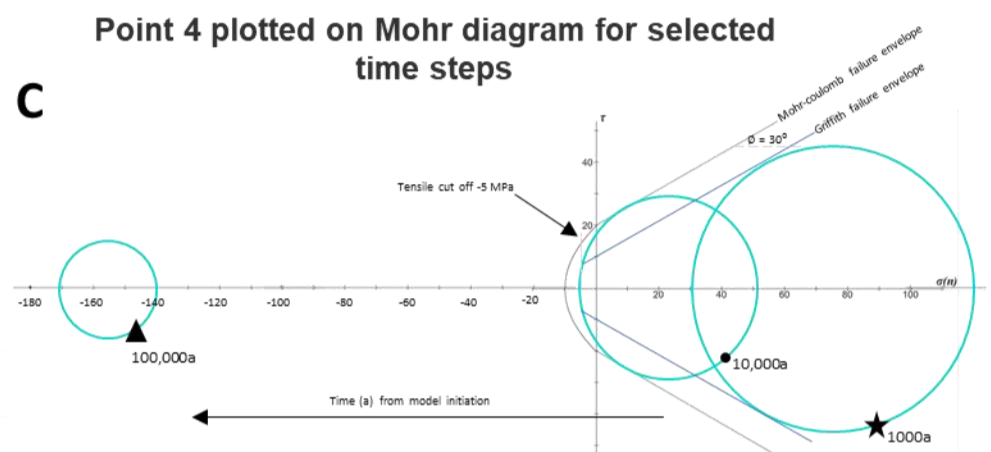
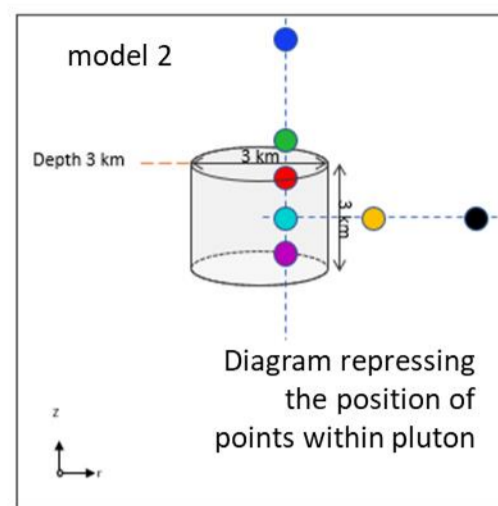
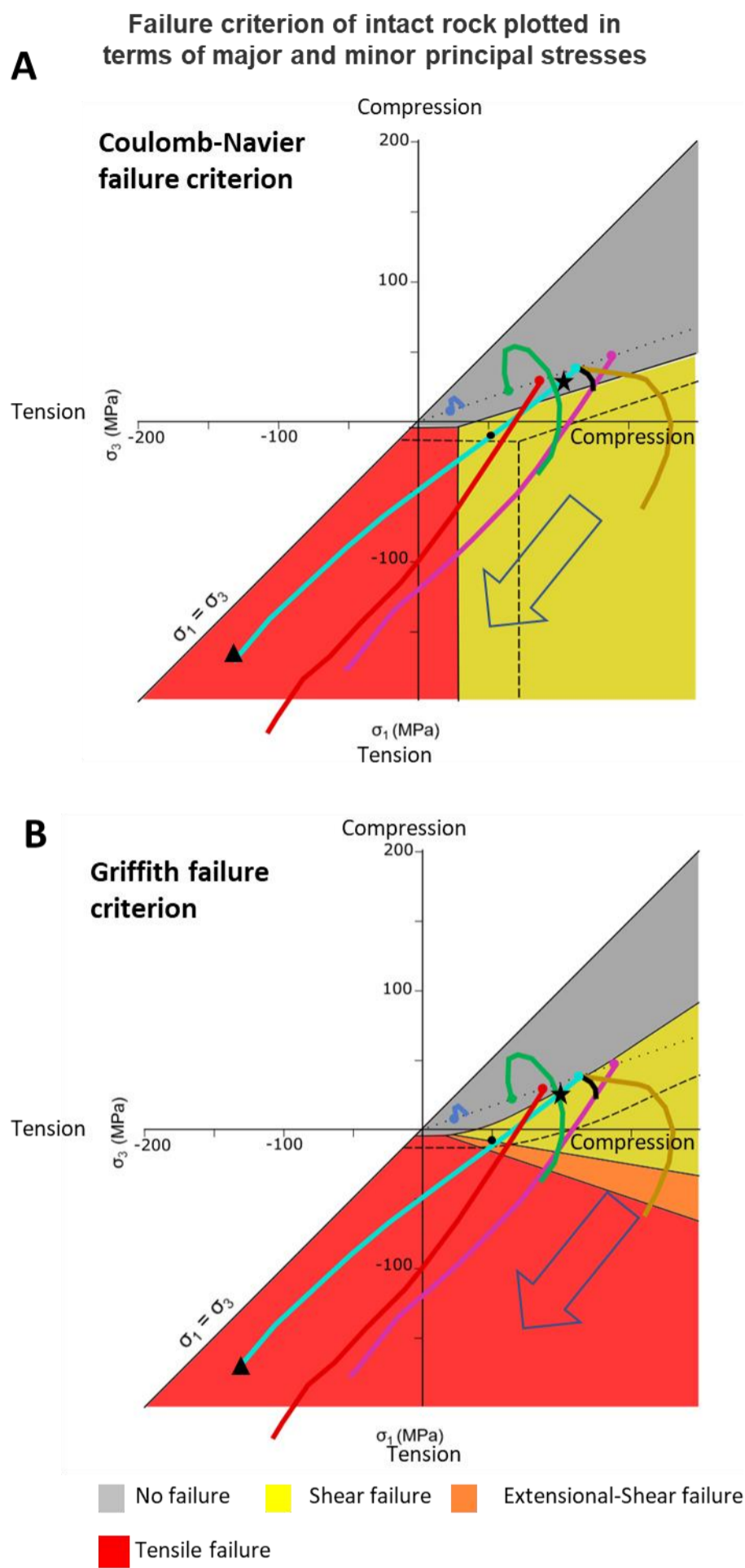


Figure 3.17. Stress paths for selected points. (A - B) Plotted on a maximum (σ_1) – minimum (σ_3) principal stress plot for model 2. Compression positive overlain on (A) Coulomb-Navier and (B) Griffith failure domain plots. Points mark the starting stresses in the no failure domain (grey), large arrow shows cooling direction and movement of stress paths. (C) Point 4 plotted on Mohr diagram at selected time steps as shown, lower images failure domains for selected time steps for model 2, see Figure 3.18 (p.71) for details on the section images. Inset shows position of point 4 (blue) for reference, see Figure 3.9 p.59 for details.

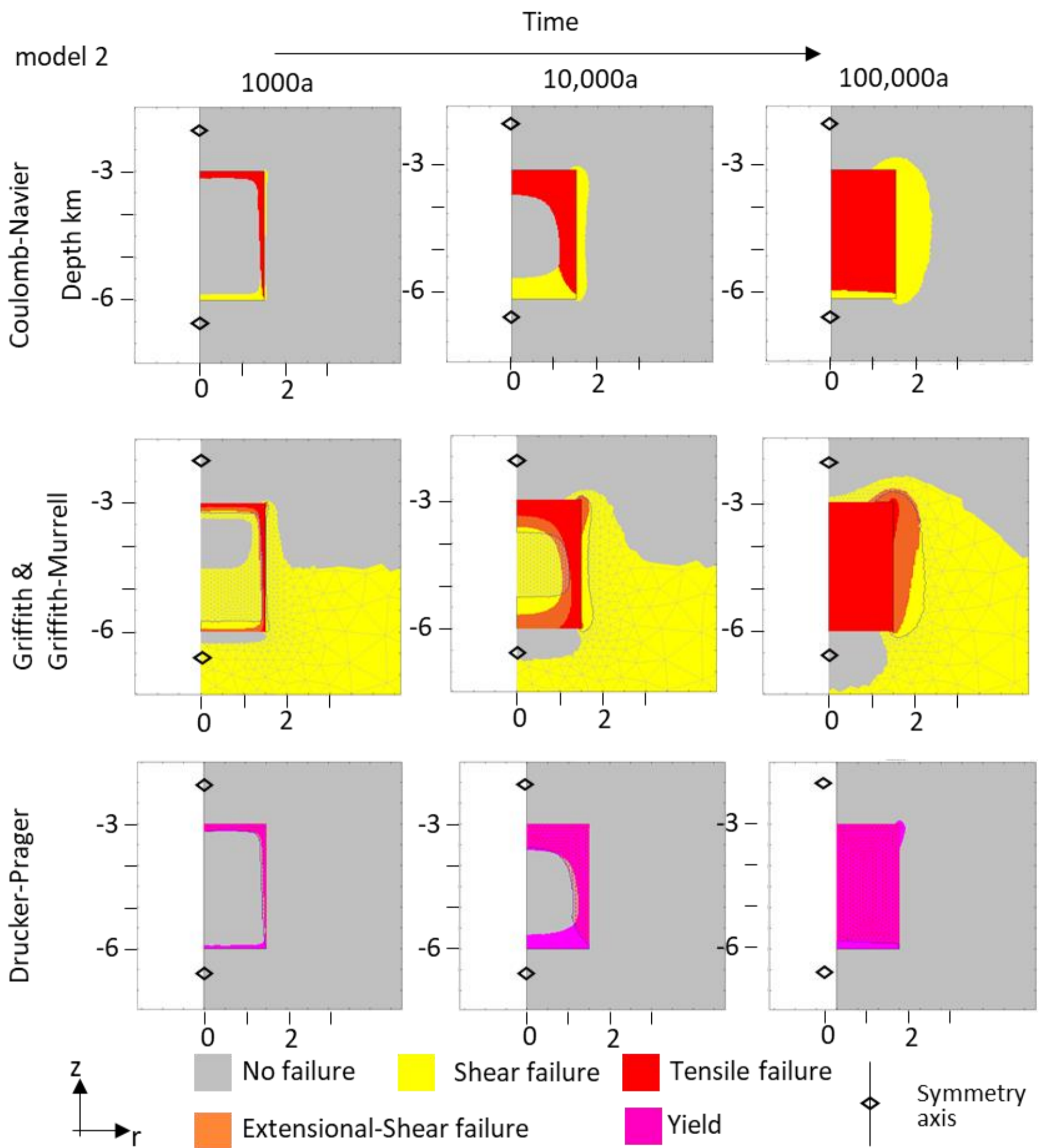


Figure 3.18. Failure domains for selected time steps for model 2. Coulomb-Navier, Griffith, Griffith-Murrell and Drucker-Prager criterion for both temperature independent (Table 3.4). The Griffith-Murrell no failure domain is shown as the grey wireframe overlay. Tensile failure domain is shown as a red wireframe over the Drucker-Prager failure domain.

3.4.6. Grid Resolution and Timesteps

Grid, resolution and timesteps are all defined in the models. The selection of these parameters is based on the modelling dimension (Figure 3.8). Sensitivity testing for modelled time steps and grid resolution were run for models. The applied time step has no influence on resulting temperature change (e.g., point 4 in model 2, appendix A, A3-9 A p.331). For the same model and point the grid resolution has a greater influence on modelling results although this is still minimal (see appendix A, A3-9 B p.331).

3.4.7. Model Run Time

Once set up, model 1 (two-dimensional) took ~ 10 minutes to run, model 2 (asymmetric) took 40 minutes to run and model 3 (~4 hours) on a machine with 64-bit windows machine.

3.4.8. Summary

Two-dimensional modelling results in a slower cooling for a given point than the equivalent asymmetric or three-dimensional modelling. Asymmetric or three-dimensional model result in similar cooling histories in the pluton (Figures 3.14). In the host rock of model 1, the two-dimensional model, points close to the pluton margin are heated to a greater extent than the equivalent points in the asymmetric or three-dimensional models (Figure 3.12). The difference in cooling rate does not significantly alter the predicted stress orientation or magnitudes (Figures 3.13 & 3.14). Strain energy for a given point in the two-dimensional model is lower than equivalent points in the asymmetric or three-dimensional models (Figures 3.15 & 3.16). Failure occurs progressively from the margins. The time and mode of failure is influenced by the applied failure criterion (Figure 3.17 & 3.18). Grid resolution and timestep do not alter results.

Part 2

3.5. COMSOL® Models Based on Published Models

Models were run during initial set up of models in COMSOL® (Table 3.5) and provided a useful test of model setup.

Table 3.5. COMSOL® models based on published models

Model number	Based on	Material properties table number	Failure criterion	Model description
K-1	Knapp, 1978			Model geometry based on thesis.
K-2				Infinitely elongate dyke Host rock geometry extended vertically and horizontally
G-1	Gerla, 1988	Table 3.4	Coulomb-Navier	Model geometry based on thesis, Infinitely elongate cylinder: magma chamber 2 km pluton 4km diameter
G-2				magma chamber 1 km pluton 4 km diameter
G-3				magma chamber 0.5 km pluton 4 km diameter
G-4				Diamond Joe Stock geometry following workflow of Berbauer, 1998 no tectonic load
G-5				Diamond Joe Stock geometry following workflow of Berbauer, 1998 with tectonic load
B-1	Bergbauer, 1998	Cartridge pass 3.6		Circular pluton
B-2				Rectangular pluton
B-3				Hour glass wide pluton
B-4				Hour glass thin pluton
B-5				Cartridge pass Granodiorite thermal only
B-6				Cartridge pass Granodiorite thermal and tectonic
B-7				Cartridge pass Granodiorite tectonic only
B-8				Lake Edison thermal only 3.5 km depth
B-9				Lake Edison thermal only 7 km depth
B-10				Lake Edison thermal and tectonic 7 km depth
Z-1	Žák et al., 2006	Tables 3.4	Drucker-Prager	Tanvald pluton temperature independent material properties
Z-1b				Temperature independent mechanical properties
Z-2		Table 3.10		Temperature dependant material and mechanical properties
Z-2 b		Linear material / mechanical properties		

3.5.1. Infinite dyke, Knapp (1978)

Two vertical two-dimensional conductive plane strain models were setup in COMSOL® (models K-1 and K-2, Figure 3.19). The pluton geometry was defined as a rectangle, 3 km wide and 4.5 km vertical height. The top of the pluton was set at a depth of 4.5 km. In Model K-1 the host rock domain is defined as a rectangular block 18 km wide and 9 km vertical height. In model K-1 The base of the host rock domain was set to be the same as the base of the pluton at 9 km, comparable to the Knapp, 1978 model. To determine the influence of the modelled host rock boundaries on results, the host rock geometry was extended to 50 km wide and 20 km high (model K-2). Initial pluton temperature was set to 900 °C and host rock geotherm to 15 °C/km (Knapp, 1978). Material properties in both the pluton and host rock domains were set to values as given in part 2 Table 3.4 p.50. These values differ from values given by Knapp 1978 who defined phase change with material properties as temperature and pressure dependent. These values were chosen to simplify the modelling set up and to assess the influence of not accounting for phase change or temperature dependent material properties.

Resulting temperature distributions (Figures 3.19 to 3.21), principal stress trajectories (Figure 3.22), stress magnitudes (Figure 3.23) and failure domains (Figures 3.24 & 3.25) calculated in COMSOL® are like those given by Knapp (1978). Comparison highlights that simplifying model material parameters and not accounting for phase change (i.e., after Bergbauer, 1998) does not significantly alter modelling results.

Minor differences in results are due to the different material properties applied in the COMSOL® models which result in the COMSOL® models cooling moderately faster than the model presented by Knapp (1978) (Figures 3.19 to 3.21). The position of the 300 °C contour at 100,000 years calculated in COMSOL® is comparable to the position of the 400 °C contour given by Knapp, 1978 and by 300,000 years the COMSOL® model is cooler than that given by Knapp (1978) (Figure 3.20). In Model K-2 at both 100,000 years and 300,000 years after model initiation the 300 °C contour in the COMSOL® models is in a comparable position to the 400 °C contour given in Knapp (1978) (Figure 3.20). The dimension of the host rock influences the geometry of the isotherms as the pluton cools (Figure 3.20) but has a limited influence on modelling results (Figure 3.22 & 3.23). As found by Knapp (1978) shear and then tensile fracturing domains move from the top and sides of the pluton as it cools. Shear failure occurs in the host rock around the top of the pluton (Figures 3.24 & 3.45).

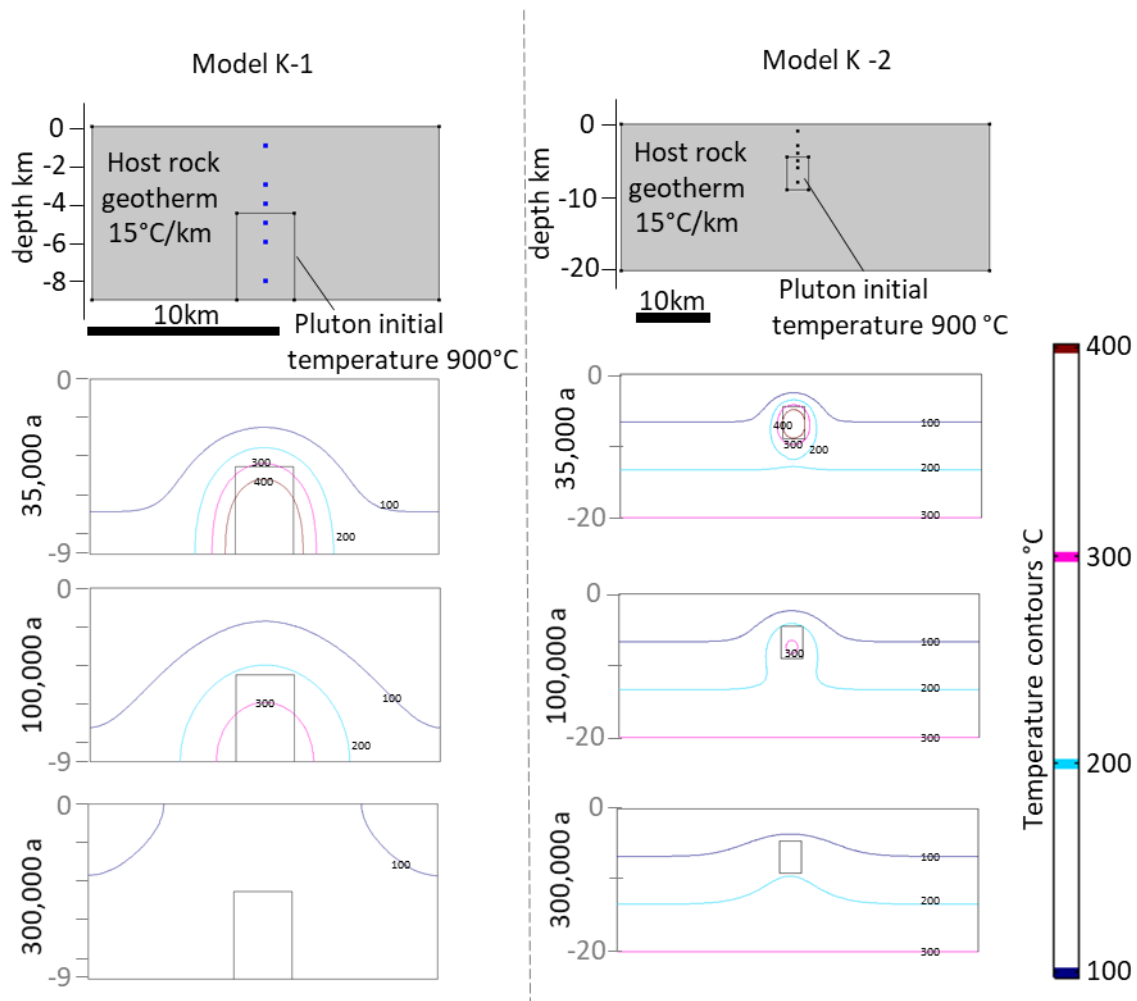


Figure 3.19. Isotherms showing the cooling of the plutonic body for models K-1 and K-2 at selected time steps in years after model initiation. The initial pluton is the same size and only the size of the host rock domain is altered. Pluton temperature is set to 900 °C and host rock geotherm to 15 °C /km. Resulting isothermal contours as a result of cooling have slightly different geometries depending on the base position of the host rock.

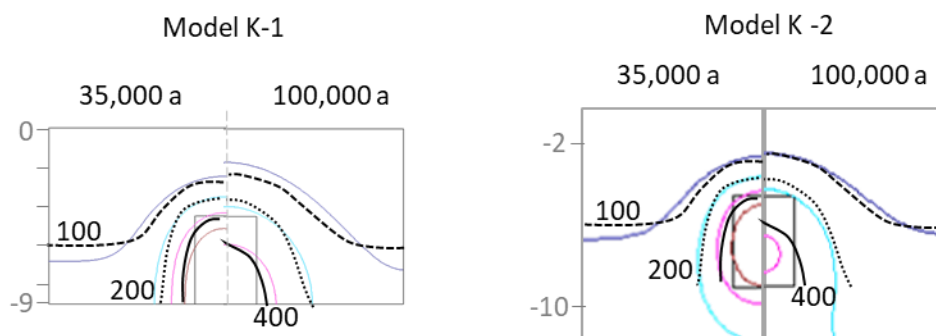


Figure 3.20. In the bottom row of images contours the COMSOL® models are compared to contours calculated by Knapp, 1978. Knapp models shown as back lines as labelled (°C) redrawn from Knapp, 1978 (Fig.11 p.65). Comparison is made for two selected time steps.

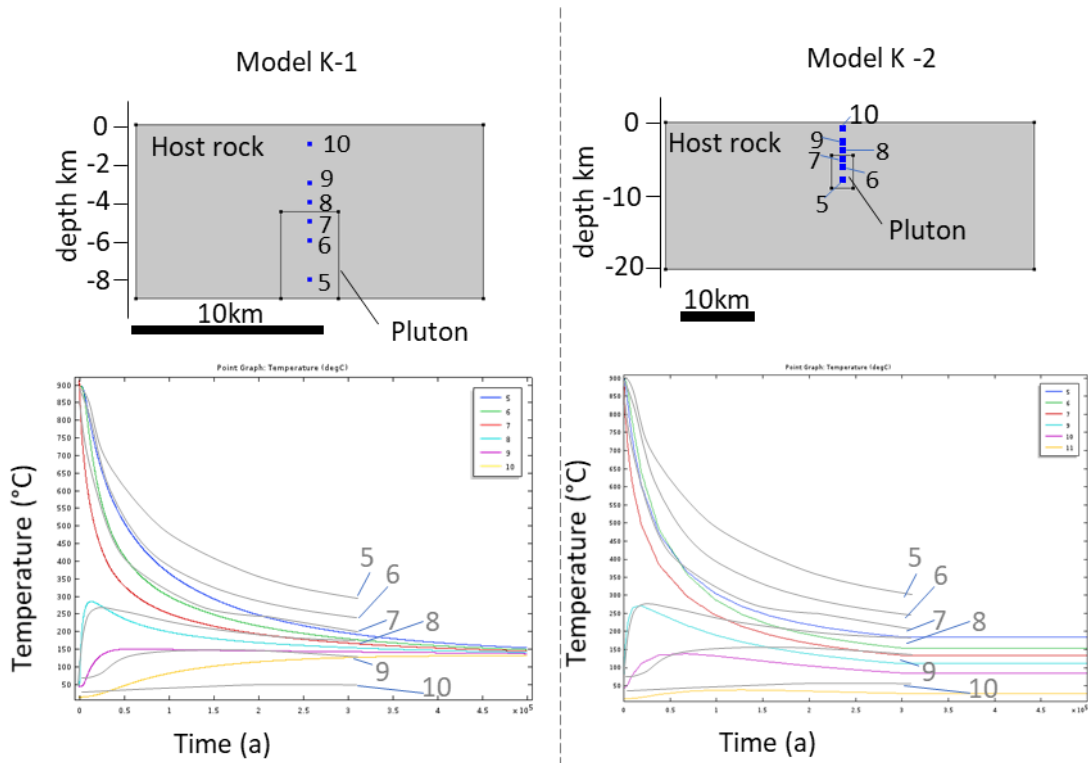


Figure 3.21. Temperature vs time graphs for selected points within the host rock and pluton. Points 5, 6 & 7 within the pluton continually cool while the host rock, points 8, 9 & 10 are initially heated before cooling. The rate of cooling is inversely proportional to the distance from the pluton margin. Grey lines (labelled for equivalent point number) redrawn from Knapp (1978) (Fig.12 p.67). As for figures 3.19 & 3.20, these graphs highlight the faster cooling rate in the COMSOL® in comparison to the Knapp models.

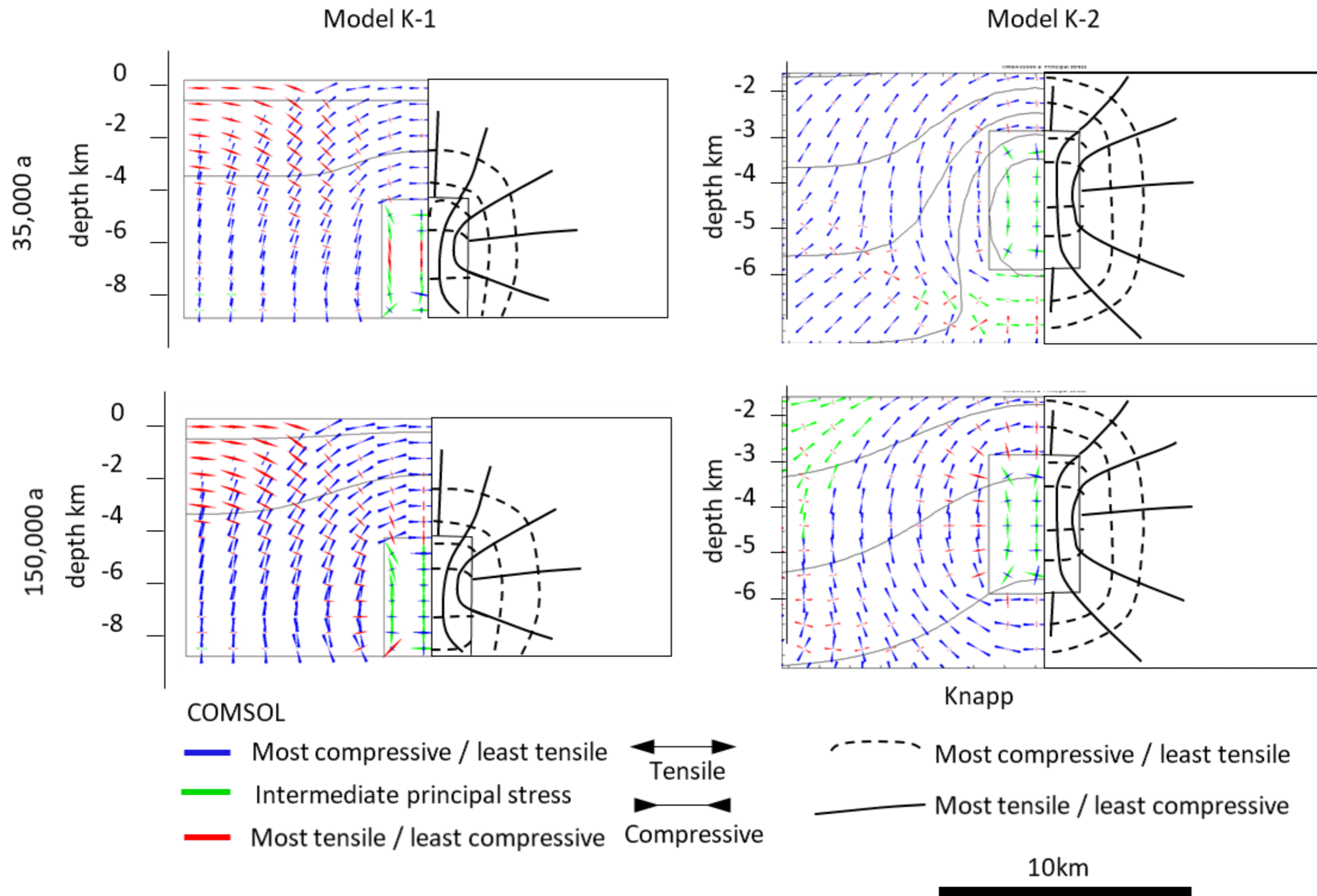


Figure 3.22. Principal stress trajectories in the cooling pluton for models K-1 and K-2 at selected time steps in years after model initiation and temperature contours (grey). Results from COMSOL® are shown on the left and trajectories calculated by Knapp (1978) (Fig.18 p.85) are shown on the right, dashed black line maximum compressive stress direction and solid black line minimum compressive stress orientation. In COMSOL® Maximum compressive stress is blue, intermediate green and minimum red, arrow directions show if stress magnitudes are compressive (pointing inwards) or tensile (pointing outwards). Maximum compressive stress is radial around the pluton in the host rock and approximately parallel to the shortest margin within the cooling pluton.

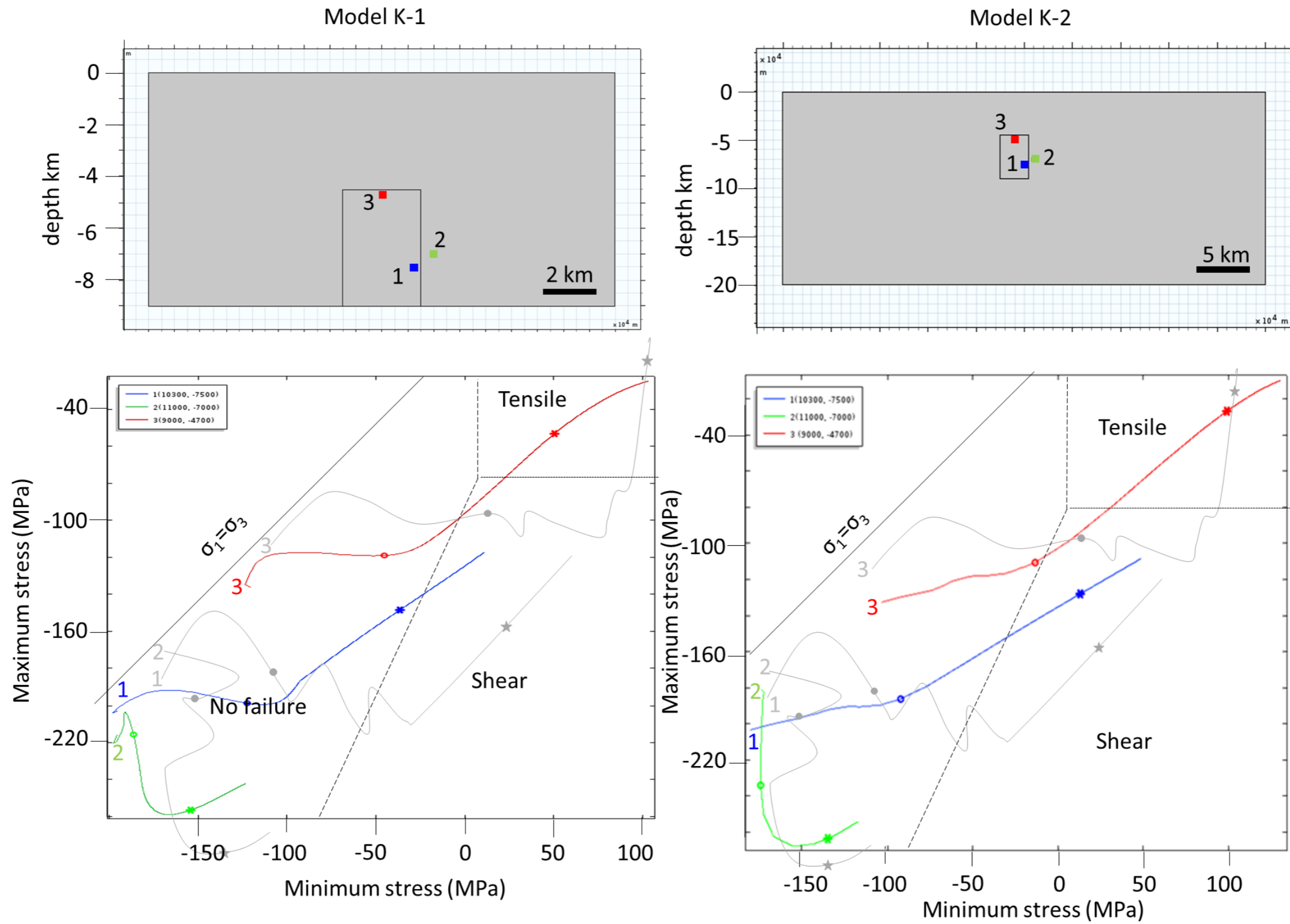


Figure 3.23. Stress paths calculated at selected locations within the COMSOL® model (tensile positive). Circle marks 5,000 years and the star 100,000 years after model initiation. Black lines show brittle failure regimes of the Coulomb-Navier criteria as defined by Knapp (1978). Compressive strength is -100 MPa, and tensile strength is 5 MPa. Grey lines are for equivalent points as those given in Knapp (1978) (Fig.20 p.89). Lines calculated in COMSOL® are less complex than those of Knapp (1978) which account for pressure change as a result of phase change.

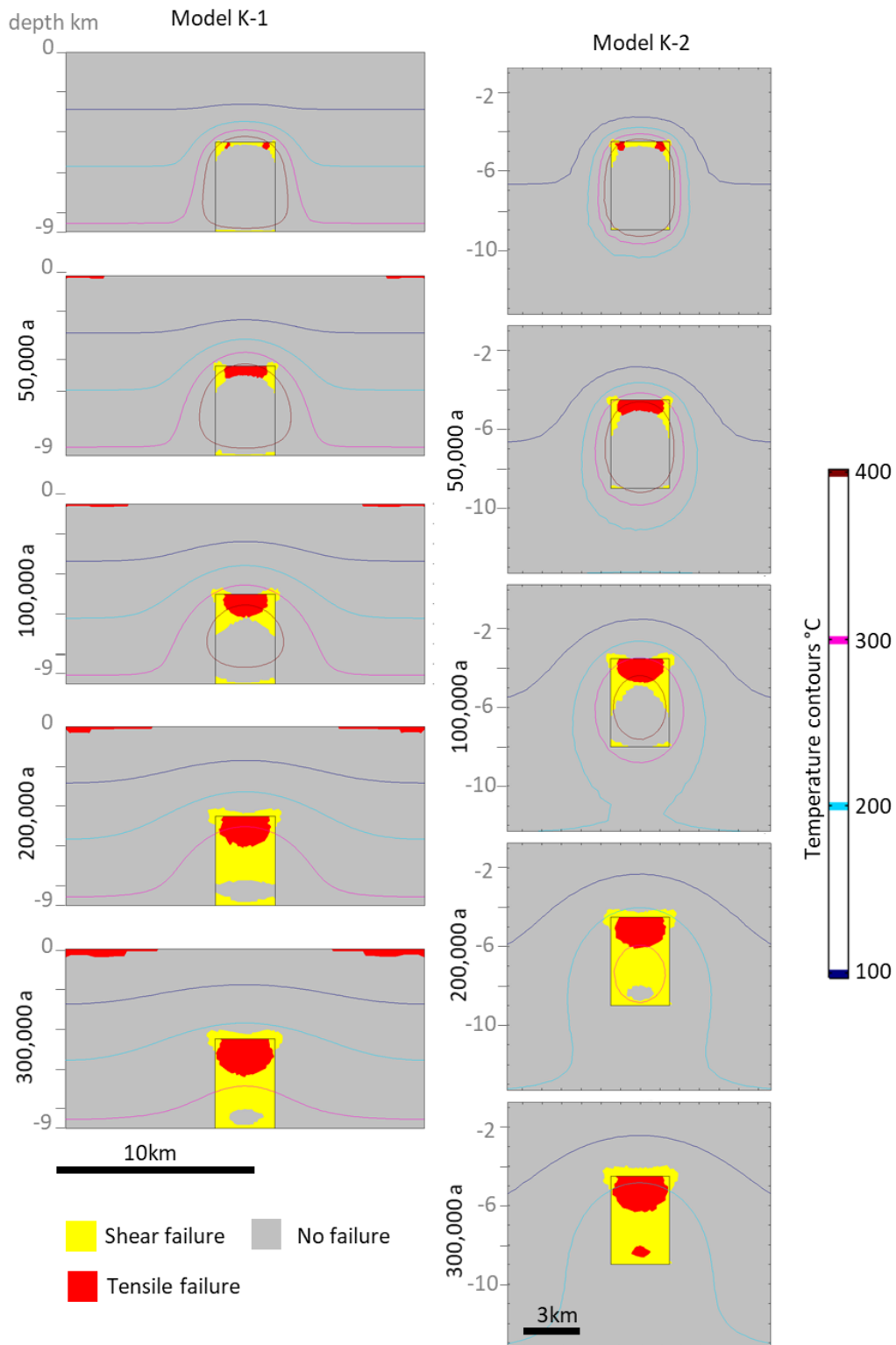


Figure 3.24. Calculated failure domains for the Coulomb-Navier failure criterion in the cooling pluton for models K-1 and K-2 at selected time steps in years after model initiation. Thermal fracturing occurs progressively by shear and then tensile failure in the pluton and shear failure around the pluton.

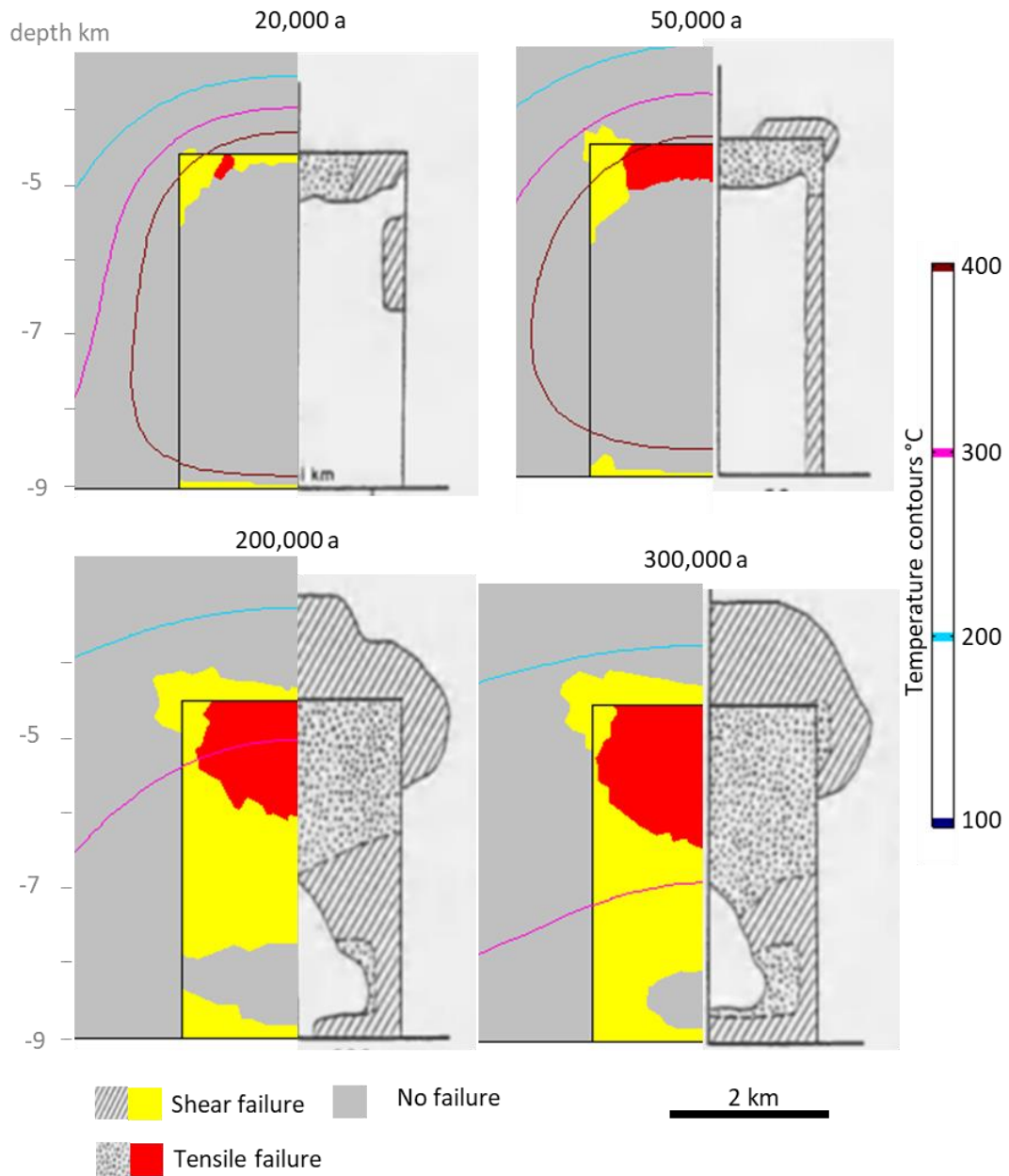


Figure 3.25. Comparison of COMSOL® model K-1 to Knapp models for selected time steps. Numbers are for thousands of years since model initiation. Images on right modified from Knapp 1978 (*Fig.24 p.98*) full unedited figure given in Figure 3.3 p41 this thesis. Copyright (1978) granted by R. Knapp.

3.5.2. Pressured Cylinder and the Diamond Joe Stock, Gerla (1983)

Three two-dimensional conductive plane strain models of pressured cylinders were setup in COMSOL® (Models G-1 to G-3, Figures 3.26) to match the models run by Gerla (1983) (Figure 3.27). Variation in initial temperature and magma pressure were also tested (Figure 3.38). Gerla (1983) compared the numerical models of the pressurised cylinder with fracture patterns in the Diamond Joe stock. In COMSOL® two models (models G-4 and G-5) were set up using the margin geometry of the Diamond Joe stock (Figures 3.29 to 3.31).

For models G-1 to G-3 the pluton is taken as a horizontal map slice through a pressurised cylindrical tube which is infinitely long in the out of plane direction. After Gerla, 1983, the cylinder has an 8 km diameter, the approximate size of the Diamond Joe stock. The magma chamber radius is reduced in each of the models G-1 to G-3 and is 2 km, 1 km and 0.5 km respectively. Initial pluton temperature is set to 920 °C and the host rock to 150 °C. The regional maximum horizontal stress is set to 135 MPa in the y direction and the minimum horizontal stress is set to 45 MPa in the x direction (Gerla, 1983). In models G-1 and G-2 magma pressure is equal to the maximum horizontal stress (135 MPa). In model G-3 magma pressure is increased by 20% to 162 MPa. These values differ from values given by Gerla 1983 who does not state the Young's modulus or coefficient of thermal expansion used in his models (Table 3.2, p.40).

Modelling results for models G-1 to G-3 are shown at 100,000 years after model initiation (Figure 3.26). Comparison of results to models presented by Gerla, 1983 (Figure 3.27) highlights the similarity in orientation of the maximum compressive stress direction and failure mode despite differences in the predicted temperature distribution and strain energy. Model differences are related to the different material properties applied in COMSOL®. For example, the strain energy calculated in COMSOL® is lower than those calculated by Gerla (1983). This is related to the solid thermomechanical parameter (Table 3.2, p.40) which is half in COMSOL® than that given by Gerla (1983).

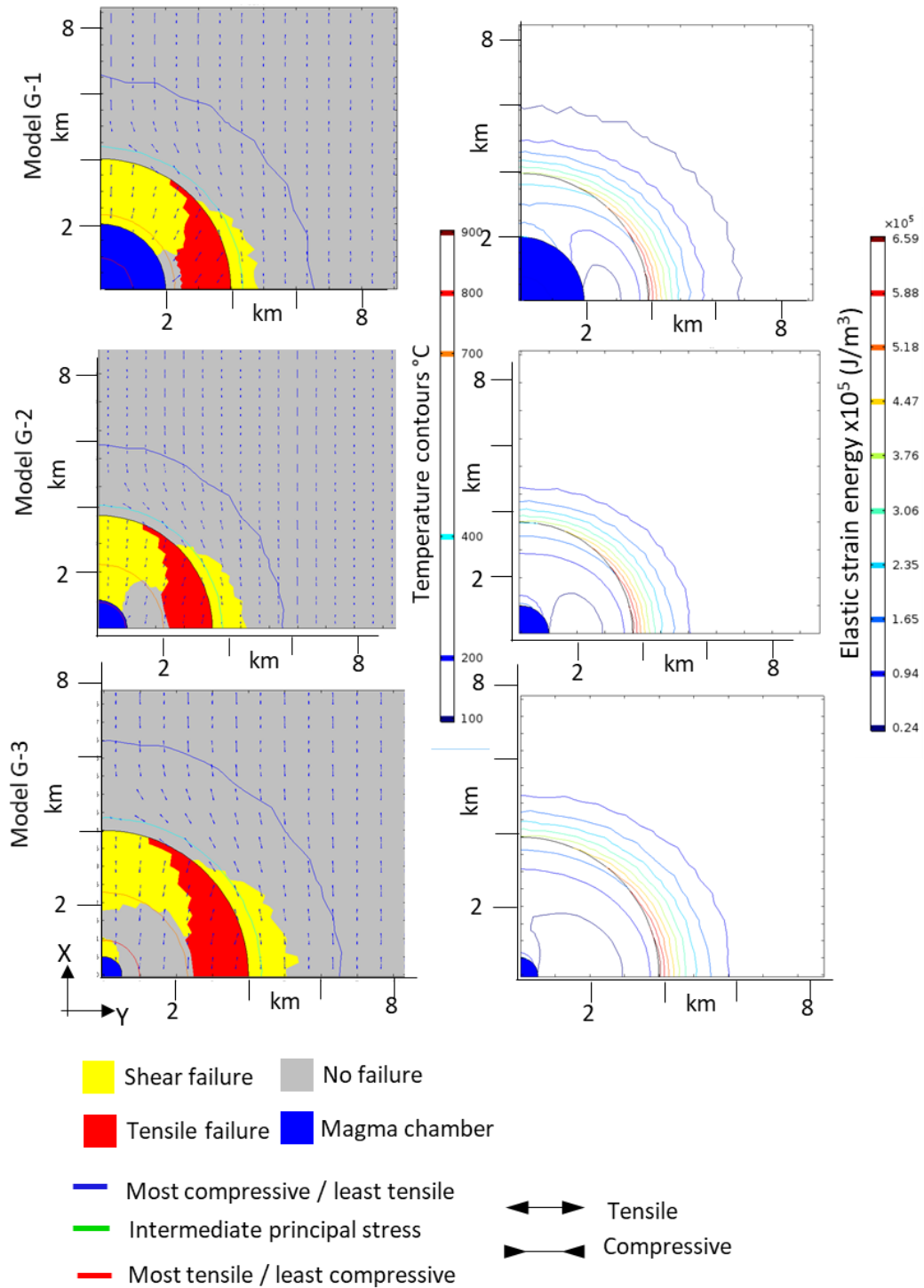


Figure 3.26. Plan view of temperature, stress and strain energy (J/m^3) values calculated in COMSOL® models G-1 to G-3 at 100,000 years after model initiation. Pluton temperature is set to 920 °C and host rock to 150 °C (depth ~ 2 km assuming a geotherm of 75 °C /km). Maximum horizontal stress (y-direction) is set to -135 MPa and minimum horizontal stress (x-direction) is set to -45 MPa. In Models G-1 and G-2 magma pressure is equal to the maximum horizontal stress (135 MPa). In model G-3 magma pressure is increased by 20% to 162 MPa. Brittle failure domains are coloured. Compare to Figure 3.27.

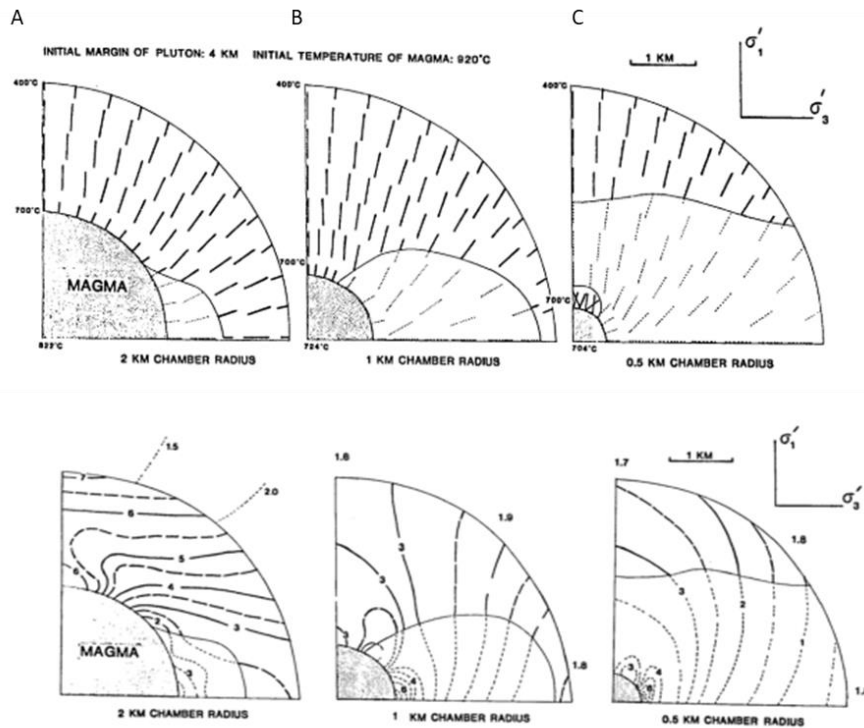


Figure 3.27 Stress and strain energy predicted in a pressured cylinder for varying chamber radius. Top row: Solid lines strike of predicted vertical fractures based on the direction of maximum compressive stress, dashed lines represent areas that are not in failure. Horizontal stresses are set to 135 MPa in the y direction and 45 MPa in the x direction. For 4 km radius pluton with (A) 2 km radius magma chamber, (B) 1 km radius magma chamber and (C) 0.5 km radius magma chamber. Magma pressure is set to 135 MPa in models with a 2 and 1 km radius magma chamber and 162 MPa for the model with a 0.5 km radius magma chamber. Bottom row: Contoured theoretical elastic strain energy at three stages of crystallization (J/cm³). Dotted contour lines indicate values of strain in areas that are predicted not to fracture. Copyright (1983) *Fig.24 p54 and Fig.35 p57* granted by P. Gerla.

Removing magma pressure from the models reduces early shear failure near the magma chamber but overall has a minimal influence on the modelled results (Figure 3.28). The influence of lowering the regional load on modelling results was tested (Figure 3.28). The regional load was reduced to 75 and 15 MPa and magma pressure to 45 MPa (Gerla, 1988). Reducing the regional load reduces the alignment of the plane perpendicular to the minimum principal stress with the regional load (Figure 3.28). The lower values of regional tectonic stress were chosen by Gerla (1988) to best fit mapped radial orientations of fractures in the Diamond Joe stock (Figure 3.28). Based on this modelling and field work Gerla (1988) inferred that east-northeast oriented compression during early Laramide orogeny led to pluton emplacement. This was followed by reversal of the regional stress

field, in shallow levels, to a N35°W orientated compressive field during cooling and fracturing as a result of arching in the upper crust.

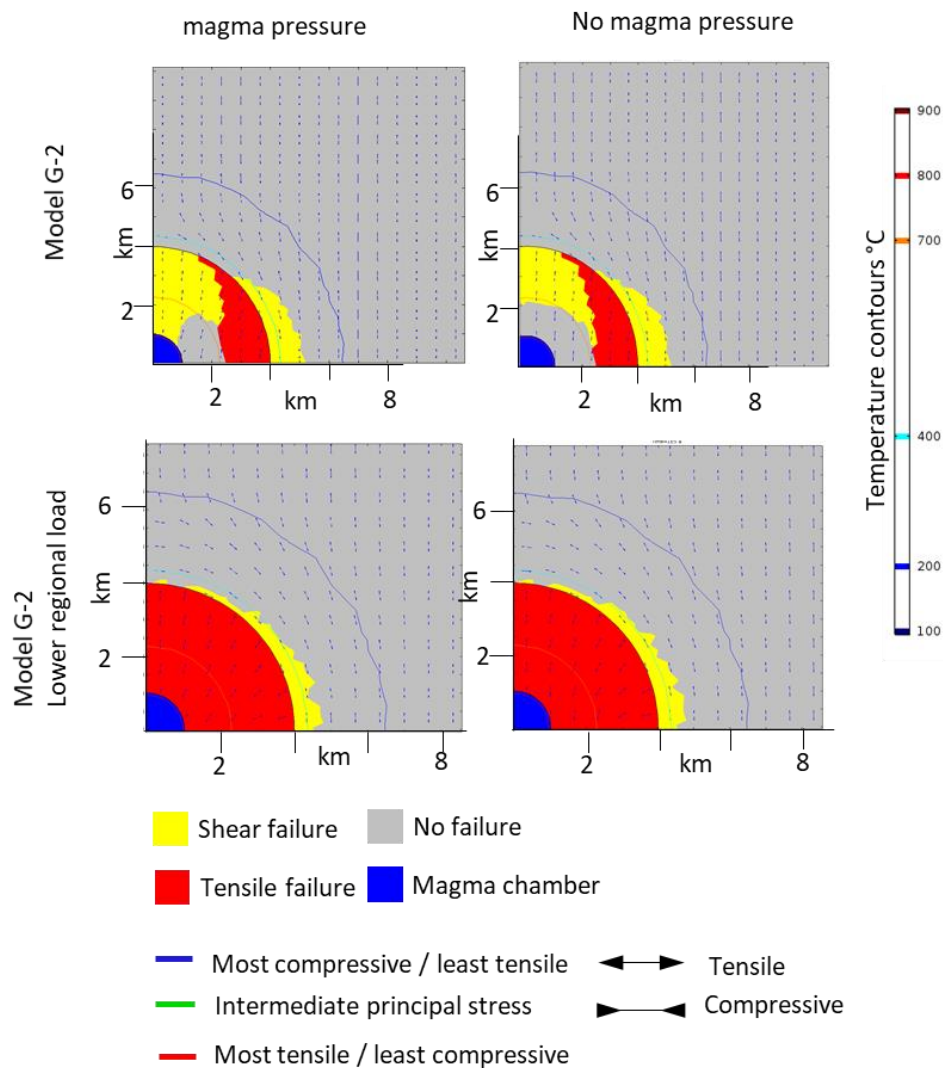


Figure 3.28. Variations of model G-2 calculated in COMSOL® showing effect of not accounting for magma pressure and lowering the regional load. Pluton temperature is set to 920 °C and host rock to 150 °C (depth ~ 2 km assuming a geotherm of 75 °C/km). Top row: Maximum horizontal stress (y-direction) is set to 135 MPa and minimum horizontal stress (x-direction) is set to 45 MPa. Bottom row: Maximum horizontal stress (y-direction) is set to 75 MPa and minimum horizontal stress (x-direction) is set to 15 MPa.

Modelling results are compared to a representative diagram of radial fractures (after Gerla, 1983, 1988) and a lineament interpretation of the satellite image (Figure 3.29). Non-radial fracture patterns were removed from Gerla's (1983, 1988) interpretation due to the dominant radial pattern predicted during numerical modelling of the infinite cylinder.

Based on the modelling workflow of Bergbauer (1998) the mapped boundary geometry of the Diamond Joe stock was used to directly model thermal history and predict principal stress directions. Initial pluton temperature was set to 920 °C and host rock to 200 °C (Gerla, 1988). Two models were run one with an isotropic initial stress field (model G-4) and the second with the proposed anisotropic regional tectonic load (model G-5, Figure 3.30). In models G-4 and G-5 the stock geometry is rotated 35° clockwise so that in model G-5 the regional maximum compressive stress (75 MPa) is aligned with the y axis. Modelling results are compared to a representative diagram of radial fractures (after Gerla, 1983, 1988) and a lineament interpretation of the satellite image (Figure 3.29). Non-radial fracture patterns were removed by Gerla (1983, 1988) from his presented interpretation (Figure 3.29B) due to the dominate radial pattern predicted during numerical modelling of the infinite cylinder.

Modelling results (Figure 3.30) suggest that there is a better fit of predicted stress orientations to lineament interpretation when tectonic load is not accounted for in the earlier cooling history (Figure 3.30 D, Model G-4 at 5,000 years after model initiation). Contrary to Gerla, 1983, 1988, that in the case of the Diamond Joe stock the plutonic geometry has more of an influence on fracture orientations than the regional tectonic load. Radial fractures, to the right of the Gunsight fault and below the Silvertrails lineament only predicted in the model G-5 which accounts for regional tectonic load. As the other fracture orientations in the numerical model are not readily matched to the model G-5 it may be possible that the radial fractures in this location are related to tectonic movement on the Gunsight fault. Application of the Coulomb-Navier failure criteria suggest that tensile failure is likely to predominate within the pluton (Figure 3.31), which is the dominant failure mechanism observed in the field (Gerla, 1983).

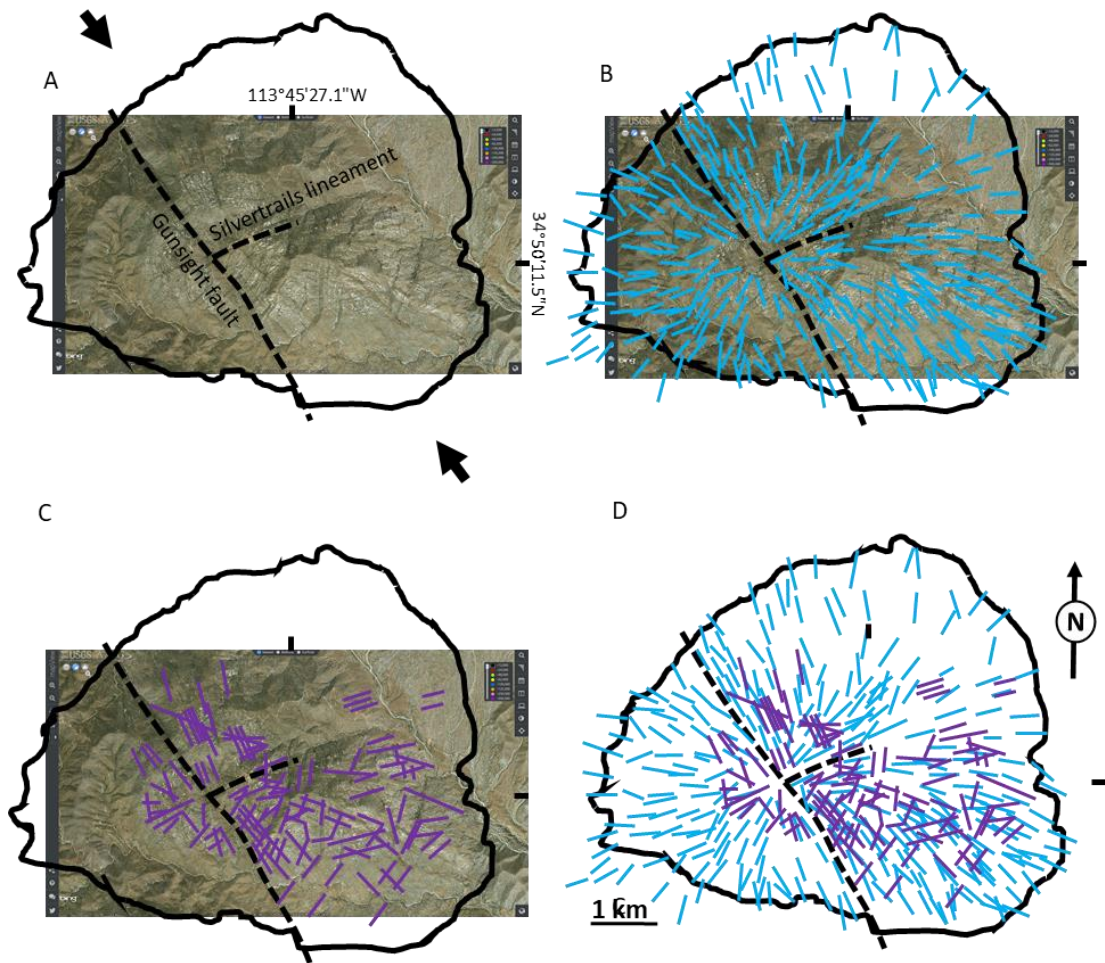


Figure 3.29. Lineament interpretation of the Diamond Joe stock. (A) Mapped boundary overlain on satellite image. Dashed lines position of prominent linear features redrawn after Gerla (1983). Inferred $N35^{\circ}W$ direction of maximum horizontal stress is shown by black arrows. (B) strikes of radial fracture sets (redrawn from Gerla, 1983 Fig.16 p37) the lines are representative trends and Gerla (1983, 1988) removed the other non-radial trends (as identified in C) from this interpretation. (C) Interpretation of linear trends on aerial photograph, the $\sim NE$ trend is identified in the SE quadrant of the stock. (D) overlay of interpretations given in B and C.

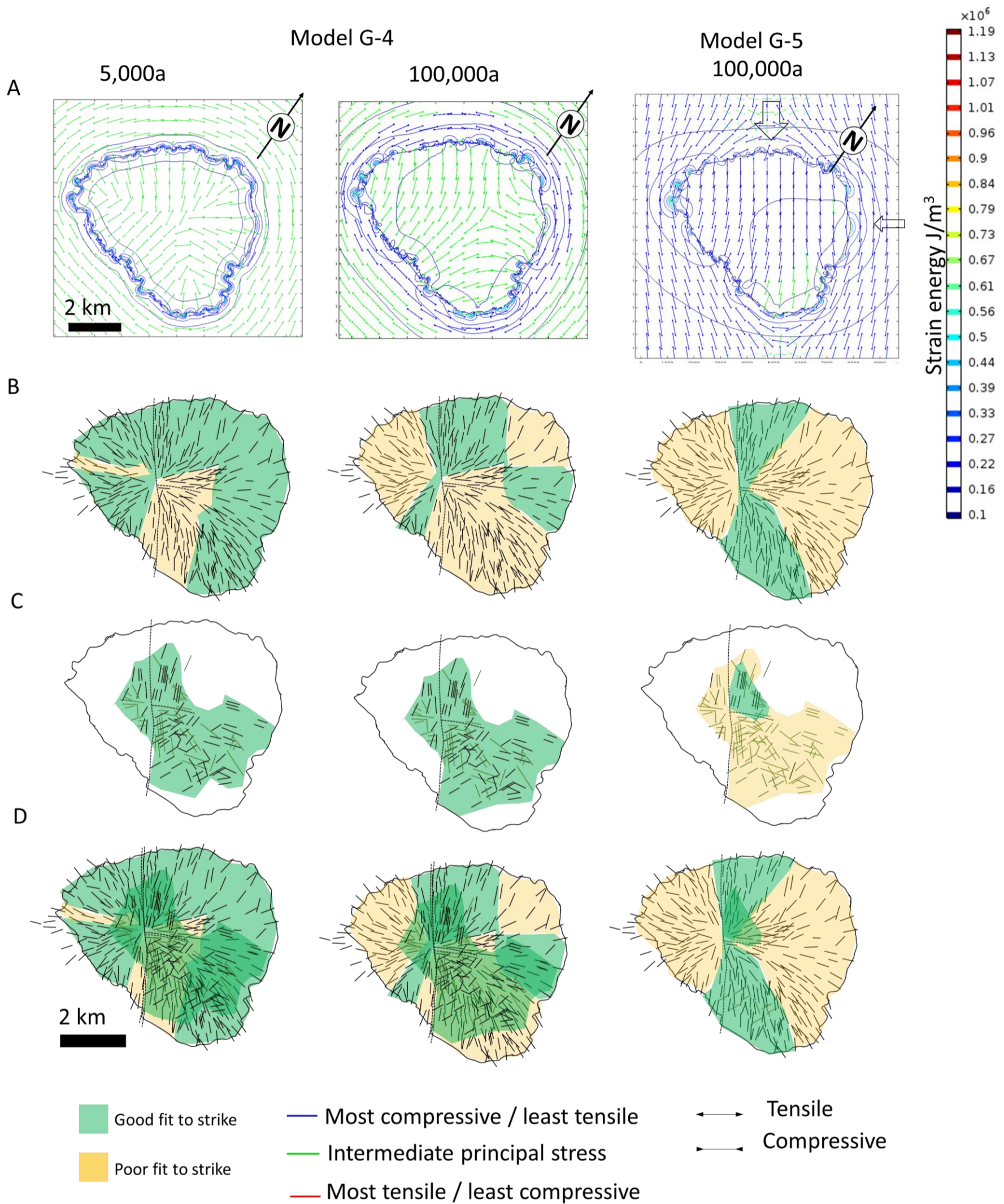


Figure 3.30. Numerical models of the Diamond Joe stock and comparison to lineament maps. Model G-4 horizontal stresses equal, model G-5 horizontal stresses are not equal, maximum horizontal stress is in a NW-SE direction, modelled maximum compressive stress of 75 MPa in y direction and 15 MPa in x direction after Gerla (1983). (A) principal stress direction and contours of strain energy for Model G-4 is shown for two-time steps and model G-5 for one-time step as principal stress orientations do not change over time. (B) and (C) comparison of COMSOL® models to interpreted fracture orientations given in Figure 3.29, colour mapped green for when $<15^\circ$ and orange when $>15^\circ$ difference in strike of plane perpendicular to the minimum principal stress. (D) overlay of the fit for both (B) and (C) at the given time step.

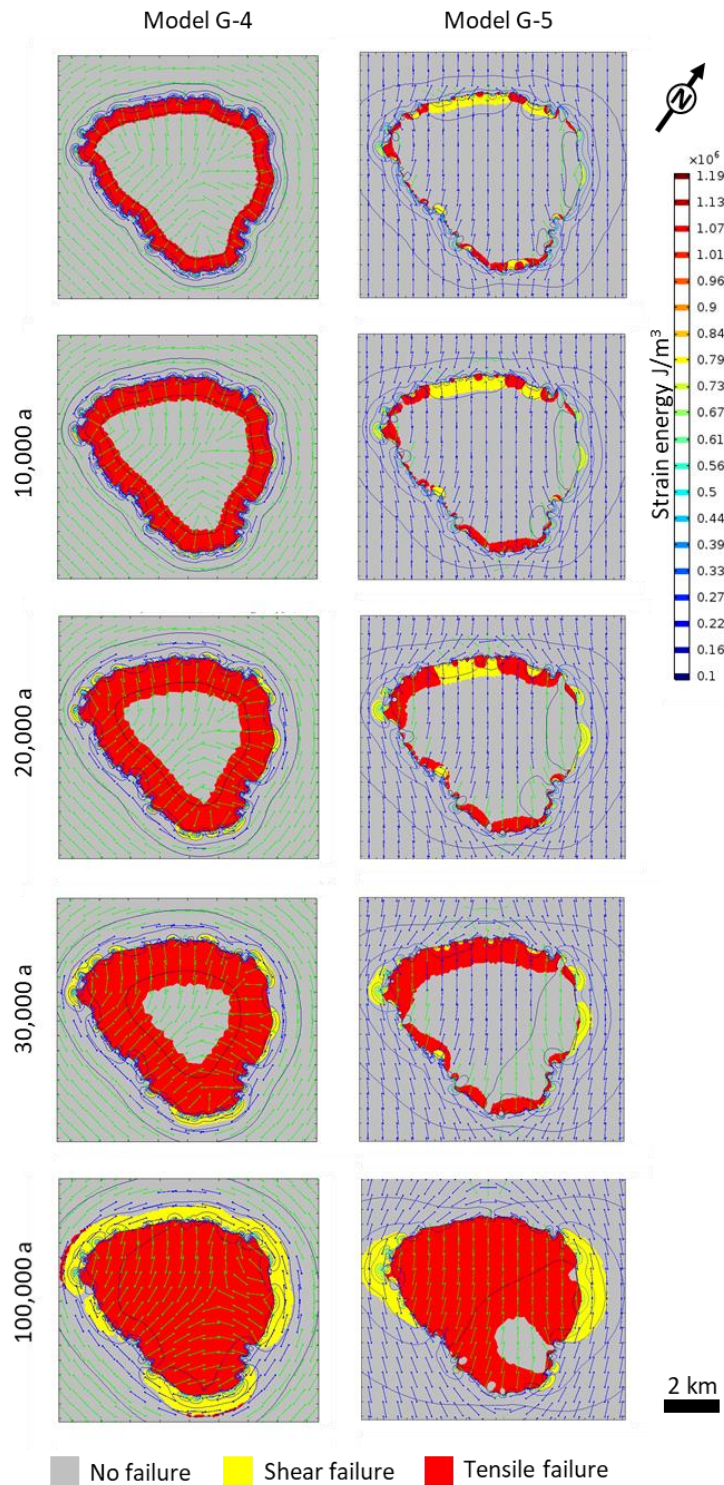


Figure 3.31. Calculated failure domains for the Coulomb-Navier failure criterion in the cooling pluton for models G-4 and G-5 at selected time steps in years after model initiation. Model G-4 thermal fracturing occurs progressively by tensile failure in the pluton and shear and tensile failure around the pluton. In model G-5 both shear and tensile failure occur within the pluton and the location of shear failure in the host rock is limited. Contours strain energy (J/m^3) pattern.

3.5.3. Geometric shapes, Cartridge Pass and Lake Edison granodiorites, Bergbauer (1998)

Models of basic geometric shapes (models B-1 to B-4) and models of the Cartridge Pass Granodiorite (models B-5 to B-7) and Lake Edison Granodiorite (model B-8 to B-10) were set up as two-dimensional plane stress models. Conductive cooling of the plutonic body was modelled. Initial temperatures and material parameters of these models are given in Table 3.6. Mechanical properties are taken from Table 3.4. Best fit tectonic loads suggested by Bergbauer (1998) were applied in models B-6 and B-10. The thermal histories and developed stresses in all models are like those predicted by Bergbauer (1998) (Figures 3.32 to 3.36).

Table 3.6. Initial temperatures, material properties.

		Basic geometries and Cartridge Pass Bergbauer et al., 1998 Models B-1 to B-7	Lake Edison Bergbauer and Martel, 1999 Models B-8 to B-10
Initial pluton temperature	°C	750	800
Initial host rock temperature	°C	300	230
Density	kg/m ³	2630 *	2630 *
Heat capacity at constant pressure	J/(kg.K)	775 *	775 *
Thermal conductivity	W/(m.K)	2.79 ‡	4.99 ‡
Young's modulus	GPa	30.4	30.4
Poisson's ratio		0.25	0.25
Coefficient of thermal expansion	1/°C	8 x 10 ⁻⁶ †	8 x 10 ⁻⁶
Thermal diffusivity	m ² / s	1.37 x 10 ⁻⁶	2.45 x 10 ⁻⁶

* Values from MATLAB script given at end of Bergbauer (1998).

† Value in paper is given as 1.8 x 10⁻⁶ but this is assumed to be a type error, based on value in Skinner (1966) and solid thermomechanical parameter given in the paper.

‡ Values calculated from Thermal conductivity = Thermal diffusivity x density x specific heat capacity.

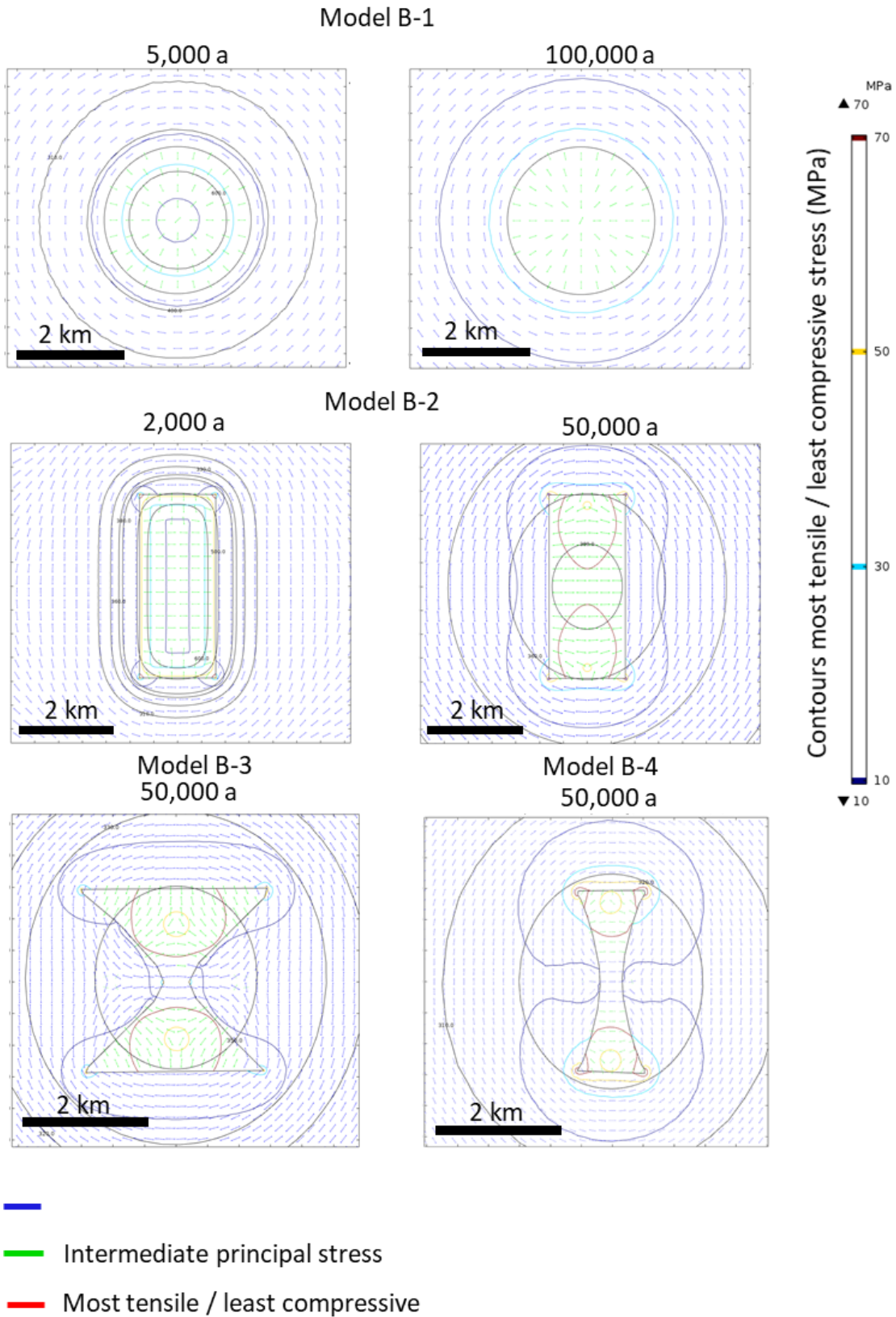


Figure 3.32 A. Development of stresses within plutons and host rock in map view for given time steps for a circular intrusion, rectangular intrusion hourglass intrusions (after Bergbauer et al., 1998). Compare with Figure 3.33 B (next page).

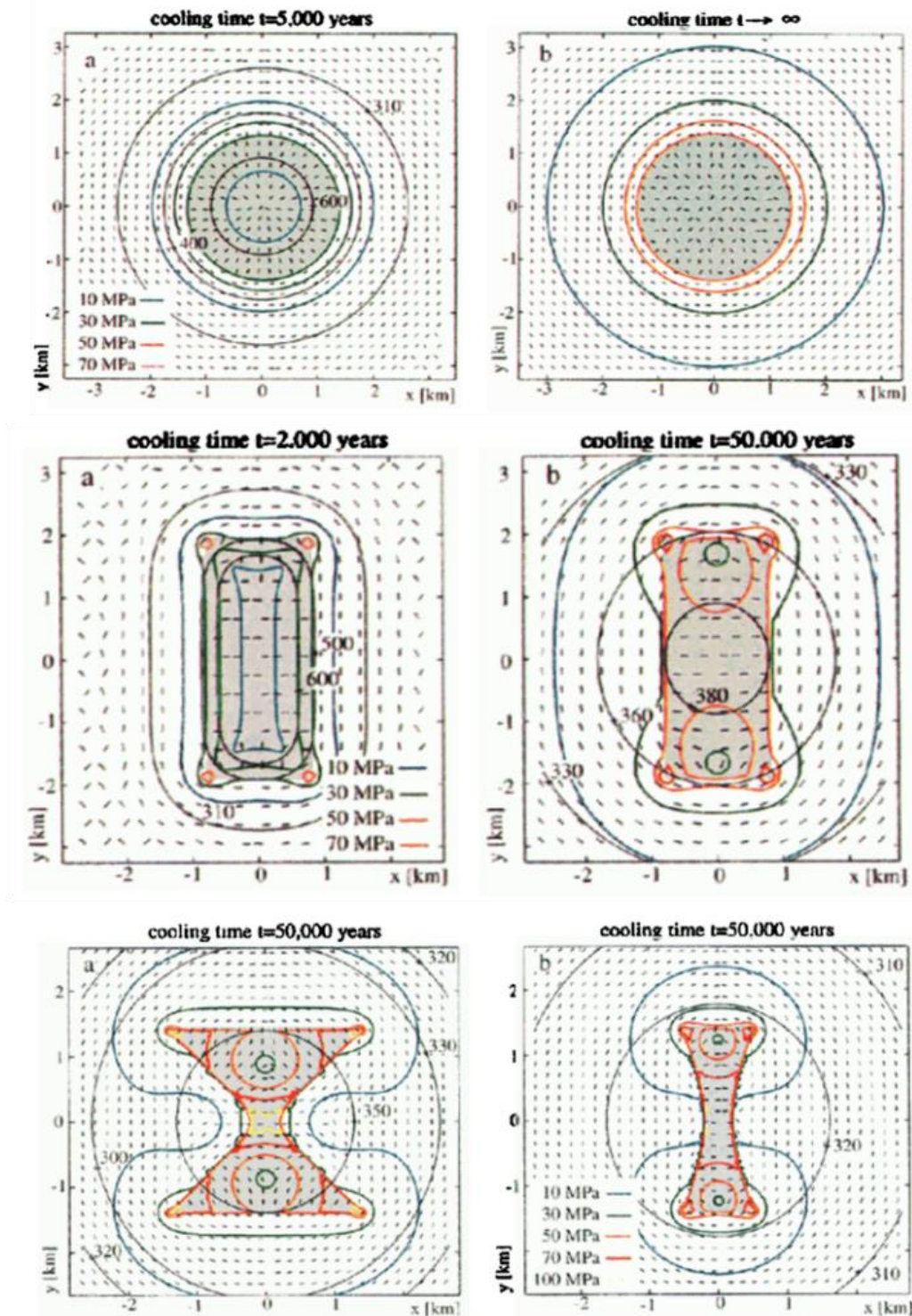


Figure 3.32 B. Development of stresses within plutons (grey) and host rock in map view for given time steps for a circular, rectangular and hourglass intrusions. Coloured contours show most tensile stress magnitudes and black contours the temperature for the given time after emplacement. Tick marks are perpendicular to the direction of most tensile stress. In circular intrusions, the direction of maximum compressive stress is therefore radial. In rectangular geometries, away from the margins, the maximum principal stress preferentially aligns to the short axis. From Bergbauer et al. (1998). Copyright (1998) *Fig.1 – 3 p.709* AGU. Duplicate of Figure 3.2 p.42 this thesis.

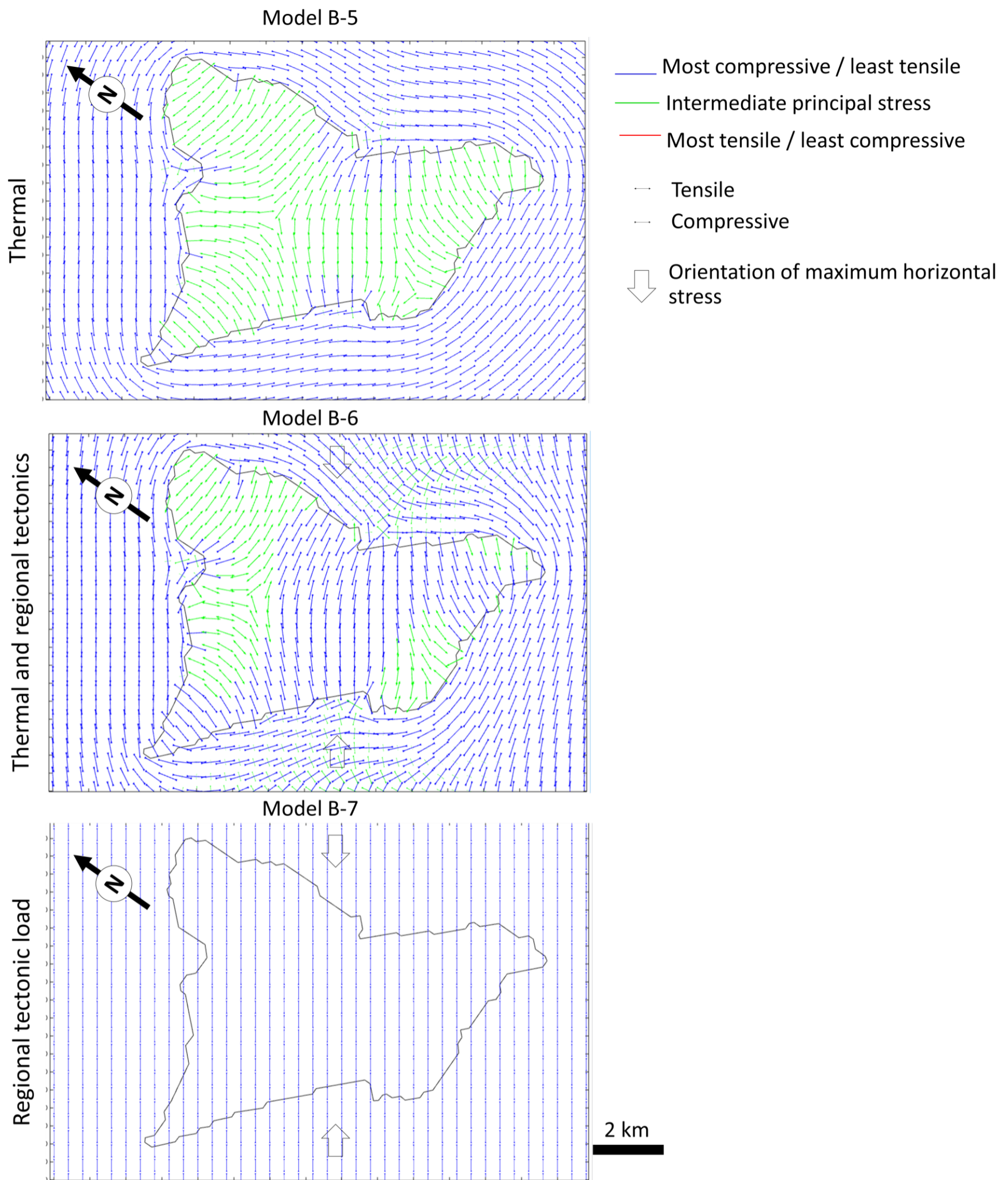


Figure 3.33. Numerical models of the Cartridge Pass granodiorite 50,000 years after model initiation. Model B-5 thermal stress only, model B-6 thermal and tectonic stress, model B-7 tectonic stress only.

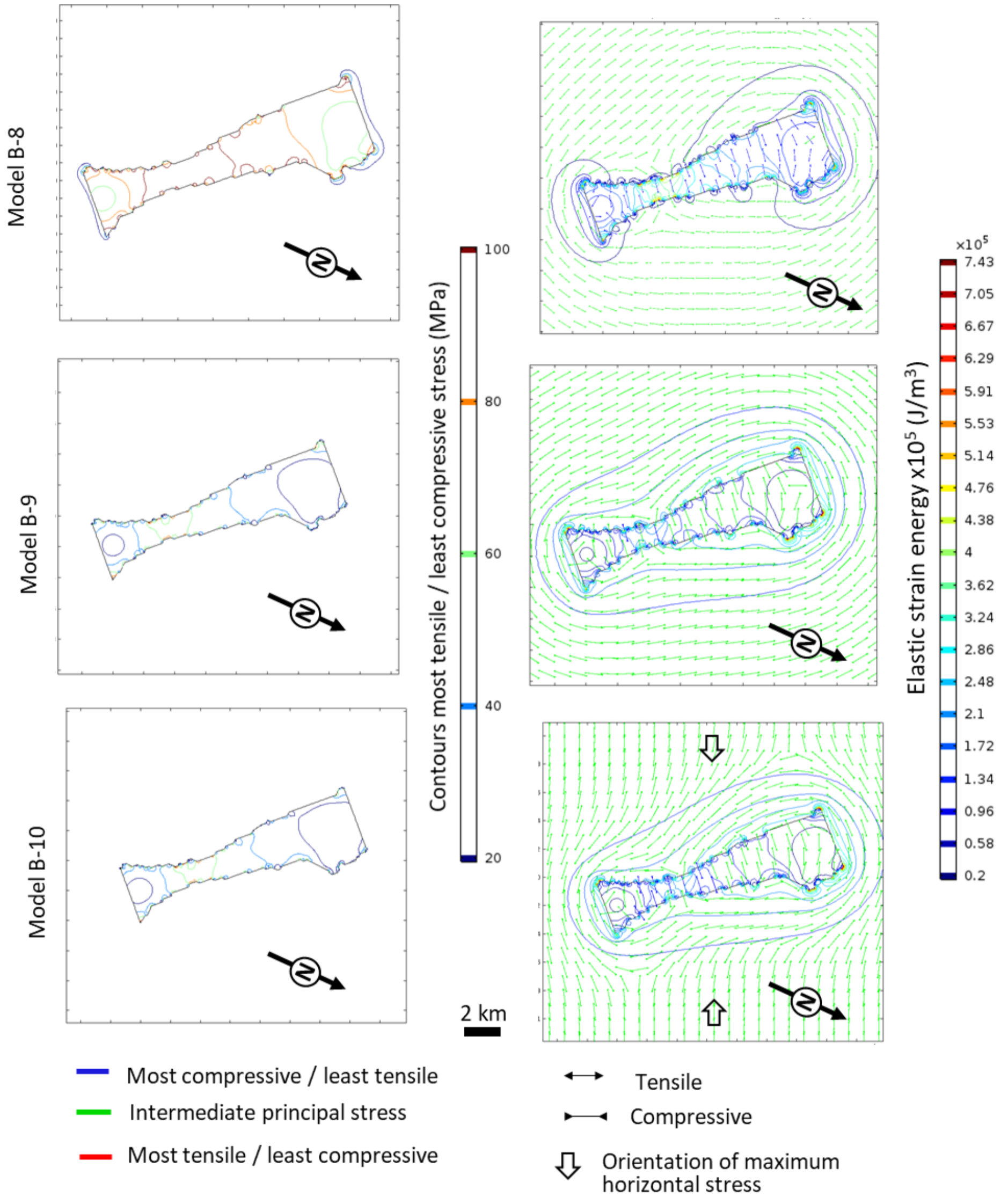


Figure 3.24. Numerical models of the Lake Edison granodiorite 1,000,000 years after model initiation. Model B-8 thermal stress only at a depth of 3.5 km, model B-9 thermal stress only at a depth of 7 km, model B-10 thermal and tectonic stress at a depth of 7 km.

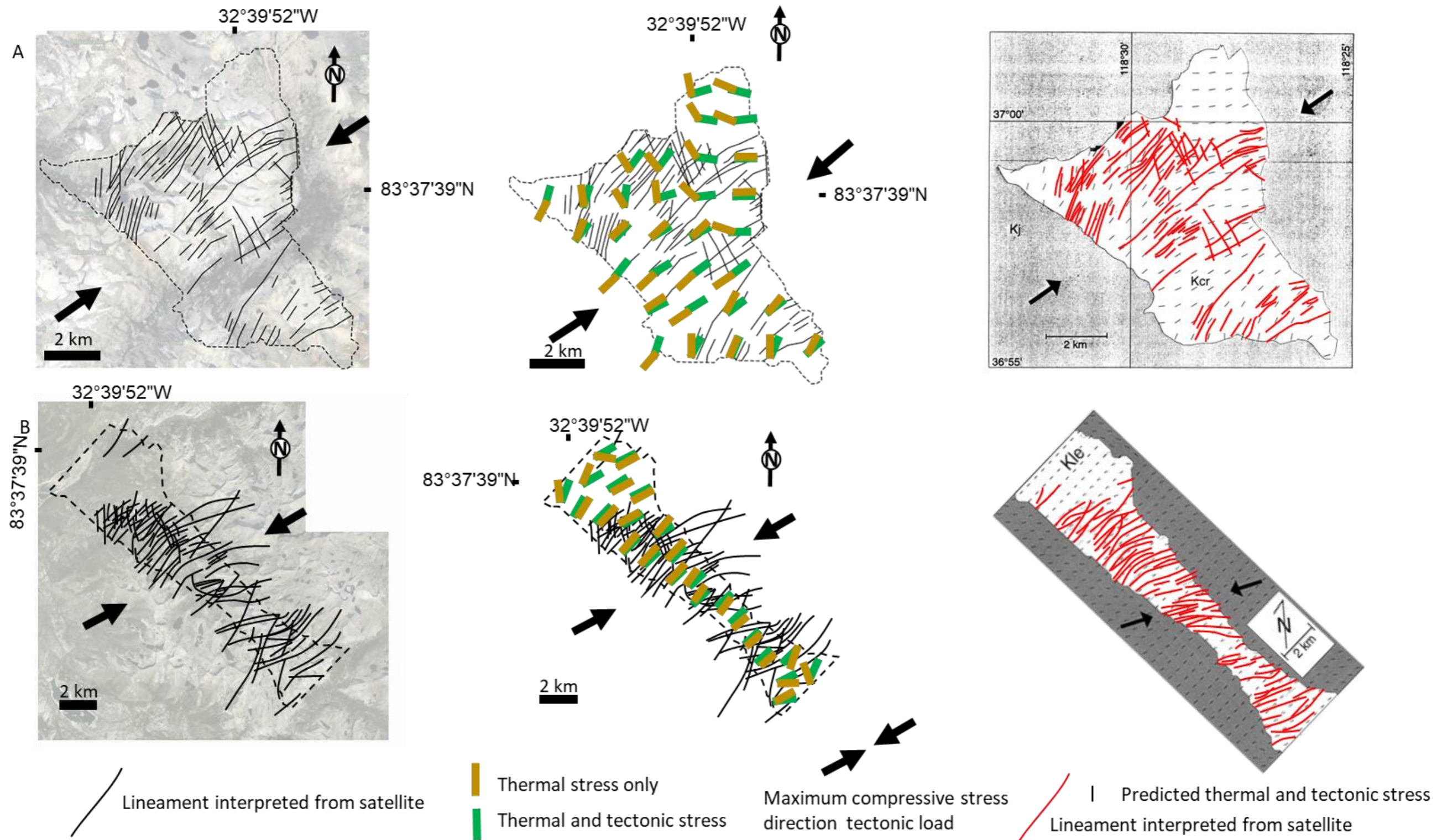


Figure 3.35. Comparisons of lineament interpretation from (A) Cartridge Pass granodiorite (top row) and (B) Lake Edison granodiorite (bottom row) with modelled thermal and thermal & tectonic stresses from COMSOL®. Modelling results from Bergbauer and Martel (1999) are shown for comparison. Bergbauer and Martel, 1999 models (last column): short black ticks are the modelled most compressive stress trajectories due to thermal and regional tectonic stresses. (A) Granodiorite of Cartridge Pass at 0.9 million years after cooling and (B) Lake Edison Granodiorite after 86 million years of cooling. Black arrows show the direction of the applied regional most compressive horizontal stress. Copyright (1999) Fig.7 p.831 Fig.8 p.833 with permission from Elsevier (Duplicate of Figure 3.4 p42 this thesis).

Bergbauer (1998) used modelling results to suggest that tectonic load was necessary to best match fracture traces predicted from numerical models of plutons (Figure 3.35). Despite this some areas in the models do not match particularly well and in areas where the best match is observed, predictions from thermally loaded models have a similar trend.

Differences in the pattern of predicted principal stress and the photolineament interpretation in the case of the Cartridge Pass granodiorite and the Lake Edison granodiorite have been explained by Bergbauer (1998) as due to (1) the presence of non-thermal lineaments, (2) material anisotropy (e.g., presence of shear zones and dyke-like intrusions) influencing the stress field, (3) the mapped shape of the intrusive contact, (4) stress redistribution due to fracturing resulting in multiple fracture orientations, or (5) an incorrectly assumed tensile strength value at the point of failure as principal stress directions change overtime. Bergbauer (1998) suggests that the last two explanations are less likely, due to the good fit in orientation in other parts of the intrusive bodies. An alternative explanation may be related to only selecting one orientation of fracture for comparison. Multiple sets of fractures of varying orientations may have formed at one point in the pluton due to shear failure or rotation of the principal stress axes over time (Figure 3.16).

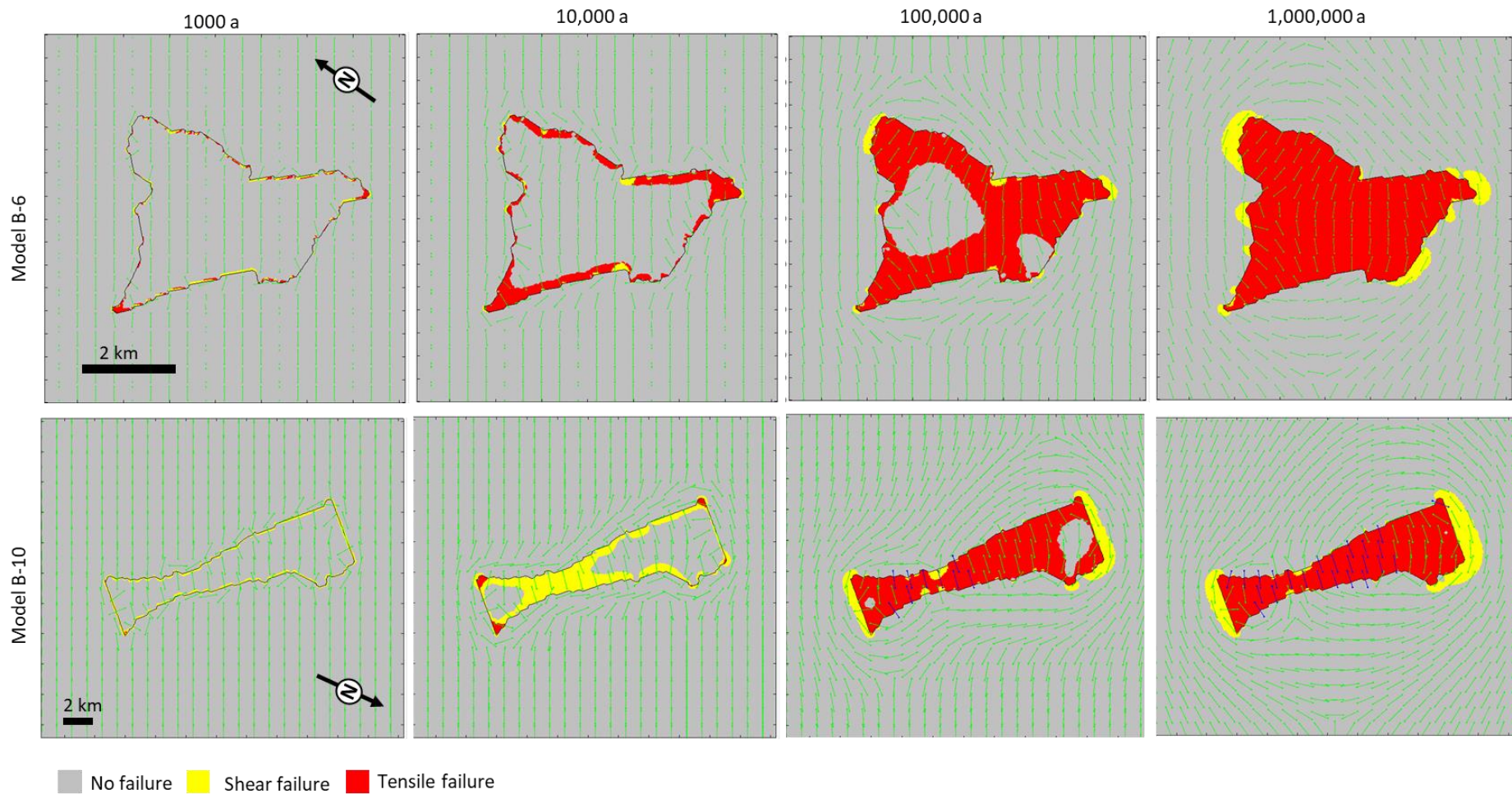


Figure 3.36. Calculated failure domains for the Coulomb-Navier failure criterion in the cooling pluton for models B-6 and B-10 at selected time steps in years after model initiation. Model B-6 thermal fracturing occurs predominately by tensile failure in the pluton, localised shear failure occurs within and round the Cartridge Pass granodiorite. In model B-10 shear failure dominates the early failure mechanism followed by tensile failure.

3.5.4. The Tanvald Pluton, Žák et al. (2006)

Map-view two-dimensional conductive plane strain models were setup in COMSOL® (models Z-1 & Z-2, Figure 3.37). Pluton and host rock geometry is defined after Žák et al. (2006). Initial pluton temperature is set to 800 °C and host rock geotherm to 300 °C/km (Case 2 Žák et al., 2006). Conductive cooling of the plutonic body was modelled. Initial temperatures and material parameters of model Z-1 are given in Table 3.4 and temperature dependent modelling parameters used in model Z-2 are given in Table 3.7. Models Z-1 and Z-2 are compared to assess the effects of temperature dependent material and mechanical properties on results.

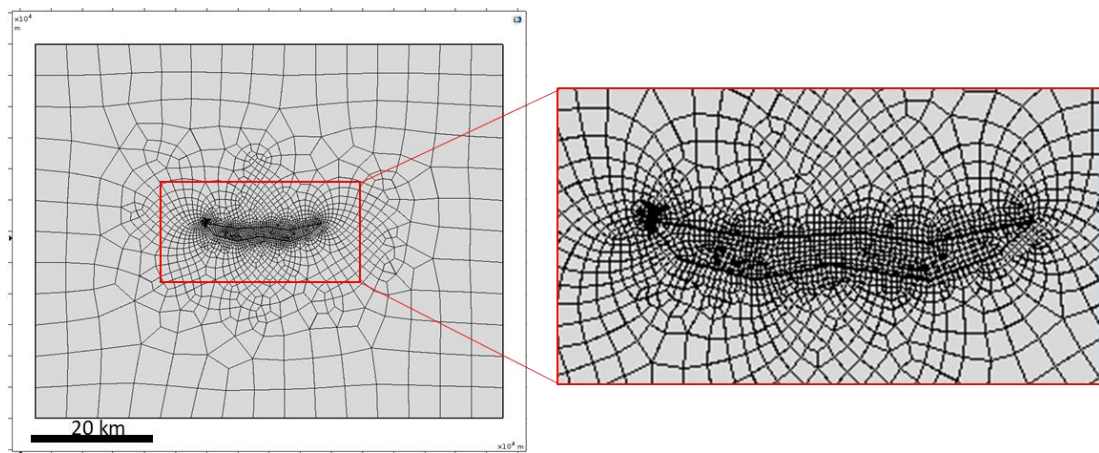


Figure 3.37. Geometry and grid used in COMSOL® to model the Tanvald pluton.

Table 3.7. Temperature dependent material and mechanical properties defined in model Z-2

Granite		Temperature °C					
		20	200	400	600	800	1100
Density	kg/m ³	Constant at 2600					
Heat capacity at constant pressure	J/(kg.K)	766	968	1149	1226	1226	1415
Thermal conductivity	W/(m.K)	2.4	1.9	1.6	1.5	1.5	1.6
Young's modulus	GPa	56	Linear				0
Poisson's ratio	-	0.11				0.5	
Coefficient of thermal expansion	1/°C	0	Linear		15e-6	0	
Tensile strength	MPa	21	Linear				0
Compressive strength	MPa	229	Linear				0
Phyllite							
Density	kg/m ³	Constant at 2600					
Heat capacity at constant pressure	J/(kg.K)	613	920	1226	1415	1533	1839
Thermal conductivity	W/(m.K)	3	2	1.5	1.3	1.3	0.9
Young's modulus	GPa	76.5	Linear				0
Poisson's ratio	-	Constant at 0.2					
Coefficient of thermal expansion	1/°C	0	Linear		15e-6	0	
Tensile strength	MPa	22.8	Linear				0
Compressive strength	MPa	126	Linear				0
Granite and Phyllite							
Cohesion [†]	MPa	22.6	22.5	20.7	16.2	10.4	0
Angle of internal friction [†]	°	50.2	49.1	38.8	26.2	6.9	7.3

Unless stated values after Žák et al. (2006) see appendix Table A3-3 p311 for details.
[†] Values taken from Heuze (1983)

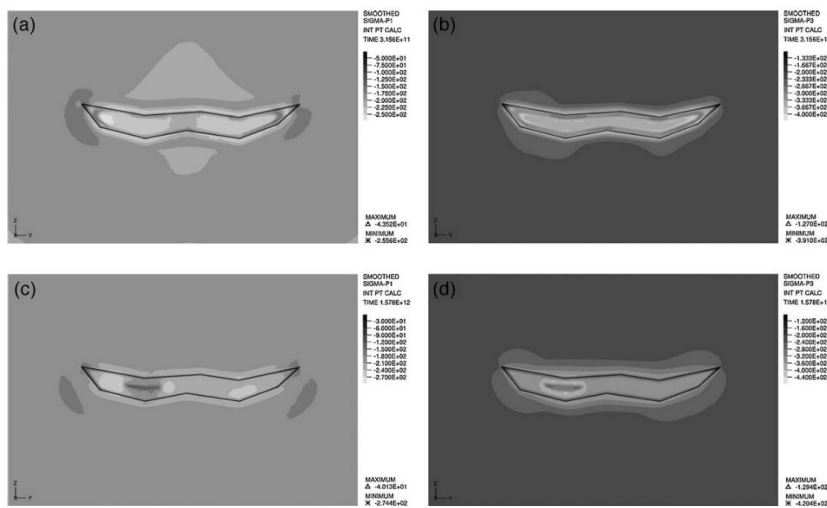
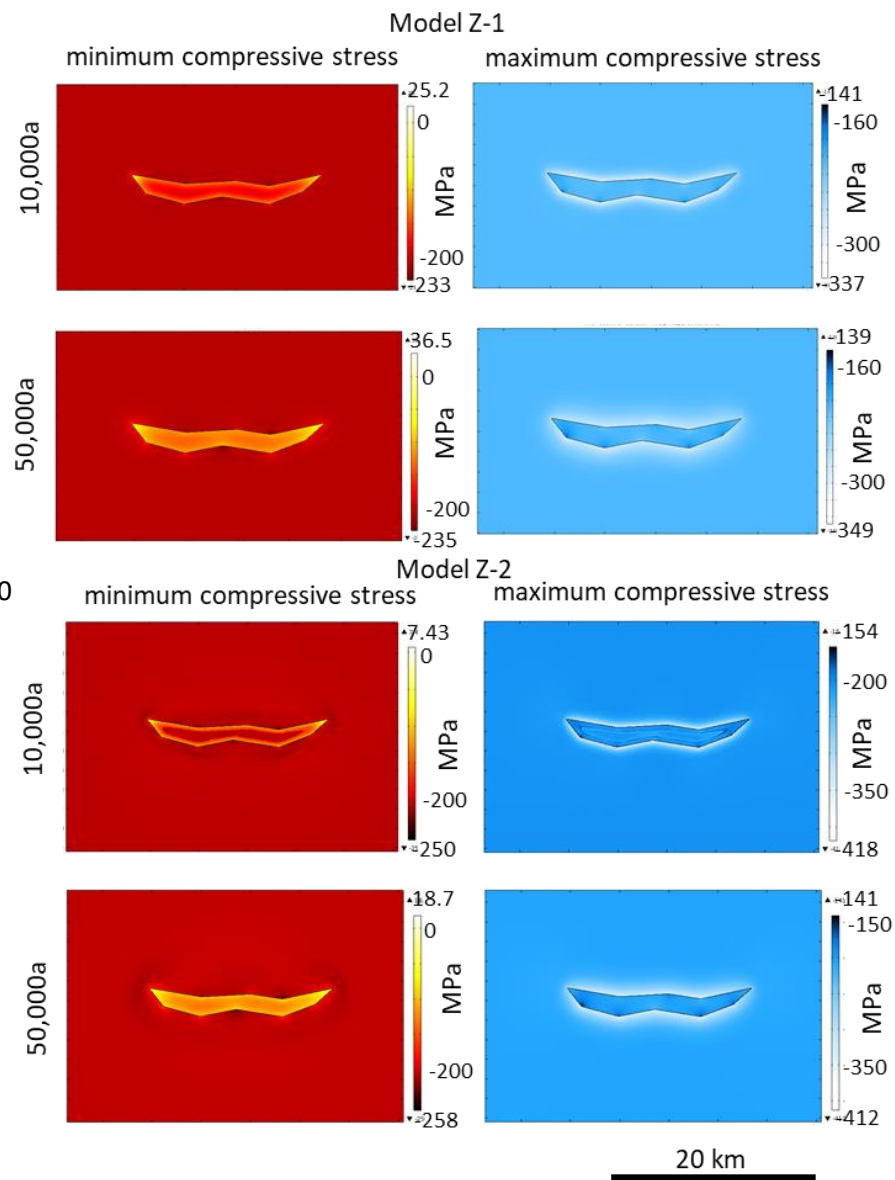


Figure 3.38. Comparison of maximum and minimum principal stress values 10,000 years and 50,000 years after model initiation in years of COMSOL® and Žák et al. (2006) models. Top Image from Žák et al. (2006). Copyright (2006), Fig.19 p303 with permission from Elsevier (Duplicate of Figure 3.1 p39 this thesis). Numerical model of the Tanvald pluton contoured for the maximum (P1) and minimum (P3) principal stresses (MPa), compression negative. Top row (a & b), 10,000 years after model initiation and bottom row (c & d) 50,000 years after model initiation.



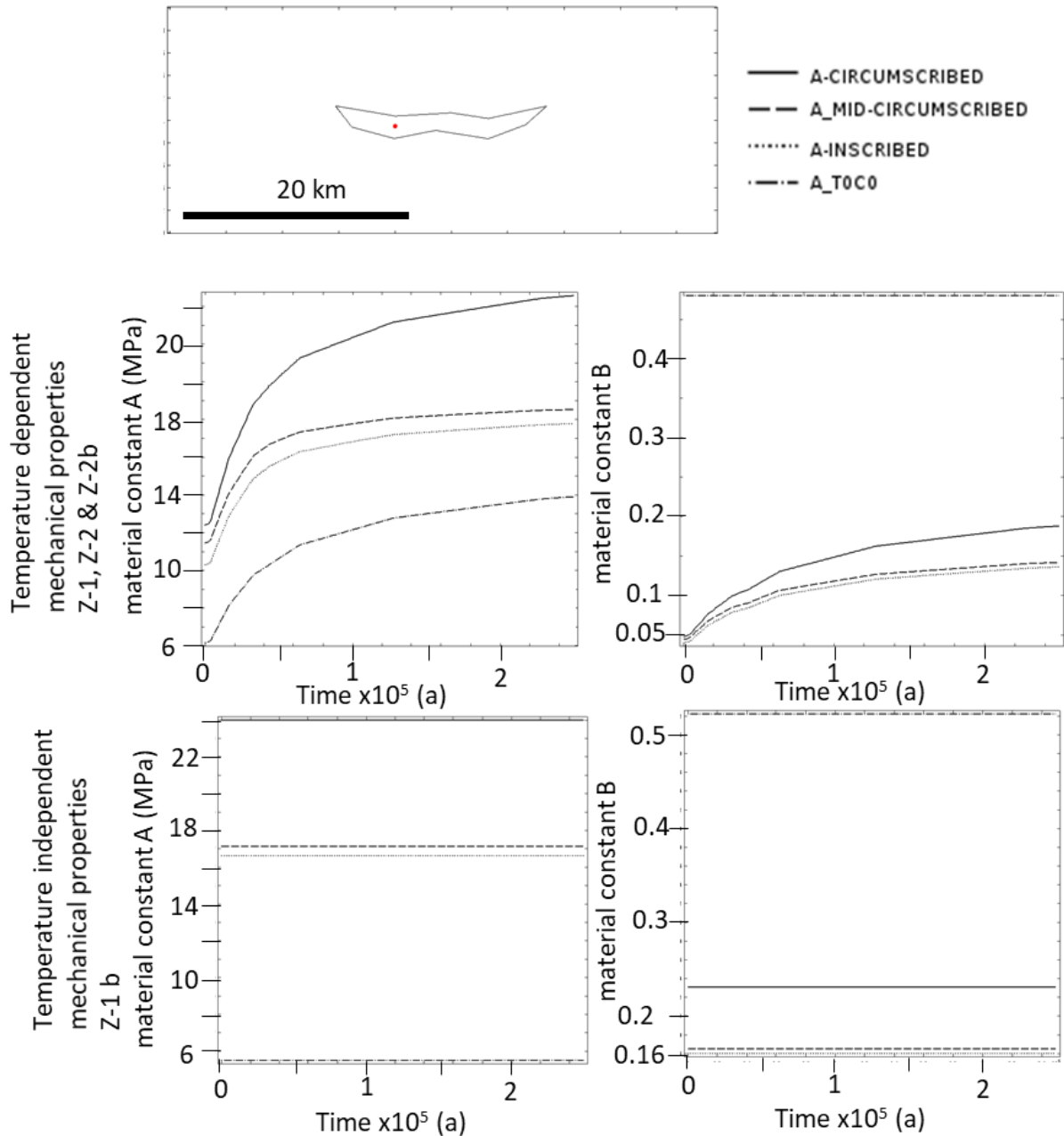


Figure 3.39. Influence of mechanical properties on material constants calculated of the Drucker-Prager yield criterion.

Modelling results are comparable to those presented in Žák et al. (2006) and highlight that temperature dependent material properties have a limited effect on modelling results (Figures 3.37 to 3.39). Applied mechanical properties influence the applied failure criterion by controlling the values of the material constants of the Drucker-Prager yield criterion (Figure 3.39). Prediction of failure is therefore very sensitive to the selected temperature dependent material and mechanical properties.

Applying the given temperature dependent material properties and Drucker-Prager criterion predicts that no failure will occur as a result of thermal stresses at the modelled depth of 8 km, assuming equal vertical and horizontal stresses, estimated to be 205.6 MPa (Žák et al., 2006). Modelling a gravitationally loaded crust, where the vertical stress is estimated to be 204 MPa and horizontal stress is 64 MPa, results in failure (Figure 3.40). Orientation of the modelled principal stresses is predominantly controlled by the geometry of the pluton. At early time steps in models minimum compressive stress is preferentially parallel to the intrusion margins with some variability being observed away from the margins. Overtime the minimum compressive stress rotates to preferentially parallel the long axis of the pluton.

Assuming a gravitationally loaded crust and that at early time steps areas in failure are not numerical errors (as assumed by Žák et al., 2006) then, based on Anderson failure angles, NW-SE and NE-SW fractures may have formed (Figure 3.40). Following the same principle, failure at later time steps would then be interpreted to form as approximately N-S trending joints. As this joint orientation is not observed in the field, it would have to be inferred that later fracturing events did not occur.

Uncertainties in the time of emplacement of the Tanvald pluton to surrounding larger plutonic bodies (see Žák et al., 2006) and the tectonic regime at time of emplacement may influence the predicted orientations. Another explanation for the limited match between predicted and measured fracture orientations, may relate to the scale of fractures recorded. Lineaments at the km scale, as used for comparison in the other examples presented here, cannot be observed in the Tanvald pluton on satellite images as the area is populated and forested.

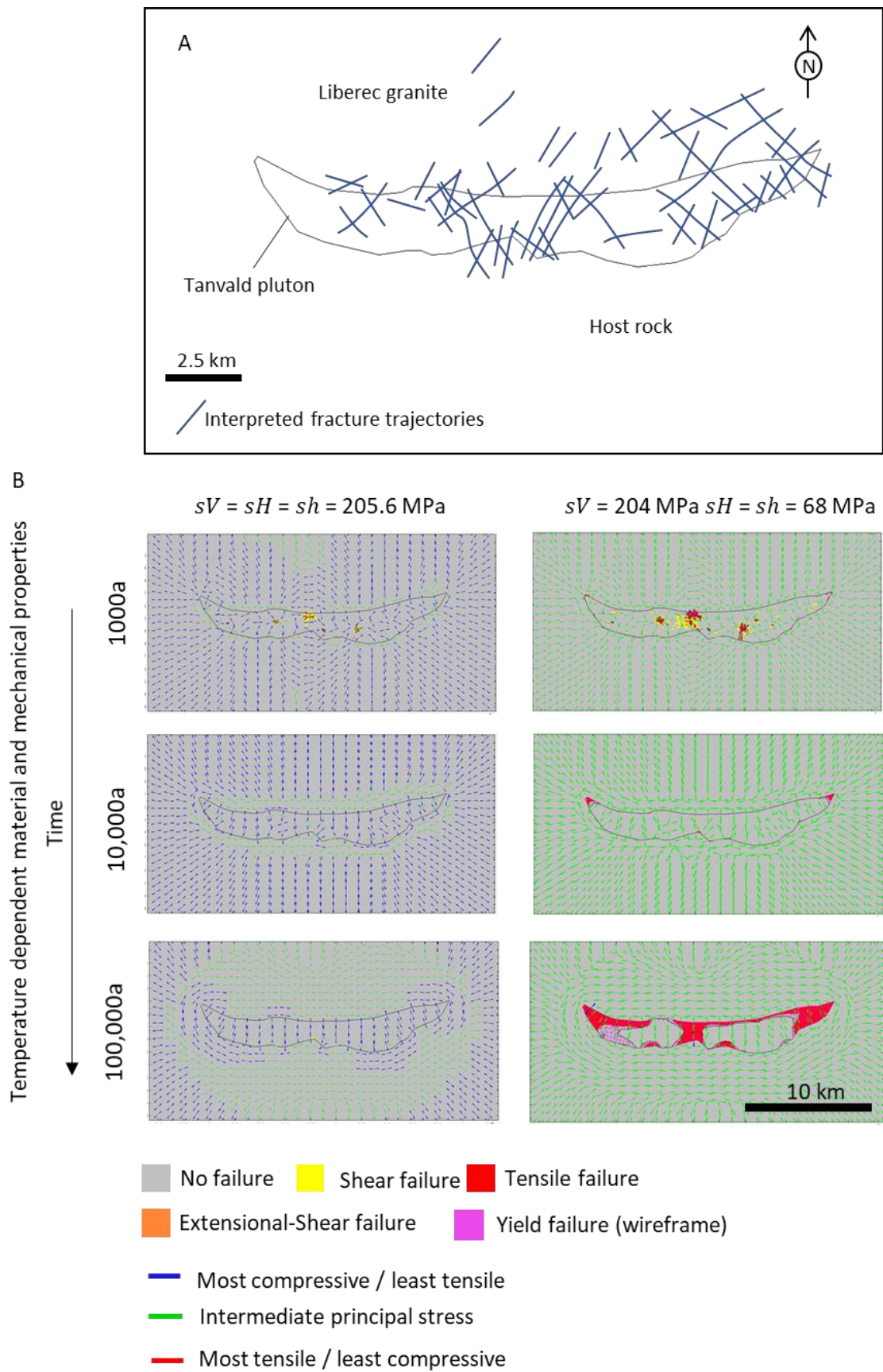


Figure 3.40. A. sketch map of the Tanvald plutonic body showing fracture trajectories interpolated from outcrops. B. numerical models of the Tanvald pluton, using mapped boundary.

3.6. Summary

Over time the direction of conductive heat loss from an intrusion is influenced to a greater extent by the overall pluton geometry than by margin geometry (Figure 3.41). The rate of heat loss is controlled by the material properties and a balance between the initial pluton temperature and host rock temperature. Cooling influences both the orientation and magnitude of the predicted principal stresses.

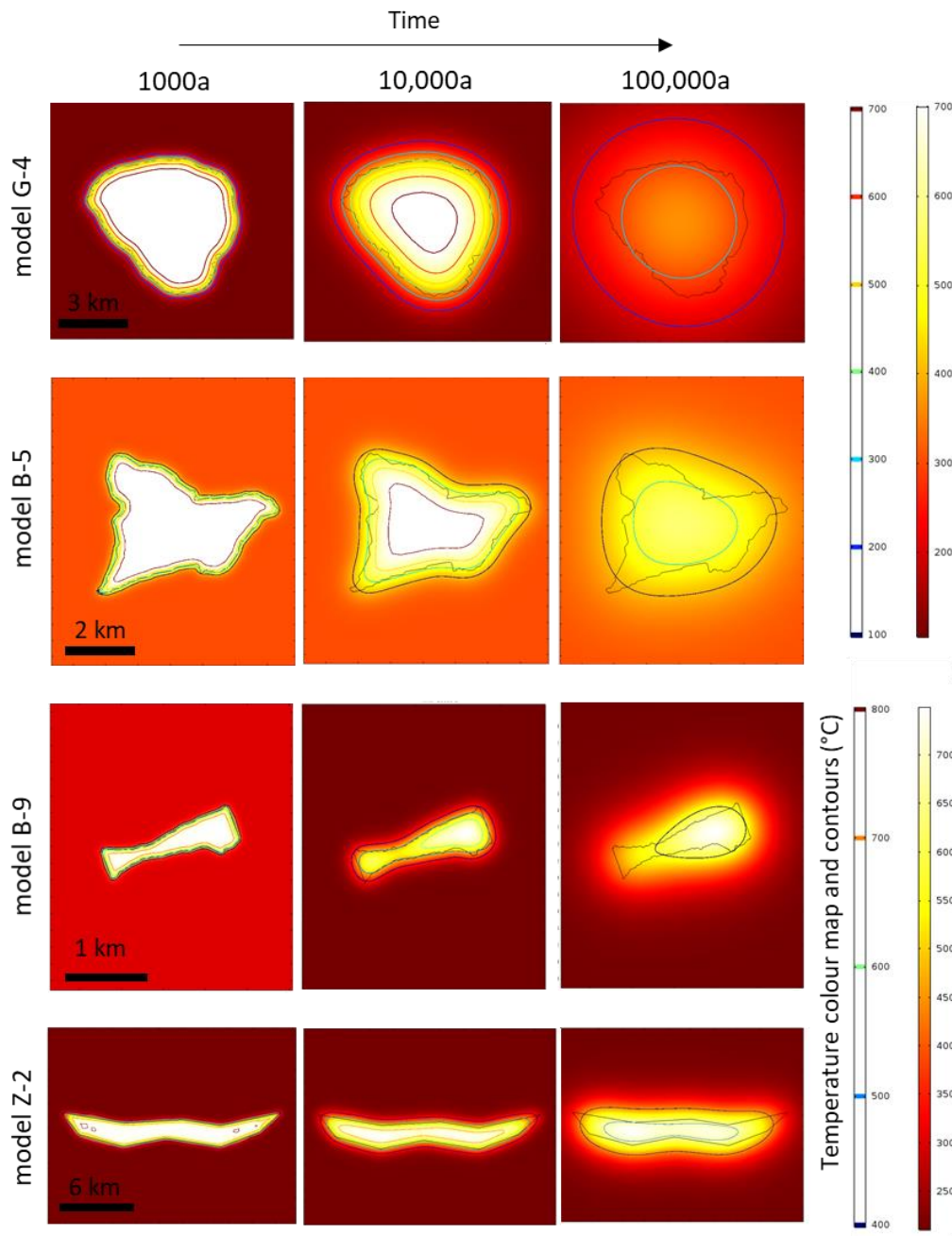


Figure 3.41. Thermal history predicted from two-dimensional modelling of the Diamond Joe stock (model G-4), Cartridge Pass granodiorite (model B-5), Lake Edison granodiorite (model B-9) and the Tanvald pluton (model Z-2). Coloured and contoured for temperature in °C.

Predicted failure patterns are sensitive to the selected temperature dependent properties. The examples of plutonic bodies (Diamond Joe Stock, Cartridge Pass granodiorite and the Lake Edison granodiorite) show a broad match between predicted principal stress orientations and photolineament interpretation. The comparison of single fracture orientation at a given location may however be misleading as rotation of principal stresses during cooling and progression of failure mode from shear and tensile failure domains may mean that multiple sets of fractures with varying orientations are formed. Lineament maps also highlight multiple fracture orientations.

Part 3

3.7. COMSOL® Model Variations

Models (Table 3.8) have been run to investigate the influence of modelling dimension (presented in part 1), depth, geometry, in-situ stress, initial temperature distributions and the defined material and mechanical properties. In addition to these models the influence of temperature dependent mechanical properties is investigated for models 2, 4 – 6 and 19.

The importance and implication of modelling assumptions are outlined below. The assumptions made in the models include:

- (1) Geometry of the pluton
- (2) Depth of emplacement
- (3) Emplacement mechanism (rate of emplacement, number and timing of incremental intrusions)
- (4) Initial temperature of the pluton and host rock
- (5) In-situ stresses
- (6) Cooling mechanism
- (7) Rheology
- (8) Material and mechanical properties
- (9) Failure criterion
- (10) Numerical model dimension (i.e., 2D, 2D-axisymmetric or 3D), grid resolution and modelled time step.

Table 3.8. COMSOL® models run

Model number	Modelling dimension	Geometry	Depth (km to top)	Initial temperature (°C)	Geothermal gradient (°C/km)	In suit stress (MPa)	Material properties table number
Modelling dimension (Part 1: Figure 3.9 to 3.18)							
1	2D	Cir 3	3	750	35	-	3.4
2	AS	Cyl 3-3	3	750	35	-	3.4
3	3D	Cyl 3-3	3	750	35	-	3.4
Depth variation (Figure 3.38)							
4	AS	Cyl 3-3	1	750	35	-	3.4
5	AS	Cyl 3-3	5	750	35	-	3.4
6	AS	Cyl 3-3	7	750	35	-	3.4
Initial temperature variation (Figure 3.39)							
7	AS	Cyl 3-3	3	900	35	-	3.4
8	AS	Cyl 3-3	3	750	55	-	3.4
9	AS	Cyl 3-3	3	750	15	-	3.4
In situ stress (appendix A3-12)							
10	3D	Cyl 3-3	3	750	35	x 40	3.4
11	3D	Cyl 3-3	3	750	35	y -40	3.4
12	3D	Cyl 3-3	3	750	35	y -100	3.4
Material properties variation (Figure 3.40)							
13	AS	Cyl 3-3	3	750	35	-	Rho3.11
14	AS	Cyl 3-3	3	750	35	-	Cp3.11
15	AS	Cyl 3-3	3	750	35	-	k3.11
16	AS	Cyl 3-3	3	750	35	-	E3.11
17	AS	Cyl 3-3	3	750	35	-	nu3.11
18	AS	Cyl 3-3	3	750	35	-	alpha3.11
19	AS	Cyl 3-3	3	750	35	-	3.11
Geometry variation (Figure 3.37)							
20	AS	Cyl 3-1.5	3	750	35	-	3.4
21	AS	Cyl 3-6	3	750	35	-	3.4
22	AS	Cyl 6-6	3	750	35	-	3.4
23	AS	Cyl 3-0.7	3	750	35	-	3.4
24	AS	Sph1 1.5	3	750	35	-	3.4
25	3D	Cu1 3-3-3	3	750	35	-	3.4
26	3D	Rect1 6-3-1.5	3	750	35	-	3.4
27	3D	Rect2 1.5-3-6	3	750	35	-	3.4
28	3D	Rect3 3-3-6	3	750	35	-	3.4
29	3D	Hg1 6-3/0.5-1.5	3	750	35	-	3.4
30	3D	Hg2 6-3/1-1.5	3	750	35	-	3.4

As – Axisymmetric

Cir = Circle #diameter [km], Cyl = cylinder #diameter–vertical thickness [km], Sph = sphere #radius [km], cu = cube #length–width–vertical height [km], Rect = rectangle #length–width–vertical height [km] and Hg = hourglass #length–width widest/narrowest–vertical height [km].

(1) Geometry of the Pluton

A cylindrical geometry with a radius of 1.5 km and vertical thickness of 3 km and depth to the pluton top of 3 km is used as a base case to test other modelling assumptions against i.e., emplacement depth (models 4 - 6), initial temperature distributions (models 7 - 9), material property variation (models 13 - 19). A cylindrical geometry was chosen as it can be represented in all three

modelling dimensions (part 1, Figure 3.9, p58). The geometric dimensions of models (1 – 19) are based on the Alta Stock in Utah. In chapter 4, models are extended into three-dimensions using mapped boundaries allowing for comparison of numerical model predictions and field data.

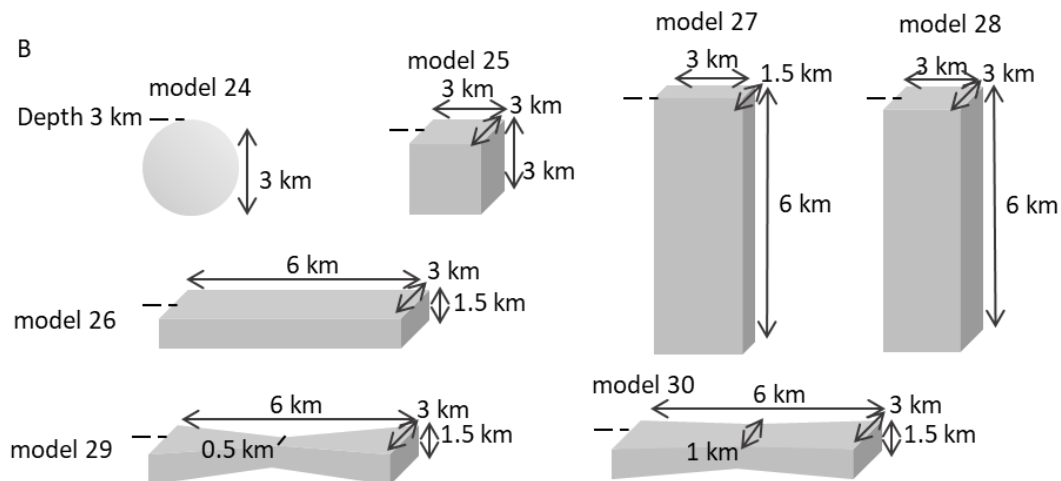
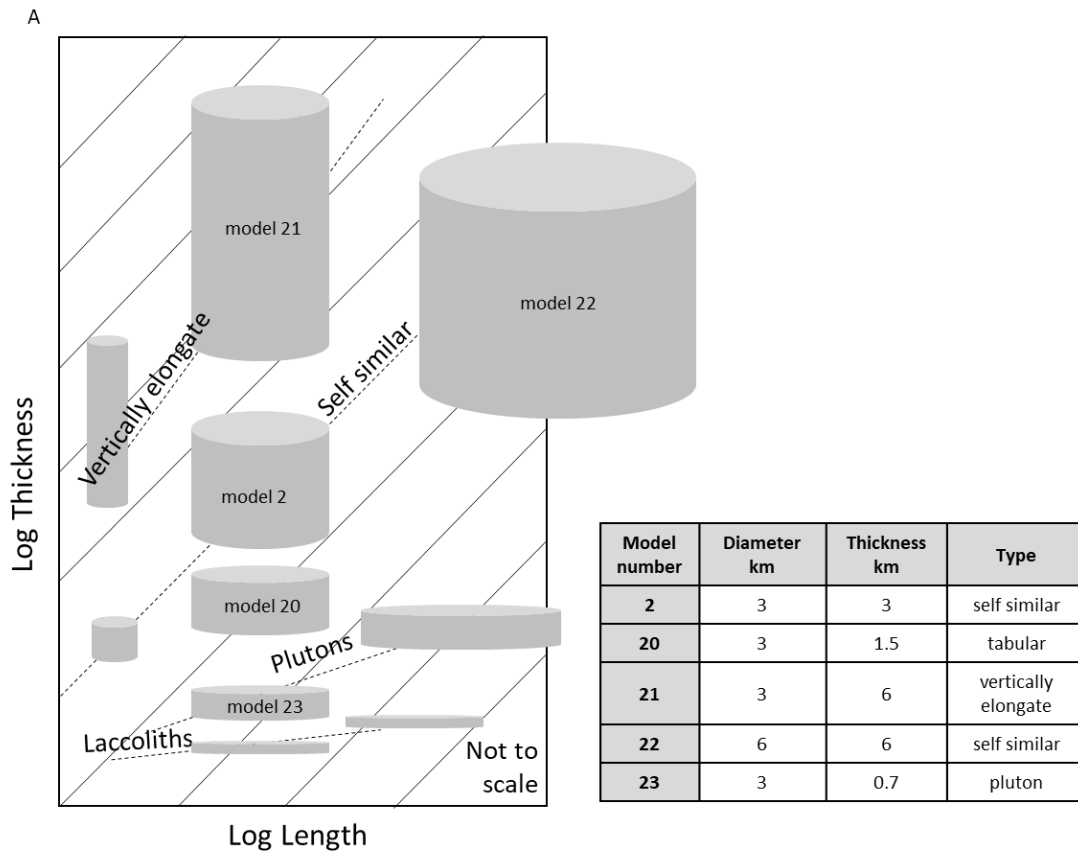


Figure 3.42. Schematic diagram showing variation in model geometry (A) thickness and volumes of modelled cylinders (models 2, 21 – 23) (B) other geometries (models 24 – 30).

Other three-dimensional geometries tested include cylinders with varying radii and thickness (Figure 3.42 A, models 20 - 23), spheres and cubic geometries (Figure 3.42 B, models 24 – 30). Geometry is investigated as it has been shown to be critical in controlling the thermal stress distribution and resulting predicted stress orientations (Gerla, 1983; Bergbauer et al., 1998; Koenders and Petford, 2003; Bergbauer, 1998; Bergbauer and Martel, 1999).

(2) Depth of Emplacement

The depth at which the top of the plutonic body was placed in the host rock domain was varied and tested for top pluton depths of 1, 3, 5 and 7 km (Figure 3.43). The influence of emplacement depth on fracturing for the same geometry and initial conditions has not previously been tested (Knapp, 1978; Gerla, 1983; Bergbauer, 1998; Koenders and Petford, 2003; Žák et al., 2006; Mondal and Acharyya, 2018) where only one depth is modelled. Depth of the plutonic body has the potential to alter the time and mode of failure and its mode. Žák et al., 2006 suggest based on the Drucker-Prager yield criterion that at depths of ~8 km fracturing due to thermal stresses does not occur whereas Bergbauer 1998 suggest that modelled stresses, at similar depths, are sufficient to result in fracture.

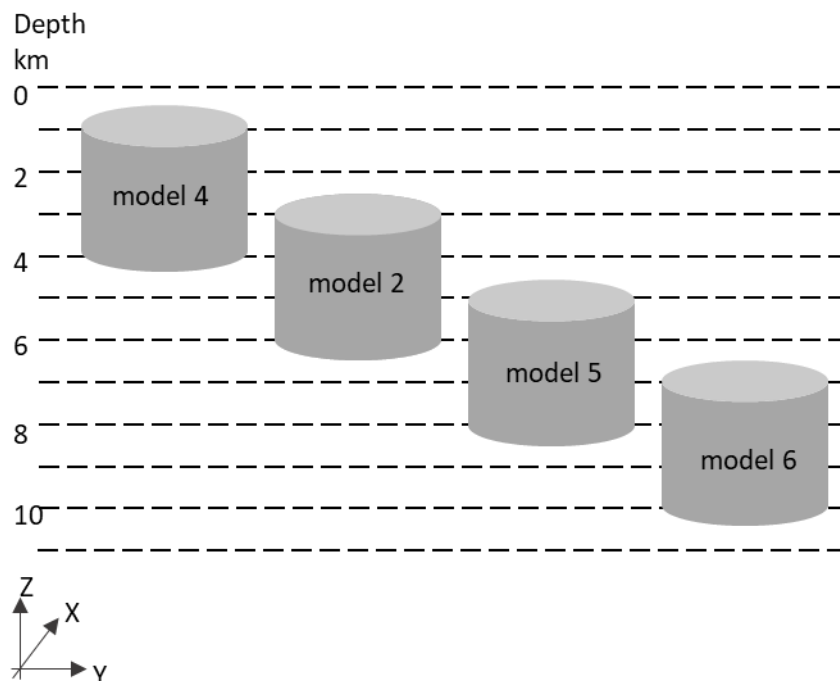


Figure 3.43. Schematic diagram showing variation in model depth (models 2, 4 – 6).

(3) Emplacement Mechanism

In the models presented here it is assumed a single unit of magma is instantaneously emplaced (Gerla, 1983; Knapp, 1978; Bergbauer, 1998; Koenders & Petford, 2003; Žák et al., 2006). This means that the models are representative of an igneous unit which has experienced a single cooling history. This assumption holds true for plutonic bodies when the rate of emplacement is relatively fast (> 2 cm/year; Norton and Knight, 1977) compared to the cooling time or there are not large time gaps between incremental intrusions (e.g., Bergbauer 1998). Stresses within the host rock as a result of emplacement are also not accounted for. These stresses may influence fracture patterns within the host rock (e.g., Gudmundsson, 2012) and therefore have the potential to alter host rock failure.

(4) Initial Pluton and Host Rock Temperature

The pluton is set to a homogenous initial temperature of $750\text{ }^{\circ}\text{C}$ after Bergbauer et al., 1998 (Table 3.9). The influence of a higher initial temperature of $900\text{ }^{\circ}\text{C}$ (after Knapp, 1978) is tested in models 7 (Figure 3.44).

The given host rock geothermal gradient is important as it controls the rate of heat removal from the intrusion. The initial temperature of the host rock is based on an assumed geothermal gradient. A geothermal gradient of $35\text{ }^{\circ}\text{C}/\text{km}$ is applied in the models presented in this work. The influence of applying a lower geothermal gradient $15\text{ }^{\circ}\text{C}/\text{km}$ and a higher geothermal gradient of $55\text{ }^{\circ}\text{C}/\text{km}$ are also tested (c.f. models 2, 8 & 9).

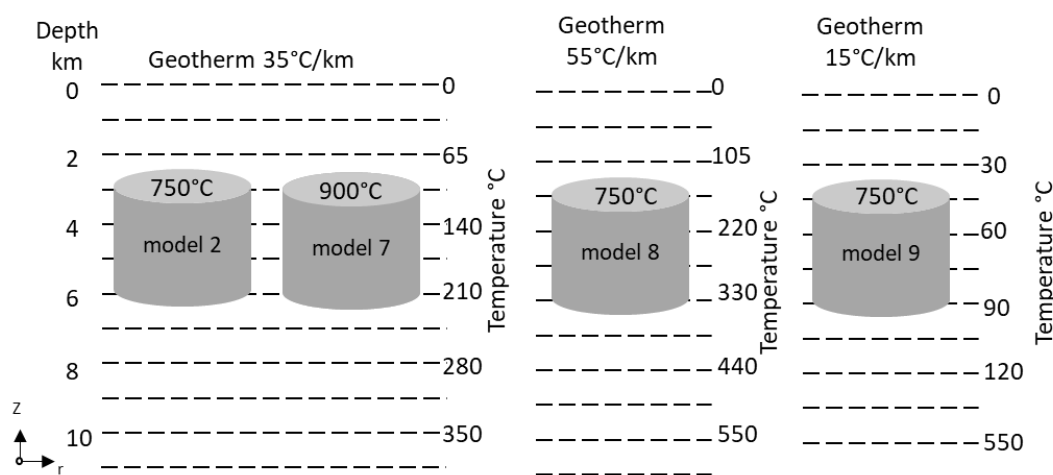


Figure 3.44. Schematic diagram showing variation in initial temperatures (models 2, 4 – 6).

The selected geothermal gradient of 35 °C/km is based on the average crustal geothermal gradient (e.g., Bergbauer, 1998). Higher geothermal gradients are used when it is assumed that the host rock temperature has been increased due to heating of the crust by previous intrusions (i.e., 150 °C/km Gerla, 1983; 50 °C/km; Žák et al., 2006). Lower geothermal gradients (i.e., 15 °C/km; Knapp, 1978) are used to account for the likelihood of hydrothermal fluid convection in the host rock.

Table 3.9. Initial temperature and assumed liquidus and solidus temperatures from previous publications

Reference	Pluton initial temperature °C	Geothermal gradient °C/km	Emplacement depth km	Host rock 2D map temperature* °C	Liquidus °C	Solidus °C
Knapp (1978)	900	15	4.5 top 9 km base	n/a		
Gerla (1983)	920	150 – 75 **	< 1 – 2 ***	150		
Bergbauer et al. (1997) Lake Edison	750	85 - 43	3.5 – 7	300	-	750
Bergbauer et al. (1998) basic geometries/ Cartridge Pass	750	35	8.6 ***	300	-	750
Bergbauer and Martel (1999) Lake Edison	800	28	3.5 – 14 8 ***	230	-	-
Koenders and Petford (2003)	Dimensionless					
Žák et al. (2006) case 1 consistent with metamorphic conditions	750	50 **	8 ***	400	1100	700
Žák et al. (2006) case 2 extreme thermal loading	800	37.5 **	8 ***	300	1100	700
Mondal and Acharyya (2018)	800	35	6 ***	210	800	-

* based on given depth and geothermal gradient
** calculated from given host rock temperature and given emplacement depth
*** based on map slice

(5) In-situ stress

The initial in-situ stress is given as a uniaxial stress state defined by the gravitational load. This is the most commonly applied reference stress state applied in the crust in the absence of tectonic loads (Martin-Velazquez et al., 2009). The gravitational load is defined on a horizontal surface, so that the influence of topographic relief is not modelled (c.f. Miller and Dunne, 1996).

Tectonic loads can be added to the gravitation load to modify the maximum and minimum horizontal stresses. Application of tectonic load has been shown to significantly influence the orientation of the resulting principal stresses calculated for a cooling pluton (Gerla, 1983; Bergbauer, 1998; Bergbauer et al., 1998; Bergbauer and Martel, 1999). Tectonic loads applied in previously published models are given in Table 3.10.

Table 3.10. Initial in-situ stresses assumed in previous publications

Reference	Regional tectonic load maximum	Regional tectonic load minimum	Magma pressure
	MPa		
Knapp (1978)	-	-	Varied vertically
Gerla (1983)	135 MPa	45 MPa	Equal to regional maximum principal stress (135 MPa) and increased 20 % radius of hole 0.5 km to 162 MPa.
Bergbauer et al. (1998) Cartridge Pass Granodiorite	-40 MPa (N55E)	-10 MPa (N35W)	-
Bergbauer and Martel (1999) Lake Edison Granodiorite	Trends N70E	Within 40 MPa of the maximum tectonic load	-
Žák et al. (2006)	Lithostatic pressure 205.6 MPa at ~8 km depth		Vertical pressure top and base of pluton 150 MPa.

(6) Cooling Mechanism

Models only account for cooling via conduction. Conductive cooling is modelled as it is likely to dominate the early cooling history of plutonic bodies. See section 2.4.2 p.27 - 28 and section 3.2.3 p.50 - 51 for details.

(7) Rheology

To simplify the model elastic behaviour in homogenous solids is assumed. At confining pressures and temperatures < 800 °C, strain rates are on the order of 10^{-5}s^{-1} and rocks can be assumed to have a linear response the stress (Knapp, 1978).

(8) Material and Mechanical Properties

Material properties of the pluton and host rock are taken to be the same. Temperature independent material properties (Table 3.4 p.57) are applied to models 1 – 12 & 20 to 30). The effect of temperature dependent values (Table 3.11) are tested in models 13 to 19. To assess the influence of the temperature dependence, each of the material properties are tested individually (models 13 – 18). Temperature dependent material properties are based on Hezue (1983). Graphs showing a range of temperature dependencies for the material and mechanical properties are given in Figures 3.45 and 3.46. Tabulation of the data plotted in figures is given in appendix A Tables A3-2 to A3-4 p.305 – 306.

Table 3.11. Temperature dependent material and mechanical properties defined in models

		Temperature °C					
		20	200	400	600	800	1100
Density *	kg/m ³	2469	2145	1769	1494	1075	649
Heat capacity at constant pressure *	J/(kg.K)	815	965	1133	1129	1179	1242
Thermal conductivity *	W/(m.K)	2.6	2.1	1.7	1.5	1.3	1.3
Young's modulus *	GPa	30.3	23.7	16.4	9.1	1.8	0
Poisson's ratio *	-	0.25	0.25	0.25	0.25	0.25	0.5
Coefficient of thermal expansion *	1/°C	0	3.6e-6	7.6e-6	12e-6	15e-6	0
Tensile strength *	MPa	14	12	11	5	2	0
Compressive strength †	MPa	230	238	246	177	111	14
Cohesion *	MPa	22.6	22.5	20.7	16.2	10.4	0
Angle of internal friction *	°	49.1	38.8	26.2	14.8	6.9	7.3

* Values after Heuze (1983) see appendix Table A3-2 p.305
† Values after Saiang (2012)

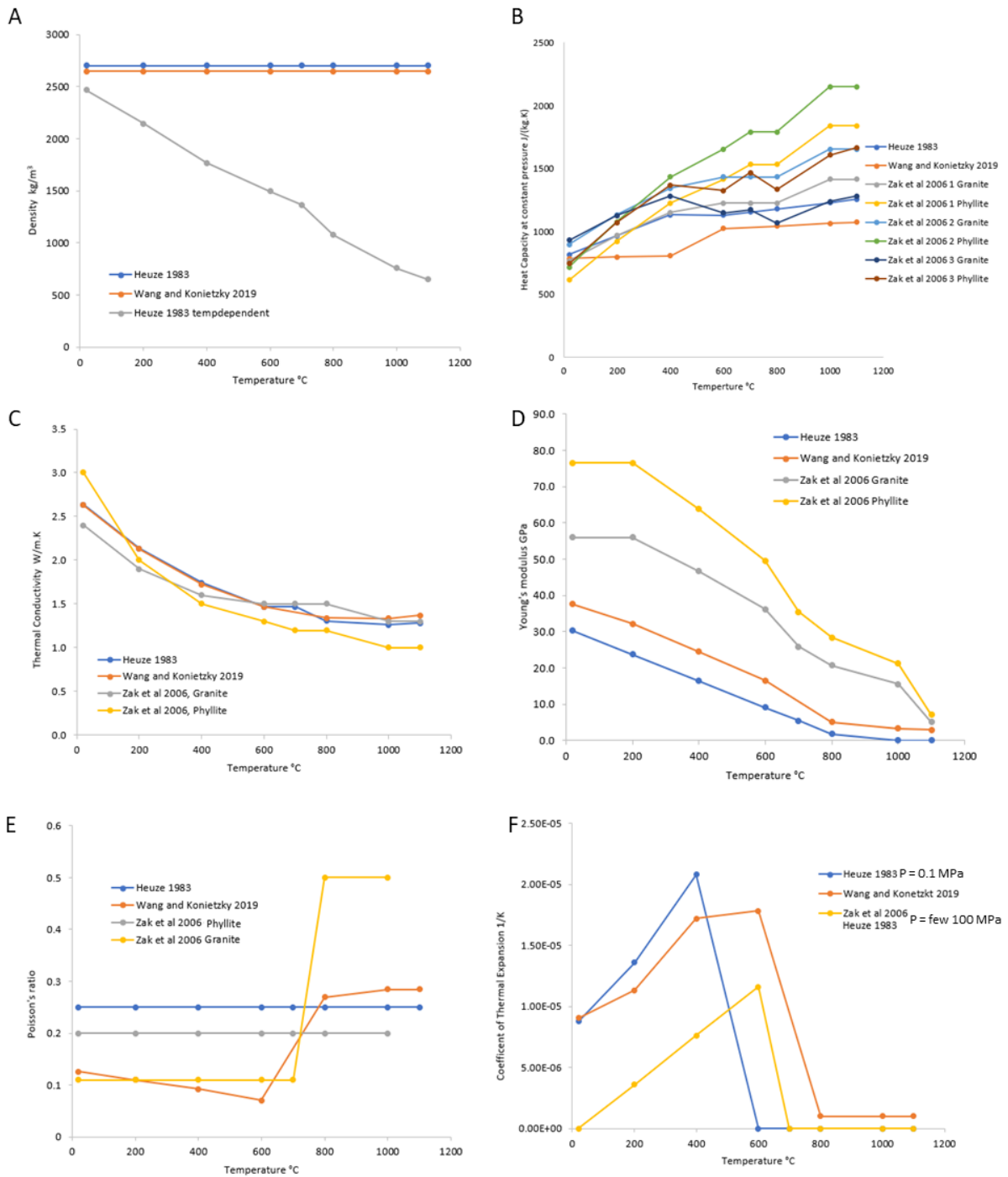


Figure 3.45. Graphs of material property variation with temperature. See appendix A Tables A3-2 to A3-4 p.305 - 306 for tabulated values. Temperature dependent (A) density, (B) heat capacity at constant pressure, (C) thermal conductivity, (D) Young's modulus, (E) Poisson's ratio and (F) coefficient of thermal expansion.

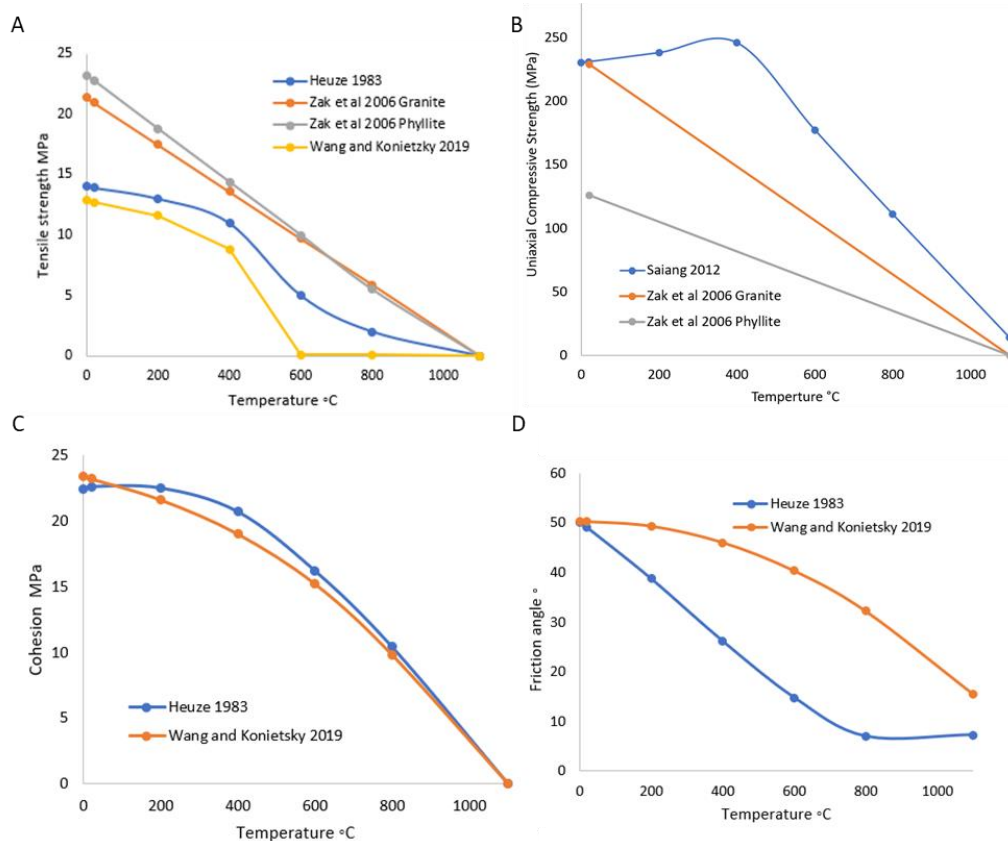


Figure 3.46. Graphs of mechanical property variation with temperature. See appendix A Table A3-5 p.306 for tabulated values. Temperature dependent (A) tensile strength, (B) uniaxial compressive strength, (C) cohesion and (D) friction angle.

(9) Failure Criteria

The applied failure criteria are outlined in section 3.2.2 p.50. The influence of temperature dependent mechanical properties is tested (section 3.8.5. p.121).

Fractures as a result of cooling are presumed to occur in a similar manner to equivalent rocks and analogous conditions in laboratory tests (Nelson, 2001). It is also assumed that the numerical models are representative of the local state of stress at the time of fracture formation. Stress redistribution as a result of fracturing is not included in the models. This simplification has been shown to be a reasonable approximation (Knapp, 1978).

(10) Modelling Dimension, Grid Resolution and Model Time Step

Grid, resolution and time steps are all defined in the models. Grid size is based-on the modelling dimension A time step of 1000 years over 1 million years was set for each of the models. See chapter 3 part 1 for additional details.

3.8. Modelling Results

3.8.1. Intrusion Depth

Increasing the intrusion depth influences the orientation and magnitude of the principal stresses and therefore the resulting failure mode at a given point over time (Figures 3.47 & 3.48 and appendix A Figure A3-1 p.308). With increasing depth shear failure is more likely to occur than tensile failure (Figures 3.48).

At shallower depths the switch in orientation of the minimum compressive stress within the pluton from radial to concentric is less likely to occur and in the host rock the maximum compressive principal stress is less likely to incline to horizontal around the top and base of the pluton (Figure 3.48). In the example models presented in Figure 3.48 the switch in principal stress orientation within the pluton does not occur below 4 km depth. Principal stress magnitudes are more compressive in deeper plutonic bodies (Appendix A A3-1c p.310).

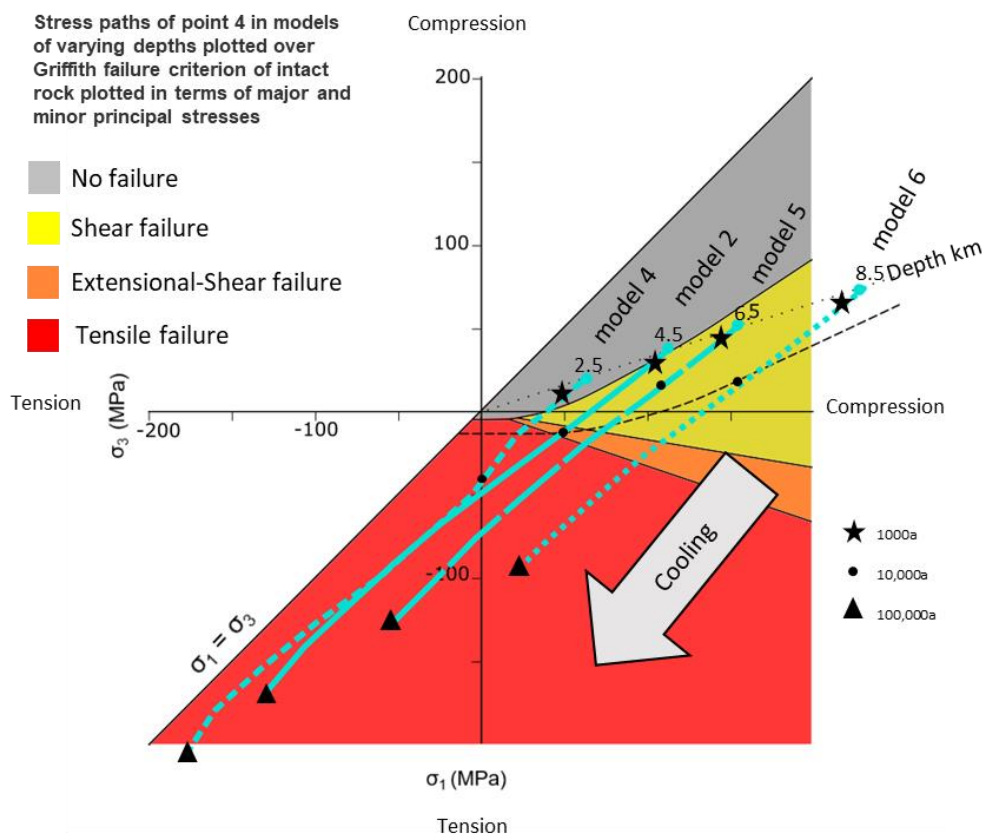


Figure 3.47. Stress paths for selected points (point 4, at varying depths as labelled) on a maximum (σ_1) – minimum (σ_3) principal stress plot (compression positive) with the Griffith failure domain plots. Points mark the starting stresses in the no failure domain (grey), large arrow shows cooling direction and movement of stress paths.

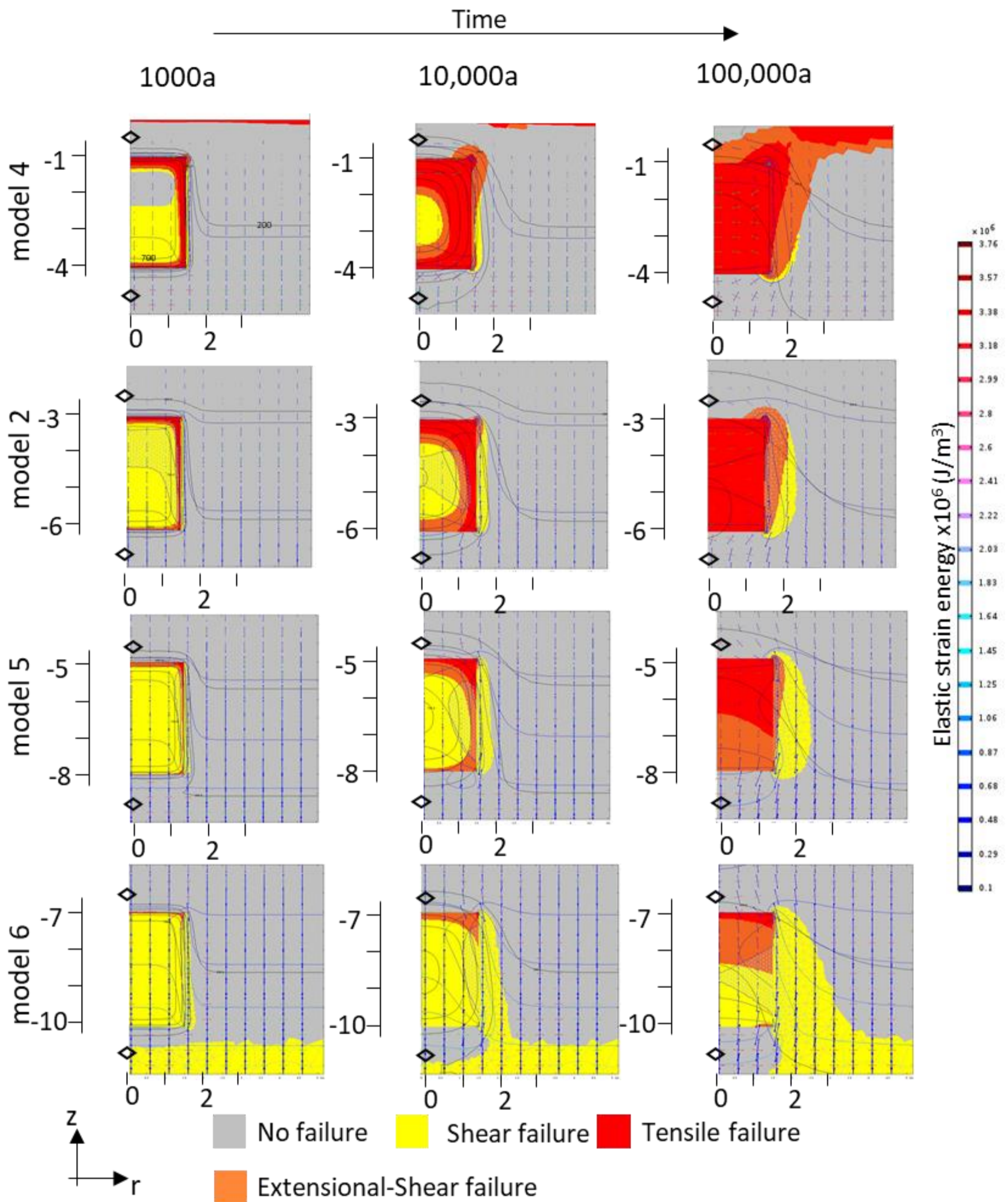


Figure 3.48. Influence of depth on failure domains of the Griffith and Griffith-Murrell criterion accounting for temperature independent material and temperature dependent mechanical properties. The domain of no failure for the Griffith-Murrell criterion is shown as the grey wireframe overlay. Increasing depth increases the shear failure domain and modifies the geometry of the three-dimensional failure domain.

3.8.2. Initial Temperature Distribution

The initial temperature distribution has limited effect on the orientation of the predicted principal stress (Figure 3.49). Increasing the pluton temperature relative to the host rock geothermal gradient (model 7 c.f. model 2) increases the magnitude of the principal stresses (appendix A Figure A3-2b p.312). Increasing or decreasing the geothermal gradient relative to the pluton (models 8 & 9 c.f. model 2) reduces the magnitude of the predicted principal stresses (appendix A Figure A3-2b p.312). These changes however have limited overall effect on the geometry of failure domains and only influence the time of failure (Figure 3.49).

3.8.3. In-Situ Stress

As the predicted magnitude of thermal stress is on a similar order of magnitude to the in-situ stresses the thermal stress interacts with the in-situ stress to control stress orientation and magnitude. When the horizontal stresses are not equal the orientation of the principal stresses preferentially align to the regional tectonic loads e.g., when maximum compressive stress is vertical, the minimum compressive stress aligns to the direction of the minimum horizontal stress (Figure 3.50, appendix A A3-3 p.314 – 316).

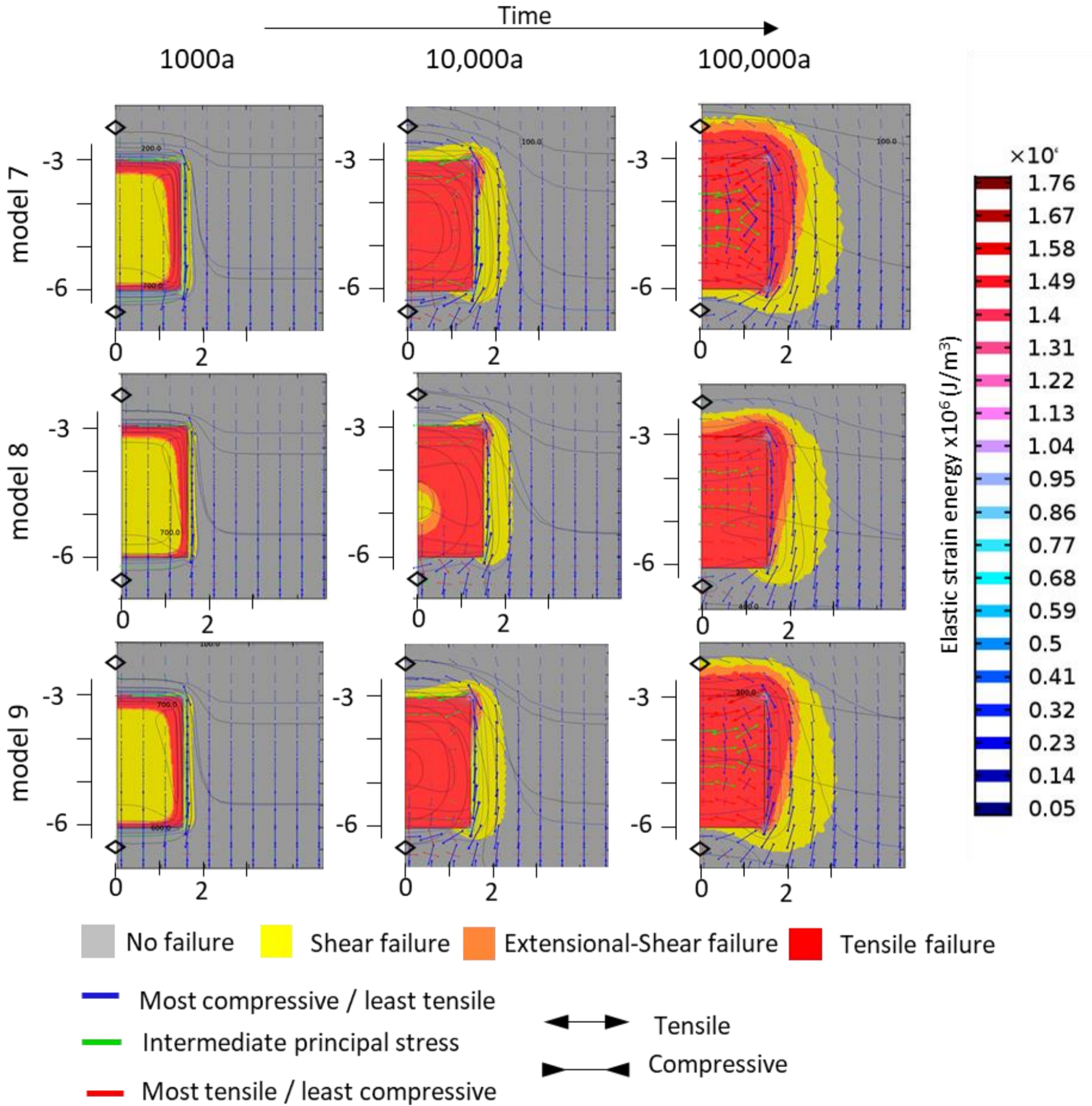


Figure 3.49. Influence of initial temperature distribution on failure domains of the Griffith and Griffith-Murrell criterion accounting for temperature dependent mechanical properties. The domain of no failure for the Griffith-Murrell criterion is shown as the grey wireframe overlay.

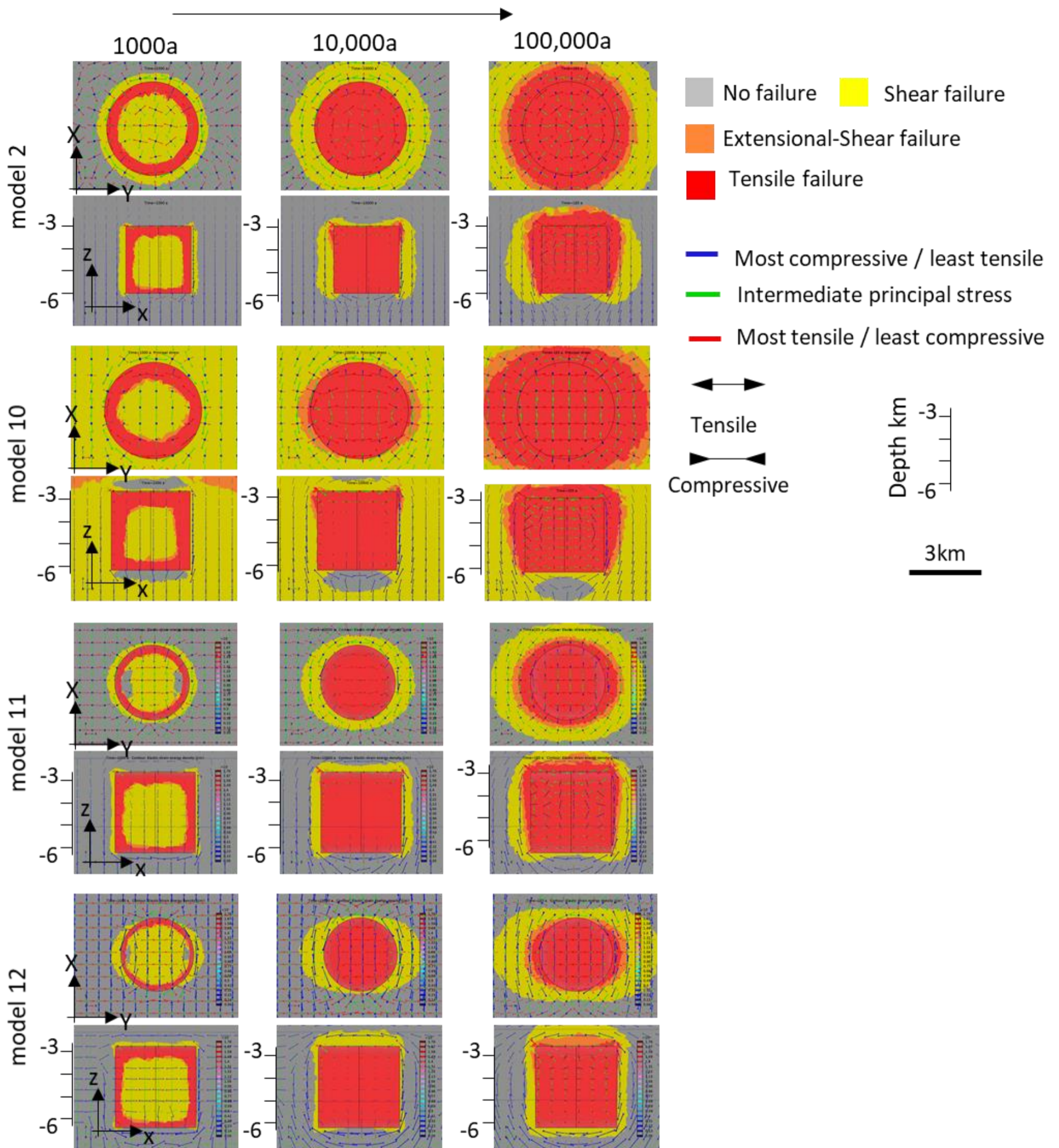


Figure 3.50. Influence of regional stress on failure domains of the Griffith criterion in three-dimensional models. Model 2 vertical stress (σ_V) > maximum horizontal stress (σ_H) = minimum horizontal stress (σ_h), model 10 E-W extension $\sigma_V > \sigma_H > \sigma_h$, model 11 E-W compression $\sigma_V > \sigma_H > \sigma_h$, model 12 E-W compression $\sigma_H > \sigma_V > \sigma_h$. X-Y slice at a depth of 4 km.

3.8.4. Temperature Dependent Material Properties

Accounting for temperature dependency of material properties influences the time and shape of failure domains. The material properties that have the greatest influence are the density, Young's modulus and coefficient of thermal expansion (Figure 3.51).

Accounting for a decrease of density with decreasing temperature (appendix A Table A3-2 model 13 p.305), the rate of cooling increases resulting in stress paths moving through failure domain more quickly (appendix A Figure A3-4 model 13 p.317). Increasing the Young's modulus with decreasing temperature (model 16), modifies the stress paths so that there is less change in the minimum compressive stress in the early cooling stages (Figure 3.51; appendix A Figure A3-4c model 16 p.319). This means the pluton remains in the no failure domain for longer before failure (Figure 3.51, model 16). Accounting for a decrease in the coefficient of thermal expansion with decreasing temperature (model 18), results the overall magnitude of stress decreasing and stress paths initially moving towards and then away from the tensile failure domain (Figure 3.51; appendix A Figure A3-4c model 18 p.320).

Accounting for the temperature dependence of material properties results in a more complex failure sequence. Stress paths migrate away from no failure through failure domains and then back towards the no failure domain (Figure 3.52 model 19). Depth influences these results (Figure 3.52). Increasing the solid elastic thermomechanical parameter (the product of the Young's modulus and coefficient of thermal expansion) increases the values of predicted thermal stress. The solid elastic thermomechanical parameter is variable over time, defined by the Young's modulus increases with decreasing temperature the coefficient of thermal expansion increases (Figure 3.53).

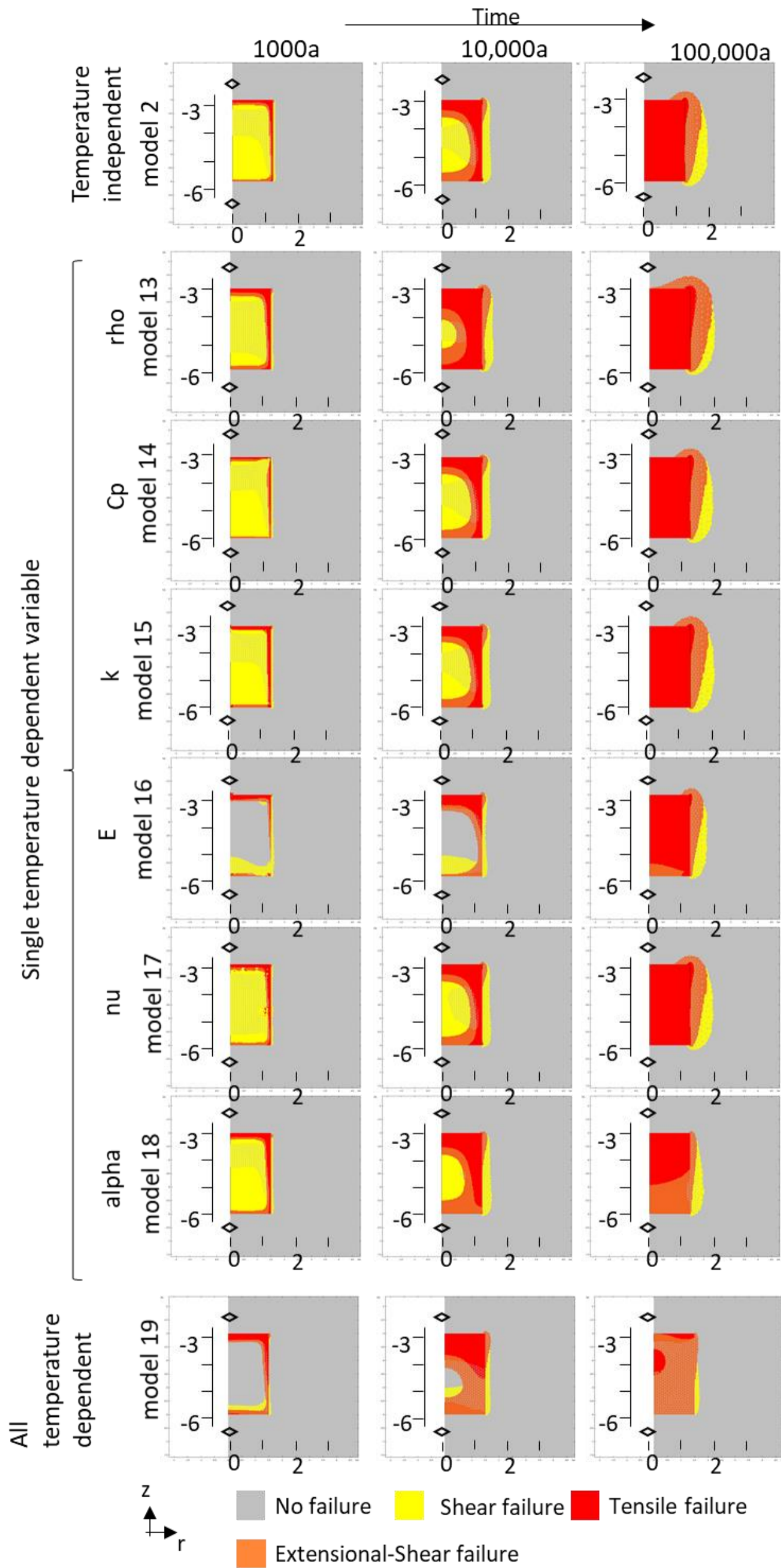


Figure 3.51. Griffith and Griffith-Murrell failure domains for selected time steps for models 13 – 18 with selected temperature dependent material properties, as labelled. Model 2, temperature independent material properties, shown for comparison. The domain of no failure for the Griffith-Murrell criterion is shown as the grey wireframe overlay. All models have temperature independent mechanical properties.

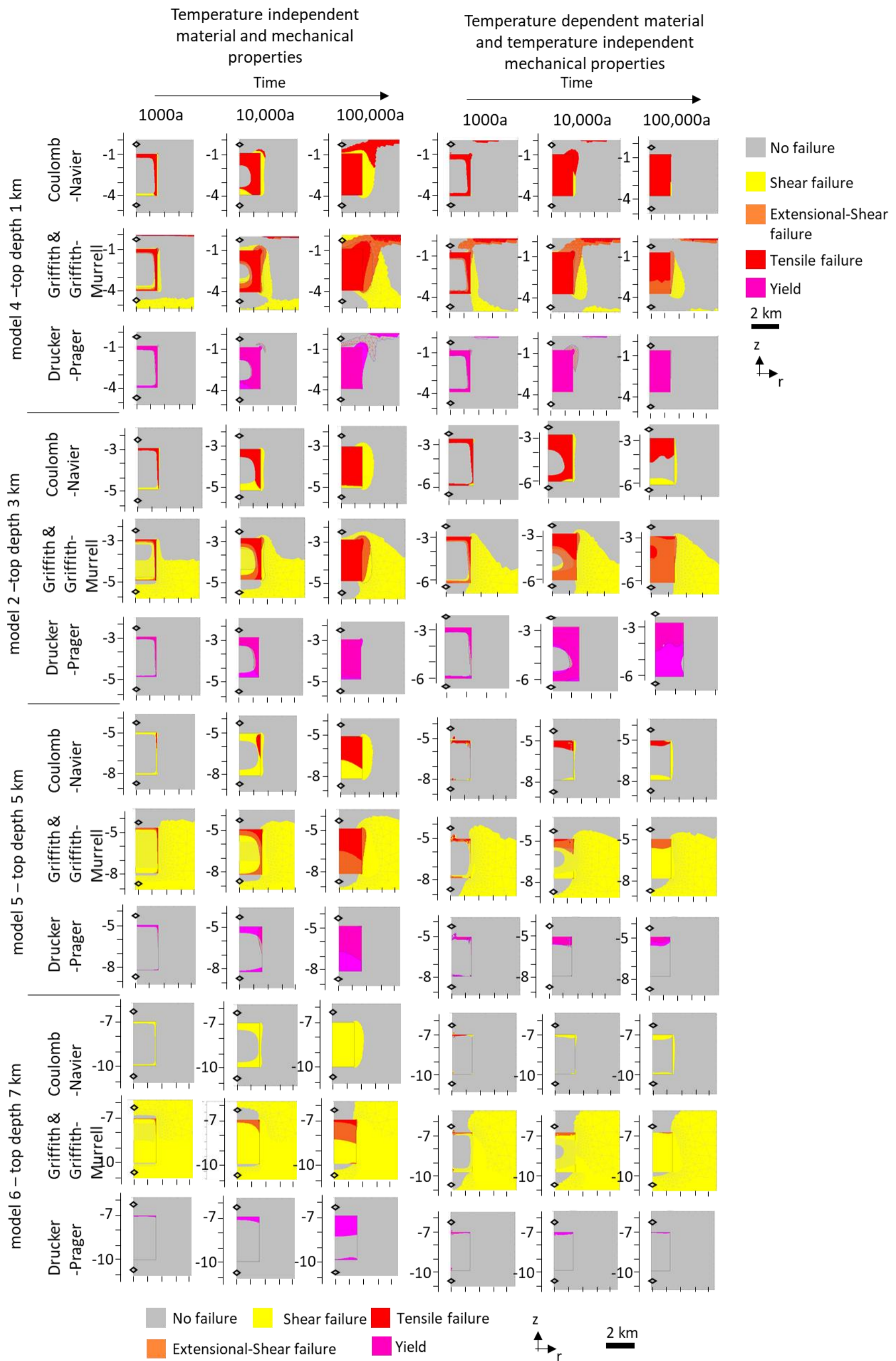


Figure 3.52. Influence of depth for the applied failure criterion. Left column material and mechanical properties are temperature independent and right column material properties temperature dependent and mechanical properties are temperature independent. The domain of no failure for the Griffith-Murrell criterion is shown as the grey wireframe overlay.

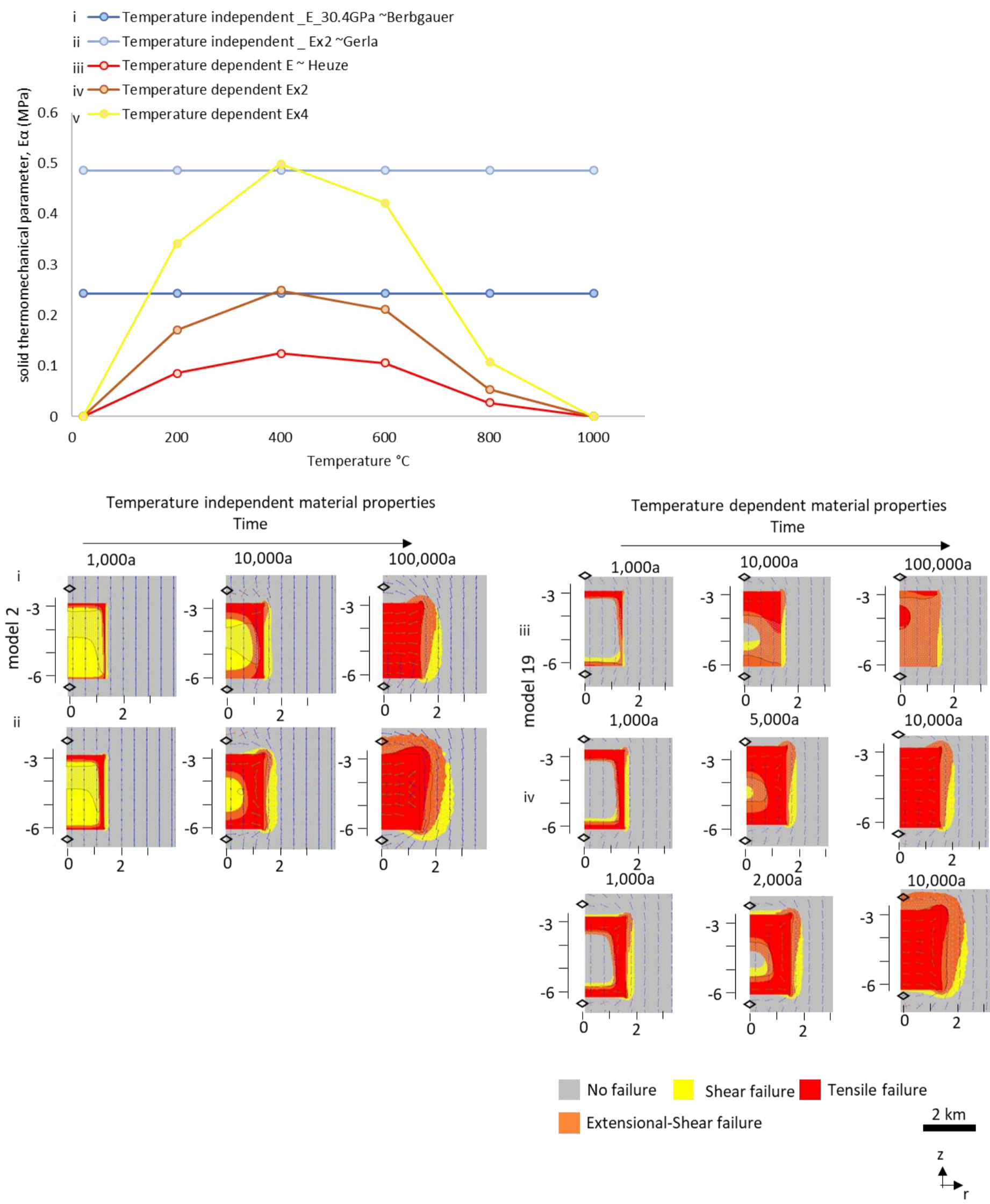


Figure 3.53. Graph of the solid thermal mechanical parameter and its influence on Griffith and Griffith-Murrell failure domains. The domain of no failure for the Griffith-Murrell criterion is shown as the grey wireframe overlay.

3.8.5. Temperature Dependent Mechanical Properties

When temperature dependent mechanical properties are accounted for the failure domains in the host rock are reduced in size. Accounting for the intermediate principle using the Griffith-Murrell criterion stress significantly alters the geometry of the no failure domain (Figure 3.54). With increasing depth, the pluton is less likely to fail and when it does shear failure is more likely to occur than tensile failure (Figure 3.54).

Temperature dependence of mechanical properties influences the angle of shear failure (Figure 3.55) so that accounting for temperature dependent material properties (e.g., model 19) means the angle of shear failure becomes more variable (Appendix E.1. p.359).

3.8.6. Pluton Geometry

Pluton geometry affects the magnitude and orientation of the principal stresses, influencing the time of failure and geometry of the failure domains. Despite this, the sequence of failure is comparable for varying geometries (Figures 3.56 & 3.57, appendix A A3-5 & A3-6 p.321 – 328).

For doubly curved surfaces (i.e., spheres or saddles) the plunge of the radial minimum compressive stress parallels the dip of the nearest margin (models 24, 29 & 30, Figure 3.57). Where two perpendicular surfaces meet (i.e., vertical side and horizontal top and base), the principal stress axes are deflected forming arcuate patterns curved away from corners (Figures 3.56 & 3.57).

As geometries cool the plane perpendicular to the minimum compressive stress may switch from tangential to radial moving inwards and downwards from the top of the intrusion. The plane dips towards the outer margin. This switch is most distinct in plutons that are vertically elongate e.g., Figure 3.56 models 2 and 21, Figure 3.57 model 27. This switch does not occur in model 28, which although vertically elongate has equal map view dimensions. The switch is also influenced by pluton depth and does not occur in deeper plutonic bodies (see section 3.7.1). In tabular geometries the switch in direction of the plane perpendicular to minimum compressive stress is not observed (e.g., model 23 & 26).

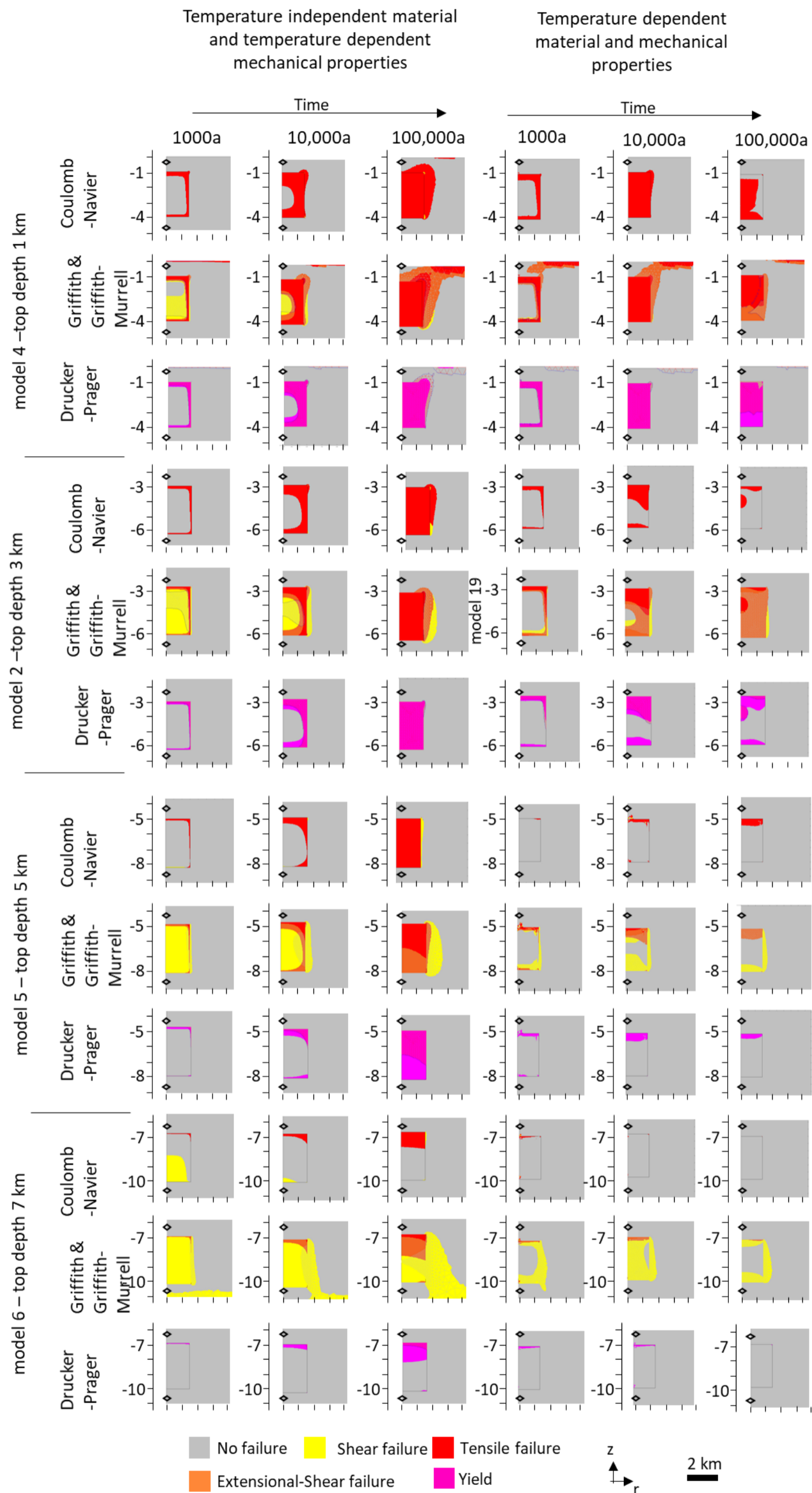


Figure 3.54. Influence of temperature dependent mechanical properties for the applied failure criterion for varying depths. For both temperature independent and dependent material properties. The domain of no failure for the Griffith-Murrell criterion is shown as the grey wireframe overlay.

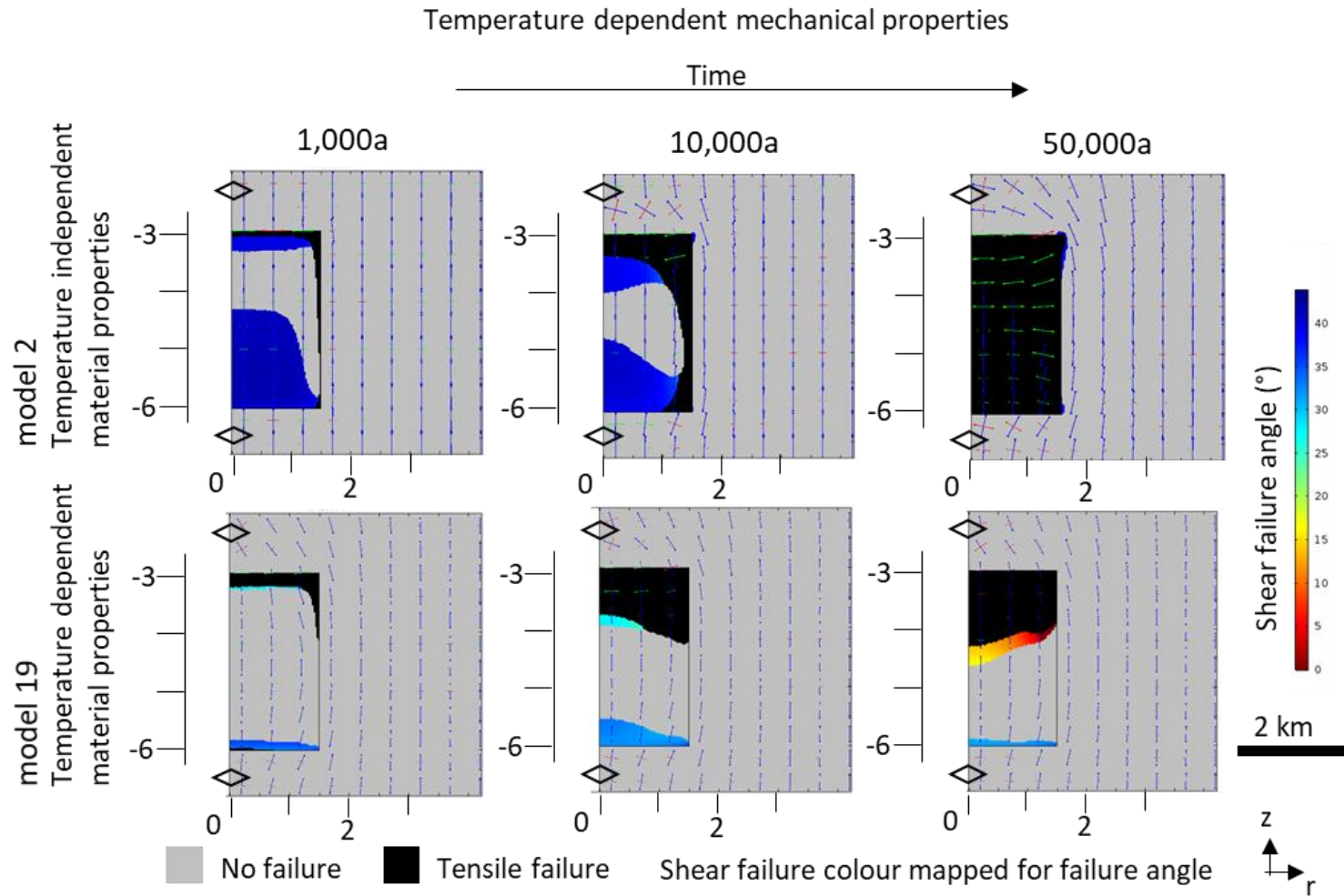


Figure 3.55. Model 2 (temperature independent material properties) and model 19 (temperature dependent material properties) for the 3D Griffith-Murrell criterion, assuming temperature dependant mechanical properties. The domains of shear failure are colour mapped for predicted failure angle from the plane of the maximum compressive / least tensile and intermediate principal stress (equation 14 p.53). See appendix E.1 for animation file.

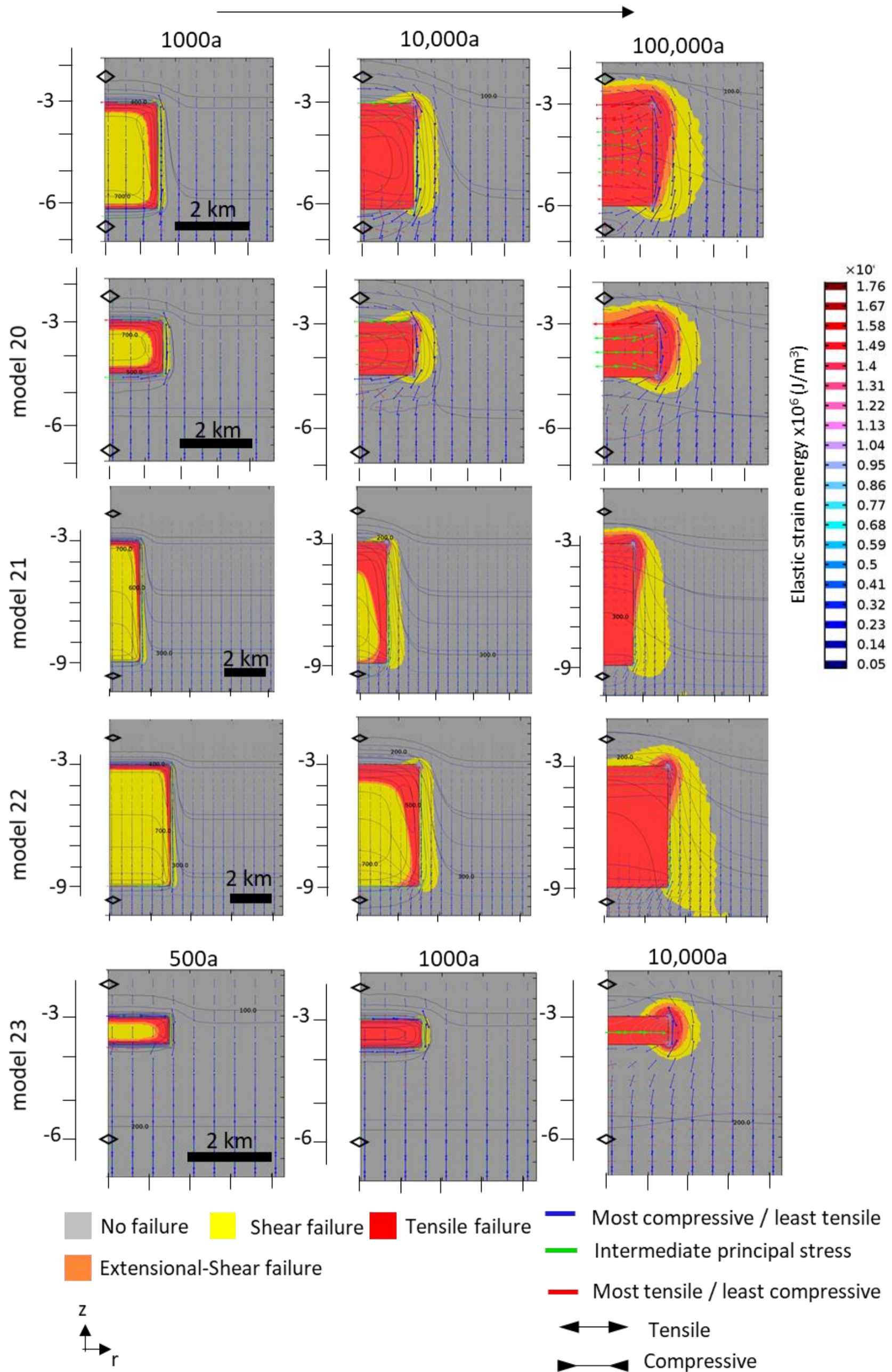


Figure 3.56. Influence of cylindrical geometry on stress orientation and the predicted Griffith domains failure domains.

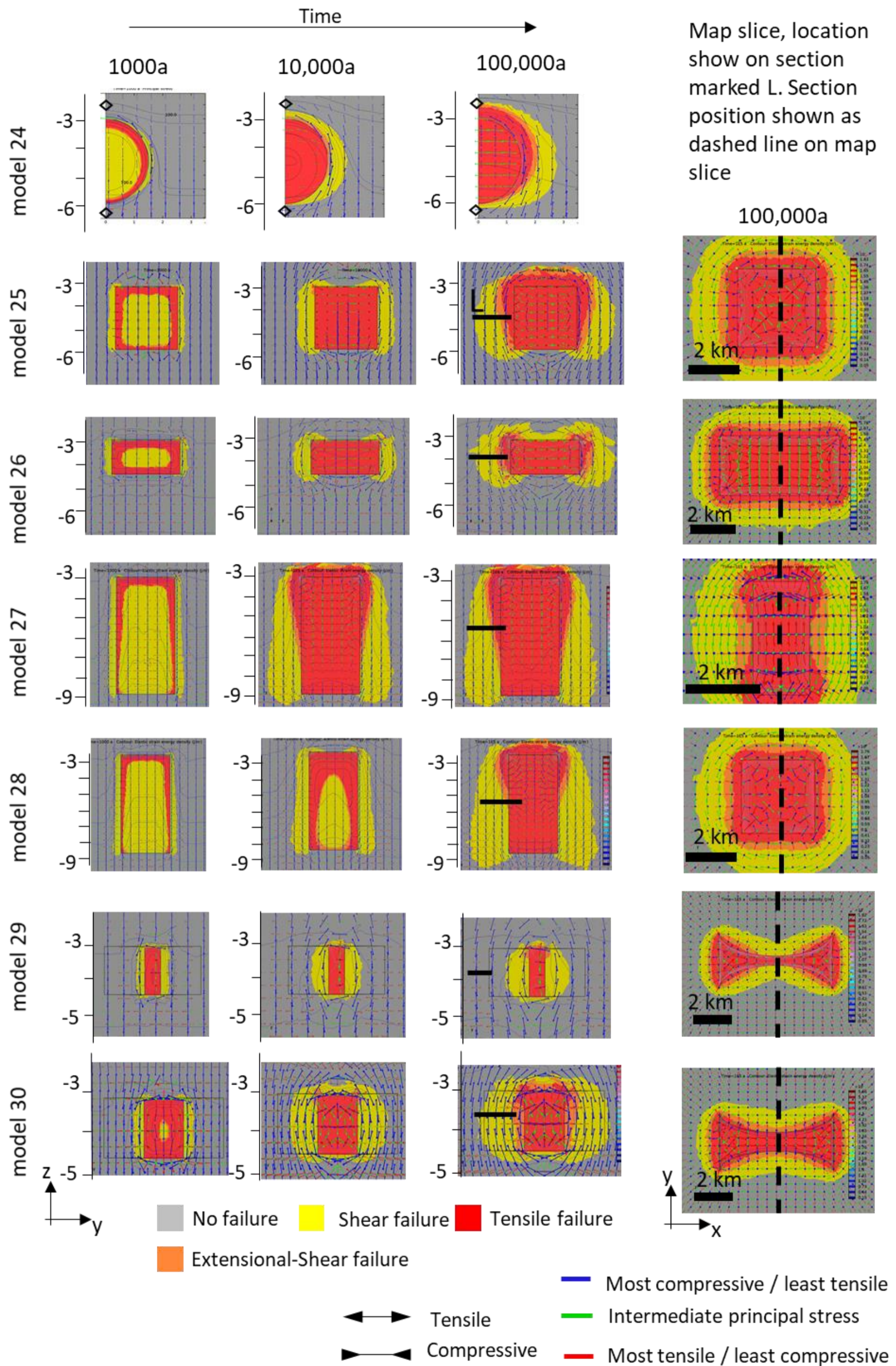


Figure 3.57. Influence of non-cylindrical geometries on stress orientation and the predicted Griffith domains failure domains.

3.9 Discussion

3.9.1. Rotation of the Principal Stress Axes

In map view the predicted orientation of least-compressive stress / most-tensile stress directions are initially parallel to the isothermal contours, so that the minimum principle stress is parallel to the margin. As cooling proceeds the least-compressive stress / most-tensile stress direction preferentially parallels the long axis of the intrusion. In three-dimensional models the relationship between isotherms and the intermediate principal stress is less clear. However, a later switch in orientation of the least-compressive stress / most-tensile stress and intermediate principal stress directions from concentric to radial around the top of a plutonic body is apparent. The switch is dependent on the intrusion geometry, i.e., dimensions and depth (Figures 3.58 & 3.59). The initial temperature distribution between the pluton and host rock only influences the timing of the orientation of principal stresses.

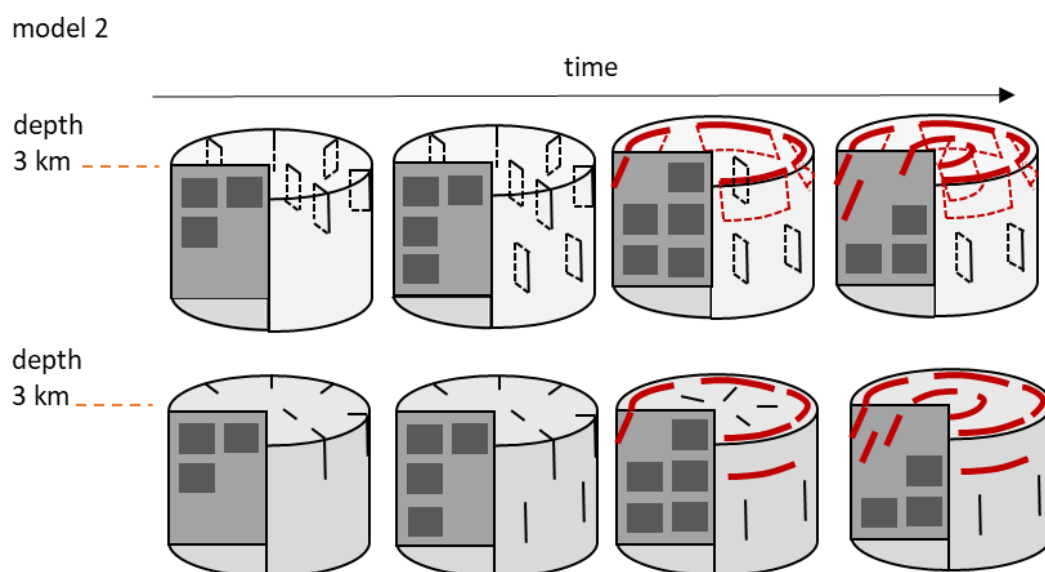


Figure 3.58. Schematic diagram of planes perpendicular to minimum tensile stress in cooling plutonic bodies of model 2. Top row: the cylindrical geometry is shown with transparency to highlight the geometry of the plane. The cut away and lower row are show without transparency. Early orientations are outlined in black and shown as grey plane in the cut away. The rotation of the orientation over time is shown by the red planes which dip outwards towards the margins. The orientation of the plane in host rock is parallel to the pluton margins (not shown).

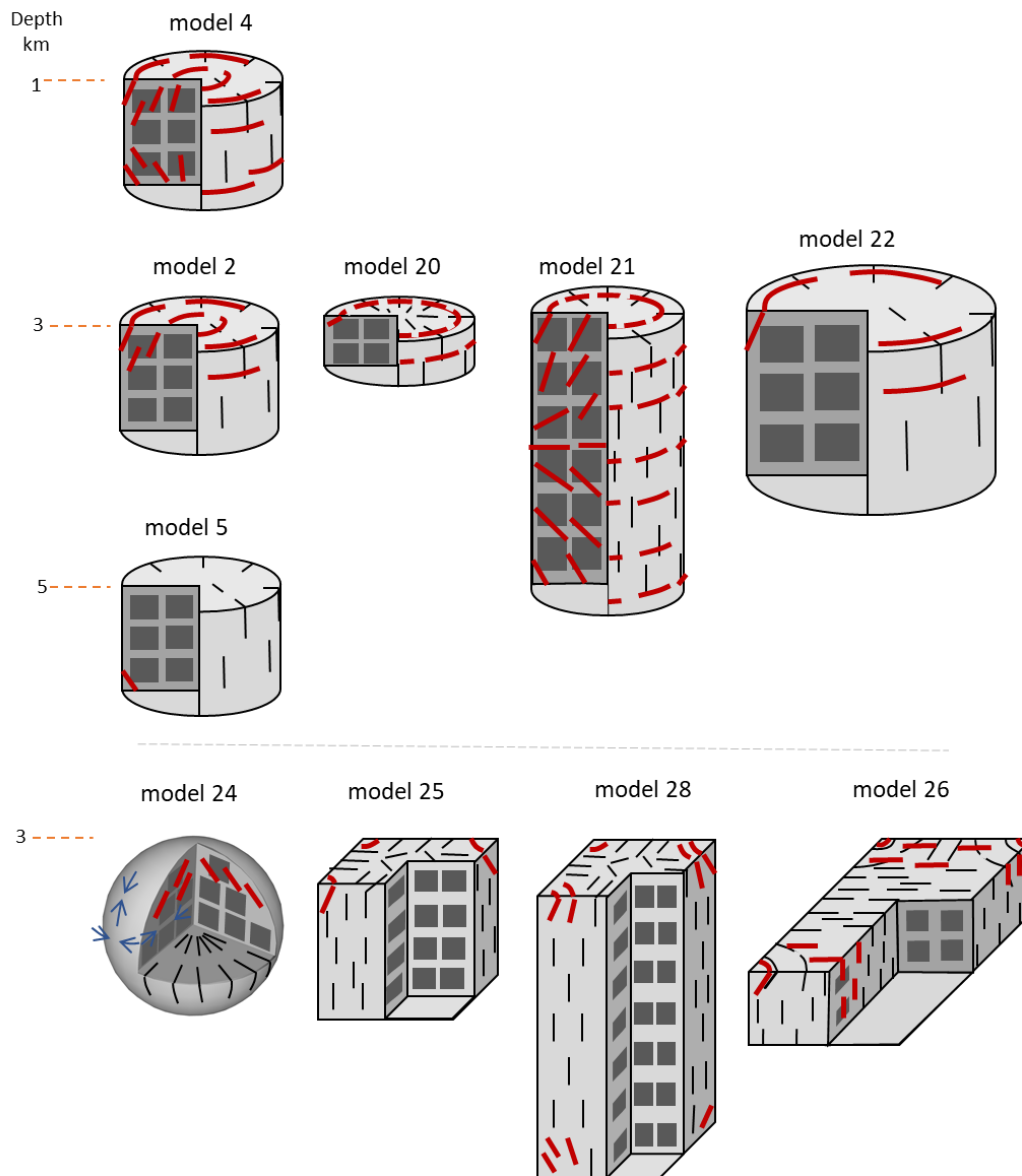


Figure 3.59. Schematic diagram of planes perpendicular to minimum tensile stress in cooling plutonic bodies of varying geometries and depths. Early orientations are shown in grey and later orientations in red. Orientation in host rock is parallel to the pluton margins (not shown).

Including anisotropic, in-situ, horizontal stresses, of a similar order of magnitude as the thermal stresses, strongly influences the orientation of predicted principal stresses (Figure 3.60). The axis of the least compressive / most tensile stress aligns with the orientation of the minimum horizontal stress defined by the regional load. If tectonic load values are increased towards the magnitudes of thermal stress the influence of the pluton geometry diminishes and the influence of tectonic load direction on predicted principal stress orientations, increases (Figure 3.60). The late rotation of principal stress directions may be influenced by early fracturing events.

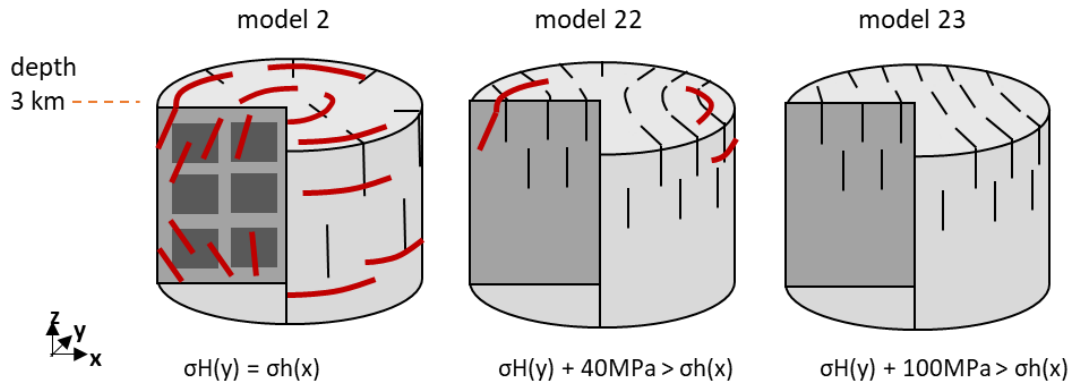


Figure 3.60. Schematic diagram of planes perpendicular to minimum tensile stress in cooling plutonic bodies with anisotropic horizontal stress. Maximum horizontal stress (σ_H) in models 22 and 23 is parallel to the y axis. In model 2 the maximum (σ_H) and minimum (σ_h) horizontal stresses are equal. Early orientations in grey and later orientations in red. In model 23 rotation does not occur as tectonic load dominates the control on principal stress axes orientation. Orientation in host rock is parallel to the pluton margins (not shown).

3.9.2. Stress Magnitudes

Stress magnitudes are greatest where heat loss is fastest i.e., at intrusion corners and where the intrusion is narrowest. Stress magnitudes are strongly influenced by the values of Young's modulus and coefficient of thermal expansion. Increasing the solid elastic thermomechanical parameter (the product of the Young's modulus and coefficient of thermal expansion) increases the values of predicted thermal stress. Tectonic loads and depth influence the initial stress at a given point and therefore the timing of the failure domains which a specific point passes through. Fluid pressures, which are not included in the models, would also influence the starting point of the failure paths. Increasing fluid pressures would push stress paths towards the tensile failure domain.

3.9.3. Failure Criteria

Modelling highlights the complex interplay of parameters which influence the spatial and temporal variation of fractures that may result from thermal stress. Pluton geometry (i.e., shape and depth), the in-situ stress field and the solid thermomechanical parameter have the greatest influence on the predicted principal stress orientation and magnitude. When the failure criterion is exceeded failure progresses from the pluton margins as it cools, regardless of geometry (i.e., shape and depth), initial temperatures or material properties. In the host, rock failure is preferentially located around the top of the intrusive body.

As cooling proceeds the stress magnitudes become tensile and differential stress reduces (Figure 3.61 A and Figure 3.17, p.70). At shallow emplacement levels < 5 km, tensile stresses are generated as a result of cooling (Figure 3.61 B.). At greater depths, the confining pressure due to gravitational loading, means the modelled stresses remain compressive (Figure 3.47 p.115). Failure, as a result of intrusive cooling, is therefore less likely in deeper plutons. This is also the case in models of the Tanvald pluton (Žák et al., 2006) which show that thermal stresses are unlikely to have had a significant influence on fracture generation at depths ~ 8 km (see section 3.5.4. p.97 – 102). With increased depth, shear mode failure is more likely as differential stresses are greater (Figure 3.61 B). Host rock failure is less likely with increasing depth even when temperature dependent material and mechanical properties are considered.

As well as depth, the initial differential stress is also influenced by the initial temperature field (Figure 3.61 C.) and in-situ stress (Figure 3.61 D.). Within a homogenous horizontal stress field, the depth at which stresses remain compressive is dependent on the plutonic volume and dimensions. Reduction of the minimum principal stress moves the stress paths towards the extensional-shear failure domain reducing time in the shear failure domain (Figure 3.61 D). Variation in geometry influences the cooling rate of a given point and therefore the differential stress magnitudes (Figure 3.16. F).

Accounting for temperature dependent material and mechanical properties (Figure 3.61 E). influences the spatial and temporal positions of predicted failure domains (Figure 3.51 p.121 and Figure 3.51 p.122). Accounting for temperature dependent mechanical properties results in modification of the failure envelope during cooling. The stable field (area of no fracture) increases as cooling proceeds as, values of the angle of internal friction and cohesion are modelled to both increase with decreasing temperature. The angle of shear failure is also influenced, so that when temperature dependent material properties are accounted for (e.g., model 19) the angle of shear failure becomes more variable (Figure 3.55, p.126). Temperature dependent material properties result in an initial increase and then decrease in stress magnitudes so that the modelled stresses move towards and then away from the failure envelope (Figure 3.61 E and Figure 3.53 p.123).

Mohr circles expand beyond the failure envelope (Figure 3.61) as the models do not account for the influence of fluid pressures or mechanical processes such as fracturing on stress distributions. Reactivation of existing fractures may also influence the predicted failure angles in plutonic bodies.

Point 4 (4.5 km) plotted on Mohr diagram for selected time steps and models

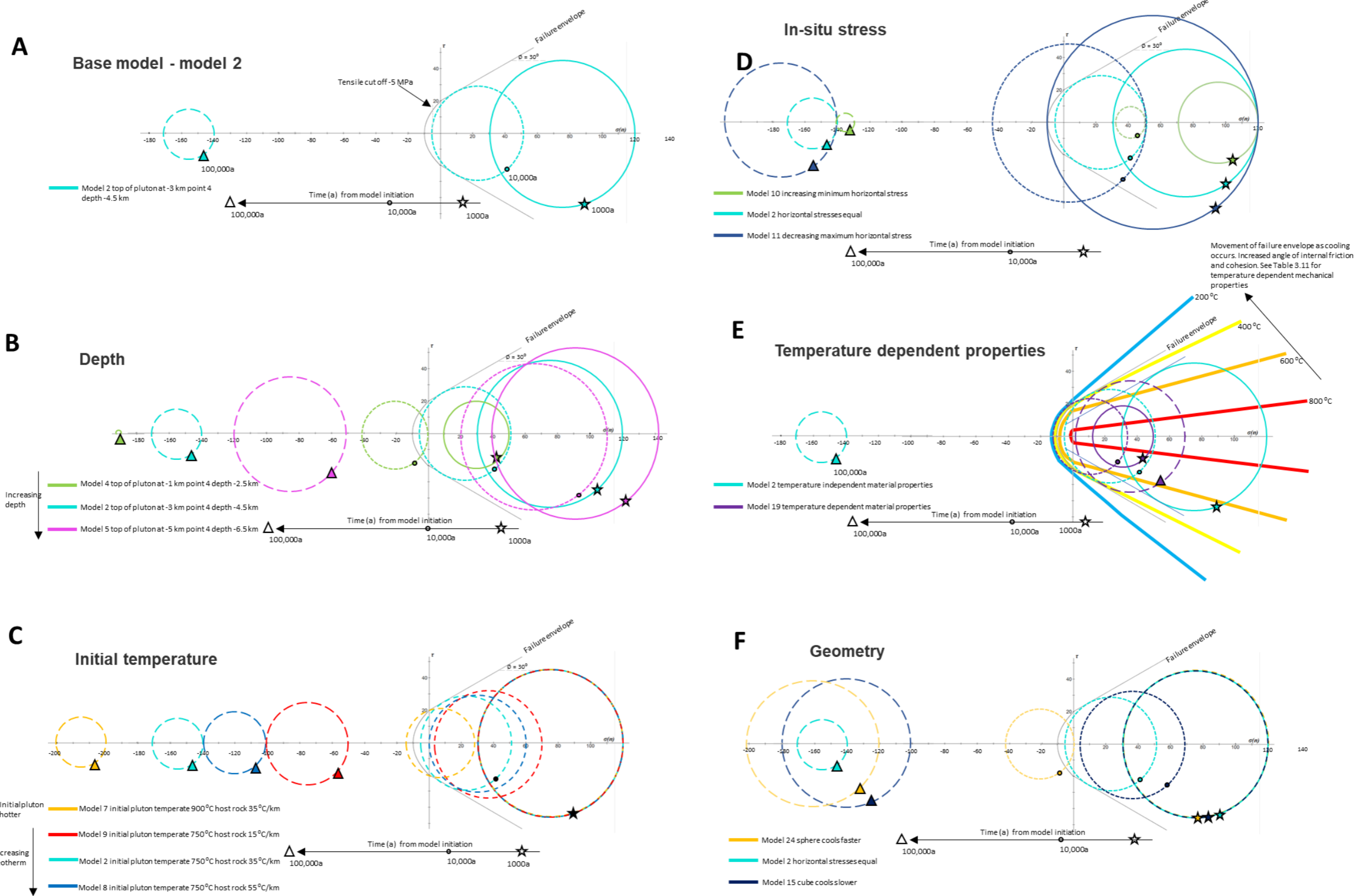


Figure 3.61. Effect of initial conditions on failure mode. Point 4 plotted on Mohr diagram for selected time steps and models. Point 4 is at a depth of 4.5 km in the pluton. Mohr circles plotted for (A) based case model, (B) variation in depth, (C) variation in initial temperature, (D) variation in in-situ stress, (E) application of temperature dependent material properties and (F) variation in geometry.

3.9.4. Implications of Numerical Models for Understanding Fracturing in Cooling Plutons

The models provide an initial insight into heat loss from an intrusive body. These models highlight the influence of conductive cooling considered to be the most important factor in early cooling history prior to the development of a hydrothermal system. Coupled chemical and mechanical processes will also influence the thermal history. For example, heat generated by magma crystallisation could reduce the cooling rate. Mechanical processes are likely to increase the cooling rate, as fracturing would increase permeability and therefore allow convective heat transfer. Permeability and stress distributions will also be influenced by the precipitation and annealing of minerals in fractures, which could reduce permeability, convective heat flow and the cooling rate (see chapter 2 p.29).

Three-dimensional modelling results highlight that rotation of the stress axis may occur during cooling and could potentially results in multiple fracture orientation forming. The effectiveness of the simplification of the models can only be addressed through comparison of modelling results to field examples, which account for geometry, emplacement depths and likely in-situ stress at the time of cooling.

3.10. Conclusions

Numerical models investigating the likelihood of fracturing resulting from the cooling of plutonic bodies have been run. The models of conductive cooling of a hot body in an elastic plate were set up and run in COMSOL Multiphysics[®]. These models have been benchmarked against existing two-dimensional numerical models and extended into the third dimension. Models highlight that thermal changes resulting from cooling plutons have an important control on the orientation and magnitude of stress.

The models presented here highlight that the magnitudes of stress predicted from the models vary over time and are enough to result in failure. The predicted stress magnitude is influenced by pluton geometry (i.e., volume and depth), applied material properties and initial temperature distribution. The orientation of predicted principal stress is influenced by the plutonic geometry and strongly influence by in-situ stresses. In-situ stress is defined by gravitational load (i.e., depth) and regional tectonic setting i.e., relative magnitude of vertical and horizontal stress. Over time the orientation of the principal stress may rotate as the pluton cools i.e., the minimum horizontal stress within the pluton may change from concentric to radial. This effect is greatest in vertically elongate plutonic bodies where horizontal dimensions are not equal. All else being equal, this effect is greater in volumetrically smaller and in shallower plutons. Within the host rock, the maximum compressive stress parallels the pluton margin and the minimum compressive stress is radial away from the pluton. The maximum compressive stress at the top and base of the pluton therefore changes from initially vertical to horizontal. The orientation of principal stress in the host rock is also likely to be influenced by pre-existing anisotropies in the crustal stress field which are not included in the models.

Predicted failure is influenced by the applied failure criterion, material and mechanical properties, the initial in-situ stress (i.e., anisotropic regional loads and depth), pluton geometry (i.e., shape and volume), and the initial temperature distribution. Despite these variations, failure progresses inwards from the margins as the pluton cools and influences the host rock around the pluton. Increasing the pluton depth means that failure is less likely to occur and the failure that does occur, is more likely to be shear failure.

The models presented here are most applicable to plutonic bodies that are emplaced at rates greater than 2 cm / year, without significant cooling between emplacement of successive units, at early stages of cooling before significant fracturing of the host rock has occurred and advective cooling related to hydrothermal systems is limited. The applicability of these models can only be tested through comparison to fractures in plutonic bodies.

4. The Alta Stock

This chapter describes numerical modelling and comparison to field data of the Alta stock in Utah. An introduction is given in section 4.1 (p.137). Following this, a geological overview of the Alta stock is given, section 4.2 (p.142). Field data is described in section 4.3 (p.144). Numerical modelling method is outlined in section 4.4 (p.165) and results are presented in section 4.5 (p.173). Numerical modelling results are compared to field data on section 4.6 (p.188). The discussion, section 4.7 (p.196), focusses on fracture evolution at Alta. Conclusions are presented in section 4.8 (p.203). Data is given in the associated appendix B and digital appendix E files.

The results described in this chapter were presented at AGU 2018, Ellis, J.F, Blenkinsop, T. and Davies, H. The Origin of Fractures in Plutonic Rocks: field evidence and three-dimensional numerical modelling of the Alta Stock, Utah AGU 2018.

4.1. Introduction

The Alta stock is located at the highest part of the Central Wasatch mountain range, Utah. Elevations range from 2,600 m at the town of Alta to 3,290 m at Mt Wolverine. The stock is accessible from Salt Lake City (approximately 20 miles southeast) at the Snowbird ski resort and to the west from Brighton, numerous hiking trails are found within the area. The Alta stock is used as an example to compare the numerical modelling developed in chapter 3 to field data (Figure 4.1).

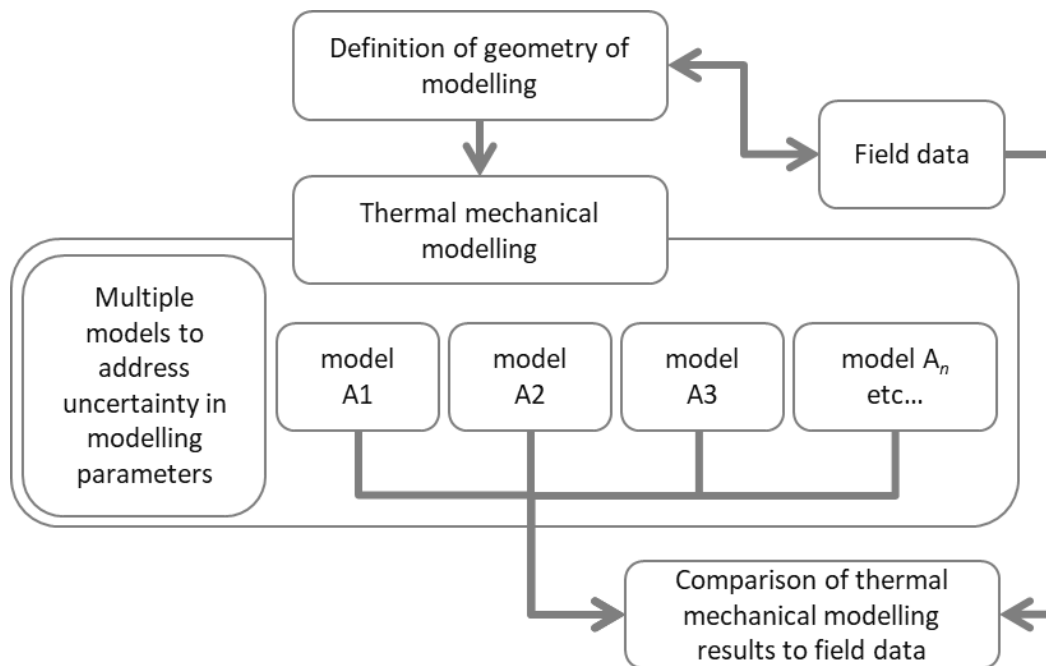


Figure 4.1. Summary of workflow, comparison of numerical models and field data.

Geological mapping of the area is published by the USGS and can be found on the USGS/AASG National Geologic Map Database. On these maps the geometry of the Alta stock is based on work completed by Wilson (1961). Host rock geometry is defined from mapping by Calkins et al., 1943. Historic mine workings (pre-dominantly Pb-Ag) are found along the contact with the host rock and surrounding area (Butler and Loughlin, 1912).

Systematic fracture patterns within the intrusion have previously been identified. Wilson (1961) produced the first map of joint orientations within the stock (Figure 4.3). Identifying steeply dipping (> 60°) joint systems formed of 1 to 4 fracture sets grouped by orientation. Vein sets (John, 1991, Figure 4.4) and microcrack orientations (Ren et al., 1989; Kowallis et al., 1995) have also been studied. The fracture orientations identified in these studies trend NNE to NE, N and NNW, have been

attributed to cooling, Basin and Range tectonics, or local stresses (Wilson, 1961; John, 1991; Ren et al., 1989; Kowallis et al., 1995).

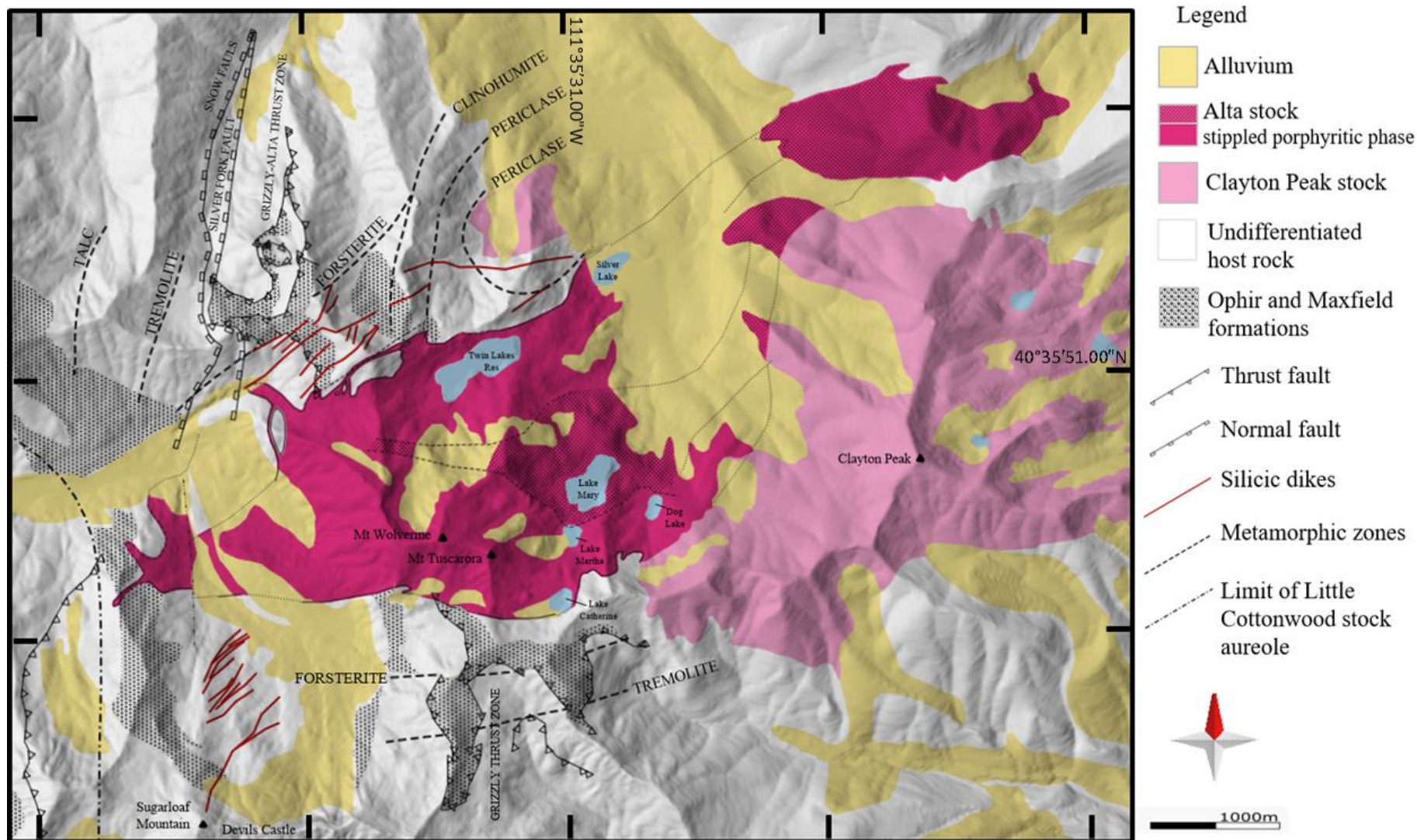


Figure 4.2. Geological map of the Alta stock and surrounding area. Non-porphyritic (light fuchsia) and porphyritic (stippled, darker fuchsia) phases of the Alta stock are shown. These phases have a gradational contact except in the south where there is a sharp boundary. Geological units and structures are based on USGS map GQ-534 (https://ngmdb.usgs.gov/Prodesc/proddesc_1849.htm) overlain on topographic surface. Contact aureole domains based on mapping by Cook and Bowman (1994).

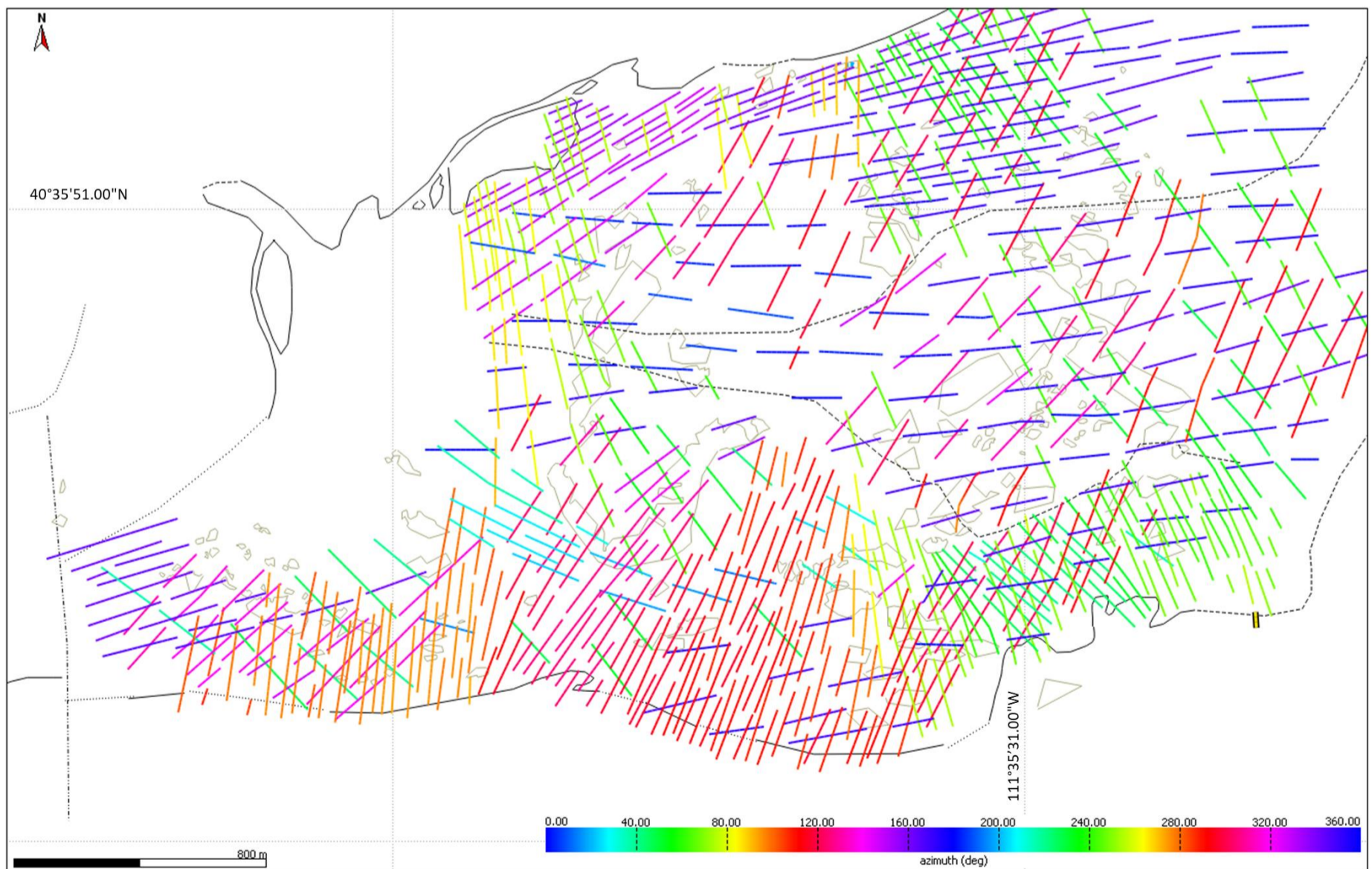
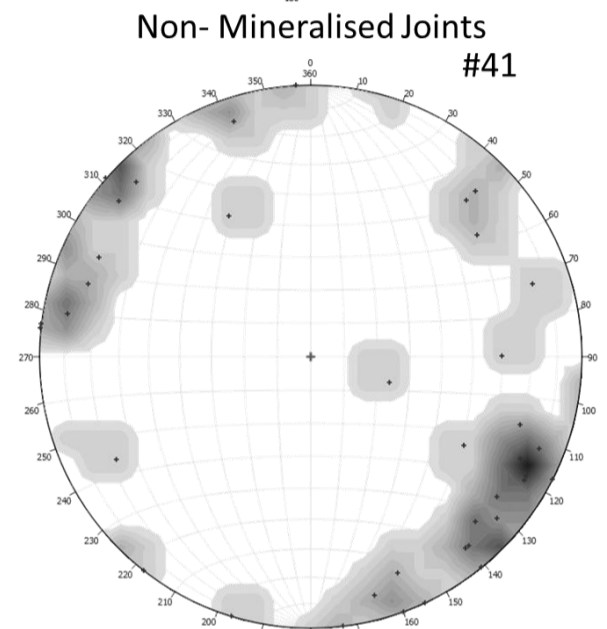
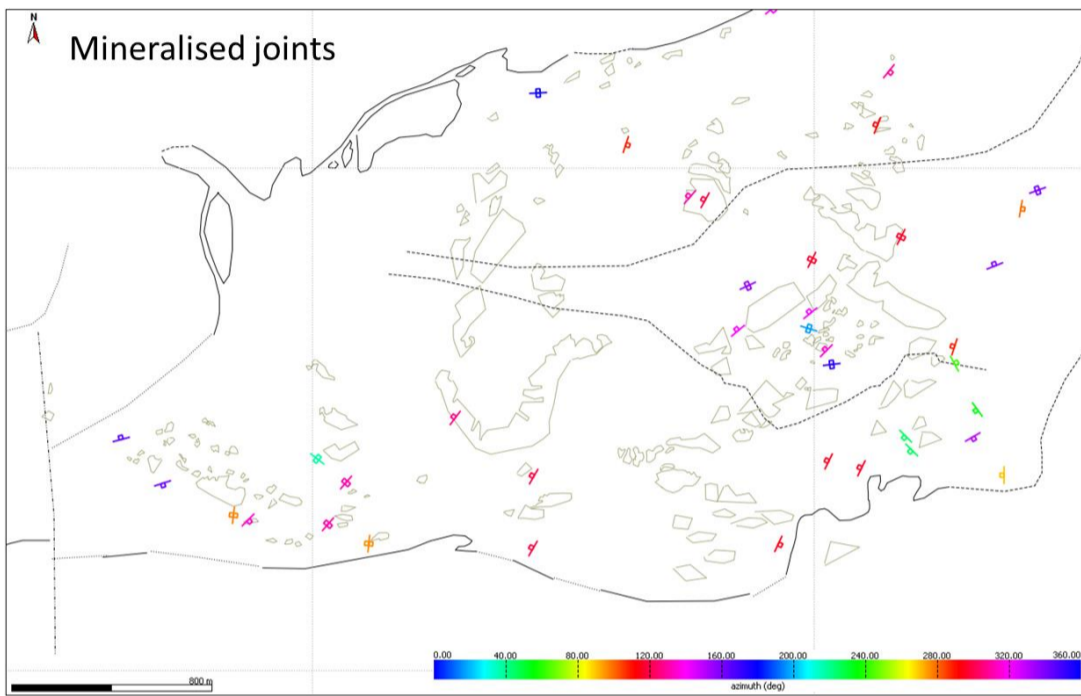
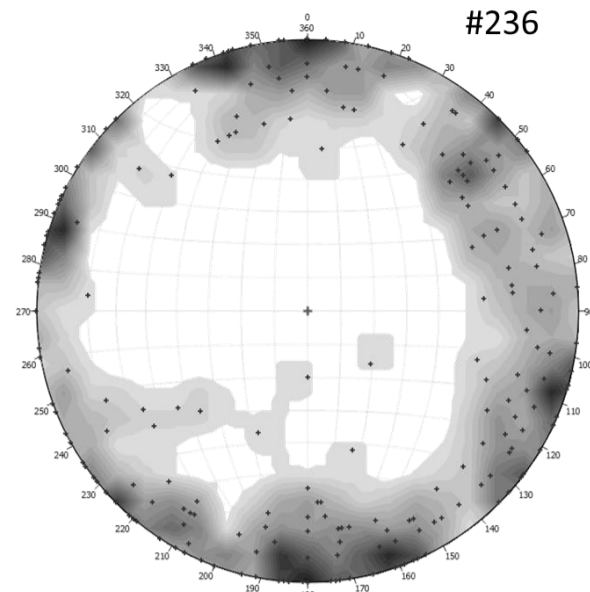
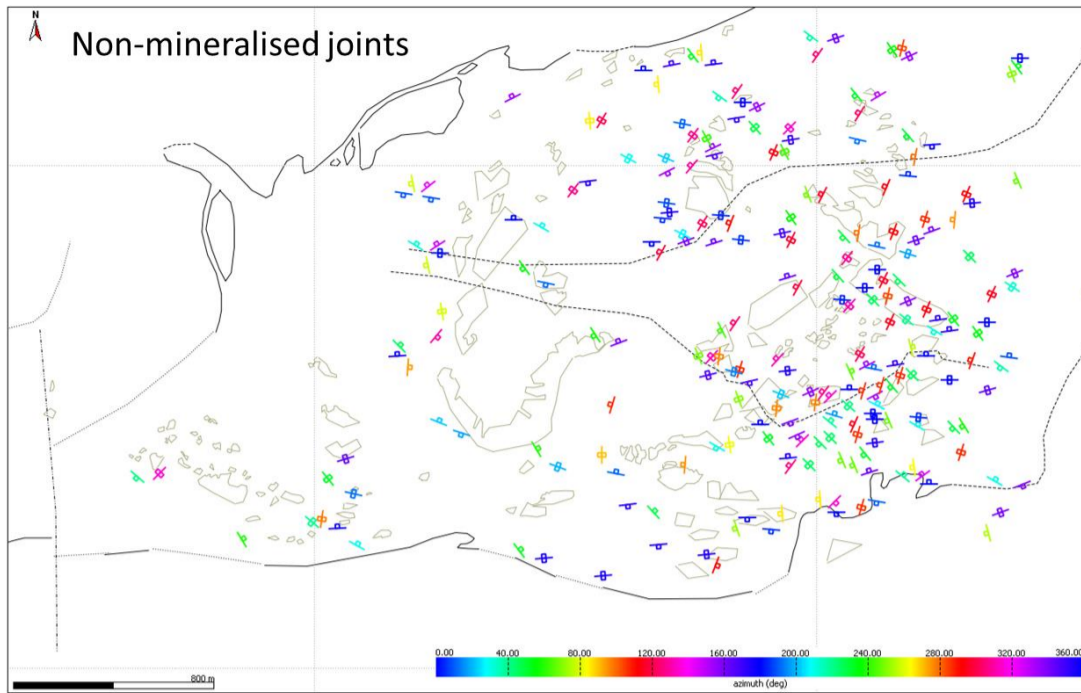


Figure 4.3. Published mapping of orientation data of joints and veins recorded by Wilson (1961). Lower-hemisphere equal-area stereonet projection of poles of joint and mineralised joints. Total number of measurements plotted given by stereonet. Lower image is a generalised interpretation of strike directions and qualitative interpretation of joint spacing, the lines do not represent individual joint planes. Data was digitised in MOVE™ from figures given in Wilson, 1961 and colour mapped for orientation. Stereonets contoured for density (interval 5, significance 3, grid 20) percent per 1-percent area.

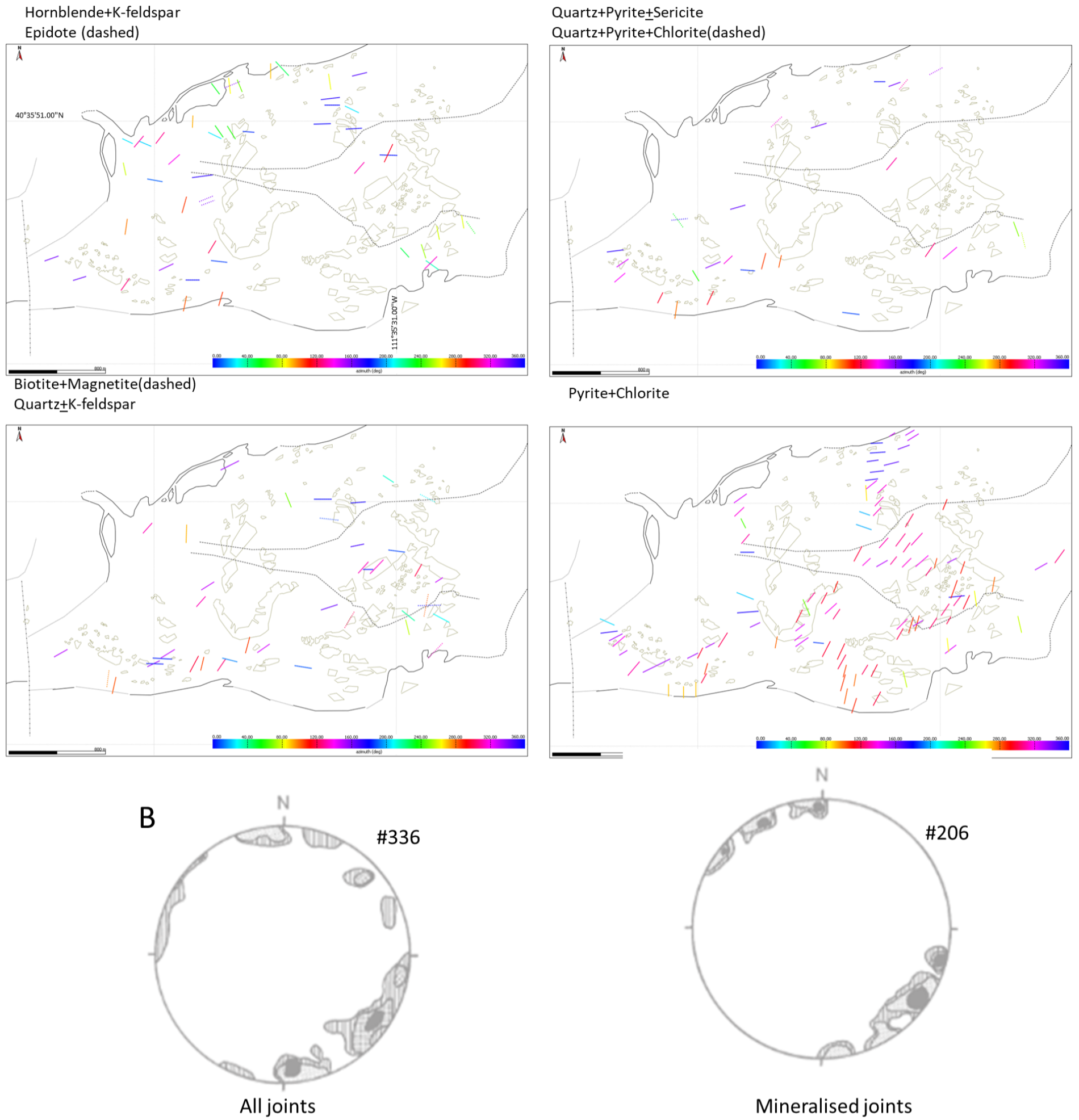


Figure 4.4. Published mapping of joints and veins recorded by John (1991) separated by mineral fill. Lower-hemisphere equal-area stereonet projection of poles to joints (left) and mineralised joints (right). Total number of measurements plotted is given by each stereonet. Data was digitised in MOVE™ from figures given in John, 1991 and colour mapped for orientation. Stereonet contours at 5 (lined), 6.5 (stippled), and 8 (black) percent per 1-percent area.

4.2. Geological Overview

Sedimentary host rocks primarily consist of quartzites (Precambrian Big Cottonwood and Cambrian Tintic Formations) and pelitic units (Cambrian Ophir Formation) capped by carbonate rocks (Cambrian Maxfield and Mississippian Fitchville, Deseret and Gardison Formations). The sedimentary formations have a generally northerly strike and predominantly dip to the east. They are deformed by north-south folding and pre-intrusive thrusting. In the Alta area thrusting is represented by the Alta-Grizzly Thrust zone (Figure 4.2). This thrust repeats a portion of the carbonate section, placing Cambrian Maxfield over the Upper Mississippian Deseret and Gardison Formations. Folding of sediments around the Alta stock is marked by the upward bending of the eastward dipping Alta-Grizzly Thrust zone into a faulted syncline. To the southwest, the Alta stock intrudes the older Clayton Peak stock (quartz monzodiorite to quartz monzonite, 35.5 ± 1.5 Ma U-Pb zircon, Vogel et al., 2001).

The mid-Tertiary Alta stock (34.3 ± 1.5 Ma; U-Pb zircon, Vogel et al., 2001) has a mapped aerial area of approximately 10 km² (Figure 4.2). The stock extends 8 km along an NE trend and has an elongate sigmoidal shape in map view (Figure 4.2). The stock margins are steeply dipping at the surface and the minimum vertical thickness is estimated at 3 km based on paleodepth calculation, outcrop and mine working exposures (John, 1989; Cook and Bowman, 1994). The granodiorite to quartz-monzonite stock is mapped with a central leucocratic phase (porphyritic phase) and a more mafic equigranular border phase (non-porphyritic phase) (Figure 4.2). A sharp contact between these phases can only be mapped along the southern contact, marked by the later porphyritic phase cutting aplite dykes within the non-porphyritic phase (Wilson, 1961). Elsewhere, the boundary between these phases is transitional and impossible to distinguish reliably in hand sample (Wilson, 1961; Bartley et al., 2008). Estimates of emplacement depth range from ~3.5 km to 7 km (Johnson, 2009). These estimates are calculated from stratigraphic reconstruction (6.25 km; Wilson, 1961) and fluid inclusion data assuming lithostatic conditions (6.3 km in the west and 3.7 km in the east; John, 1991).

Metamorphism associated with the stock has affected the host rocks up to two kilometres from the southern intrusive contact (Cook and Bowman, 1994) (Figure 4.2). Several kilometres to the east the younger granite to granodiorite Little Cottonwood stock (30.5 ± 0.5 Ma; U-Pb zircon, Vogel et al., 2001) outcrops. Its contact aureole overprints the western margin of the Alta stock (Cook and Bowman 1994).

Studies on the regional paleostress field suggest rotation of the maximum horizontal stress from NE-SW in the Eocene and early Oligocene to ~E-W in the Late Oligocene and Early Miocene, NW in the Mid-Miocene (Kowallis et al., 1995) and subsequently ~N-S related to Basin and Range tectonics

(Ren et al., 1989). Post-emplacment, the stock has been tilted 15° – 20° to the east as a result of tilting in the footwall of the Wasatch fault (John, 1989, 1991) (Figure 4.5). Structural relationships have been used to infer left-lateral strike slip motion on an east-west trending basement structure during emplacement of the stock. These relationships suggest magma emplacement related to NW-SE extension within an extensional step-over (Vogel et al., 2001). Incremental emplacement (syntaxial crack-seal) is suggested by AMS studies (Bartley et al., 2008) and Ti-in-quartz geothermometry (Johnson, 2009).

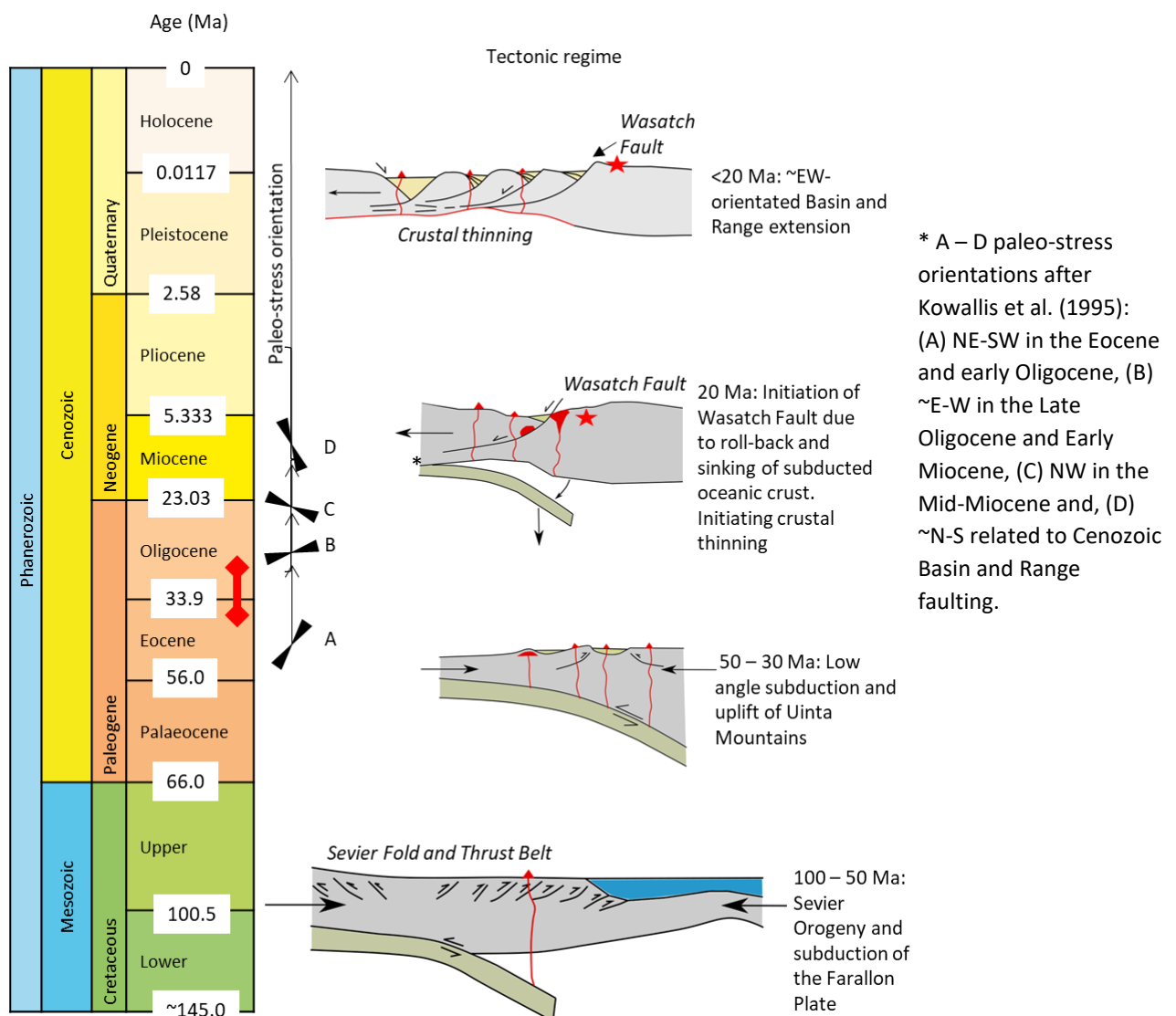
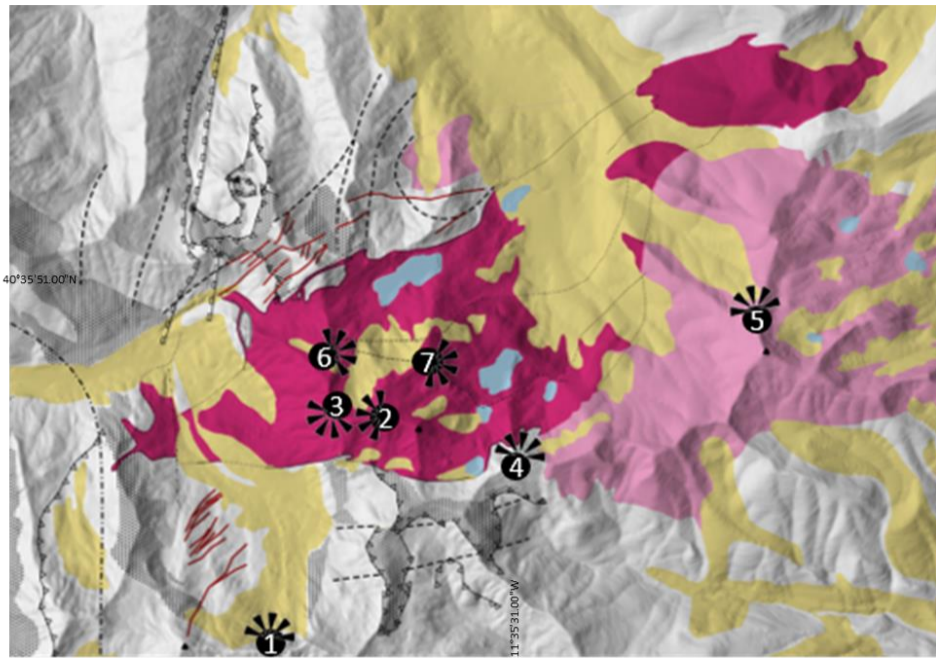


Figure 4.5. Tectonic evolution of the Wasatch fault and surrounding area. Alta is emplaced in the footwall of the Wasatch fault, representative position shown by a red star. Red line on geological timeline marks the timing of the intrusive rocks of interest (36-30 Ma). Tectonic regimes redrawn after R. Harris <http://sipes.org/wp-content/uploads/2015/06/Central-Wasatch-Range-Field-Trip-Guide-reduced.pdf>.

4.3. Field Data

Data presented here is for field work carried out over two field seasons in 2016 and 2017 for this study. Annotated panoramic photos giving an overview of the field area are presented in Figure 4.6. The collected data was compiled using FieldMove Clino version 2.4.0 and data files can be found in the digital appendix E. The field work focused on the collection of orientation data for aplite dykes across the stock, and joint orientations collected using circular scan lines (Zeeb et al., 2013) from seven selected outcrops. Where relevant, field data collected by Wilson, 1961 and John, 1991 is referenced.



- Al Alluvium
- qm Little Cottonwood stock quartz monzonite
- gd Alta stock granodiorite
- gp Alta stock porphyritic granodiorite
- cp Clayton peak granodiorite
- ☒ Ophir and Maxfield formations

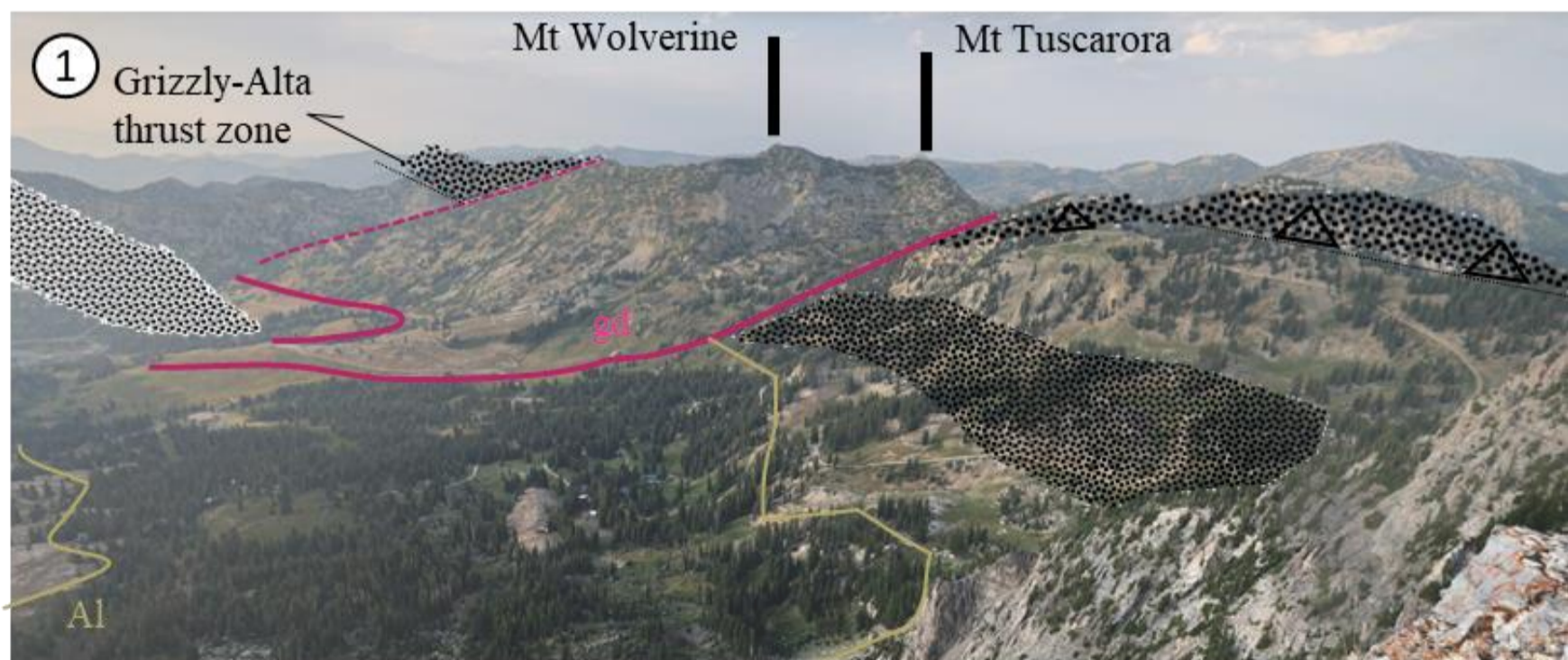
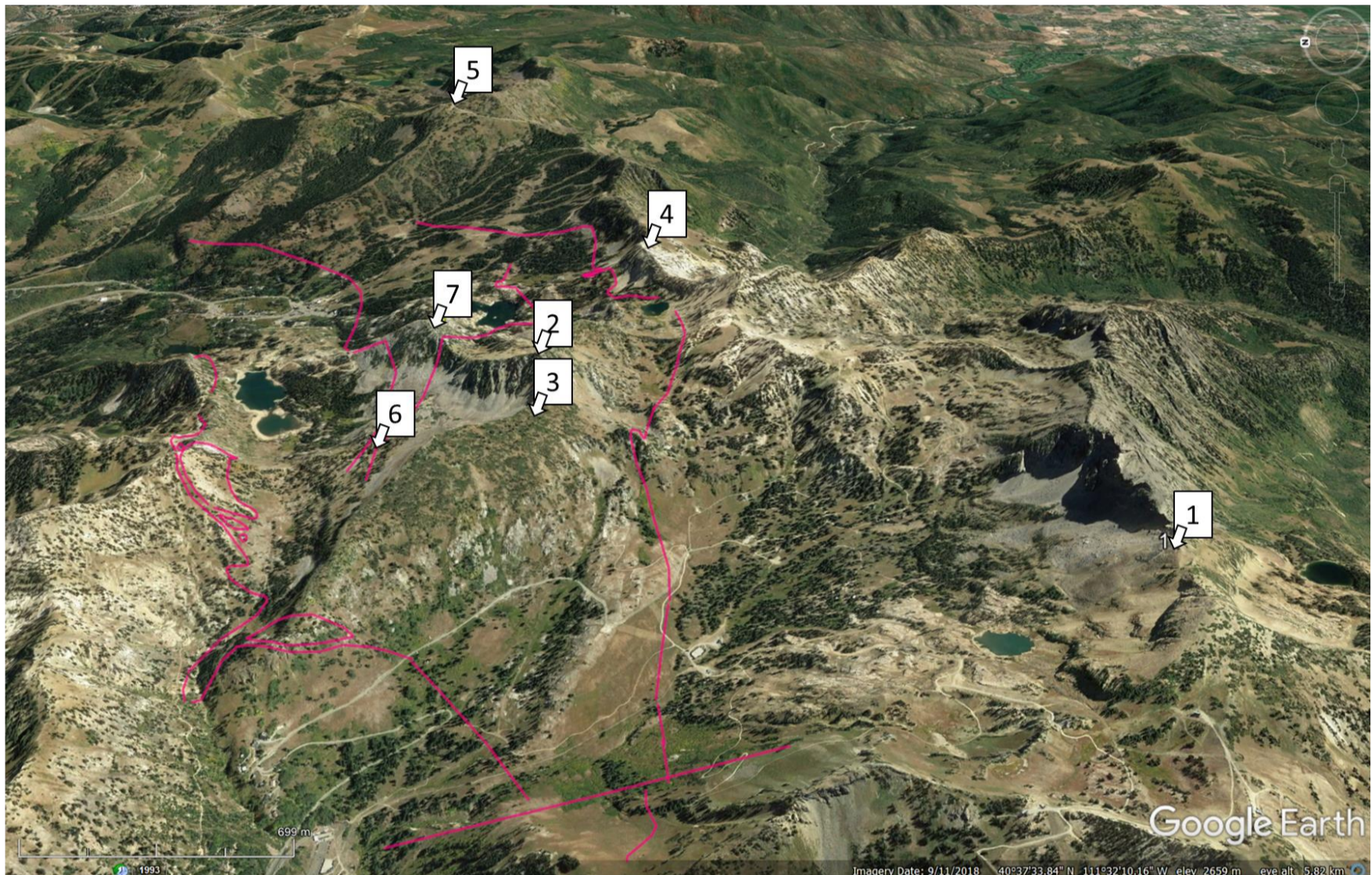


Figure 4.6. Annotated panoramic photos of the field area around the Alta stock. Locations and view directions are given on map and oblique Google map view, looking east. Boundaries of the Alta stock are shown by pink lines. Numbers refer to photos. Photos 2 – 7 are given on next page.

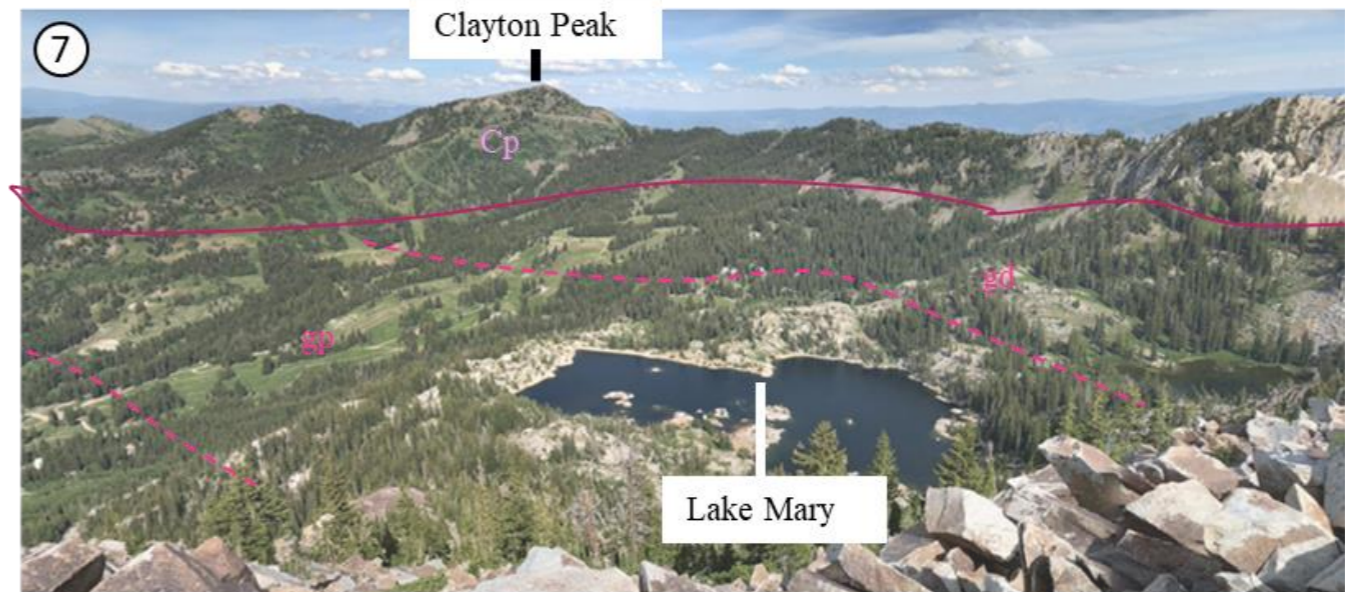
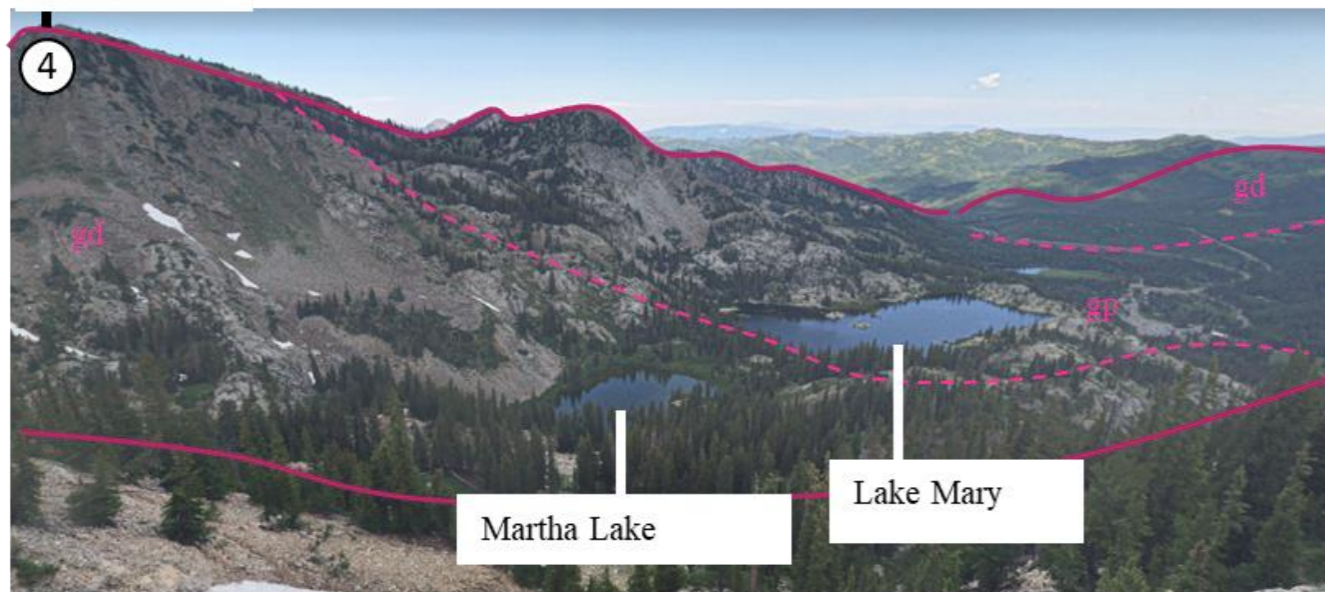
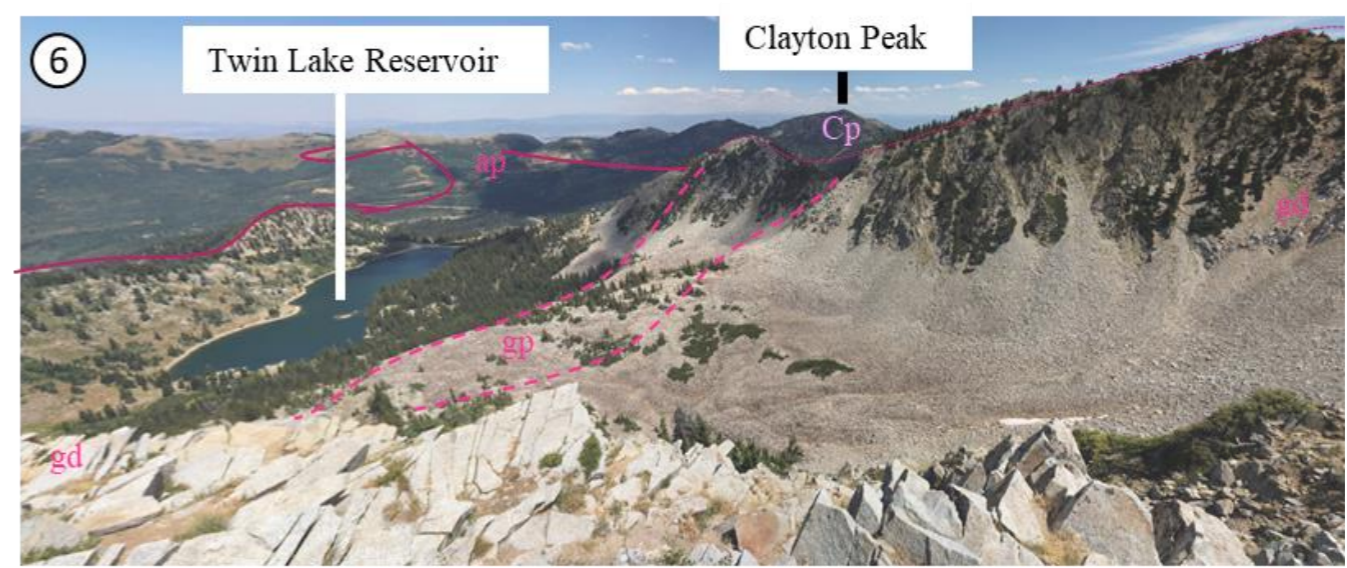
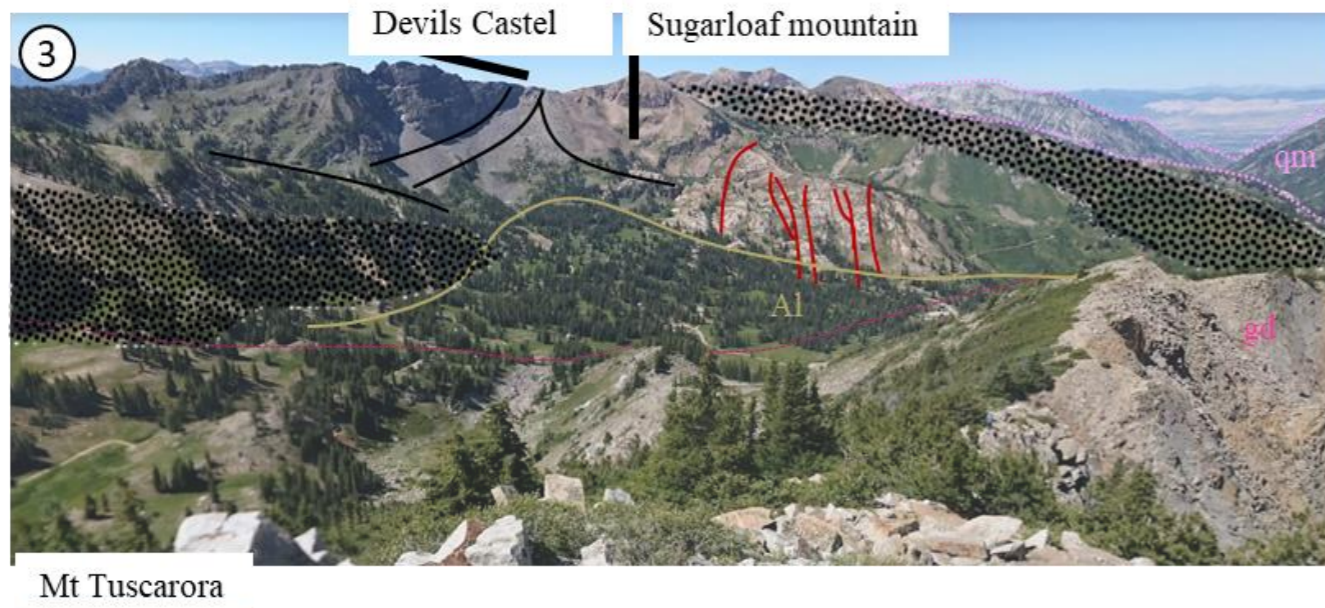
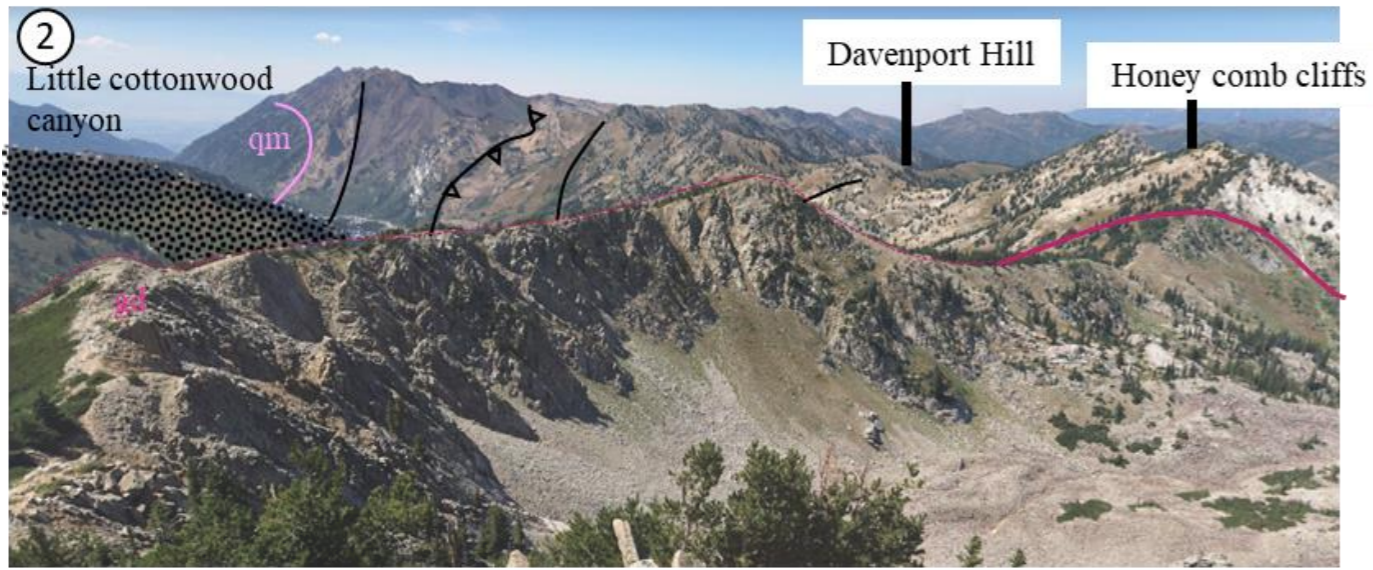
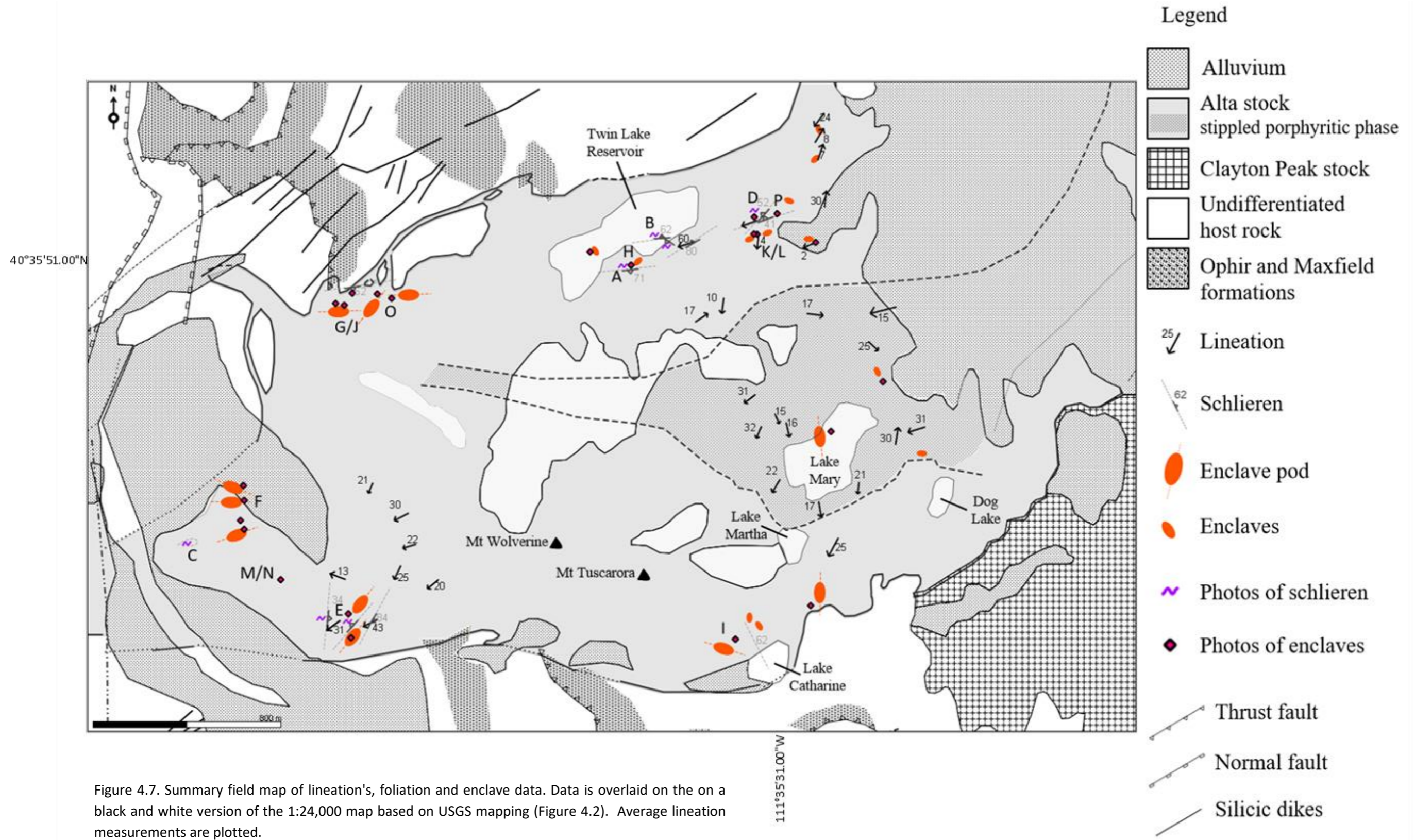


Figure 4.6. Continued.

4.3.1. Primary Structures (foliations, lineations and enclaves)

Measurement of primary igneous flow structures recorded include the lineation of mafic crystals, orientations of schlieren and enclaves and groups of enclaves forming pods (>20 individual closely spaced enclaves) (Figure 4.7). The most common lineation trend of mafic crystals is south westerly and plunging on average 21° (range $2^\circ - 60^\circ$), the preferred orientation is not strongly developed. Schlieren which are located around the margins of the stock (Figure 4.7) typically dip steeply and are sub-parallel to the margins of the stock. Their length varies from a few meters up to a minimum of 8 m (length measurements are constrained by outcrop exposure) (Figure 4.8). One example of elliptical schlieren was observed (Figure 4.8 C). Enclaves are distributed throughout the stock (Figure 4.7). Fewer enclaves were observed in the centre of the stock, although this may in part be due to difficulty in accessing outcrops due to steep cliffs.



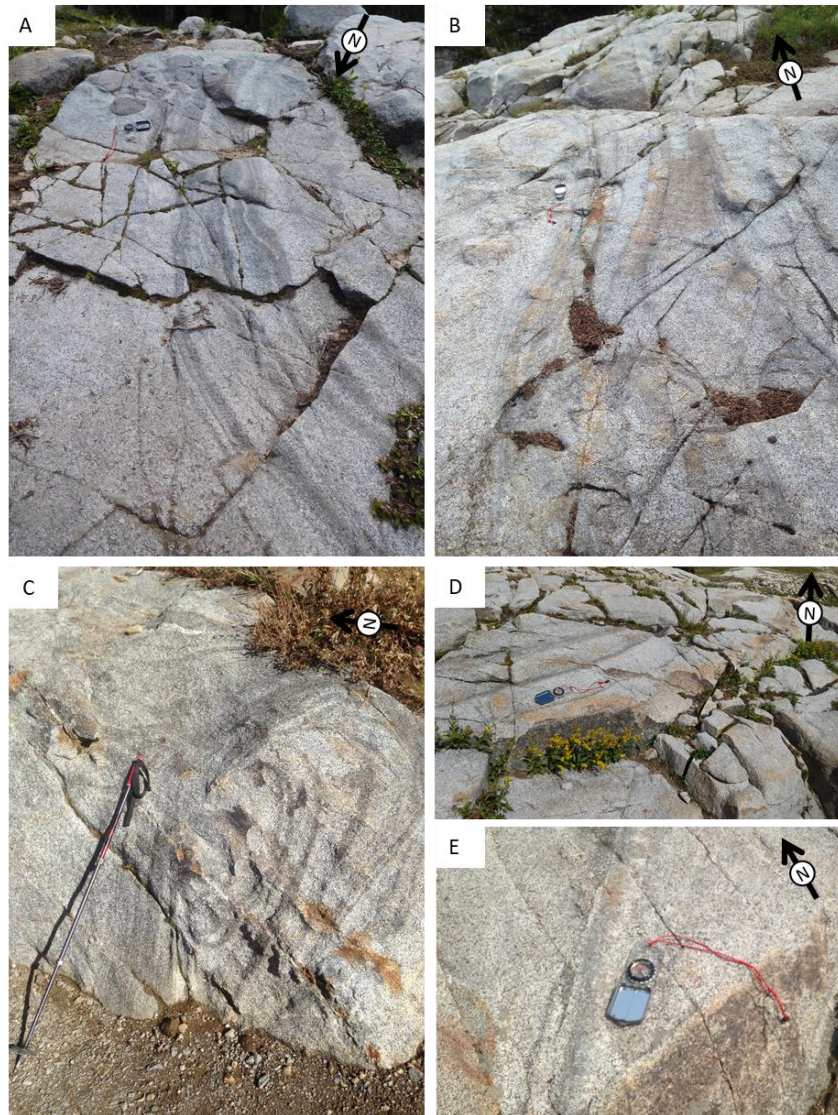


Figure 4.8. Photos of schlieren (A - E, letters correspond to locations marked on Figure 4.7). Schlieren are typically steeply dipping and elongate, length varies from a few meters up to 8 meters (maximum length constrained by outcrop exposure), (C) example of elliptical schlieren.

Enclaves occur as pods (Figures 4.10 F - J) or distributed (Figures 4.10 K - P). The form and size of the enclaves vary but they are generally rounded to elliptical and 5 to 50 cm along the long axis. Some large enclaves (5 – 10 m, long axis) are observed dispersed in the north-east area of the stock (Figure 4.9 K – L). Enclave pods are found along the western and southern margins of the stock (Figure 4.7). Some pods have a sharp margin (N to NW side) but are gradational on the opposing margin (Figure 4.9 F – I). Fractures and aplite dykes that cut the enclaves typically continue through the enclaves and the stock. In three cases persistent closely spaced (1 – 10 cm) fractures were observed within moderately size enclaves (~1 m long-axis) and do not visibly continue into the stock. These fractures strike ~NE-SW (Figures 4.10 J, O & P).

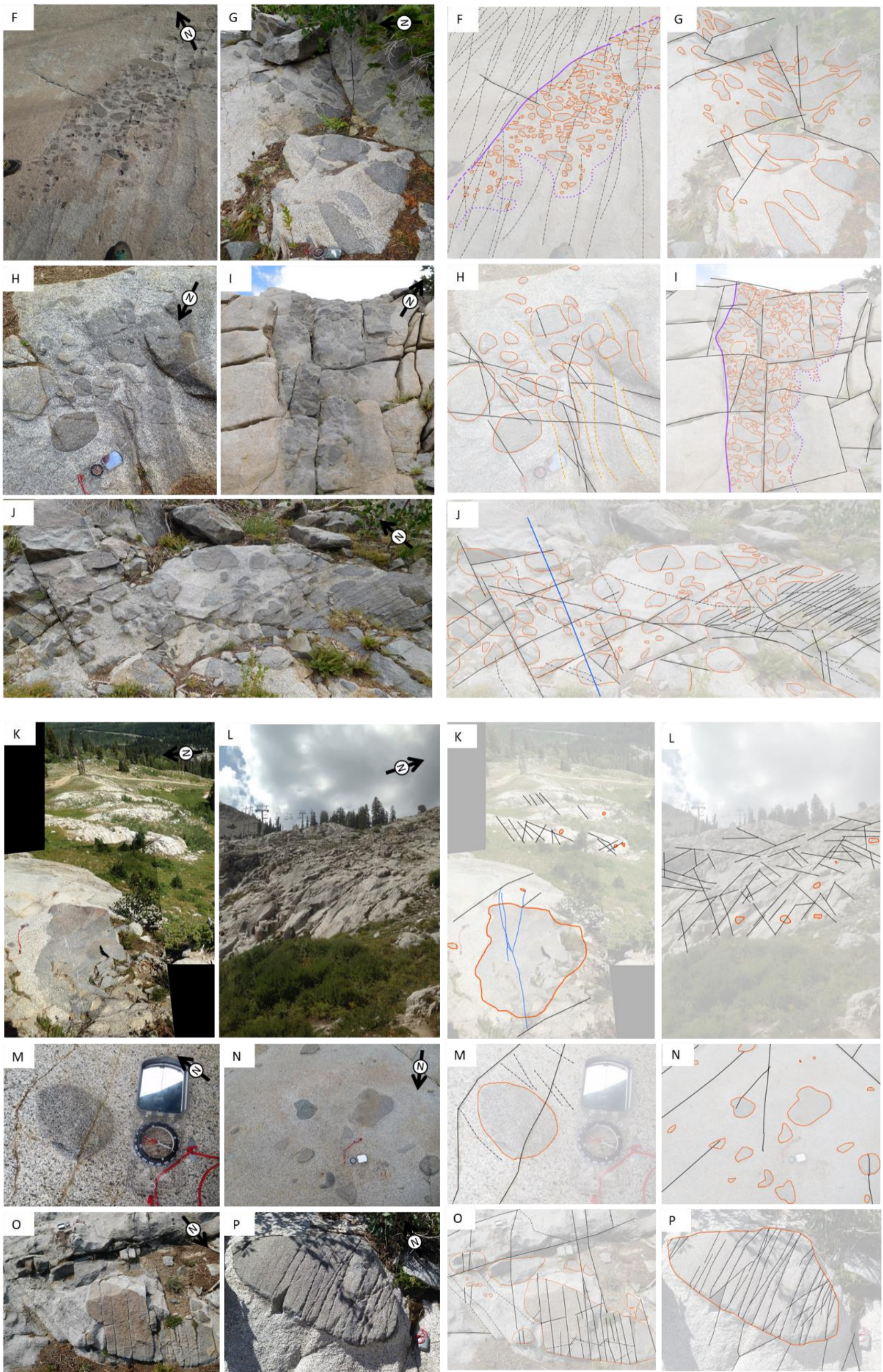


Figure 4.9. Photos of enclaves (F – P, letters correspond to locations marked on Figure 4.7). The enclaves occur as pods (F - J) or distributed (K – P). Interpreted overlays are given. Orange line outline enclaves, black line joints, veins black dashed line, schlieren light orange dashed lines, aplite dykes blue lines. Purple lines interpreted on F and I show sharp (solid) and dispersed (dashed) margins of enclave pods.

4.3.2. Aplite Dykes

Aplite dykes are generally steeply dipping (70° - 90°) and orientated at high angles to the stock margins (Figure 4.10). Straight-walled dykes (1 – 3 cm thick) are exposed for up to 20 m along strike (constrained by exposure) and are typically fine grained with sharp margins (Figures 4.11 A & B). In places they are wider (10 – 20 cm thick) and have pegmatitic textures (Figures 4.11 C & D). Some aplites display evidence of emplacement into a deforming host (Figures 4.11 E - J). Anastomosing networks can also be found (Figures 4.11 K & L). Sinuous and anastomosing aplites are located around the western margin of the stock where greater paleodepths are estimated (~ 5.5 km, fluid inclusion study, John, 1989).

The most common aplite dykes, with sharp margins, extend throughout exposures (maximum outcrop extent ~ 20 m). Terminations of aplites were not observed (Figures 4.11 A, B, M – Z). Aplite dykes pre-date joints sets, but post-date enclaves as evidenced by the intersection of enclaves by the aplite dykes (Figures 4.11 Y & Z). In only one location close to the northern margin of the stock were mineralised joints observed to offset an aplite dyke (Figure 4.11 X).

Conjugate pairs of aplites are common and predominantly located along the northern margin of the stock and along the southern contact between the non-porphyrific and porphyritic phases (Figure 4.11 M - W). The thickness of the pairs of conjugate dykes are similar. Evidence of minor shear compared to opening (average slip to opening ratio 1:2) was observed on the crossing conjugate dykes and where aplites cross enclave markers (Figure 4.11 M – Z). Shear sense on aplite dykes was recorded as both compatible (Figure 4.11 N, P, Q, R, T, U & V) and non-compatible (Figure 4.11 M, O & S) with the shortening direction within the acute bisector. The acute angle of intersecting dykes is $\sim 40^{\circ}$ for conjugate dykes where the shortening direction intersects the acute bisector. Where the shortening direction intersects the obtuse angle, angles in the shortening direction range between 120° – 150° (tabulated data in appendix B Table B4-1 p.332). Other examples of crossing aplites are interpreted as only representing opening displacement (e.g., Figure 4.11 P, V & W).

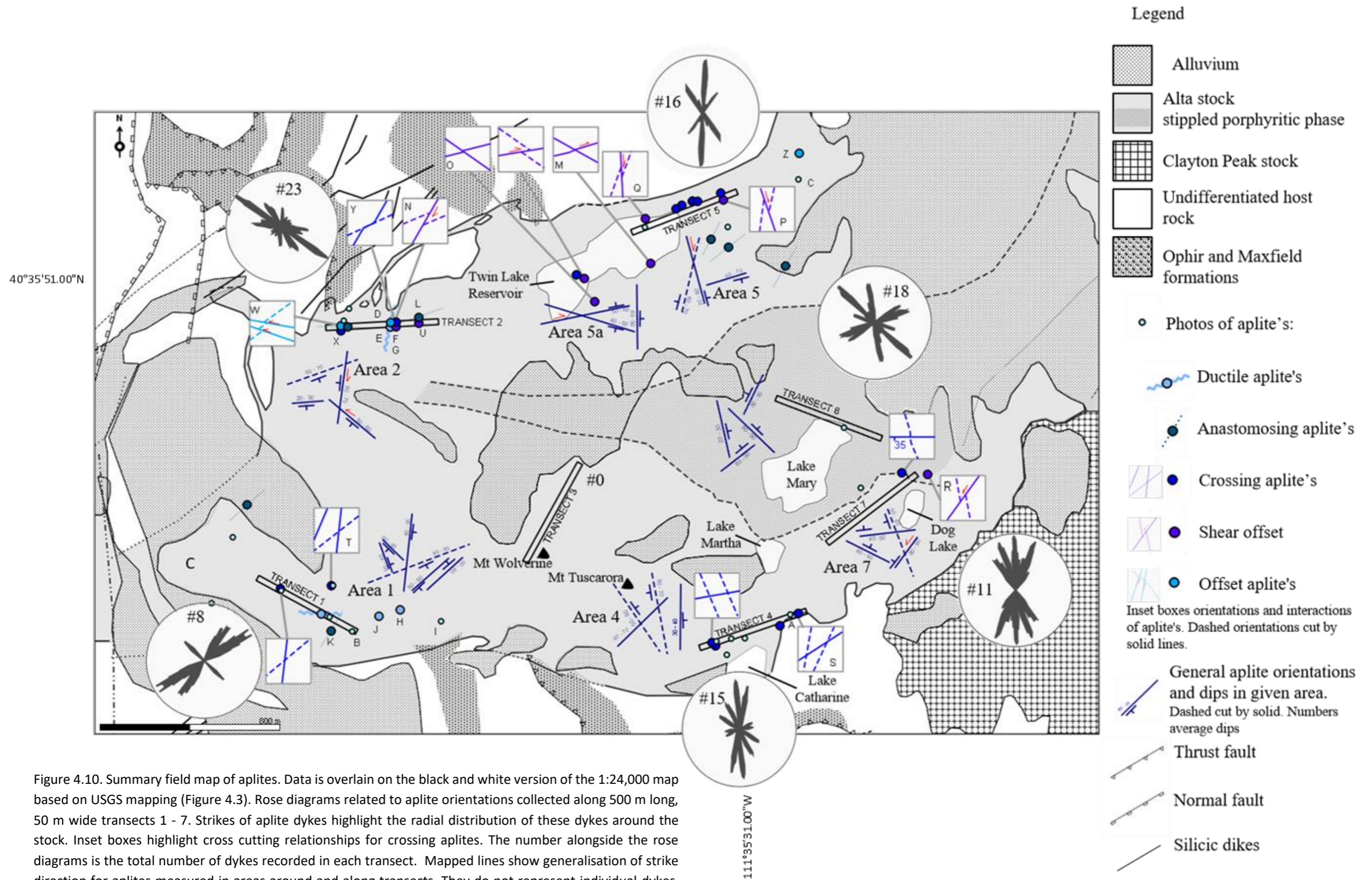


Figure 4.10. Summary field map of aplites. Data is overlain on the black and white version of the 1:24,000 map based on USGS mapping (Figure 4.3). Rose diagrams related to aplite orientations collected along 500 m long, 50 m wide transects 1 - 7. Strikes of aplite dykes highlight the radial distribution of these dykes around the stock. Inset boxes highlight cross cutting relationships for crossing aplites. The number alongside the rose diagrams is the total number of dykes recorded in each transect. Mapped lines show generalisation of strike direction for aplites measured in areas around and along transects. They do not represent individual dykes. Cross-cut dykes are shown by dashed lines. Letters refer to photo locations given in Figure 4.11.



Figure 4.11. Photos of aplites. Photos M – Z following page. (A & B) examples of fine aplites, (C & D) examples of pegmatitic textures in wider aplite dykes, (E – J) examples of deformed aplites, (K – L) anastomosing networks of aplite dykes, (M – R) conjugate sets of aplite dykes, (S – T) examples of cross-cutting aplite dykes, (U – X) Offset aplite dykes, and (Y – Z) aplite dykes cutting enclaves. Note, NE-SW white lines in J are surface marks due to winter walking in crampons.

4.3.3. Mineralised and Non-Mineralised Fractures and Veins

Up to seven mineralized (mineralized coating on open fracture surfaces) or non-mineralized fracture sets occur within a single outcrop (Figure 4.14). Typically, two to three of the fracture sets are well defined and are commonly near-to-orthogonal, forming rectangular (Figures 4.14 L1 – L6) or rhombus (Figure 4.14 L7) sectional geometries. Mineralised fractures pre-date the non-mineralised fractures.

Veins (infilled) contain assemblages of hornblende, epidote, quartz, K-feldspar, pyrite, sericite and chlorite (John, 1991). Veins typically show minimal fill (>0.5 mm), except for quartz veins which may be up to 5 mm wide. Based on outcrop measurements the dominant strike of mineralized fractures across the stock is NE-SW (Figure 4.12).

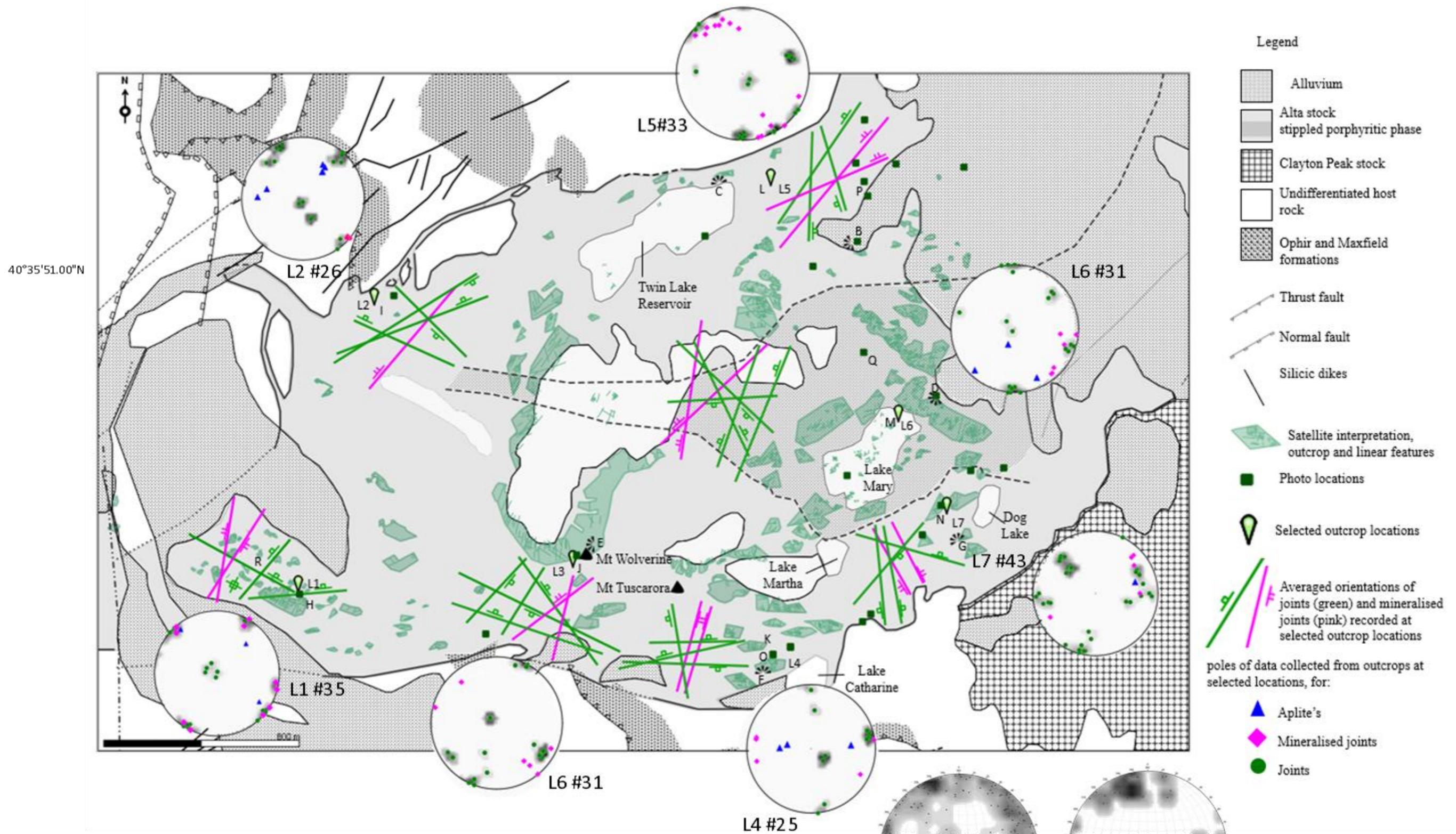


Figure 4.12. Summary field map of joint data. Overlaid on the on a black and white version of the 1:24,000 map based on USGS mapping (Figure 4.3). Stereonets of fracture orientation's collected at selected locations L1 – L7. Mapped lines show generalisation of strike direction for fractures recorded at selected outcrops. They do not represent individual joint traces. Letters refer to photo locations given in Figures 4.13 & 4.14. Stereonets (lower hemisphere, equal area) of all joints and mineralised joints recorded across the stock, highlighting the dominant NE-SW trend of mineralized fractures (pink diamonds). Stereonets can be compared with data collected by Wilson, 1961 and John,1991 Figures 4.3 & 4.4 p.140 – 141.

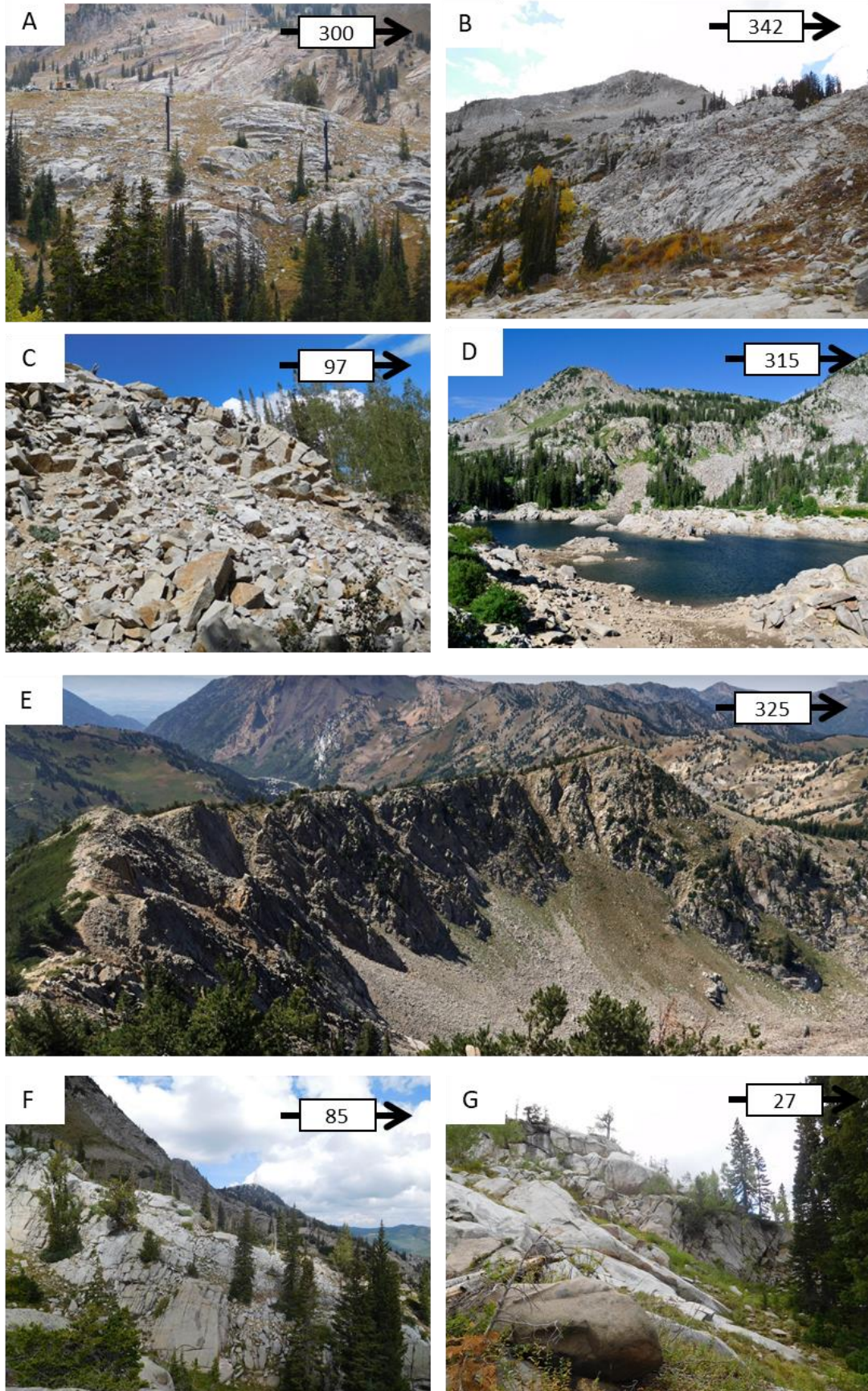


Figure 4.13. Photos of joints. Locations marked on Figure 4.12. Gentle curvature of joint strikes over distance can be observed in photos B, D and F. Orientation of photo is given.

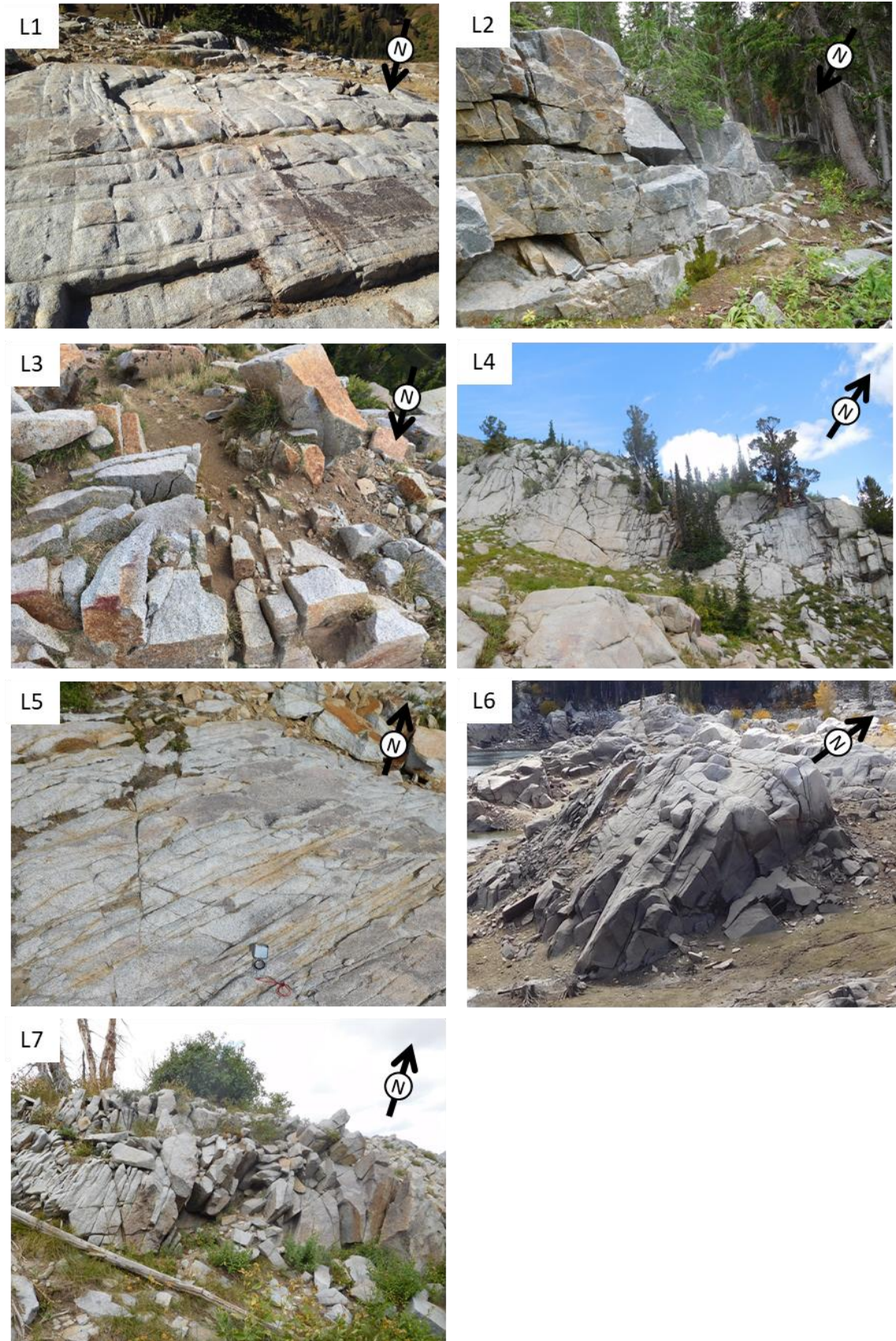


Figure 4.14. Photos of selected outcrops. Fracture orientations and topological analysis were completed at these locations for comparison to numerical models. Locations marked on Figure 4.12 L1 – H, L2 – I, L3 – J, L4 – K, L5 – L, L6 – M and L7 – N.

Fractures are typically continuous along strike for several tens of meters, constrained by exposure. In some cases, strikes gently curve, which can be observed where outcrop extents are greater than 10 m. Interpretation of linear features of aerial photographs (Figure 4.15) suggest fracture trends may extend for kilometres. Several lineament orientations are clearly distinguishable on aerial photographs these include NE, NW and ENE trends (Figure 4.15). The relative importance of these orientations varies across the stock. To the west a NE-SW orientation dominates and to the east two additional orientations E-W and NNE-SSW orientations are also apparent (Figure 4.15). Between 3 to 5 lineament trends of varying orientation and spacing are identified in selected locations (Figure 4.16).

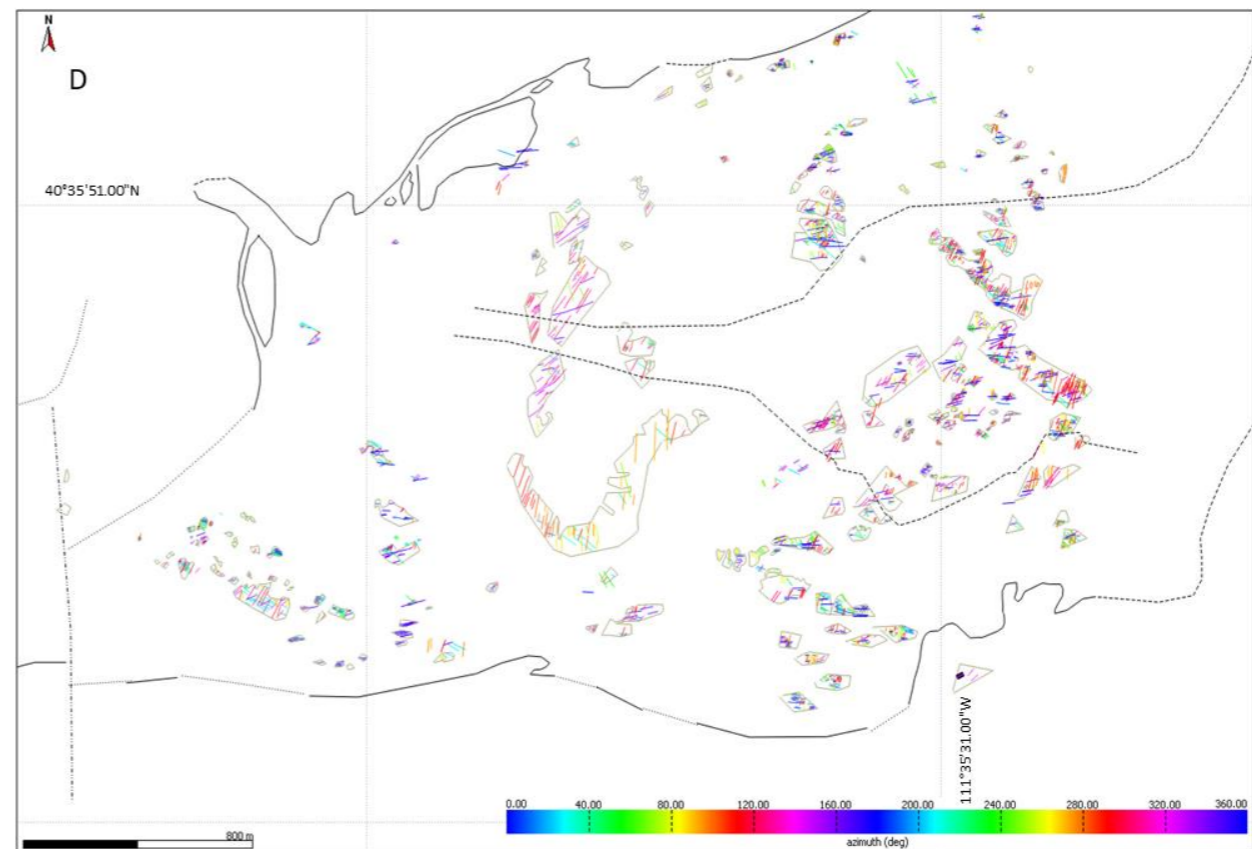
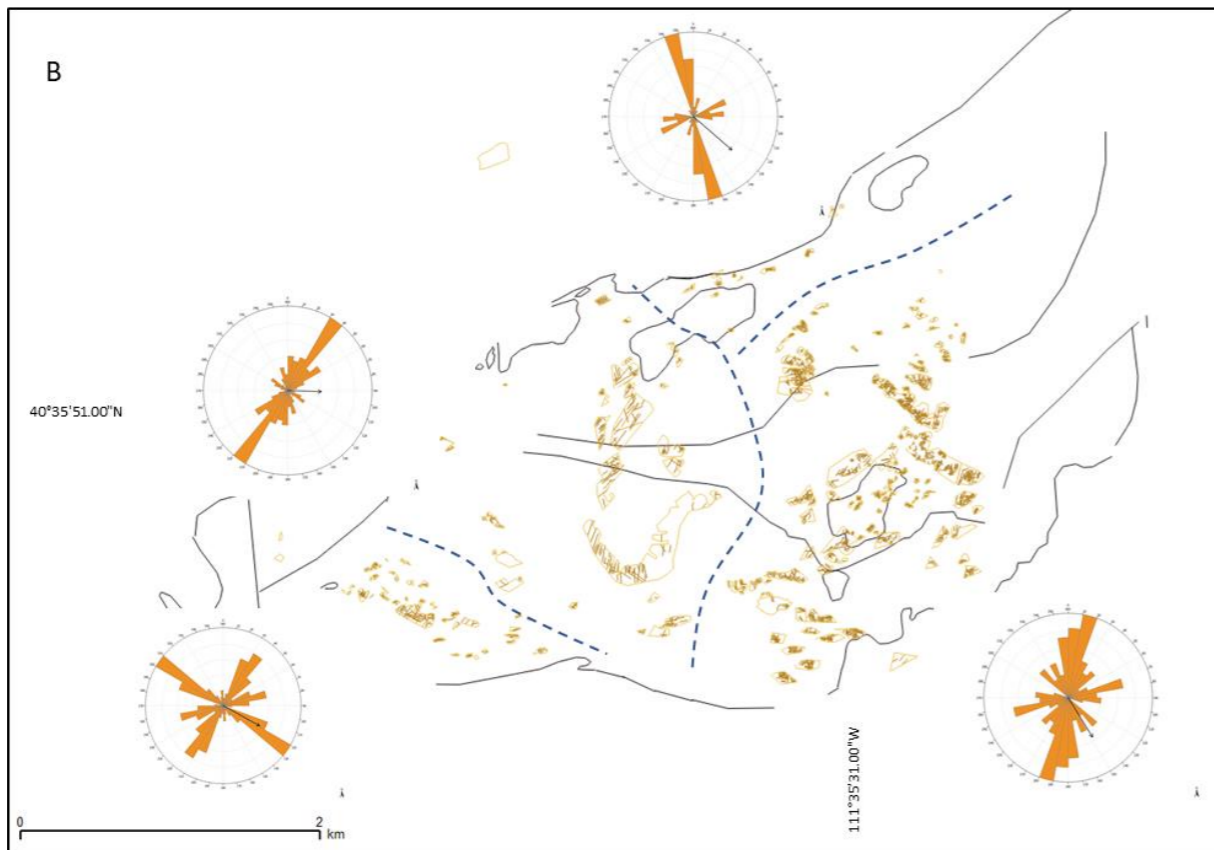
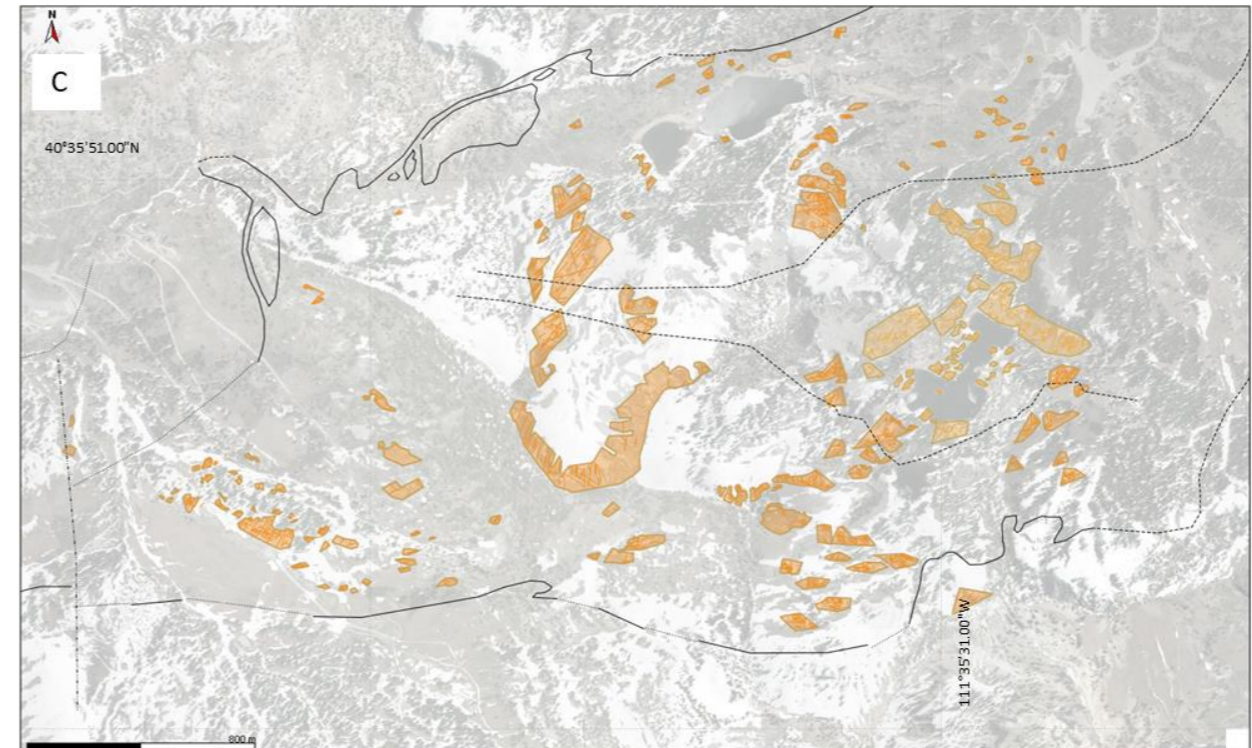
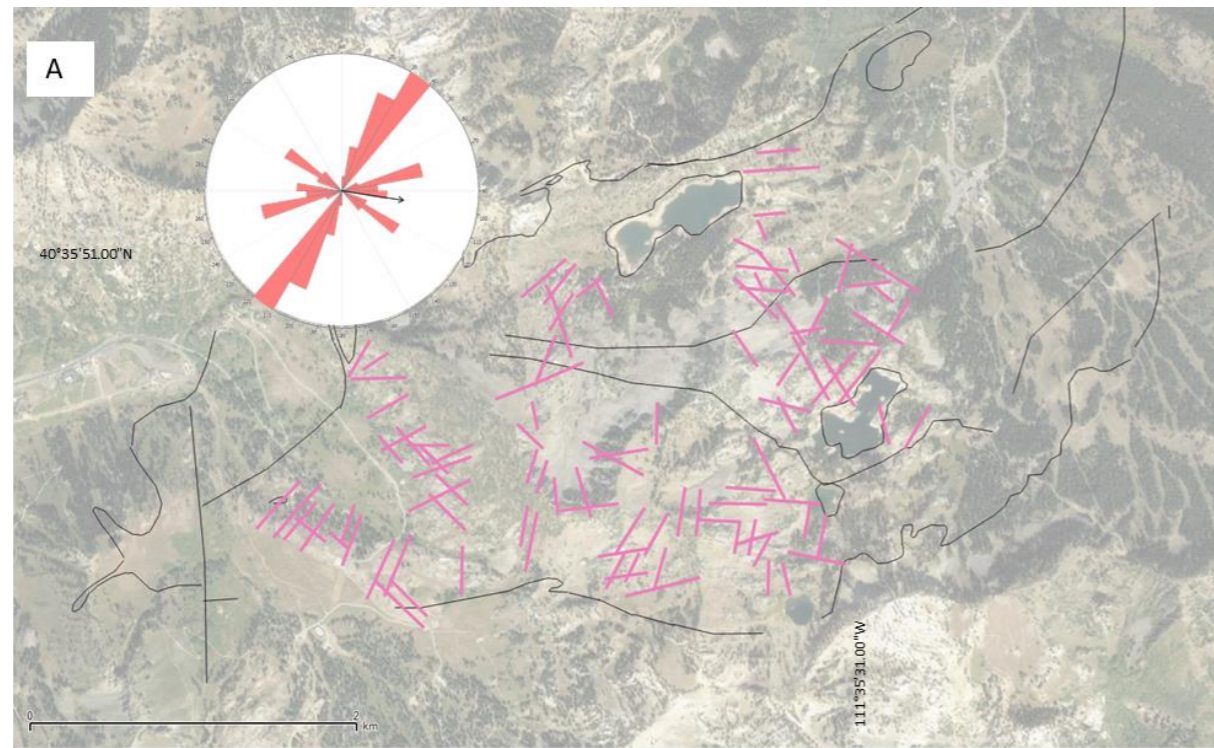


Figure 4.15. Interpretation of lineaments on satellite image at a scale of (A) 1:10,000 and (B) 1:1000. For the 1:1000 scale, interpretation is also overlain on the satellite image (C) and coloured mapped for azimuth (D). Satellite images used HRO 2012 (12.5 cm) and HRO 2006 (25 cm) available from <https://raster.utah.gov>

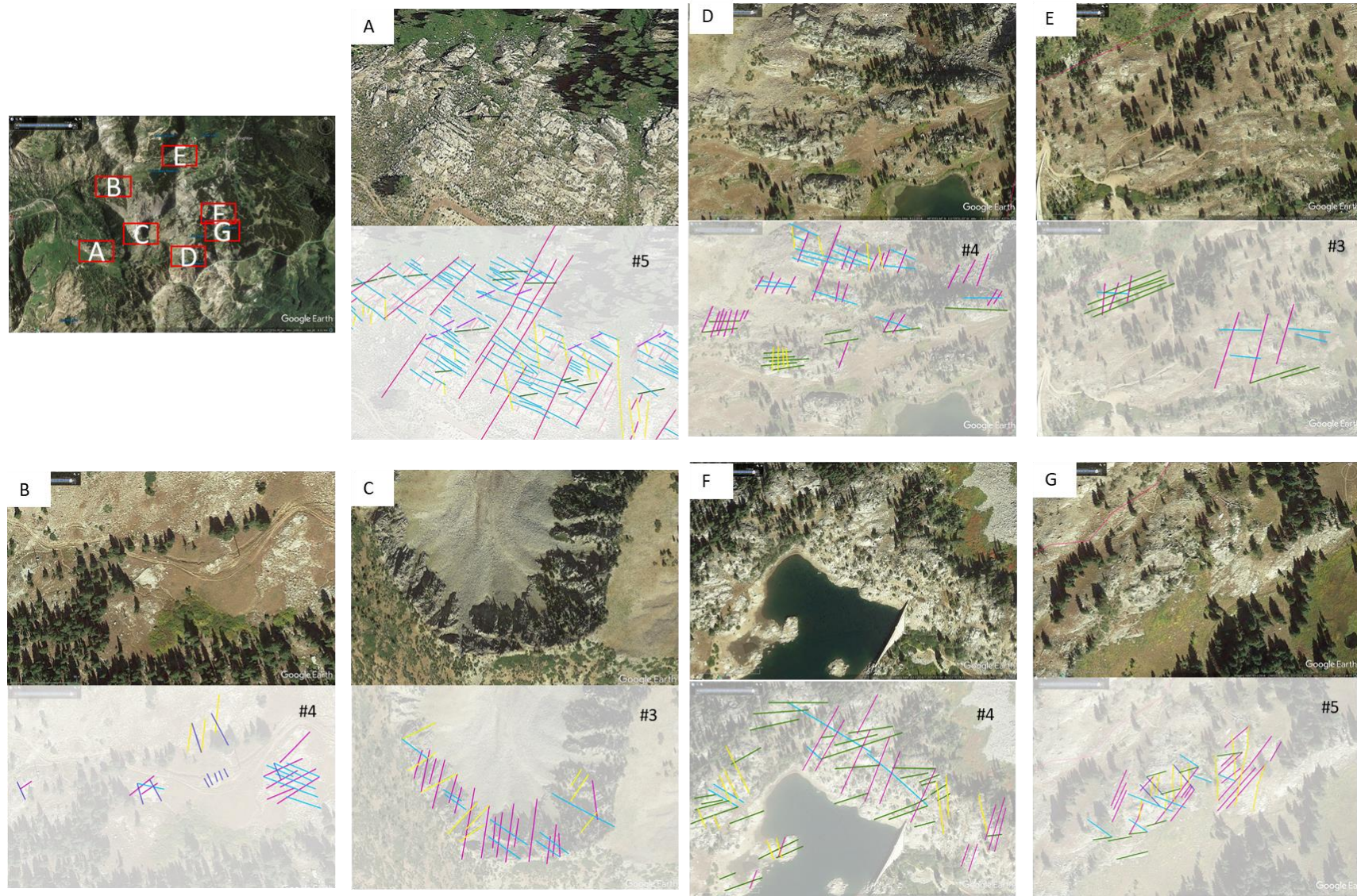
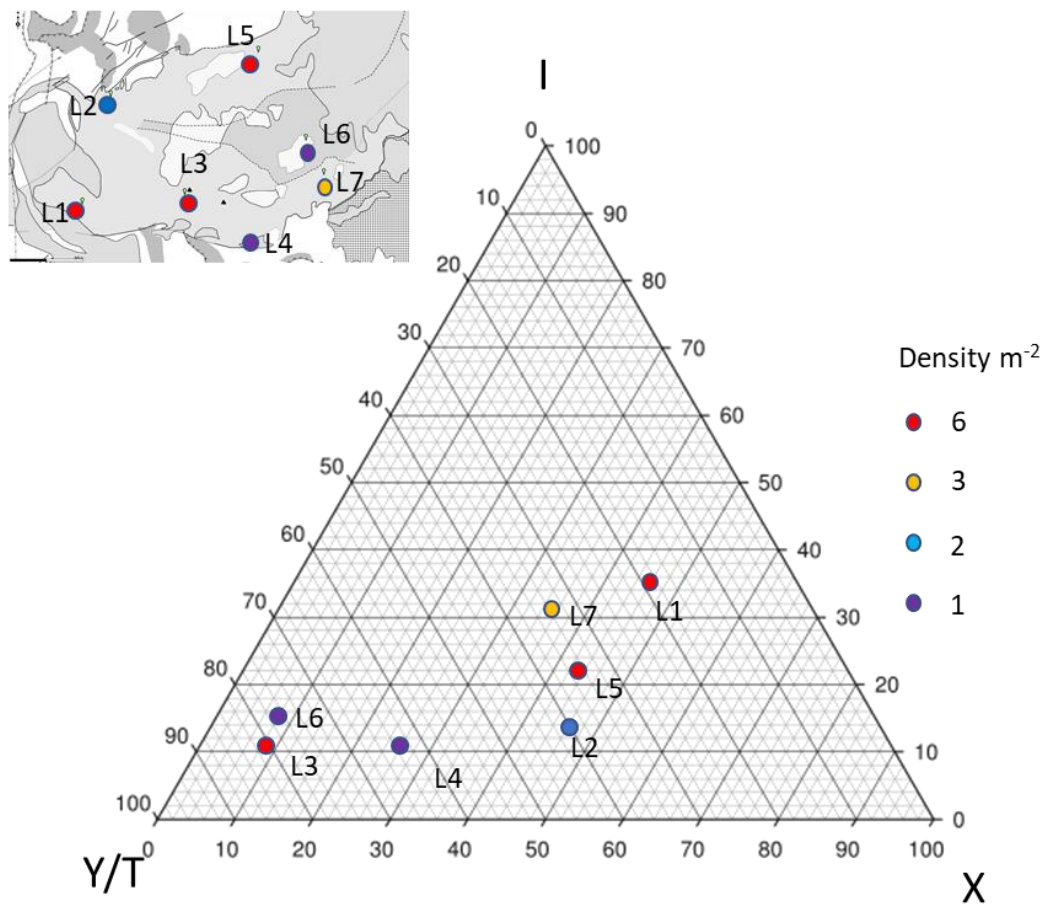


Figure 4.16. Interpretation of lineaments on aerial photos at selected locations A – G (shown on inset). Three to five lineament sets defined by orientations can be observed at each location. Colours identify different orientation sets at each location, colours are not correlated for the different locations.

The spacing between parallel joint sets varies from ~20 cm to > 1 m. Fracture intensity varies between outcrops and domains where increased fracturing is evident. This is particularly notable in Figure 4.13 F where domains of highly fractured rock are separated by domains of less fractured rock (highly fractured domains are typically 5 - 10 m wide). Measured density (P_{20} number of fractures per unit area) values vary between selected locations (range 1 – 6 m^{-2}). Mean trace length is inversely proportional to the density; increasing in outcrops with lower density (Figure 4.17). Density values do not show a clear correlation to the spatial distribution (e.g., distance from margin, paleo-depth or relationship to porphyritic and non-porphyritic phases) of selected outcrops across the stock (Figure 4.17).



	L1	L2	L3	L4	L5	L6	L7
scan line radius (m)	1	1	0.5	1	1	1	1
density p_{20} (m^{-2})	6	2	6	1	6	1	3
mean trace length (m)	1	3	2	5	2	9	2

Figure 4.17. Topology plot based on data collected from circular scan lines. Locations colour mapped based on fracture density. Density calculated after Zeeb, 2013.

Fracture surfaces are smooth to slightly rough and no fractographic markings (surface markings, see literature review section 2.2.1 p.21 for a description of these features) where noted. Although minor (<2 cm) offset of an aplite dyke was noted on mineralised fractures at one outcrop (Figure 4.11 X), no discernible strike separation was observed on other mineralised fractures. Fracture sets are observed to stop abruptly or offset against each other. Abutting relationships are not consistent between sets. Circular scan line analysis (Figure 4.18) suggests that cross cutting joints (X-nodes) are more common in outcrops closer to the margin and abutting (T-nodes) are relatively more abundant in the central outcrops (L3 & L6) (Appendix B Table B4-2, p.333).

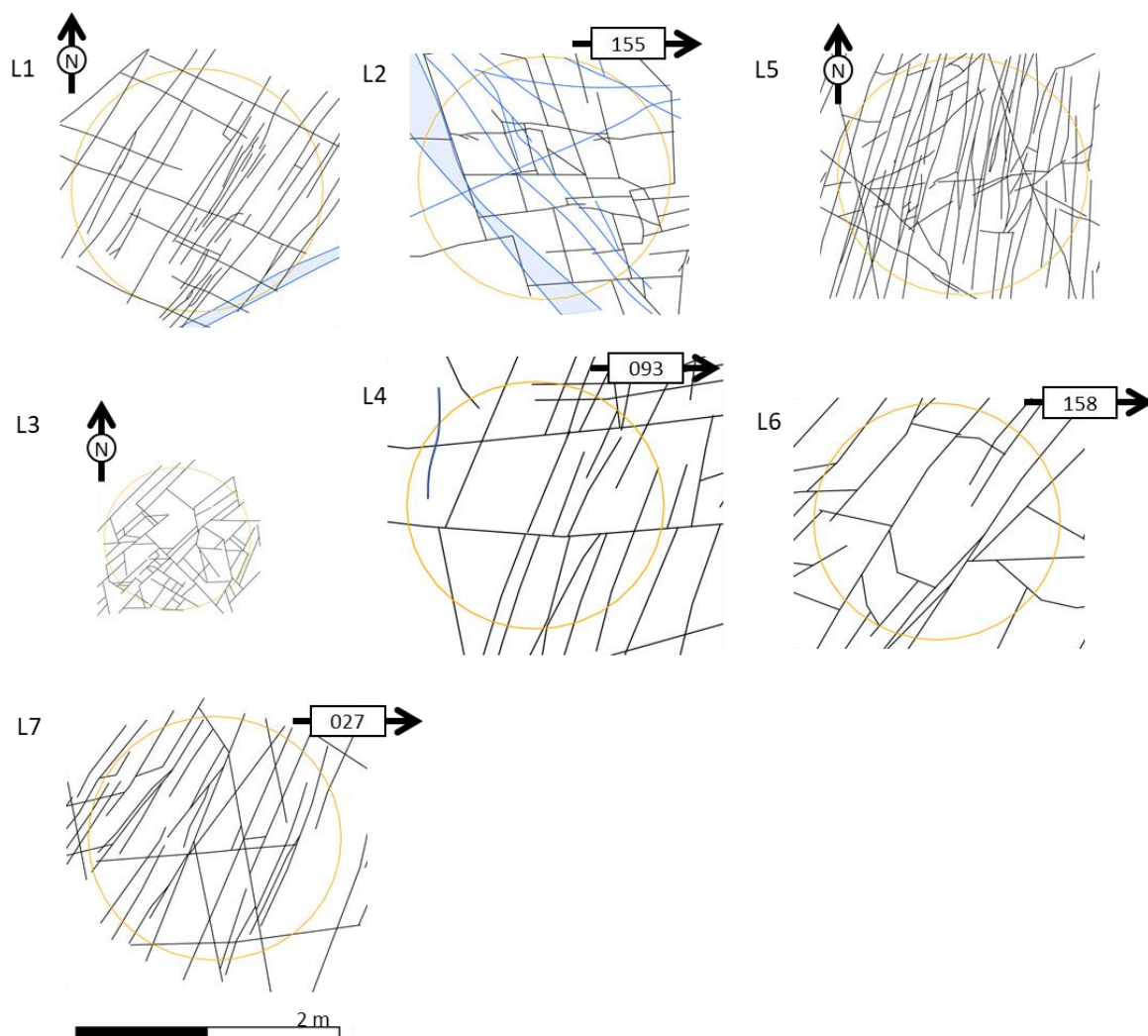


Figure 4.18. Circular scan line analysis and topological analysis. Circular scan lines in orange, diameter 2 m for locations L1, L2, L4 – L7 and 1 m for location L3. Locations L1, L3, L5 recorded on near flat surfaces and locations L2, L4, L6 & L7 recorded on near vertical outcrops. Locations relate to photos of outcrop locations in Figure 4.12, L1 – H, L2 – I, L3 – J, L4 – K, L5 – L, L6 – M and L7 – N (appendix B Table B4-2 p.333).

4.3.4. Significance of the Structural Data

The planar structures of the stock are interpreted as primary flow structures resulting from deformation of the host during solidification of the stock. Although weakly developed the dominant south-westerly plunge of hornblende mineral alignment is interpreted by Calkins et al. (1943) and Wilson (1961) to indicate up-to-the-east emplacement of magma at moderate to low angles. Rotation of the stock accounting for Basin and Range rotation (20° down-to-the-east rotation) would return the average plunge (21°) of these lineations to nearly horizontal. The slight variation in lineation orientations within the central porphyritic phase may be evidence of the variation of flow direction or related to distance from the margin.

The earliest evidence of fracturing in the Alta stock is recorded by aplite dykes, which are cut by both mineralized and non-mineralized fractures. Aplites show a range of styles that probably relate to multiple events in the cooling history. Some aplites formed earlier than the inner porphyritic phase, which can be observed to cut aplite dykes along its southern margin (Wilson, 1961). Aplites that display evidence of emplacement into a deforming host are found in the western margin of the stock. This could be representative of dyke formation at or near to the brittle-viscous transition or related to the fact that exposures to the west represent the greatest paleodepths of the stock (~6.3 km; fluid inclusion data, John, 1991). Straight walled aplite dykes record both pure opening and opening with minor shear. Shear movement on the aplites pre-dates the formation of joint sets. The shear sense on conjugate aplites is compatible with the shortening direction in some cases interesting the acute angle and in other cases the obtuse angle (appendix B Table B4-1 p.332). Where the shortening direction intersects the obtuse angle the offset may be interpreted as : (1) apparent due to opening of existing conjugate fractures; the result of (2) fracture rotation by distributed pure-shear from combined contraction and extensional deformation, unidirectional contraction or unidirectional extension; or, (3) the orthogonal switching of principal-stress directions (Figure 4.19).

Mapping identifies similar joint and vein orientations to those identified by Wilson, 1961 and John, 1989, 1991 (Figure 4.3 & 4.4). One significant difference in the orientation data collected is that no horizontal (<10° dip) fracture sets were recorded by Wilson, 1961 and John, 1989, 1991. Some of the ~horizontal fracture sets formed early as indicted by occasional aplite intrusion, however no mineralisation was observed in the horizontal joints.

No discernible strike separation was observed on mineralized or non-mineralized fractures at all but one outcrop (close to the northern margin) within the stock. These fractures are therefore interpreted to indicate predominantly opening mode failure. Fluid inclusion evidence suggests that mineralised fractures are likely to have formed during cooling of the stock and precipitated from

dominantly magmatically derived hydrothermal fluids (John, 1989). The strong NE trend of veins corresponds to the estimated NW-SE extensional paleostress direction at the time of emplacement (Ren et al., 1989; Kowallis et al., 1995; John, 1991).

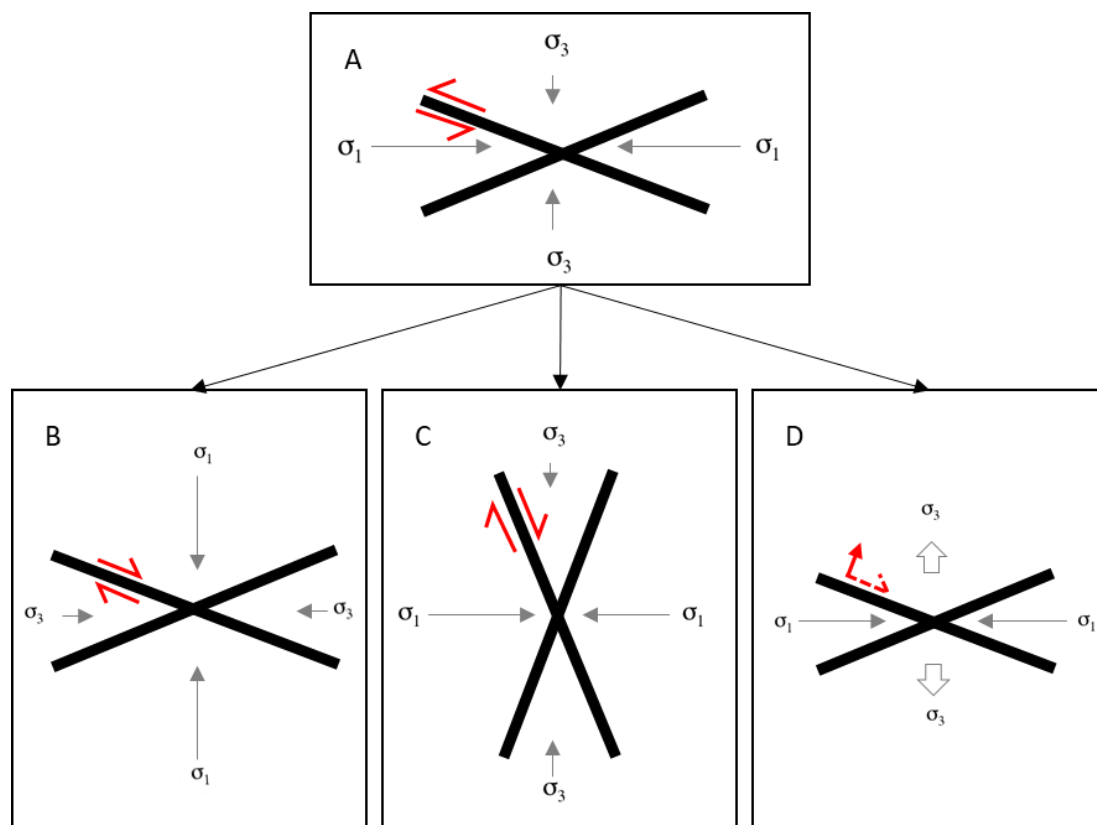


Figure 4.19. Kinematics that may result shear offset on conjugate dykes comparable with the shortening direction in the obtuse angle. (A) Initial shear fracture formation with shortening direction in towards the acute angle (B) orthogonal rotation of stress field after formation (C) continued shortening and fault rotation via distributed pure-shear deformation by combined contractional and extensional deformation, distributed unidirectional extension or distributed unidirectional contraction (after Yin and Taylor, 2011) and (D) extension on shear fractures.

There is no obvious correlation between abundance of joints and veins with distance from the margin or paleodepth across the stock (this study and John, 1991). The total number of fractures per metre values given by John, 1991 are < 1 to >20 fractures per metre. Density of fractures in the central porphyritic intrusion recorded at Location 6, in this study, gives a density of 1 m^{-2} , lower than the average density value of 4 m^{-2} for outcrops recorded in the outer non-porphyritic phase. There is however significant variation in the density values in the non-porphyritic phase (range $1 - 6 \text{ m}^{-2}$). As only one density measurement was made in the porphyritic phase there is not enough data to confirm if there is a difference in the relative density of fracturing between the two phases as suggested by Wilson (1961).

4.4. Numerical Modelling

4.4.1. Overview

Following the modelling approach developed in chapter 3, conductive cooling models were setup using COMSOL Multiphysics® v5.3. The stock is modelled as a three-dimensional hot solid within a colder homogenous elastic domain (cf. Knapp, 1978; Gerla, 1988; Bergbauer, 1998; Žák et al., 2006). The model predicts the orientations and magnitudes of principal stresses (compression positive) related to cooling, gravitational and regional tectonic loads. Uncertainty in the initial boundary conditions (initial stress field, stock geometry and depth of emplacement) was assessed by running ten models with varying parameters (Table 4.1). The Griffith-Murrell failure criterion (Murrell, 1963) is used in order to account for the effects of true triaxial stress (Descamps and Tshibangu, 2007). The models assume a temperature-dependent tensile strength. The variation of the tensile strength of the stock with temperature was estimated from experimental data for granite (Heuze, 1983). Sensitivity tests were completed for run time and grid resolution. See chapter 3 (p.51 – 55) for additional details on the set up of the applied failure criterion.

Table 4.1. COMSOL® models run

Model number	Modelled geometry			Initial material and mechanical parameters		Initial temperature distribution		Initial stress field	
	Stock thickness (km)	Depth to top of stock (km)	Host rock	Material properties	Mechanical properties	Stock temperature (°C)	Host rock Geotherm (°C/km)	In situ stress gravity	In situ stress tectonic load *
A1	3	3.5	hr1	fix	Td	825	55	gr1	none
A2	1.5	3.5	hr1	fix	Td	825	55	gr1	none
A3	16.5	3.5	hr1	fix	Td	825	55	gr1	none
A4	3	5	hr1	fix	Td	825	55	gr1	none
A5	3	3.5	hr1	fix	Td	825	55	gr1	NE-100
A6	3	3.5	hr1	fix	Td	825	55	gr1	NE-40
A7	3	3.5	hr1	fix	Td	825	55	gr1	NW40
A8	3	3.5	hr1	fix	Td	825	55	gr1	NS-40
A9	3	3.5	hr1	fix	Td	825	55	gr1	EW-40
A10	3	3.5	hr1	fix	Td	825	55	gr1	NW-40

hr1 – host rock geometry 100 km² and 20 km thick
 Fix – fixed material properties as given in Table 4.3 p171
 Td – temperature dependant mechanical properties given in Table 4.4 p171
 gr1 – gravity
 * Values as applied in COSMOL®, convention tension positive.

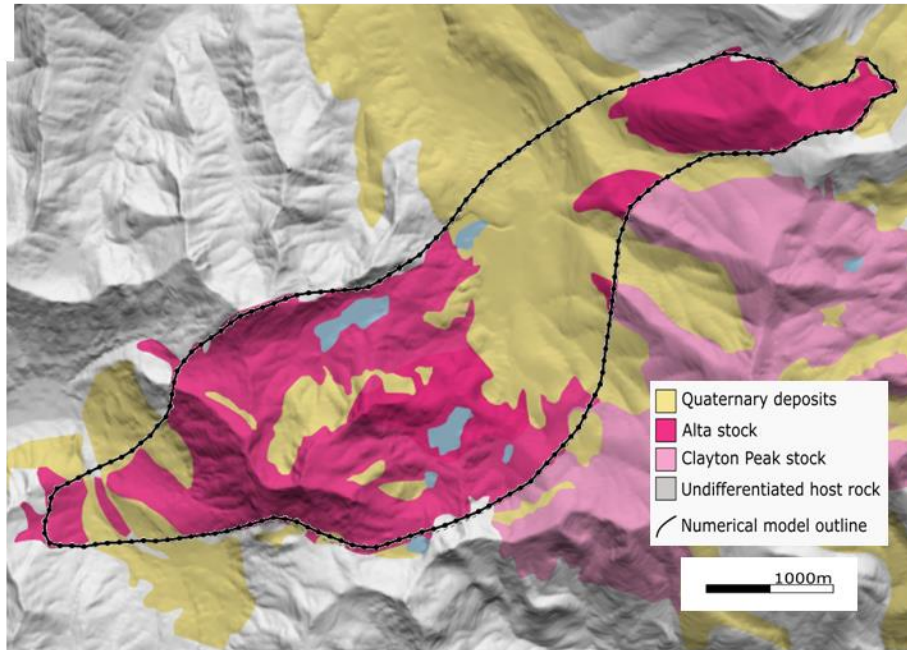
4.4.2. Modelling Geometry

The host rock modelling domain was defined by a uniform block with map area of 100 km² and thickness of 20 km, large enough so that the temperature at the model boundaries did not vary. The stock's geometry was simplified by sampling external mapped boundaries of USGS map GQ-534 at 100 m intervals (Figure 4.20) and extended into three-dimensions using a cylindrical projection. The geometry was rotated to remove rotation related to later Cenozoic faulting so the top and base of the stock were modelled horizontal surfaces (Figure 4.20). Based on field evidence a thickness of 3 km and a depth of 3.5 km to the top was applied to the stock (models A1, A5 – 10). Sensitivity tests for stock thickness (models A2 & A3, Figure 4.21) and depth (model A4) were run (Table 4.1). Comments for the reasons for selection of geometries for sensitivity testing are given in Table 4.2.

Table 4.2. Reasoning for Variations in Modelled Geometry

Vertical thickness		
Modelled parameter	Comments on reason for section	Model number(s)
1.5 km	Minimum intrusion thickness based on outcrop and mine workings (Cook and Bowman, 1994). Note assuming 20° dip towards the East caused by Basin and Range rotation this form does not geometrically work with present day topography, unless stock has an irregular upper surface.	A2
3 km	Equivalent to the thickness required to cover range of paleodepths (6.3 km in West and 3.7 km in East) recorded from fluid inclusion data (John, 1991) including the 0.3 km additional vertical extent beyond present erosional level (Cook and Bowman, 1994).	A1, A5 to A10
~ infinitely thick	maximum thickness extended to base of model.	A3
Depth of emplacement		
Modelled parameter	Comments on reason for section	Model number(s)
3.5 km	Minimum estimate based on estimates taken from fluid inclusion studies.	All except A4
5 km	Maximum estimate based on stratigraphic reconstruction (Wilson, 1978) and used by Cook and Bowman, 1994 for numerical model.	A4

A



B

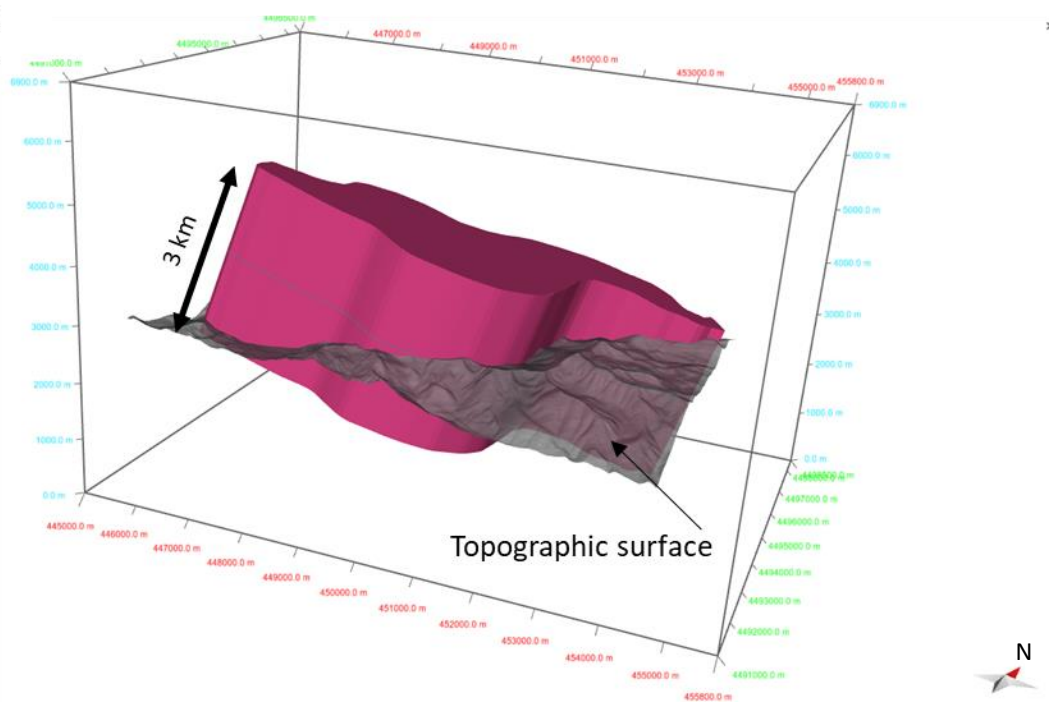


Figure 4.20 Modelled stock geometry. (A) geology map of the Alta stock overlain on topographic surface showing simplified boundary lines for intrusion geometry sampled at 100m (B) 3D projection of stock geometry (pink volume) intersecting present day topographic surface, thickness of stock shown is 3 km.

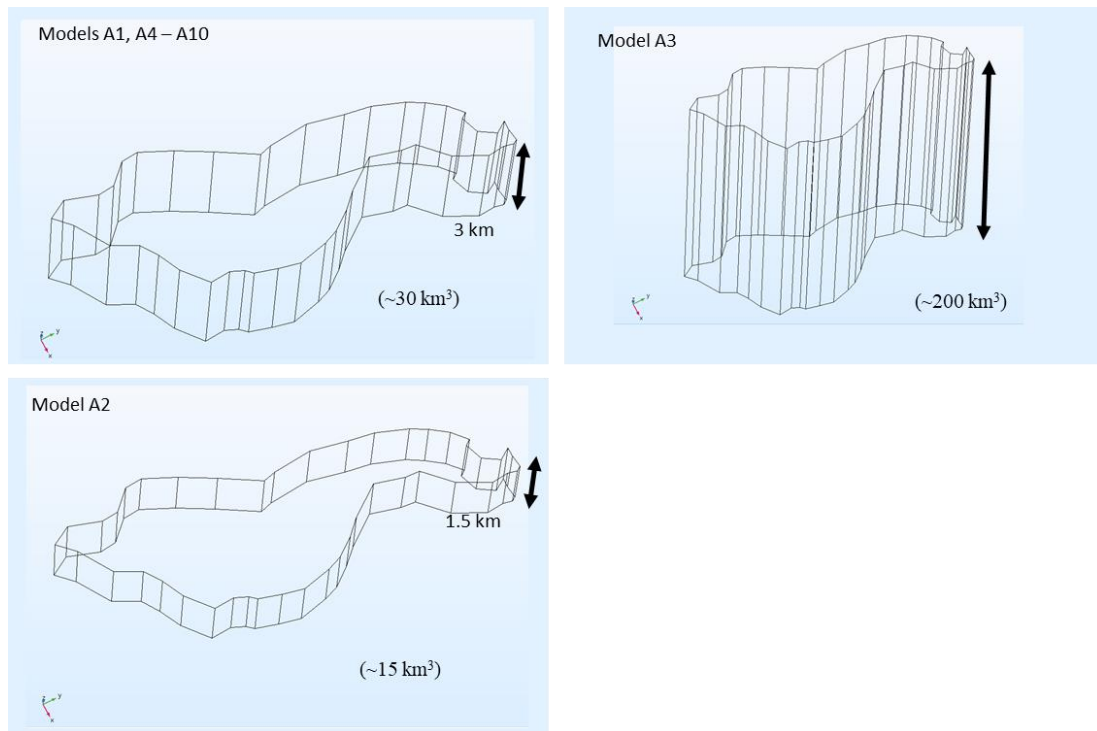


Figure 4.21. 3D models of stock for numerical modelling showing variations in thickness. Basin and Range rotation is removed so that the top and base of the stock are modelled as horizontal surfaces.

4.4.3. Material and Mechanical Properties

Material properties, density, specific heat and conductivity for the stock are taken from Cook and Bowman (1994) and Young's Modulus, Poisson's ratio and the coefficient of thermal expansion are assumed from appropriate values (after Bergbauer and Martel, 1999 given in Table 4.3). The host rock is modelled as a homogenous isotropic unit. Density, specific heat and conductivity are taken from an average of units estimated by Cook and Bowman (1994). The boundary defining the stock separates it from the material properties of the host rock domain. The tensile strength is defined as temperature dependent after Heuze (1983) Table 4.4.

Table 4.3. Material Properties

	Unit	Stock	Host rock
Density	kg/m ³		2700 *
Heat capacity	J/(kg.K)	1450 *	1025 *
Thermal conductivity	W/(m.K)	1.8 *	2.3 *
Coefficient of thermal expansion	1/K		8e-6 †
Young's modulus	Pa		3.04e10 †
Poisson's ratio	-		0.25 †

* After Cook and Bowman, 1994. 1150 J/(kg.K)+300 J/(kg.K) accounting for latent heat of crystallisation
For host rock the average from units 1-4 is taken
† After Bergbauer and Martel, 1999

Table 4.4. Mechanical Properties

	Temperature dependent *	
	Temperature °C	Tensile strength MPa
Tensile strength	0	14
	200	13
	400	11
	600	5
	800	2
	1100	0

* Temperature dependent tensile strength values based on experiments of Heuze (1984). From experiments on Westerly and Charcoal granites over temperature from 20 – 1100 °C at low strain rates of 10⁻⁶/sec.

4.4.4. Gravitational and Tectonic Loads

A gravitational body load is applied to both the stock and host rock domains. The influence of a regional tectonic stress was accounted for in models A5 – A10. Tectonic stress is added as a boundary condition by adding a uniaxial load to the stress tensor. Tectonic load can be modelled by either lowering the minimum horizontal stress (i.e., decreasing the NW-SE horizontal stress, model A7) or increasing the maximum horizontal stress values (i.e., increasing the NE-SW horizontal stress, models A5 and A6). Models A5 and A7 are considered to be endmember models that allow for overall NW-SE extension. The uniaxial load values added to the stress tensor are based on the given horizontal gravitational load, that result in the (1) maximum horizontal stress becoming horizontal (model A5), (2) the minimum horizontal stress equal to zero (model A7) and (3) an intermediate compressive load (models A6, A8 – A10). The influence of the orientation of the tectonic load based on increasing the maximum horizontal stress is tested for comparison (models A6, A8 – A10).

4.4.5. Initial Temperature Distributions

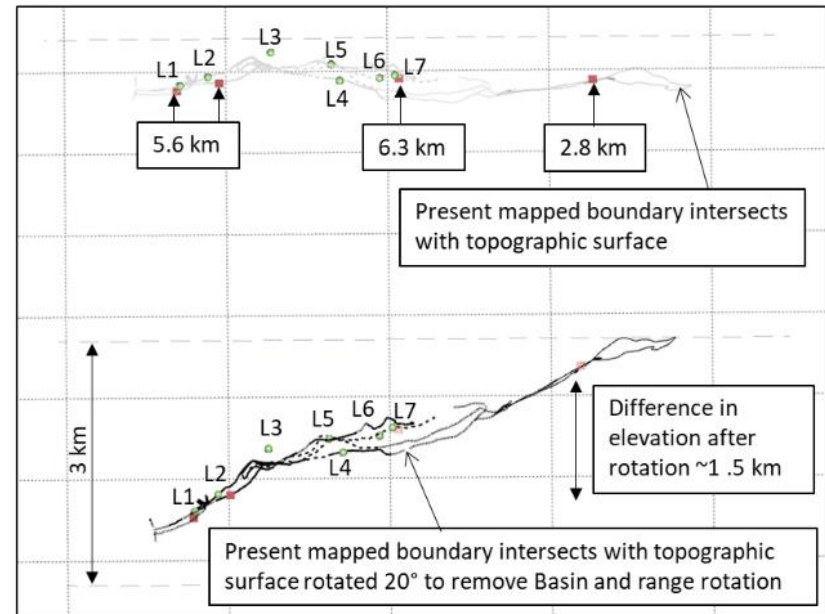
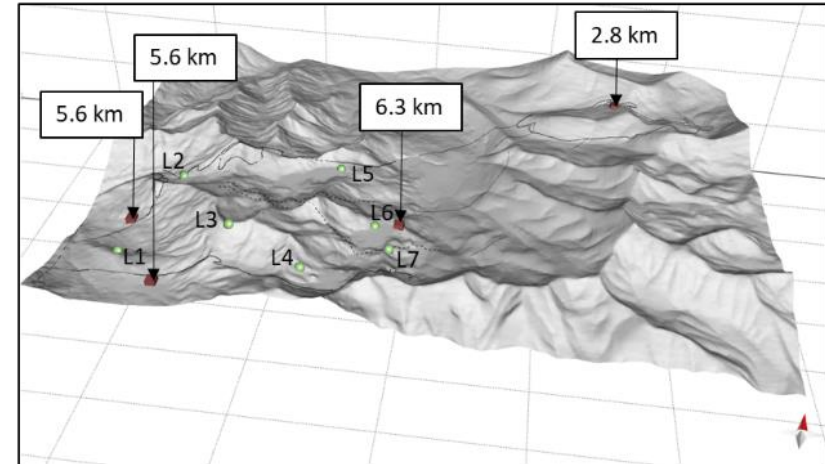
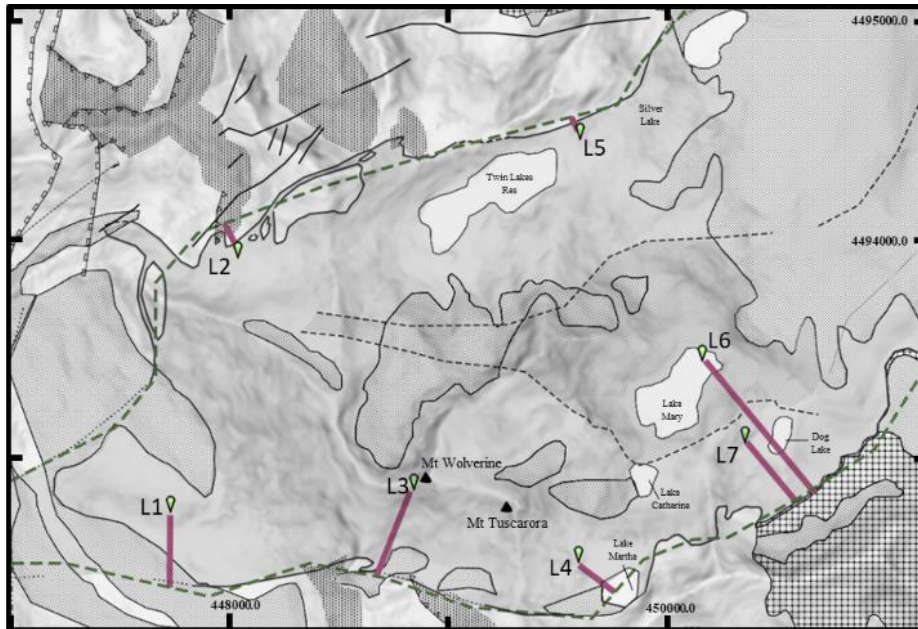
An initial uniform temperature of 825 °C was applied. This temperature is based on results of zirconium geothermometry giving a maximum temperature estimate for the stock (Cook and Bowman, 1994). This temperature is slightly higher than estimates of the solidus temperature for Alta (725 – 770 °C John, 1991; 750 °C minimum temperature Wilson, 1961). Within the host rock a geothermal gradient of 55 °C/km was used to account for the probability of elevated host rock temperatures as a result of emplacement of the nearby intrusions (after Cook and Bowman, 1994). The predicted isotherms and resulting thermal stress distributions assume that the stock was instantaneously emplaced.

4.4.6. Grid Size and Modelling Time Steps

A maximum meshed tetrahedral element size with an edge length of 400 m was used within the stock, increasing to 2 km at the boundaries of the host rock domain. The models were run for a million years using a time step of 10 years. These parameters were selected based on repeatability of modelling results and run time.

4.4.7. Model Outputs

The cooling process was considered to be complete when the temperature within the stock reaches 100°C of the applied geotherm at the equivalent depth and the thermal distribution lacked any abrupt changes (Žák et al., 2006). Outputs from the model include the magnitude and orientation of the principal stresses, the strain energy and, failure mode at given timesteps. Data from selected locations (Figure 4.22) are extracted and plotted. The calculated eigenvectors (given in terms of the direction cosines) exported from COMSOL® were converted to plunge and plunge directions of the principal axes for comparison with field data plotted on stereonet (Appendix C workflow C5-4 p.338). Although calculated assuming engineering standard (tension positive), model outputs for the magnitudes of principal stresses are presented in the geological convention of compression positive. Results presented as 2D images are taken from horizontal slice at a depth of 5 km for models A1, A3, A5 – A10, a depth of 4.25 km for model A2 and 6.5 km for model A4, the central elevation in the stock based on the modelled depth.



Location	D_WGS_1984 UTM Zone12N [km]			Perpendicular distance to nearest margin [m]	Confidence in boundary position
	x	y	z		
1	447.7292	4492.7814	2.8	330	Poor \pm 90
2	448.0393	4493.9514	3	130	OK \pm 70
3	448.8498	4492.8836	3.3	420	OK \pm 70
4	449.6075	4492.5498	3.1	210	Poor \pm 90
5	449.61500	4494.4975	2.9	70	OK \pm 70
6	450.1773	4492.8836	2.9	790	good \pm 50
7	450.3743	4493.1010	2.9	360	good \pm 50

Figure 4.22. Field locations. Basin and Range rotation is removed giving paleodepth for extraction of points from numerical models for comparison with field data.

4.5. Numerical Modelling Results

4.5.1. Cooling History

Heat conduction results in initial cooling of the stock and heating of the surrounding host rock which then cools (Figures 4.24, 4.25 and Appendix B, Figure B4-2, p.335). Cooling at the centre of the stock is prolonged compared to that of the margins. The rate of cooling is inversely proportional to the distance from the margins resulting in a heterogeneous thermal distribution, which is hotter in the centre than at the margins. When applying an initial homogeneous temperature of 825 °C, a geothermal gradient of 55 °C/km in a 3 km thick stock with top depth at 3.5 km (models A1, A5 to A8), the cooling process is complete 100,000 years after model initiation (Figure 4.24 A). The temperature in the host rock increases up to 2 km from the margin, reaching temperatures slightly higher than 600°C at the margins of the stock (Figures 4.24 & 4.25).

Stock thickness (models A2 & A3) and depth (A4) also influences the cooling rate. The thinner stock, model A2, cools faster and the cooling at the centre is completed 60,000 years after model initiation (Figure 4.23 and Appendix B, Figure B4-2, p.335). The thicker stock takes longer to cool, taking 1,000,000 years to cool to a similar temperature at a depth of 5 km as measured in model A1. Models of the same geometry but different depths (e.g., model A1 and model A4) take approximately similar times to cool. For Model A4 the cooling process is complete 100,000 years after model initiation, the overall temperature of the stock remains higher than for the shallow buried model A1 (Figure 4.23 and appendix B Figure B4-2 p.335).

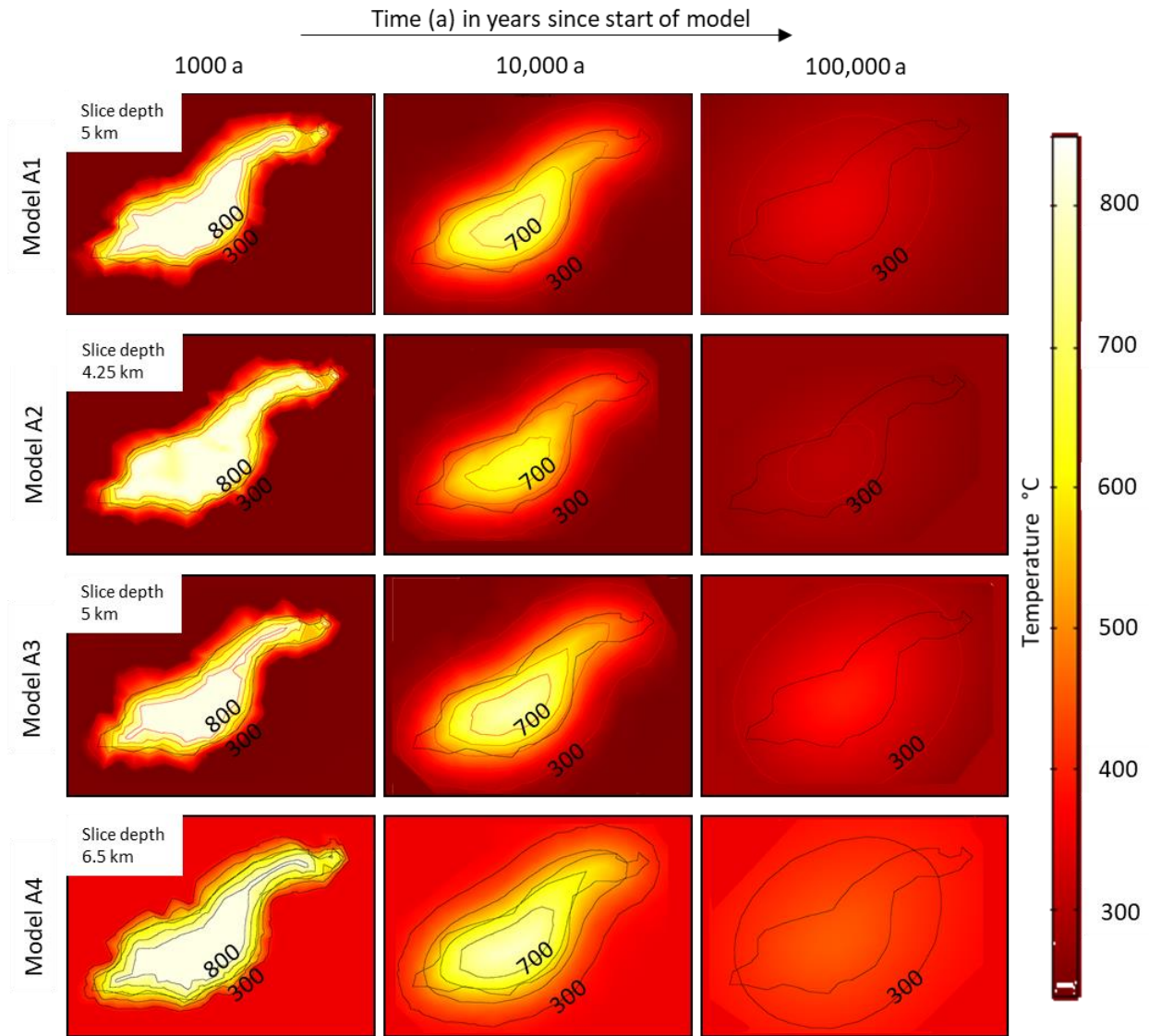


Figure 4.23. Thermal models for slices taken from models A1 – A4 at selected time steps (see Table 4.1 p.165 for description of models). The thermal history of model A1 is equivalent to the thermal histories of models A5 – A10. For models A1 and A3 a slice is cut at a depth of 5 km, for model A2 at a depth of 4.25 km and for model A4 at a depth of 6.5 km. The horizontal slice through the model is taken at the centre of the stock. Contours of temperature (°C) is shown for 100 °C intervals and key levels are labelled.

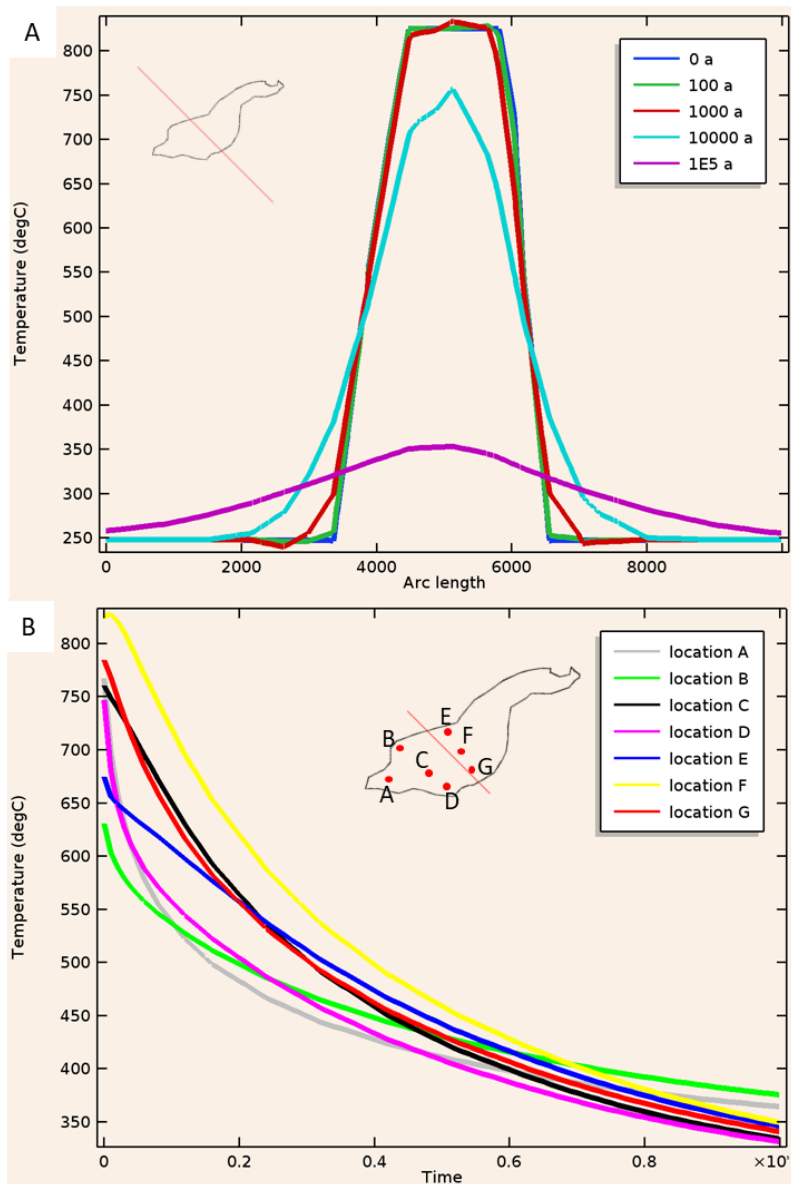


Figure 4.24. Thermal history of model A1. (A) a NE-SW line cut through the numerical model at a depth of 5km (as shown on inset) and (B) temperature plotted against time for selected points for model A1, refer to Figure 4.22 p.172 for depths of selected points. The cooling process is considered to be complete at 100,000a when the temperature within the stock reaches 100°C of the applied geotherm at the equivalent depth and lacked any abrupt changes. See appendix B Figure B4-1 p.334 for equivalent graphs for models A2 – A4.

4.5.2 Principal Stress Orientations

Orientations of the intermediate (green) and maximum principal stresses (blue), assuming compression positive, are presented in Figures 4.25 to 4.30 for selected time steps. The minimum principal stress (σ_3 not shown) is perpendicular to the plane fitted to the intermediate and maximum principal stresses (the $\sigma_1\sigma_2$ plane), this plane represents expected orientations of opening mode fractures. Orientations of the principal stresses are modified by the additional of a regional load (models A5 – A10).

Orientations related to thermal load only (models A1 – A4)

For model A1, a 3 km thick stock with top depth at 3.5 km, the $\sigma_1\sigma_2$ plane is initially randomly orientated. The maximum principal stress is vertical and intermediate principal stress horizontal. Upon cooling of the stock, the $\sigma_1\sigma_2$ plane aligns perpendicular to the margins of the stock. Centrally, orientations of the $\sigma_1\sigma_2$ plane are variable but preferentially parallel to the NE-SW long axis of the stock (Figure 4.25 A, > 100a). As cooling continues the orientation of the plane rotates so that it is parallel to the short axis of the stock (Figure 4.25 A, >10,000a), perpendicular to the stock margin. Within the host rock the $\sigma_1\sigma_2$ plane is initially orientated perpendicular to the margins and rotated to be parallel to the margins of the stock as the host rock cools after being heated (Figure 4.25 A). Over time the maximum and intermediate principal stresses switch in some places to become horizontal and vertical respectively. This switch is most prevalent at the margins and where the stock width is thin. Depth within the stock also influences the orientation of the plane (Figure 4.25 B) which is more variable in the early cooling history (Figure 4.25 B, < 1000a).

Stock thickness and depth influence the time at which the $\sigma_1\sigma_2$ plane aligns perpendicular to the margins (Figure 4.26). The area over which the maximum principal stress switches with the intermediate principal stress, becoming horizontal, increases for the thicker stock (model A3) and decreases in the thinner (model A2) and deeper buried (model A4) stocks (Figure 4.26).

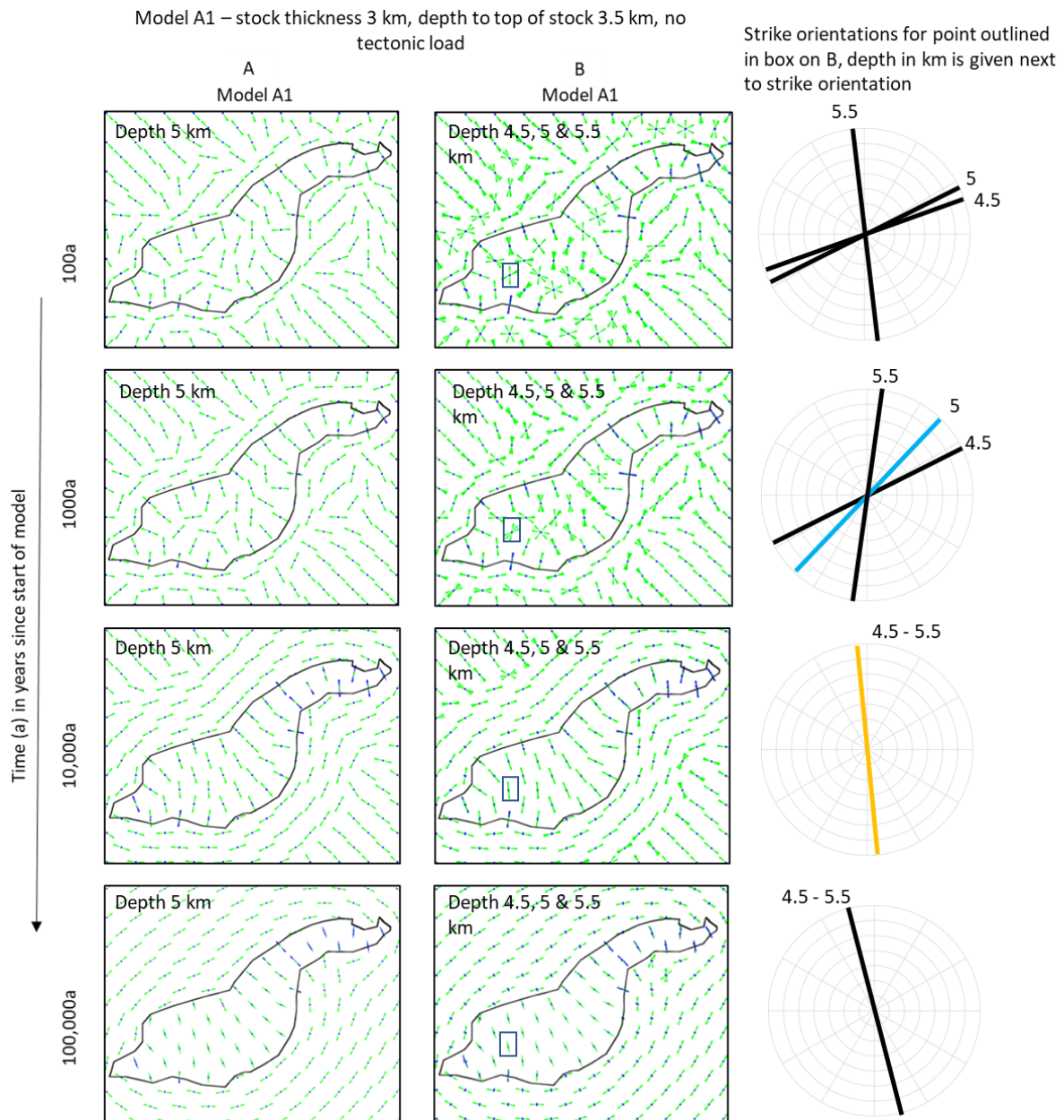


Figure 4.25. Principal stress directions over time for model A1. (A) on a horizontal plane at a depth of 5 km, (B) on horizontal planes overlain at depths of 4.5, 5 and 5.5 km to highlight variation in orientation with depth. Maximum principal stress blue and intermediate principal stress green. Minimum principal stress direction is not shown, it would be perpendicular to a plane fitted to the maximum and intermediate principal stress directions. Coloured strikes, blue (1000a) and orange (10000 a) on rose plots, used as reference in Figure 4.30 p.138.

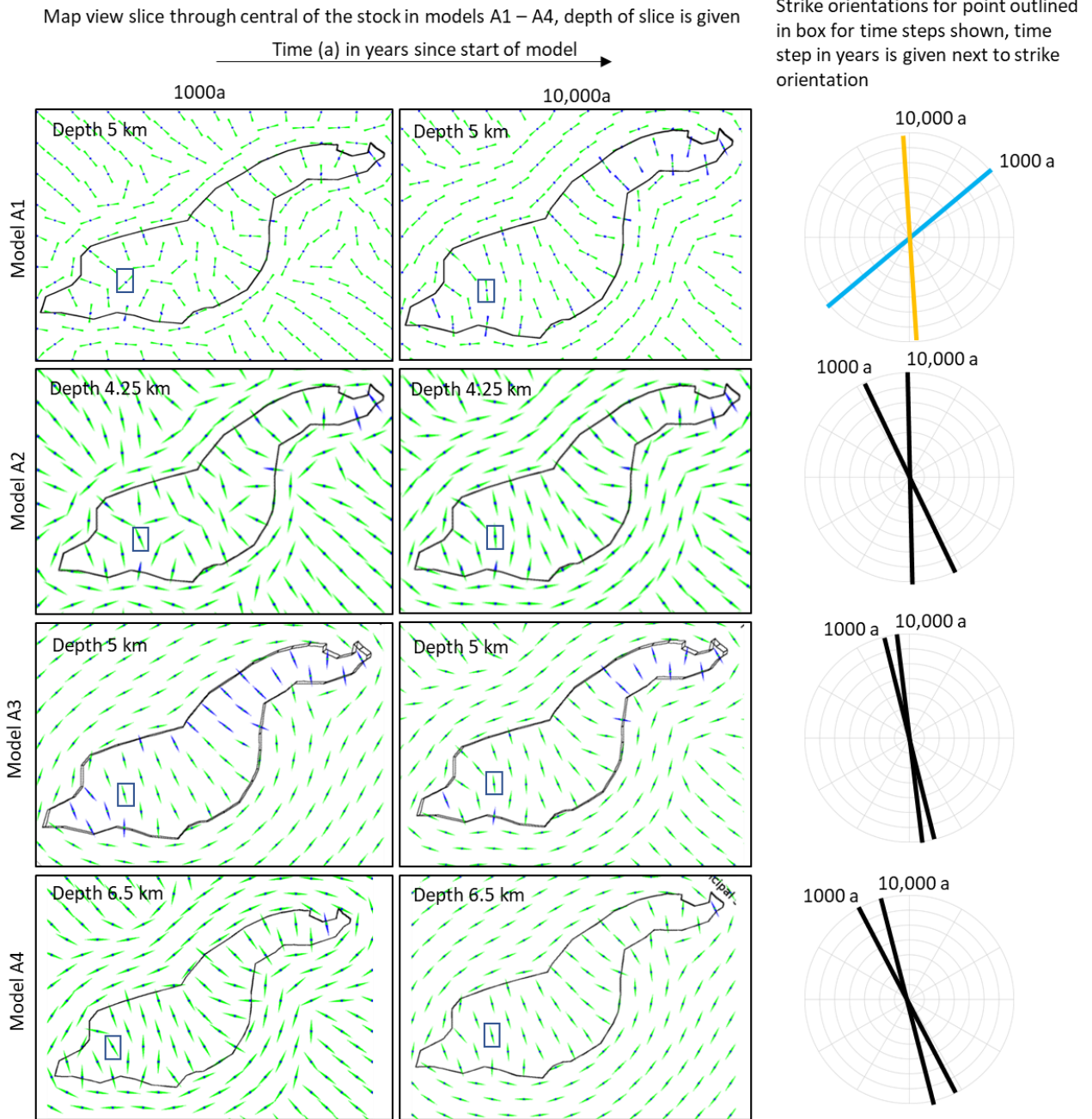


Figure 4.26. Comparison of principal stress directions over time for models A1 – A4 on a horizontal plane. Models A1 and A3 slice at a depth of 5 km, for model A2 at a depth of 4.25 km and for model A4 at a depth of 6.5 km. Coloured strikes, blue (1000a) and orange (10000 a) on rose plots, used as reference in Figure 4.30 p.138.

- Model A1 - reference model (stock thickness 3 km, depth to top of stock 3.5 km and no tectonic load)
- Model A2 - thinner stock (stock thickness 1.5 km, depth to top of stock 3.5 km and no tectonic load)
- Model A3 - thicker stock (stock thickness 16.5 km, depth to top of stock 3.5 km and no tectonic load)
- Model A4 - deeper stock (stock thickness 3 km, depth to top of stock 5 km and no tectonic load)

Orientations related to thermal and regional load (models A5 – A10)

When a compressive load is applied the maximum principal stress may be modelled as horizontal and the intermediate principal stress vertical (Figure 4.27). Initially, the orientation of the $\sigma_1\sigma_2$ plane parallels the orientation of the maximum compressive stress of the applied regional load (maximum horizontal stress aligned NE-SW). Over time the $\sigma_1\sigma_2$ plane aligns with the directions predicted by thermal loads. The amount of rotation depends on the relative levels of tectonic and thermal stress, greater rotation toward the thermal pattern occurring when the tectonic load is lower (cf. Figures 4.28, model A5 and Figure 4.28, model A6). There is less variation in orientation of the principal stress axes with depth when tectonic loads are applied (cf. Figures 4.26B model A1 (no tectonic load) to 4.28B to 4.20B (tectonic loads)).

Lowering the minimum horizontal stress (model A7, Figure 4.29) compared to increasing the maximum horizontal stress results in similar orientations being predicted (cf. Figures 4.28 & 4.29). Varying the orientation of the regional load modifies orientations of the principal stress axes (Figures 4.30).

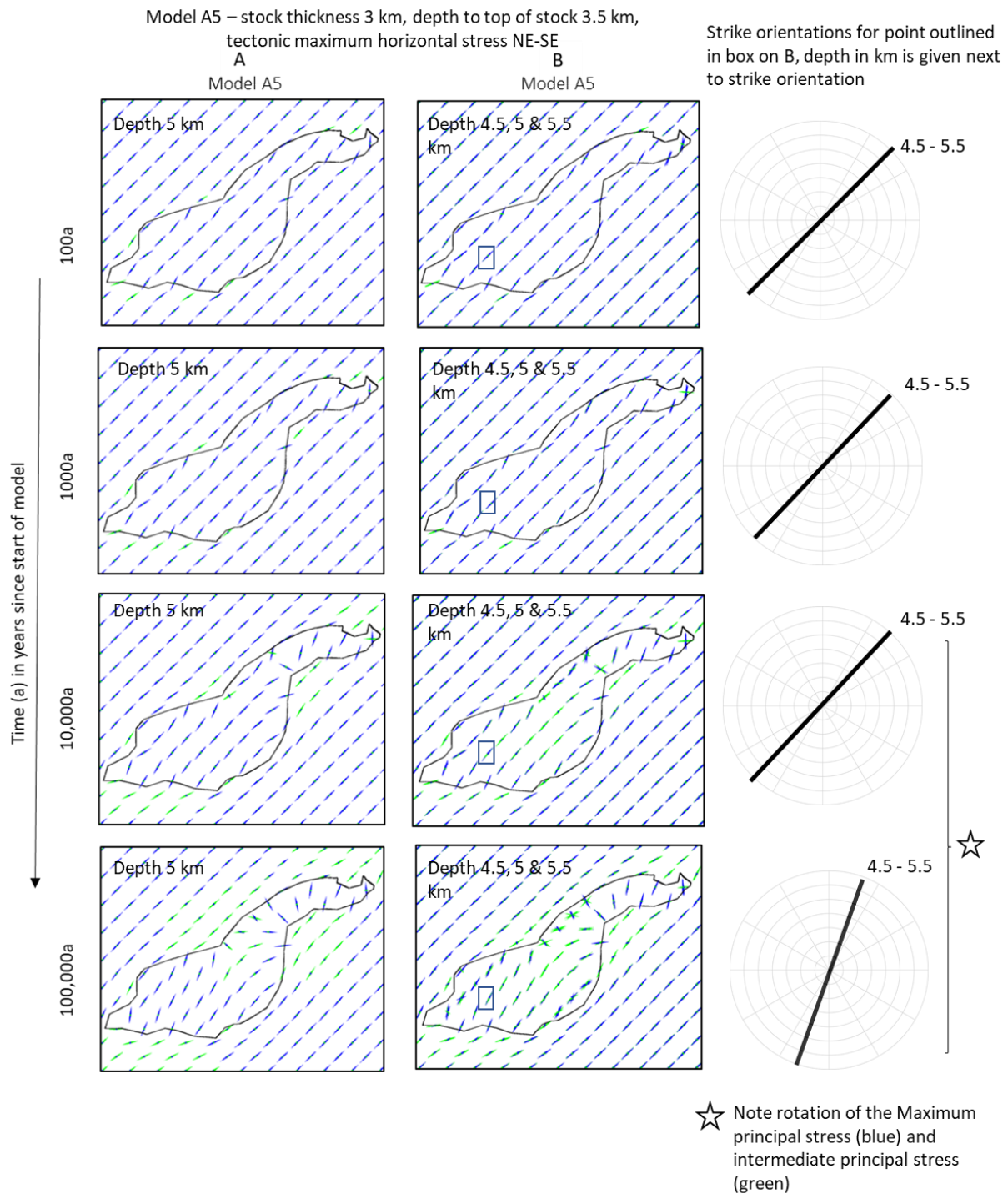


Figure 4.27. Principal stress directions over time for model A5. (A) on a horizontal plane at a depth of 5 km, (B) on horizontal planes at depths of 4.5, 5 and 5.5 km to highlight variation in orientation with depth, cf. with Figure 4.25 B minimum variation in strike direction with depth is observed. Maximum principal stress blue and intermediate principal stress green. Minimum principal stress direction is not shown.

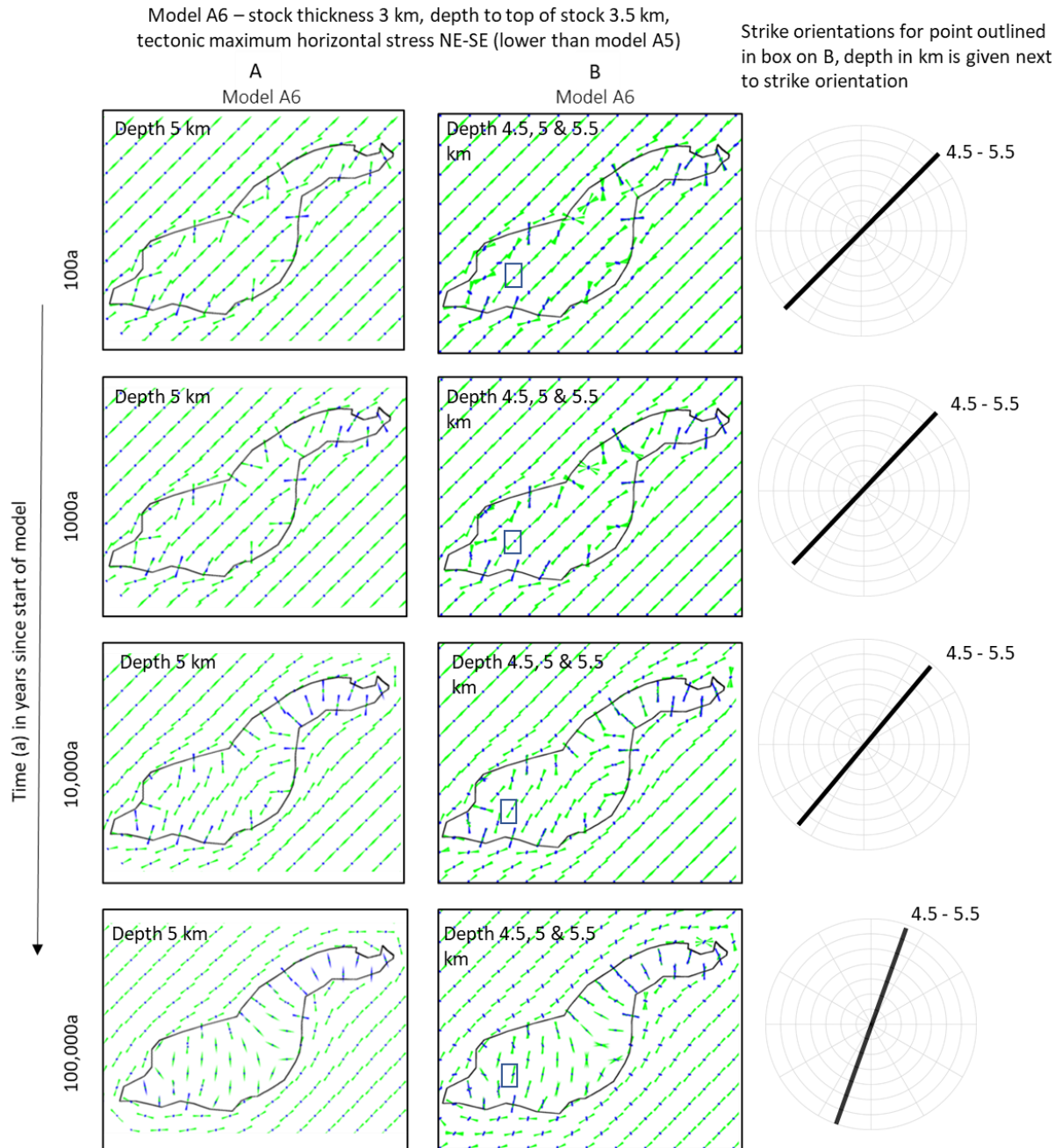


Figure 4.28. Principal stress directions over time for model A6. (A) on a horizontal plane at a depth of 5 km, (B) on horizontal planes at depths of 4.5, 5 and 5.5 km to highlight variation in orientation with depth. Maximum principal stress blue and intermediate principal stress green. Minimum principal stress direction is not shown. Increasing the maximum horizontal stress orientated NW-SE.

Model A7 – stock thickness 3 km, depth to top of stock 3.5 km,
 tectonic maximum horizontal stress NE-SE (lowering NW minimum)

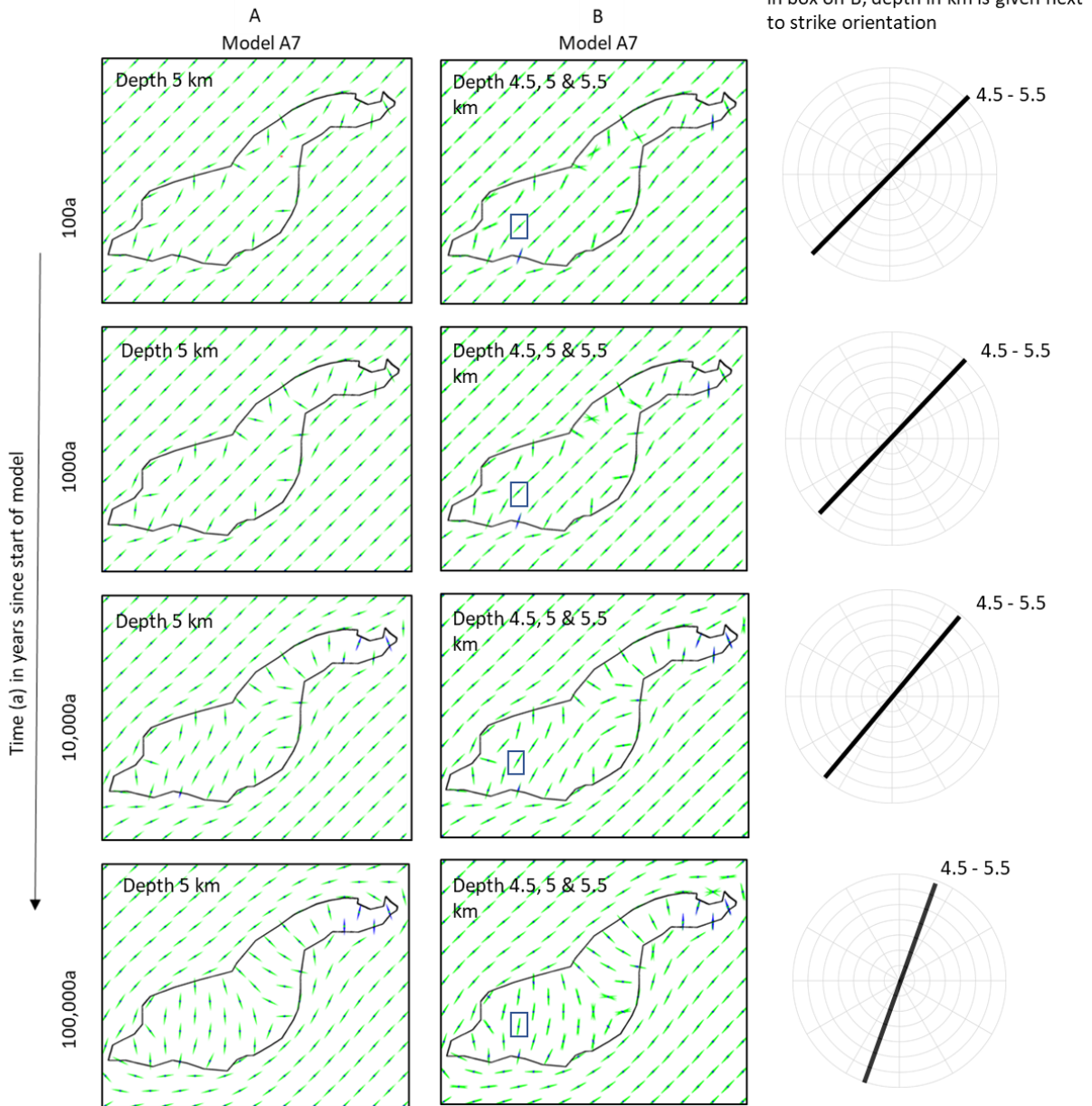


Figure 4.29. Principal stress directions over time for model A7. (A) on a horizontal plane at a depth of 5 km, (B) on horizontal planes at depths of 4.5, 5 and 5.5 km to highlight variation in orientation with depth. Maximum principal stress blue and intermediate principal stress green. Minimum principal stress direction is not shown. Lowering the minimum horizontal stress orientated NE-SW.

4.5.3. Stress Magnitudes and Failure Modes

The tensile stresses are highest where the stock cools fastest, at the margins (Figure 4.31). The initial stress magnitude is modified when a tectonic load is applied. The time for model initiation at which the stress paths, for any given point, cross failure domain boundaries of the applied Griffith-Murrell Failure criterion are influenced by the initial stress magnitude and temperature. As the stock cools the regions of shear and extensional-shear propagate inwards and shrink as the region of tensile failure expands. The timing and temperature of failure varies with the initial conditions, but the failure sequence is unchanged. The progression of failure mode remains the same in all models; shear, extensional-shear and finally tensile (Figure 4.32).

In models A1 – A4 no tectonic load is applied, maximum (σ_H) and minimum (σ_h) horizontal loads are initially equal and given by the gravitational load. In model A5 the minimum horizontal load in the NE-SW direction is decreased, comparable to the proposed stress field at the time of emplacement. In all models the failure domains move inwards as the stock cools, progressing from shear, to extensional-shear and then tensile failure at any given location. The inward propagation of the failure domains from all margins of the stock is only altered in the deeper (model A4) and thicker stock (model A3) where tensile failure only occurs from the top and side margins. Modelling highlights the limited influence of boundary conditions on the predicted failure sequence.

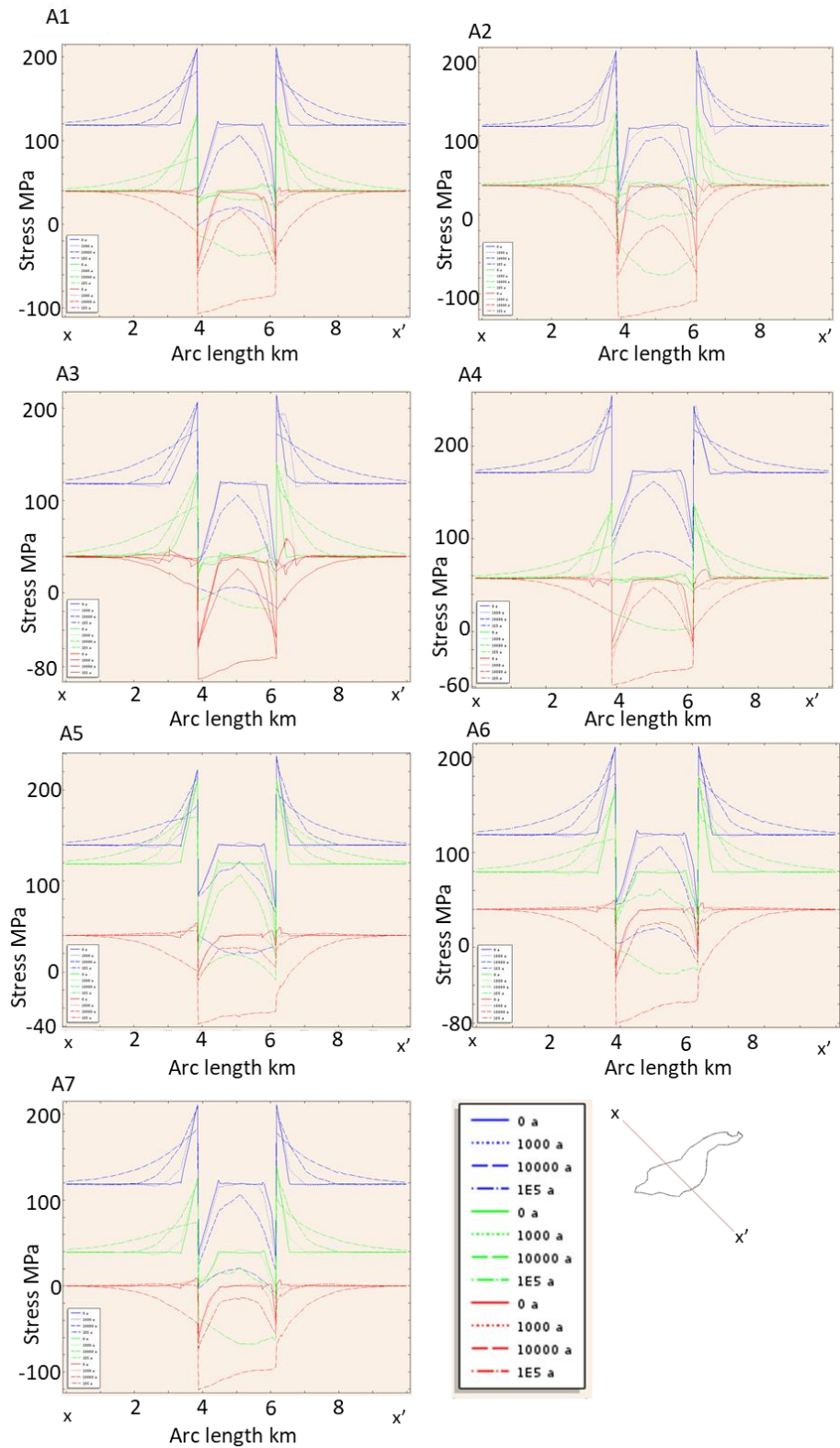


Figure 4.31. Principal stress magnitudes for selected time steps of a NE-SW 2D line cut through numerical models A1 – A7. The position of the sliced 2D line shown on inset. Stress magnitudes for blue maximum compressive stress, green intermediate compressive stress and red minimum compressive stress. See appendix B Figure B4-2 p.335 for equivalent graphs of models A8 – A10.

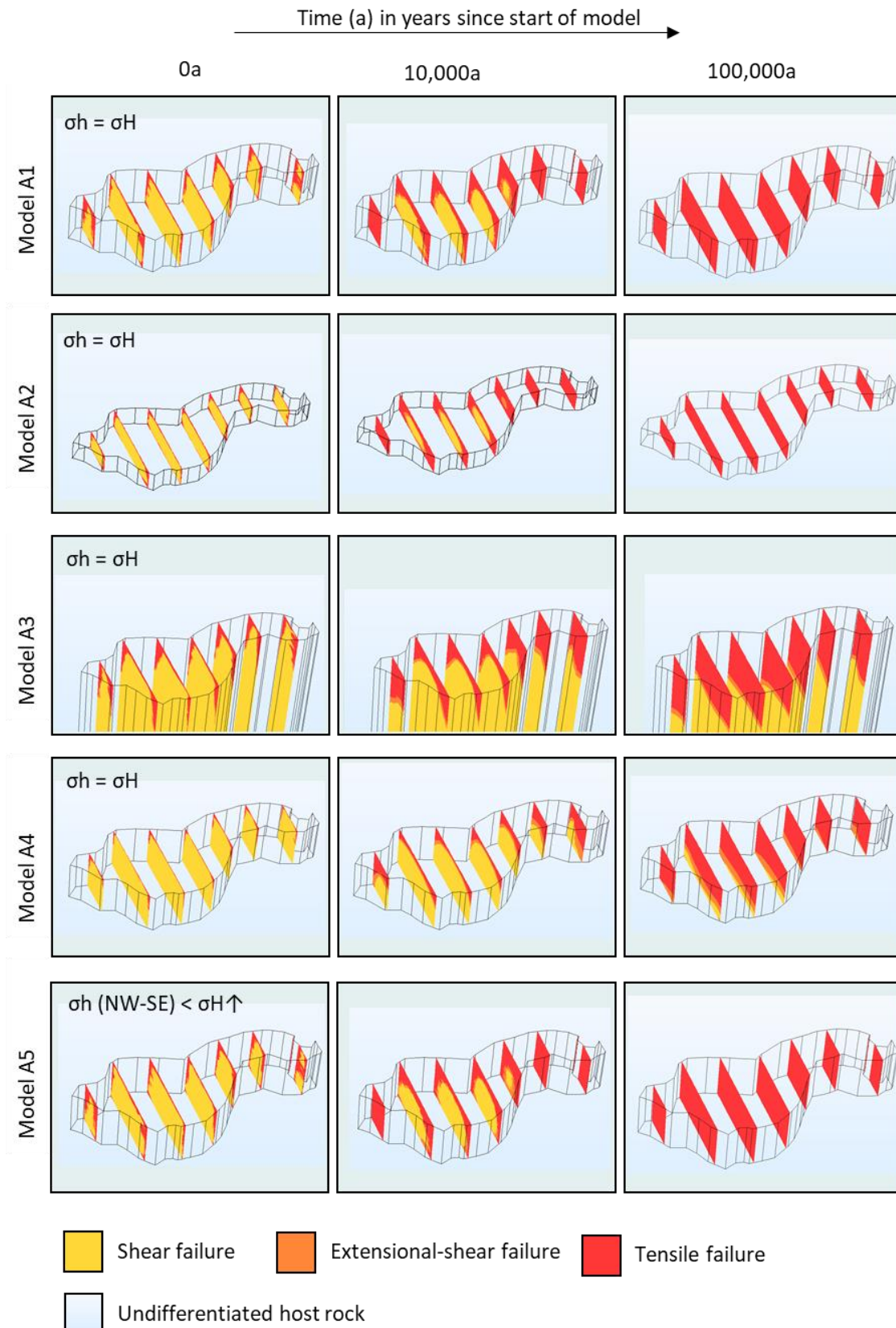


Figure 4.32. Calculated failure modes within the stock for oblique view on selected sections looking north, of the numerical models for selected times from model initiation. Stock thickness 3 km in models A1 & A3 – A5, 1.5 km in model A2 and 16.5 km in model A3. Depth at top of stock 3 km.

4.5.4. Elastic Strain Energy

Elastic strain energy patterns are comparable for all models (Figure 4.33). Values are highest in the host rock around the stock and within the stock where boundaries are concave inwards. Elastic strain energies are compared as Gerla (1983) suggested a correlation to fracture densities (See chapter 3, section 3.1. p.45)

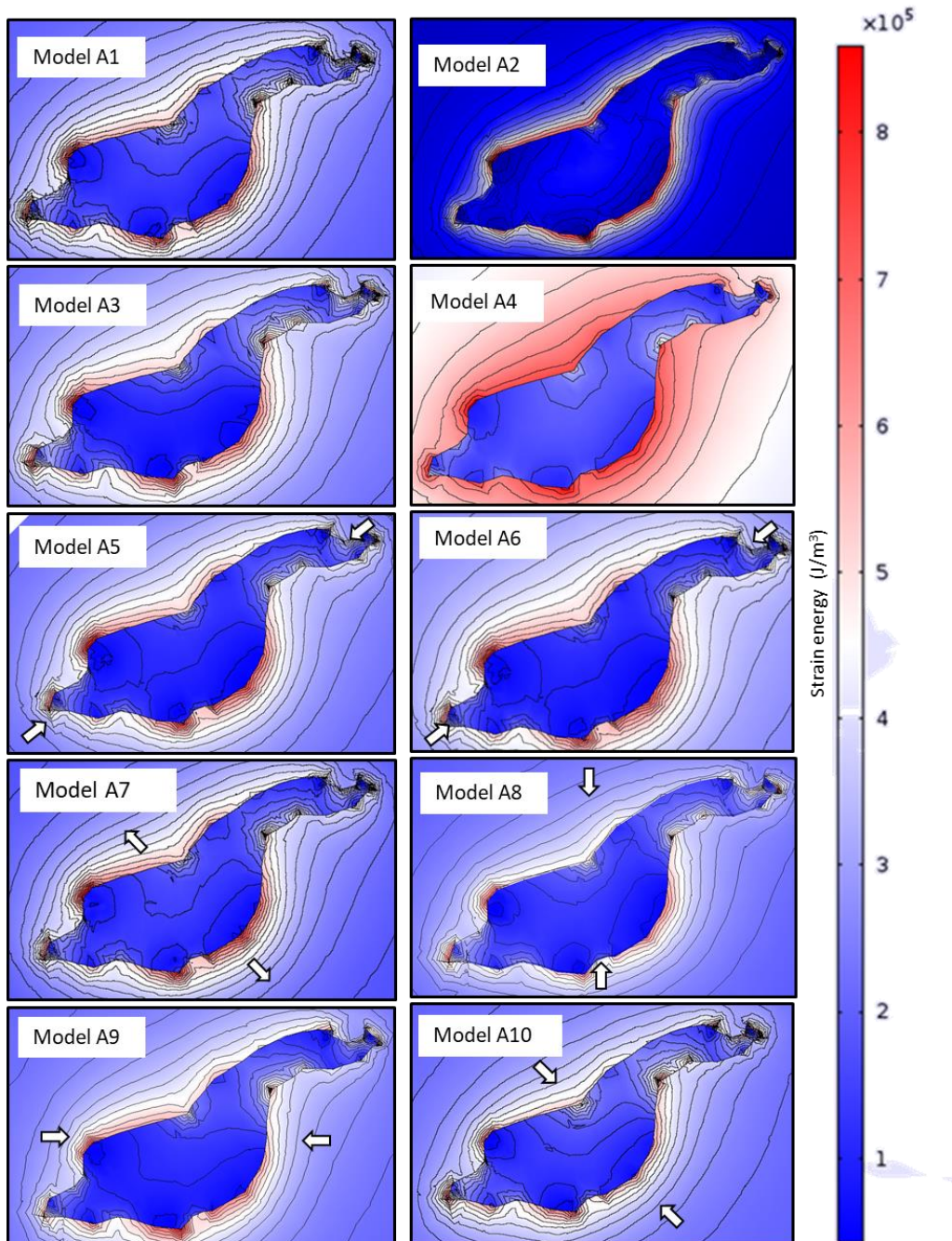


Figure 4.33. Strain energy (J/m^3) plotted for models A1 – A10. For models A1 and A3, A 5 – A10 slice is cut at a depth of 5 km, for model A2 at a depth of 4.25 km and for model A4 at a depth of 6.5 km.

4.6. Comparison of Numerical Models to Field Data

4.6.1. Orientation Comparison

Principal stress orientation is variable depending on time from model initiation, tectonic load, and to a lesser extent depth within the stock. Within the stock trends of the $\sigma_1\sigma_2$ plane are orientated NNE, NE, NW and NNW. The NNE and NE trends are related to thermal loads and the NW to NNW orientations to models in which the minimum horizontal stress is orientated NE-SW (models A5 - A7). These orientations are comparable to lineaments interpreted on satellite images (Figure 4.34) and those highlighted in previous interpretations (Wilson, 1961; Ren et al., 1989; John, 1991; Kowallis et al., 1995). The ~E-W orientation of lineaments interpreted on the satellite images and identified by Wilson, 1961 (Figure 4.34 & 4.35), predominantly located in the central phase, are not predicted in the numerical models.

Models at depth 5 km and time steps labelled (A) 1000, (B) 10,000 and (C) 100,000 years

Models at depth 5 km and time steps 1000 a, 10,000 a and 100,000 a

Models over satellite interpretation

Models over Wilson (1961) joint schematic

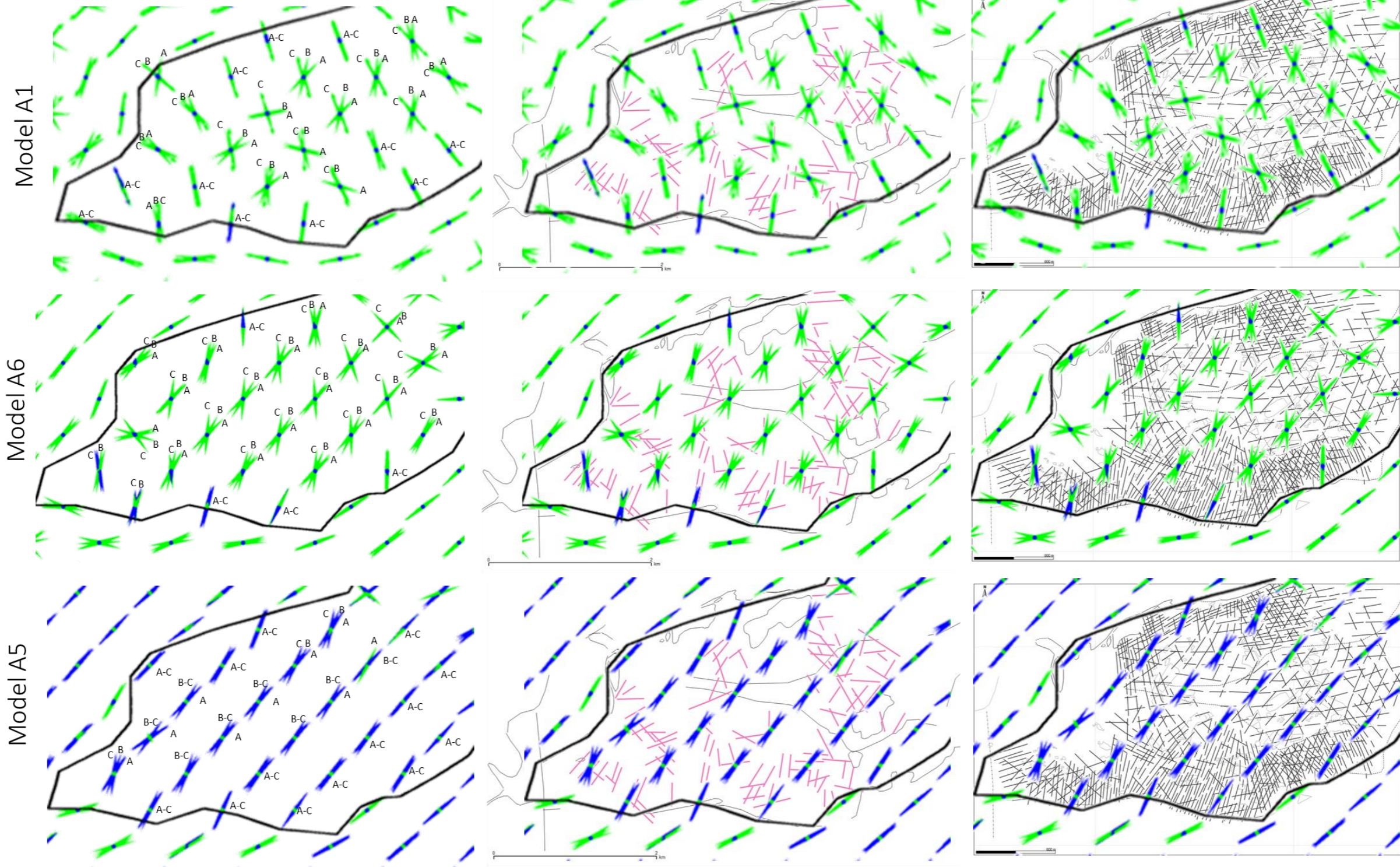


Figure 4.34. Comparison of satellite interpretation (left) and Wilson (1961) schematic representation of joint direction and spacing (see Figure 4.3 p.140) (right) with numerical model orientation at a depth of 5 km at 1000 years, 10,000 years and 100,000 years for models A1, A5 and A6. Blue maximum principal stress, green intermediate principal stress.

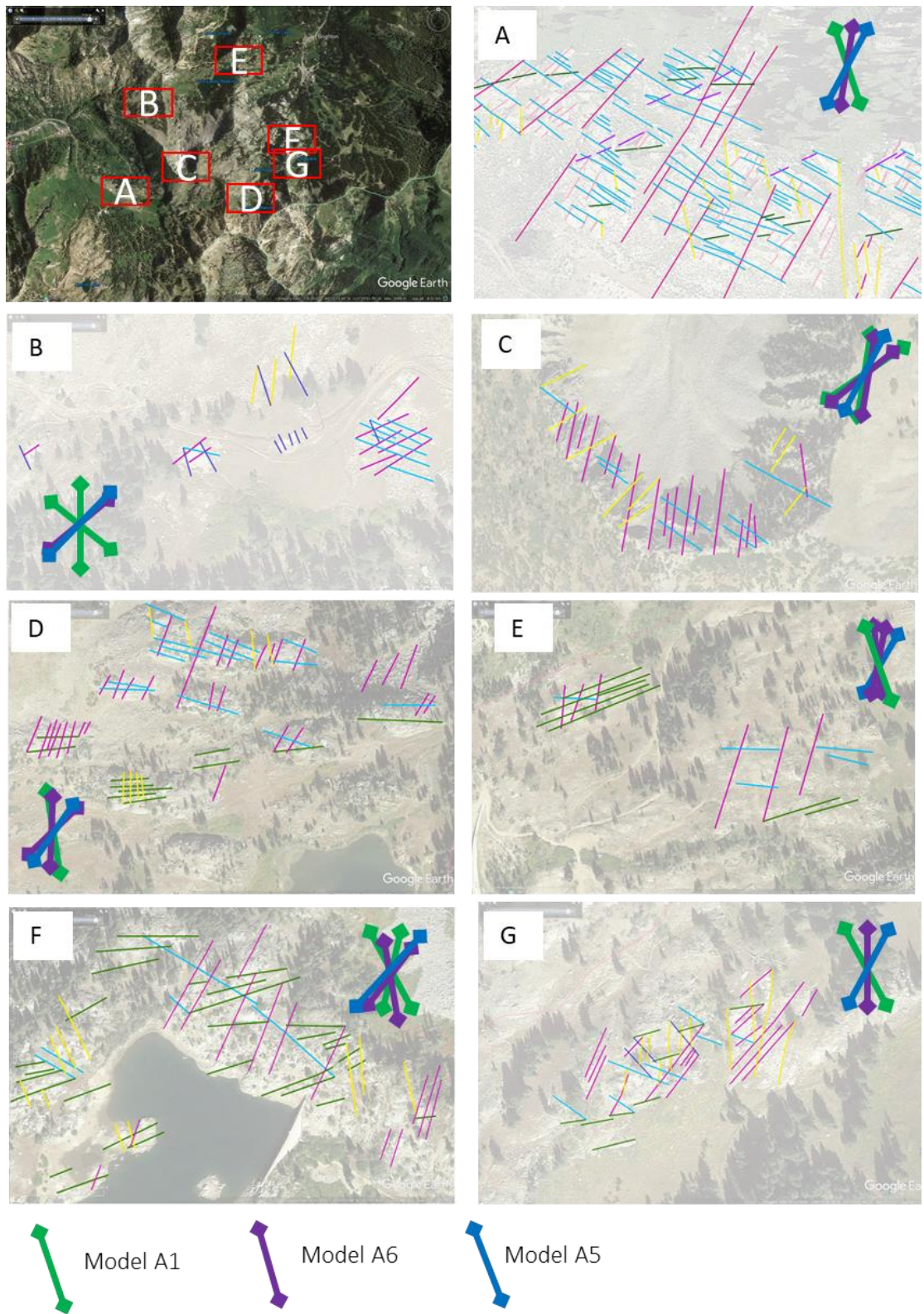


Figure 4.35. Comparison of satellite interpretation and strike of the maximum-intermediate principal plane for numerical model orientation at a depth of 5 km at 1000 years, 10,000 years and 100,000 years for models A1, A5 and A6. Interpretation of lineaments on aerial photos at selected locations A – G (shown on inset). Three to five lineament sets defined by orientations can be observed at each location. Colours identify different orientation sets at each location, colours are not correlated for the different locations (see Figure 4.16).

Kinematic interpretations of dykes show a good fit to maximum principal stress directions predicted from numerical models with applied tectonic loads (Figure 4.36). The predicted orientation of the maximum compressive stress from model A5 which intersects the obtuse angle (Figure 4.36 M, O & S) and the acute angle (Figure 4.36 N, P, Q, R & T) are consistent with the interpreted shear sense. In examples of aplites interpreted as opening mode, the modelled maximum principal stress is predicted to be perpendicular to the opening direction (e.g., Figure 4.36 W; see appendix B, Table B4-1 p.332 for tabulated data).

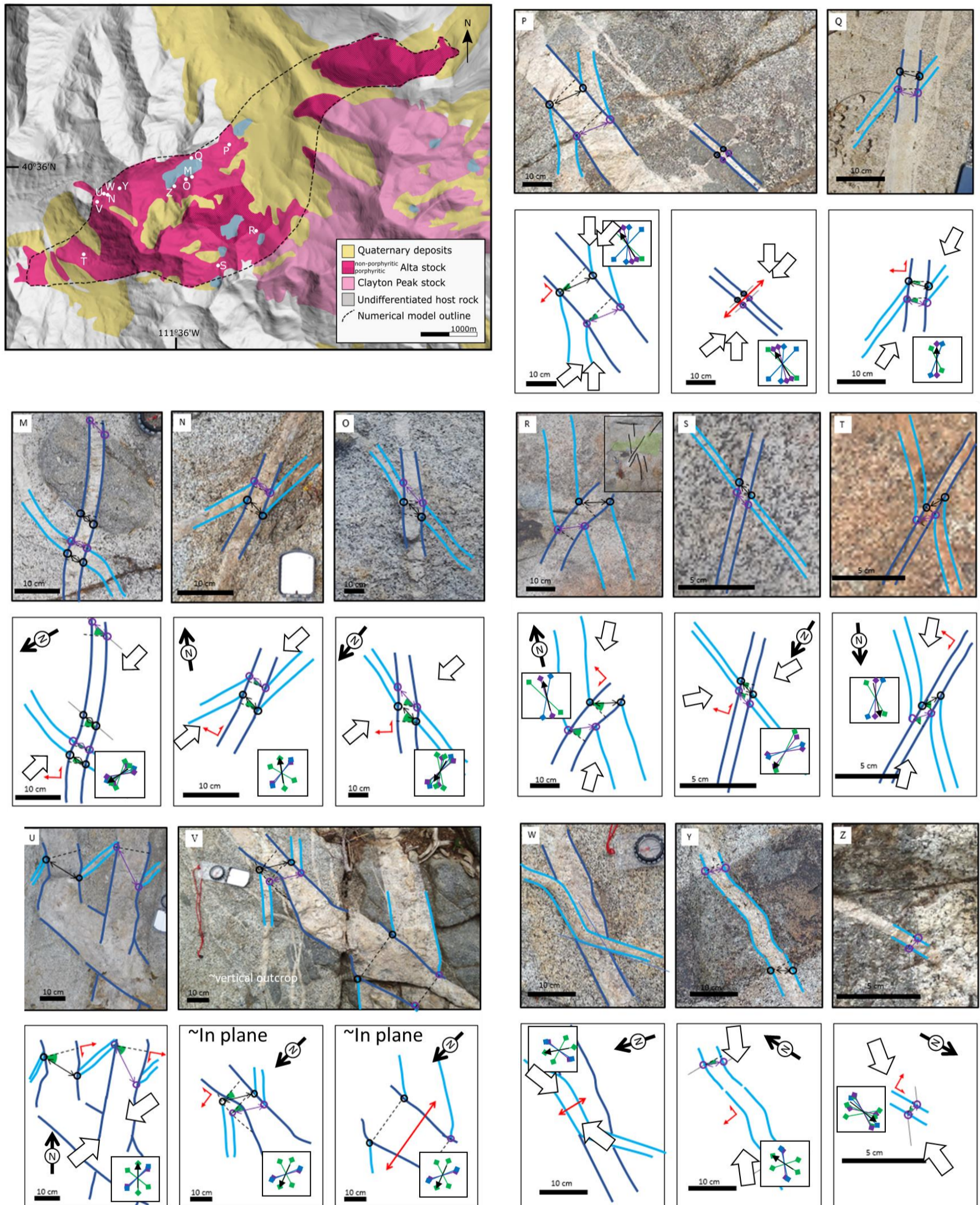


Figure 4.36. Comparison of kinematic dyke interpretation and numerical model orientations at 1000 years, 10,000 years and 100,000 years for models A1, A5 and A6. White arrows are based on model A5 and fit with the interpreted kinematics on dykes. Kinematic interpretation of aplite dykes is shown as; dilation direction (purple and black arrows) and opening angle of aplite dykes. M, O and S, are interpreted to have non-Andersonian-type opening directions on conjugate shears.

Field data at selected locations compared to numerical models show variability in match of orientations (Figure 4.37). Locations L1 to L4, L6 & L7 show a reasonable correlation between mineralised joint orientations recorded in the field and orientations of tensile failure predicted from modelling when a tectonic load is included. Location L5 does not show a good fit to mineralised fracture orientations in any model (Figure 4.37). This is the only field location that shows shear offset along these joints (Figure 4.12 X p.155 & 4.14 L15 p.157). The shear failure at this location (L5), which has a wide distribution of measured mineralised joint orientations, may perhaps be related to a later tectonic event resulting in shear.

Poles to extensional-shear failure correspond to field data at L2 and poorly at L4 and L7, in other locations no match to mineralised or non-mineralised joints is observed (Figure 4.37). At locations L2, L4 and L7 both thermal model (model A1) and models that include tectonic load (models A5 – A7) show a reasonable match to different clusters of fractures recorded in field data. Location L3 and L6 only have a reasonable match to models which include the regional load. This difference may reflect the distance from the stock margin. Locations L2, L4 & L7 are closer to the margins (< 400 m) and locations L3 and L6 are further from the margins. L1 which is located < 400 m from the margin fits the models which include a tectonic load (models A5 to A7). The level of confidence in the boundary geometry at location A is low, and an inaccurate geometry may be the reason that the thermal only model does not fit well. The match between field data and numerical models is directly related to the distance from, and confidence in, the modelled boundary geometry.

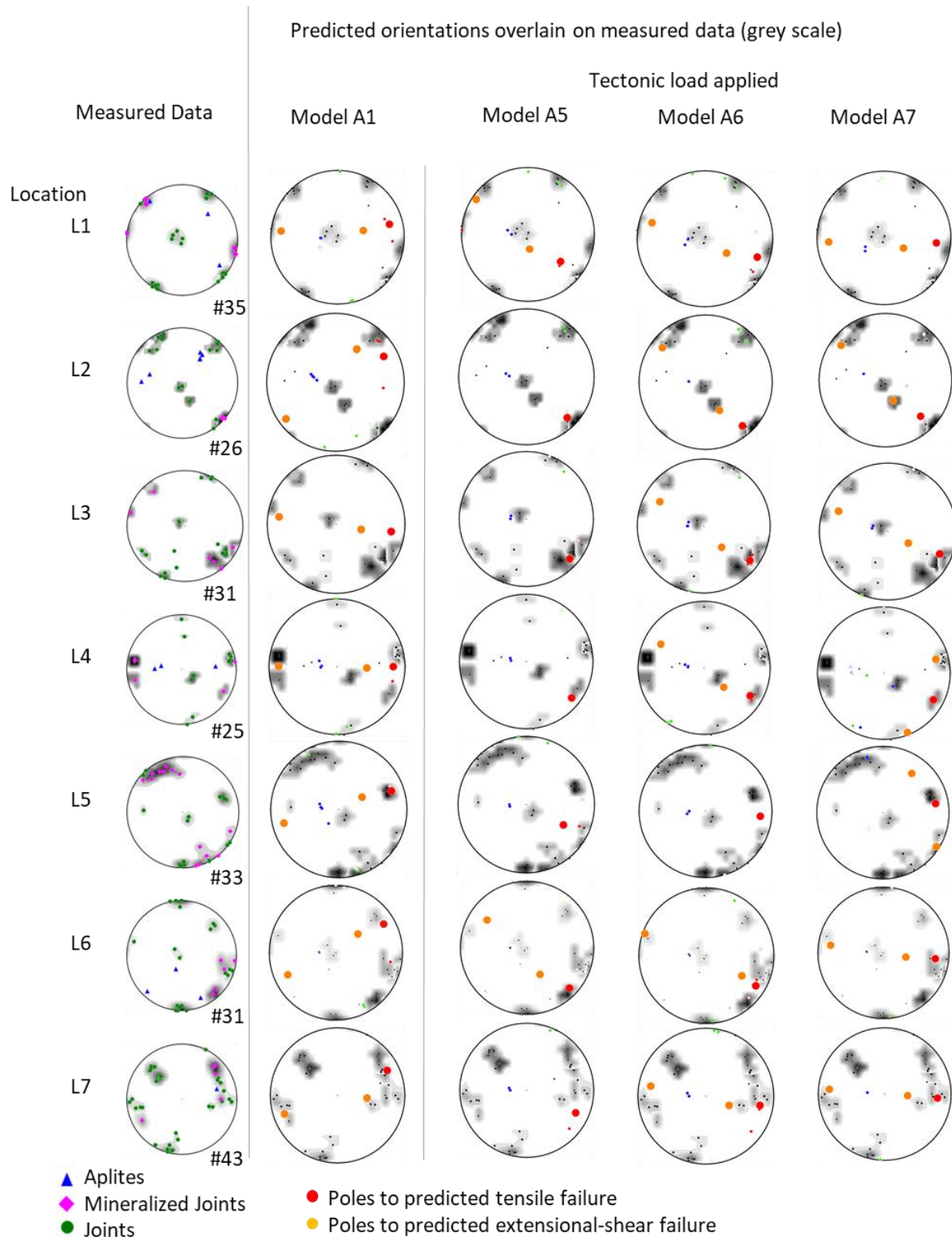


Figure 4.37. Poles predicted for fracture orientations based on failure criterion from numerical models are overlain on stereonets of field data. Red poles tensile and orange poles extensional-shear. Shear failure orientations have a similar trend to extensional-shear failure planes and are not plotted. Numerical model orientations are corrected for 20° eastward Basin and Range rotation. Field data collected at each location is shown in grey.

4.6.2 Strain Energy Compared to Fracture Density

Comparison between elastic strain energy and fracture density is limited by the relatively few points measured in the field. However, density calculation based on the representative joint map produced by Wilson (1961) shows that the distribution of fracture density is similar to the predicted elastic strain energy variation (Figure 4.38).

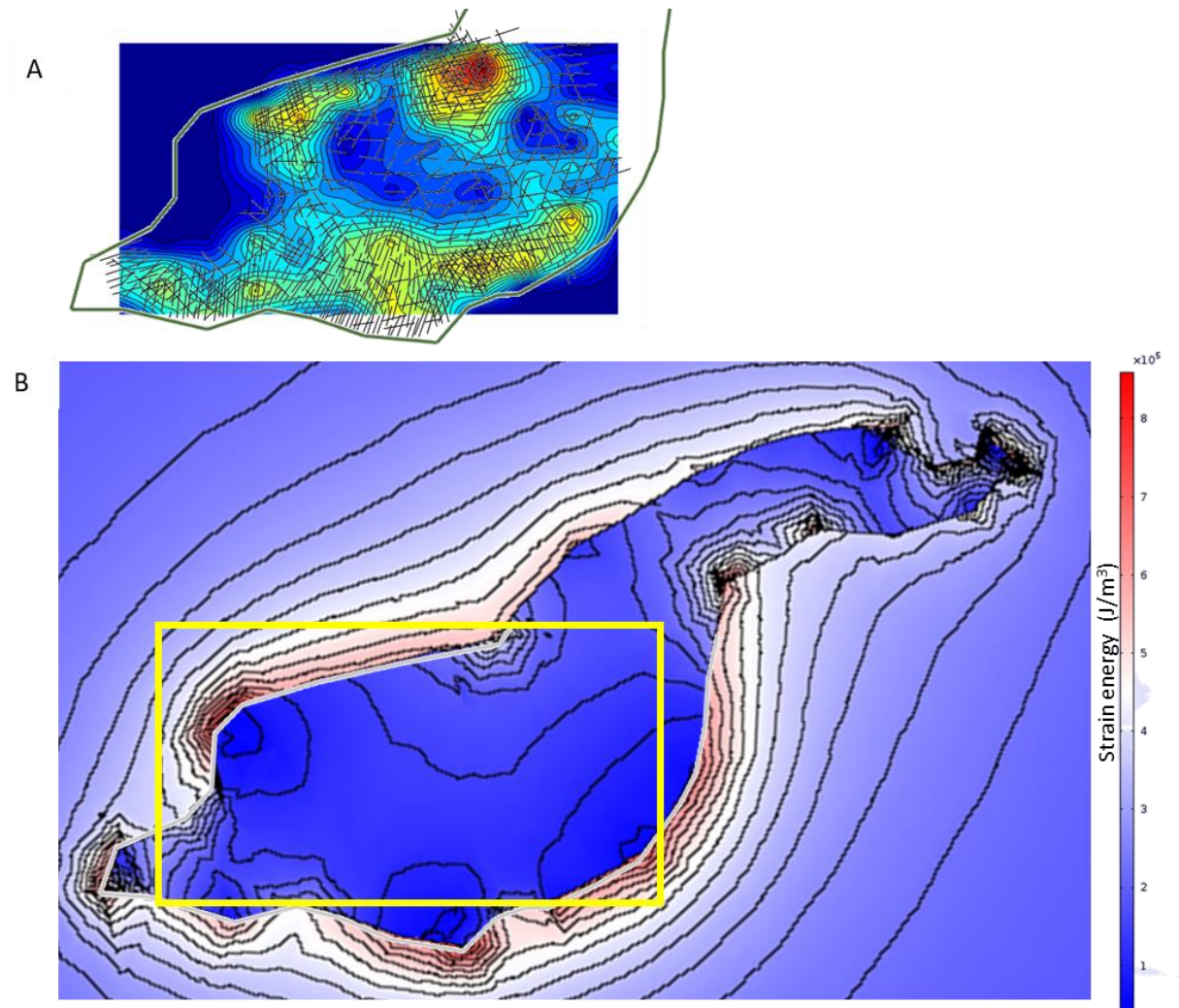


Figure 4.38. Comparison of (A) calculated joint density based on schematic representation of joint direction and spacing (Wilson, 1961) and (B) strain energy (J/m^3) predicted from numerical modelling.

4.7. Discussion

4.7.1. Failure Sequence

Numerical models developed in chapter 3 are applied to the Alta stock. The applied failure criterion results in a sequence of shear, extensional-shear and tensile failure. This sequence is comparable with the field observations at Alta in which mixed-mode failure recorded by aplite dykes is followed by tensile failure recorded by mineralised and non-mineralised joints. The applied boundary conditions mean that the stock is entirely in shear failure at model initiation (Figure 4.32 p186).

Observed aplite dykes in the non-porphyrific phase of the Alta stock are interpreted to record a transition from emplacement into a deforming host to brittle extensional-shear and tensile failure. Deformed aplites (i.e., those with non-straight margins) are observed along the western margins which correlates with the greatest paleodepth estimates of (~6.4 km, fluid inclusion studies; John, 1991) of the exposed stock. Close to the margins of the stock straight-walled aplites are typically oriented perpendicular to the stock margins. Close to the margin conjugate pairs of straight-walled aplites record evidence of extensional-shear failure. This distribution may reflect the timing of aplite formation relative to failure at the margins, or possibly faster cooling rates at the margins resulting in the preservation of extensional-shear failure. Within the central porphyritic phase, aplites show tensile opening and have variable orientations that are not correlated to the geometry of the stock margin. This may imply that margin geometry has less of a controlling influence on fracture geometry with distance from the margin.

Clear evidence of early shear failure is not apparent in the field. Shear failure may not have occurred or been preserved. This may be because the temperature at which the stress path was in the shear failure domain was higher than permitted for brittle failure, alternatively without the presence of intrusive material or mineralizing fluids, early fractures could be easily annealed (Balk, 1937; Hutchinson, 1956; Hibbard and Watters, 1985). The predicted temperatures at which stress paths cross into the extensional-shear failure domain (Figure 4.39 p.198) are near to the temperature of the brittle-viscous transition in granitoid rocks for modelled normal or longitudinal strain rate, calculated as temperature difference over time, of 10^{-15} s^{-1} (Fournier, 1999; Violay et al., 2017). The presence of deformed aplites along the western margin of the stock suggests that some early fracturing did occur close to the brittle-viscous transition. As there is evidence for the formation of dykes at or near to the brittle-viscous transition, mechanisms of failure forming early dykes may be different from

those forming later fractures. The application of alternative failure criterion to assess the influence of the brittle-viscous transition on fracturing may therefore be applicable.

The failure sequence recorded in a cooling stock depends on the temperature experienced along the stress path and is influenced by the conditions defining the imposed stress state. Not included in the model are (1) stress redistribution due to failure, (2) the influence of fluids and, (3) initial heterogenous thermal distributions potentially related to incremental emplacement, all of which may alter the stress paths and failure sequence.

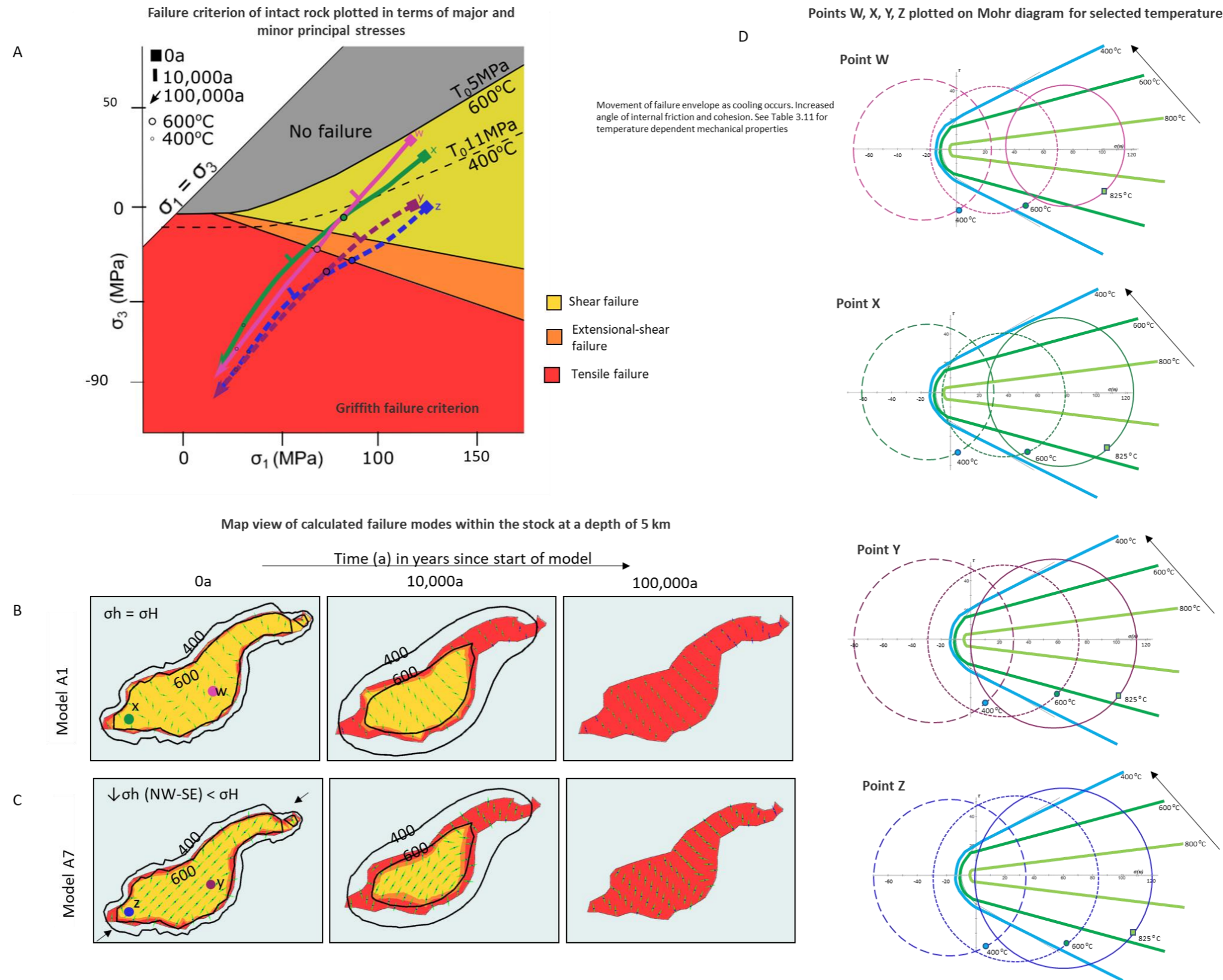


Figure 4.39. Griffith failure criteria plotted on σ_1 - σ_3 graph (compression positive). Four domains of fracturing are recognized; no failure, shear failure, extensional-shear (E-S) and tensile failure. As tensile strength increases with decreasing temperature the failure boundary shifts. Failure boundaries for tensile strength 5 MPa (~600 °C) and 11 MPa (~400 °C) are plotted. (B) model A1 and (C) Model A7. Stress redistribution due to fracturing is not accounted for, so the stress path moves continuously through fracturing modes (Gerla, 1988; Knapp, 1978). (D) Stresses for points W, X, Y, Z (W & Y, depth 4.5 km and X & Z, depth 5.5 km) for model initiation (825°C) and when point is at 600 °C and 400 °C plotted as Mohr diagrams.

4.7.2. Cooling History

The stock is modelled as a hot body which continually cools from its margins. Therefore, cooling is protracted in the centre of the stock compared to that of the margins. The stock is assumed to be a homogenous instantaneously emplaced unit. In previous modelling this assumption is justified because stock emplacement is considered to be rapid relative to the time required for substantial cooling (Bergbauer and Martel, 1999; Bergbauer et al., 1998; Žák et al., 2006). At Alta it has been argued that the stock grew via a process of syntaxial crack-seal, in which the ~NE orientated stock was centrally fed and progressively dilated outwards in an ~NW-SE orientation over an extended period of 1 million years (Bartley et al., 2008). Theoretically the thermal stress distribution may be altered by long term emplacement and/or cooling of pre-existing pulses of magma.

Despite the possibility of incremental emplacement, it is believed that the assumption of cooling from a homogenous unit is valid. Plutons emplaced incrementally at growth rates of <2 cm/yr can maintain temperatures at or above >500 °C for extended periods (Norton and Knight, 1977; Hanson and Glazner, 1995; Bartley et al., 2008). It is estimated that the Alta stock grew at a rate of ~1 - 2 mm/year (Bartley et al., 2008). The estimated growth rate of Alta therefore potentially allowed the temperature of the stock to remain high during emplacement. The absence of a well-defined primary fabric relating to incremental dykes at Alta and loss of primary fluid inclusions as a result of recrystallization (John, 1989) also support the idea that Alta remained at a high temperature during its emplacement history. The only evidence of cooling prior to emplacement of later pulses is along the southern boundary between the porphyritic and non-porphyritic phase where the porphyritic phase cuts aplites and fractures in the non-porphyritic phase. However, the whole stock likely remained at a high temperature during emplacement.

The syntaxial mechanism of emplacement, where new material is added centrally, would result in the centre of the stock remaining hotter for longer. This is comparable to the applied thermal model, which assumes cooling from a homogenous instantaneously emplaced unit. Thermal models reflecting a syntaxial emplacement or a second phase of intrusion do not significantly alter the predicted orientations of the principal stresses (Figure 4.40). This is partly related to the distribution of heat reflecting the elongate nature of the stock. The applied thermal model influences the timing and temperature of failure which may modify the cooling time of the stock. The use of a homogenous initial temperature distribution may explain the better fit between field data and modelling results close to the margins, where initial conditions will have a smaller influence on modelling results.

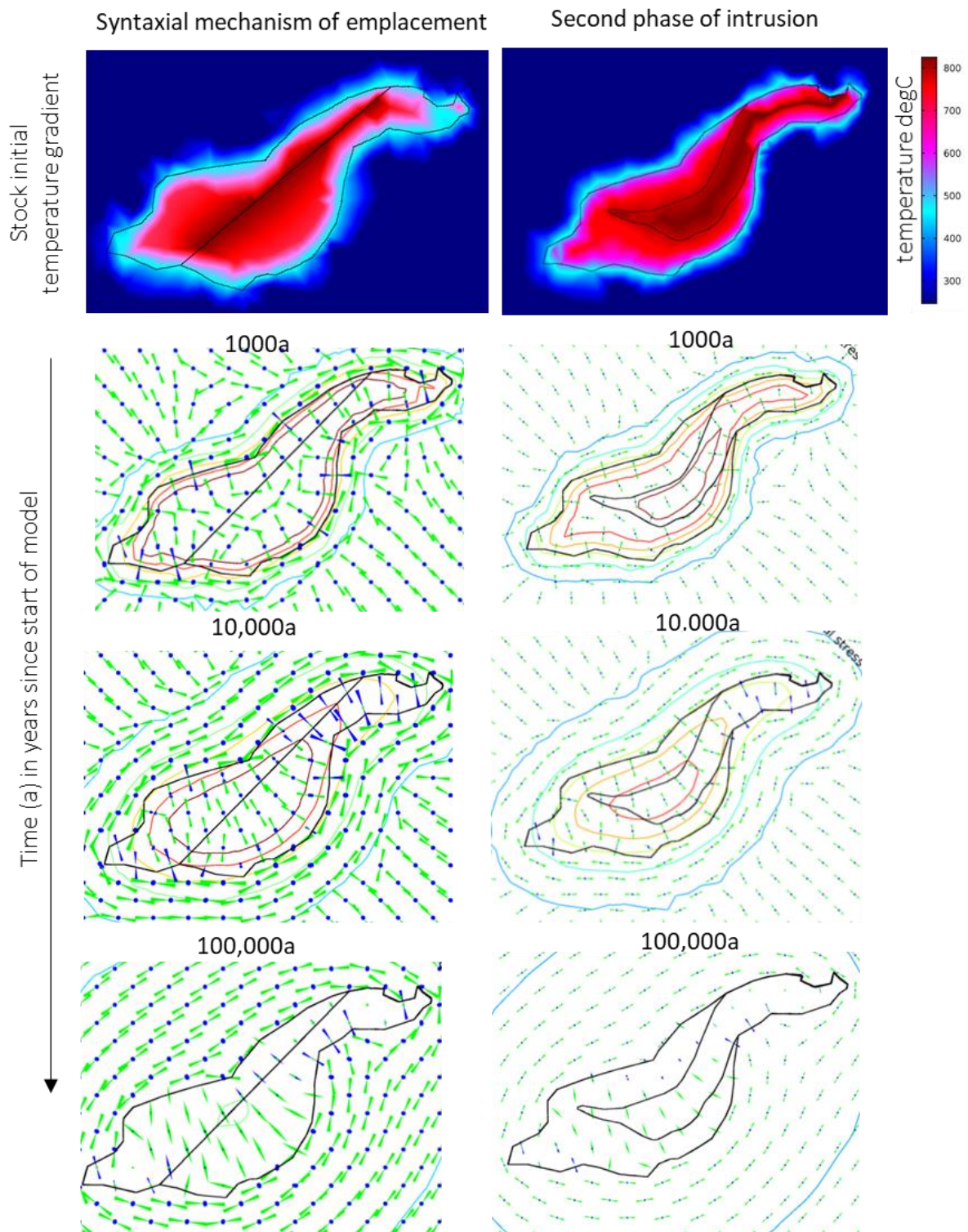


Figure 4.40. Alternative thermal models with initially non uniform thermal distributions.

The geotherm of the host rock was set to 55 °C/km to account for an increase in host rock temperature as a result of emplacement of the surrounding early plutonic bodies (after Cook and Bowman, 1994). Other numerical models have also raised the geotherm for this reason (e.g., 150

°C/km Gerla, 1983; 50 °C/km; Žák et al., 2006). Although the geotherm has been modelled as linear, it is possible that only the geotherm at shallower crustal levels < 7 km is influenced by the emplacement of the surrounding plutons, resulting in a non-linear geotherm, and lower temperatures at 20 km depth (e.g., Ratschbacher et al., 2018). Modelling the geotherm as non-linear does not influence the modelling results.

4.7.3 Stress Field and Tectonic Setting during Cooling

Without a regional load (model A1, Figure 4.25), the minimum principal stress axes is parallel to the stock margins and therefore preferentially parallel to the ~NE-SW long axis of the stock. Resulting in a NW-SE orientated $\sigma_1\sigma_2$ plane. When a uniaxial tectonic load is applied, so that the minimum horizontal stress is orientated NW-SE, the $\sigma_1\sigma_2$ plane axis aligns NE-SW (models A5 – A7, Figures 4.27 – 4.30 p.180 – 183). Depending on the magnitude of the tectonic load, over time the $\sigma_1\sigma_2$ plane may rotate towards the ~NW-SE thermally controlled orientation. This effect is strongest within 400 m of the stock margins. As a result, cooling joint orientation is likely to be variable depending on pluton geometry and regional tectonic load.

The orientation of the aplite dykes and mineralized joints compared to the modelling results suggest that the initial stages of stock cooling were influenced by an anisotropic regional stress field, where the minimum horizontal stress is orientated NW-SE. This stress field is comparable to the proposed stress field at the time of emplacement (Ren et al., 1989; Vogel et al., 2001). A NE-SW fracture orientation is also the most prominent trend recorded in micro-crack data by Ren et al. (1989), who suggest that this orientation relates to the regional stress field at the time of cooling (Figure 4.41 A). In contrast, a similar study on micro-cracks at Alta by Kowallis et al. (1995) found a near random scatter of the microcracks (Figure 4.41 B). Kowallis et al. (1995) concluded that the stock was either shallowly emplaced or the stress field was close to isotropic during the time of emplacement. They group samples from six or more undisclosed locations across the stock, combining orientation data that may be influenced by the geometry of the stock margin possibly resulting in apparently random scatter in orientation data. As a breakdown of data at the recorded locations is not given this cannot be confirmed.

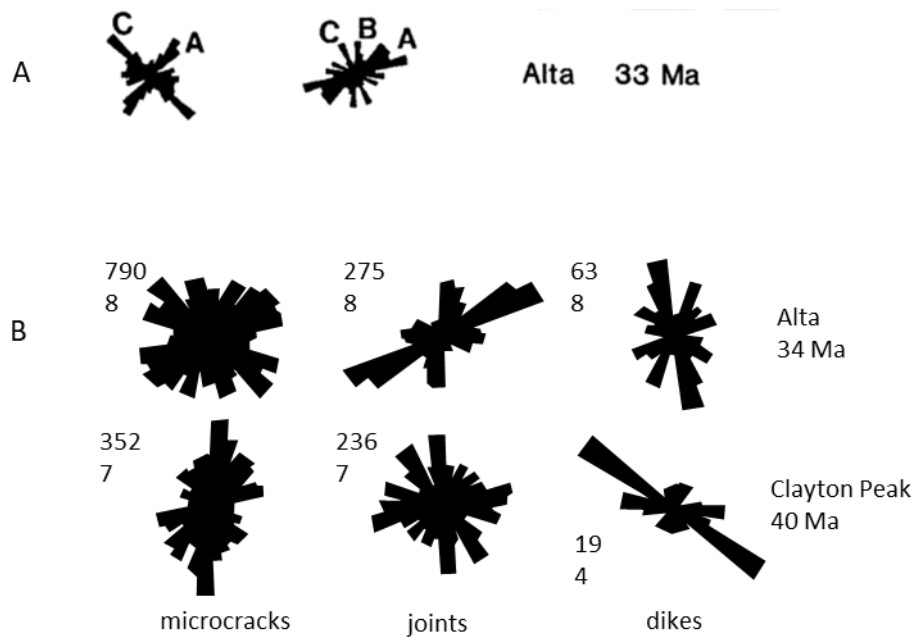


Figure 4.41. Paleostress orientations from (A) Ren et al., 1989 orientations labels A – C regional stress at time of cooling, B – Bains and Range, C – local stress. Copyright GSA (1989), fair use policy and (B) orientations for microcracks, joints and dykes tope number, number of measurements and bottom is the number of stations redrawn from Kowallis et al., 1995.

Interestingly the orientation of the predicted maximum principal stress in models where tectonic loads are included, in which the minimum horizontal stress is oriented NW-SE, corresponds to the correct sense of slip recorded on all conjugate aplite dykes. Flat lying fractures are not predicted by the numerical modelling, assuming Andersonian failure. This suggests that either stress rotation or other mechanisms of failure such as post-cooling deformation and exhumation may be the cause of these fractures.

4.8. Conclusions

Field evidence and modelling show that fracture systems in plutonic rocks can have complex and diverse origins. In the Alta stock, early fractures (preserved by aplite dykes) show evidence of mixed-mode deformation, whereas later mineralised and non-mineralised fractures are predominantly opening-mode. At Alta aplite dykes record that shear or extensional-shear may be the earliest failure mode in a pluton, preceding tensile failure, and occurring at or near the brittle-viscous transition. This contrasts with prevailing notions that cooling fractures result from opening mode failure. Key field observations include:

- Deformed aplite dykes with non-straight margins are interpreted as evidence of emplacement into a deforming host. Observations of this type of aplite intrusion are restricted to western outcrops of the intrusion, correlating with the deepest estimates of paleodepths (~6.4 km based on fluid inclusion studies by John, 1991).
- Straight walled aplite dykes record both minor hybrid mode failure (along the northern margin of the stock and the southern contact between the porphyritic and non-porphyritic phases) and opening mode failure (ubiquitous through-out the stock).
- Conjugate dyke sets intersect with acute angles of between 30° - 60°. Dykes of the same pair are of similar thicknesses, suggesting that they formed under similar fluid pressures and conditions. Measured slip to opening ratio on conjugate dykes average is on the order of 1:2. The shortening direction interpreted based on sense of shear recorded on crossing dykes is interpreted to intersect the acute and obtuse angles of dykes. Where the shortening direction is interpreted to intersect the obtuse angle, it may be: (1) apparent due to opening of existing conjugate fractures, (2) the result of fracture rotation by distributed pure-shear from combined contraction and extensional deformation, unidirectional contraction or unidirectional extension, or (3) the orthogonal switching of principal-stress directions. The angle in the direction of shortening for conjugate dykes in which the shortening direction intersects the acute angle is consistently around 40°. Where the shortening direction intersects the obtuse angle, angles in the shortening direction range between 120° – 150°.
- Mineralised joints predominantly trend NW-SE though out the stock, comparable to the orientation of the maximum principal stress direction predicted in numerical models with a tectonic load applied.
- Non-mineralised fractures have variable orientations across the stock.

The numerical models apply to fractures developed during cooling of the Alta stock and predicts a sequence of shear, extensional-shear and tensile failure. Even with some uncertainty with

the model boundary conditions, the modelled failure sequence is comparable to the field observations at Alta in which extensional-shear failure is followed by tensile failure. The predicted failure sequence of the cooling stock depends on the temperature experienced along a stress path and is influenced by the imposed stress state. Variation to the initial conditions (e.g., stock depth, initial temperature distribution, tectonic load) does not significantly alter the failure sequence. Stress path trajectories predicted by the models may be altered by redistribution of stress due to fracturing, the presence of fluids, or initial heterogeneous thermal- or stress-fields related to the tectonic setting:

- Annealing or filling of early formed fractures may limit the influence of stress redistribution during cooling.
- Incremental emplacement, which was not modelled, could locally alter the cooling history.
- Increasing fluid pressures are likely to move the failure criterion closer to the tensile failure domain, reducing the likelihood of shear failure.

The orientation of principal stress directions predicted in the models are variable over time and dependent on regional tectonic loads. When no regional load is applied, the $\sigma_1\sigma_2$ plane preferentially trends perpendicular to the margins and over time rotates towards parallel to the narrowest, ~NW-SE, dimension of the stock. When a regional tectonic load is included in the model, the $\sigma_1\sigma_2$ plane initially strikes NE-SW, perpendicular to the minimum horizontal stress of the regional load. This plane then rotates toward a thermally controlled orientation, in which this plane is preferentially ~NW-SE. The amount of rotation is dependent on the margin geometry and relative orientations and magnitudes of thermally and regionally imposed stresses. The maximum principal stress orientations predicted in models where the minimum horizontal stress is oriented NW-SE correlates with the sense of shear observed on all aplite dykes.

5. Bingham Canyon

This chapter describes two-dimensional numerical modelling of the Bingham Canyon Cu-Mo-Au porphyry deposit and compares the results to field data. An introduction to fracture networks in porphyry systems and an overview of work completed at Bingham Canyon is given in section 5.1 (p.206). A geological overview of the Bingham Canyon deposit is given in section 5.2 (p.208). A description of early fractures found in and around the Bingham Canyon deposit is given in section 5.3 (p.212). The applied workflow is described in section 5.4 (p.216). Numerical modelling results are presented in section 5.5 (p.226) and compared to field data in section 5.6 (p.234). The discussion, section 5.7 (p.236), focusses on fracture evolution at Bingham Canyon. Conclusions are presented in section 5.8 (p.239). Based on the results it is suggested that thermal stress may have influenced early fracture trends at Bingham Canyon. The influence of thermal stress on early fracture and stockwork formation may apply to other porphyry deposits and vein networks hosted in intrusive rocks. A description of workflows used for data transfer between MOVE™ and COMSOL Multiphysics® is given in the appendix C (p.336 – 345). Data is provided in digital appendix E.

Kennecott Utah Copper (KUC) provided the 2017 Bingham Canyon mine model and copy of the MSc thesis by Grün (2007). The Grün's (2007) thesis contains tabulated lists of data used in the analysis presented in this chapter.

The results described in this chapter were presented by Ellis J.F. to Rio Tinto in December 2018 and at the Materials Network Modelling Workshop in Cardiff, June 2019 as a presentation and poster.

5.1. Introduction

Porphyry systems are characterised by complex fracture networks. These networks are formed of spatially and temporally variable fracture and vein systems located in and around intrusive bodies (Tosdal and Richards, 2001 and references therein; Gruen et al., 2010; Harris and Holcombe, 2014). Subvertical patterns of veins observed within porphyry stockworks are typically either pluton-centred (systematic radial-concentric or non-systematic) or aligned to form systematic strike-parallel patterns (Gustafson et al., 1975; Heidrick and Titley, 1982; Titley, 1990). The nature of these arrays results from the relative importance of magmatic and tectonic forces. Systematic patterns may become chaotic at shallower depths where lithostatic loading is lower (e.g., Titley, 1990; Tosdal and Richards, 2001 and references therein, see section 2.1.2 p.19 – 20 for additional details). Distinct mineral infill and alteration assemblages reflect the temperature evolution of the system (e.g., Sillitoe, 2010).

At the large Bingham Canyon Porphyry Cu-Mo-Au deposit veins are considered to be roughly radial to the earliest and volumetrically largest porphyry intrusion (Redmond et al., 2004; Gruen et al., 2010; Redmond and Einaudi, 2010). The approximately radial pattern observed at Bingham Canyon is suggested to result from pressure driven rock extension and to be influenced by regional extension (Gruen et al., 2010; Redmond and Einaudi, 2010). Variations in orientations from the radial pattern are explained by fracturing due to magmatism and hydrothermal circulation (Richards and Tosdal, 2001; Grün, 2007; Gruen et al., 2010).

Since the discovery of the Bingham Canyon deposit in 1863 it has been one of the most studied copper porphyry systems in the world (e.g., Steinberger et al., 2013; Krahulec, 1997; Steinberger et al., 2013). Available data includes geological mapping (Hintze, 1980; Boutwell et al., 1905; Tooker et al., 1970; Morton, 1975; Biek et al., 2007), geochemical data of ore evolution (Rose, 1961; Field and Moore, 1971; Roedder, 1971; Moore and Nash, 1974; Parry et al., 1978; Reid, 1978; Waite et al., 1997; Inan and Einaudi, 2002; Cunningham et al., 2005; Core et al., 2006; Stavast et al., 2006; Seo et al., 2012) and hydrothermal alteration data (Bray, 1969; Moore, 1978; Reid, 1978; Landtwing et al., 2010). Synthesis of this information has been used to produce a detailed understanding of the deposit's intrusive history and paragenesis (Farmin, 1933; Warnaars et al., 1978; Lanier et al., 1978; Redmond et al., 2004; Core et al., 2006; Redmond & Einaudi, 2010; Gruen et al., 2010; Kloppenburg et al., 2010b; von Quadt et al., 2011; Steinberger et al., 2013; Zhang, and Audétat, 2017).

5.2. Geological Overview

The Bingham Canyon deposit is located within the eastern part of the Oquirrh Mountains, ~32 km southwest of Salt Lake City, Utah (Figure 5.1, inset). The deposit is hosted within a large Eocene to Oligocene volcano-plutonic complex (the Bingham Canyon magmatic complex, emplaced between 38.1 and 37.8 Ma; U-Pb Zircon; von Quadt et al., 2011).

In map-view the Bingham Canyon magmatic complex is approximately rectangular to equidimensional (~3 km² northeast-southwest and ~2.5 - 3 km² northwest-southeast; Figure 5.1) as defined by the pre-mineralized equiangular monzonites of the Last Chance stock (38.55±0.19 Ma, U-Pb zircon: Parry et al., 2001) and the Bingham stock. These stocks are connected by the Phoenix dyke (Lanier et al., 1978). The equiangular monzonite (MZ) forming these stocks has steep margins that have vertical dimensions equal to, or greater than, map view dimensions (minimum drilled volume 5.9 km³ based on a minimum estimate of vertical thickness of ~2 km below the 2010 mine surface; Redmond and Einaudi, 2010; Steinberger et al., 2013). The MZ is intruded by a series of ore-related porphyries and dykes (Redmond and Einaudi, 2010). These include the quartz monzonite porphyry (QMP), the porphyritic quartz monzonite Ohio Copper Dyke and latite to quartz latite porphyry dykes and sills (age range 37.74 ± 0.11 Ma to 37.07±0.21 Ma; ⁴⁰Ar/³⁹Ar isotopes of hydrothermal biotite: Parry et al., 2001).

The QMP is the volumetrically largest (minimum drilled volume 0.8 km³, Steinberger et al., 2013) and earliest of the intruding porphyries (Redmond and Einaudi, 2010). The QMP is located along the north-western margin of the Bingham Stock and forms a dyke-like elongate body (Figure 5.2), ~350 m-wide and 1,500 m along a ~northeast axis in map view, and dips ~55 to 60° to the north-west (Redmond and Einaudi, 2010). The boundary between the QMP and MZ is gradational. Mineralisation is centred on the south-eastern contact of the QMP and associated with zoned hydrothermal alteration extending into the monzonite and host rock enclaves of the Bingham Stock, forming a cap around a barren core (Atkinson and Einaudi, 1978; Babcock et al., 1995; Redmond et al., 2004; Gruen et al., 2010; Landtwing et al., 2010; Redmond and Einaudi, 2010; Steinberger et al., 2013). The QMP is cut by laterally extensive (> 8 km), steeply dipping (60° to 75°) northeast trending latite to quartz latite porphyry dykes (widths 10 to 80 m). The dykes are mineralized but to a lesser extent than the QMP.

The Bingham magmatic complex is intruded into several deformed lithotectonic units. The host rocks of the main mineralised intrusive units are the Pennsylvanian age Butterfield Peaks Formation (late Morrowan to Desmoinesian) and overlying Bingham Mine Formation (Missourian to Virgilian) of the Oquirrh Group (Boutwell et al., 1905; Tooker et al., 1970; Lanier et al., 1978; Babcock

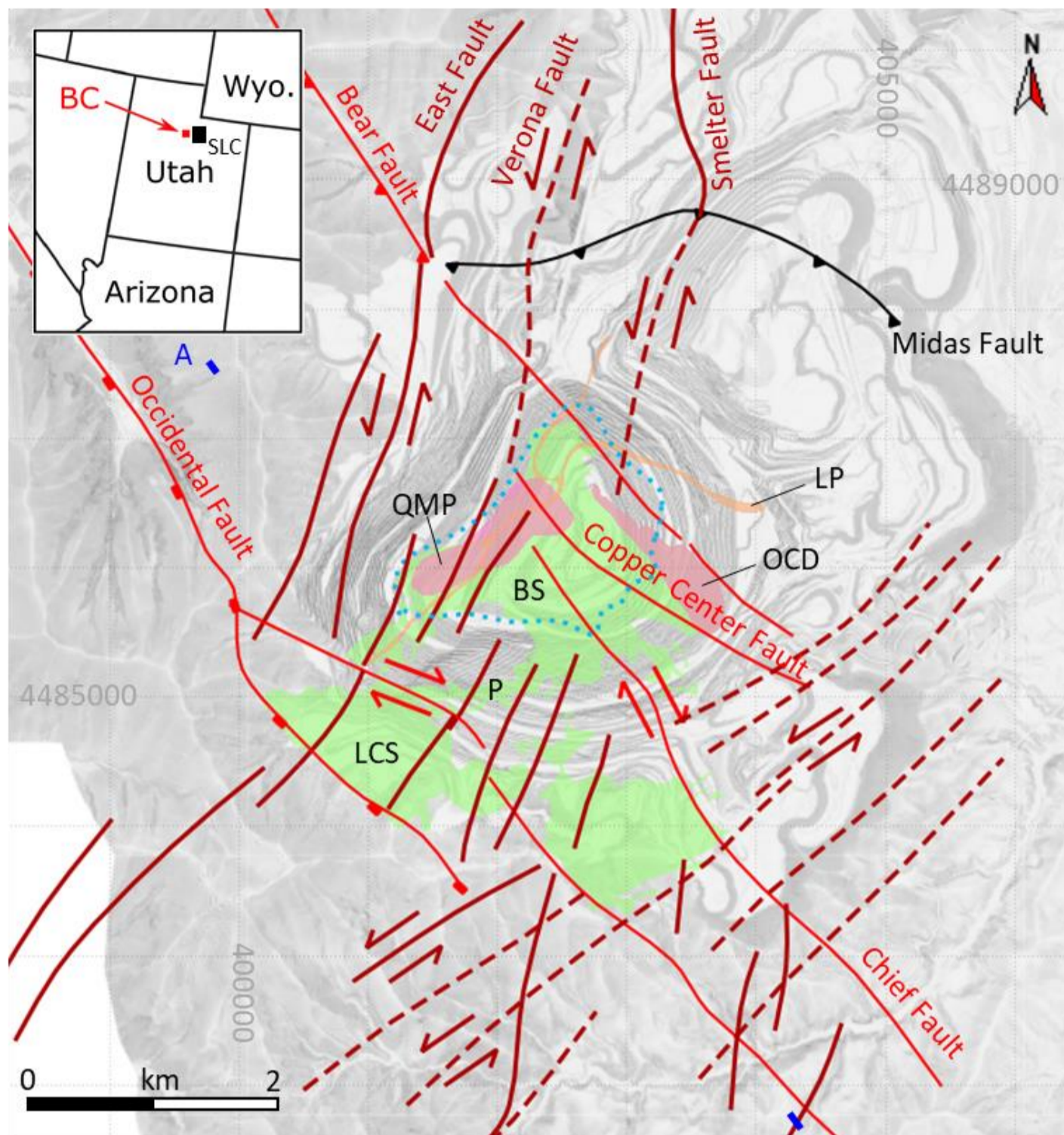
et al., 1995). These units are mainly composed of arkosic orthoquartzites and lesser limestone, calcareous siltstone and sandstones (Calkins et al., 1943; Tooker et al., 1970; Babcock et al., 1995). The Bingham Mine Formation is dominated by quartzites. Structure within the Bingham Mine Formation can be identified by marker beds including the Parnell calcareous sandstone bed and the Jordan and Commercial limestone beds (Figure 5.2). Near the base of the Bingham Mine Formation, the Jordan and Commercial limestone beds and associated skarns form two economically important units (Babcock et al., 1995). Mineralised skarns are found close to and within the enclaves distributed throughout the Bingham stock (Atkinson and Einaudi, 1978).

Prior to the emplacement of the Bingham Canyon magmatic complex, host rock sediments were faulted and folded during the mid-Jurassic Elko orogeny and Late Cretaceous Sevier orogeny (Lanier et al., 1978; Babcock et al., 1995; Presnell and Parry, 1996; Presnell, 1998). Host rock structure can be picked out from the Jordan, Commercial and Parnell beds found within the Bingham Mine Formation (Figure 5.2).

Sedimentary rocks generally strike northeast and dip moderately to the northwest. Near the Bingham Canyon magmatic complex strikes are deflected and trend east-west and northwest-southeast. East-west compression during the Sevier orogeny resulted in thrusting (represented by the southwest dipping Midas thrust in the mine area) and the formation of non-cylindrical shear folding (the Copperton anticline and Rood and Apex folds) (Babcock et al., 1995). The broad open north-west trending Bingham syncline is thought to result from emplacement of the Bingham Canyon magmatic complex (Gruen et al., 2010).

The Bingham Canyon magmatic complex was emplaced in these units at the base of a stratovolcano at an estimated paleodepth of ~ 2 km (Waite et al., 1997; Maughan et al., 2002). At depth (> 5km) the system is thought to link to a large (approximately 2,000 km³) east-west trending batholith (Waite et al., 1997; Steinberger et al., 2013).

The position of the Bingham Canyon magmatic complex is thought to have been controlled by the Uinta axis (see Figure 1.2 p.8), an east-west trending structural boundary separating Archean crust in the north from Paleoproterozoic terrane in the south, and its interaction with the Cretaceous-Tertiary north-south Sevier thrust belt (Presnell, 1998; John, 1997). Space for the emplacement of the Bingham Canyon magmatic complex may have been created by conjugate slip on steeply dipping (~75°) northwest (e.g., the Bear and Occidental faults) and north-northeast-trending faults (e.g., the East fault) and their interaction with low-angle faults (e.g., the Midas thrust) (Kloppenburg et al., 2010b).



- Igneous rock types**
- Quartz Latite and Latite porphyry dykes
 - Quartz Monzonites
 - Equigranular Monzonite
 - >0.35 wt.% Cu grade shell
- Faults**
- NW-trending
 - Normal fault
 - Reverse fault
 - Shallow angle thrust
 - NE-trending (dashed inferred)

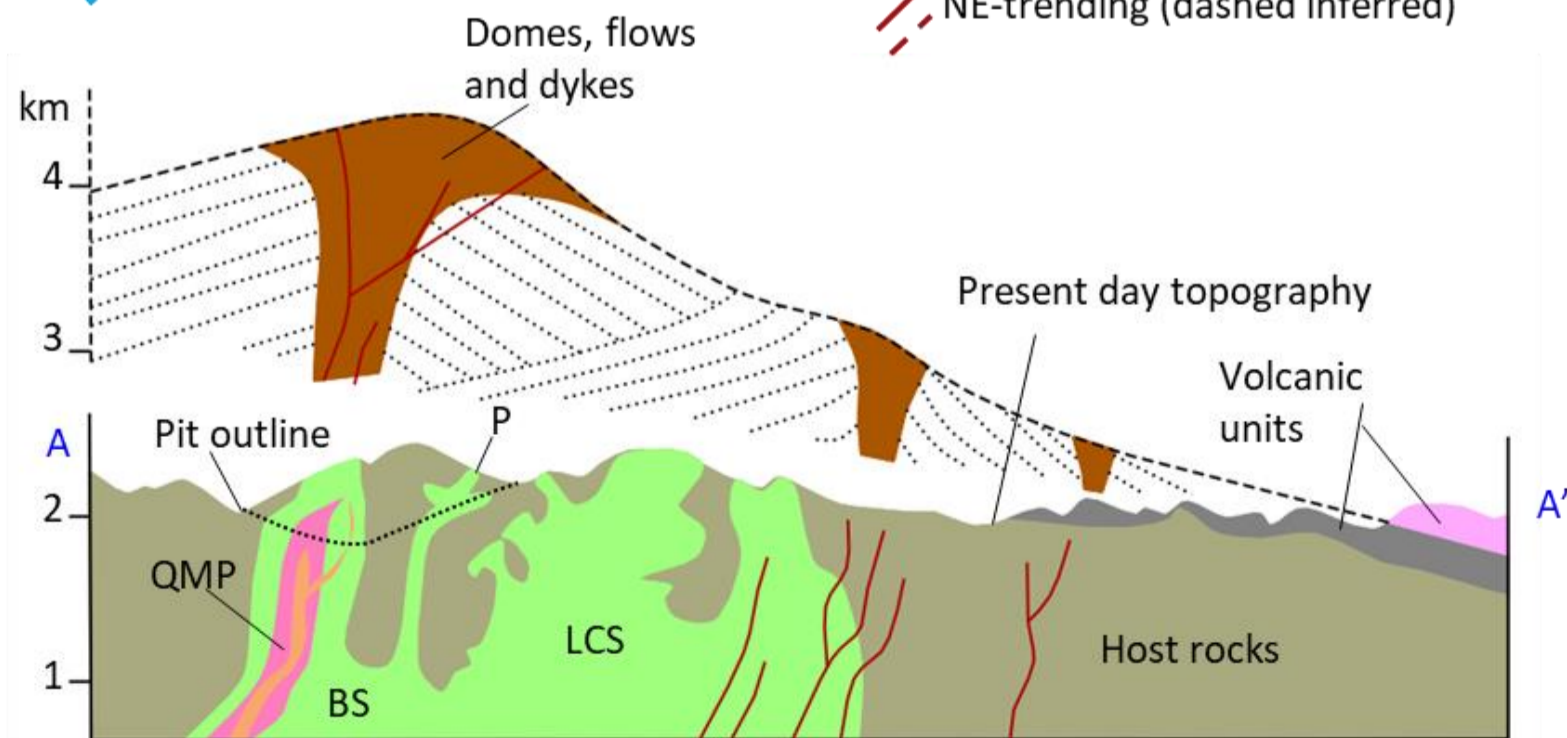


Figure 5.1. Regional geological map and section of the Bingham Canyon magmatic complex. Geological map of the Bingham area showing main elements of the fault framework and intrusive units after Kloppenberg et al. (2010b) SLC – Salt Lake City, BS – Bingham stock, LCS – Last Chance stock, QMP – quartz monzonite porphyry, OCD – Ohio Copper Dyke. Inset showing location of the Bingham Canyon deposit in Utah. Northwest-southeast cross section showing the hypothetical stratovolcano above the Bingham Canyon magmatic complex (modified from Denio and Keith, 1997; Waite et al., 1997).

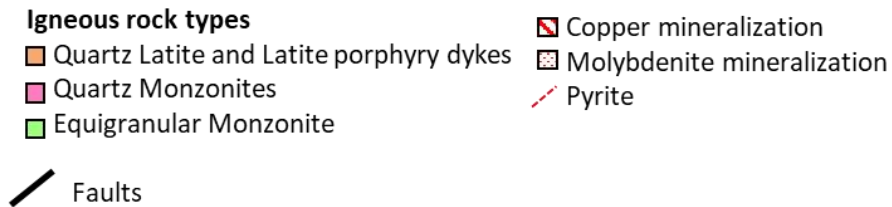
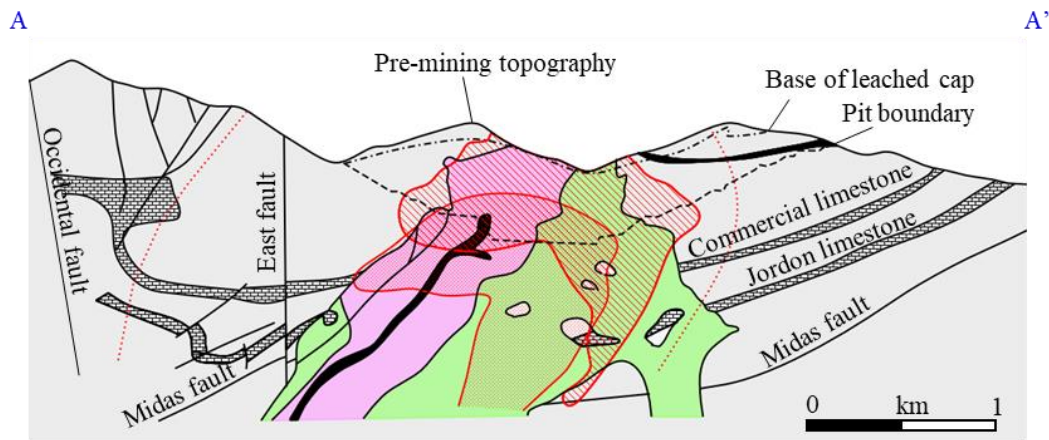
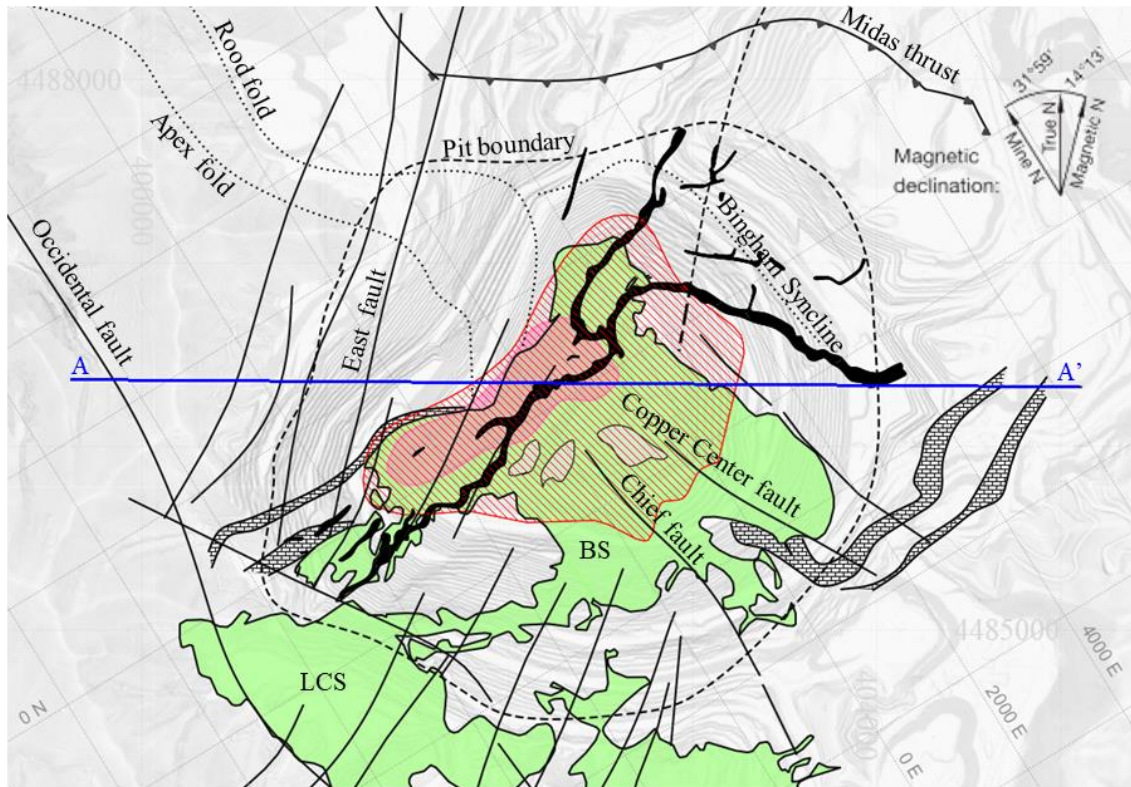


Figure 5.2. Local geological map and section of the Bingham Canyon magmatic complex. Geological map of the Bingham area showing main elements of the fault framework and intrusive units after Grün, 2007. BS – Bingham stock, LCS – Last Chance stock, QMP – quartz monzonite porphyry, OCD – Ohio Copper Dyke. East-west cross section showing the structure of the Bingham Canyon deposit (modified from Babcock et al., 1995).

Activation of the two conjugate sets of steep faults is thought to have resulted in local extension into which the dykes and sills of the Bingham Canyon magmatic complex intruded (Kloppenburg et al., 2010b). The geometry of the QMP and latite dykes is interpreted to infer an active northwest-southeast extensional regional stress field during emplacement (Redmond and Einaudi, 2010).

Post emplacement and mineralisation, Miocene Basin and Range tectonics have tilted the deposit and host rocks 10° to 30° down to the east (Table 5.1). This tilting was the result of extensional movement on approximately north-trending faults (Presnell, 1998; Vogel et al., 2001). This regional east-west extension was associated with the development and movement on northwest-trending normal faults (Lanier et al., 1978) and reactivation of some of the pre-existing northeast-trending structures (Presnell, 1998).

Tilting estimate	Method	Reference
15° to 30° eastward	Attitude of pyroclastic rocks on eastern range front	Smith, 1961
~ 25° eastward	Assuming axis of metal was vertical	Atkinson and Einaudi, 1978
17° eastward	Tilting of ore shell	Lanier et al., 1978
10.8±4.0° eastward	?	Melker and Geissman, 1998 (given in Maughan and Keith 2002)
30° eastward	Tilting of QMP to near vertical	Redmond and Einaudi, 2010

5.3. Early Fracturing in and around the Bingham Canyon Magmatic Complex

Geometric relationships between the intrusions, vein generations and mineral distribution have been documented within the stocks (Redmond et al., 2004; Tooker, 2005; Gruen et al., 2010; Styles et al., 2011). Three key vein generations include the stockwork veins, molybdenite-veins and late quartz-pyrite veins associated with sericitic alteration (QSP veins). The classification is based on mineral characteristics and cross cutting relationships (Gruen et al., 2010). The early stockwork veins are associated with Cu-Au and were emplaced post-QMP intrusion and pre-latite dykes. Molybdenite-veins post-date latite dykes (Redmond et al., 2004; Inan and Einaudi, 2002; Landtwing et al., 2010). The later, quartz-pyrite vein stage is associated with sericitic alteration (QSP veins) and post-dates economic mineralisation (Redmond et al., 2004; Redmond and Einaudi, 2010; Gruen et al., 2010).

Vein distribution and orientation is variable across the deposit (Figure 5.3, Gruen et al., 2010). Stockwork and molybdenite-veins are most abundant in the centre of the pit. Stockwork veins have an approximately radial orientation centred on the QMP intrusion. Molybdenite veins are the least abundant vein type in the measured data and have a variable orientation. The resulting molybdenite mineralization has a similar shape but deeper distribution to the copper ore shell (Figure 5.1). QSP veins are frequent around the periphery of the QMP and strike away from the axis of the elliptically shaped QMP intrusion (Figure 5.3).

Mineralisation is associated with zoned hydrothermal alteration and forms a cap around a barren core (Babcock et al., 1995; Gruen et al., 2010; Landtwing et al., 2010; Steinberger et al., 2013). The main pulse of Cu-Au mineralization is centred in the early quartz stockwork veins on the south-eastern contact of the QMP, extending into the monzonite and host rock enclaves of the Bingham stock (Atkinson and Einaudi, 1978; Redmond et al., 2004; Redmond and Einaudi, 2010). Copper mineralization is estimated to have occurred at temperatures of 320 °C to 430 °C and pressures of 9 to 26 MPa. The later molybdenite-veins are estimated to have formed at temperatures of 360 °C to 580 °C and at pressures of 14 to 71 MPa (Redmond et al., 2004; Landtwing et al., 2010). Re-Os dating of molybdenite veins gives ages of 37.3 to 36.8 Ma (Chesley et al., 1997). Dating therefore suggests the ore-related hydrothermal alteration began shortly after monzonite emplacement (around 0.75 million years; Parry et al., 2001; Gruen et al., 2010; Landtwing et al., 2010; Redmond and Einaudi, 2010).

The evolution of the vein network has been related to a stress field fluctuating between magmatic control (low differential stress) and tectonic control (Figure 5.4 after Gruen et al., 2010). The vein geometry progression from irregular wavy to straight-walled is consistent with a transition

from plastic to brittle conditions during cooling (Fournier, 1999; Redmond and Einaudi, 2010). The maximum principal stress during vein formation is estimated to be approximately parallel to the north-west dip of the QMP stock (Gruen et al., 2010). Magmatic stresses are attributed to doming above the QMP, resulting in a roughly radial pattern of fractures around the stock. A later tectonic stress regime of north-northwest extension is inferred to control the elongate nature of later porphyry intrusive bodies and dykes and to have influenced later fracturing events (Grün, 2007; Gruen et al., 2010).

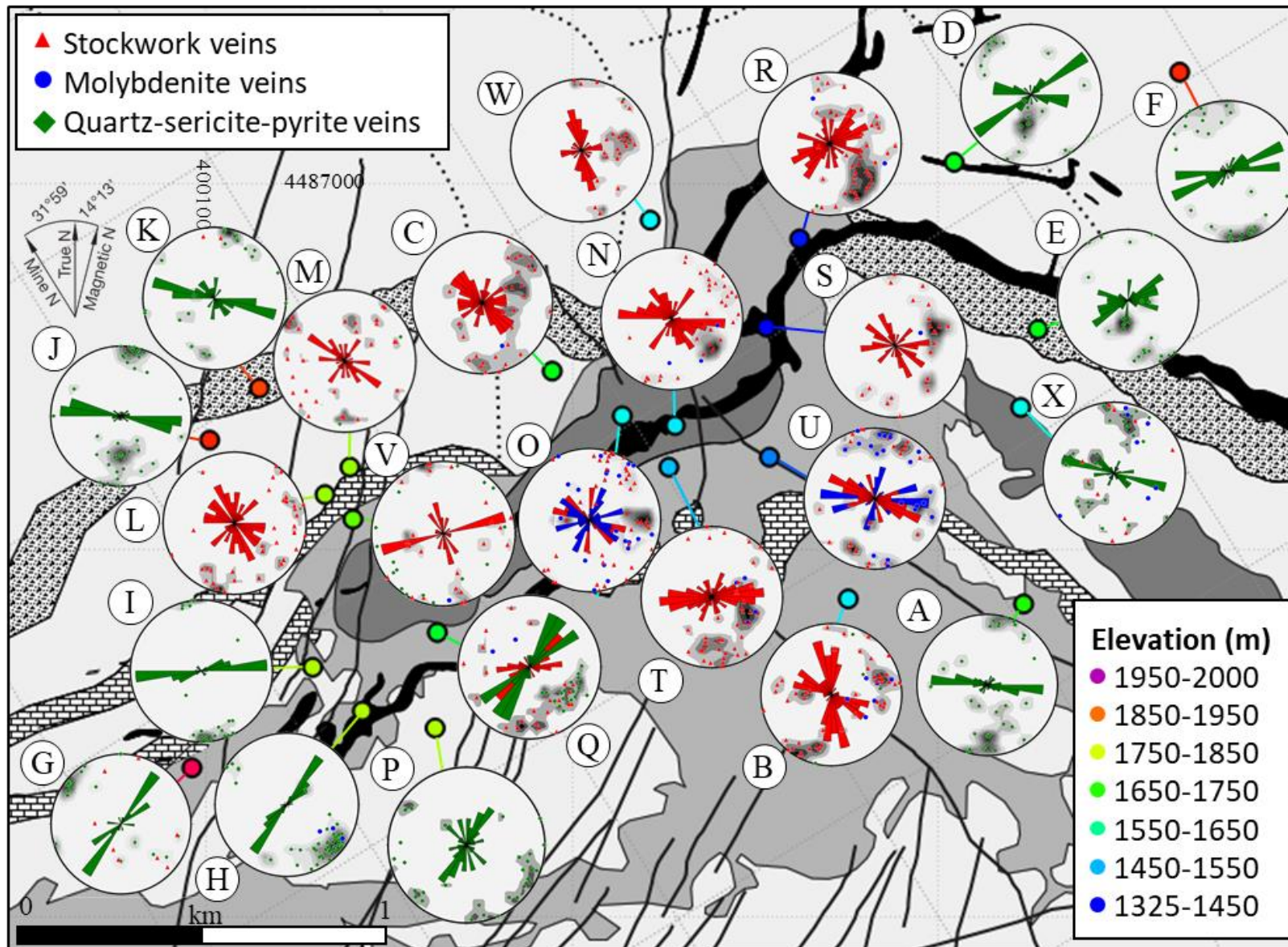


Figure 5.3. Veins plotted as poles on equal area lower hemisphere Schmidt nets. Vein types are distinguished by coloured triangles, circles and diamonds. Contour for density 1% area (interval 5, significance 3, grid 20). Rose diagrams, coloured for vein type, are overlain. Rose diagrams are only shown for locations with more than 20 readings for vein type. Locations are colour mapped for elevation. Data from Grün (2007) and this study.

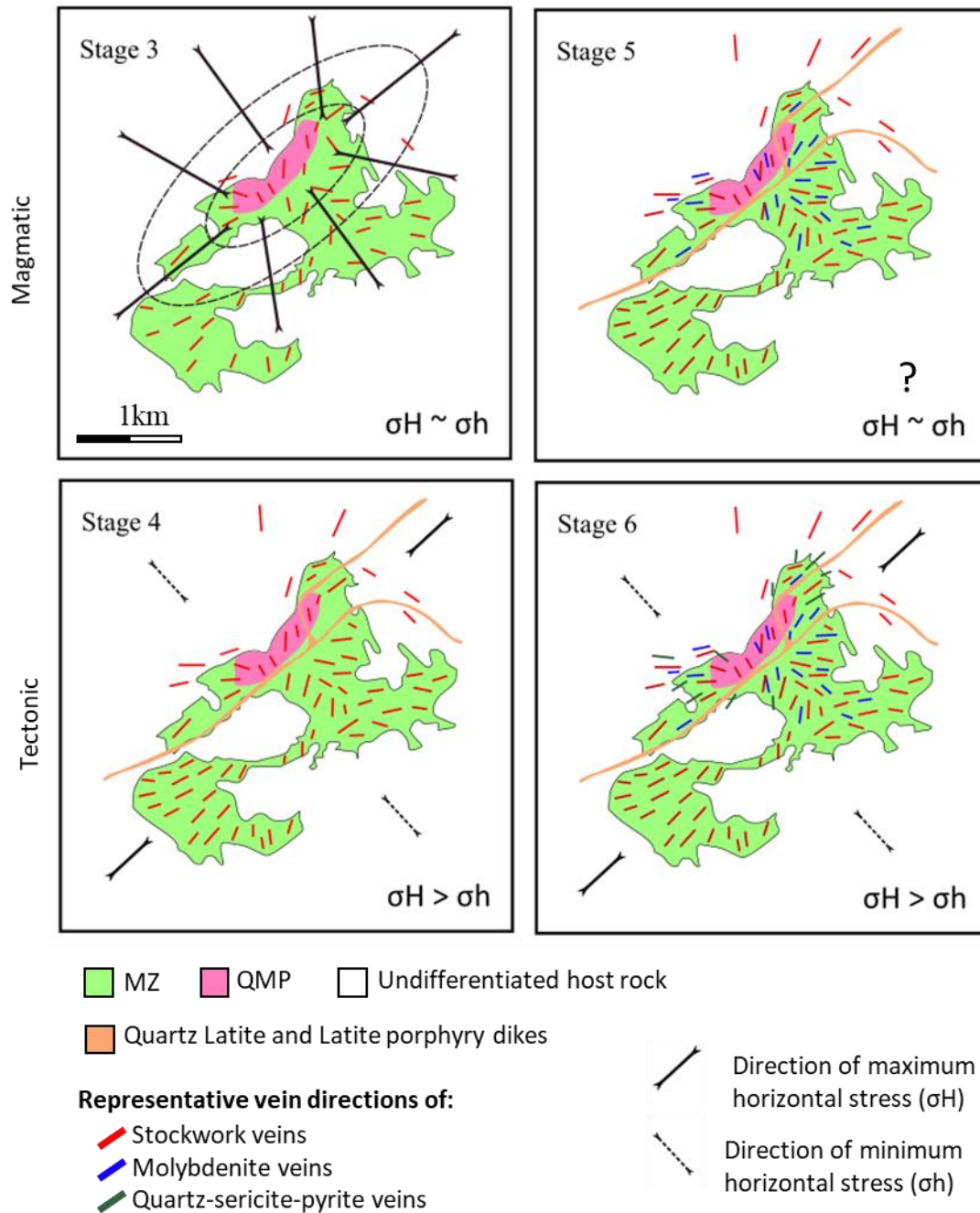


Figure 5.4. Map sketches illustrating the sequence of vein formation at the Bingham Canyon deposit after Gruen et al. (2010). Sketches illustrate the geometry of intrusions and the orientation of veins and idealised local stress regime variation between magmatic, when horizontal stresses are near subequal (stages 3 and 5), and tectonic when horizontal stresses are significantly different (stages 4 and 6). Doming above the QMP intrusion due to underlying fluid overpressure is suggested to approximately control the radial fracture patterns (Gruen et al., 2010). Stages 1 – 2 of this model, not shown, relate to the emplacement of the MZ and QMP stocks prior to formation of veins referred to in this study.

5.4. Methodology

Numerical modelling of cooling plutonic rocks has shown that thermal stresses should have an important control on early fracture orientation (see chapter 3). Despite the expected influence of temperature on early fracture formation, hydraulic pressure and local stretching of the host rock are generally considered to be the most important fracture-forming processes in mineralised intrusions (Burnham, 1979; Gustafson and Hunt, 1975; Fournier, 1999). In this study the results of numerical modelling are compared to paleostress estimates calculated from vein orientations measured during field work. This comparison is used to determine the influence of thermal stress on fracture orientations and veining events at the Bingham Canyon magmatic complex. Figure 5.5 shows the implemented workflow.

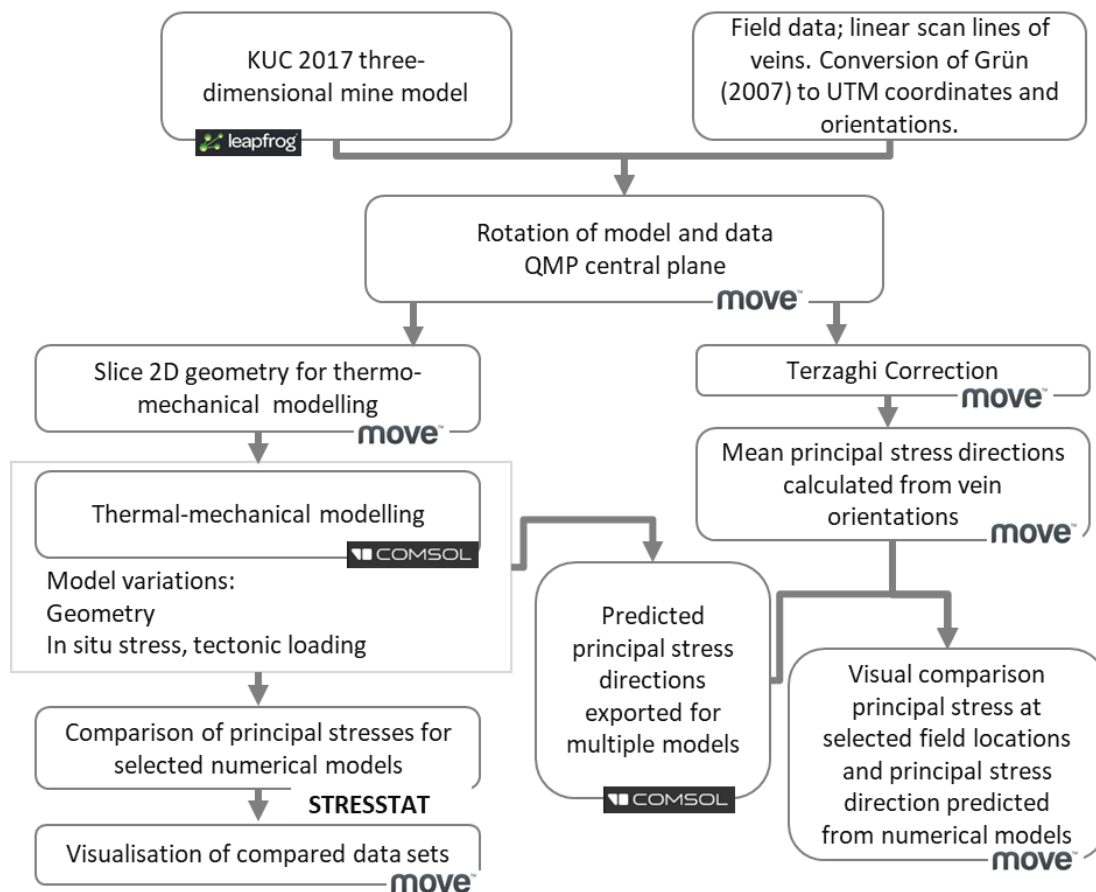


Figure 5.5. Workflow. COMSOL Multiphysics®, MOVE™ and Leapfrog are commercial software packages. STRESSTAT was developed by Lisle and Orife, (2002) and Orife and Lisle (2003).

5.4.1. Numerical Modelling

The workflow is based on models developed in chapter 3. The Bingham Canyon magmatic complex is modelled as a hot domain within a colder host rock domain (Bergbauer and Martel, 1999; Žák et al., 2006). Seven two-dimensional models are run (Table 5.2). The boundaries defining the Bingham Canyon magmatic complex and key host rock units were obtained from the Kennecott Utah Copper (KUC) 2017 three-dimensional mine model (appendix C workflow C5-1 p.336). The full 3D model was too complex a geometry to import and run in COMSOL Multiphysics® even with downsampling.

Prior to numerical modelling the Kennecott Utah Copper (KUC) 2017 the three-dimensional mine model was rotated so that the QMP stock was vertical (Figure 5.6). The central plane of the QMP intrusion was rotated to vertical as the maximum principal stress for vein formation is estimated to be approximately parallel to the north-west dip of the QMP stock (Gruen et al., 2010). Rotation of the QMP stock to vertical means that the maximum principal stress recorded from the field is near vertical (Grün, 2007; Gruen et al., 2010) and can be compared to the two-dimensional numerical models, where one principal stress is fixed to vertical.

Models BC-1 to BC-4 are based on horizontal sections from the rotated KUC 2017 mine model (Figure 5.7). Model BC-5 is a representative section averaged from the geometry of models BC-1 to BC-4 (Figure 5.8). In model BC-6 internal host rock enclaves were removed from the intrusion to assess enclave influence on model results. In model BC-7 the influence of tectonic load is tested.

Table 5.2. COMSOL® models runs

Model number	Description
BC-1	2d level 1 see Figure 5.5
BC-2	2d level 2 see Figure 5.5
BC-3	2d level 3 see Figure 5.5
BC-4	2d level 4 see Figure 5.5
BC-5	Representative section, see Figure 5.6
BC-6	Representative section no enclaves
BC-7	Representative section tectonic load

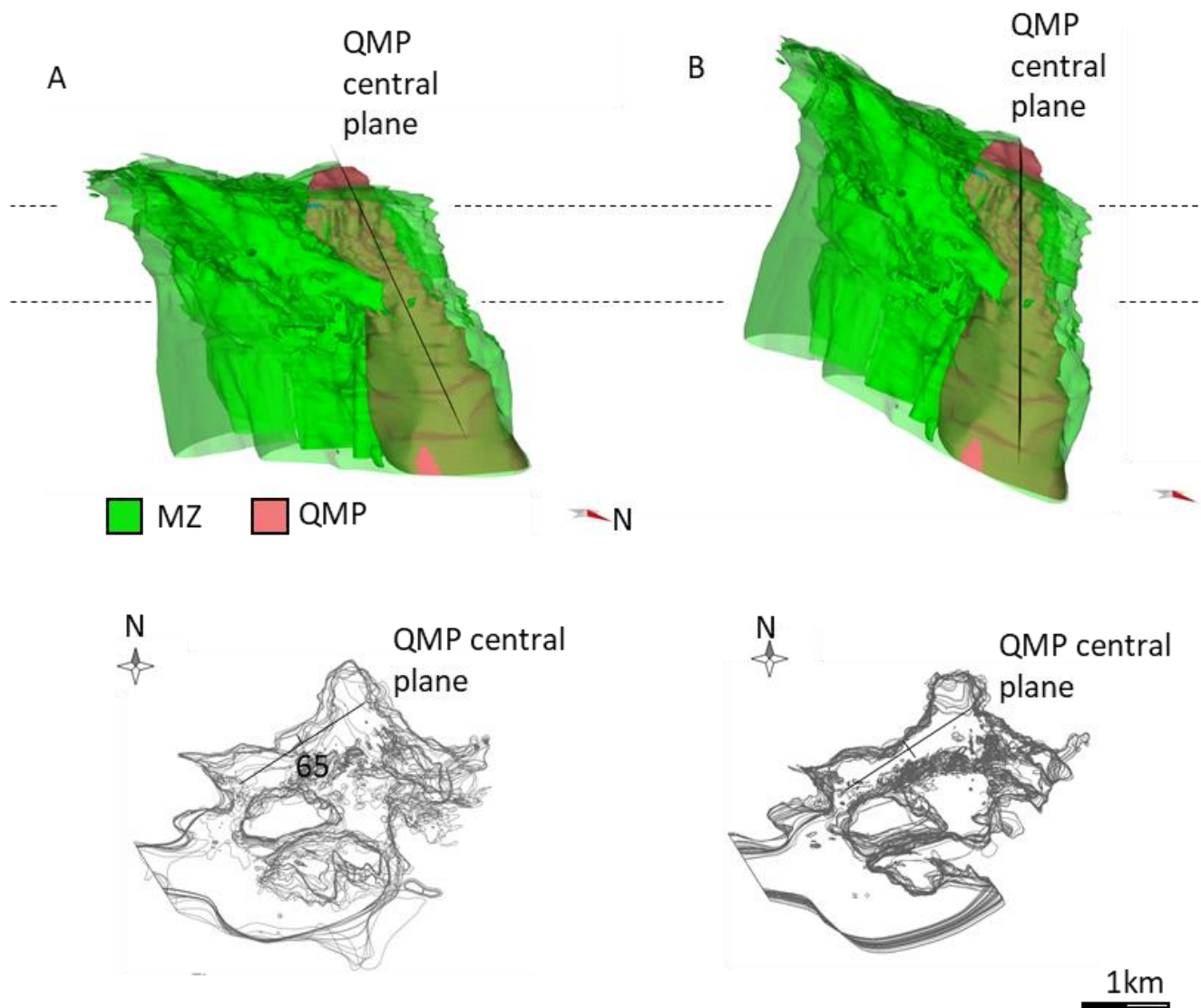


Figure 5.6. Monzonite (MZ) and quartz monzonite porphyry (QMP) from the Kennecott Utah Copper (KUC) 2017 three-dimensional mine model. Top row images show the three-dimensional model of the Bingham and Last Chance stocks (green) and QMP (pink). Bottom images are map projections of multiple horizontal sections cut through the model between the interval given by the dotted lines. (A) Model prior to rotation (B) rotated around the QMP central plane. After model rotation stock margins are near vertical.

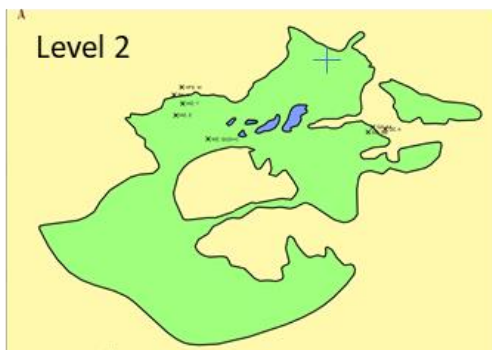
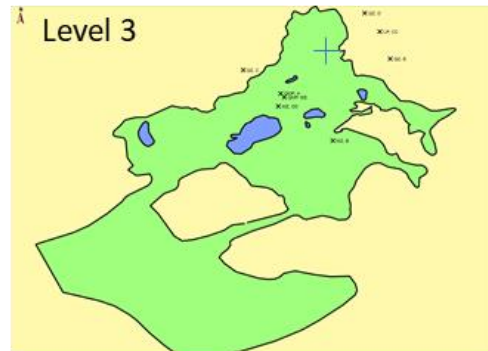
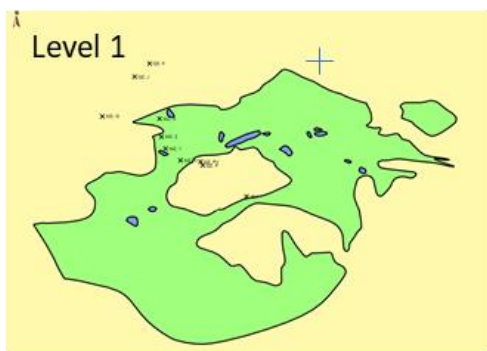
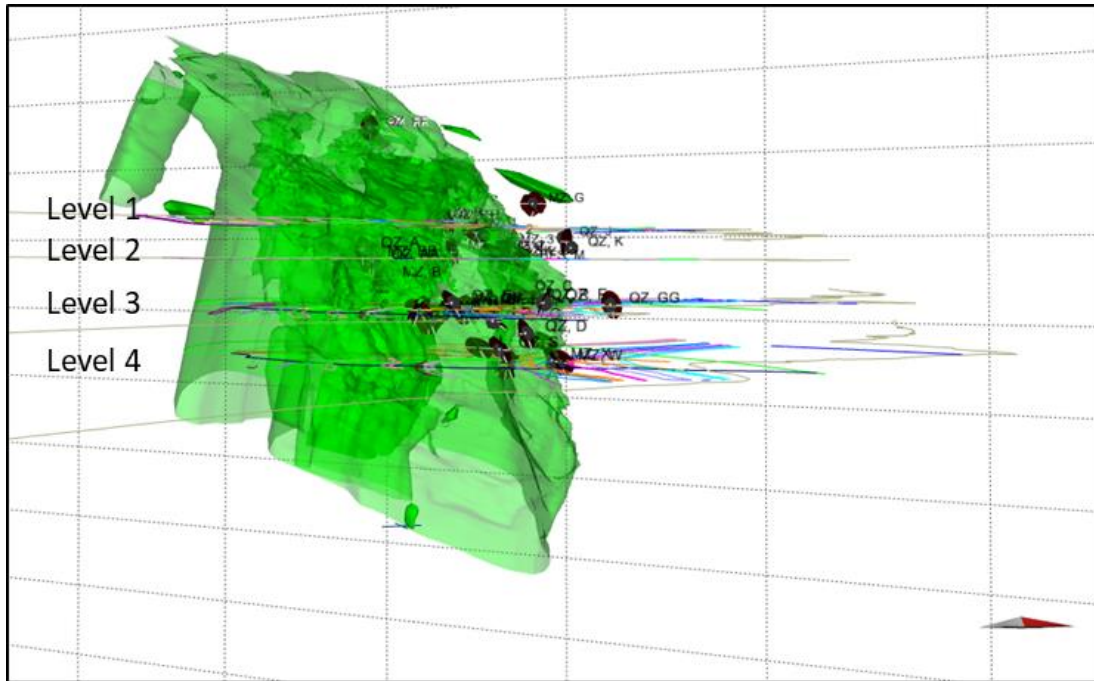


Figure 5.7. Levels sliced from KUC 2017 mine model used as geometries in models BC-1 to BC-4. Blue cross marks x 0, y 0 position in the rotated mine model.

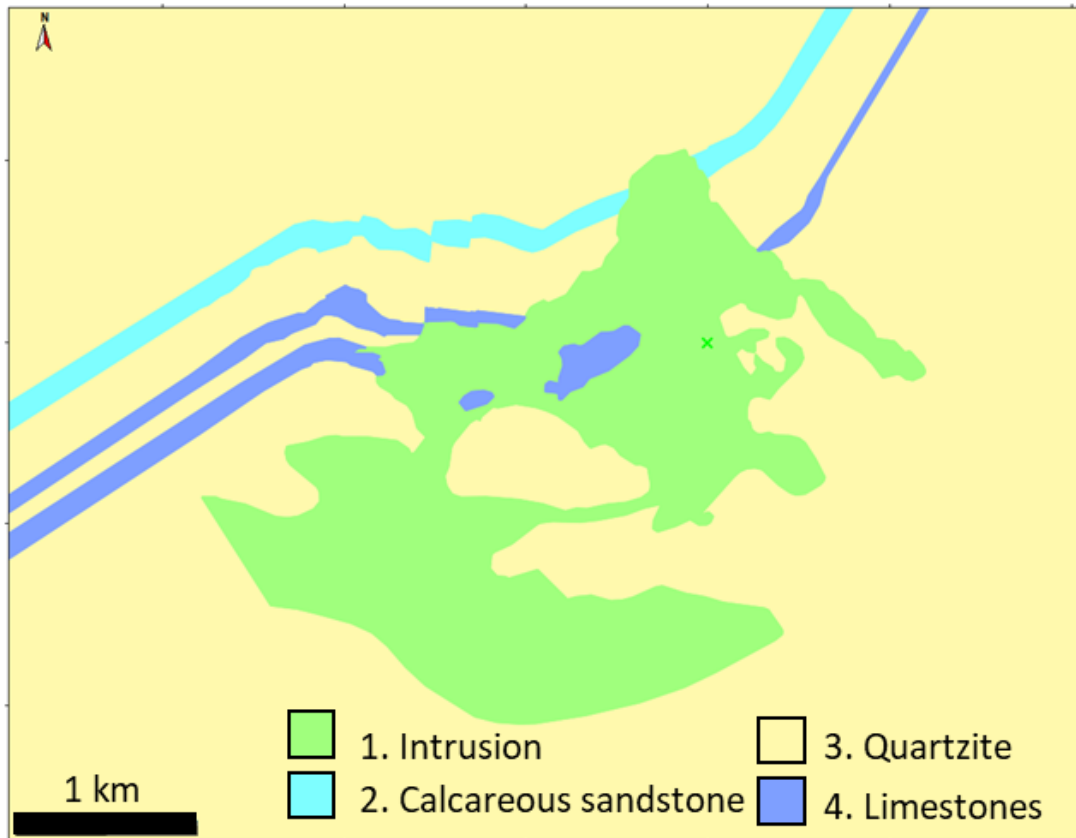


Figure 5.8. Geometry used in models BC-5 to BC-7. Limestone enclaves within the intrusion are not included in model BC-6.

The geometry of the Bingham Canyon magmatic complex used in the model is based on the outer limit of the modelled intrusions. The Bingham Canyon magmatic complex is treated as a homogenous unit and intrusive units. The MZ and QMP units and minor latite dykes are not distinguished. Although units were emplaced incrementally, the gradational boundaries between the MZ and QMP intrusions suggest that temperature remained high during emplacement and only local reheating occurred after QMP intrusion (Redmond et al., 2004). The latite dykes are volumetrically small and are unlikely to have had a significant effect on the thermal history.

In the two-dimensional model, the Bingham Mine Formation host rock domain is divided into three separate units including quartzites, and the Parnell, Jordan and Commercial beds (Figure 5.8). The boundary of this domain is a square of 100 km² so that the boundary remains at a constant temperature during modelling (e.g., Bergbauer and Martel, 1999; Žák et al., 2006). The Bingham Canyon magmatic complex is positioned approximately at the centre of the host rock square.

Material properties are characterized by the density, heat capacity, conductivity and coefficient of thermal expansion (Table 5.3). As no direct measurements of the thermal properties of the Bingham Canyon magmatic complex and host rock were available, values are based on data from similar studies and rock types given in literature.

Table 5.3. Material properties of the domains defined in the thermomechanical model

Parameter		1. Intrusion	2. Calcareous sandstones	3. Quartzite	4. Limestones
Density	[kg/m ³]	2880 [*]	2700 [†]	2600 [*]	2800 [*]
Young's Modulus	[GPa]	27.5 [*]	20 [§]	23.5 [*]	34 [*]
Possion's ratio	[1]	0.2 [*]	0.21 [§]	0.27 [*]	0.25 [*]
Thermal conductivity	[W/(m. K)]	1.8 [†]	2.2 [†]	3 [†]	2 [†]
Heat capacity at constant pressure	[J/(kg. K)]	1450 [†]	1000 [†]	1100 [†]	1050 [†]
Coefficients of thermal expansion	[1/K]	8 e-6 [‡]	10e-6 [‡]	7e-6 [‡]	8e-6 [‡]

* Styles, et al., 2011.
† Cook, S.J. and Bowman, J.R., 1994.
§ Gercek, H., 2007.
‡ Huotari, T. and Kukkonen, I., 2004.

Uniform temperature values were assigned to the intrusion unit and host rock domains. The initial temperature of the Bingham Canyon magmatic complex was set to 750 °C. In the host rock the selected temperature was based on a geothermal gradient of 35 °C/km (e.g., Bergbauer and Martel, 1999). For the two-dimensional models a host rock temperature of 140 °C was used, estimated as the temperature at a depth of ~4 km. Sensitivity tests for the QMP intrusion being hotter relative to the MZ stocks were also run (see appendix C. Figure C5-4 p.345). The initial temperature variation makes no difference to modelling results.

In model BC-7, a regional tectonic load was defined with minimum horizontal stress in a northwest-southeast orientation (328° – 148°), minimum horizontal stress was lowered by 50% of the estimated horizontal load. The horizontal load was estimated to be approximately 1/3 of the overburden at 4 km depth (section 2.5.1. equation 2 p.30). The estimated tectonic load orientation is based on the elongate geometry of the QMP and LP dykes and inferred emplacement into an extensional stress regime (Redmond and Einaudi, 2010; Gruen et al., 2010).

The boundary lines of the defined geometries were sampled at 100 m. In the two-dimensional models a maximum meshed triangular element size of 200 m was used within the stock, increasing to 10 km at the boundaries of the host rock domain. In the three-dimensional models a minimum element size of 50 m was set in the intrusive domain and minimum element size of 100 m in the host rock domain. The models were run for a million years using a time step of 100 years. These parameters were selected based on repeatability of modelling results and run time.

5.4.2. Field Data and Estimation of Paleostress

Within the mine a complex array of fractures representing fracturing events throughout the entire geological and recent excavation of the mine exist (Figure 5.10). Vein orientation data was used to estimate the stress distribution of the early fracturing events. This is because vein fills can be used to identify fractures that were open during the early hydrothermal history of the deposit.

Vein orientations and aperture, were collected along linear scan lines and paleostress orientations were estimated (after Grün, 2007). Field data used, included that collected by Grün (2007) and additional data collected in this study in 2017 and 2018 (appendix C Figure C5-1, p.341). Using the rotation function in MOVE™ stereonet analysis, the data was rotated around the QMP central plane to be comparable to the rotation applied to the KUC 2017 three-dimensional mine model (appendix C workflow C5-1, p.336). Data collected by Grün (2007) was then rotated from mine North to UTM north prior to analysis (appendix C workflow C5-2, p.336). A table relating the field location labels from Grün (2007) and field work in this study to the labels given in Figures 5.3, 5.9 & 5.16 can be found in appendix C Table C5-7 p.342.

Prior to estimates for minimum tensile stress orientation, the data was corrected for scan line bias using Terzaghi correction (Terzaghi, 1965) in MOVE™ 2018.2. The recorded orientation measurements are plotted as poles on the lower hemisphere Schmid equal area projection. Paleostress tensors were established at locations with a minimum of 20 orientation measurements for a given vein type. It is assumed veins formed by Mode I failure.

The geometrical distribution of the vein system is used to determine the paleostress tensor (Jolly and Sanderson, 1997). The axis of the dominant minimum compressive stress is taken to be in the direction of the highest pole density (André et al., 2001; Grün, 2007; Harris and Holcombe, 2014). The angles of maximum and intermediate stresses are calculated in MOVE™ based on the method of Jolly and Sanderson (1997). The strike of the plane perpendicular to this pole is assumed to represent the preferred paleostress orientation of the resulting vein array. After rotation of data around the

QMP central plane the inferred paleostress has a subvertical maximum compressive stress axis and sub horizontal intermediate and minimum compressive stress orientations (Figure 5.9).

The vein array is used to calculate the paleostress tensors and give an estimation of the orientation of the σ_1 - σ_2 plane (perpendicular to the minimum compressive stress σ_3) plane. This method assumes the veins provide a reasonable representation of the stress state in the rock at the time of their formation and that:

- veins of a given type are contemporaneous.
- the dominant fracture array exploited by the vein network formed early in the cooling history and developed with respect to the stress field at any given point.
- any fractures without mineral fill were not preserved and did not influence the stress state of the rock during subsequent fracturing events.
- early veining events are sealed due to mineral precipitation so that the rock mass can be considered a homogenous unit during subsequent fracturing events.

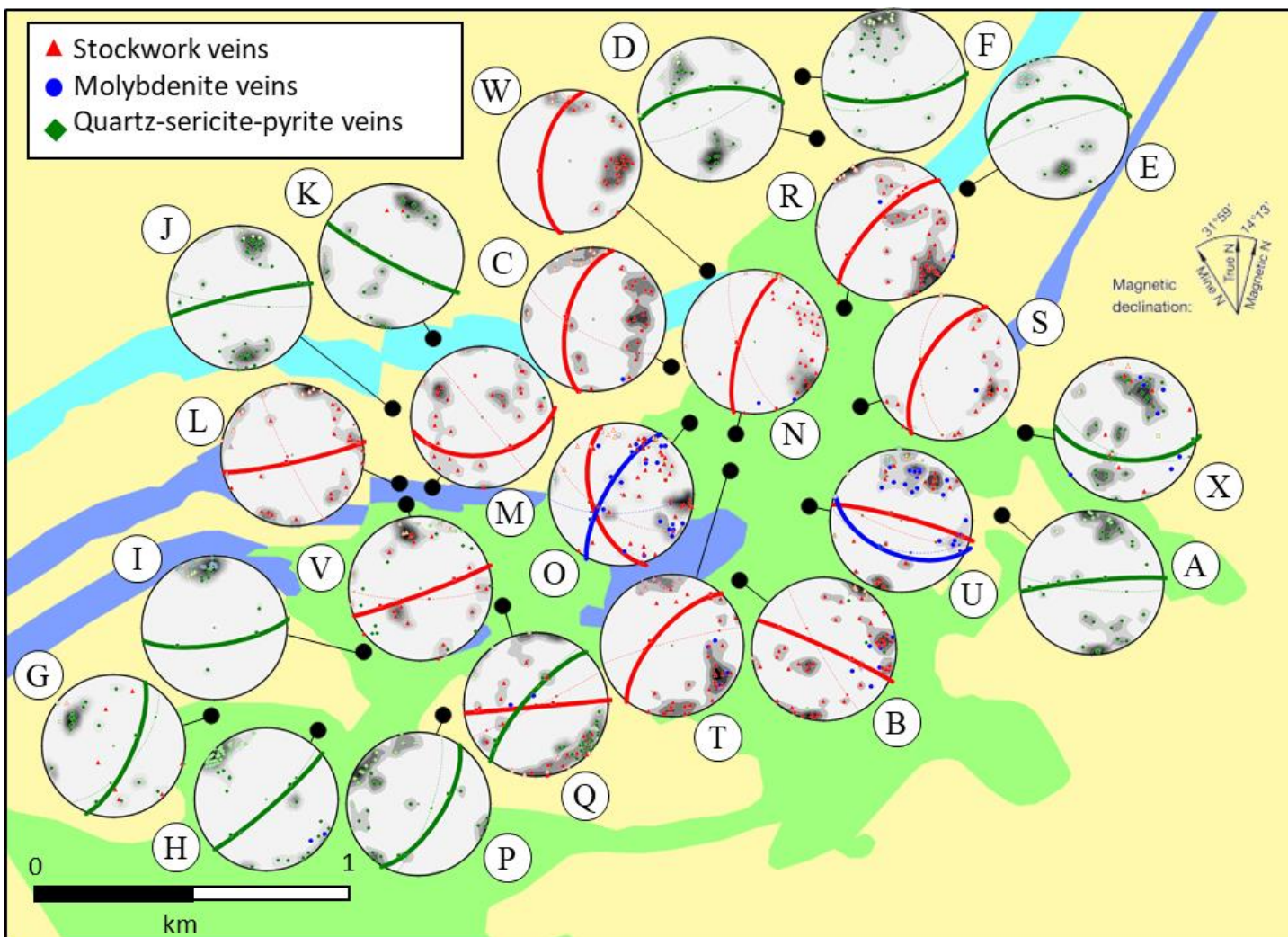


Figure 5.9. Summary of surface measurements (poles) and estimated paleostress orientations. All data is rotated around the QMP central plane and relative to true north. Poles of vein type are represented by red triangles (stockwork veins), blue circles (molybdenite veins) and green diamonds (QSP veins). Planes are representative of the σ_1 - σ_2 plane (perpendicular to the minimum compressive stress, σ_3) estimated from paleostress analysis. Dashed lines are paleostress planes without the Terzaghi bias correction applied.

5.4.3. Comparison of Numerical Models

Calculated principal stress orientations in models BC-5 to BC-7 (i.e., the two-dimensional representative model with different initial conditions) are compared statistically using STRESSTAT (Lisle and Orife, 2002; Orife and Lisle, 2003). Data is compared on a grid of 100 m spacing over the intrusion (Figures 5.12).

STRESSTAT calculates the stress difference (D) between two given stress tensors (Lisle and Orife, 2002; Orife and Lisle, 2003). Data is imported to STRESSTAT as a text file that compares pairs of sequential rows of stress tensors. Each row contains five, tab separated, numbers in the order: maximum compressive principal stress plunge (a1), maximum compressive principal stress plunge azimuth (p1), minimum compressive principal stress plunge (a3), minimum compressive principal stress plunge azimuth (p3) and the stress ratio (R) (Lisle and Orife, 2002). The stress ratio (R) is defined as: $\phi = (\sigma_2 - \sigma_3) / (\sigma_1 - \sigma_3)$; $\sigma_1 > \sigma_2 > \sigma_3$ where compression is considered positive. The resulting stress difference values are defined as: very different ($D > 1.71$), different ($D 1.01 - 1.71$), similar ($D 0.66 - 1.01$) or very similar ($D < 0.66$) (Orife and Lisle, 2003). Results of the comparison between given models are loaded as points in MOVE™ and the D values coloured mapped based on the given ranges of D.

5.4.4. Comparison of Numerical Models to Field Data

Comparison is made between the strike direction of the plane perpendicular to the minimum principal stress direction from the numerical models and the equivalent paleostress direction estimated from field data. Principal stress orientation data was exported from COMSOL Multiphysics® and loaded into MOVE™ for comparison with paleostress orientations estimated from field work (appendix C workflows C5-3 to C5-5, p.337 - 338).

The Wilcoxon signed-rank test is used to assess if samples from the field data and selected time-steps of COMSOL Multiphysics® models are statistically different. It is applied as the difference between the two samples cannot be assumed to have a normal distribution. The null hypothesis is that the median difference between pairs of observations is zero.

The difference in strike directions between each sample site and the numerical model is classified as $< 20^\circ$ difference (green), 20° to 30° difference (orange) or $> 30^\circ$ difference (red). The classification is based on uncertainty inherently included with in the models as a result of field data collection and boundary geometry shape. The ranges for classification of fit between orientation data is based on data uncertainty.

5.5. Numerical Modelling Results

Results from models BC-5 to BC-7 are presented. Models BC-1 to BC-4 (appendix C Figure C5-2 & C5-3, p.343 - 344) were run to confirm the geometry selected for use in models B-5 to BC-7 was reasonable. Modelling outputs include the cooling history, orientations of the principal stress axes, the magnitude of principal stresses and the elastic strain energy (considered by Gerla (1983) to possibly correlate to fracture density). The time steps presented are chosen to highlight key changes in the direction of the principal stresses over time.

5.5.1. Cooling History

The intrusive domain cools continuously. The margins of the intrusion cool the fastest. As the intrusion cools, the thermal pattern becomes roughly elliptical, elongate along an approximately northeast-southwest trend. Two centres located centrally within the Bingham stock and Last Chance stock remain hottest for longest (Figure 5.10). Within the host rock and enclave domains, temperatures initially increase and then decrease. As the enclaves are heated and then cool their influence on the cooling patterns is reduced. Enclaves and narrow domains of host rock are heated to temperatures comparable to the intrusive domain. Temperature in the surrounding host rock reaches a maximum of ~400 – 500 °C.

Cooling times are influenced by the initial temperature and thermal conductivity of the units. Using the values given in Table 5.3, the centre of the stock cools to within 100 °C of the host rock temperature (105 °C) 10,000 years after model initiation (Figure 5.11). If initial temperature of the intrusion is decreased to 550 °C, the estimated maximum temperature for magmatic-hydrothermal fluids in porphyry systems (Berger et al., 2008), the cooling time is decreased by 100,000 years (Figure 5.11, and appendix C Figure C5-4, p.345). Increasing the thermal conductivity value increases the rate of cooling, which is likely to be high due to fluid flow and convective heat transfer. Patterns of principal stress at times of similar temperature distributions are unaffected by these changes.

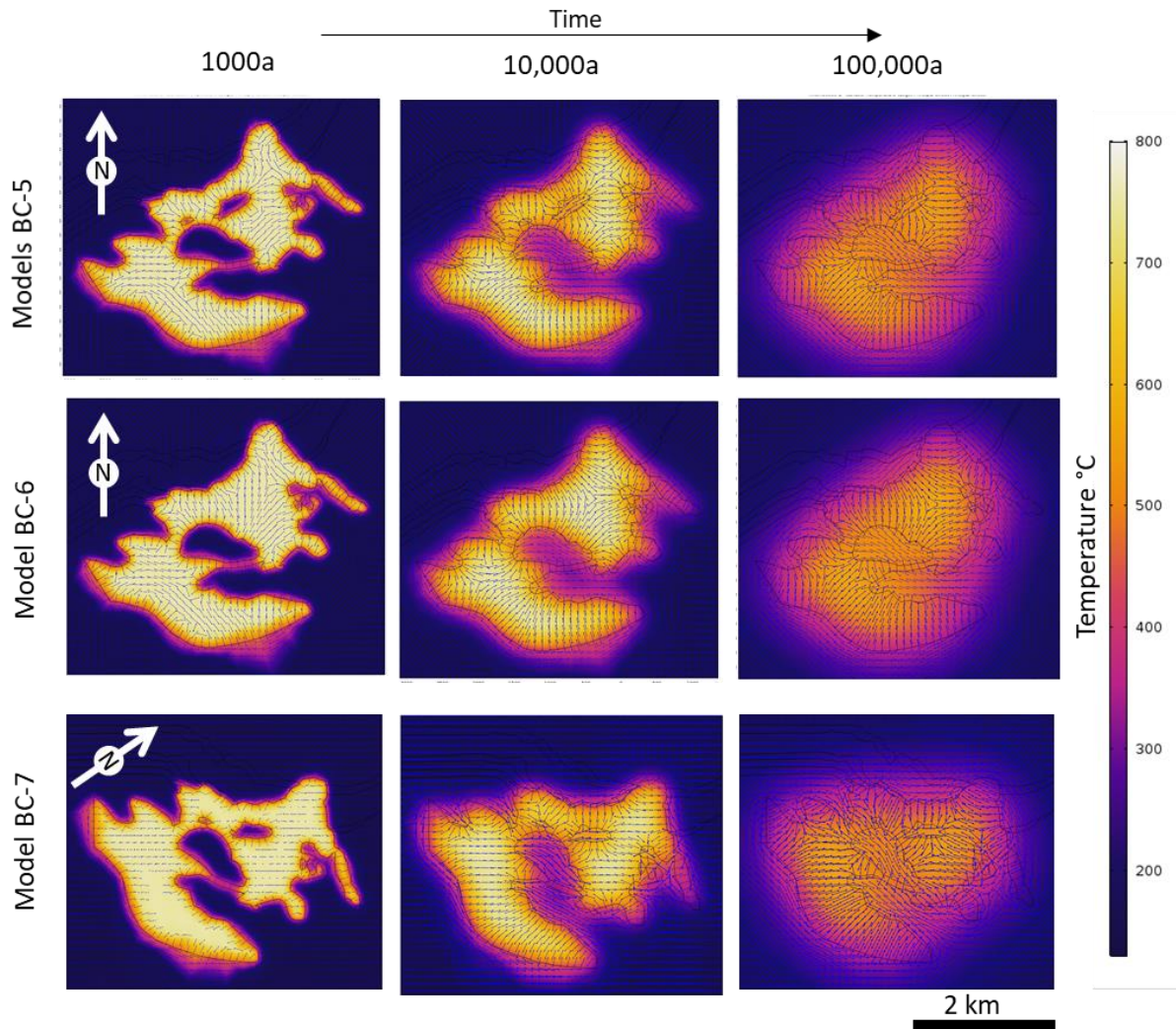


Figure 5.10. Colour map of temperature distribution over time. Model BC-5 includes enclaves and model BC-6 excludes enclaves. Model BC-7 includes tectonic load. a: cooling time in years from model start. As cooling progresses a similar NE-SW trending elliptical cooling pattern forms as enclaves are initially heated and then cooled.

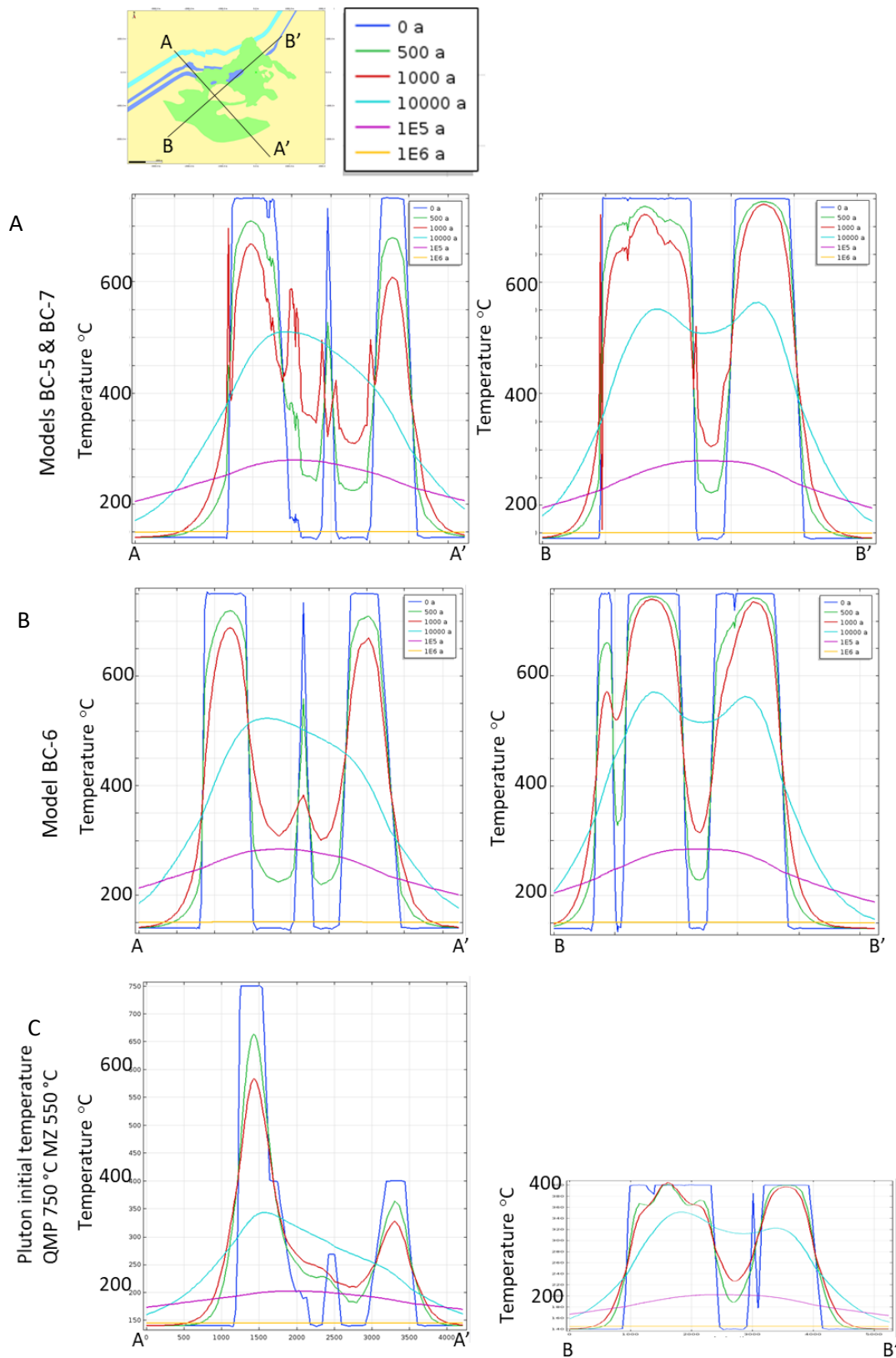


Figure 5.11. Temperature over time for sections A-A' and B-B'. Temperature over time shown for (A) models BC-5 & BC-7 which are the same, (B) model BC-6 where enclaves are not modelled and for (C) model BC-5 variation, QMP temperature is set to 750 °C and MZ intrusion to 550 °C (see appendix C Figure C5-4 p.345 for images of this model). COMSOL Multiphysics® x-y points for lines: A x -2000 m y 800 m A' x 500 m y -2600 m B x -3000 m y -2600 m B' x 1000 m y 800 m.

5.5.2. Principal Stress Orientations

As cooling proceeds, stress orientations are strongly controlled by the margin geometry of the Bingham Canyon magmatic complex, the modelled enclaves and the application of a regional load. The orientation of the plane perpendicular to the minimum compressive stress changes with time (Figure 5.10). Within the pluton, this orientation is approximately radial around the Bingham Canyon magmatic complex and around enclaves (model BC-5, Figure 5.12 A). Away from the margins and within the intrusive domain, the minimum principal stress rotates significantly over time (D values between different times >1.01 ; Figure 5.12 B). Within the enclaves and the host rock block bounded by the Phoenix dyke predicted orientations are parallel to bedding. In the model without internal enclaves (model BC-6), orientations in the areas of enclaves align northeast-southwest (Figure 5.12 C & D). This is approximately orthogonal to directions within and around enclaves when they are included in model BC-5 (D values within the enclaves are > 1.01 ; Figure 5.12 C). Over time, orientations around the enclaves (Figure 5.12 B) preferentially rotate to orientations similar to models without enclaves ($D < 1.01$; Figure 5.12 D). Orientations in the enclaves included in model BC-5 trend approximately perpendicular to orientations when enclaves are not modelled (model BC-6, stress difference values $D > 1.01$; Figure 5.12 D).

In the host rock domain, the orientations perpendicular to the least compressive stresses are initially perpendicular to the margins of the intrusive domain and are similar for models BC-5 and BC-6 (Figures 5.12 A - D). Over time this orientation becomes parallel to the margins. As orientations are initially perpendicular to pluton margins and then become parallel to pluton margins, the change in the modelled orientation is very significant ($D > 1.71$; Figure 5.12 B). Lithological variation defined in the host rock domain has very little effect on modelled orientations (Figures 5.12).

The applied northwest to southeast regional extension (model BC-7) means that early orientations of the plane perpendicular to the minimum principal stress align approximately northeast-southwest. Applying a greater magnitude of northwest-southeast extension makes this orientation dominate for longer. The application of regional tectonic load in model BC-7 (Figure 5.12 E & F), compared to no regional load being applied (model BC-5, Figure 5.12 A & B) influences the early principal stress orientations to the northwest and southeast of the intrusive domain ($D > 1.01$; Figure 5.12 E). As orientations in the host rock in model BC-7 rotate over time they become like that of model BC-5 (Figure 5.12 F). Over time the difference in the orientations of stress direction when tectonic load is applied is restricted to the margins of the intrusive domain (Figure 5.12 F).

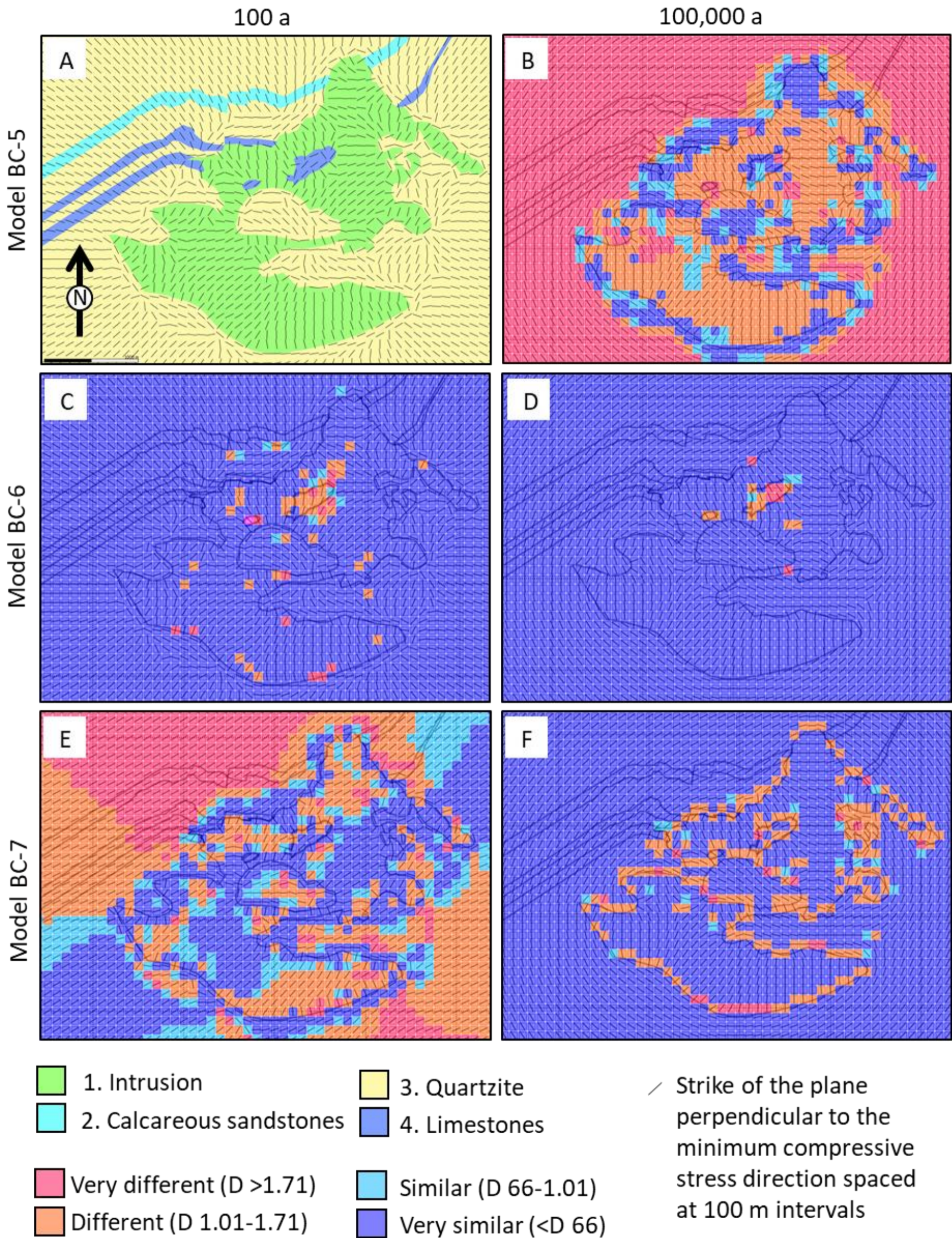


Figure 5.12. Results and comparison between numerical models presented as maps with lines perpendicular to the predicted direction of least compressive stress for models BC-5 to BC-7. (A) Domains are coloured based on material properties defined in the model (Table 5.3), (B-F) maps are coloured for stress difference calculated using STRESSTAT, models are compared to model BC-5 at 100 years and 100,000 years after model initiation. Data is compared on a grid of 100 m spacing over the intrusion.

5.5.3. Elastic Strain Energy

Elastic strain energy (considered by Gerla (1983) to possibly correlate to fracture density) is greatest at the intrusion margins (Figure 5.13). Comparison between elastic strain energy and fracture density is limited by the relatively few points measured in the field in this study and by Grün (2007). However, density is roughly similar where elastic strain energy values are highest in the centre of the QMP (c.f. Figure 5.13 and 5.14).

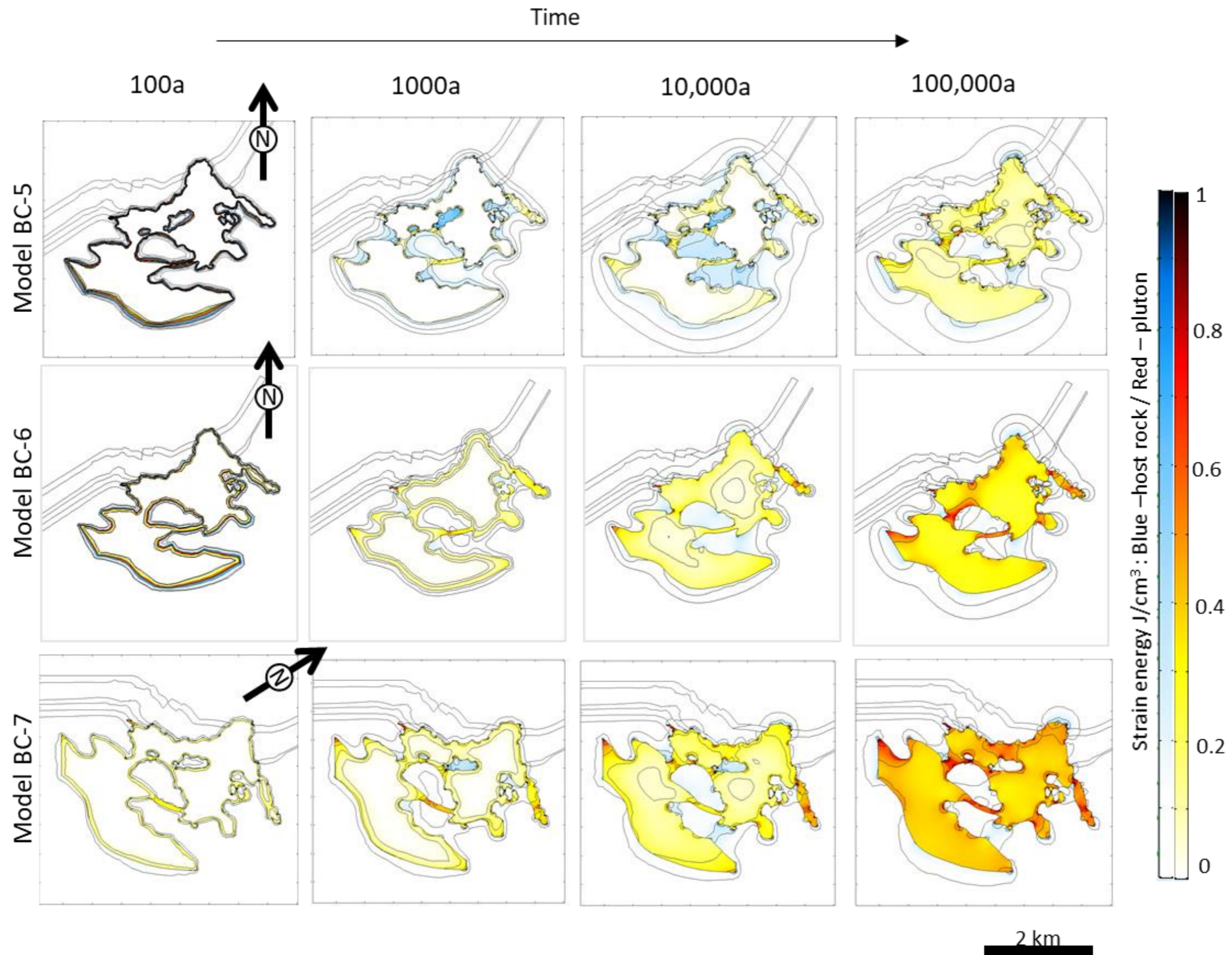


Figure 5.13. Strain energy (J/m^3) plotted for models BC-5 to BC-7. See appendix C Figure C5-3 (p.344) for strain energy calculated for models BC-1 to BC-4

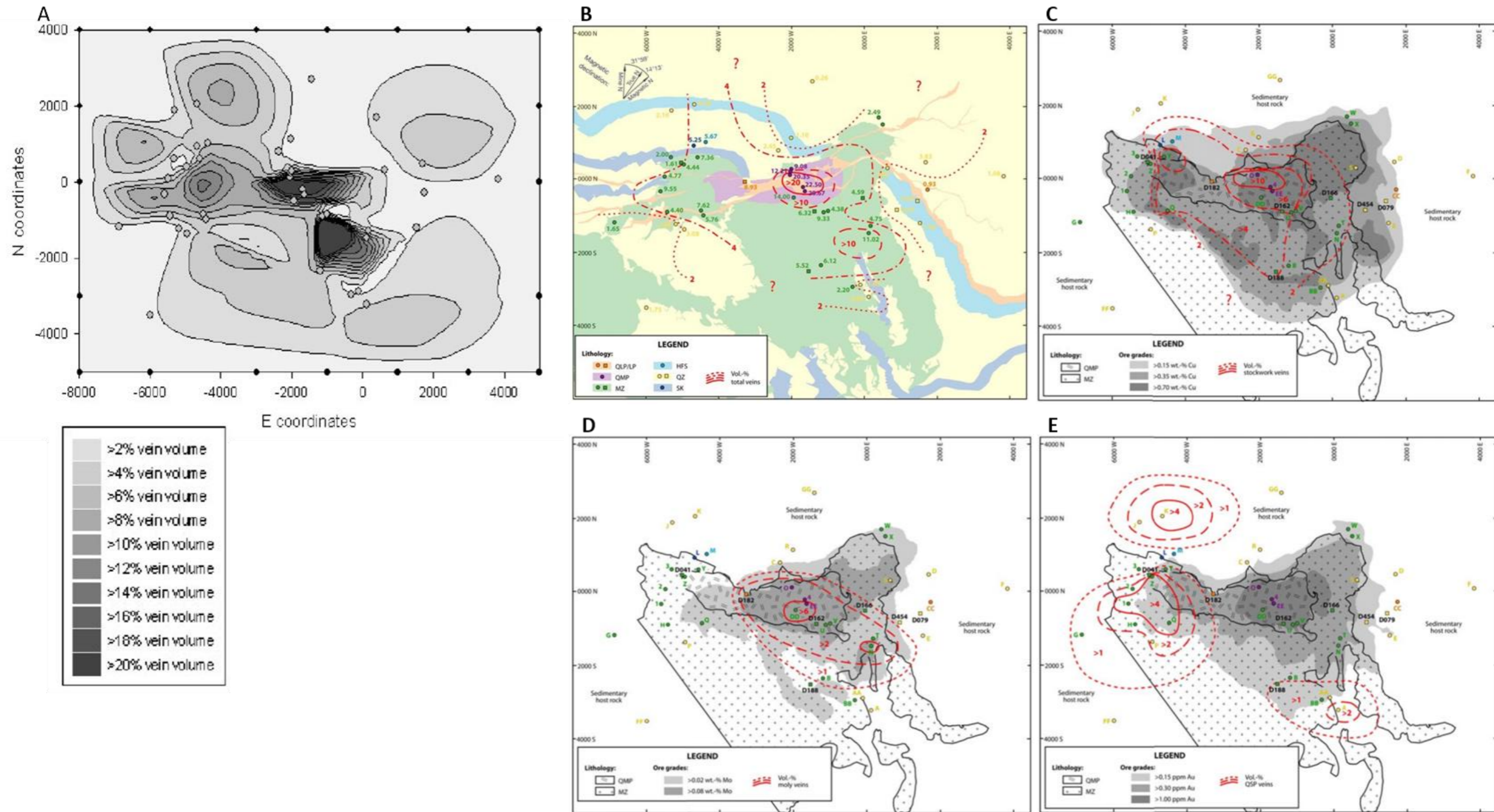


Figure 5.14. Density plots from Grün (2007). Grids are labelled relative to mine north. (A) Linear density plots automatically generated in SigmaPlot, input data location marked as points, (B) manually drawn vein density contours (red lines), (C) Stockwork vein density, (D) molybdenite vein density and, (E) QSP vein density. Copyright (2007) Fig.2-8 p.31, Fig3-6 p.39 and Fig.3-9 p.44 ETH Zurich.

5.6. Comparison of Numerical Models to Field Data

Comparison of model BC-5 with field data shows a better match than between models BC-6 and BC-7 and the field data (Table 5.4, Figure 5.15). Weaker matches between the models and field data are observed at the earlier presented timestep (Figure 5.15 A, D and G) and later time steps at the end of the model run (Figure 5.15 C, F and I).

Table 5.4. Wilcoxon signed-rank test. Comparison of the orientation of field data and selected time steps from the given COMSOL Multiphysics® model

	p	Null at 0.05	
Field data vs Model BC-5 100 a	0.792	Accept	
Field data vs Model BC-5 1,000 a	0.068	Accept	
Field data vs Model BC-5 1,000,000 a	0.002	Reject	Data significantly different
Field data vs Model BC-6 100 a	0.143	Accept	
Field data vs Model BC-6 1,000 a	0.040	Reject	Data significantly different
Field data vs Model BC-6 1,000,000 a	0.002	Reject	Data significantly different
Field data vs Model BC-7 100 a	0.792	Accept	
Field data vs Model BC-7 1,000 a	0.028	Reject	Data significantly different
Field data vs Model BC-7 1,000,000 a	0.003	Reject	Data significantly different

In the model BC-5 the weakest match between the modelled orientations and field data are observed for 5 of the 27 paleostresses calculated from veins. These locations are in the host rock to the north of the Bingham stock (QSP veins; location E), near to the north-western margin of QMP (molybdenite-veins; location O), close to the boundary between the north western margin of the intrusive domain and the host rock (stockwork veins; location V) and near to the margin of one of the enclaves (stockwork and QSP veins; location Q). The five paleostresses in this model that result in a weaker comparison to the numerical model may be related to the proximity of sample locations to the margins of the intrusive units. The geometry of the margins in these models is only a representation of the actual geometry and local deviation could significantly alter the predicted principal stress orientations (see figure appendix C Figure C5-2, p.343).

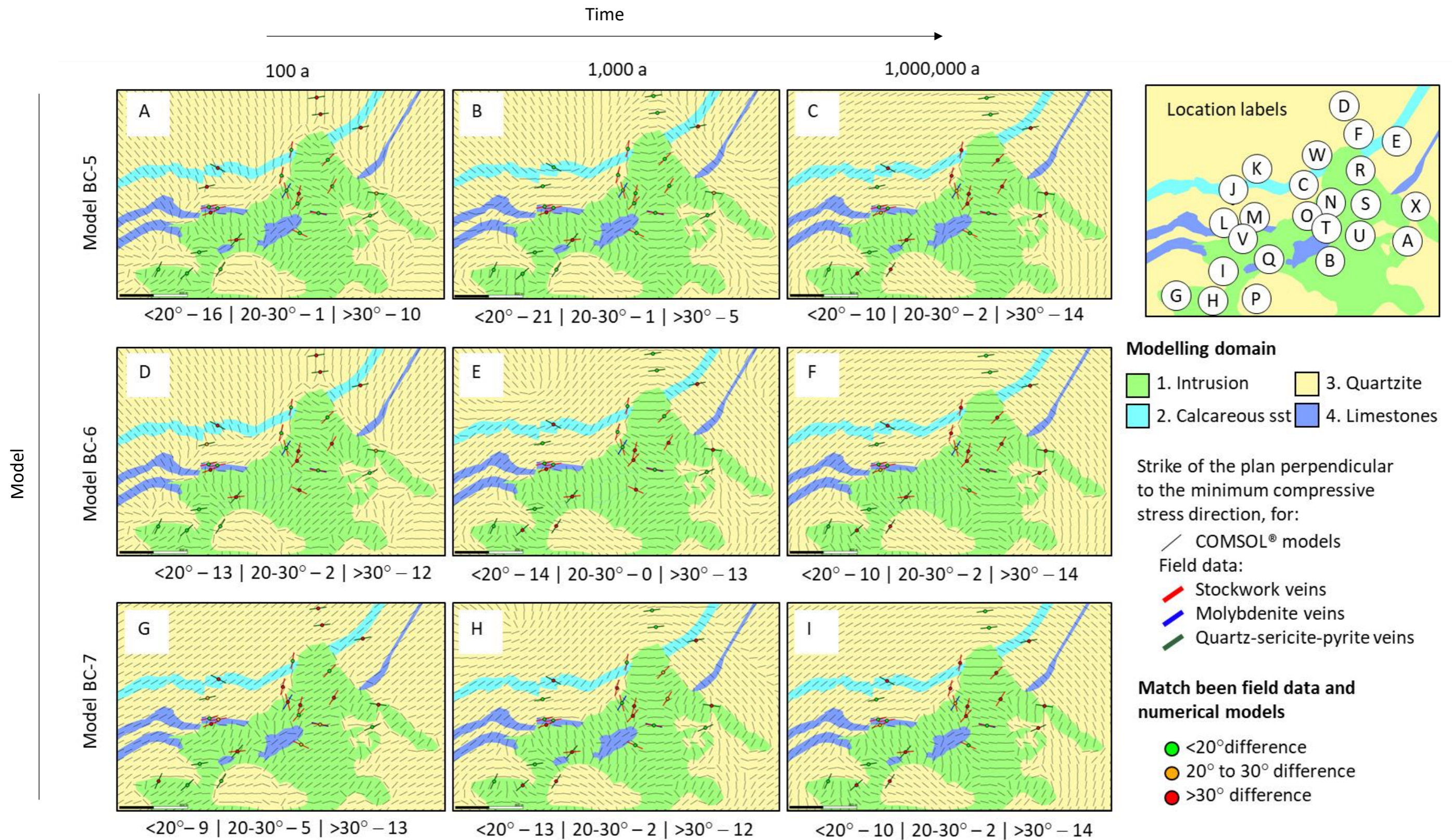


Figure 5.15. A. Comparison of field data and numerical model predictions. The plane perpendicular to the minimum compressive stress estimated from field measurement orientations of all measured vein types at given locations is compared with numerically modelled orientations for models BC-5 to BC-7 at time steps 100 years, 1,000 years and 1,000,000 years. Numerical model orientations are shown in grey on a grid at 100 m spacing. Estimated orientation from field data shown as coloured lines with points marked for closeness of fit to the numerically modelled orientations. The best fit between the two data sets is to model BC-5 at cooling time 1,000 years after model initiation.

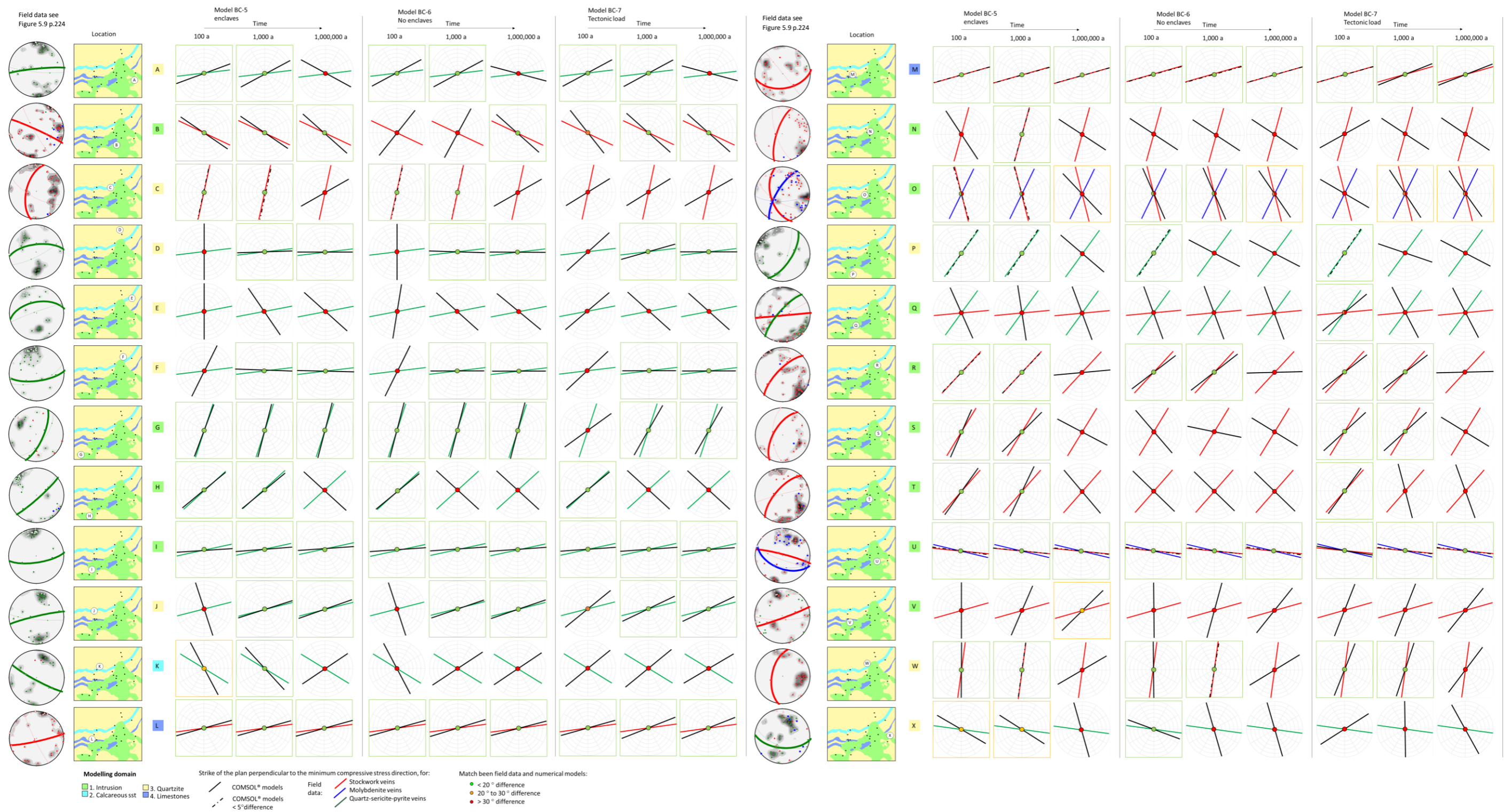


Figure 5.15. B. Comparison of field data and numerical model predictions. The plane perpendicular to the minimum compressive stress estimated from field measurement orientations of all measured vein types at given locations is compared with numerically modelled orientations for models BC-5 to BC-7 at time steps 100 years, 1,000 years and 1,000,000 years. Estimated orientation from field data shown as coloured lines central points marked for closeness of fit to the numerically modelled orientations. The best fit between the two data sets is to model BC-5 at cooling time 1,000 years after model initiation.

5.7. Discussion

5.7.1. Stress Evolution

Models highlight the influence that cooling may play in controlling stress distributions and resulting fracture patterns. However, the models do not rule out other processes that may have an influence on the stress field evolution over time (e.g., Gustafson and Hunt, 1975; Burnham, 1979; Burnham and Ohmoto, 1980; Fournier, 1999; Tittley, 1990; Gruen et al., 2010; Tosdal and Richards, 2001; Harris and Holcombe, 2014).

Cooling results in changes in direction of the thermal stress state over time, providing a mechanism for change in local stress conditions during development of fracture networks (c.f. Boutwell et al., 1905 *p.61*). The patterns of vein orientations at Bingham are likely to be controlled by the cooling history of the intrusive geometry (Figure 5.16, c.f. Figure. 5.4 *p.215*). Variation in the geometry of veins at hand-specimen scale is likely to be controlled by local stress modifications influenced by existing fractures and fluctuating fluid pressures (c.f. Richards and Tosdal, 2001).

The modelling presented here only relates to fracturing due to cooling after emplacement of the MZ and QMP. The model does not account for stress redistribution as a result of earlier fracturing events, emplacement of the intrusive bodies or later latite dykes. These model simplifications may be reasonable as early veining events are sealed due to mineral precipitation so that the rock mass can be considered a homogenous unit during sequential fracturing events (Tosdal and Richards, 2001) and because the latite porphyry dykes are volumetrically small (Redmond and Einaudi, 2010; Steinberger et al., 2013).

5.7.2. Cooling History

The Bingham Canyon magmatic complex is modelled as a homogenous unit, representing the combined geometries of the MZ and QMP bodies. However, the Bingham Canyon magmatic complex was formed from a series of intrusive bodies where incremental emplacement and cooling history may be influenced by repeated intrusion. Emplacement histories and related cooling histories are complex, related to multiple interlinked processes (Tittley, 1990; Richards and Tosdal, 2001). The grain size of the MZ suggests rapid cooling, while larger phenocrysts within an aplitic groundmass in the QMP suggest fluid saturation or longer residence time during partial crystallisation of the magma before rapid cooling (Steinberger et al., 2013).

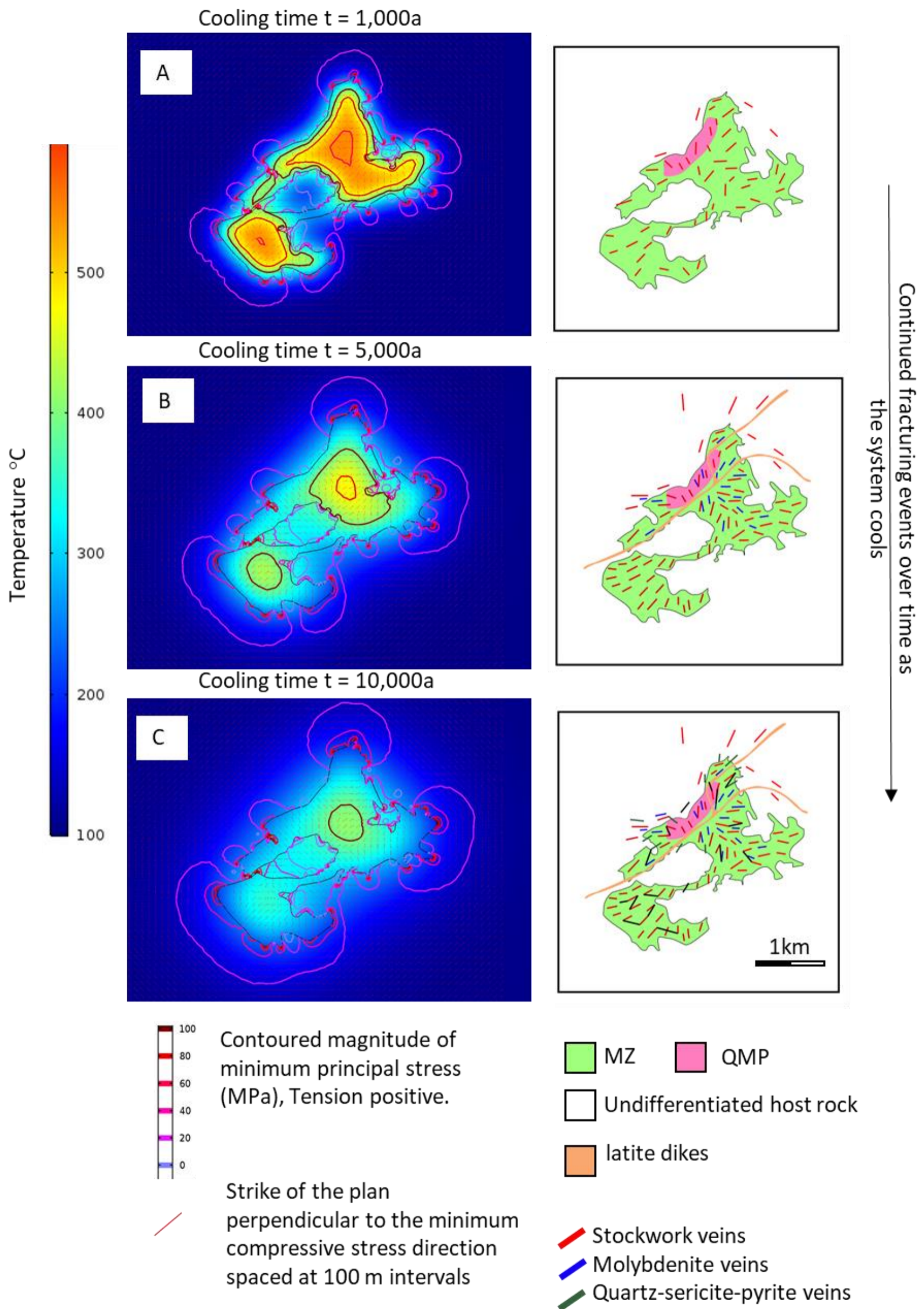


Figure 5.16. Map sketches illustrating the evolution of the stress field related to thermal cooling over time (left) and resulting fracture orientations (right) when regional stresses are initially subequal, based on model BC-5. The evolving thermal stress field provides a mechanism to explain the mine-scale trends in paleostress orientation predicted from field data. Vein distributions can be explained by the thermal stress field without having to infer regional tectonics c.f. Figure 5.4 p.215. (A – C) cooling continuum over approximate a 200 – 300 °C temperature drop. (A) quartz stockwork veins equivalent to stage 3 Figure 5.4 (B) emplacement of latite dykes and moly-veins equivalent to stages 4 and 5 Figure 5.4 (C) formation of QSP veins equivalent to stage 6 Figure 5.4 p.215.

The lack of clearly defined boundary between the MZ and QMP stocks suggest temperatures ≥ 500 °C could have been maintained for the duration of emplacement (Norton and Knight, 1977), so that the assumption of rapid emplacement relative to the time required for substantial cooling, as in other models of cooling plutons, is likely to be valid (Bergbauer and Martel, 1999; Žák et al., 2006). This may not be the case in other porphyry intrusions depending on the time of emplacement relative to the time of vein formation.

5.7.3. Comparison of Field Data and Numerical Models

Orientation information from numerical modelling and field data are used to assess modelling results. Ranges of fit are defined based on the data uncertainty controlled by data collection methods, model rotation and simplification of the boundary geometries in the numerical models. The Wilcoxon signed-rank test (Table 5.4) is applied to test if field data is significantly different from the selected time steps in the end member models (BC-5 – enclaves/ no tectonic load, BC-6 - no enclaves / no tectonic load and BC-7 – enclaves / tectonic load). Results of this statistical comparison show that in all cases predicted orientation at later time steps are significantly different (95 % confidence) than field data. Early modelled results are not significantly different. The fit of modelling results from earlier time steps suggested that the influence of thermal stress as a result of cooling influences fracture orientations and vein events in the Bingham Canyon magmatic complex. Model BC-5 at early time steps (100 and 1000 years after model initiation) has the best match between field data and numerical model results, suggesting that enclaves influence the cooling history and thermal stress orientation. Influence of tectonic load reduced the number of comparable locations between field data and numerical model results.

Comparison of the data set is limited by the time taken for comparison of the data set. The comparison could be made stronger by comparing all time steps. However, the time taken for export of data from COMSOL Multiphysics® for all time steps at each point and conversion to orientations for comparison with the field data excluded the possibility of this during the duration of this study. Each export for a single time step for one model ~13 hours, conversion of data ~2 hours. Assuming an 8-hour working day, for a model run at 10-year model intervals it would take 51.3 years to extract and compare the data or at 100-year model intervals 5 years per model. The time steps selected and presented here are considered a reasonable reflection of the full data set.

5.8. Conclusions

Thermomechanical modelling of the Bingham Canyon magmatic complex highlights the potential influence of thermal stresses on the orientation of early fractures. The match between the thermally predicted and measured principal stress orientations provides an explanation for the dominant vein orientation around the Bingham Canyon magmatic complex (c.f. Grün, 2007; Gruen et al., 2010). Modelling results suggest that at the deposit scale thermal loading influences the dominant trend of the fracture network.

- Models predict variation in the trend of the plane perpendicular to the minimum compressive stress over time. The amount of variation in the trend over time is spatially variable; the greatest variation is in the host rock while in the intrusive units, variability is greatest away from the modelled domain margins. The best match between modelled results and estimates for field data is for orientations predicted at early stages of cooling without tectonic loads applied.
- The trend of the plane perpendicular to the minimum compressive stress varies with depth at a given time step. The amount of variation in the trend with depth is spatially variable. The greatest variation is in the intrusion domain away from the modelled domain margins. Variation in the host rock is lower, being greatest where host rock is heated and then cooled.
- As the temperature of the enclaves is increased the geometry influences the trend of the plane perpendicular to the minimum compressive stress. Over time, as the enclaves cool with the intrusive domain, their influence over the principal stress trends within the intrusive domain diminishes and orientations rotate to match models which do not include enclaves.
- Increasing the initial temperature of the QMP body relative to that of the MZ does not significantly influence the trend of the plane perpendicular to the minimum compressive stress. This can be explained due to the elongate nature of the QMP body where most tensile stress would be expected to trend parallel to the longest sides of an elongate body (e.g., Bergbauer et al., 1998; Koenders and Petford, 2003). Lowering the initial temperature of the intrusive domain only influences the magnitudes of the principal stress predicted and does not influence the predicted principal stress directions.
- Tectonic loading significantly alters the trend of the plane perpendicular to the minimum compressive stress in the host rock. The trend within the intrusive domain varies depending on the relationship of the tectonic load to the domain boundary geometry. Tectonic control on fracture orientation cannot be ruled out but thermal control without tectonic influence matches the dominant orientations of estimated paleostress calculated from field data the best.

6. Analogue Modelling

This chapter describes experimental observations of desiccating corn-starch, and the formation of fractures in this material. The general modelling aims are described in section 6.1 (p.242). Following this, published experiments of fracture formation in drying starches are reviewed in section 6.2 (p.244). The methodology developed to form corn-starch masses and the experimental procedure is outlined in section 6.3 (p.247). Scaling relationships between the analogue models and plutonic intrusions are presented in section 6.4 (p.251). The results are presented in section 6.5 (p.253). In the discussion, section 6.6 (p.270), results are compared to conceptual and numerical models of plutonic fractures and previous desiccation experiments. Conclusions are summarised in section 6.7 (p.275). Photos of each sample and measured weight at the given time intervals are presented in Table D6-2 appendix D (p.346 – 358).

The results described in this chapter were presented as a poster at the 2018 Tectonics Study Group meeting (Ellis, J.F. and Blenkinsop, T., 2018. Analogue modelling of fractures in cooling intrusions). Results from key samples have been published in Tectonophysics (Ellis, J.F. and Blenkinsop, T., 2019. Analogue modelling of fracturing in cooling plutonic bodies).

The Cardiff Undergraduate Research Opportunities Programme (CUROP 2017) was awarded to fund an undergraduate student (Hamid Reza Sha Mohammadi, ShaMohammadiH@cardiff.ac.uk) to test the initial experimental set up. Samples produced during this work are clearly marked in appendix D Table D6-1 p.346 – 347.

6.1. Modelling Aims and Approach

As the direct observation of fracture formation in cooling plutons is not possible, analogue models are a useful tool (e.g., Hubbert, 1937; Koyi, 1997). Various mechanisms and geometries of fractures resulting from the cooling of intrusive rocks have been proposed. In the Cloos model five key sets of fractures are suggested to predominantly result from emplacement forces (Balk, 1937; see Chapter 2). In contrast, two-dimensional numerical models predict vertical fractures that result from the contraction of cooling bodies, these models do not account for emplacement forces (e.g., Martel and Bergbauer, 1997; Bergbauer et al., 1998; see Chapter 3).

Analogue models that have been used to directly investigate fracture formation within cooling igneous rocks, include moving wet clay (Riedel, 1929; Balk, 1937: *p.29 plt12*), interaction of contracting two-dimensional films to investigate the formation of micro-scale joints in cooling volcanic rocks (Samanta, 2001), desiccation of air-exposed starch flour investigating the processes of columnar joint formation and tensile-crack morphology (e.g., Müller, 2001) and, the recording the energy of crack released during the heating and cooling of basaltic rocks by measurement of acoustic emission (Browning et al., 2016). No previously published analogue models were found to be comparable to fracturing resulting from contraction of a volume, the process for early fracture formation suggested by numerical modelling. The aim of the analogue modelling developed here was to investigate fracture geometries resulting from the contraction of a volume, comparable to numerical models of cooling plutonic bodies. The influence of depth and geometry on fracture patterns was tested and compared to the results to conceptual and numerical models.

Initial trials showed that dehydration of buried starch flour to be a workable analogue. Drying of water saturated corn-starch is analogous to cooling, as both are diffusive processes (Müller, 1998a). Starch experiments have previously been used to give insights into column formation in cooling lava flows (an end member of fracture patterns resulting from cooling of igneous rocks) (Müller, 1998a, 1998b; Toramaru and Matsumoto, 2004; Goehring et al., 2006; Morris, 2012) and studies of tensile-crack propagation and crack morphology (Müller and Dahm, 2000; Müller, 2001).

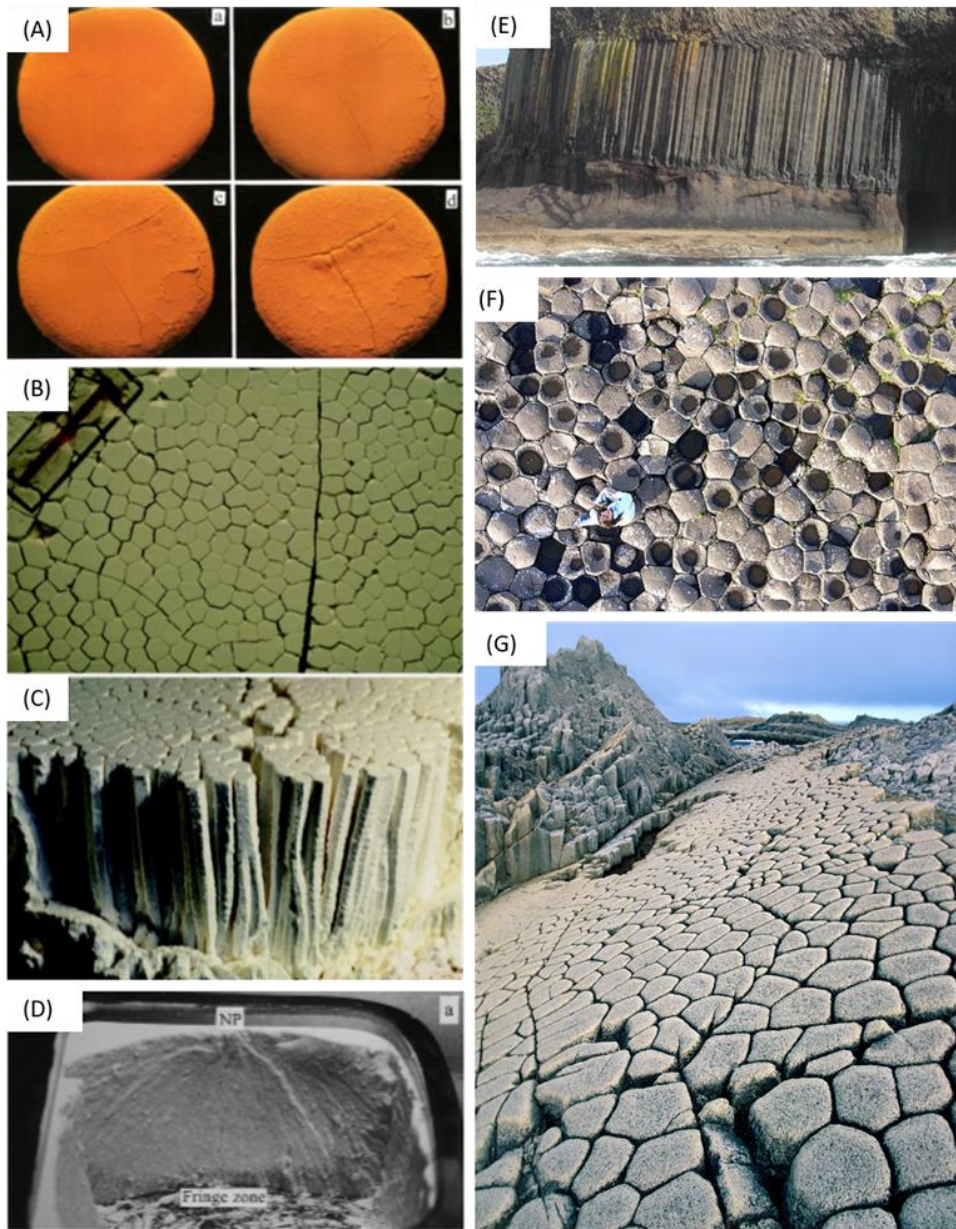


Figure 6.1. Examples of experimental results from drying corn starch and field examples of columnar joints. (A) Type I crack formation on drying corn starch slurry. Images from Müller (1998) Copyright (1998) American Geophysical Union; (B & C) columnar joint formation in corn-starch (Type II cracks). Images from Müller (1998b) Copyright (1998), with permission from Elsevier; (D) fracture surface in corn-starch. Images from Müller (2001) Copyright (2001), with permission from Elsevier; (E) Columnar joints Staffa, Argyll Scotland; (F) Aerial view of columnar joints Giants Causeway Copyright nickrussill and (G) columnar joints separated by larger cracks Cape Stolbchaty, Kunshir Island copyright lusika33.

6.2. Theoretical Background of Fracture Formation in Starch Flours

The drying of wet starch flours has been shown to be a suitable analogue to the formation of columnar joints in cooling basaltic flows (Müller, 1998a,b, 2001; Toramaru and Matsumoto, 2004; Goehring et al., 2006; Goehring and Morris, 2008; Morris, 2012a,b), tensile crack formation analogous to drying muds (Walker, J., 1986; Goehring 2003, 2013; Akiba et al., 2017) and, tensile joint formation processes (Müller and Dahm, 2000; Müller 2001). Properties of corn-starch are summarised by Müller (1998b), Rust et al., (2012) and Akiba et al., (2017).

Columnar joint patterns are formed as wet starch slurries are dried from a single free surface (Figure 6.1 A - C). The outcome of desiccation of wet starch via evaporation is volume reduction. As a result of contraction stresses are developed which exceed the tensile strength of the starch resulting in fracture formation (Müller, 1998a,b, 2001). When starch slurries are dried from a single free surface two phases of cracking are identified: primary fracturing (type I cracks) resulting from the uniform decrease in water content and secondary fracturing (type II cracks) resulting from non-uniform drying (i.e., Müller, 1998a; Toramaru and Matsumoto, 2004; Goehring, 2003; Nishimoto et al., 2007).

Type I cracks are analogous to the formation of fractures in drying mud, forming where the surface tension is eliminated (Walker, J., 1986; Müller, 1998a; Goehring 2003, 2013; Akiba et al., 2017) (Figure 6.2 A). The angle between joining fractures may evolve over time (i.e., Goehring 2013). Prior to the formation of surface cracks, fractures extending vertically through the damp starch mass may initially divide the sample into larger blocks (Müller, 1998a; Akiba et al., 2017). This process has been likened to the formation of mega-joints and then columns in lava flows (Müller, 1998a) (Figure 6.1 G). The exact conditions that result in the early formation of mega columns in lava flows is however unknown (Spry, 1962). These fractures may display fractographic markings on their surfaces (Müller and Dahm, 2000; Müller 2001) (Figure 6.1 D). Plumose lines radiate away from the rupture point, indicating the local rupture direction. The rupture velocity during formation of these fractures in starches decreases with depth. It is suggested this change in rupture velocity is due to a decrease in tensile strength with depth as water concentration increases (Müller and Dahm, 2000). The process is considered to be analogous to the formation of tensile cracks in sedimentary units (Müller and Dahm, 2000; Müller 2001).

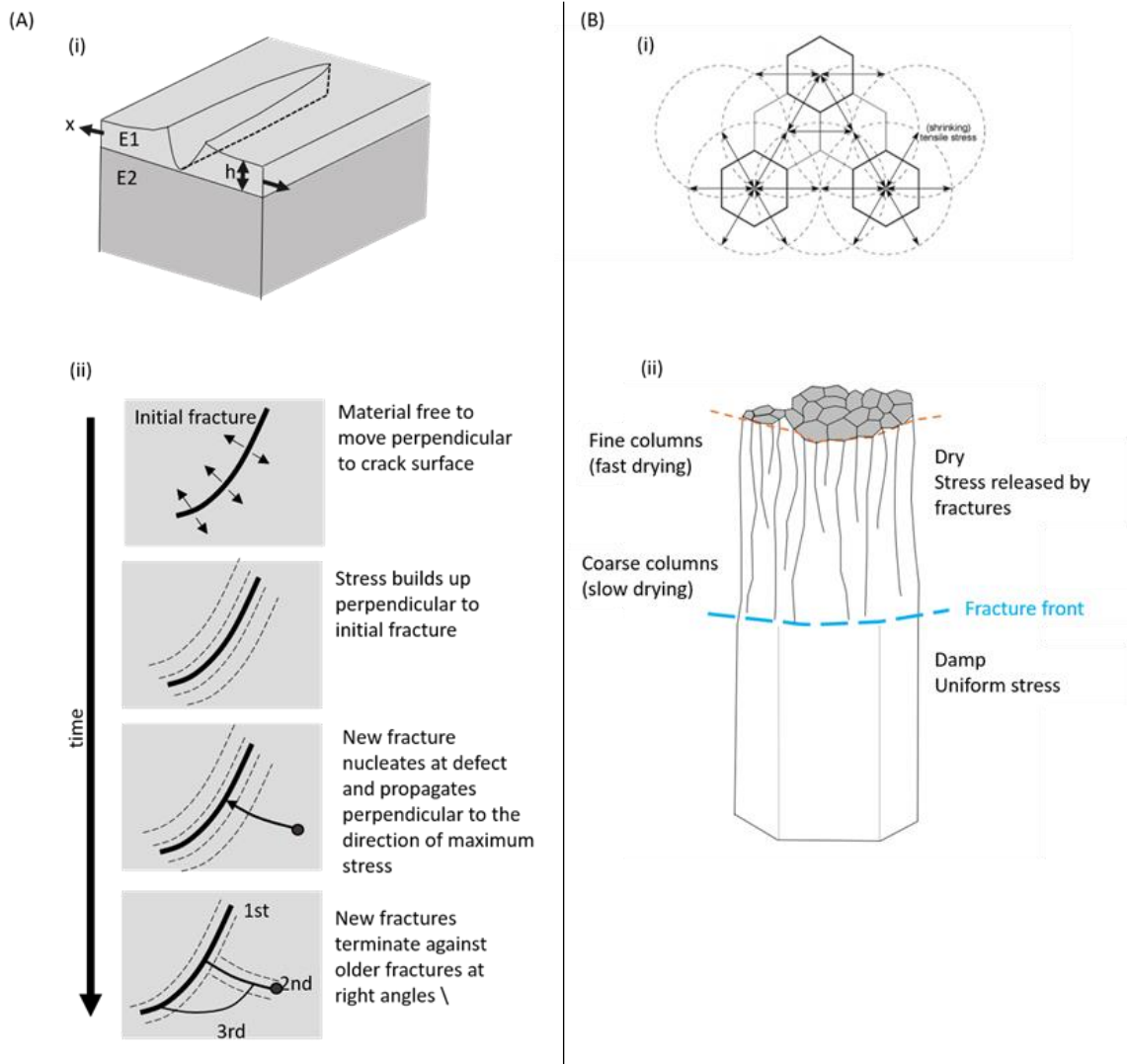


Figure 6.2. Mechanisms of fracture formation in drying corn-starch. (A) diagrams of thin film fractures (Type I cracks) modified from Goehring (2003, 2013) (i) film of height (h) under stress (x) with elastic properties $E1$ and adhere to a thicker substrate with possibly different elastic properties $E2$, channel cracks may open and propagate across the film. The crack releases stress preferentially perpendicular to its propagation direction. (ii) Interaction of channel cracks, later cracks will curve to intersect earlier cracks at right angles. (B) diagrams of columnar joint formation in corn-starch (second generation cracks) (i) map view of hexagonal joint pattern due to tensile stresses towards equally distributed drying centers in homogenous material redrawn from <http://www.files.ethz.ch/structuralgeology/jpb/files/english/4joints.pdf> and (ii) Columnar joint pattern formed contracting volume with a free surface at the top modified from Goehring and Morris (2005).

Type II crack patterns organise into polygonal joints when the critical desiccation rate ($0.8 \times 10^{-2} \text{ g/cm}^2\text{h}$) is exceeded (Figure 6.2 B, Müller, 1998a; Toramaru and Matsumoto, 2004). Fracture patterns become more regular and self-organise into columnar joints with depth (Figure 6.1 B & C). The shapes of the polygons may vary from pentagons to hexagons. It has been suggested that pentagonal column shapes form preferentially during faster desiccation and hexagons at slower




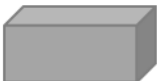

desiccation rates (Toramaru and Matsumoto, 2004). A range of column sizes can be produced for any given evaporation rate (Goehring and Morris, 2005; Goehring et al., 2006; Goehring and Morris, 2008). The control on the size of the columnar joints formed in drying starch is debated but has been related to the concentration gradient (Müller, 1998a), the desiccation rate (Toramaru and Matsumoto, 2004) and the thickness of the crack front (Goehring and Morris, 2005). When desiccation rates are $> \sim 1.4 \times 10^{-2}$ (g/cm²h) (the normal columnar joint regime) the average cross-sectional area is inversely proportional to the average desiccation rate (Toramaru and Matsumoto, 2004). The difference between the spatial and time scales of formation of columnar joints in drying starch and basaltic columns (2 to 3 orders of magnitude; Müller, 1998a,b; Goehring et al., 2006) is suggested to result from the difference between the thermal diffusivity of basalt (0.9 to 1.2 mm²/s) and the hydraulic diffusivity of starch (0.01 to 0.03 mm²/s) (Müller, 1998a).

6.3. Method

Slurry mixtures of 250 g corn-starch (Brown & Polson brand) and 250 ml water (mixed with ~1tsp of bleach to prevent mold growth, c.f. Goehring and Morris, 2005) were prepared. Rice flour was also tested as an alternative to corn-starch, but not used due to mould growth (samples 59, 60 and 65). A 1:1 ratio of starch to water was used to fully saturate the starch grains (Müller, 1998a).

To generate volumes, acetate containers were constructed, filled with the corn-starch slurry and part dried to form starch patties. These acetate moulds were constructed by folding and taping acetate sheets to five different geometries (Table 6.1). These include three types of cylinders (geometries A – C), bricks (geometry D) and cylindrically projected hourglass geometries (geometry E). Geometries B – E were run to compare the influence of initial geometry with depth and drying method investigated with geometry A. The mould geometries were selected to represent basic shapes and produced on a scale practical for lab work.

Table 6.1. Acetate mould geometries

	Geometry	Dimensions (cm)		
		diameter	height	
	(A) Cylinder	4	4	
	(B) Flat-cylinder	10	2	
	(C) Tall-cylinder	4	10	
		width	length	thickness
	(D) Brick	4	8	4
	(E) Hour glass	4 narrowing to 1	8	2

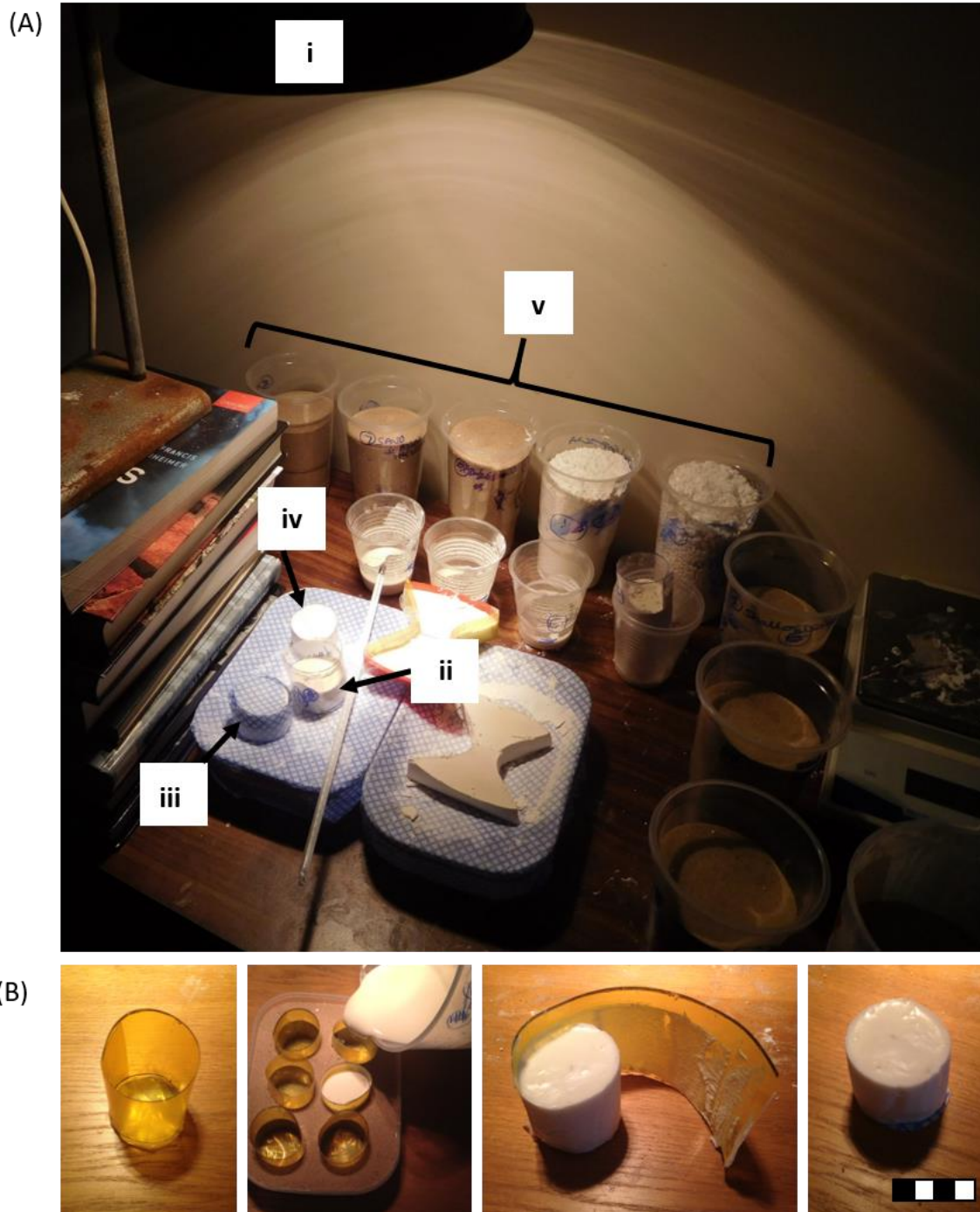


Figure 6.3. Experimental set-up. (A) i. 250 W halogen heat lamp positioned at ~50 cm from bench, various experiments for short cylinder and hourglass geometries are laid-out for the various drying methods; ii. in mould, iii. cloth covered, iv. air exposed and v. buried. (B) method for forming corn-starch patties; taped acetate mould, 40 mm diameter and height; corn-starch slurry poured into moulds that are placed in sand to maintain shape and prevent leaks; removal of acetate mould once corn-starch patty formed after leaving under heat lamp; corn-starch patty prior to burial.

The slurry was poured into the acetate containers and dried to the point that it formed a coherent wet mass, before surface cracks formed. This was achieved by placing the mould 50 cm from a 250 W heat lamp (temperature ~30°C) for 1 hour (Figure 6.3 A). Various distances and drying times were tested for the heat lamp. Testing of heat lamp distances and drying time required was carried out by an undergraduate student during a summer project funded by CUROP. The partly dried corn-starch patties were removed by cutting the tape (Figure 6.3 B).

Various methods of drying the corn starch patty were then applied. These included drying under the heat lamp with or without the mould, air drying the patty in the mould, or burying the patties removed from the mould. In two cases the slurry was poured directly into sand without forming a moulded geometry (samples 48 & 49). Oven dried sand, corn-starch and calcium chloride desiccant (brand, Kontrol Krystals) were used as the burial media to investigate the difference between the influences of drying rate and depth.

For geometry A, the 4 cm by 4 cm cylinder, the burial depth in sand to top of the sample, was 5 mm, 10 mm, 20 mm, 40 mm, 60 mm. Two deeper samples buried at 75 mm and 145 mm were run during the CUROP project. Three repeats of each sand buried sample were completed to test reproducibility. In the samples where corn-starch and desiccant were used as the burial medium, samples were buried at 5 mm, 20 mm, 40 mm and 60 mm. These samples were placed in cloth to help with the removal. Cloth encased, lamp dried samples (samples 7 & 8) and sand buried sample (depth 20 mm, sample 21) were run as a control for comparison with the other burial media. In one sample an external force was applied to the patty by squeezing prior to burial (sample 58). A total of 60 samples were prepared and dried for the 4 cm by 4 cm cylinders. Geometries B – E were buried to a depth of 30 cm.

Drying rate was recorded in grams for selected samples using a mass balance scale to a precision of two decimal places. The mass of selected samples was recorded every hour for the first 12 hours of drying and then every 24 hours. Once the weight reduced by ~30% of the original mass the samples were broken vertically in half to examine the internal fracture patterns. The drying time depended on drying rate up to a maximum of 6 weeks. Lamp dried samples (samples 1 to 10) were left for 1 day (no mould) to 6 days (in mould), air dried samples were left for 17 days (samples 11 & 12) and sand buried samples for a maximum of 6 weeks (samples 13 to 49 & 58). The corn-starch buried samples were left for 3 days (sample 50), 6 days (sample 51), 9 days (sample 52), and 12 days (sample 53). This was significantly less than the equivalent sand buried (>30 days). Desiccant-buried samples (samples 54 to 57) were left for a maximum of 5 days for the sample buried to 60 mm (sample 57), the shallowest buried sample (buried to 5 mm) was left for 1 day (sample 54).

Photography was used to capture the resulting fracture patterns. Quantitative analysis of the surface fracture pattern (Type I cracks) was undertaken for samples where the surface patterns were entire (not broken or obscured by sand embedded in the surface). Fracture apertures, fracture length, topology, polygon area and polygon number were measured and density and intensity calculated. Topology was measured using the method of Sanderson and Nixon (2015). Intensity of fracturing on the surface is recorded as length of fractures per area ($P_{21} - \text{mm}^{-1}$). Density of fracturing is recorded as the number of fractures per unit area ($P_{20} - \text{mm}^{-2}$). Samples were broken vertically in half to examine the internal fracture patterns. All samples are listed (Table D6-1), and photos of each sample is given in appendix D (p.346 – 358).

6.4. Scaling

The analogue models are scaled to ensure they are geometrically, kinematically and dynamically similar as possible to their natural analogue (Hubbert, 1937; Merle, 2015), in this case cooling plutonic bodies.

6.4.1. Geometric Scaling

A length scaling ratio of 10^{-5} is assumed so that 1 cm in the models is equivalent to 1 km in nature. The range of geometric shapes found in plutonic bodies in nature is extensive (e.g., Mendel, 2011). The shape and size selected for the analogues presented in this work were chosen based on numerical modelling of fracture in cooling cylindrical bodies presented by Knapp (1978), Knapp and Norton (1981) and Bergbauer (1998). For example, geometry A is most comparable to plutonic bodies of steep sided stock like geometry with volumes of $\sim 50 \text{ km}^3$. Stocks are typically emplaced in shallow-to-mid crustal ranges 1 – 6 km depth (Menand, 2011), comparable to analogue burial depths of 10 – 60 mm.

6.4.2. Dynamic Scaling

The gravity field and density are imposed by the modelling conditions and materials used. The density of dried sand was around 1600 kg/m^3 and the wet starch around 1500 kg/m^3 . The initial analogue material density is approximately half that of natural rocks (typically $2600 - 3000 \text{ kg/m}^3$; Wyllie, 1971). The density of dry desiccant is $\sim 250 \text{ kg/m}^3$ and corn starch $540 - 630 \text{ kg/m}^3$, dependant on compaction (loose to tight). These comparatively low-densities are not considered to be a critical factor in the experimental set-up as running these models allows a comparative assessment of burial depth and drying rate to be made.

6.4.3. Kinematic Scaling

Drying rate is influenced by burial depth and model scaling. The run time of most models buried in sand varied between 21 and 39 days. Hydraulic diffusivity of starch (0.01 to $0.03 \text{ mm}^2/\text{s}$) (Müller, 1998a) is ~ 2 to 3 orders of magnitude slower than the thermal diffusivity of basalt (0.9 to $1.2 \text{ mm}^2/\text{s}$) (Müller, 1998a,b; Goehring et al., 2006). Based on this relationship, model run times would scale to natural processes of 2,000 – 40,000 years. Assuming the three orders of magnitude difference the scaled model run times are similar to estimates of solidification time (32,000 years) in numerical models of Knapp and Norton (1981). This rate may be modified by many other processes not included in numerical models (Knapp, 1978). One of the most significant influences of the thermal evolution is

likely to be related to incremental growth history (Glazner et al., 2004; Annen, 2009; Menand, 2011; Annen et al., 2015). Comparable to numerical modelling (i.e., Norton and Knight, 1977; Hanson and Glazner, 1995; Bergbauer and Martel, 1999; Žák et al., 2006; Bartley et al., 2008) analogues are representative of a pluton at the point of crystallisation, with an evolutionary history that maintains its temperature prior to cooling as a single unit.

The rheological properties of drying starch-water mixture changes from liquid with low viscosity to a brittle material with high viscosity and non-zero values of shear modulus and tensile strength (Müller, 1998a). The cohesion of starches ranges from 40 Pa – 260 Pa, depending on water saturation (Stasiak et al., 2013). The analogue material cohesion is therefore $\sim 10^{-6}$ times lower than natural rocks and suitably scaled (Holohan et al., 2008; Warsitzka et al., 2013). The internal friction angle of starch flours (37°; Stasiak et al., 2013) is comparable to that of rocks (30° – 40°; Byerlee, 1978). Despite the differences in microstructure and elastic properties of the analogue material and igneous rocks, fracture processes are similar as the contraction stress exceed the material strength (Müller, 1998a). The scaling of brittle material behaviour is theoretically time-independent (Merle, 2015).

6.5. Results

6.5.1. Geometry A

Comparison of fractures formed from four methods of drying for the 4 cm by 4 cm cylinder (geometry A) are presented in Figure 6.4. Traces of top surface fracture and internal fracture patterns are sketched. The geometry of surface and internal fractures varies with burial depth, burial medium and drying method. The normalised weight over time for these samples is presented in Figure 6.5. Drying rates are fastest for the non-buried lamp dried samples (Table 6.2 p.256).

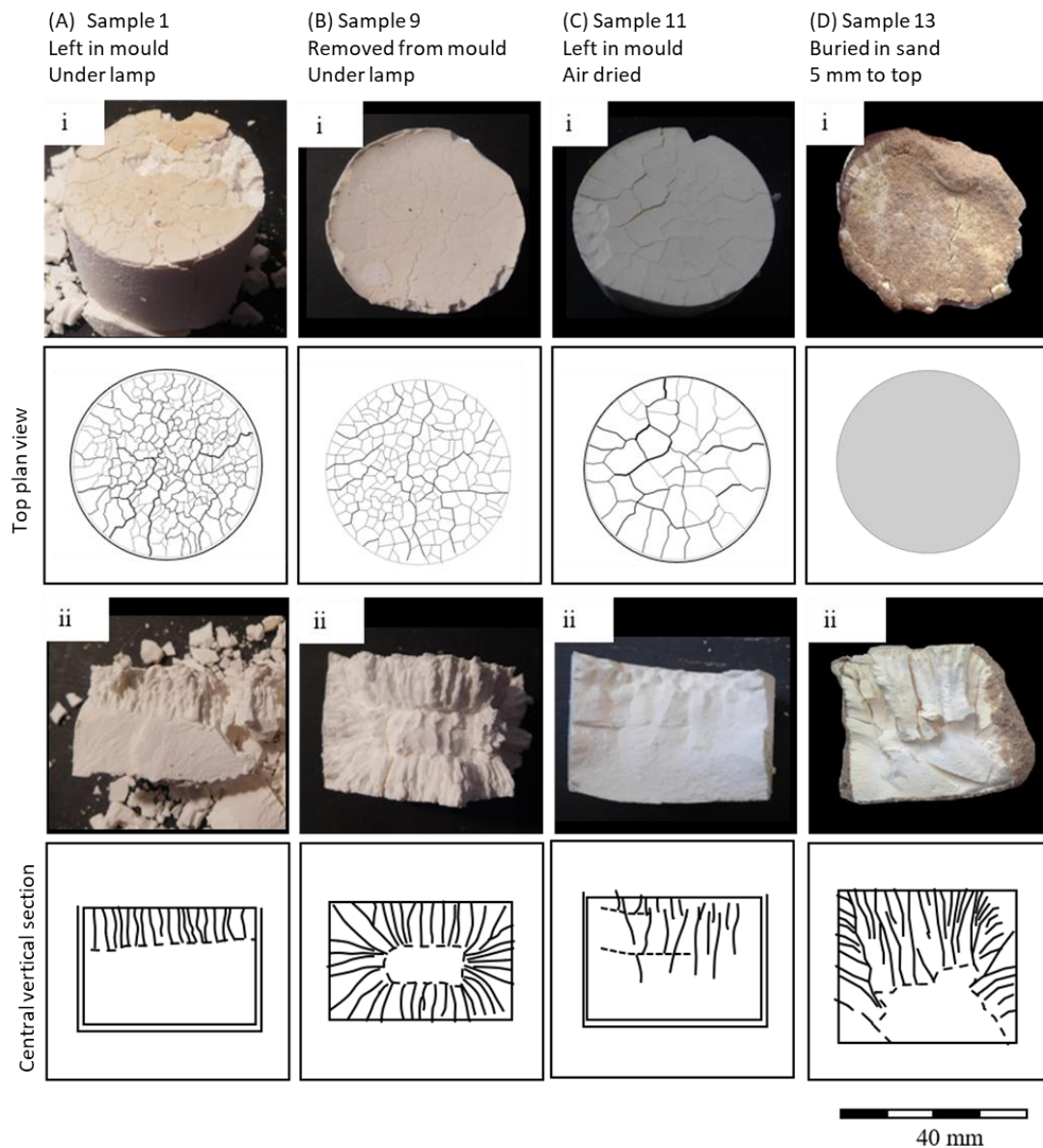


Figure 6.4. Comparison of drying methods for 40 mm by 40 mm cylinders (i) top surface of dried corn-starch patties (ii) broken vertically in half to reveal internal fracture patterns. These samples were generated as starch-patties under the heat lamp before leaving to dry.

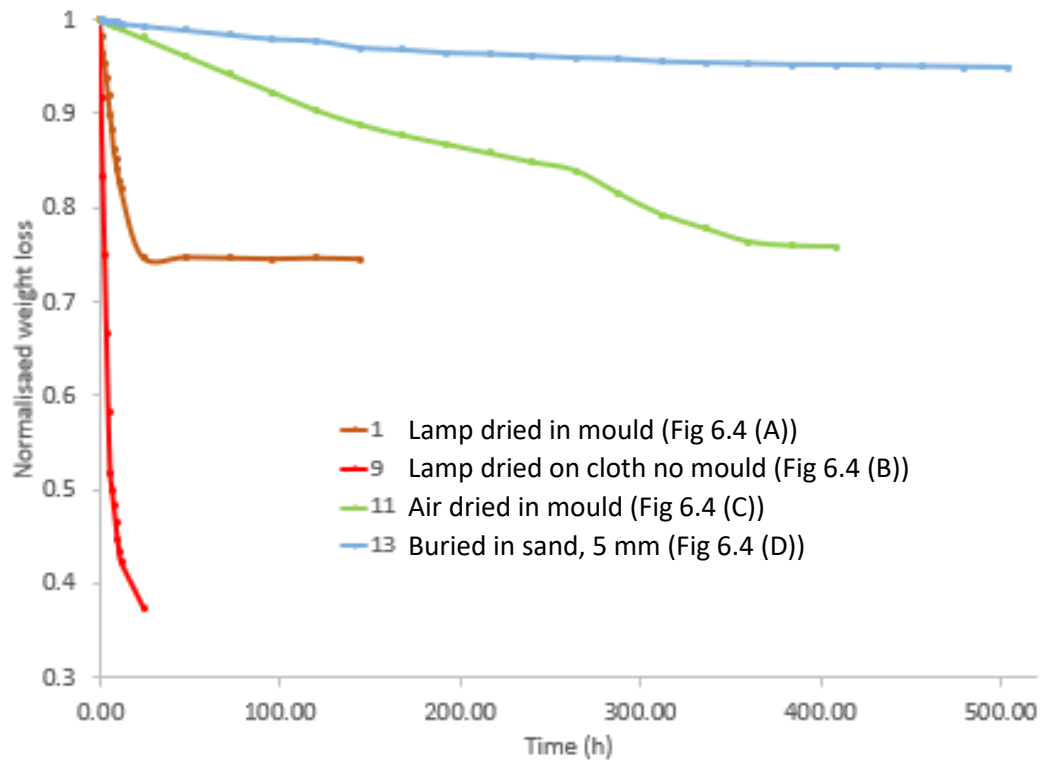


Figure 6.5. Graph of normalised weight against drying time for selected samples given in Figure 6.4.

Table 6.2. Quantitative analysis of top surface pattern

Sample number		Average		Total number of segments	Total length	Total number of edge fractures	Average		Density from segments P_{20}
		Burial depth	desiccation rate 24 hours*				distance from edge	Intensity P_{21}	
		mm	g/cm ² h	#	mm	#	mm	mm ⁻¹	mm ⁻²
1	LM-0-40-1	0	6e-2	444	911	45	2	0.72	0.35
2	LM-0-40-2	0	5e-2	617	1067	35	3	0.85	0.49
6	LB-0-40-2*	0	*	687	1098	35	4	0.87	0.55
7	LC-0-40-1	0	2e-2	561	1037	40	4	0.83	0.45
9	LN-0-40-1	0	2e-2	571	1029	41	4	0.82	0.45
11	AM-0-40-1	0	4e-2	97	395	21	6	0.31	0.08
16	BS-10-40-1	-10	5e-4	703	1139	49	2	0.91	0.56
17	BS-10-40-2	-10	3e-4	586	1008	46	3	0.80	0.47
23	BS-20-40-2	-20	2e-4	103	406	17	6	0.32	0.08
24	BS-20-40-3	-20	2e-4	126	441	23	6	0.35	0.10
27	BS-30-40-2	-30	1e-4	70	315	14	10	0.25	0.06
28	BS-30-40-3	-30	2e-4	40	247	13	8	0.20	0.03
29	BS-35-40*	-35	*	144	526	26	10	0.42	0.11
32	BS-45-40	-45	3e-4	22	172	8	9	0.14	0.02
39	BS-60-40-1	-60	*	31	242	13	10	0.19	0.02
42	BS-75-40*	-75	*	18	166	8	11	0.13	0.01
51	BC-20-40	-20	2e-4	201	576	28	3	0.46	0.16
52	BC-40-40	-40	1e-4	46	252	14	7	0.20	0.04
53	BC-60-40	-60	2e-4	50	255	13	8	0.20	0.04
58	BS-20-40-L1	-20	2e-4	100	401	17	4	0.32	0.08

*assuming surface area of 12cm² for samples left in mould and a surface area of 75cm² when removed from mould

Map view surface fracture patterns

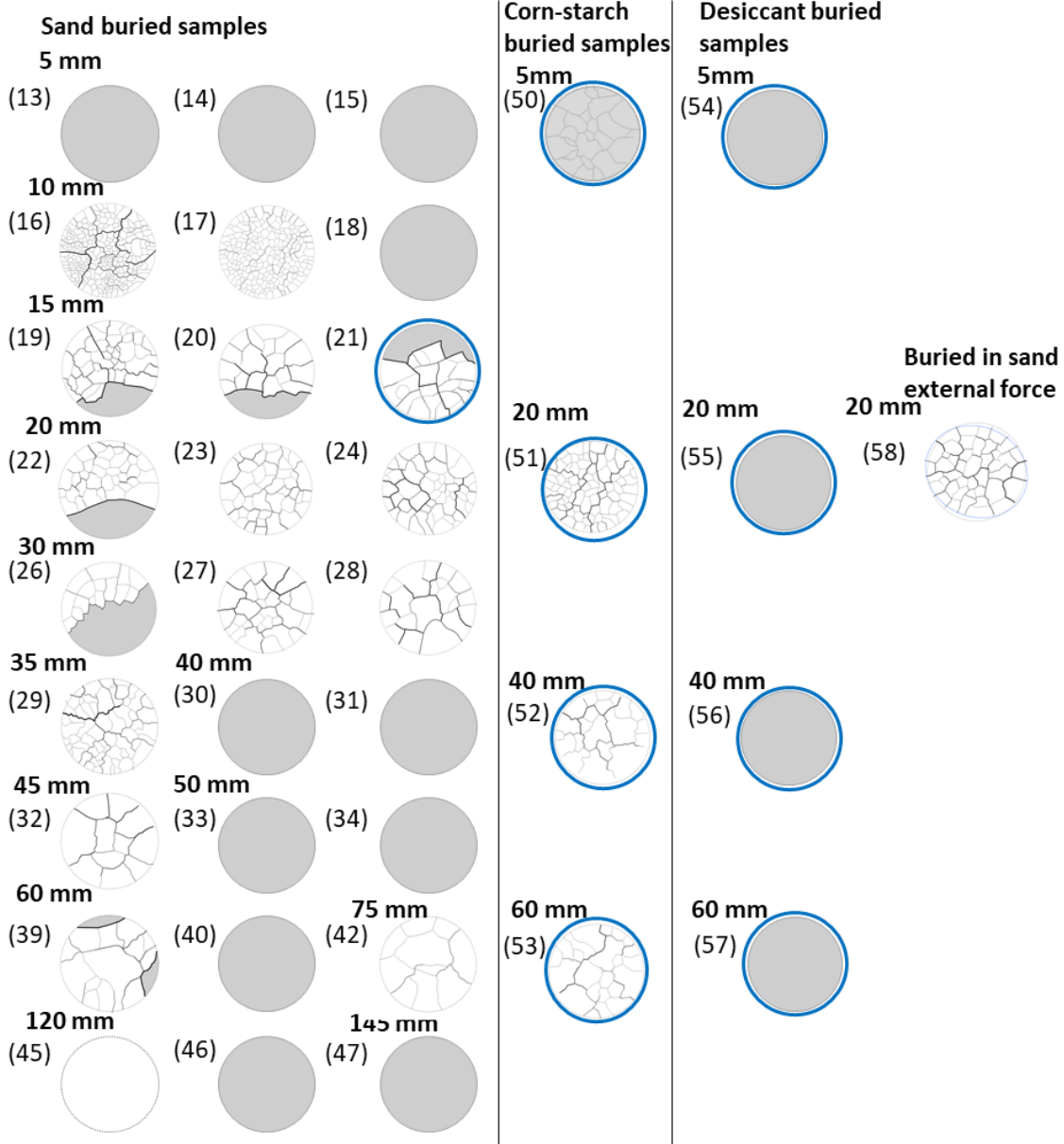
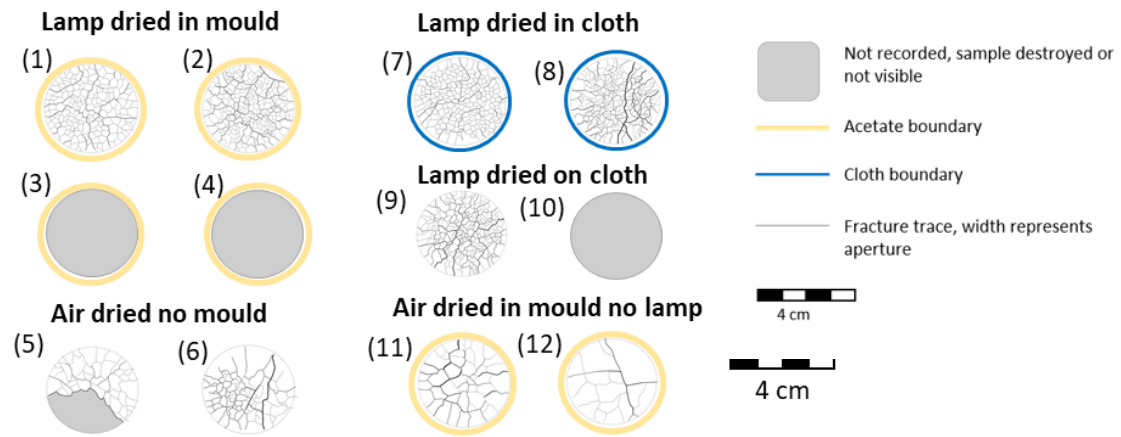


Figure 6.6. Line diagrams map view of surface fracture patterns. Samples which did not fracture are not shown.

The fastest dried samples (under the lamp) have the greatest number of surface fractures and form small blocks (~ 0.1 cm – 0.5 cm) with irregular edges (Figure 6.6). Air-dried and buried samples form larger surface blocks (~ 0.5 cm to 1 cm). Larger block sizes dominate in the buried examples (Figure 6.6). Surface blocks form more angular geometries in the corn-starch buried example than in the sand buried samples without a cloth cover (c.f. samples 51 with samples 22 – 24 and sample 60 with sample 39, Figure 6.6). Sample 21 was buried in sand with a cloth cover for comparison and fractures have a similar angular relationship as the corn-starch cloth covered samples. Surface patterning on the desiccant buried samples was not visible.

Fracture traces in the buried examples are smoother than in the lamp-dried examples. Fracture networks on the top surface can be described as random and irregular in the lamp dried examples to random and regular in the air dried and buried examples (Figure 6.6). Surface patterning is influenced by the application of an external force. When an external force is applied prior to burial, fracture traces preferentially align to the direction of the maximum applied force (sample 58, Figure 6.6). In all the samples the fractures extending from the top surface margins are oriented perpendicular to the margin. The trace length of fractures perpendicular to the margins are shortest in the lamp dried examples (~0.1 cm, i.e., samples 1 & 2 Figure 6.6), increasing in trace length with depth of burial (~ 1 cm at a burial depth of 75 cm, i.e., sample 42 Figure 6.6, Figure 6.7). The total trace length of all combined fractures decreases in buried samples as fewer fractures formed. Fracture intensity (P_{21}) decreased as the rate of drying slows and as burial depth increases (Table 6.2 and Figure 6.8). P_{21} values for lamp dried examples are $\sim 0.85 \text{ mm}^{-1}$, comparable to the shallow (10 mm) sand buried samples. P_{21} values are $\sim 0.3 \text{ mm}^{-1}$ for 20 mm sand buried examples and 0.2 mm^{-1} for 30 mm for buried examples (Figure 6.8). Similarly fracture density P_{20} based on the number of segments per area decreases as the rate of drying slows and as burial depth increases (Table 6.2). Fracture apertures vary between 0.1 and 0.6 mm. A visual representation of varying apertures on the top surface is given in Figure 6.6. A higher proportion of thin apertures are recorded for the non-buried and shallow buried samples. Fracture traces on the sides of the cylinder are like the top surface of exposed air-dried samples (Figure 6.9A). In buried samples the pattern of fracturing is different, being dominantly perpendicular to the top surface (Figure 6.9 B). Topological assessment of fracture traces on the top surface demonstrates that edge I-node number decreases in buried samples. Only the externally loaded samples contain internal I-node terminations. There is little correlation between the proportion of Y- and X- terminations within in the samples. A slightly higher proportion of X- nodes are recorded in the air dried and shallow buried sampled but this may be down to the scale of fractures intersections below a scale which is visible to the naked eye (Figure 6.10).

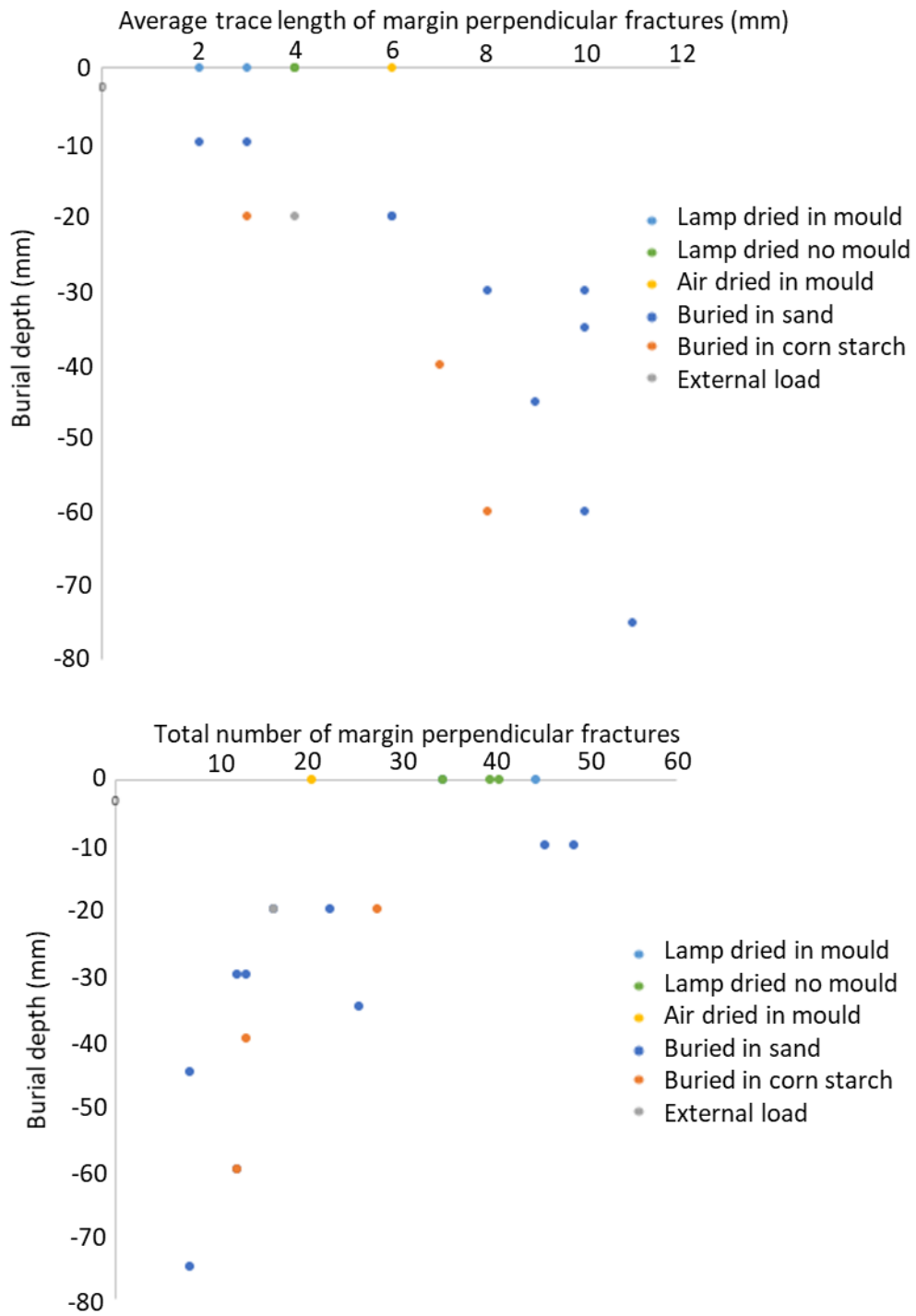


Figure 6.7. Plots of number of trace length and total number of sample edge fractures against burial depth.

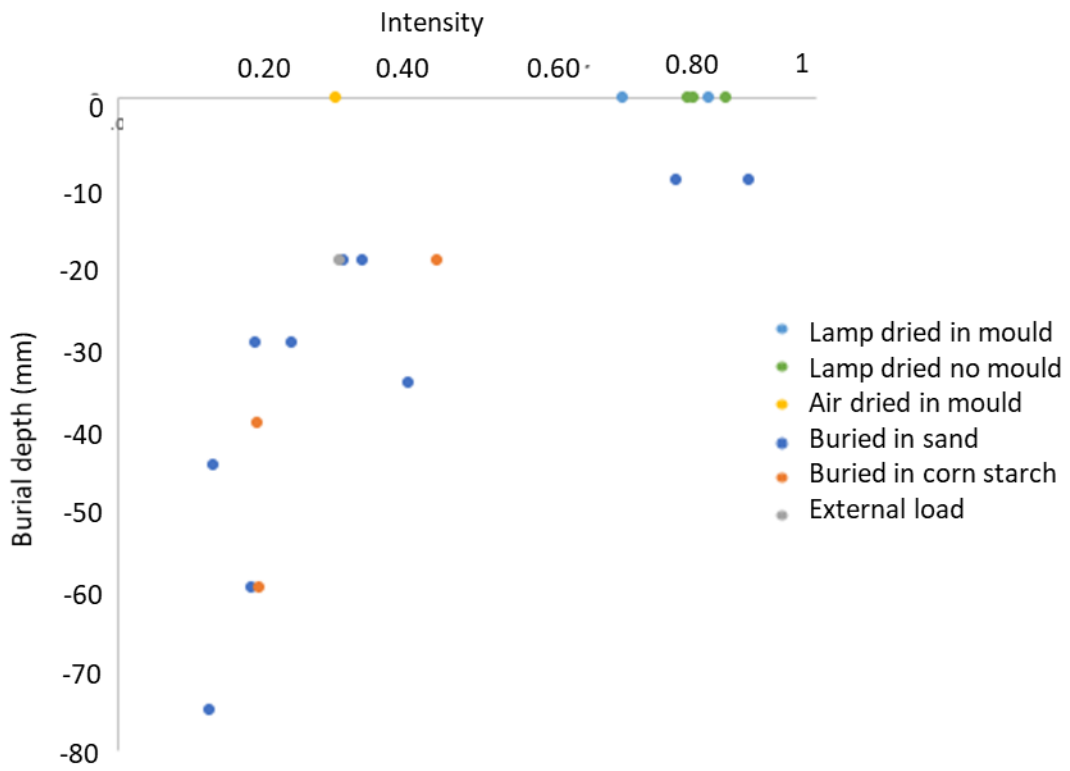


Figure 6.8. Plot of top surface fracture intensity value (Table 6.2) plotted against burial depth.

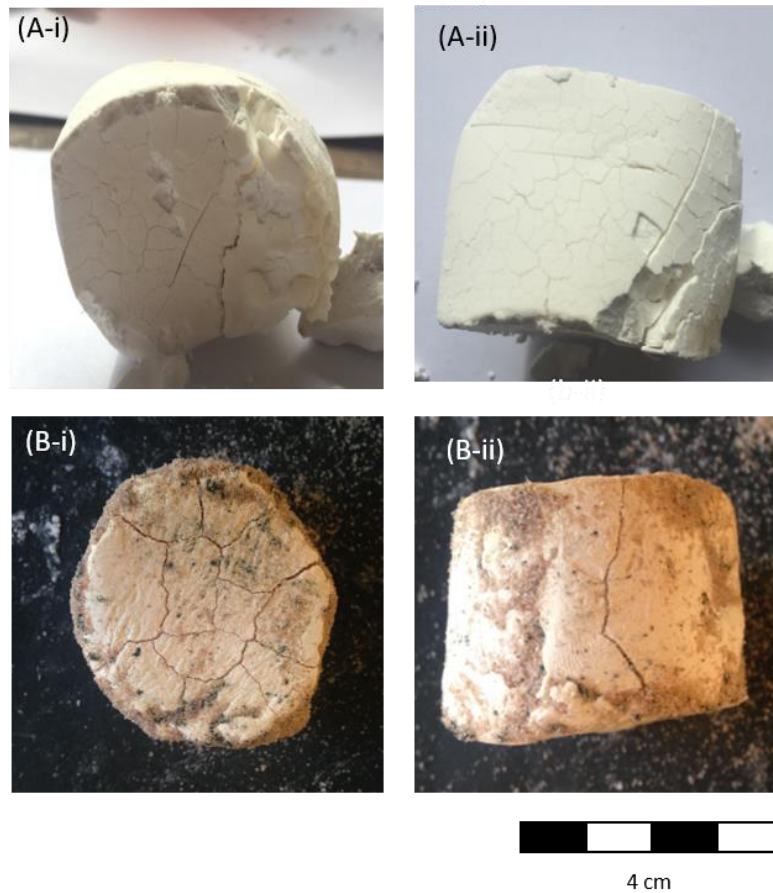


Figure 6.9. Comparison of top and side fracture patterning, (i) top surface of dried corn-starch patties (ii) side fracture pattern. (A) air dried out of mould (sample 6) and (B) sand buried (sample 32).

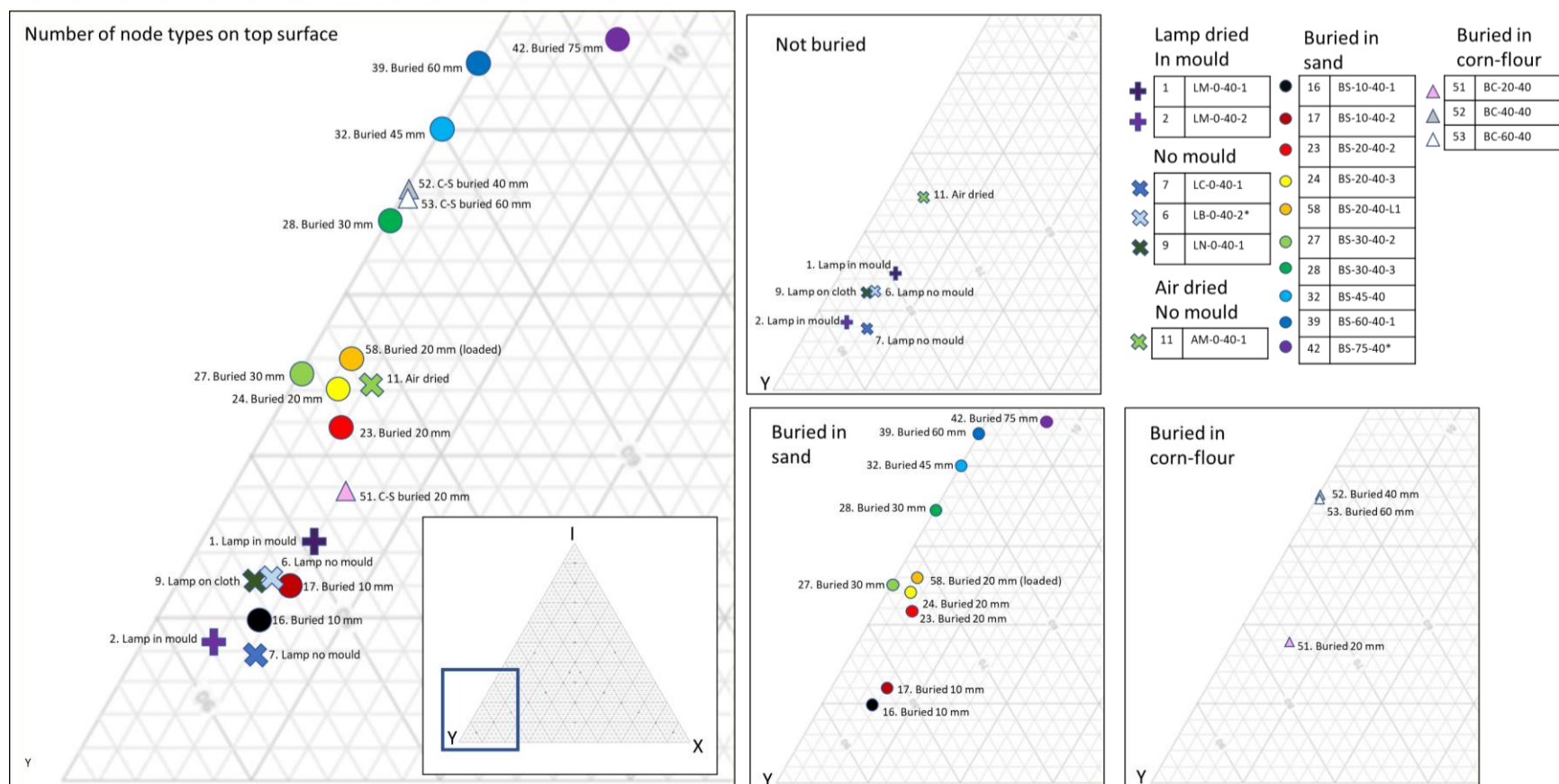
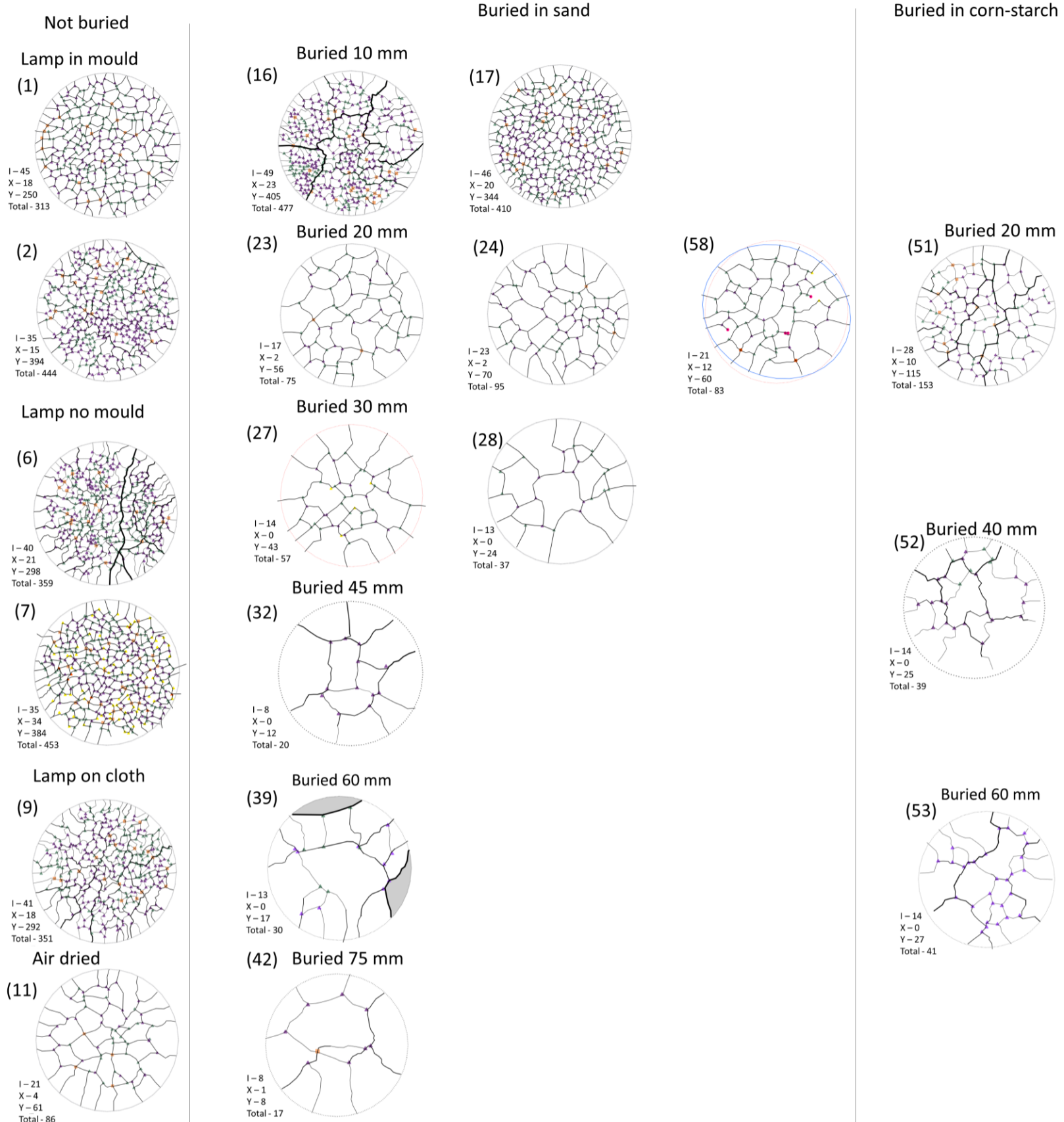


Figure 6.10. Topological analysis for top surface fractures plotted on a I-Y-X diagram. Internal I node marked as circle, Y nodes triangle and X nodes square. Edge I nodes are not marked but are include in the I node count (see appendix D Table D6-3 p.358 for tabulated data).

Internal section fracture pattern

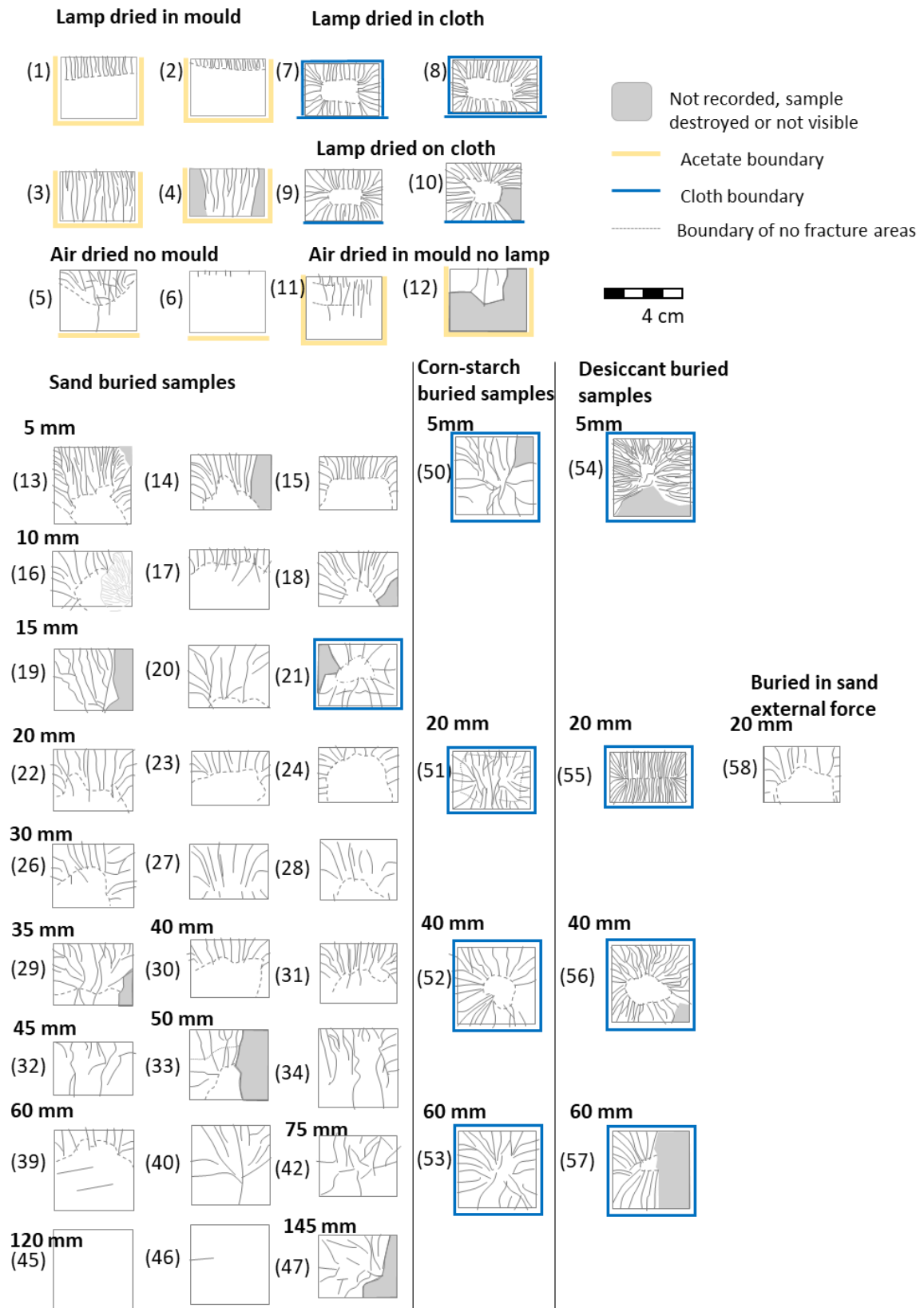


Figure 6.11. Line diagrams of internal fracture patterns. Samples which did not fracture are not shown.

Internally formed fractures extend up to a sharp boundary with damp, unfractured corn-starch, marked by a dashed line in Figure 6.11. The density of fracturing decreases towards the centre and bottom of each sample.

Lamp dried examples produced smaller (1 mm spacing) and more frequent columns (i.e., samples 1 - 4, Figure 6.11) than air-dried examples (~2 to 4 mm spacing i.e., sample 11, Figure 6.11). Fractures formed when the patty is suspended on a cloth creates ~1 mm diameter column's perpendicular to every margin of the sample (i.e., samples 9 & 10, Figure 6.11).

In the buried patties (Figure 6.6) fractures curve downwards from the top surface and margins. Internal fracture orientations are non-columnar to roughly columnar and to various degrees are curved. Orientations of fractures formed are near vertical and perpendicular to the margins or concentric to the margins and curve downwards. The fractures are not as distinct as the fractures formed in lamp and air-dried examples (i.e., samples 13 – 47, Figure 6.11) and are more widely spaced (2 – 3 mm).

The patties that were buried deeper have fewer and less curved fractures than those with shallow burial and are observed to coarsen and appear to become more planar with depth (Figures 6.11 & 6.12). Fractures decrease in number towards the centre and bottom of each sample. In samples that were cloth covered prior to burial (i.e., samples 21, 50 to 57, Figure 6.11) fractures formed approximately perpendicular to the top, sides and base. Fractures are finely spaced (~ 1 mm columns) in desiccant-buried samples (samples 54 to 57, Figure 6.11) and corn-starch columns are spaced at ~2 to 4 mm (samples 50 to 53, Figure 6.11). The influence of burial depth and related drying rate is presented in Figure 4.13. Fractures in the slower dried and deeper samples are fewer in number and more widely spaced.

Where the corn-starch slurry was added directly to the sand without moulding (samples 48 & 49) fractures did not form. A cemented zone of sand formed around the corn-starch and probably prevented evaporation of water (Figure 6.14). Fractures also did not form in seven of the buried samples (35 to 38, 41, 43 & 44, 48 & 49, Figure 6.14). It is assumed that water did not sufficiently evaporate from these samples, as the patty was still damp and had not fully dried.

In two of the samples (33 & 55) early fractures formed through the entire depth of the corn-starch patty. Plumose textures formed on these early fractures (Figure 4.15 A). They formed early when the starch patties were still damp.

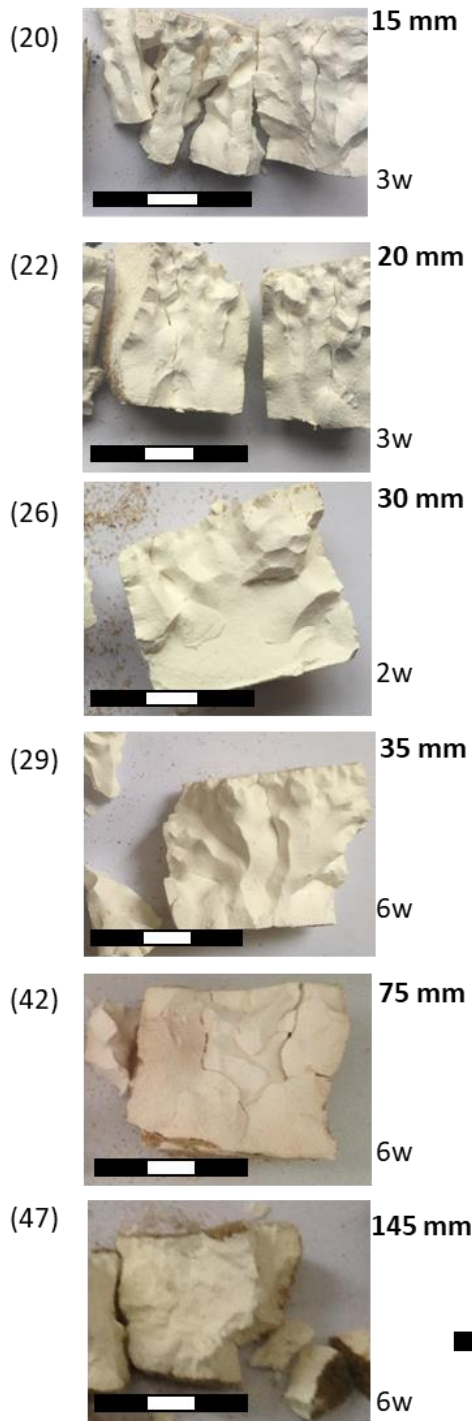


Figure 6.12. Comparison of varying internal fracture patterns with burial depth for 40 mm by 40 mm cylinders. Sand buried samples. Sample number and depth to top of sample given. Approximate length of time left to dry given in weeks.

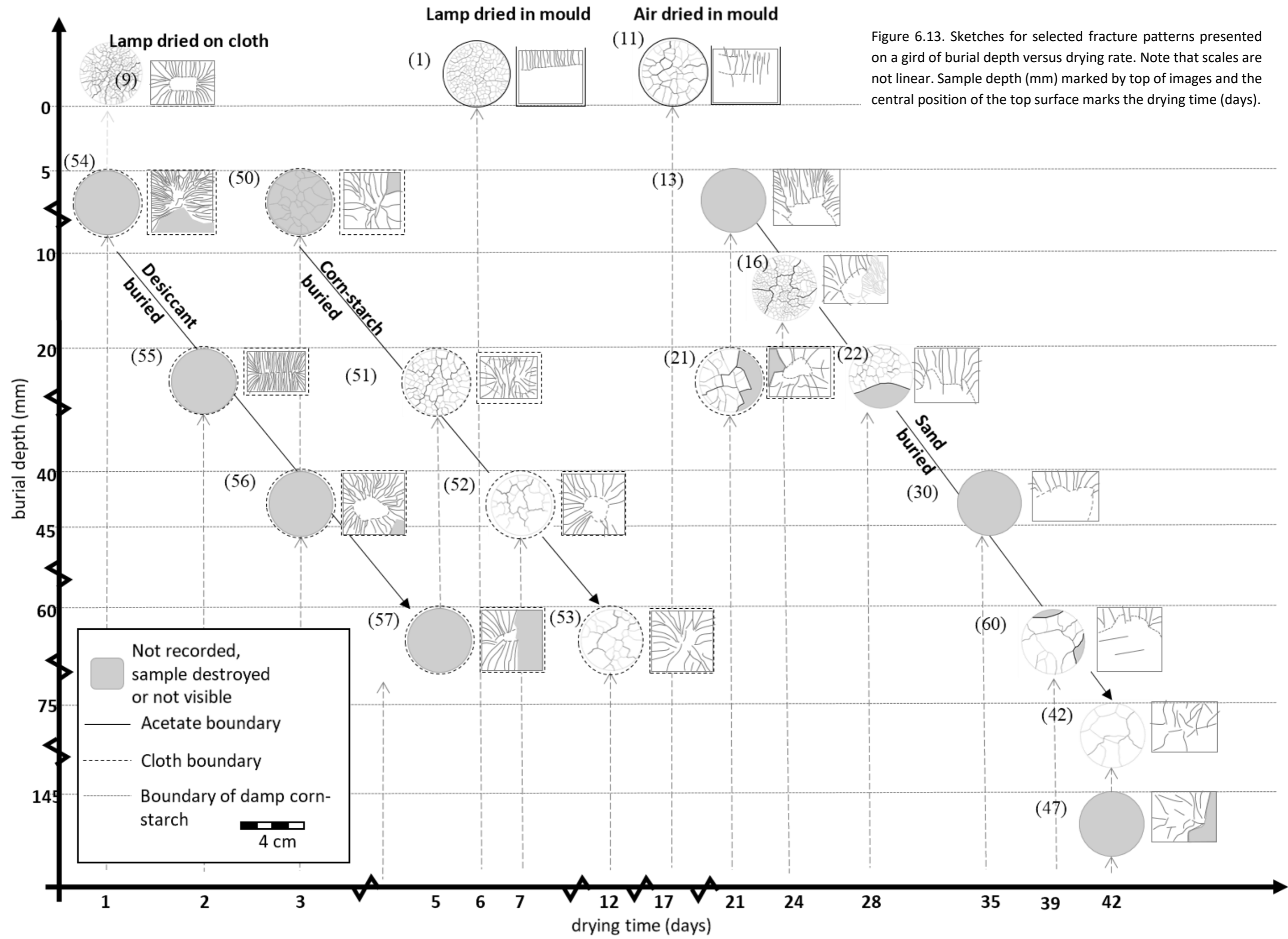


Figure 6.13. Sketches for selected fracture patterns presented on a grid of burial depth versus drying rate. Note that scales are not linear. Sample depth (mm) marked by top of images and the central position of the top surface marks the drying time (days).



Figure 6.14. Example of samples in which no fractures formed. (i) top surface of dried corn-starch patties (ii) broken vertically in half to reveal no internal fracture patterns. For (A) sample 45 and (B) sample 48. Scale bar 5 cm.

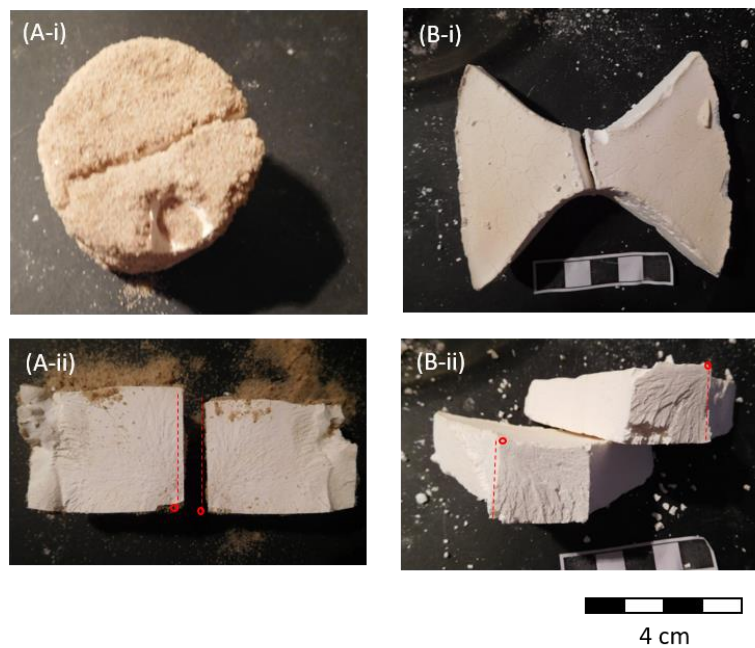


Figure 6.15. Examples of fractures extending the entire height of the geometry with plumose pattering on surfaces. For (A) sample 33 and (B) sample 77 (i) top surface and (ii) vertical fracture surface. Initiation point marked with open red circle. Red dashed line are matching sides of samples showing both sides of the plumose structures on the fracture surface.

6.5.2. Geometries B - E

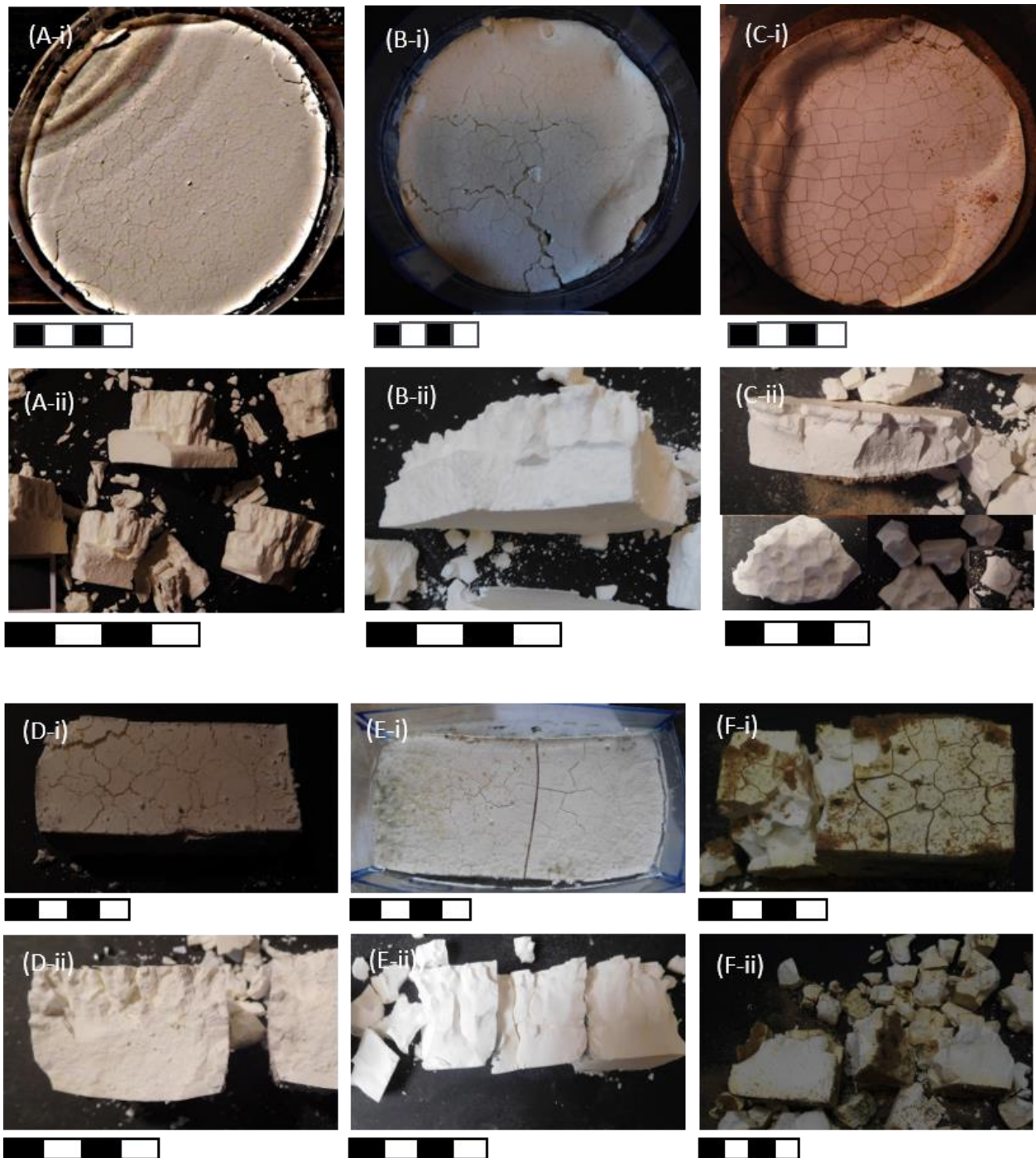


Figure 6.16. Comparison of fractures formed for geometries B and D for various drying methods. for flat cylinder; 10 cm diameter, thickness 2 cm and rectangle; width and height 4 cm and length 8 cm (i) top surface of dried corn-starch patties (ii) broken vertically to reveal internal fracture patterns. (A) left in mould under lamp (sample 61), (B) left in mould no lamp (sample 62), (C) buried in sand (sample 63), (D) left in mould under lamp (sample 71), (E) left in mould no lamp (sample 74), and (F) buried in sand (sample 75). Scale bar 4 cm.

Modifying the geometry to a flat cylinder (geometry B, samples 61 to 65), brick (geometry D, samples 71 to 76) and hour glass (geometry E, samples 77 - 79) results in a similar style of fractures as for the short cylinders described above (Figure 6.16). The tall cylinder (geometry C, samples 67 to 70) did not result in internal fracturing as for the other samples. Full going fractures formed in five of the samples (69, 74, 77 to 79). Plumose fractures formed on three of these fracture surfaces (samples 77 to 79, Figure 6.15 B). Plumose structures appear to form when rupture occurs on samples when they are still damp.

The top surface patterns for the flat cylinder (geometry B) with a diameter of 100 mm and left under the heat lamp to dry (Figure 6.16 A), air dried (Figure 6.16 B) and buried in sand to a depth of 5 mm (Figure 6.16 C), have a similar patterning of surface fracturing to the 40 mm by 40 mm cylinders.

Desiccation of a flat cylinder of rice starch under the heat lamp (Figure 4.17) over seven days resulted in the cylinder reducing in size from diameter 10 cm and height 2 cm (157.08 cm^3) to diameter 8 cm and height 1.2 cm (60.32 cm^3), a decrease in volume of 96.71 cm^3 (~40% volume decrease), which is a total mass loss of 97.84 g. Surface fractures are more prominent on the base than the top. Initial surface fractures were perpendicular to the margin but also formed parallel / concentrically as well at around 0.5 to 1 cm from the margin. The fractures perpendicular to the margins propagated most of the way to the centre of the cylinder. Internally 0.5 cm columns formed vertically from the top surface.

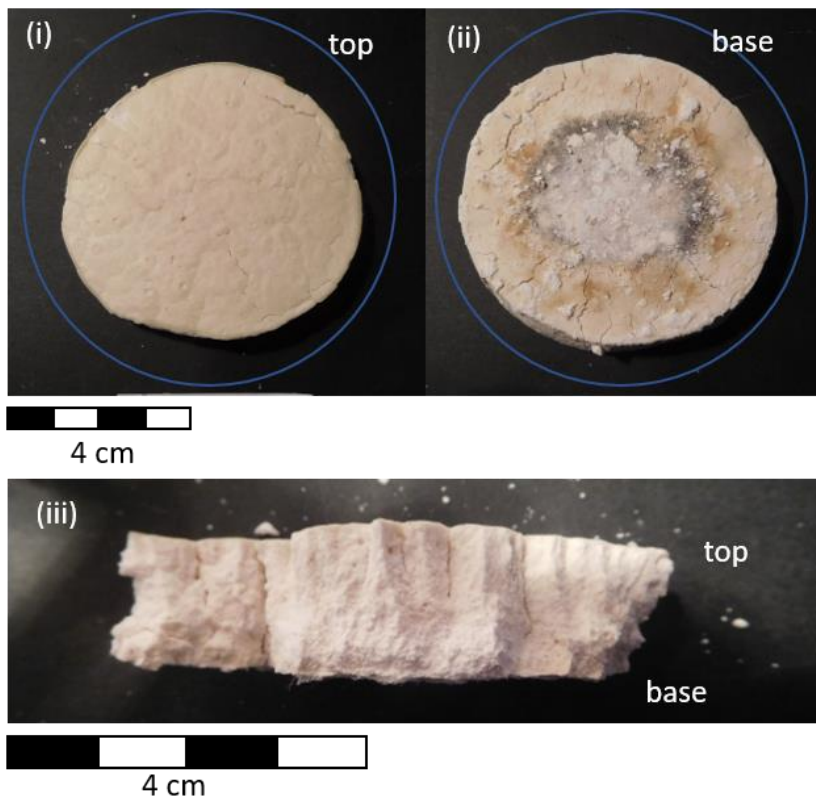


Figure 6.17. Rice starch flat cylinder 10 cm diameter, thickness 2 cm. Sample 66 (i) top surface (ii) bottom surface, black and white mold can be seen growing on the bottom. Blue line around photos (i) and (ii) mark the original extend of the rice starch prior to contraction during drying, (iii) large columnar joints are formed internally.

6.6. Discussion

6.6.1. Experimental Results

Trace lengths of fractures visible on the top surface are greatest when samples are buried deeper or dried more slowly. The total number of fracture traces on the top surface reduces in the slower dried and deeper buried samples while the lengths and smoothness of these fractures increases (c.f. samples 1 and 11, Figure 6.13). This variation suggests that fractures formed on the top surface are dependent on drying time which influences the length and spacing of resulting fractures. Longer drying times result in fewer and longer fractures. The increase in smoothness of the formed fracture trace with increased drying time may suggest that local stresses from grain boundaries have less effect with slower desiccation rates, in agreement with Akiba et al. (2017).

The orientation of fractures formed on the top surface is also influenced by external loading. It is possible that either development of shear zone or grain alignment in the partly consolidated starch-patty influence the propagation direction of cracks resulting from stresses during drying. Fracture patterns formed in drying corn-starch have been shown to be influenced by the application of faraday waves to the wet mixture (Nakayama et al., 2013; Nandakishore and Goehring, 2016). The influence of external loading of the body is also identified in numerical modelling and in the field. Additional testing to quantify the external force would be required to analyse the effects of external loads in detail.

As with fractures formed on the surface of the sample, increasing burial depth and decreasing drying rate result in fewer fractures forming internally. Internal fracture orientations are dependent on the margin of the sample from which drying occurs (i.e., vertical or horizontal). In geometry A, the contraction of the cylindrical volume results in radial and inward dipping fractures, related to radial and vertical tensile forces. The change in dip of concentric fractures indicates a change in stress direction with depth both within the sample and with burial depth (c.f. Odone et al., 1999).

6.6.2. Experimental Uncertainties

Several errors are likely to be inherent in the modelling procedure:

- (1) A variation in the desiccation rate was noted between experiments run during the summer July 2017 CUROP project (faster) and later experiments (slower) run in December 2017. This is likely related to differences in the temperature and humidity levels (Table 6.3). Air humidity likely controls the initial hydration level of corn-starch (Goehring 2003) and sand. For the post-

CUROP experiments the sand was oven dried around 120°C for 4 hours to minimise its water content. Air temperature also likely influenced drying rates.

Table 6.3. Temperature and humidity values for Cardiff for July and December 2017, data from <https://www.timeanddate.com/weather/uk/cardiff/historic?month=7&year=2017>

	July 2017	December 2017
Maximum temperature °C	26	13
Minimum temperature °C	9	-1
Mean temperature °C	17	6
Maximum humidity %	100	100
Minimum humidity %	37	61
Mean humidity %	83	90

- (2) The corn-starch slurry was mixed with water in batches of ~250 g corn starch. This was found to be the most suitable volume to allow for mixing. This means that there may be some variation associated with the volume of each component (corn-starch, water and bleach) in each slurry batch. Because of variability in the initial hydration levels and variation in mixtures Goehring (2003) estimated a maximum 5% accuracy in the preparation of the mixtures. A similar level of error is expected here.
- (3) In some cases, the moulds leaked from the taped margins. Once wet it was not possible to re-tape. Further leakage was prevented by placing the mould in a small cup and topping-up the slurry and placing sand around until the pressure outside prevented additional escape of the corn-starch slurry.
- (4) Lamp dried models took longer than a day to dry and when left unattended (i.e., overnight) the heat lamp was switched off to reduce fire risk. In some of the experiments the rate of drying is seen to decrease during these periods.
- (5) The scaling of the sample sizes was selected to allow practical handling in the lab and reasonable drying times. Although they are not scaled to the 2 to 3 orders of magnitude as estimated from experiments forming columnar joints (Müller, 1998a,b; Goehring et al., 2006), similar surface fracture patterns are produced when the diameter of samples is varied, therefore suggesting that fracture orientation and scale is independent of sample size.

6.6.3. Additional Modelling

Modelling results could be further investigated through statistical analysis of internal fracture patterns. This could be done using either x-ray tomography or possibly using a resin to glue the models and slice them to view under a microscope. Analysis using x-ray tomography could provide insight into internal fracture propagation, by scanning the sample as drying proceeds. Microscopic analysis might

reveal insight into the mechanism of failure. Additional models could be run to access the influence of applying an external load prior to burial, the test example (sample 58) showed that applying an external load prior to burial influenced the resulting fracture patterns.

6.6.4. Comparison to Fracture Orientations in Conceptual Models

The analogue modelling produces fractures that formed by contraction of drying corn-starch. The radial fracture patterns (Figure 6.18) mimic orientations of margin perpendicular fractures predicted by numerical models with circular geometries (c.f. Bergbauer et al., 1998).

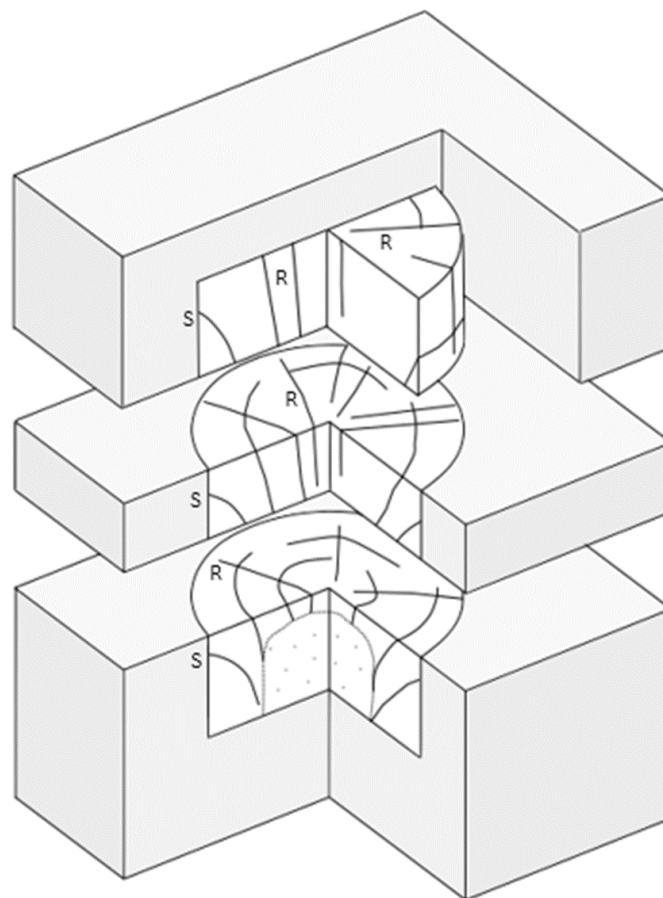


Figure 6.18. Sketch of key internal fracture orientations produced in sand buried corn-starch patties. R, fractures near vertical with radial strikes; S, fractures from vertical margins, curve downwards and strike concentrically around the sample. Stippled area nonfractured domain of damp corn-starch.

The orientation of the concentric fractures from the analogues (Figure 6.18) are comparable to marginal fissure orientations in the Cloos model (see Chapter 2, Figure 2.1. p.14). Although the analogue models presented do not rule out the formation or movement of marginal fissures due to

emplacement forces, as suggested by Cloos, fractures of similar orientations may be produced by cooling and contraction.

6.6.5. Comparison to Numerical Models

In circular two-dimensional numerical models, the predicted plane perpendicular to the minimum compressive stress forms a radial pattern (Figure 6.19. B). This radial plane is expected to be in the orientation of Mode I tensile failure. Fracture patterns formed on the surface at the out edge of the top surface (Figure 6.19. A) and internally in the analogue models (see Figure 6.18, R-fractures) are equivalent to this orientation. However, radial fractures on the top surface of the analogue models are only observed to extend radially from the external edge of the top surface for a set distance, dependant on drying rate. Towards the centre of the top surface the radial pattern changes and becomes tangential and radial (e.g., Figure 6.19. A). This is different from the two-dimensional numerical models which would suggest that radial fractures would propagate to the centre of the circle (Figure 6.19. B). In cylindrical numerical models the intermediate principal planes curves down and rotates over time (Figure 6.19. B). The amount of curvature with depth of the intermediate principal stress direction is influenced by depth (see chapter 3) this orientation is comparable to those formed internal in analogue models (cf. Figure 6.19 C and Figure 6.18, S-fractures).

Application of failure criterion to numerical models predicts that shear failure will occur prior to tensile failure. The failure mode of the fracture in the analogue models cannot easily be determined, it is assumed to be predominantly tensile failure, although this cannot be confirmed. Microscopic work may provide additional insight into the failure mode in the analogue models.

Volume change in three dimensions as a result of temperature change can be approximated as $\Delta V = \beta V \Delta T$, where, V – volume, ΔV – change in volume, β - coefficient of volume expansion and $\beta \approx 3\alpha$ where α is the coefficient of linear expansion, ΔT is the change in temperature. Based on this the volume change for a 50 km³ volume cooled by 500 °C were α is 8e-6 (1/°C) then volume change would be expected to be 0.6 km³ ~ 1% volume change. The volume change in analogue models formed of corn-starch was undetectable. Test models run using rice starch results in a ~40% volume decrease considered to be too large to be comparable to the volume change of cooling plutonic bodies.

6.6.6. Comparison to Columnar Joint Formation in Drying Corn-Starch

Fractures presented in the buried analogues result from drying and contraction of corn-starch masses and are different from previously published experiments (e.g., Müller, 1998a, 1998b;

Toramaru and Matsumoto, 2004; Goehring et al., 2006; Morris, 2012) where drying was from a single planar surface and resulted in the formation of columnar joints.

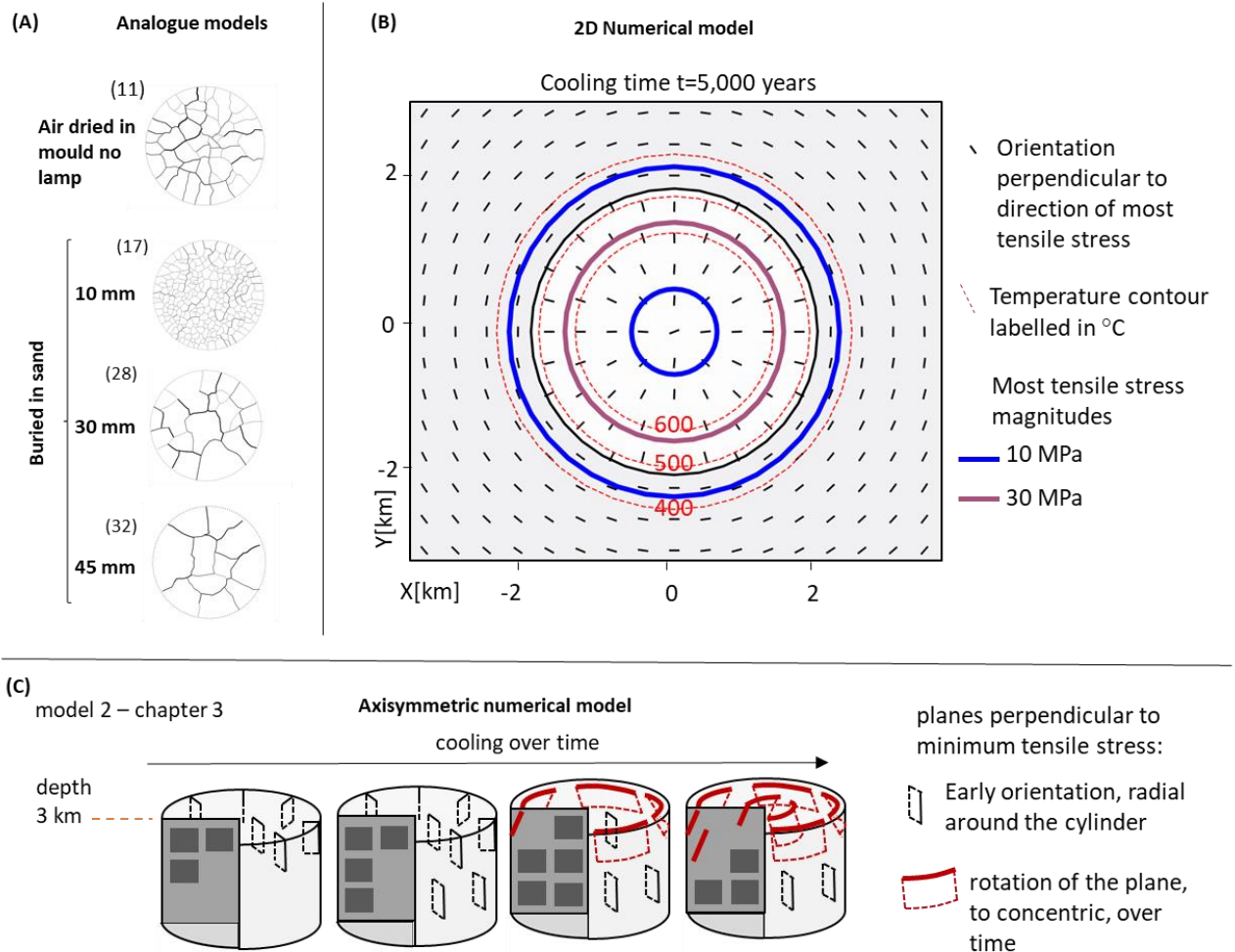


Figure 6.19. Comparison of analogue and numerical models. (A) Fractur patterns examples of the map view top surface of selected analogue samples, fractures at the edge of the top surface are radial around the sample, the distance of the radial fractures is dependent on drying rate. (B) Two-dimensional numerical model of a cooling pluton (after Bergbauer et al., 1998) the predicted orientation of the plane perpendicular to the direction of most tensile stress is radial around the pluton. This lane would be expected to be parallel to Mode I fractures. (C) Schematic diagram of planes perpendicular to minimum tensile stress predicted in axisymmetric numerical models (see chapter 3). The cylindrical geometry is shown with transparency to highlight the geometry of the plane. The cut away is show without transparency. Early orientations are outlined in black and shown as grey plane in the cut away. The rotation of the orientation over time is shown by the red planes which dip outwards towards the margins. (duplicate of Figure 3.58., P131).

Propagation directions of non-buried samples are compared to geometries found in columnar joints formed in cooling lava flows (Figure 6.20). Columnar joints formed in the samples presented

here are not as clearly defined as in published experiments (cf. Figure 6.1 p.243 with Figure 6.4 p.253). Rates of drying are slower in samples than previous experiments. The average desiccation rate ($0.3e-2 \text{ g/cm}^2\text{h}$) calculated for sample 11 (air dried in mould) and the average desiccation rates ($0.1e-2 - 0.01e-2 \text{ g/cm}^2\text{h}$) calculated for the buried samples are lower than the calculated critical desiccation rate for column formation ($0.8e-2 \text{ g/cm}^2\text{h}$) (Toramaru and Matsumoto, 2004). The critical desiccation rate for column formation may be lower in our models than in the Toramaru and Matsumoto (2004) experiments because of water retention in the burial media.



Figure 6.20. Comparison of corn-starch columnar joints to columnar joints found in the field. (A-i and C-i) sample 9, (A-i) sample 3, (d-i) sample 11, (A-ii) The Giant's Organ, Northern Ireland copyright Noelle Kelly, (B-ii) Boyabat, Turkey copyright Alican Aslan, (C-ii) Basalt columns at Devil's Postpile, California copyright Lee Foster and (D-ii) Jeju Island, South Korea copyright Jean-Noël Vignaroli.

6.7. Conclusions

Corn starch patties, buried to different depths under various media, are potential analogues of cooling plutons. The analogue modelling presented here was used to investigate fracture orientations that could result directly from the contraction of a volume. The process of contraction in the analogues is comparable to numerical models (c.f. Chapter 3). These models differ from other analogue models of fracturing in cooling plutons that did not consider contraction of a three-dimensional mass (e.g., Müller, 1998a, 1998b; Toramaru and Matsumoto, 2004; Goehring et al., 2006; Morris, 2012).

A method whereby corn-starch patties could be part solidified and removed from a mould prior to drying was successfully developed. The depth and geometry of the drying corn-starch volumes was varied. Despite uncertainties associated with the geometric scaling of the samples, analogue modelling has proved to be a useful exercise in considering variables and resulting fracture patterns from contraction of a three-dimensional mass.

Fracture geometry formed in the samples is controlled by both margin orientation and burial depth of the drying patty. Increased burial depth reduces the total number of fractures formed and the curvature of fractures. For buried samples with geometry A, cylindrical geometry, two key fracture orientations are formed: near vertical, perpendicular to the margins, and concentric to the margins, curving downwards. These fracture orientations are comparable to the radial fractures suggested by numerical modelling of cooling, and the marginal fissure orientations of the Cloos model respectively. In contrast to the Cloos model, the analogues suggest that marginal fissure orientations could result from contraction, rather than emplacement forces.

7. Synthesis

7.1. Addressing the Hypotheses

This thesis aimed to understand the influence of thermal stress on fracture formation in cooling intrusive rocks. Understanding and modelling these fractures is valuable for both fluid flow modelling (e.g., Gustafson and Krásný, 1994; Petford, 2003; Genter et al., 2010) and geotechnical analysis (e.g., Price, 1979; Segall and Pollard, 1983a,b; Christiansen and Pollard, 1997). Four research hypotheses and research objectives were developed to investigate the effects of thermal stress on fracturing in cooling plutonic bodies (chapter 1, section 1.5, p 11). The research objectives have been met by developing three-dimensional thermomechanical models (chapter 3), application of these models to case study examples (chapters 4 & 5) and the development of analogue models (chapter 6). The main conclusions from this thesis are discussed in context of the hypotheses proposed.

Hypothesis 1. Fracture sets of various orientations may be generated as stresses evolve in plutonic bodies during cooling.

Multiple sets of fractures with varying orientations are often recorded in field studies of fractures in plutonic rocks. Typically, two near vertical fracture sets, forming orthogonal patterns, intersect with diagonal and horizontal sets (e.g., Balk, 1937; Heidrick & Titley, 1982). Often mineral coating or fracture infill can be used to infer if these fractures are formed simultaneously in the early cooling history of the intrusive body (Balk, 1937; Hutchinson, 1956; Hibbard and Watters, 1985). In contrast, two-dimensional map view thermomechanical models of cooling plutonic bodies have been used to predict a single fracture orientation at any given location within the pluton (Gerla, 1983; Bergbauer, 1998; Mondal and Acharyya, 2018) and do not investigate the variation in orientation at a given point.

Three-dimensional numerical modelling developed in chapter 3 highlights that the principal stress directions, in some cases, may switch during cooling. The minimum principal stress may change from margin parallel to margin perpendicular. The questions of whether this switch could result in multiple fracture orientations was addressed through analogue modelling (chapter 6). Analogue modelling, using drying corn-starch patties, resulted in both radial and tangential fractures forming, supporting the idea that orthogonal fracture sets may be generated from evolving stresses in plutonic bodies during cooling.

Hypothesis 2. The relative importance of thermal and regional stresses that result in failure and fracture formation may vary during plutonic cooling.

The conceptual model of Heidrick & Titley (1982) highlights the relative importance of thermal and regional stresses, through identification of a spectrum of pluton centred and strike-parallel fracture sets. Thermomechanical modelling compared to field examples has also previously highlighted the importance of regional stress in influencing predicted orientations (e.g., Gerla 1988; Bergbauer, 1998). This is because the magnitude of thermal and crustal stresses are comparable.

As shown in chapter 3, modelled cooling histories of plutonic bodies are influenced by variables such as the initial temperature and defined thermal conductivity. Different variables controlling the initial model conditions may modify the temporal evolution and stress magnitude. However, there is a limited influence on the predicted orientation of principal stresses. The orientations are controlled by the pluton geometry and in-situ stress field. In anisotropic horizontal stress fields, the minimum principal stress preferentially parallels the margins and long axis of plutonic bodies. For applied regional loads the minimum principal stress within and around the pluton preferentially aligns to the least horizontal regional load. Within the pluton the orientations are also influenced by plutonic geometry. The relative magnitude of thermal and regional tectonic stress determines which stress dominates the orientation. Over time, in models, the thermal stresses are predicted to have a greater influence on orientation than the regional in-situ stress.

The magnitudes of tensile stress resulting from cooling are greatest where plutonic bodies are thinnest and cool the fastest. The magnitudes of tensile thermal stress resulting from cooling of plutonic bodies may offset compressive in-situ stresses resulting in fracture. The interaction of pluton geometry, overburden, regional and thermal stress, and fluid pressures means that the resulting stress path can be variable. The resulting stress path evolution and failure mode will therefore be dependent on initial conditions.

The relationship between the thermal and regional stresses is critical in controlling the orientation and stress paths experienced by a point within a cooling intrusion. As a result, fracture patterns may vary temporally and spatially.

Hypothesis 3. Stress paths for a given point within a plutonic body may pass through different failure fields i.e., failure in tension or shear.

Cooling fractures in intrusive rocks are typically considered to result from opening mode failure and in the Cloos model these fractures are classified as joints. Despite this, classification of cooling fractures as joints is cautioned against by Price (1966) as these fractures often display evidence for shear. Comparison of predicted stress paths in thermomechanical models by Knapp (1978) Gerla (1988) and in chapter 3, this thesis, highlights that shear failure may precede tensile failure in cooling plutons. The timing of shear can be hard to distinguish as it may be due to later reactivation.

The Griffith & Griffith-Murrell failure criteria applied to thermomechanical models of the Alta stock shows a sequence of failure transitioning from shear to extensional shear to tensile failure (chapter 4). The earliest record of failure in the Alta stock is observed as aplite dykes. These display a range of deformation styles interpreted to include emplacement into a deforming host, extensional-shear and opening mode failure. Early shear failure, as predicted by the numerical models, may not be preserved because the temperatures were above the brittle-viscous transition (Fournier, 1999; Violay et al., 2017).

The failure sequence predicted by the thermomechanical models is dependent on the temperature experienced along a stress path and the in-situ stress state. The models do not account for stress redistribution due to fracture initiation. Fracturing events are likely, at least locally, to result in modification to the stress field and to the propagation direction of the fracture (e.g., Renshaw and Pollard, 1994). Despite not accounting for stress redistribution as a result of fracturing, numerical models provide a reasonable match to field data. This suggests that early fractures have a limited effect on ongoing fracturing during cooling. This may be the result of high temperatures (>600 °C) where fractures may be annealed or infilled.

Hypothesis 4. Depth and temperature dependent material properties will influence stress path evolution and control the resulting failure mechanism and timing.

Numerical models of Žák et al. (2006) highlight that a model accounting for temperature dependent properties and the Drucker-Prager yield criterion does not predict failure as a result of cooling of the modelled deep (~8 km) Tanvald pluton. Depth and temperature dependence of material and mechanical properties are systematically tested here (chapter 3) and compared to the applied failure criterion.

With increasing depth failure is less likely to occur, as thermal stresses do not exceed the brittle failure criterion as a result of overburden. The depth at which stresses remain compressive is determined by the pluton volume, dimension and in-situ stress state. Tensile stresses as a result of cooling are generated at shallow emplacement levels < 5 km for a pluton with volume of ~21 km³. If the failure criterion is exceeded failure propagates inwards from the margins as cooling proceeds.

Accounting for temperature dependent properties leads to the prediction of more complex failure sequence, in which stress paths migrate away and then towards the domain of no failure. The solid elastic thermomechanical parameter (the product of the Young's modulus and coefficient of thermal expansion) has the greatest influence of all the material properties influencing the spatial and temporal positions of the predicted failure domains. Accounting for temperature dependent mechanical properties reduces the area of failure and decreases the likelihood of shear failure as the domain of shear failure decreases with increasing tensile strength related to a decrease in temperature.

Modelling results are sensitive to both the modelled depth and applied material properties and will influence the stress history experienced at a point within the pluton. In turn this will influence the resulting failure mechanism and time of predicted failure and predicted fracture patterns.

7.2. Limitations with Numerical Modelling

Three-dimensional modelling is limited by the capability of the software and hardware. Complex geometries, such as the KUC 2007 representation of the Bingham Canyon magmatic complex (chapter 5), are too complex for the software to handle. Models simplifying three-dimensional geometries to cylindrical projections, with horizontal tops and bases did run. It would be expected that geometries with non-vertical and non-horizontal surfaces would locally impact the predicted principal stress orientation. Predicted orientations from two-dimensional models are comparable to results from three-dimensional models cut on a horizontal plane, centrally through thick plutonic bodies.

Numerical models simplify the cooling history of the pluton to conductive cooling. Many factors may alter the cooling rate of a plutonic body e.g., latent heat of crystallisation, convective cooling and incremental emplacement (also see section 2.4.2. p.27). Comparison of Knapp, 1978 and COMSOL® models (chapter 3 section 3.5.1 p.74 - 80) highlights that accounting for phase change does not significantly alter modelling results. The magnitude of predicted stress will alter depending on the rate of heat loss from the modelled plutons. Predicted orientations of principal stresses will primarily be controlled by plutonic geometry, volume and depth. Incremental emplacement and stress distributions within the host rock are likely to be the main factors that would alter the initial predicted orientations of the principal stress axes. Modifying the initial host rock temperature i.e., increasing the geothermal gradient to account for emplacement of surrounding intrusions (e.g., Cook and Bowman, 1994) or decreasing the gradient to account for increases cooling due to convection (e.g., Knapp, 1978) has limited influence on predicted orientation of the principal stress axes. Within the host rock the geothermal gradient is modelled as linear. This may result in modelling an unrealistic temperature with depth (chapter 4 section 4.7.2. p.200).

As these numerical models only account for instantaneous emplacement and conductive cooling the models are most comparable to plutonic bodies that are (1) emplaced at rates greater than 2 cm / year, (2) have limited time gaps between incremental emplacement and, (3) in systems at early stages of cooling before significant fracturing of the host rock and/or development of hydrothermal systems

The prediction of the failure mode and timing is dependent on the applied failure criterion. There are numerous failure criteria available (Colmenares and Zoback, 2002; Rahimi and Nygaard, 2015; Ma et al., 2017) which could have been applied to modelling. The factors which will influence

the results most significantly are temperature dependence of the physical properties, fluid pressures and the potential for stress redistribution as a result of fracturing.

Changes in fluid pressure are likely to influence the stress paths of any selected point and influence the mechanical behaviour of the rock mass. The completed modelling focused on conductive cooling and did not account for fluid pressures (See section 2.4.2 p.27 – 28). This assumption is justified as conductive cooling is likely to dominate the early cooling history of plutonic bodies and early thermal stress history prior to the development of advective cooling processes (e.g., Jaeger and Carslaw, 1959; Knapp and Norton, 1981; Gerla, 1988; Bergbauer et al., 1998). A wide range of fluid pressures associated with intrusive bodies can be expected relative to pore fluids in the host rocks and late stage volatiles in cooling plutons (e.g., 0 – 500 MPa: Burnham, 1979). Uncertainty exists in understanding the time and pressure of initial fluid exsolution and transition from the magmatic to hydrothermal stage of fluids in plutonic systems (e.g., Fournier, 1999, 2007). Despite the likelihood of fluids and their influence on failure, simplification of models to conductive cooling appears to reasonably match orientation data recorded from the field (i.e., chapters 4 and 5).

7.3. Summary

The major findings of this research are:

1. Thermal stress is likely to play a significant role in fracture formation within cooling intrusive rocks. Comparison of numerical models and field data highlights the likely influence that thermal stresses may play in controlling stress distribution and resulting fracture patterns. Modelling simplified cooling histories therefore provides a powerful tool for the prediction of paleostress and resulting failure in cooling plutons. The examples presented here highlight that thermal stresses may influence fracture patterns at both the pluton and at the local scale.
2. Fracturing related to cooling in plutonic bodies may show transitions from shear to extensional shear to tensile failure. This contrasts with prevailing notions that cooling fractures result from opening mode failure. The failure sequence recorded in a cooling pluton depends on the temperature experienced along a stress path and the in-situ stress state. At the Alta stock (chapter 4) evidence of this failure sequence is interpreted to be recorded in the evolution of fracture filling from aplites (extensional shear failure) to mineralization in veins and non-mineralised joints (tensile failure).
3. Thermal-mechanical modelling of the Bingham Canyon magmatic complex (chapter 5) highlights the potential influence of cooling stresses on the orientation of early mineralisation-hosting fractures. The model provides an explanation for the dominant paleostress orientations estimated from vein trends around the Bingham Canyon magmatic complex, implying that thermal stresses as a result of conductive cooling influenced the trends of the fracture network. The influence of thermal stress on early fracture and stockwork formation may apply to other porphyry deposits and vein networks hosted in intrusive rocks.
4. The rotation and switch of principal stress directions during cooling (chapter 3) may result in fractures of multiple orientations. Analogue modelling (chapter 6) supports the idea that multiple fracture orientations may result from contraction of a three-dimensional volume, analogous to thermal cooling of plutonic bodies. Resulting fracture orientations are also influenced by plutonic geometry, in-situ stress, fluid pressures, failure mode and temperature dependent mechanical properties.

7.4. Future Research

7.4.1. Application of Numerical Models

This research focuses on the relationship between thermal stress and fracturing in intrusive bodies. The practical application of this study for generating attributes to guide geological fracture modelling for industrial applications is significant. Future work could apply the developed modelling technique to help guide field identification of likely cooling fractures, aiding characterisation of this type of fracture. Modelling could also be applied to address uncertainty and improve the understanding of the paleostress history for a given intrusion at the time of cooling. This could be done through the modelling of multiple scenarios, with varying regional in-situ stress, and comparison to mapped fracture patterns in the field. Application of the modelling approach to other porphyry deposits and vein networks hosted in intrusive rocks may assist with the development of conceptual models of fracturing in these systems.

In order to apply the modelling technique developed in this thesis to a given intrusion, thermomechanical modelling should be closely linked to field mapping of the intrusive geometry and fractures. The numerical models should be run along-side field mapping and an iterative approach of comparison of data sets should be used to guide modelling. Two-dimensional models can give a reasonable estimate of thermal stress orientations, where geometry and paleostress are known, allowing models to be simplified when the three-dimensional geometry is not known. Three-dimensional modelling can be beneficial in considering local variation of principal stress direction. Software and hardware capability currently limits the level of complexity of three-dimensional models that can be used as input. Incorporating temperature dependent properties is also not a necessity as predicted principal stress directions are not significantly altered. However, the predicted failure mode and timing will influence resulting fracture patterns.

7.4.2. Extension of Numerical Models

Outstanding research questions that could be addressed include assessment of: (1) fracture interaction and its influence on later fracture formation, (2) the best failure criteria to apply in cooling intrusive rocks, including assessment of the influence of non-brittle deformation on later brittle deformation (this could include temperature dependant properties based on the cooling of fresh igneous material rather than reheated rocks), (3) the influence of incremental emplacement on thermomechanical modelling results, and (4) the influence cooling mechanism and hydrothermal fluids could be assessed.

Research into fracture interaction and propagation has predominantly focused on fracture interaction in sedimentary rocks and generally in two-dimensional homogenous units (e.g., Pollard and Aydin, 1988). Understanding the characteristics, interaction and propagation of fractures in heterogenous massive rocks would aid with understanding the processes of fracturing in igneous rocks. Further analysis of the three-dimensional topology of fracture in intrusive rocks would be a fascinating topic (e.g., Bahat, 2012; Gonzalez-Garcia et al., 2000; Dowd et al., 2009). New and developing methods to characterise the three-dimensional topology of fracture networks (e.g., Sanderson and Nixon, 2015; Seers and Hodgetts, 2016) could be applied to this research. Additionally, using predictions from thermomechanical modelling as anisotropies in numerical models of fault propagation in intrusive rocks would be interesting. As highlighted by Crider, 2015 early fractures are likely to influence the propagation direction of faults in crystalline rocks.

The failure models applied in this thesis have focused on brittle failure criterion. Study of the Alta stock (chapter 4) highlights that earliest fracturing events record high temperature failure at or near the brittle viscous transition when the pluton is in a “semi plastic” state. Applying and developing failure criteria that focus on the brittle viscous transition (e.g., Miehe et al., 2015), may provide intriguing insights into the early cooling history of plutonic rocks. Understanding the differences, if any, between temperature dependant properties of rocks that are reheated and cooled versus properties resulting from cooling of molten rock would be interesting even if a little difficult.

The influence of incremental emplacement could be further investigated. Thermomechanical modelling could be combined with models of incremental emplacement (e.g., Annen, 2009; Annen, 2011; Annen et al., 2015). The rate of emplacement could be varied and the influence on predicted stress magnitude and orientation could be assessed. Comparison of this type of model with field studies is however complicated due to current uncertainty in pluton emplacement mechanisms and resulting pluton geometries (e.g., Glazner et al., 2004; Cruden and McCaffrey, 2001; Menand, 2011). In addition, it would be interesting to model stress anisotropy in the host rock. Models of stress in the host rock related to intrusion emplacement and stresses around structures such as faults and folds (e.g., Vigneresse et al., 1999; Gudmundsson, 2012; Browning and Gudmundsson, 2015) could be used to address the influence on stresses within the pluton.

Thermomechanical models could also be extended to take account of pore fluid pressure and hydrothermal circulation within and around plutons (e.g., Cathles, 1981; Clemens and Mawer, 1992) which have the potential to alter the rate of cooling within plutonic bodies. As with all modelling, field work will be critical to verifying any developed numerical models.

A. Chapter 3 Appendix

Table A3-1. Failure Criterion as applied in COMSOL® (compression negative)

Navier-Coluomb *	
Shear failure	$\text{if}(\text{solid.sp3} < C0 + \text{solid.sp1} * (\tan(\pi/4 + (\text{int13}/2))^2) \& \& \text{solid.sp3} < C0 + T0 * (\tan(\pi/4 + (\text{int13}/2))^2), 1, 0)$
Tensile failure	$\text{if}(\text{solid.sp1} > T0 \& \& \text{solid.sp3} > C0 + T0 * (\tan(\pi/4 + (\text{int13}/2))^2), 1, 0)$
Shear failure angle	$1/2 * \text{atan}(1/(\text{int13}))$
Griffith & Murrell-Griffith	
3d failure domain	$(\text{solid.sp1} - \text{solid.sp2})^2 + (\text{solid.sp2} - \text{solid.sp3})^2 + (\text{solid.sp3} - \text{solid.sp1})^2 > 24 * -T0(T2) * (\text{solid.sp1} + \text{solid.sp2} + \text{solid.sp3})$
Shear failure	$\text{if}((\text{solid.sp3} - \text{solid.sp1})^2 > (8 * -T0) * (\text{solid.sp3} + \text{solid.sp1}) \& \& (\text{solid.sp3} + 3 * \text{solid.sp1}) < 0 \& \& 4.828 * (\text{solid.sp1}) < 0, 1, 0)$
Extensional-shear failure	$\text{if}((\text{solid.sp3} + 3 * \text{solid.sp1}) < 0 \& \& 4.828 * (\text{solid.sp1}) > 0, 1, 0)$
Tensile failure	$\text{if}((\text{solid.sp3} + 3 * \text{solid.sp1}) > 0 \& \& \text{solid.sp1} > -T0, 1, 0)$
Shear failure angle	$1/2 * \text{acos}(4 * -T0 / (\text{solid.sp1} - \text{solid.sp3}))$
Drucker Prague	
Yield failure T0/C0	$(1/\sqrt{3}) * ((C0_G - T0_G) / (C0_G + T0_G)) * \text{solid.l1s} + \sqrt{(\text{solid.l12s}) - (2/\sqrt{3}) * ((C0_G * T0_G) / (C0_G + T0_G))}$
circumscribed	$((2 * \sin(\text{Int13})) / (\sqrt{3} * (3 - \sin(\text{Int13})))) * \text{solid.l1s} + \sqrt{(\text{solid.l12s}) - ((6 * \text{co_H} * \cos(\text{Int13})) / (\sqrt{3} * (3 - \sin(\text{Int13})))}$
middle circumscribed	$((2 * \sin(\text{Int13})) / (\sqrt{3} * (3 + \sin(\text{Int13})))) * \text{solid.l1s} + \sqrt{(\text{solid.l12s}) - ((6 * \text{co_H} * \cos(\text{Int13})) / (\sqrt{3} * (3 + \sin(\text{Int13})))}$
inscribed	$(\sin(\text{Int13}) / \sqrt{9 + 3 * \sin(\text{Int13})^2}) * \text{solid.l1s} + \sqrt{(\text{solid.l12s}) - (3 * \text{co_H} * \cos(\text{Int13}) / \sqrt{9 + 3 * \sin(\text{Int13})^2})}$

* Values after Knapp T0 = 5 [MPa], C0 = -100[MPa], int13 = 30[deg]
T0 – tensile strength
C0 – uniaxial compressive strength (compression negative)
Co_H – Cohesion
Int13 – angle of internal friction
format T0(T2) used for temperature decency
solid.sp3 – maximum compressive stress principal stress
solid.sp1 – minimum compressive stress principal stress

Table A3-2. Temperature dependent material properties after Heuze, 1983

Temperature	Density	Density*	Thermal diffusivity	Heat capacity at constant pressure †	Thermal conductivity †	Young's modulus ††	Poisson's ratio**	Coefficient of thermal expansion §§	Thermal Inertia §§§§
°C	kg/m ³	kg/m ³	m ² /se c	J/(kg. K)	W/(m.K)	GPa	1	1/K	J m ⁻² K ⁻¹ s ^{-½}
20		2469	1.3E-06	815	2.6	30.3		0	2408
200		2145	1.0E-06	965	2.1	23.7		Linear increase	2357
400		1769	8.7E-07	1133	1.7	16.4	0.25		2309
600	2600	1494	8.7E-07	1129	1.5	9.1			2115
800		1075	1.0E-06	1179	1.3	1.8		15e-6	2040
1000		759	1.4E-06	1230	1.3	0.0		0	2045
1100		649	1.6E-06	1255	1.3	0.0		0	2081

• Calculated, Density = thermal conductivity/(thermal diffusivity.heat capacity)

** No clear dependence on pressure or temperature

† $(6.3 \times 10^{-3} - 6.7 \times 10^{-6} \cdot T + 3.41 \times 10^{-9} \cdot T^2) \cdot 418.4$, conversion: 1 cal/cm sec °C = 418.4 W/(m.K) (Robertson, 1988)

†† Initial value 30.4 GPa

‡ Conversion: 1 cal / g. °C = 4184 J/(kg.K) (Robertson 1988)

§§at a few 100 MPa, equivalent to Žák et al., 2006

§§§§Thermal Inertia = Sqrt(thermal conductivity.density.heat capacity at constant pressure). Used for calculation of heat capacity at constant pressure after Žák et al., 2006, Table A3-3.

Table A3-3. Example of temperature dependent material properties after Zak et al., 2006

Temperature	Density	Heat capacity per Volume *		Heat capacity at constant pressure §§		Thermal conductivity		Young's modulus		Poisson's ratio		Coefficient of thermal expansion	
		MJ/K/m ³		J/(kg.K)		W/(m.K)		MPa		1		1/K	
°C	kg/m ³	G	P	G	P	G	P	G	P	G	P	G	P
20 **													
assumed	2600	2.4	2.8	766	613	2.4	3	56	76.5			0	‡
200	defined			968	920	1.9	2						
400	based			1149	1226	1.6	1.5			0.11			Linear increase
600	on			1226	1415	1.5	1.3						
700	Heuze,			1226	1533	1.5	1.2					0.2	
solidus	1983,												
800	value		linear	1415	1839	1.5	1.2		Linear decrease				15e-6 †
875	not			1415	1839	1.5	1.1						
liquidus	given in			766	613								
1000	Žák et			968	920	1.3	1					0.499 †	0
1100	al. 2006												
	paper	4.3	4.7	1149	1226	1.6	0.9	0					

* Assumed temperature, just stated as room temperature in the paper

** Calculation of heat capacity shown next page

† Žák et al., 2006 case 1 750 °C and case 2 800 °C

‡ Not given assumed to be the same as granite

§§ heat capacity at constant pressure = thermal inertia² / (thermal conductivity * density), thermal inertia calculated from values given in Heuze, 1983

G – Granite, P – Phyllite

Table A3-4. Temperature dependent material properties after Wang and Konietzky (2019)

Temperature	Density	Heat capacity at constant pressure *	Thermal conductivity **	Young's modulus †	Poisson's ratio ††	Coefficient of thermal expansion †
°C	kg/m ³	J/(kg.K)	W/(m.K)	MPa	1	1/°C
Initial values	2645	820	2.6	30.4	0.127	8 x 10⁻⁶
0	Constant	786	2.6	37.7	0.126	9.05E-06
200		796	2.1	32.1	0.110	1.13E-05
400		806	1.7	24.5	0.092	1.72E-05
600		1023	1.5	16.5	0.071	1.78E-05
800		1043	1.3	5.1	0.270	1.00E-06
1000		1063	1.3	3.3	0.284	1.00E-06
1100		1074	1.4	2.9	0.284	1.00E-06

* $0.957 + 6.59 \times 10^{-4} \cdot T, 0 \text{ }^\circ\text{C} \leq T \leq 573 \text{ }^\circ\text{C}$ (Possible type error in paper value given as 575 °C) and $1.173 + 1.238 \times 10^{-4} \cdot T, 573 \text{ }^\circ\text{C} \leq T \leq 1000 \text{ }^\circ\text{C}$
** $-5.8126 + 6.8485 \times 0.9995^T + 0.002172 \cdot T, 0 \text{ }^\circ\text{C} \leq T \leq 1200 \text{ }^\circ\text{C}$
† $1.2665 / (1 + \exp(-1.430 + 0.0034T)), 0 \text{ }^\circ\text{C} < T \leq 600 \text{ }^\circ\text{C}$ and $1 / (-109.953 + 17.542 \cdot \ln(T)), 600 \text{ }^\circ\text{C} < T \leq 1250 \text{ }^\circ\text{C}$
†† $-7 \times 10^{-4} \cdot T + 1.0052, 0 \text{ }^\circ\text{C} \leq T \leq 600 \text{ }^\circ\text{C}$ and $2.240 / (1 + \exp(13.11 - 0.020 \cdot T)), 600 \text{ }^\circ\text{C} < T \leq 800 \text{ }^\circ\text{C}$
‡ $(0.8383 - 0.00142 \cdot T)^{-1/1.7085}, 0 \text{ }^\circ\text{C} \leq T \leq 573 \text{ }^\circ\text{C}$ and $(-5.4160 + 0.0095 \cdot T)^{-1/1.5719}, 573 \text{ }^\circ\text{C} < T \leq 625 \text{ }^\circ\text{C}$ and $=0, 625 < T \leq 800 \text{ }^\circ\text{C}$
T = temperature, initial values as given in Wang and Konietzky, 2019

Table A3-5. Temperature dependent mechanical properties

	Tensile strength				Compressive Strength			Cohesion		Friction Angle	
	Heuze, 1983 *	Žák et al. 2006 Granite	Žák et al. 2006 Phyllite	Wang and Konietzky, 2019 †	Saiang 2012	Žák et al. 2006 Granite	Žák et al. 2006 Phyllite	Heuze, 1983 *	Wang and Konietzky, 2019 ††	Heuze, 1983 *	Wang and Konietzky, 2019 ††
	MPa				MPa			MPa		°	
Initial value	21 †	22.8 †	13	231	229	126	23 †	50 †			
0	14	21.4	23.2	12.9	230	233	128	22.4	23.4	50.2	50.2
20	13.9	21.0	22.8	12.7	231	229	126	22.6	23.2	49.1	50.2
200	13	17.5	18.8	11.6	238	191	105	22.5	21.6	38.8	49.3
400	11	13.6	14.4	8.8	246	148	82	20.7	19.0	26.2	45.9
600	5	9.7	10	0.1	177	106	69	16.2	15.2	14.8	40.3
800	2	5.9	5.5	0.1	111	64	36	10.4	9.8	6.9	32.2
1100	0	0	0	0	14	0	0	0	0	7.3	15.5

* Data extracted from paper using <https://apps.automeris.io/wpd/>
† initial room temperature assumed to be 20 °C not given in paper
‡ $0.9912 \cdot (1 - 4.10 \cdot T / 2483.30)^{1/4.10}, 0 \text{ }^\circ\text{C} \leq T \leq 600 \text{ }^\circ\text{C}$ and $2.610 \exp^{-0.0036 \cdot T}, 600 \text{ }^\circ\text{C} \leq T \leq 1050 \text{ }^\circ\text{C}$
†† $0.1699 \cdot (6.9845 - e^{0.001876 \cdot T}), 0 \text{ }^\circ\text{C} \leq T \leq 1000 \text{ }^\circ\text{C}$
‡‡ $-6e-7 \cdot T^2 + 3e-5 \cdot T + 1.0034, 0 \text{ }^\circ\text{C} \leq T \leq 1000 \text{ }^\circ\text{C}$
This relationship is questionable and hard to predict as it may differ dependent on granite
T = temperature

Table A 3-6. Comparison of modelling dimensions point 4

		Model number		
		1	2	3
1000 a (single arrow)	Temperature °C	497	477	449
	Sp1 MPa	-17	-19	-31
	Sp3 MPa	-49	-64	-72
	Strain energy J/m ³	-1e4	5e4	5e4
10000a (double arrow)	Temperature °C	252	206	181
	Sp1 MPa	-100	-118	-127
	Sp3 MPa	-164	-154	-162
	Strain energy J/m ³	1e5	2.4e5	2.5e5

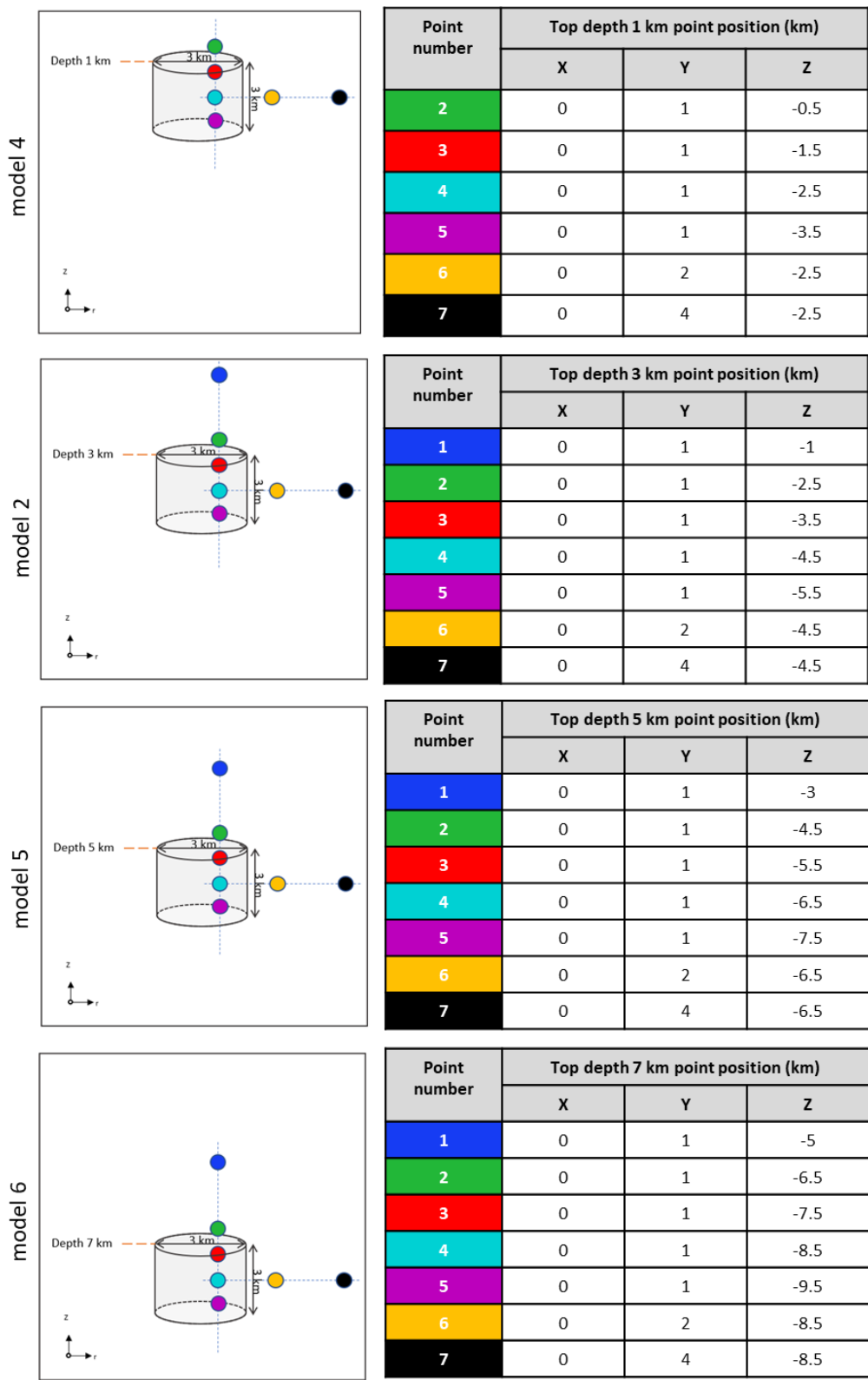


Figure A3-1a. Diagram and table showing location of the seven points selected for comparison. Model number is given. Points 1, 2, 6 and 7 are in the host rock and points 3 to 5 are within the pluton (refer to Table 3.4 p.57 for model parameters). Data is presented in parts b and c.

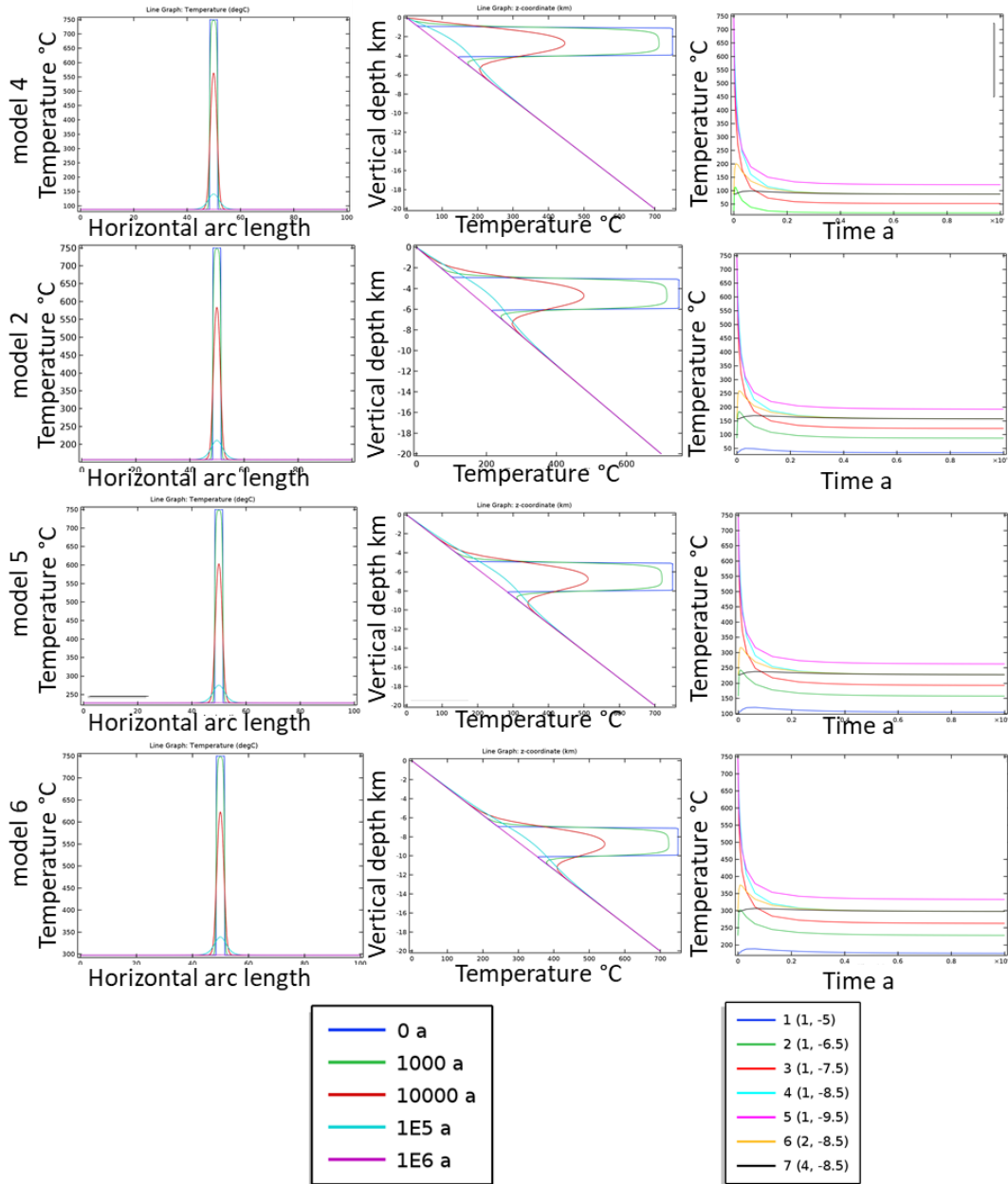


Figure A3-1b. Temperature profiles through the pluton and host rock. See Figure A3-1a for location of lines and points. Increasing depth has minimum influence on the cooling history of the pluton

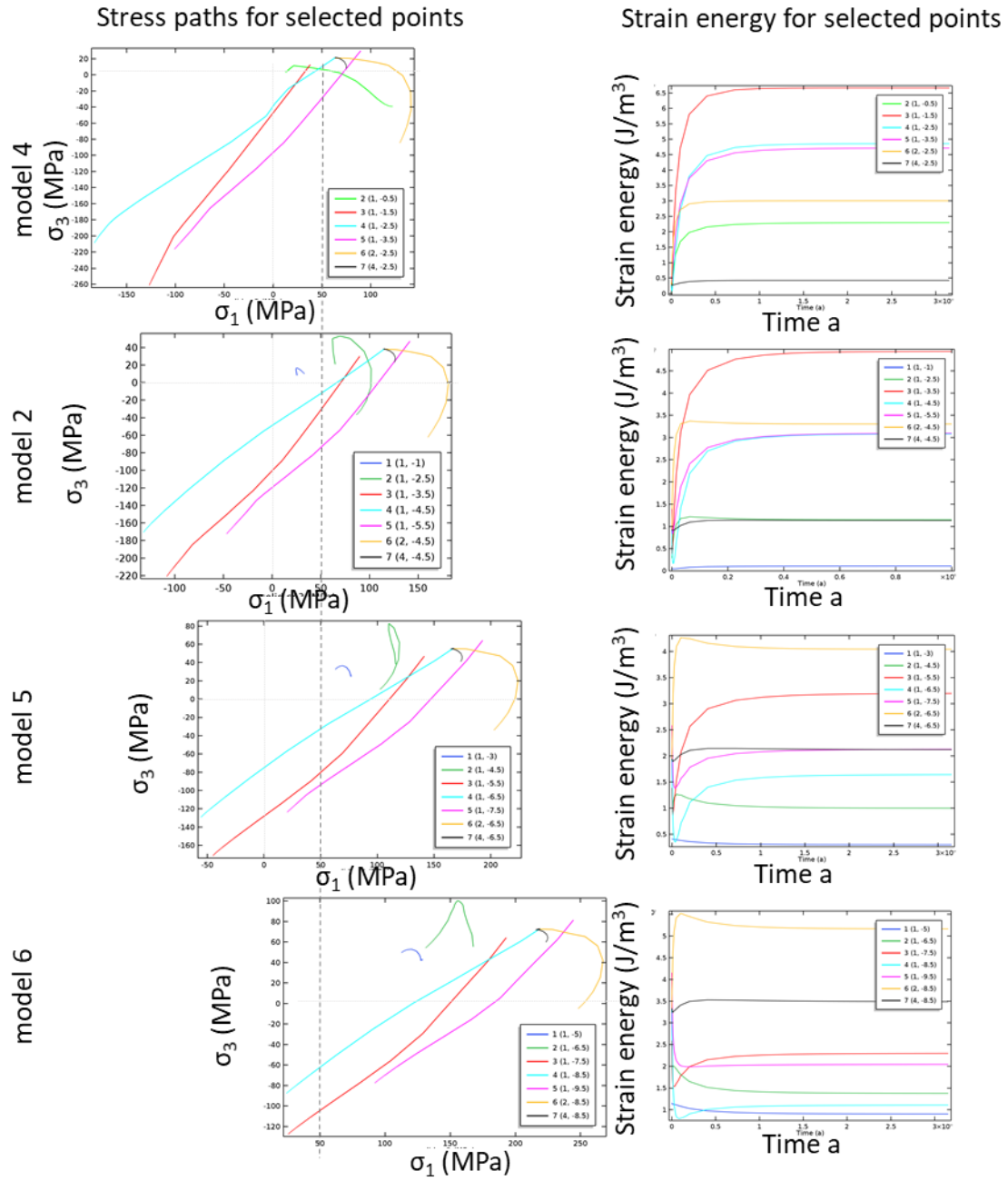


Figure A3-1c. Stress paths for selected points on a σ_1 - σ_3 plot, compression positive. Note the difference in scales, dashed line marks the maximum principal stress (σ_1) value of 50 MPa. Strain energy (J/m^3) for selected points.

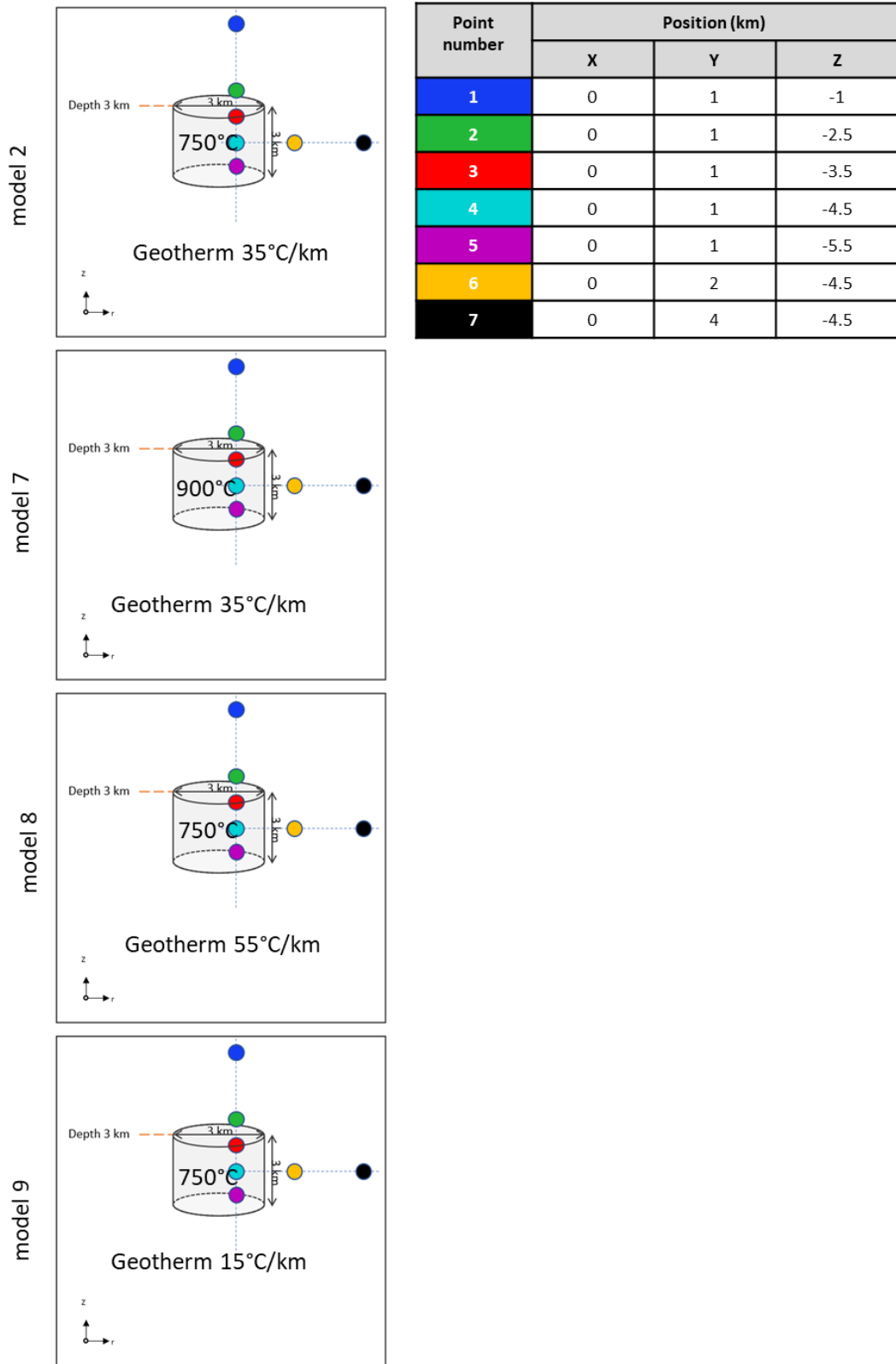


Figure A3-2a. Diagram and table showing location of the seven points selected for comparison. Model number is given. Points are in the same positions of each of the models. Points 1, 2, 6 and 7 are in the host rock and points 3 to 5 are within the pluton (refer to Table 3.4 p.57 for model parameters). Data is presented in parts b and c.

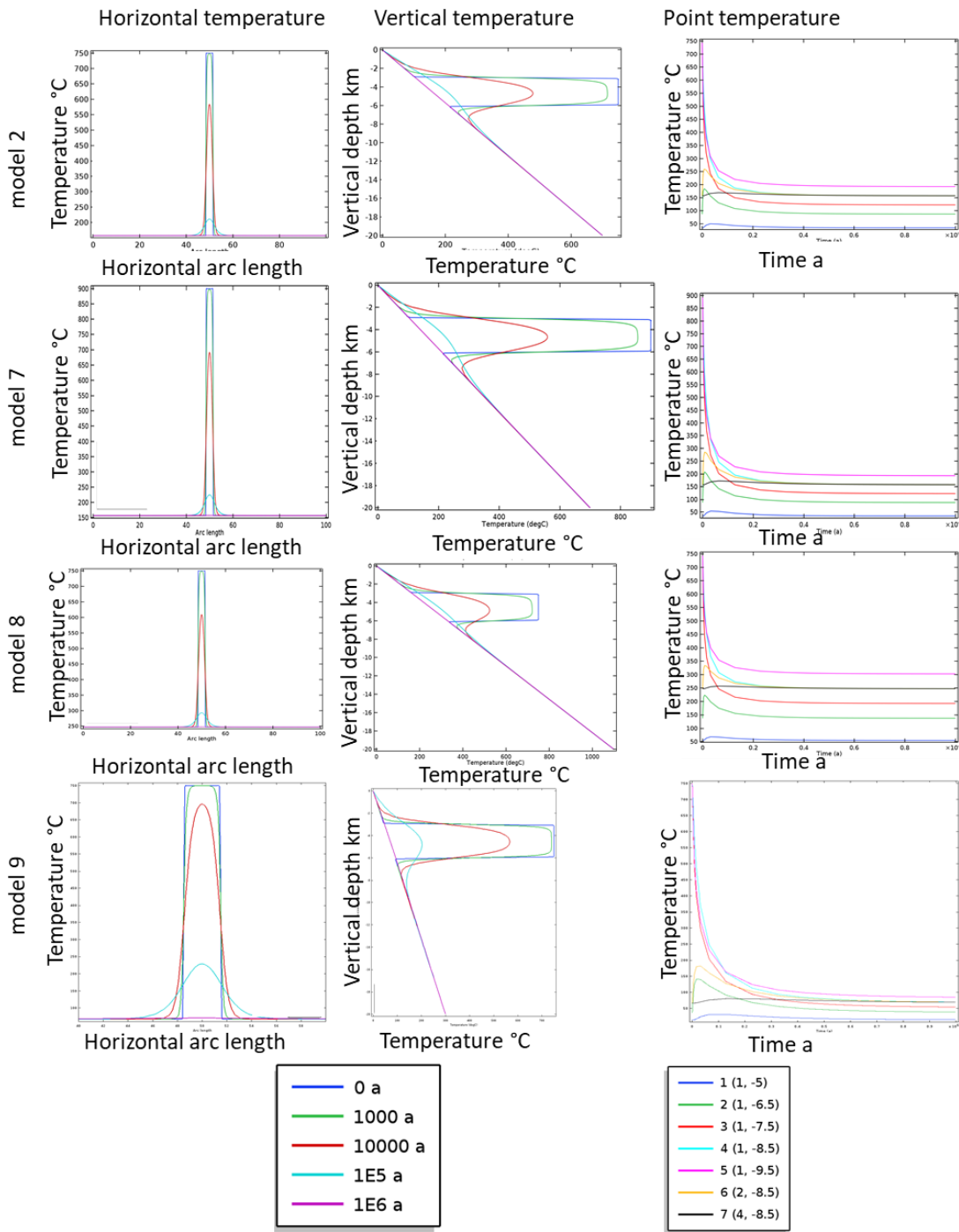


Figure A3-2b. Temperature profiles through the pluton and host rock. See Figure A3-2a for location of lines and points. Increasing depth has minimum influence on the cooling history of the pluton.

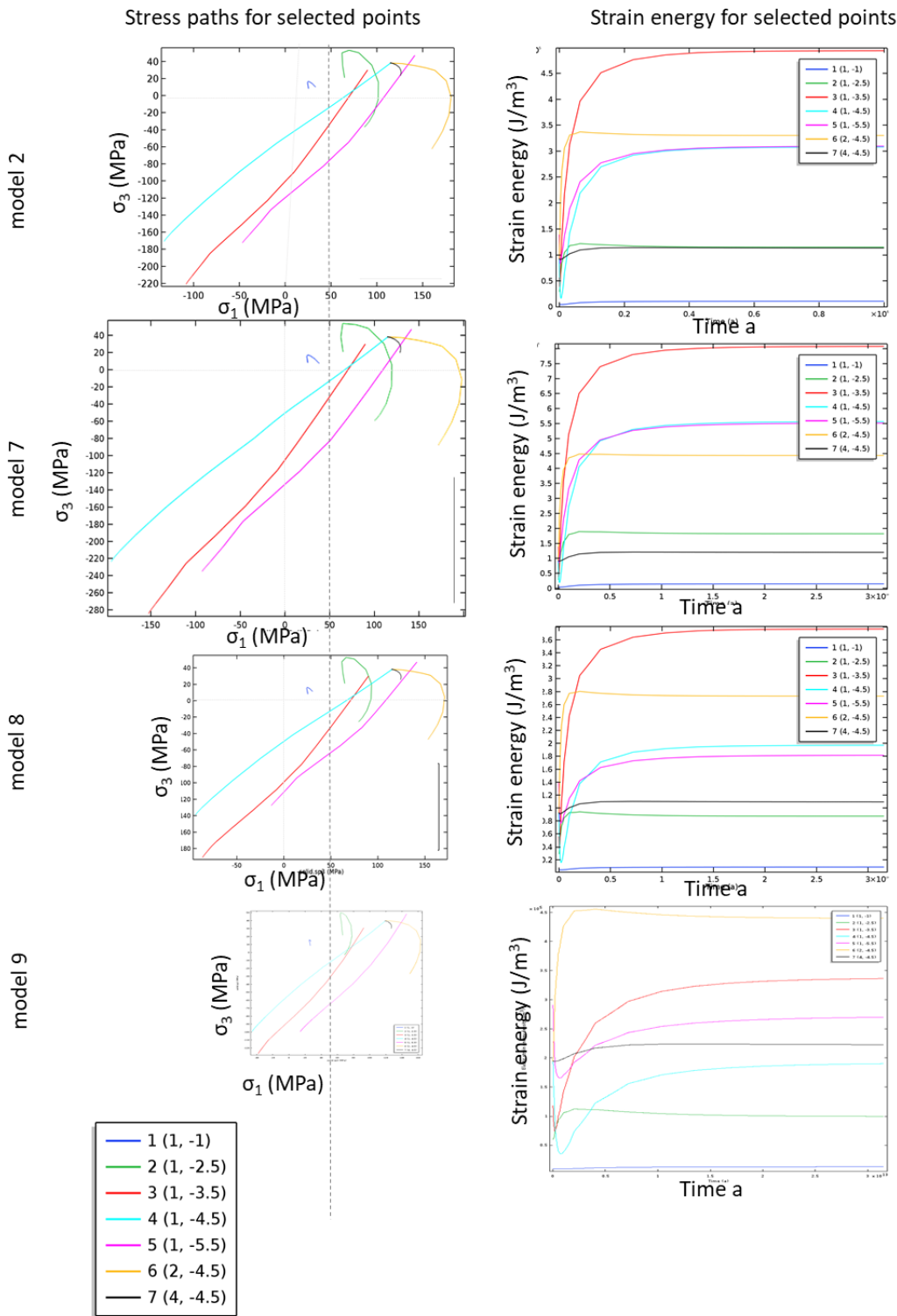


Figure A3-2c. Stress paths for selected points on a σ_1 - σ_3 plot, compression positive. Note the different in scales, dashed line marks the maximum principal stress (σ_1) value of 50 MPa. Strain energy (J/m^3) for selected points.

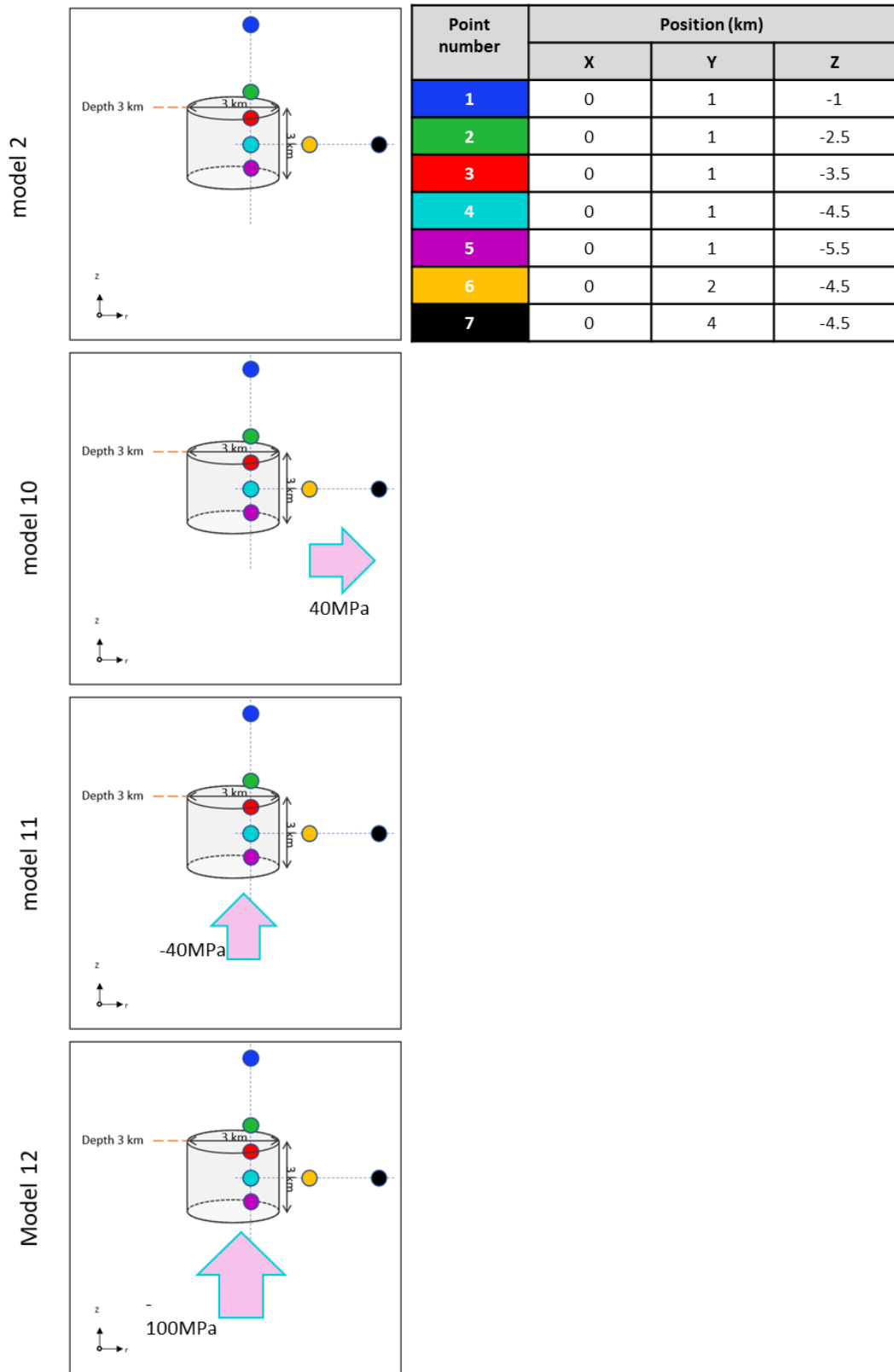


Figure A3-3a. Diagram and table showing location of the seven points selected for comparison. Model number is given. Points are in the same positions of each of the models. Points 1, 2, 6 and 7 are in the host rock and points 3 to 5 are within the pluton (refer to Table 3.4 p.57 for model parameters). Data is presented in parts b and c.

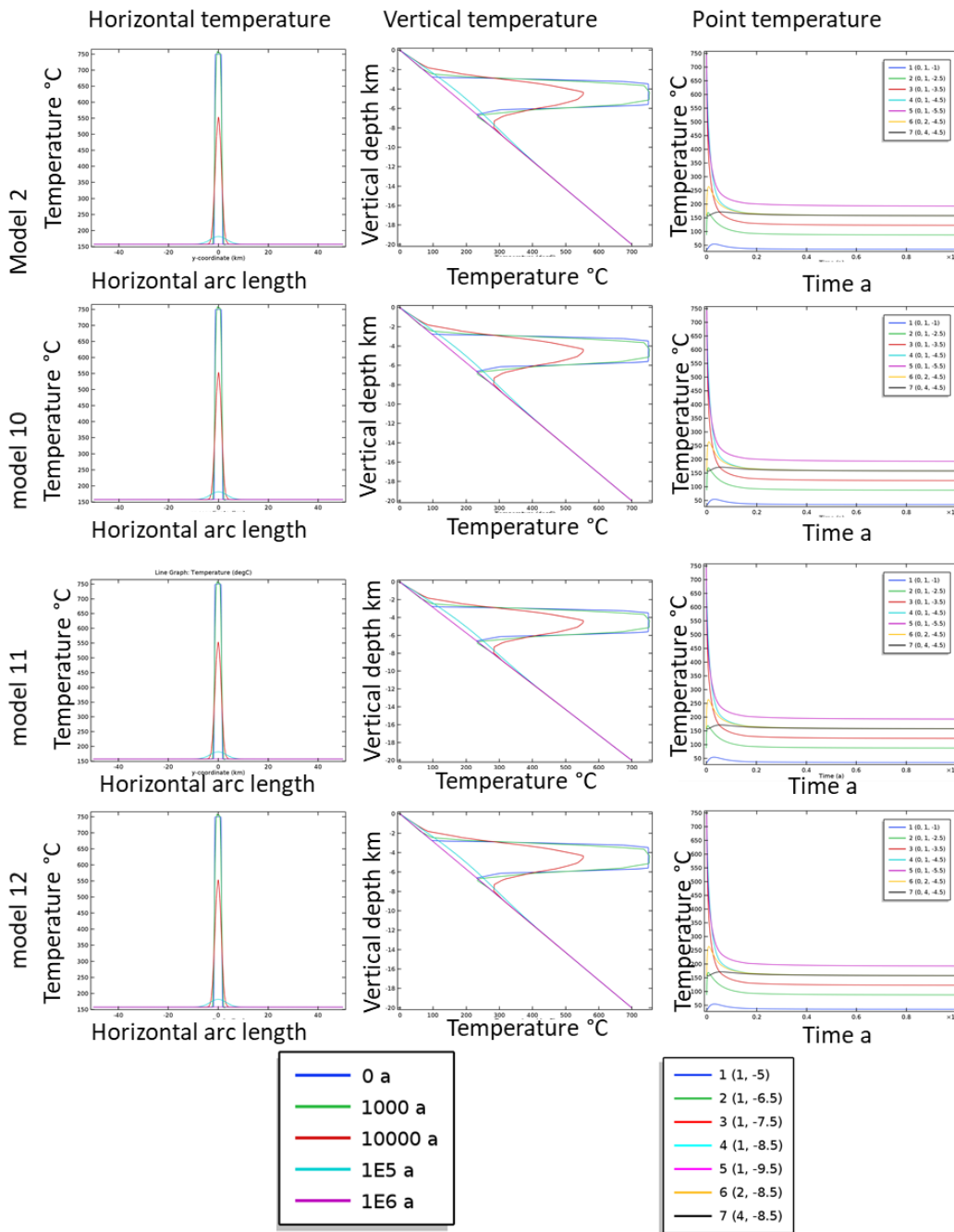


Figure A3-3b. Temperature profiles through the pluton and host rock. See Figure A3-3a for location of lines and points. Increasing depth has minimum influence on the cooling history of the pluton.

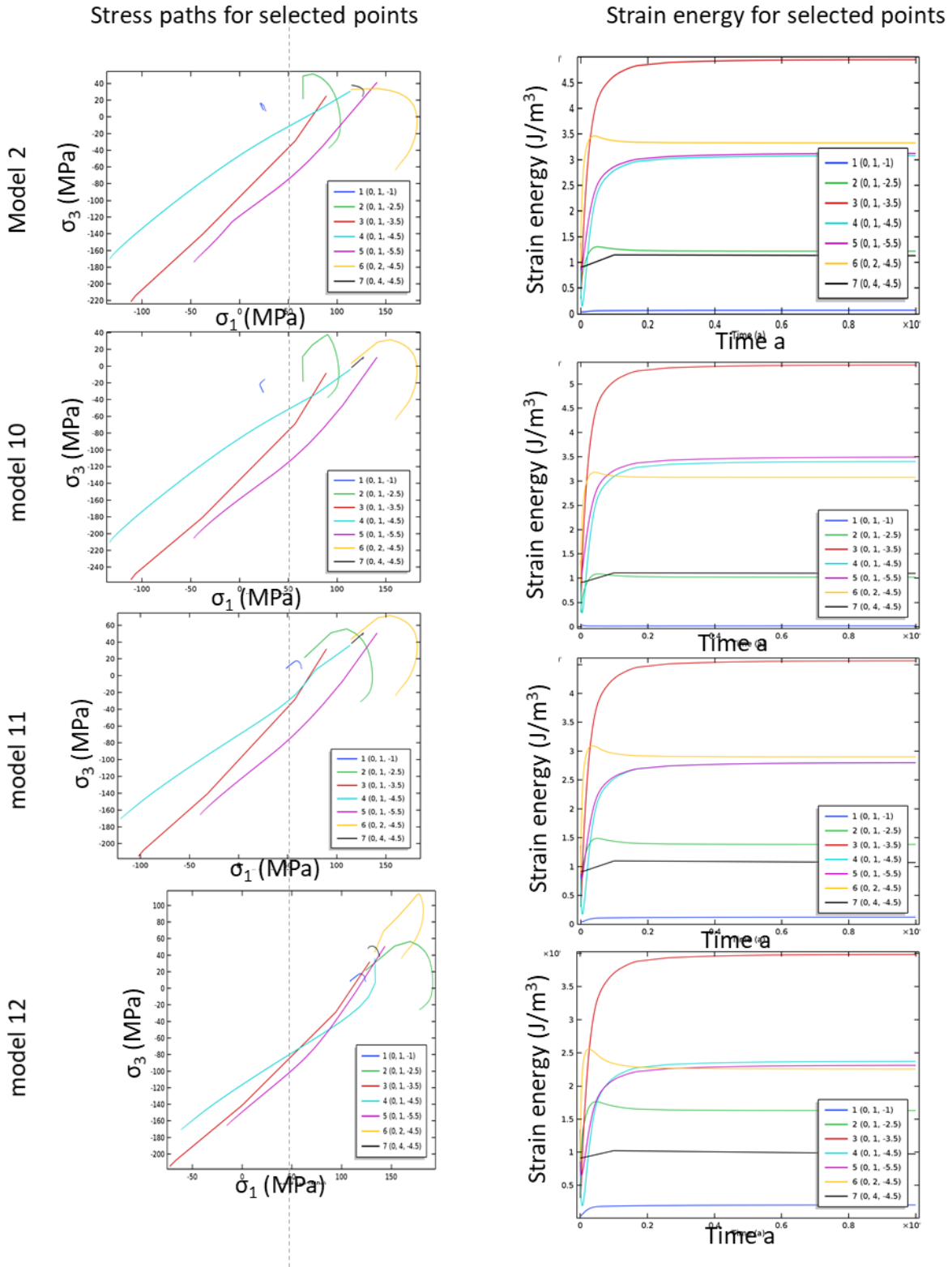
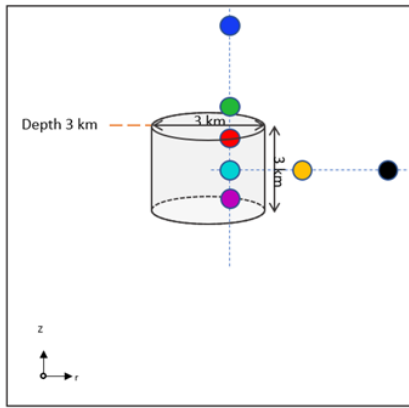


Figure A3-3c. Stress paths for selected points on a σ_1 - σ_3 plot, compression positive. Note the different in scales, dashed line marks the maximum principal stress (σ_1) value of 50 MPa. Strain energy (J/m^3 , $\times 10^5$) for selected points.

models 13 - 19



Point number	Top depth 3 km point position (km)		
	X	Y	Z
1	0	1	-1
2	0	1	-2.5
3	0	1	-3.5
4	0	1	-4.5
5	0	1	-5.5
6	0	2	-4.5
7	0	4	-4.5

Figure A3-4a. Diagram and table showing location of the seven points selected for comparison. Model number is given. Points 1, 2, 6 and 7 are in the host rock and points 3 to 5 are within the pluton (refer to Table 3.11 p110 for model parameters). Data is presented in parts b and c.

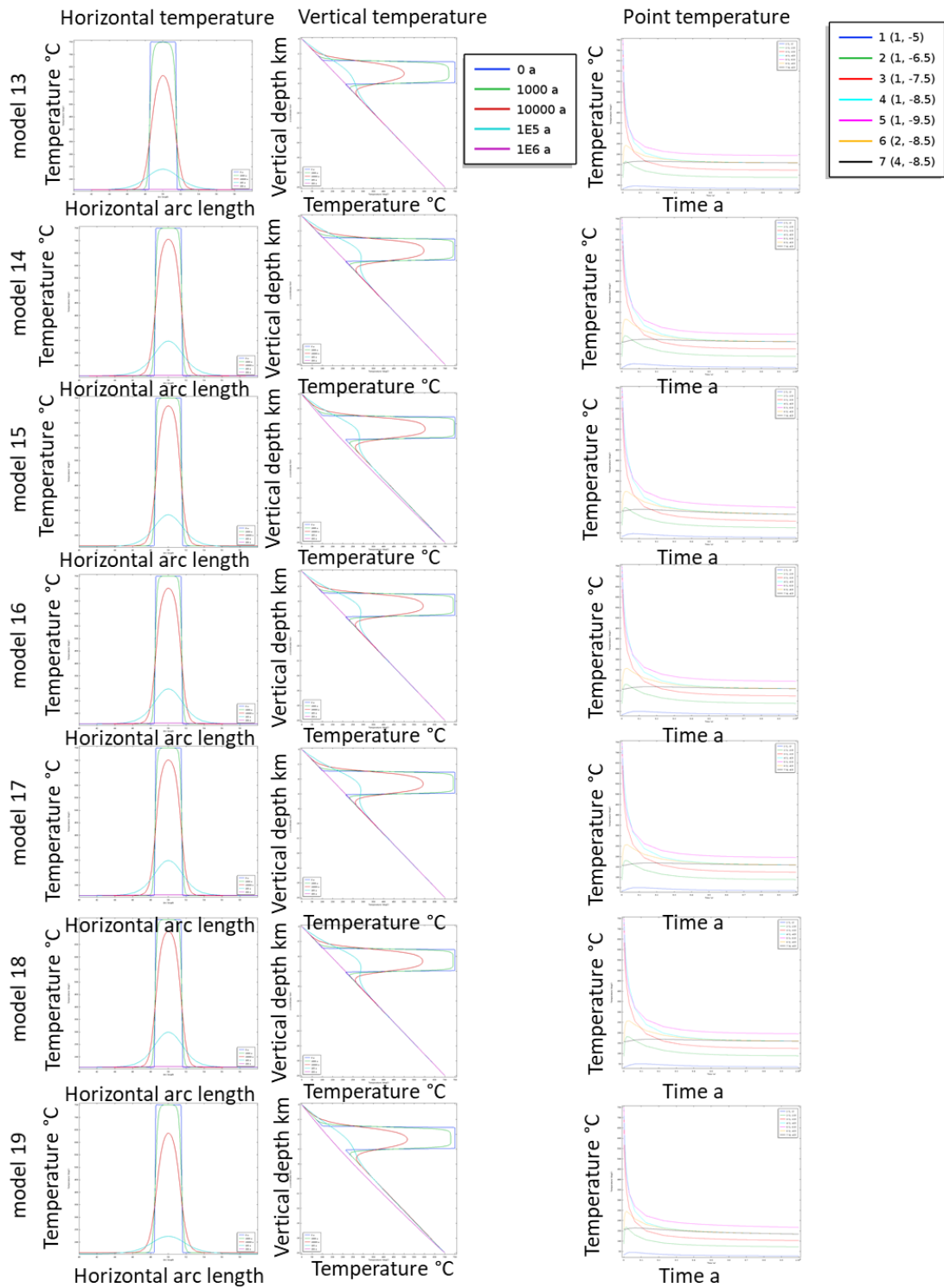


Figure A3-4b. Temperature profiles through the pluton and host rock. See Figure A3-4a for location of lines and points. Increasing depth has minimum influence on the cooling history of the pluton.

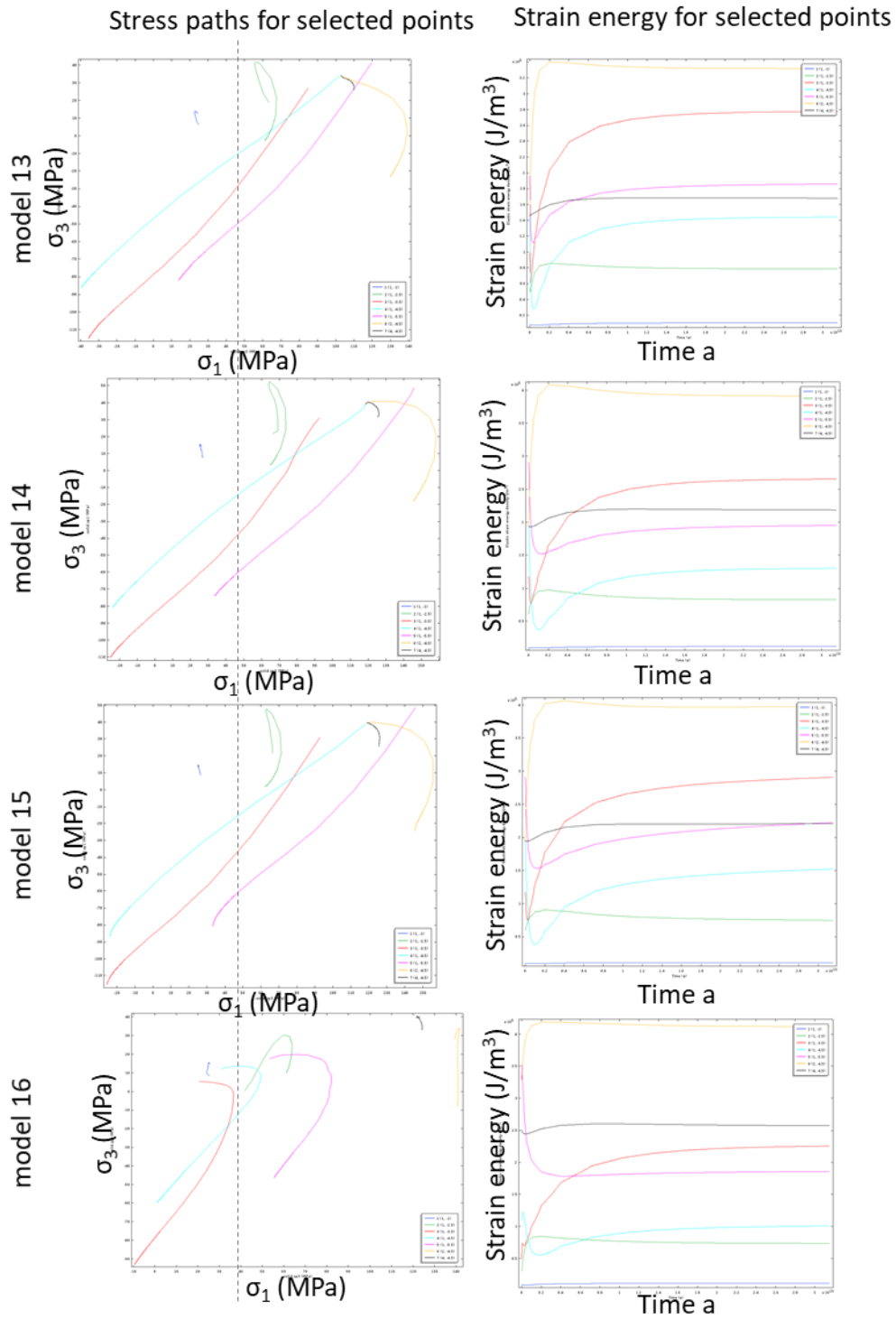


Figure A3-6c. Continued next page.

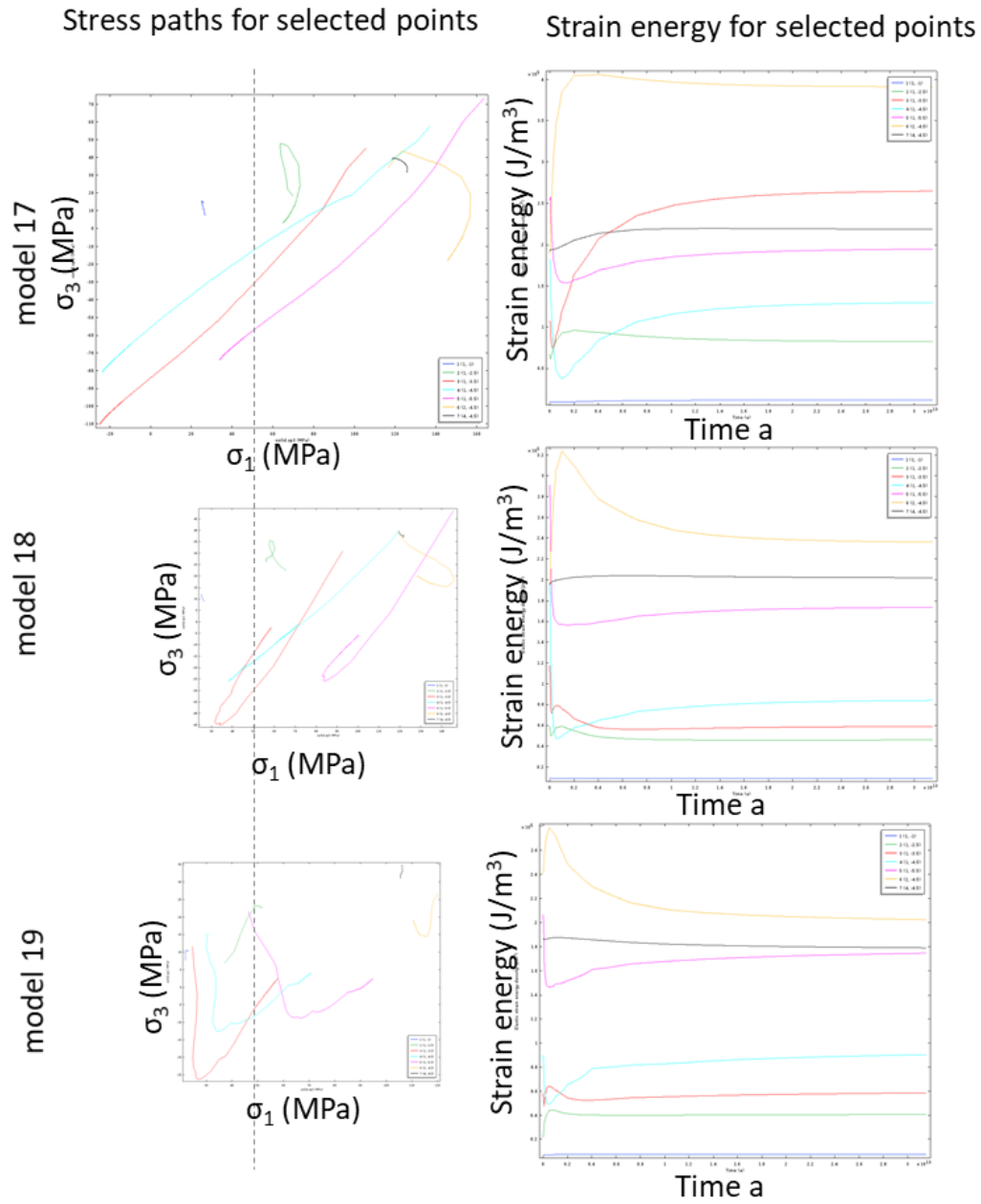


Figure A3-6c. Stress paths for selected points on a σ_1 - σ_3 plot, compression positive. Note the difference in scales, dashed line marks the maximum principal stress (σ_1) value of 50 MPa. Strain energy (J/m^3 , $\times 10^5$) for selected points.

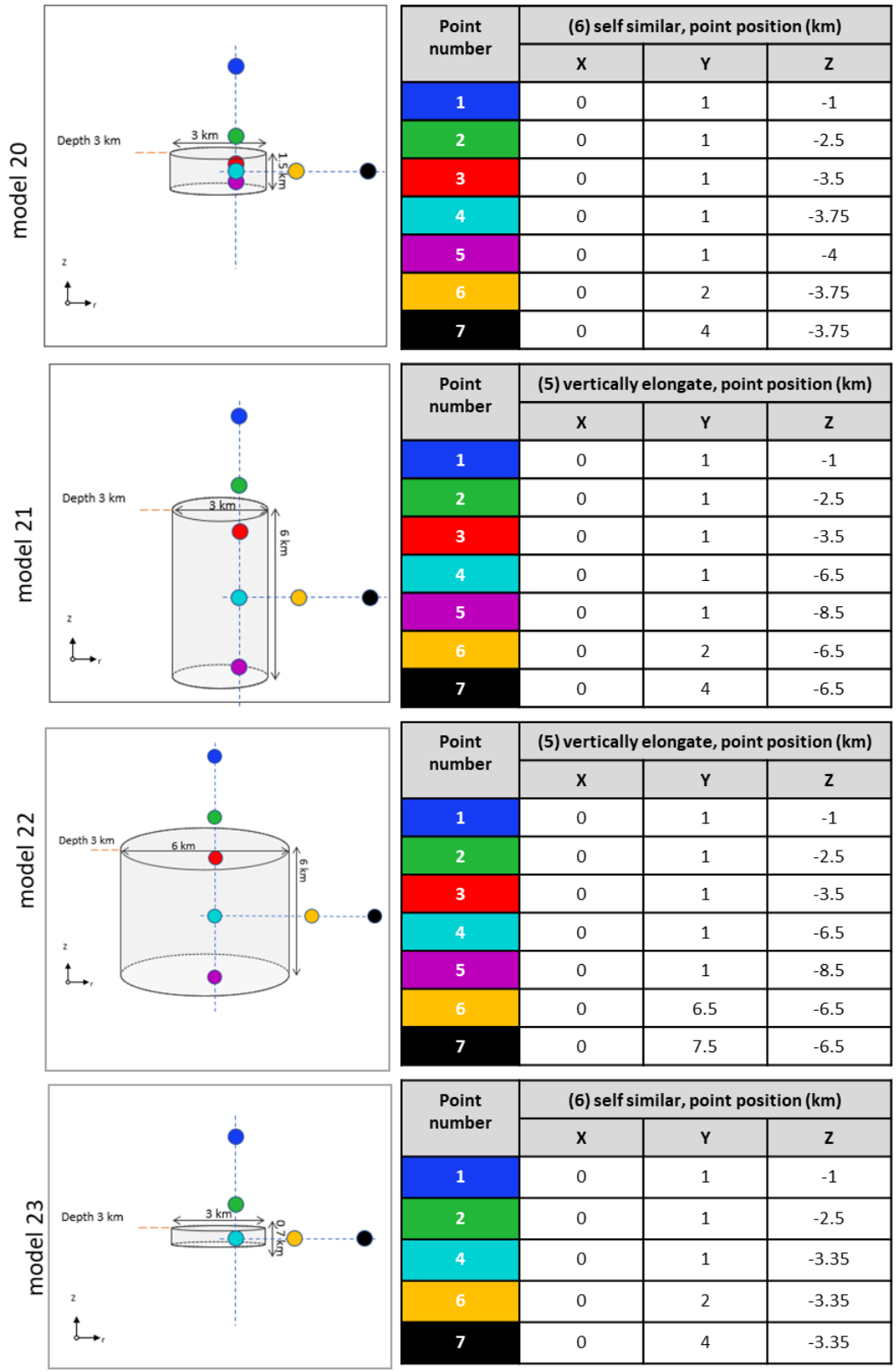


Figure A3-5a. Diagram and table showing location of the seven points selected for comparison. Model number is given. Points 1, 2, 6 and 7 are in the host rock and points 3 to 5 are within the pluton (refer to Table 3.4 p.57 for model parameters). Data is presented in parts b and c.

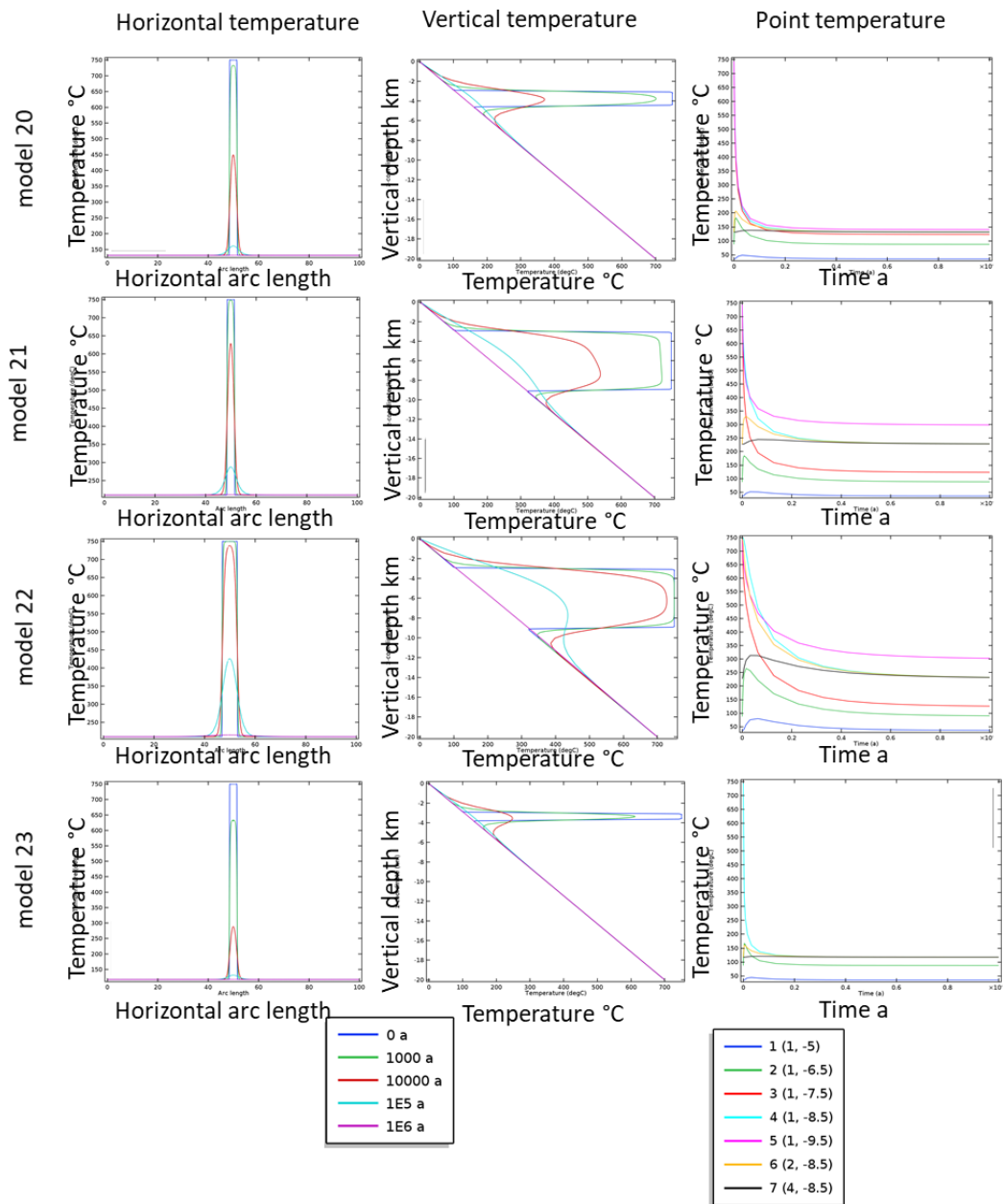


Figure A3-5b. Temperature profiles through the pluton and host rock. See Figure A3-5a for location of lines and points. Increasing depth has minimal influence on the cooling history of the pluton.

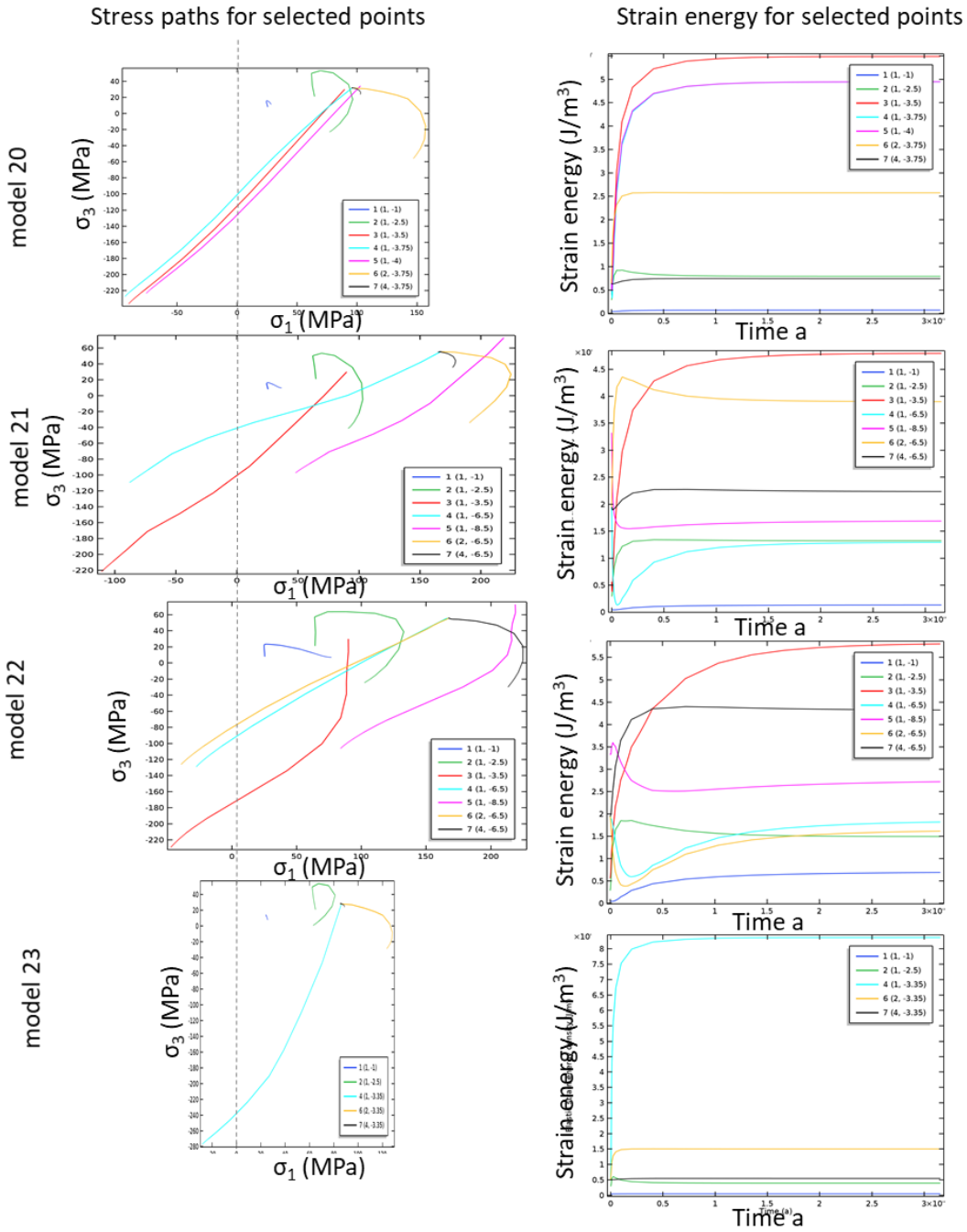


Figure A3-5c. Stress paths for selected points on a σ_1 - σ_3 plot, compression positive. Note the difference in scales, dashed line marks the maximum principal stress (σ_1) value of 50 MPa. Strain energy (J/m^3 , $\times 10^5$) for selected points.

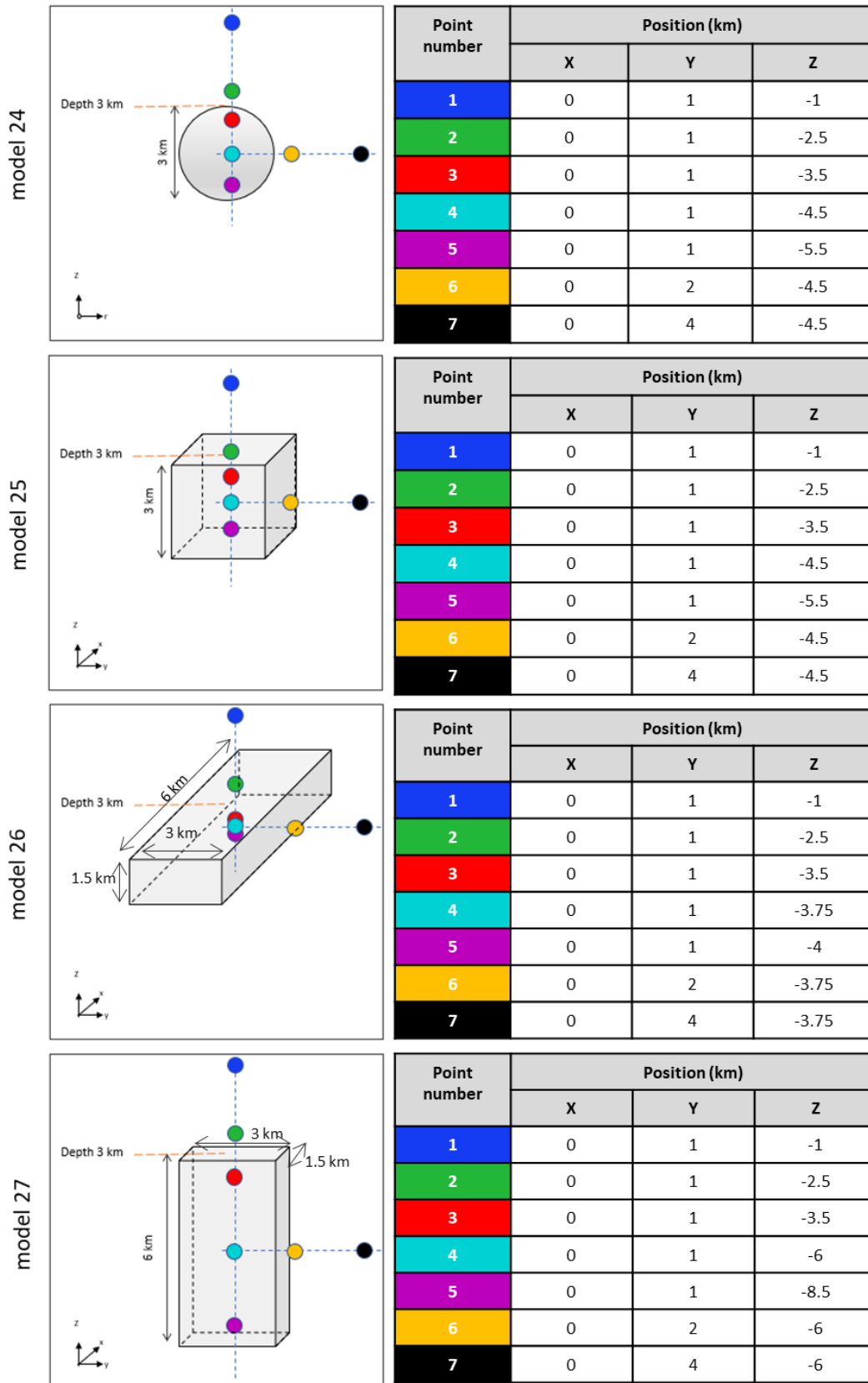


Figure A3-6a. Continued next page

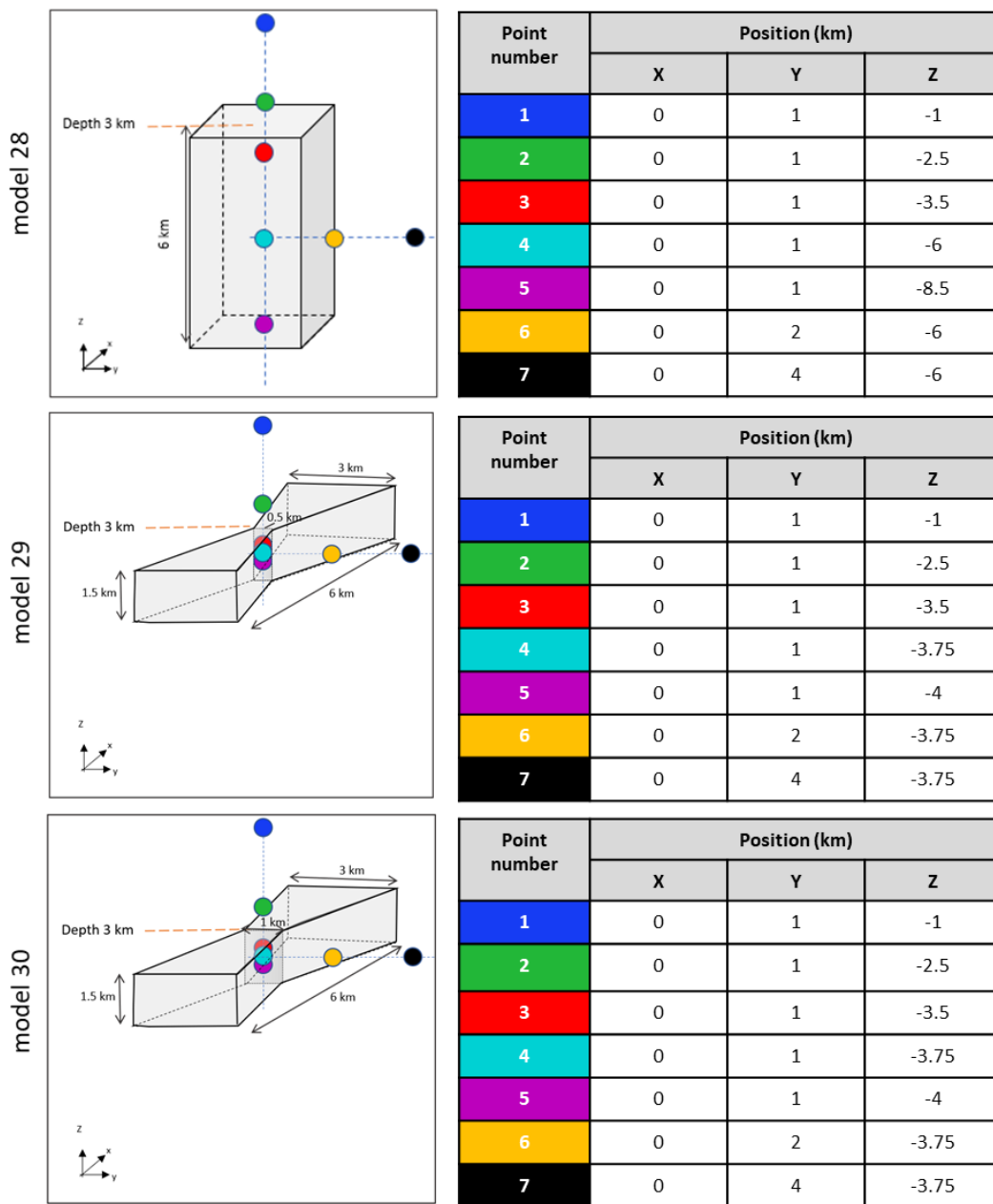


Figure A3-6a. Diagram and table showing location of the seven points selected for comparison. Model number is given. Points 1, 2, 6 and 7 are in the host rock and points 3 to 5 are within the pluton (refer to Table 3.4 p.57 for model parameters). Data is presented in parts b and c.

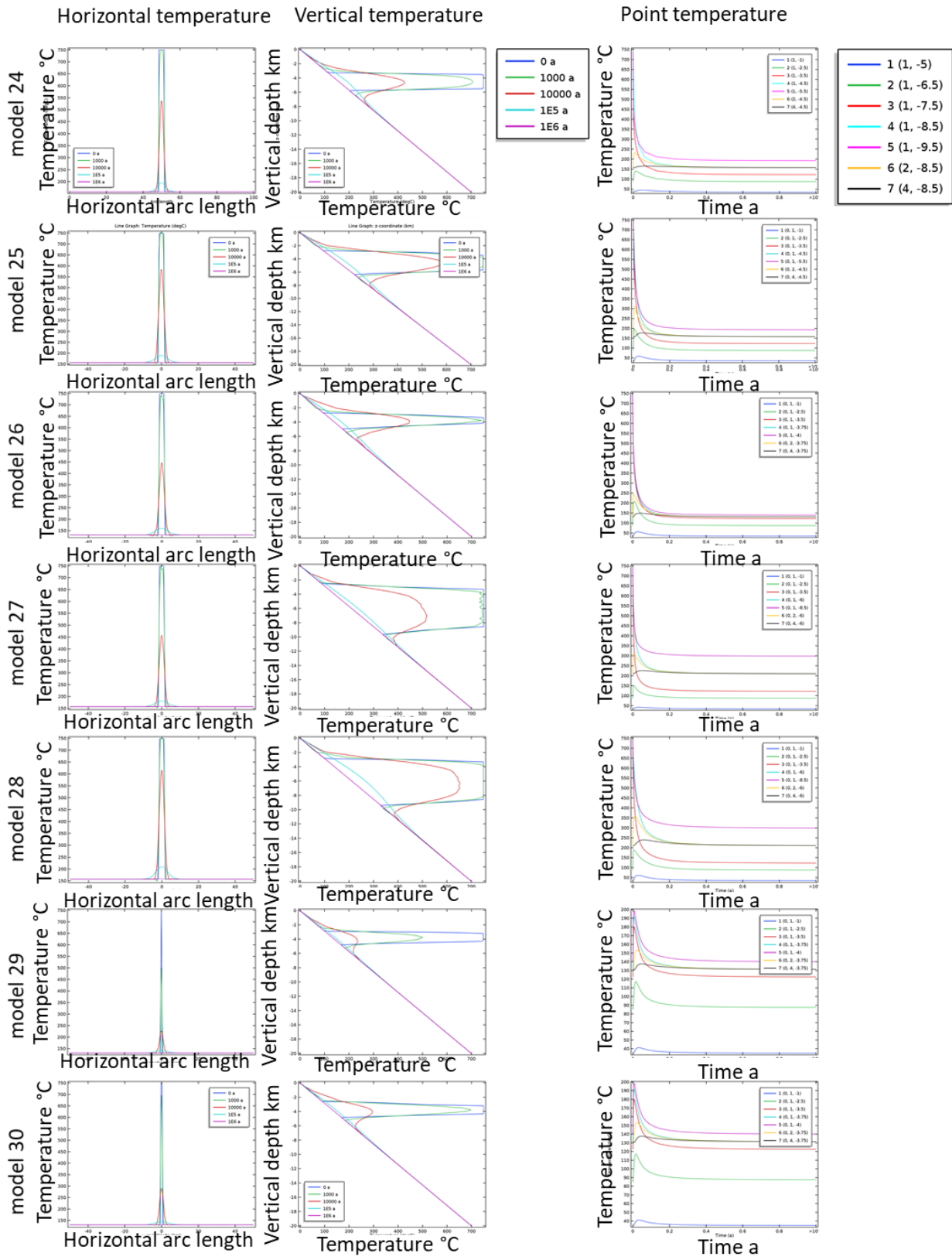


Figure A3-6b. Temperature profiles through the pluton and host rock. See Figure A3-6a for location of lines and points. Increasing depth has minimal influence on the cooling history of the pluton.

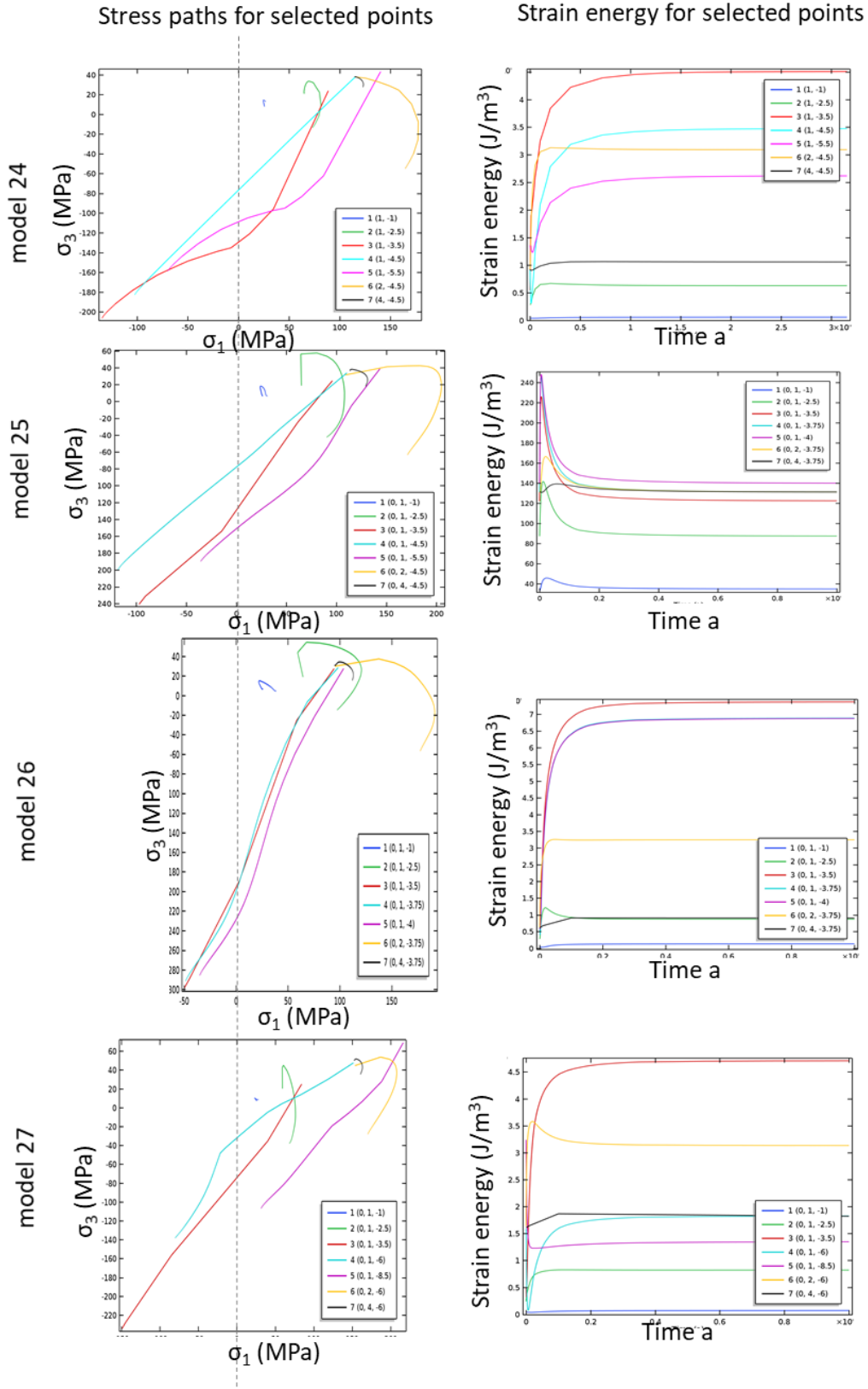


Figure A3-6c. Continued next page.

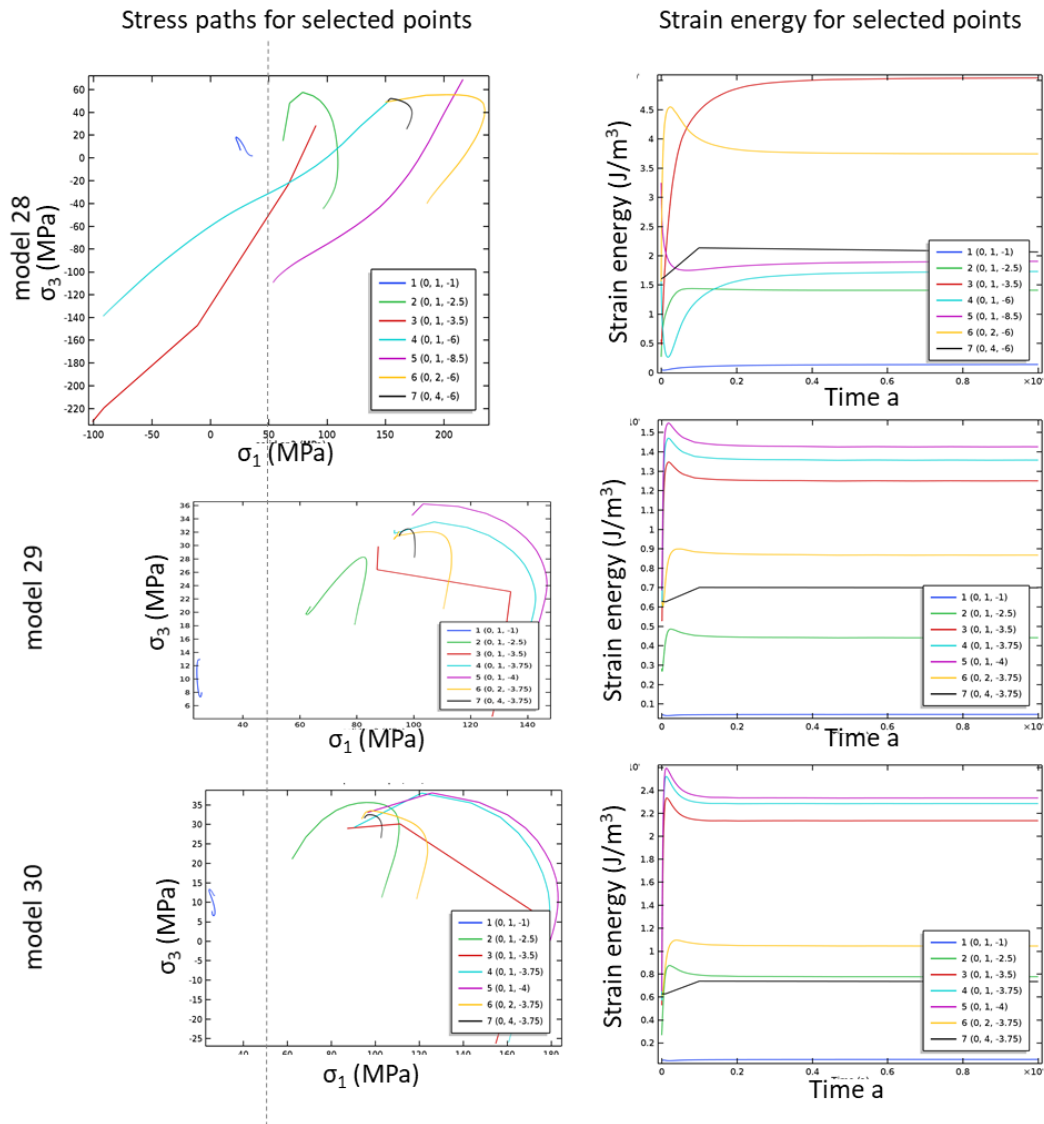


Figure A3-6c. Stress paths for selected points on a σ_1 - σ_3 plot, compression positive. Note the difference in scales, dashed line marks the maximum principal stress (σ_1) value of 50 MPa. Strain energy (J/m³, x 10⁵) for selected points.

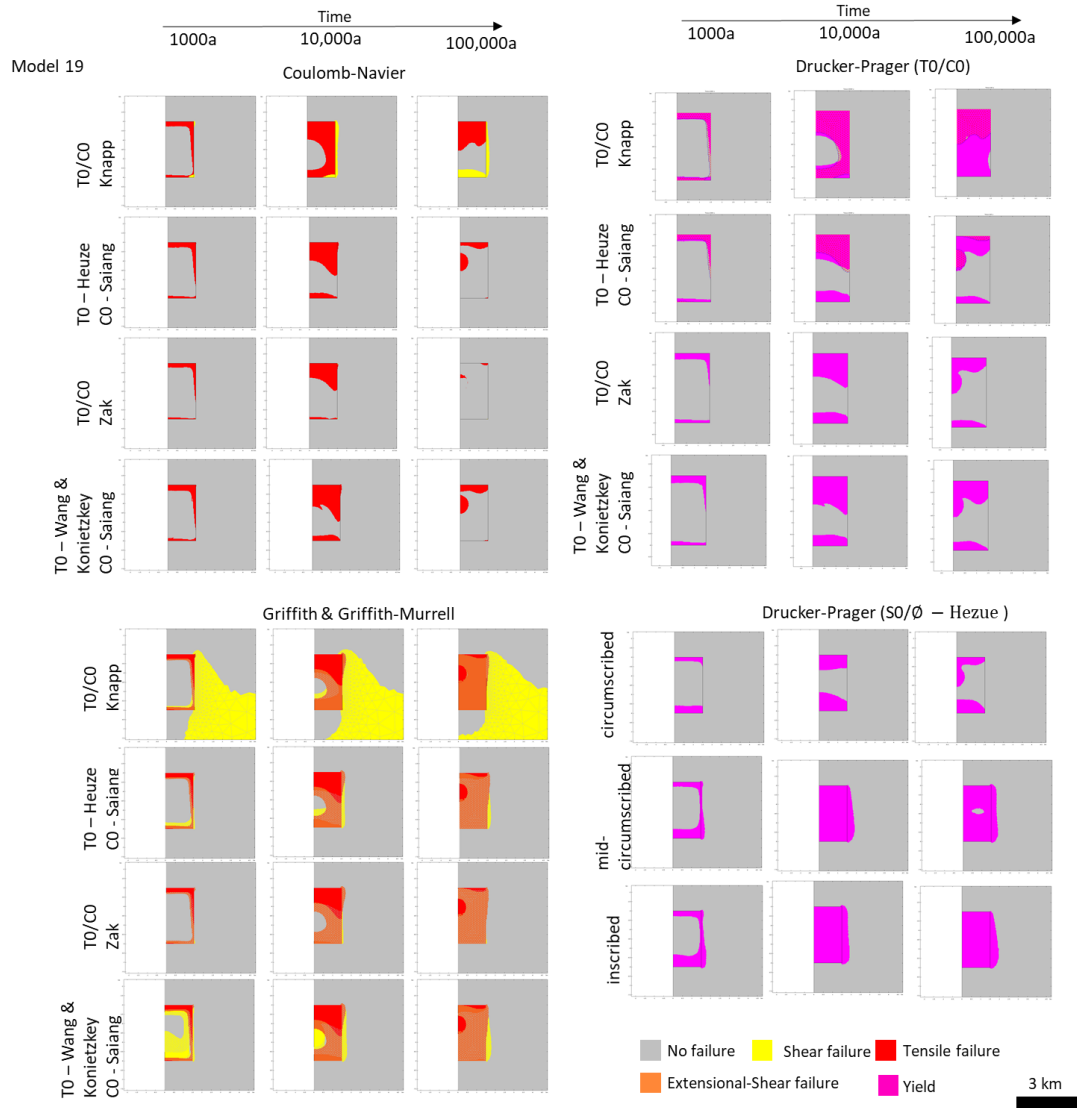


Figure A3-7. Mechanical property variation for the applied failure criterion. See Table A3-5 p312 for details of applied properties. T0 – tensile strength, C0 – compressive strength, S0 – cohesion, ϕ – angle of internal friction. Cylindrical pluton geometry top depth of 3 km, height 3 km and diameter 3 km.

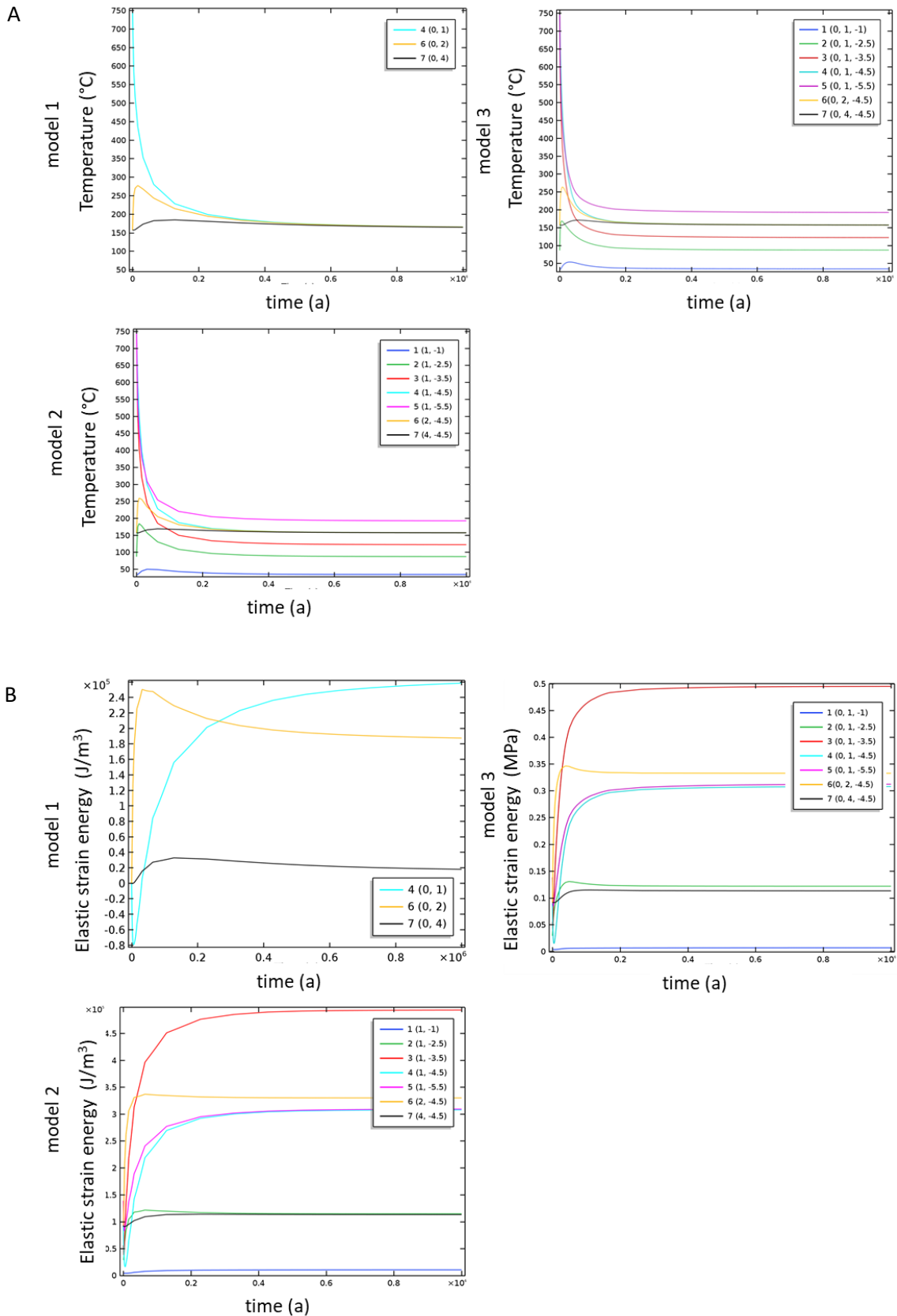
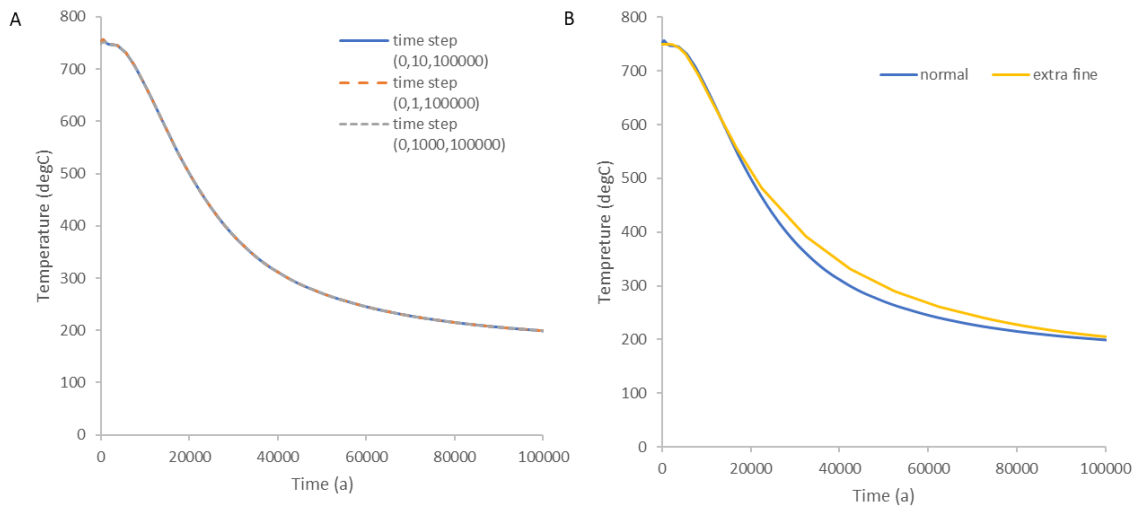


Figure A3-8. Graphs of temperature (A) and strain energy (J/m³) over time (B) for all selected points (see chapter 3 part1 Figure 3.9 p.52). This figure highlights the differences in temperature change between modelling dimensions.



Figure

A3-9. Graph of temperature over time for point 4 of model 2 for (A) comparison of timestep and (B) compared for two grid resolution. Extra fine as given in Figure 3.8 (p.56) and normal elements double the size of the grid given in Figure 3.8 (p.56). Varying time step of model calculations has no influence on modelling results.

B. Chapter 4 Appendix

Table B4-1. kinematic interpretation of aplite dykes

Aplite locality	Interpretation	Shorting direction	slip:opening ratio	Acute angle degrees of conjugates
M	right-lateral opening	Intersects obtuse angle	1:1.5 - ~1.2 / 1:4 - 1:6	60
N	right-lateral opening	Intersects acute angle	1:2 - 1:4	40
O	right-lateral opening	Intersects obtuse angle	~1:1	30
P	right-lateral opening	Intersects acute angle	1:3 - 1:4	40
P	opening	-	0:1	40
Q	right-lateral opening	Intersects acute angle	1:2.5	40
R	left-lateral opening	Intersects acute angle	1:0.6 - 1:0.4	40
S	right-lateral opening	Intersects obtuse angle	1:0.2 - 1:0.3 / ~1:1	54
T	left-lateral opening	Intersects acute angle	1:2 - 1:5	40
U	right-lateral opening	Intersects acute angle	1:2 - ~1:1.5	40
V	right-lateral opening	Intersects acute angle	01:01.4	40
V	opening	-	0:1	40
W	opening	-	0:1	40
X	later shear offset	not conjugate	n/a	not conjugate
Y	right-lateral opening	not conjugate	1:2 - ~1:1	not conjugate
Z	right-lateral opening	not conjugate	~1:3	not conjugate

Table B4-2. Topological analysis of circular scan lines for selected field locations

	L1	L2	L2AP	L2J	L3	L4	L5	L6	L7
# X	45	45	6	4	7	7	70	2	21
# Y/T	19	46	2	43	70	14	58	19	20
# I	35	15	5	11	10	7	36	4	18
TOTAL	99	106	18	58	87	28	164	25	59
EDGE	33	31	16	15	30	22	51	23	28
RADIUS METERS	1	1	1	1	0.5	1	1	1	1
DENISTY	6	2	1	2	6	1	6	1	3
INTENSITY	17	16	8	8	30	11	26	12	14
MEAN LENGTH	1	3	5	2	2	5	2	9	2
Percentage of Node Types %									
X	45.5	42.5	46.1	7	8	25	42.7	8	35.5
Y/T	19.2	43.4	15.4	74	80.5	50	35.4	76	34
I	35.3	14.1	38.5	19	11.5	25	21.9	16	30.5

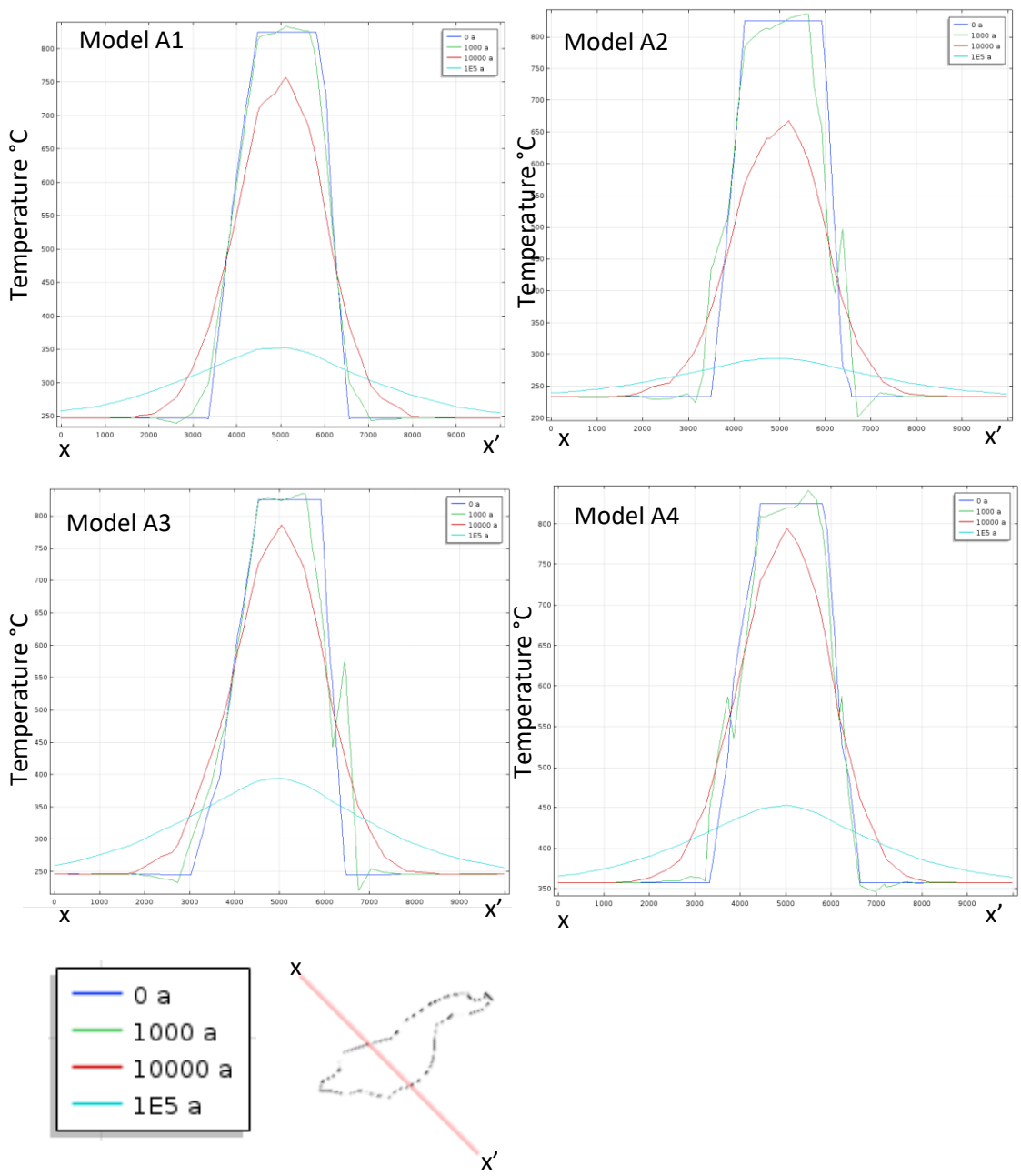


Figure B4-1. Thermal history of models A2 - 4 for a NE-SW line cut through the numerical model at a depth of 4.25 km for model A2, 5 km for model A3 and 6.5 km for model A4. See Figure 4.24 p177 for model A1.

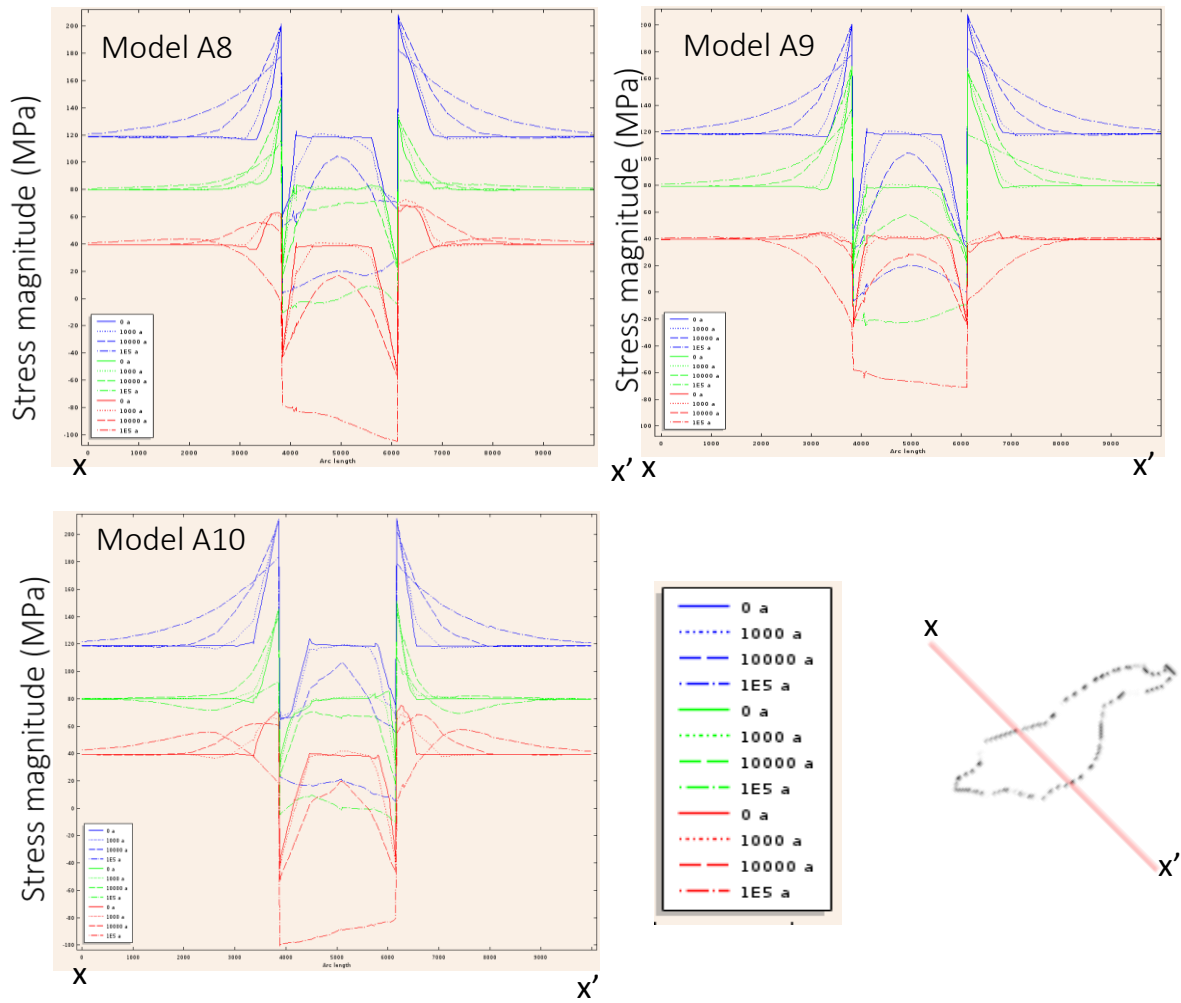


Figure B4-2. Principal stress magnitudes at selected time steps of a NE-SW 2D line cut through numerical models A8 – A10. The position of the sliced 2D line is show in Figure A4-1. Blue maximum compressive stress, green intermediate compressive stress and red minimum compressive stress. See Figure 4.31 p187 for equivalent graphs of models A1 – A7.

C. Chapter 5 Appendix

Workflow C5-1. COMSOL® geometry from MOVE™

COMSOL® geometry created from a slice of the stock outline. The slice accounts for vertical alignment of the quartz monzonite porphyry (QMP).

In the minenorth coordinate system, the QMP is initially rotated to vertical, about a plane dipping 65/000 with a transformation centre X -378.8 m, Y 198.7 m, Z 1280.3 m. Orientation data is similarly rotated on stereonet around an axis plunge 0 trend 90 rotation anticlockwise -25°.

Horizontal sections through the monzonite (MZ) intrusion were sliced. The external boundary line and internal boundaries of the MZ were manually edited to simplify boundary lines and then sampled at 5 m intervals using the DP algorithm.

The data was rotated back into mine coordinates prior to import into COMSOL®. To do this the model was rotated 31.98° around an axis with line start x 402687.1 m y 4486009.9 m z -410.7 m end x 402687.1 m y 4486694.3 m, 1057 m. the position of the rotated mine x 0, y 0 position. The rotated orientation data was corrected around the same axis plunge 65° trend 180° rotation anticlockwise - 31.98°.

The selected lines are exported as x – y coordinates in ascii file format and converted to a text file. Separate files are created for the internal and external boundaries.

The files are individually imported into COMSOL® as polygons from files. In 3D polygons are defined on a work plane and the geometry vertically extruded.

Workflow C5-2. MOVE™ MINE north to UTM coordinates

Kennecott Utah Copper (KUC) 2017 mine model in Mine North coordinates, with data in feet and elevation.

In MOVE™ conversion of data from Minenorth to UTM NAD27 12 North requires a 31.98° anticlockwise rotation (MOVE angle 328.02) with a translation of 402687.1 meters east, 4486671.0 meters north. In Utah State plane, central Zone this is Easting of 1819726.4400 and Northing of 199219.8500 from. Using x 0, y 0 in the mine model as the origin.

Conversion of orientation data from Mine North to true north is given by an taking away -31.98° from the azimuth. Rotation on stereonet around an axis plunge 90 trend 0 rotation anticlockwise - 31.98°.

Workflow C5-3. COMSOL® data export

Data exported (Table C5-1) as text file for selected time steps (100 a, 1000 a 10,000a and 100,000 a) on a given grids as listed.

Table C5-1. Data exported on gird and for selected points COMSOL®

Expression	Unit	Description
-solid.sp1	MPa	Maximum principal stress (tension positive)
-solid.sp2	MPa	Second principal stress (tension positive)
-solid.sp3	MPa	Minimum principal stress (tension positive)
solid.sp1x		Principal stress direction 1, x component
solid.sp1y		Principal stress direction 1, y component
solid.sp1z		Principal stress direction 1, z component
solid.sp2x		Principal stress direction 2, x component
solid.sp2y		Principal stress direction 2, y component
solid.sp2z		Principal stress direction 2, z component
solid.sp3x		Principal stress direction 3, x component
solid.sp3y		Principal stress direction 3, y component
solid.sp3z		Principal stress direction 3, z component
T*	degC	Temperature

* defined as T2 in 3D models

Three-dimensional models exported on a given grid (Table C5-2). Table A4 points rotated 55° anticlockwise around axis x 0, y 0 accounting for regional tectonic load.

Table C5-2. Grid coordinates COMSOL®

Grid points	Coordinates
X	range(-3500,200,1300)
Y	range(-2300,200,1500)
Z	-3.5[km] / -4.5[km] / -5.5[km] *

* exported for the three given z values separately
For the regionaltect file grid loaded from file based on points rotated 55 deg anticlockwise around X 0 Y 0

Workflow C5-4. COMSOL® data to principal stresses plunge / plunge azimuth

Data is converted to plunge and plunge directions of the principal axis. To do this the principle stress components exported from COMSOL® as eigenvectors (given in terms of the direction cosines) are converted in excel. Based on method as given in Chapter 12 Groshong, 2006.

Example of equations used in Excel to convert exported principle stress components for solid.sp1 (direction of the minimum principal stress) is given in Table C5-3.

Table C5-3. Example of conversion of eigenvectors exported from COMSOL® into plunge and plunge azimuth minimum compressive stress direction

Colum	Row 1	Description
A	Solid.sp1x numerical value	Principal stress components exported from COMSOL®
B	Solid.sp1y numerical value	
C	Solid.sp1z numerical value	
D	=ROUNDUP((DEGREES(ASIN(C1))),0)	Plunge of the minimum principal stress
E	=ROUNDUP(DEGREES(ATAN(A1/B1)),0)	Calculation and correction of plunge azimuth
F	=IF(A1<=0,180+E1,IF(B1>=0,E1,360+E1))	Plunge azimuth of the minimum principal stress*

* note for file regional tectonic then value rotated 55 degrees clockwise around vertical axis

Workflow C5-5. MOVE™ import principal stresses for visualisation

Plunge and Plunge azimuth directions can be loaded into MOVE™ as lineation data and converted to lines representing the strike direction but converting lineation data to lines based on dip azimuth directions. These lines start at the grid point exported from COMSOL®. In order to import lines with a defined length and centered on the exported COMSOL® point excel was used to convert directional data into start and end points of lines with a given length using trigonometry, outline in Table C5-4.

Table C5-4. Conversion to line start and end points of a line representing the strike direction of the maximum principal stress

Column	Row 1	Description
A	As calculated column E, Table A4.1	Plunge maximum principal stress
B	As calculated column F, Table A4.1	Plunge azimuth maximum principal stress
C	=IF(B1>180,B1-180,B1)	Angle
D	=IF(C1>90,C1-90,C1)	Angle corrected
E	Defined length of line in meters	Length of line selected for MOVE™ display
F	=(COS(RADIANS(D1)))*E1	Adjacent length
G	=(SIN(RADIANS(D1)))*E1	Opposite length
H	X value	Point x value exported from COMSOL®
I	Y value	Point y value exported from COMSOL®
J	Unique name given to each line	Given line name
K	=IF(D1>90,H1-F1,H1-G1)	Start point X
L	=IF(D1>90,I1+G1,I1-F1)	Start point y
M	=IF(D1>90,H1+F1,H1+G1)	End point X
N	=IF(D1>90,I1-G1,I1+F1)	End point y

Data then organised into rows, for each line the start point and end point of a line the same name is given. The start point is followed by the end points i.e. Table C5-5.

Table C5-5. Format of start and end point of two liens for import into MOVE™

LineNameA	startpointXLineA	startpointYLineA
LineNameA	endpointXLineA	endpointYLineA
LineNameB	startpointXLineB	startpointYLineB
LineNameB	endpointXLineB	endpointYLineB

For three-dimensional models the dip and strike of the plane perpendicular to the minimum principal stress is calculated and imported into MOVE™ as dip data. Values of minimum principal plunge and plunge azimuth are initially made positive before converting to dip and strike, Table C5-6.

Table C5-6. Conversion of minimum principal stress direction into plane representing the maximum and intermediate principal stress direction (convention assuming tension positive)

Column	Row 1	Description
A	As calculated column E, Table A4.1	Plunge minimum principal stress
B	As calculated column F, Table A4.1	Plunge azimuth minimum principal stress
C	=IF(A1<0,-A1,A1)	Plunge corrected to positive value
D	=IF(A1<0,B1-180,B1)	Plunge azimuth corrected if plunge converted from negative value step 1
E	=IF(D1<0,360+D1,D1)	Plunge azimuth corrected if plunge converted from negative value step 2
F	=90-C1	Dip of the plane perpendicular to the minimum compressive stress
G	=E1+90	Strike of the plane perpendicular to the minimum compressive stress

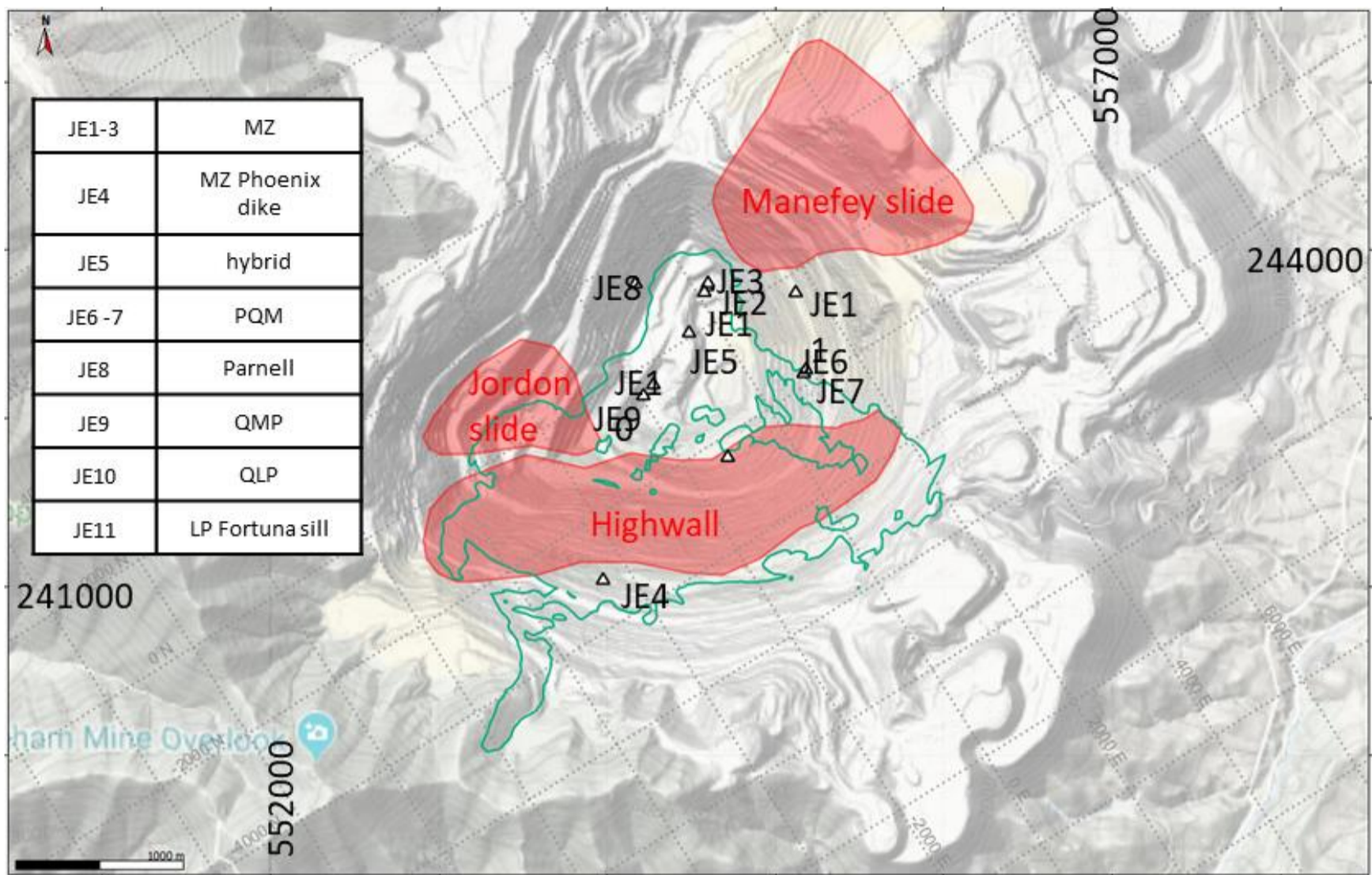


Figure C5-1. Location of data collected in this study and example photos. Bench height in photo ~40 ft (~12 meters).

Table C5-7. Point labels used on representative section

Field locations as labelled in figures chapter 6 *	Field locations as labelled from (Grün, 2007) and field work this study	Closest level models G1 – G-4
A	A	2
B	B	2
C	C	3
D	D	3
E	E	3
F	F	3
G	G	1
H	H	1
I	1	1
J	J	1
K	K	K
L	L	3
M	M	2
N	4	3
O	O/O+/O++	3
P	PandP+	1
Q	Q/Q++	2
R	JE1-3	4
S	JE5	4
T	DD	3
U	U	3
W	JE11	4
X	JE6-10	3
-	FF	1
-	JE4	1
-	GG	3
-	JE5	4
-	3	1
-	2	1
-	Y	2
-	Z	2
-	R	3
-	CC	3
-	AA	2
-	BB	2
-	WanaX	4
-	EE	3
-	V	3
-	TandN	3
-	S	4

* dash - less than 20 data point and not included in the analysis

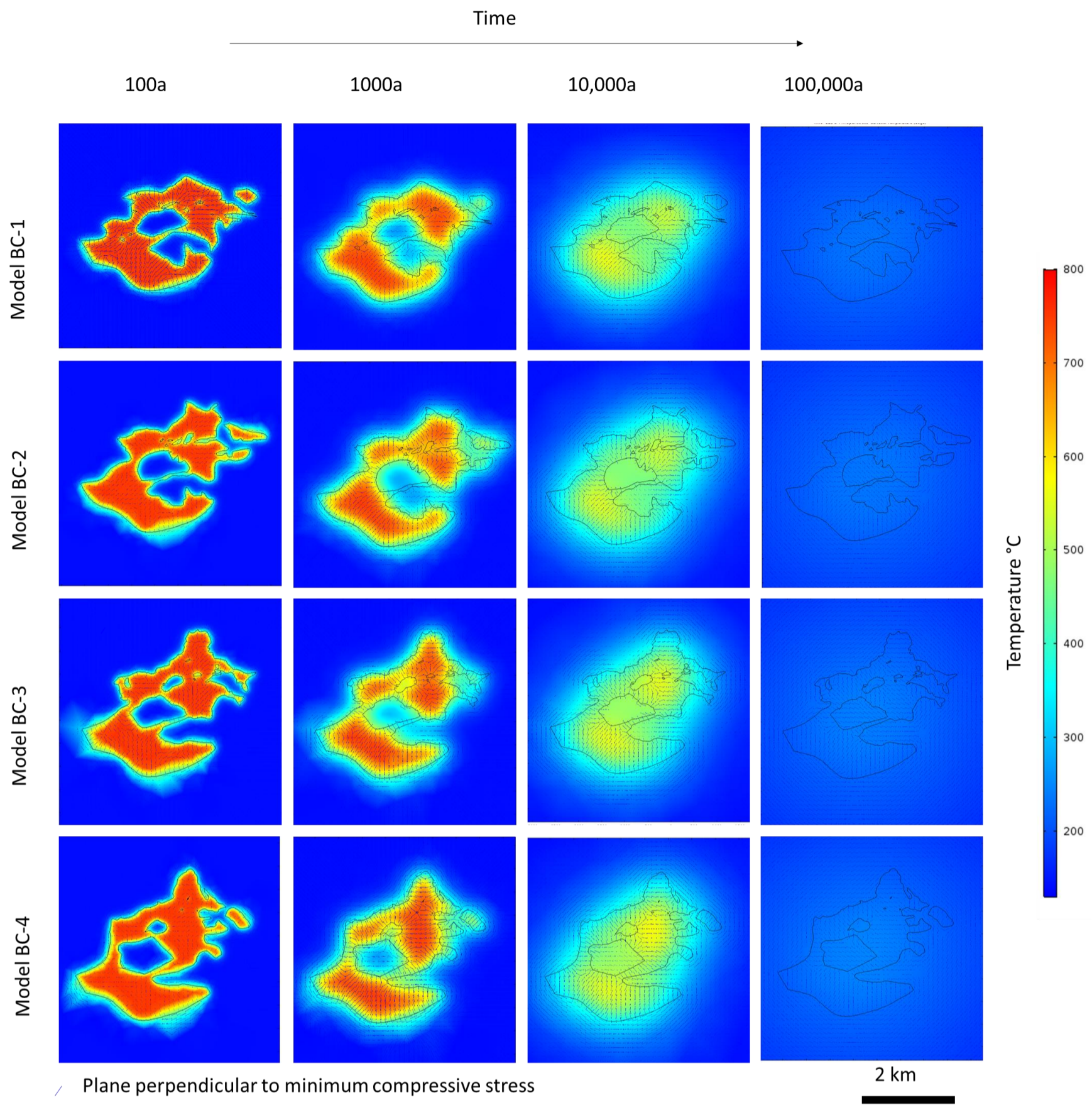


Figure C5-2. Cooling history and principal stress orientation for models BC-1 to BC-4.

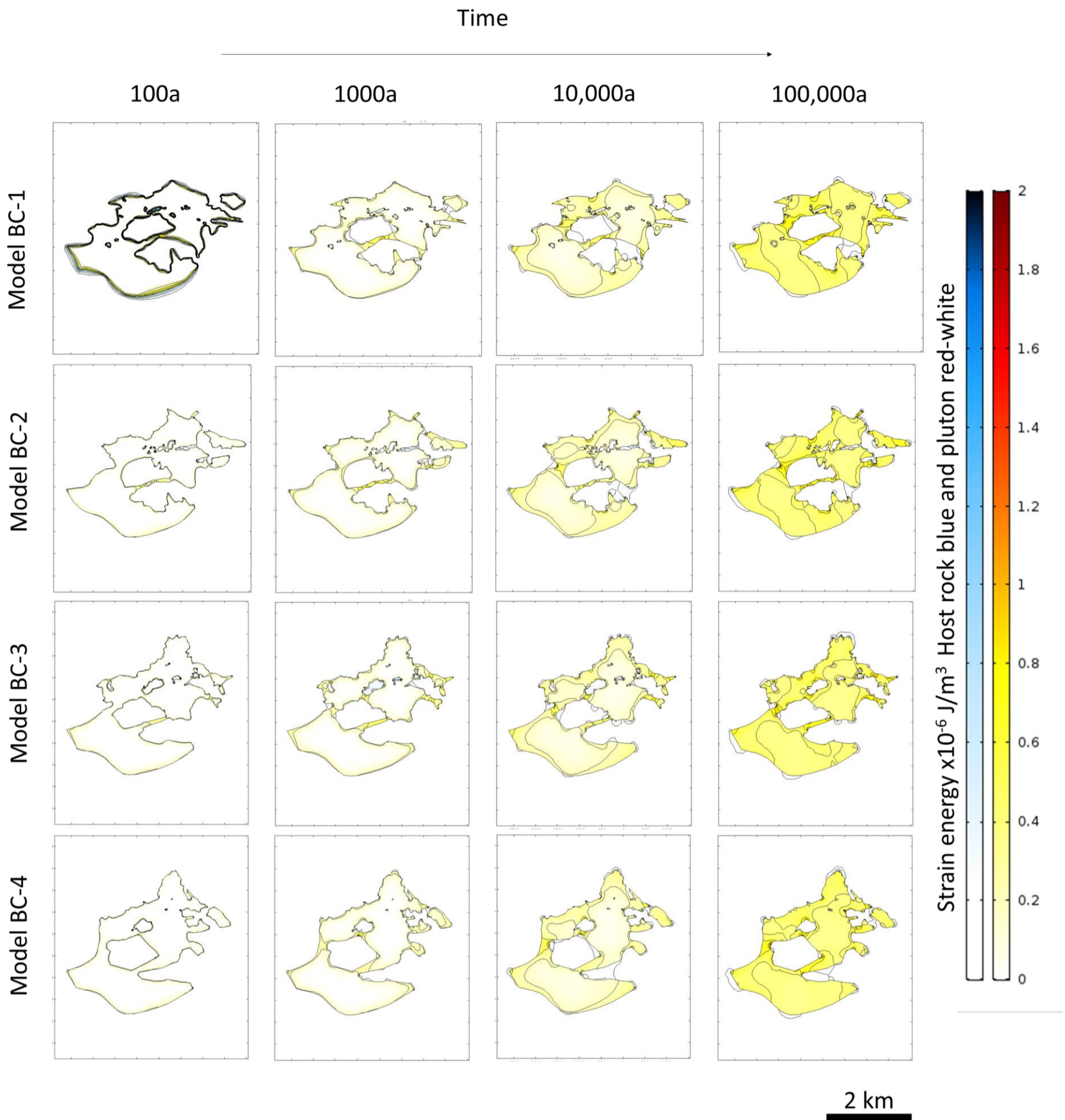


Figure C5-3. Strain energy (J/m³) for models BC-1 to BC-4.

Fig

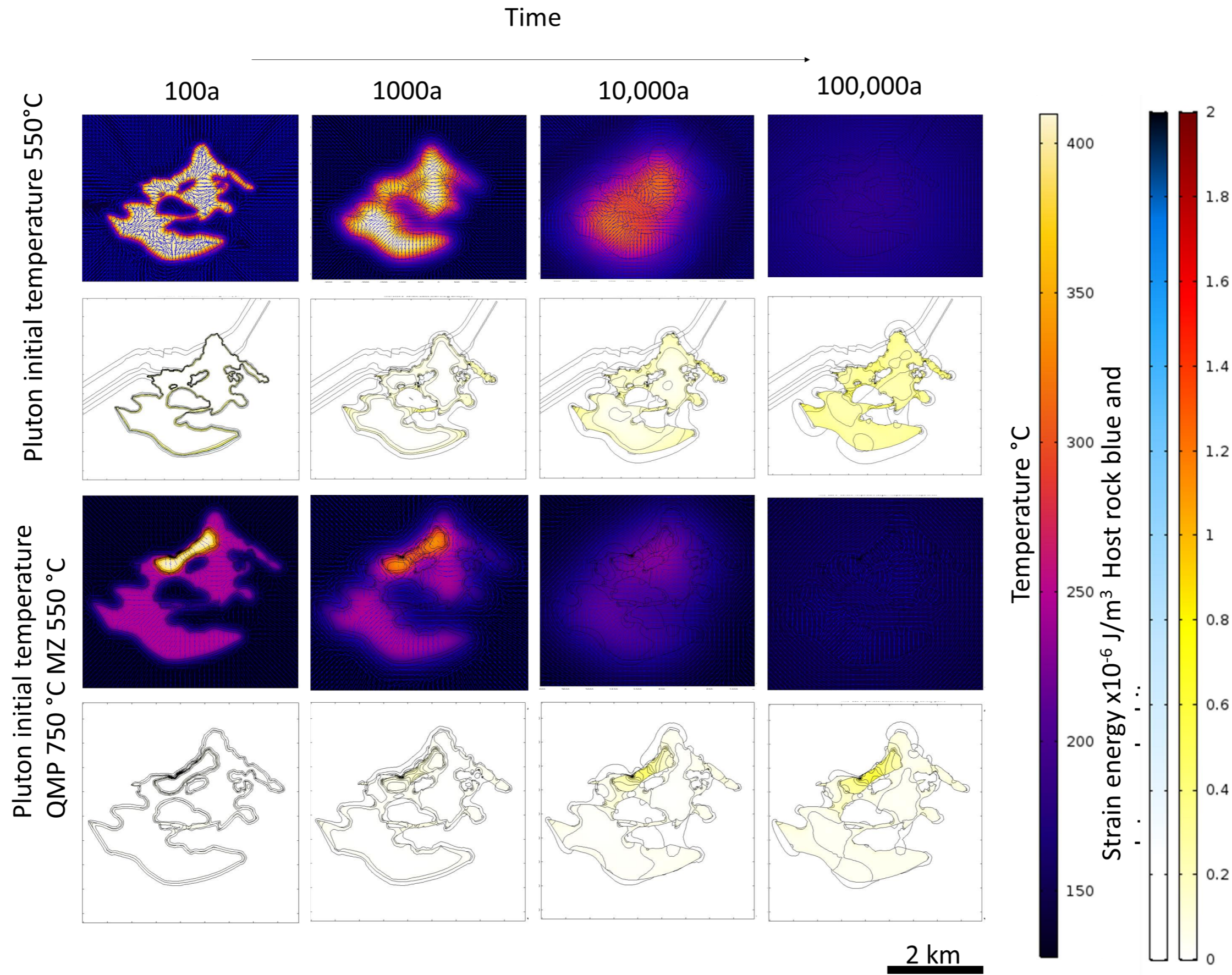


Figure C5-4. Cooling history, principal stress orientation and strain energy for varying initial temperatures of model BC-5.

D. Chapter 6 Appendix

Table D6-1. List of sample numbers. Sample number give information on the drying method, burial depth, geometry and duplicate number. The appendix slide number is given in which photographs of the dried fracture patterns are given. Experiments run in the CUROP project are marked with a star

#	Sample name	Description	Fractured ^P plumose fracture ^F full thickness fracture
1	LM-0-40-1	Lamp dried in mould	Yes
2	LM-0-40-2	Lamp dried in mould	Yes
3	LM-0-40-3 *	Lamp dried in mould	Yes
4	LM-0-40-4 *	Lamp dried in mould	Yes
5	LB-0-40-1 *	Lamp dried no mould	Yes
6	LB-0-40-2 *	Lamp dried no mould	Outside only
7	LC-0-40-1	Lamp dried in cloth	Yes
8	LC-0-40-2	Lamp dried in cloth	Yes
9	LN-0-40-1	Lamp dried on cloth	Yes
10	LN-0-40-2	Lamp dried on cloth	Yes
11	AM-0-40-1	Air dried in mould	Yes
12	AM-0-40-2	Air dried in mould	Yes
13	BS-05-40-1	Buried in sand 5 mm	Yes
14	BS-05-40-2	Buried in sand 5 mm	Yes
15	BS-05-40-3	Buried in sand 5 mm	Yes
16	BS-10-40-1	Buried in sand 10 mm	Yes ^(P)
17	BS-10-40-2	Buried in sand 10 mm	Yes
18	BS-10-40-3	Buried in sand 10 mm	Yes
19	BS-15-40-1 *	Buried in sand 15 mm	Yes
20	BS-15-40-2 *	Buried in sand 15 mm	Yes
21	BS-20-40-3 *	Buried in sand 20 mm cloth covered	Yes
22	BS-20-40-1 *	Buried in sand 20 mm	Yes
23	BS-20-40-2	Buried in sand 20 mm	Yes
24	BS-20-40-3	Buried in sand 20 mm	Yes
25	BS-20-40-4 *	Buried in sand 20 mm	No
26	BS-30-40-1 *	Buried in sand 30 mm	Yes
27	BS-30-40-2	Buried in sand 30 mm	Yes
28	BS-30-40-3	Buried in sand 30 mm	Yes
29	BS-35-40 *	Buried in sand 35 mm	Yes
30	BS-40-40-1	Buried in sand 40 mm	Yes
31	BS-40-40-2	Buried in sand 40 mm	Yes
32	BS-45-40	Buried in sand 45 mm	Yes
33	BS-50-40-1	Buried in sand 50 mm	Yes ^{(P) (F)}
34	BS-50-40-2	Buried in sand 50 mm	Yes
35	BS-50-40-3	Buried in sand 50 mm	No, damp
36	BS-50-40-4	Buried in sand 50 mm	No, damp
37	BS-50-40-5	Buried in sand 50 mm	No, damp
38	BS-50-40-6	Buried in sand 50 mm	Damp
39	BS-60-40-1	Buried in sand 60 mm	Yes

Table D6-1. Continued

40	BS-60-40-2	Buried in sand 60 mm	Yes
41	BS-60-40-3	Buried in sand 60 mm	No, damp
42	BS-75-40 *	Buried in sand 75 mm	Yes
43	BS-90-40-1 *	Buried in sand 90 mm	No, damp
44	BS-95-40-1 *	Buried in sand 95 mm	No, damp
45	BS-120-40-1	Buried in sand 120 mm	No
46	BS-120-40-2	Buried in sand 120 mm	No
47	BS-145-40-1 *	Buried in sand 145 mm	Yes
48	BS-20-V-1 *	Buried in sand 20 mm not moulded	No, damp
49	BS-20-V-2 *	Buried in sand 20 mm not moulded	No, damp
50	BC-05-40	Buried in corn-starch 5 mm	Yes
51	BC-20-40	Buried in corn-starch 20 mm	Yes
52	BC-40-40	Buried in corn-starch 40 mm	Yes
53	BC-60-40	Buried in corn-starch 60 mm	Yes
54	BD-05-40	Buried in desiccant 5 mm	Yes
55	BD-20-40	Buried in desiccant 20 mm	Yes (p) (F)
56	BD-40-40	Buried in desiccant 40 mm	Yes
57	BD-60-40	Buried in desiccant 60 mm	Yes
58	BS-20-40-L1	Buried in sand 20 mm _ squeezed	Yes
59	LM-0-40-r	Lamp dried in mould rice starch	No, damp
60	BS-20-40-r	Buried in sand 20 mm rice starch	No, damp
61	LM-0-100	Lamp dried in mould flat cylinder	Yes
62	AM-0-100	Air dried in mould flat cylinder	Yes
63	BS-30-100-1	Buried in sand 30 mm flat cylinder	Yes
64	BS-30-100-2	Buried in sand 30 mm flat cylinder	No
65	BD-30-100	Buried in desiccant 30 mm flat cylinder	Yes
65	LM-30-100-r	Lamp dried in mould flat cylinder	Yes
67	LM-0-40t	Lamp dried in mould tall cylinder	No
68	LB-0-40t	Lamp dried no mould tall cylinder	Yes
69	AM-0-40t	Air dried in mould tall cylinder	No(F)
70	BS-30-40t	Buried in sand 30 mm tall cylinder	No
71	LM-0-80/40	Lamp dried in mould brick	Yes
72	LC-0-80/40	Lamp dried in cloth brick	Yes
73	AM-0-80/40-1	Air dried in mould brick	Yes
74	AM-0-80/40-2	Air dried in mould brick	Yes (F)
75	BS-30-80/40-1	Buried in sand 30 mm brick	Yes
76	BS-30-80/40-2	Buried in sand 30 mm brick	Yes
77	LM-0-HG	Lamp dried in mould hour glass	Yes (p) (F)
78	LB-0-HG	Lamp dried no mould hour glass	Yes (p) (F)
79	BS-30-HG	Buried in sand 30 mm hour glass	Yes (p) (F)

Sample numbering system

Drying method – sample burial depth in mm – sample geometry – duplicate number i.e. (LM-0-40-1)

Abbreviations

LM – lamp dried in mould, LB – lamp dried no mould, AM – air dried in mould, BS – buried in sand, BC – Buried in corn-starch, BD – Buried in desiccant, V – not moulded directly buried in sand, r – rice starch, L – external force, HG- hour glass

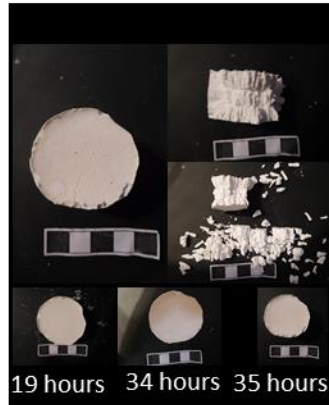
(1) LM-0-40-1



(5) LB-0-40-1*



(9) LN-0-40-1



(2) LM-0-40-2



(6) LB-0-40-2*



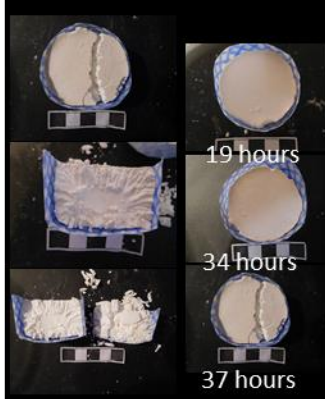
(10) LN-0-40-2



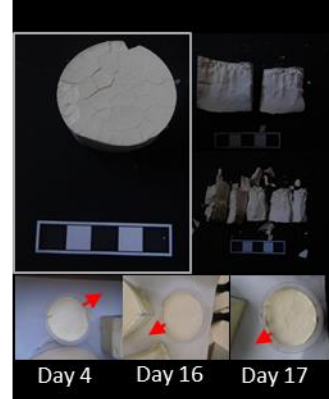
(3) LM-0-40-3



(7) LC-0-40-1



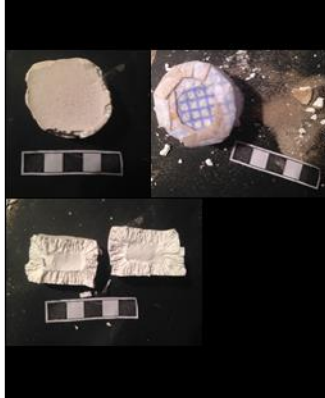
(11) AM-0-40-1



(4) LM-0-40-4



(8) LC-0-40-2



(12) AM-0-40-2



(13) BS-05-40-1



(17) BS-10-40-2



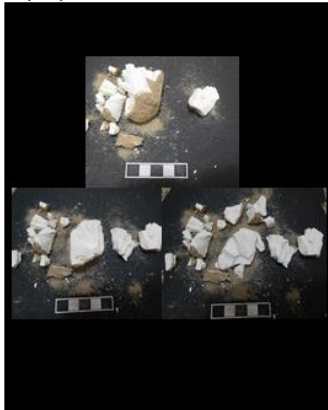
(21) BS-15-40-3*



(14) BS-05-40-2



(18) BS-10-40-3



(22) BS-20-40-1*



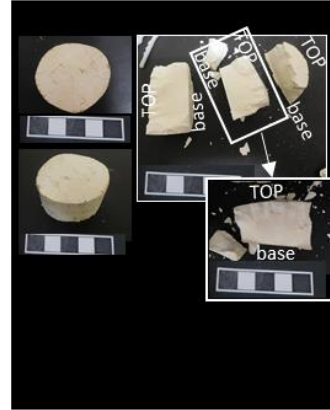
(15) BS-05-40-3



(19) BS-15-40-1*



(23) BS-20-40-2



(16) BS-10-40-1



(20) BS-15-40-2*



(24) BS-20-40-3



(25) BS-20-40-4*



(29) BS-35-40*



(33) BS-50-40-1



(26) BS-30-40-1*



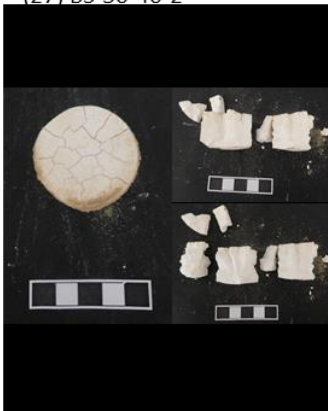
(30) BS-40-40-1



(34) BS-50-40-2



(27) BS-30-40-2



(31) BS-40-40-2



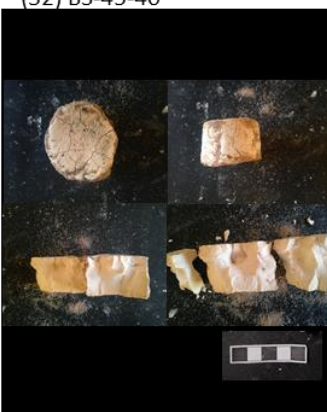
(35) BS-50-40-3



(28) BS-30-40-3



(32) BS-45-40



(36) BS-50-40-4



(37) BS-50-40-5



(41) BS-60-40-3



(45) BS-120-40-1



(38) BS-50-40-6



(42) BS-75-40*



(46) BS-120-40-2



(39) BS-60-40-1



(43) BS-90-40-1*



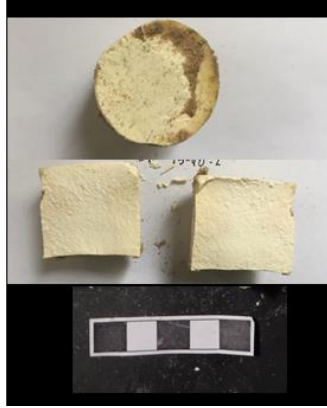
(47) BS-145-40-1*



(40) BS-60-40-2



(44) BS-95-40-1*



(48) BS-20-V-1*



(49) BS-20-V-2*



(53) BC-60-40



(57) BD-60-40



(50) BC-05-40



(54) BD-05-40



(58) BS-20-40-L1



(51) BC-20-40



(55) BD-20-40



(59) LM-0-40-r



(52) BC-40-40



(56) BD-40-40



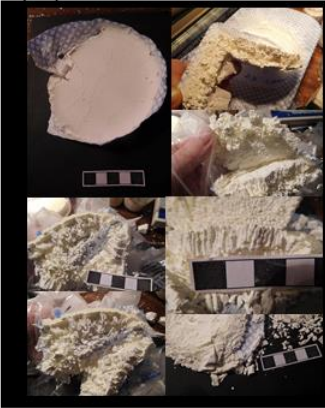
(60) BS-20-40-r



(61) LM-0-100



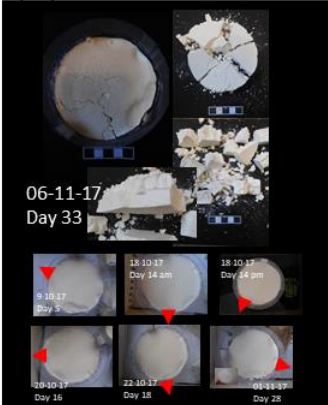
(65) BD-5-100



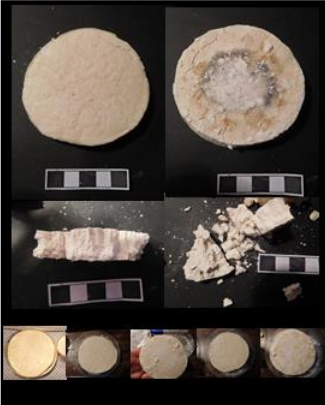
(69) AM-0-40t



(62) AM-0-100



(66) LM-5-100-r



(70) BS-30-40t



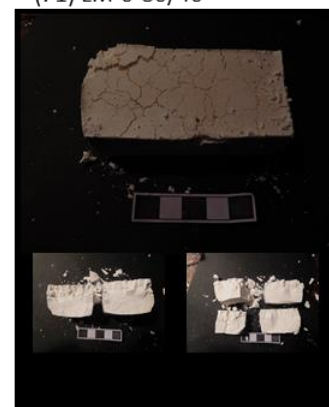
(63) BS-05-100



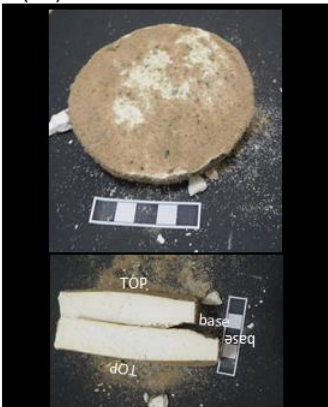
(67) LM-0-40t



(71) LM-0-80/40



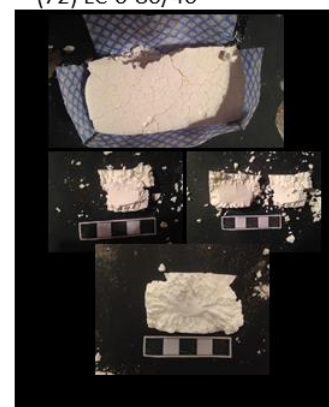
(64) BS-30-100



(68) LB-0-40t



(72) LC-0-80/40



(73) AM-0-80/40-1



(77) LM-0-HG



(74) AM-0-80/40-2



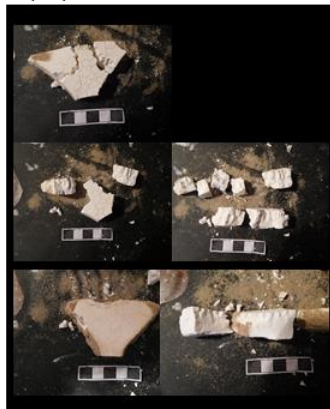
(78) LB-0-HG



(75) BS-30-80/40-1



(79) BS-30-HG



(76) BS-30-80/40-2

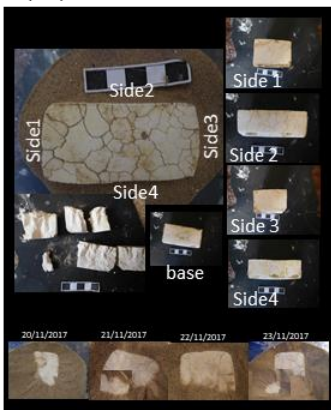


Table D6-2. Weight in grams for given sample

Time from start [h]	Sample number									
	1	2	7	8	9	10	11	12	13	14
0.00	63.52	58.2	58.12	57.45	57.9	55.45	54	53.28		
1.00	62.44	57.49	53.55	53.06	53.06	50.27	53.96	53.25	251.15	199.45
2.00	61.29	56.78	48.98	48.71	48.21	45.56	53.92	53.21	250.68	199.38
3.00	60.56	56.07	44.4	43.44	43.37	40.92	53.88	53.16	250.6226	199.34
4.00	59.55	55.36	39.83	40.13	38.52	36.49	53.83	53.18	250.5724	199.3
5.00	58.44	54.65	35.27	35.36	33.68	32.66	53.79	53.14	250.3338	199.26
6.00	57.16	53.94	32.9	33.27	30.04	28.94	53.75	53.1	250.4719	199.22
7.00	56.15	53.23	32.01	32.05	28.98	28.7	53.7	53.05	250.4217	199.18
8.00	54.77	52.52	31.12	30.96	27.95	26.56	53.66	53.01	250.3251	199.14
9.00	54.1	51.81	30.23	30.15	26.92	25.77	53.62	52.97	250.35	199.1
10.00	53.35	51.1	29.35	29.73	25.89	25.37	53.57	53.24	250.271	199.06
11.00	52.64	50.39	28.28	27.52	25.15	24.89	53.53	53.25	250.2207	199.02
12.00	52.04	49.68	27.75	27.52	24.47	23.97	53.49	53.28	250.1705	198.98
24.00	47.45	42.85	25.65	24.8	21.71	18.53	52.97	52.75	249.5678	198.5
48.00	47.45	42.89					51.93	52.59	248.3622	197.54
72.00	47.39	42.32					50.89	52.49	247.1567	196.58
96.00	47.33	41.35					49.86	52.39	245.9512	195.63
120.00	47.39	41.47					48.82	51.75	245.4866	194.67
144.00	47.33	41.79					48	51.56	243.587	193.5
168.00							47.37	51.12	243.0604	192.97
192.00							46.86	49.81	242.2045	192.54
216.00							46.34	49.39	241.9286	192.11
240.00							45.82	48.95	241.3861	191.68
264.00							45.34	48.94	240.8437	191.25
288.00							44.01	48.8	240.5602	191.02
312.00							42.79	47.55	239.7901	190.76
336.00							42	47.85	239.5241	190.22
360.00							41.23	46.01	239.2486	190.00
384.00							41	45.79	238.9705	189.78
408.00							40.96	46.46	238.9372	189.75
432.00									238.7563	189.61
456.00									238.5755	189.47
480.00									238.3947	189.32
504.00									238.2139	189.18
528.00										189.17
552.00										189.05
576.00										189.06

Table D6-2. Continued. weight in grams for given sample

Time from start [h]	Sample number									
	15	16	17	18	23	24	27	28	30	31
0.00										
1.00	249.84	237.65	194.78	199.54	201.45	234.78	196.85	237.89	265.47	196.97
2.00	249.18	237.57	194.75	199.49	201.42	234.76	196.84	237.86	265.45	196.96
3.00	249.6	237.55	194.73	199.45	201.4	234.74	196.83	237.85	265.44	196.96
4.00	249.55	237.53	194.71	199.41	201.38	234.69	196.82	237.83	265.42	196.95
5.00	249.45	237.53	194.71	199.37	201.36	234.69	196.81	237.81	265.41	196.94
6.00	249.45	237.48	194.67	199.33	201.35	234.67	196.8	237.8	265.41	196.93
7.00	249.4	237.45	194.65	199.29	201.33	234.62	196.79	237.78	265.4	196.93
8.00	249.34	237.43	194.63	199.25	201.31	234.6	196.78	237.76	265.39	196.92
9.00	249.31	237.41	194.61	199.21	201.29	234.6	196.77	237.75	265.34	196.91
10.00	249.25	237.38	194.59	199.17	201.27	234.57	196.76	237.73	265.31	196.9
11.00	249.2	237.36	194.57	199.13	201.26	234.55	196.75	237.71	265.29	196.89
12.00	248.87	237.24	194.55	199.09	201.24	234.53	196.74	237.7	265.2	196.89
24.00	248.61	236.81	194.32	198.61	201.02	234.46	196.62	237.5	265.13	196.8
48.00	247.26	235.96	193.85	197.65	200.58	234.2	196.38	237.1	264.89	196.61
72.00	246.06	234.78	192.85	196.7	200.15	232.86	196.15	236.76	264.67	196.45
96.00	244.99	233.9	192.34	195.74	199.65	232.52	195.89	236.33	264.4	196.25
120.00	243.9	232.66	191.24	194.78	199.4	232.18	195.71	235.99	264.18	196.08
144.00	242.38	231.93	190.91	193.91	199.11	231.84	195.52	235.81	263.88	195.99
168.00	241.73	231.38	190.56	193.34	198.74	231.64	195.32	235.54	263.66	195.83
192.00	241.07	230.55	189.62	192.91	198.64	231.61	195.07	235.31	263.48	195.67
216.00	240.94	229.73	188.69	192.48	198.5	231.34	194.88	235.08	263.29	195.5
240.00	240.4	229.23	188.28	192.06	198.35	231.07	194.69	234.85	263.36	195.34
264.00	239.86	228.52	187.61	191.56	198.21	230.98	194.5	234.5	263.1	195.12
288.00	239.58	228.24	187.32	191.39	198.06	230.98	194.31	234.5	263.04	195
312.00	238.82	228.03	187.23	191.13	197.84	230.74	194.24	234.44	262.94	194.98
336.00	238.53	227.69	187.19	190.59	197.72	230.44	194.06	234.3	262.53	194.92
360.00	238.26	227.5	187.02	190.44	197.24	229.9	193.46	234.03	262.51	194.84
384.00	237.98	227.37	187.1	190.15	197.16	229.78	193.38	233.56	262.34	194.59
408.00	237.95	227.45	187.18	190.2	196.94	229.59	193.06	233.39	262.34	194.4
432.00	237.77	227.38	187.14	190.12	196.52	228.88	192.69	233.1	262.24	194.27
456.00	237.59	227.35	187.1	190.11	196.33	229.04	192.55	233.08	261.95	194.26
480.00	237.41	227.22	187.06	189.93	196.14	228.69	192.41	232.73	261.96	194.1
504.00	237.23	227.16	187.03	189.86	195.94	228.41	192.26	232.32	261.72	193.93
528.00	237.2	227	186.95	189.68	195.75	228.17	192.12	232.11	261.8	193.81
552.00	237.17	226.7	186.57	189.57	195.56	227.94	191.98	231.9	261.41	193.56
576.00	237.14	226.42	186.2	189.47	195.36	227.46	191.84	231.59	261.18	193.43
600.00					195.17	227.23	191.7	231.45	261.04	193.27
624.00						227.22	191.56	231.51	261.01	193.12
648.00						227.22	191.41	231.51	260.94	193.11
672.00						227.22	191.27	231.14	260.68	192.95
696.00						227.23	191.13	230.95	260.55	192.84
720.00							190.99	230.92	260.42	192.82
744.00							190.85	230.71	260.3	192.73
768.00							190.71	230.68	260.17	192.51
792.00									259.9	192.46

Table D6-2. Continued. weight in grams for given sample

Time from start [h]	Sample number									
	32	33	34	58	50	51	52	53	54	55
0.00										
1.00	201.89	224.78	236.84	203.14	122.57	120.57	124.99	123.88	96.37	94.95
2.00	201.79	224.78	236.83	203.12	122.47	120.56	124.98	123.78	96.50	95.06
3.00	201.88	224.78	236.82	203.1	122.45	120.56	124.98	123.77	96.61	95.12
4.00	201.88	224.78	236.81	203.07	122.43	120.54	124.96	123.74	96.66	95.16
5.00	201.87	224.77	236.81	203.06	122.42	120.51	124.93	123.72	96.72	95.23
6.00	201.87	224.77	236.81	203.05	122.41	120.52	124.94	123.74	96.78	95.29
7.00	201.87	224.77	236.81	203.02	122.41	120.50	124.92	123.72	96.84	95.35
8.00	201.86	224.77	236.81	203	122.38	120.49	124.91	123.69	96.90	95.41
9.00	201.86	224.77	236.74	202.99	122.37	120.49	124.91	123.71	96.95	95.46
10.00	201.85	224.76	236.7	202.96	122.36	120.46	124.88	123.66	97.01	95.52
11.00	201.85	224.76	236.69	202.95	122.35	120.46	124.88	123.68	97.07	95.58
12.00	201.85	224.76	236.54	202.93	122.34	120.44	124.85	123.64	97.14	95.64
24.00	201.44	224.74	236.61	202.79	122.19	120.26	124.72	123.53	97.80	96.20
48.00	201.34	224.69	236.59	202.46	121.80	119.85	124.29	123.12		97.49
72.00	201.24	224.64	236.53	201.66	121.50	119.59	124.02	122.81		
96.00	201.15	224.59	236.48	201.26		119.33	123.75	122.56		
120.00	201.05	224.54	236.42	200.99		119.07	123.49	122.32		
144.00	200.99	224.5	236.07	200.69			123.23	122.06		
168.00	200.86	224.39	235.95	200.42			123.02	121.89		
192.00	200.76	224.23	235.84	200.46				121.68		
216.00	200.65	224.07	235.73	200.37				121.33		
240.00	200.17	223.91	235.61	199.99				121.06		
264.00	200.07	223.75	235.5	199.91				120.66		
288.00	200.04	223.48	235.39	199.9				120.29		
312.00	200	223.48	235.27	199.58						
336.00	199.86	223.48	235.16	199.39						
360.00	199.83	223.56	235.19	198.91						
384.00	199.67	223.43	235.2	198.82						
408.00	199.58	223.15	235.19	198.63						
432.00	199.56	223.13	234.85	198.56						
456.00	199.55	223.12	234.63	198.08						
480.00	199.45	223.1	234.63	197.83						
504.00	199.23	223.09	234.62	197.61						
528.00	199.07	223.01	234.61	197.41						
552.00	199.06	222.65	234.12	197.22						
576.00	199.05	222.64	234.02	196.91						
600.00	198.74	222.42	233.91	196.71						
624.00	198.67	222	233.79							
648.00	198.47	221.99	233.68							
672.00	198.22	221.97	233.57							
696.00	198.18	221.89	233.54							
720.00	198.13	221.88	233.34							
744.00	198.14	221.87	233.33							
768.00	198.14	221.41	233.12							
792.00	198.13	221.31	233							
816.00	198.13	220.88	232.79							
840.00	197.6	220.43	232.77							
864.00			232.66							
888.00			232.54							
912.00			232.14							
936.00			232.12							

Time from start [h]	Sample number	
	56	57
0.00		
1.00	92.45	98.73
2.00	92.47	98.84
3.00	92.57	98.90
4.00	92.72	98.98
5.00	92.73	99.01
6.00	92.75	99.07
7.00	92.81	99.13
8.00	92.83	99.19
9.00	92.86	99.25
10.00	92.95	99.31
11.00	93.00	99.37
12.00	93.07	99.44
24.00	93.66	100.08
48.00	94.86	101.36
72.00	96.04	102.76
96.00		103.76
120.00		104.97

Table D6-3. Topology count for selected samples

sample number	Excluding edge I nodes				Including edge I nodes			
	total	X	Y	I	total	X	Y	I
1	268	18	250	0	313	18	250	45
2	409	15	394	0	444	15	394	35
6	319	21	298	0	359	21	298	40
7	418	34	384	0	453	34	384	35
9	310	18	292	0	351	18	292	41
11	65	4	61	0	86	4	61	21
16	428	23	405	0	477	23	405	49
17	364	20	344	0	410	20	344	46
23	58	2	56	0	75	2	56	17
24	72	2	70	0	95	2	70	23
27	43	0	43	0	57	0	43	14
28	24	0	24	0	37	0	24	13
29	82	2	80	0	108	2	80	26
32	12	0	12	0	20	0	12	8
39	17	0	17	0	30	0	17	13
42	9	1	8	0	17	1	8	8
51	125	10	115	0	153	10	115	28
52	25	0	25	0	39	0	25	14
53	27	0	27	0	41	0	27	14
58	66	2	60	4	83	2	60	21

E. Digital Appendix (list of files)

E.1. Animations

Animation E-1. Animation of model 2 (temperature independent material properties) and model 19 (temperature dependent material properties) for the different failure criterion, assuming temperature dependent mechanical properties. The 3D no failure domain of the Griffith-Murrell criterion is overlain on the 2D failure domains as a grey wireframe. The tensile failure domain is overlain on the Drucker-Prager yield criterion as a red wireframe.

Animation E-2. Animation of model 2 (temperature independent material properties) and model 19 (temperature dependent material properties) for the Griffith-Murrell criterion, assuming temperature dependant mechanical properties. The domains of shear failure are coloured mapped for predicted failure angle. The 3D no failure domain of the Griffith-Murrell criterion is overlain on the 2D failure domains as a grey wireframe.

E.2. COMSOL® Files

COMSOL® files for chapters 3 – 5, labelled as in thesis text. For some of the larger files models in the file will have to be run to give results.

E.3. MOVE™ Files

MOVE™ files for chapters 4 and 5.

E.4. STRESSTAT

Files used in STRESSTAT from chapter 5.

E.5. Posters and Presentations

Posters and presentations given during study period.

E.6. Figure copyright permissions

Copyright permission and licence for figures reproduced in this thesis.